The Influence of the Parent Metal Condition on the Cross-weld Creep Performance in Grade 91 Steel

John A. Siefert

Department of Materials

Loughborough University

A doctoral thesis submitted in partial fulfillment of the requirements for the award of Doctor of Philosophy

July 2019

Acknowledgements

Without the support and patience from my family this thesis would not been authored. My third and fourth children arrived during this research. My wife Meredith is owed a debt of gratitude that will forever be impossible to repay. Without her unwavering support I would not have completed the process and make it through the countless weekends and a couple of vacations which were sacrificed to pull everything together.

My direct advisors, Professor Rachel Thomson and Dr. Jonathan Parker, deserve special thanks, and I forever grateful for their unwavering guidance and assistance through this marathon. I am fortunate to have forged a lasting friendship with both, and their mentoring through the last several years, including this thesis, is a testament to their faith in my abilities and willingness to educate the next generation of engineers.

They say it takes a tribe to raise a child, and this is also the case for PhD students. Thus, it is without a doubt that the execution of this thesis would not have been possible without the assistance of the following individuals: Dr. Michael Gagliano; Dr. Ryan MacLachlan; Dr. Xu Xu; Sam Davis; Dr. Geoff West; Dr. Tap Lolla; Mary Kay Havens; Scott Baily; and Kendall McCord.

Several findings from this research were leveraged through collaborative research efforts funded by the Electric Power Research Institute and with Graham Pritchard and Dr. Ian Perrin (Structural Integrity Associates) and Dr. John DuPont (Lehigh University). Through this interaction, I am fortunate to have increased my knowledge in the mechanical response of weldments and structures and enhanced my experience in the complex microstructural evolution of dissimilar metal welds. I am very grateful to Dr. Perrin and Dr. DuPont for the additional mentoring and feedback throughout the duration of my PhD studies.

Table of Contents

Nomenclature

Ac_1	Lower critical phase transformation temperature
Ac_3	Upper critical phase transformation temperature
BCC	Body centered cubic
BCT	Body centered tetragonal
BED	Backscatter electron detector imaging
CEGB	Central Electricity Generating Board (UK)
CGHAZ	Coarse grain heat affected zone
CSEF	Creep strength enhanced ferritic
CTZ	Completely transformed heat affected zone
EBSD	Electron backscatter diffraction
EDM	Electric discharge machining
EDS	Energy dispersive x-ray spectroscopy
EPRI	Electric Power Research Institute (USA)
FCC	Face centered cubic
FEG	Field emission gun
FGHAZ	Fine grain heat affected zone
FIB	Focused ion beam
GTAW	Gas tungsten arc welding
HAZ	Heat affected zone
HIC	Hydrogen induced cracking
HRSG	Heat recovery steam generator
ICHAZ	Intercritical heat affected zone
ICP-MS	Inductively coupled plasma mass spectrometry
ICP-OES	Inductively coupled optical emission spectrometry
IPF	Inverse pole figure
LMP	Larson Miller parameter
MSRC	Multiaxial stress rupture criterion
OTZ	Over-tempered heat affected zone
PAGB	Prior austenite grain boundary
PTZ	Partially transformed heat affected zone
PWHT	Post weld heat treatment
RHC	Reheat cracking

ROA	Reduction of area
SAW	Submerged arc welding
SCHAZ	Subcritical heat affected zone
SE	Secondary electron
SEM	Scanning electron microscopy
SGB	Sub-grain boundary
SMAW	Shielded metal arc welding
STEM	Scanning transmission electron microscopy
TMPZ	Tempered zone
TZ	Transformed zone
TEM	Transmission electron microscopy
TTP	Time temperature parameter
wt. %	Weight percent
XRF	X-ray fluorescence

Publications

The following conference presentations, conference papers and journal articles have been written in association with the research in this thesis:

1. [Invited presentation] J. A. Siefert, J. D. Parker and R. C. Thomson. “Influence of the Welding Thermal Cycle on the Cross-weld Creep Performance in Grade 91 Steel.” *American Welding Society Professional Program Honorary Symposium for Dr. S. David and Dr. T. DebRoy*, November 7, 2017. Chicago, IL.
2. [Conference paper] J. A. Siefert, J. D. Parker and R. C. Thomson. “Linking Performance of Parent Grade 91 Steel to the Cross-weld Creep Performance using Feature Type Tests.” *Proceedings from the Eighth International Conference on Advances in Materials Technology for Fossil Power Plants*, ASM International, 2016. pp. 531 to 544.
3. [Conference paper] J. A. Siefert, J. D. Parker, R. C. Thomson. “Factors Contributing to Heat Affected Zone Damage in Grade 91 Steel Feature Type Cross-weld Tests.” *Proceedings to the 4th International ECCC Conference on Creep and Fracture*, September 2017.
4. [Conference paper] J. A. Siefert, J. D. Parker and R. C. Thomson. “Microstructural Features Contributing to Heat Affected Zone Damage in Grade 91 Steel Feature Type Cross-weld Tests.” *Elevated Temperature Applications of Materials for Fossil, Nuclear, and Petrochemical Industries*, paper ETAM2018-6709. April 3-5, 2018, Seattle, WA.
5. [Accepted journal article] J. A. Siefert, J. D. Parker and R. C. Thomson. “Linking the Cross-weld Creep Performance to the As-fabricated Condition in Grade 91 Steel: Macro-based Assessment.” *Welding Journal* 98 (3), 2019. pp. 63-s to 77-s.
6. [Conference paper] J. A. Siefert, J. D. Parker, R. C. Thomson, R. MacLachlan and S. Yan. “Assessment and Quantification of Damage in the Grade 91 Steel Partially Transformed Zone.” *Proceedings from the Ninth International Conference on Advances in Materials Technology for Fossil Power Plants*, ASM International, 2019.

Abstract

There are thousands of technical papers, reports and other documents which seek to identify the key factors affecting the performance of Grade 91 steel. Yet, as evidenced by the recent reduction in stress allowable values for Grade 91 steel and the introduction of a Type II specification in the ASME B&PV Code, considerable uncertainty still exists regarding the performance, composition and heat treatment.

Knowledge regarding the creep performance of weldments is even more limited and opinions on damage development even more diverse. This point is pertinent whether consideration is given to laboratory cross-weld creep behavior or whether the assessment considers thick section components operating under high pressure and temperature. In part, this additional complexity is because the welding thermal cycle introduces a heat affected zone (HAZ). Although it is widely recognized that the HAZ is linked to creep failures of welds which is likely to be life-limiting in structures, there is no agreement over basic approaches such as the correct methods to characterize the microstructures formed, how to classify the structures and the specifics of the region where creep failure occurs. For example, published work states that the locations for failure should be described as the soft-zone, the subcritical heat affected zone (SCHAZ), the over tempered zone (OTZ), the intercritical heat affected zone (ICHAZ) or the fine-grained heat affected zone (FGHAZ). It is thus apparent that for cross-weld behavior in Grade 91 steel these descriptions cannot be simultaneously and technically accurate.

In addition to the disagreement on weld failure location, there is an overall lack of available information linking heat-specific creep behavior to microstructural factors which can affect the creep ductility. This lack of appreciation for heat-to-heat variability and creep ductility is widely present in the literature due to limited testing programs which typically evaluate one heat of material. Test programs evaluating behavior of CrMoV, including creep-fatigue testing, notch-bar creep tests to explore the influence of geometric notches and cross-weld tests, have shown a heat-to-heat sensitivity linked to creep ductility. The importance of creep ductility in component behavior cannot be dismissed since countless examples of in-service rupture in power generation steels have been clearly linked to microstructural or geometric features which globally or locally reduce the creep ductility. In this PhD research, two heats of

ex-service Grade 91 steel which exhibit markedly different responses to creep deformation and creep damage are evaluated in the ex-service and re-heat-treated conditions to provide for a set of HAZ-responses.

Researchers rarely include evaluation of test samples prior to fracture, let alone provide evidence for damage accumulation represented by an analysis of strain:time behavior. In general, this key omission is directly the result of performing only stress rupture tests. The cross-weld creep behavior in the present thesis is established by a relevant set of test conditions and a sample geometry purposely chosen to more justifiably link to component behavior. The current research has included measurement of strain:time providing the opportunity to analyze displacement, time to failure and the present damage. The analysis of the mechanical behavior is combined with the results of meticulous characterization regarding the location, size, nature and distribution of damage and presents a set of results unique to the field of research in creep strength enhanced ferritic (CSEF) steels and Grade 91 in particular.

A definitive outcome of the present research is the consistent observation regarding the location of damage and failure in the HAZ, which is definitively not linked to a so-called soft-zone represented in the literature as the ICHAZ, OTZ or SCHAZ. Peak damage is more clearly associated with a region in the HAZ where the peak temperature range is approximated by the Ac_1 value (e.g. ~900°C) to a value just below the minimum value for normalization (~1040°C). This range of peak temperature is clarified as the partially transformed zone (PTZ) and is consistent with a recent description purposely developed for 9 wt. % Cr CSEF steels.

The importance of parent metal creep ductility on cross-weld creep behavior is highlighted in this thesis. This point is emphasized by the comparison of the two parent materials RNT-B2 and TP1, for which the parent material deformation response is nearly identical (the variability in time to failure was only 10%), and yet the variation in the cross-weld creep time to failure is a factor 5. This deviation is only plausibly explained by features in the microstructure contributing to the noted difference in the parent metal creep ductility; the RNT-B2 and TP1 parent metal steels vary with respect to reduction of area (ROA) by a factor of 5 (15% versus 83%, respectively). The arrival at this conclusion is made possible by the fact that the weldments are fabricated using

an identical welding procedure including the weld prep geometry, filler metal, PWHT and feature cross-weld test geometry.

The assessment of damage on a local- or micro-level utilizes SEM- and TEM-based techniques. Assessment of damage in the HAZ is linked to second phase particles such as MnS or Al-rich particles (oxides or AlN). The identification of damage with high-density particles such as Laves phase or $M_{23}C_6$ is attributed to the increased probability of damage-association. It is thus concluded that a considerable distribution of cavities in the HAZ for low creep ductility parent material is associated with particles that might be controlled by modifying material specifications (e.g. a reduction in the S and/or Al content).

Although it has been 40 years since the first publications on Grade 91 steel, it is apparent that yet more research is still needed to appreciate the complexities and to enable an informed and integrated life management approach for components subjected to flexible operation for 100,000s of hours. It is hoped that the findings presented in this thesis will put to rest much of the misinformation which exists for failure location in the Grade 91 HAZ, concurrently shed light on the importance of the microstructural factors associated with creep ductility and to link these to *relevant* cross-weld creep tests. The value of relevance, when combined with a well-pedigreed set of tests and outcomes, is perhaps the most important and impactful outcome in the present research.

1 Introduction

1.1 Grade 91 Steel and Creep Strength Enhanced Ferritic Steels

The evolution of common boiler steels into the family of creep strength enhanced ferritic (CSEF) steels, including Grade 91, is illustrated in Figure 1-1 (Masuyama 2017a). Grade 91 steel, a modified variant of the conventional 9Cr-1Mo boiler steel (T9) including key additions of V, Nb and N, was first approved in 1983 by the American Society of Mechanical Engineers (ASME) for incorporation into its Boiler and Pressure Vessel Code (ASME B&PV Code) as Code Case 1943 (Gold et al. 2001). In the United Kingdom, Grade 91 steel was first installed in the Drakelow C Power Station in 1989 for a series of P91 replacement headers carrying steam in P91 piping to a P22 outlet manifold. The system in which the P91 was installed was designed for a steam conditions of 569°C and 176 barg and a design life of 150,000 hours (Blount and Taylor 1992). Today, Grade 91 steel is the most widely utilized CSEF steel for the fabrication of pressure parts in new supercritical and ultra-supercritical coal-fired power stations and modern heat recovery steam generators (HRSGs).

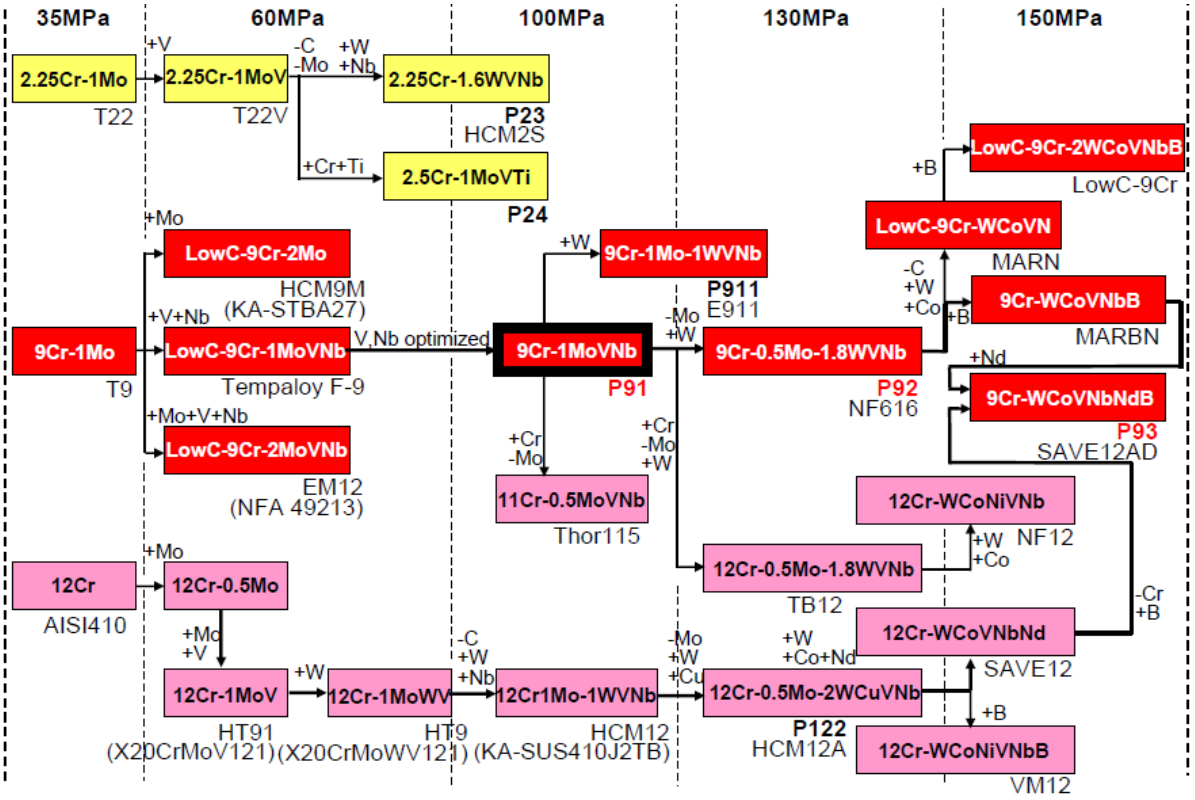

Figure 1-1. The evolution and development of ferritic boiler steels. The values given in each column indicate the stress required for creep rupture in 10^5 hours at 600°C (Masuyama 2017a).

The family of CSEF steels includes a variety of 2¼, 9 and 12 weight percent (wt. %) Cr steels such as Grade 23, Grade 24, Grade 91, Grade 92 (NF 616), E911, Grade 122, VM12SHC and more recently SAVE 12AD and THOR 115. The chemical composition ranges for these steels is referenced in Table 1-1. In general, and as highlighted in Figure 1-1, CSEF steels are broadly classified by the matrix microstructural constituent (bainite or martensite) and by the parent metal creep strength (shown as the applied stress for rupture in 100,000 hours at 600°C). A key delineation in the compositions given in Table 1-1, compared to traditional CrMo steels, is the specified additions of V, Nb, N, Ti, W, B or Co. Each of these elements has a broadly defined influence whether for solid solution strengthening, precipitation strengthening, structural stabilization (e.g. austenite or ferrite stabilizer) or corrosion resistance. These effects are summarized in Figure 1-2.

Table 1-1. Chemical composition for common creep strength enhanced ferritic steels, units wt. % and balance Fe (EPRI 2005, EPRI 2006a, ASME 2017, ASME Code Cases)
Note: *Values for Al, Co, Cu, Mn, Ni, P, S, Si not included*

Material	EN Classification (ASME B&PV Code)		C	Cr	Mo	Ti	V	W	N	Nb	B
Grade 23	7CrWMoNb9-6 (Code Case 2199)	Min	0.04	1.90	0.05	0.005	0.20	1.45		0.02	0.001
		Max	0.10	2.60	0.30	0.060	0.30	1.75	0.015	0.08	0.006
Grade 24	7CrMoVTiB10-10 (Code Case 2540)	Min	0.05	2.20	0.90	0.06	0.20				0.0015
		Max	0.10	2.60	1.10	0.10	0.30		0.012		0.007
Grade 911	X11CrMoWVNb9-1-1 (Code Case 2327)	Min	0.09	8.50	0.90		0.18	0.90	0.040	0.060	0.0003
		Max	0.13	9.50	1.10	0.01	0.25	1.10	0.090	0.100	0.006
Grade 91	X10CrMoVNb9-1 (P15E)	Min	0.08	8.00	0.85		0.18		0.030	0.06	
		Max	0.12	9.50	1.05	0.01	0.25		0.070	0.10	
Grade 92	X10CrWMoVNb9-2 (Code Case 2179)	Min	0.07	8.50	0.30		0.15	1.50	0.030	0.04	0.001
		Max	0.13	9.50	0.60	0.01	0.25	2.00	0.070	0.09	0.006
VM12-SHC	X12CrCoWVNb11-2-2 (Code Case 2781)	Min	0.10	11.0	0.20		0.20	1.30	0.030	0.03	0.003
		Max	0.14	12.0	0.40		0.30	1.70	0.070	0.08	0.006
X20	X20CrMoV11-1	Min	0.17	10.0	0.80		0.25				
		Max	0.23	12.5	1.20		0.35				

A comparison of allowable stress values for selected CSEF steels incorporated into the ASME B&PV Code is provided in Figure 1-3. It is clear in this comparison that there exists a substantial increase in allowable stress values for the family of CSEF steels over that of the widely utilized, low alloy Grade 22 steel. The increased strength for this class of high Cr CSEF steels results in a reduction in the wall thickness that is ≥60% of the requirement for the traditional CrMo low alloy steels such as Grade 22.

This is highlighted by comparison of the required wall thickness for an ultra-supercritical steam condition given in the inset image in Figure 1-3 for a steam condition of 593°C, 320 barg and an inside diameter of 200 mm. For Grade 22, the required wall thickness is 122 mm whilst for the CSEF steel grades compared in this figure, the wall thickness is reduced to ≤75 mm.

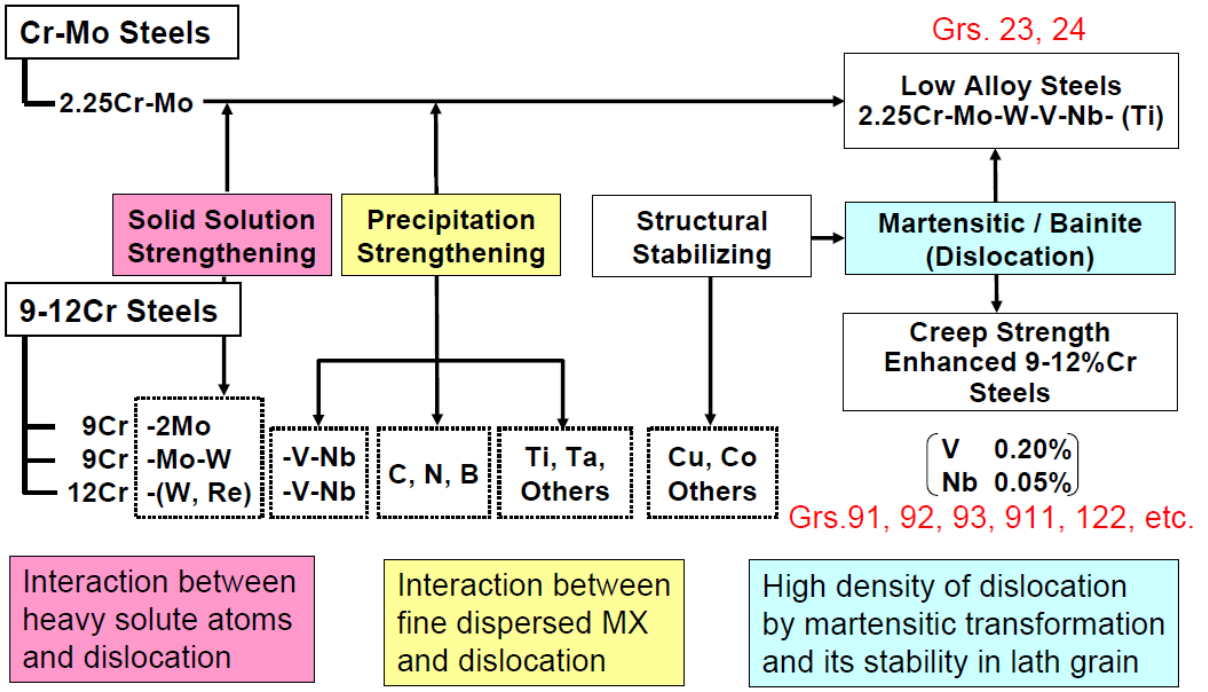

Figure 1-2. Role of elemental additions in creep strength enhanced ferritic steels (Masuyama 2017a)

The decrease in the amount of material to fabricate the component results in a direct cost saving due to a reduction in the amount of structural steel necessary during erection of the support structures, as well as a decrease in the complexity in construction. The reduction in complexity during construction can be manifested in many ways such as a reduction in the required lifting capacity, less filler material to join components and more straightforward approaches for field post weld heat treatment (PWHT). These realities result in considerable economic pressure to take advantage of the improved strength of CSEF steels in the design and fabrication of state-of-the-art power plants.

There are additional benefits specific to the martensitic class of 9 to 12 wt. % Cr CSEF steels aside from improved economic benefits and increased strength. These materials possess an advantageous combination of oxidation/corrosion resistance in steam-side and fire-side environments and desirable thermo-physical properties such

as low thermal expansion and high thermal conductivity. From a simplistic design standpoint, these materials are ideal candidates for fabrication in high temperature components operating in the creep regime.

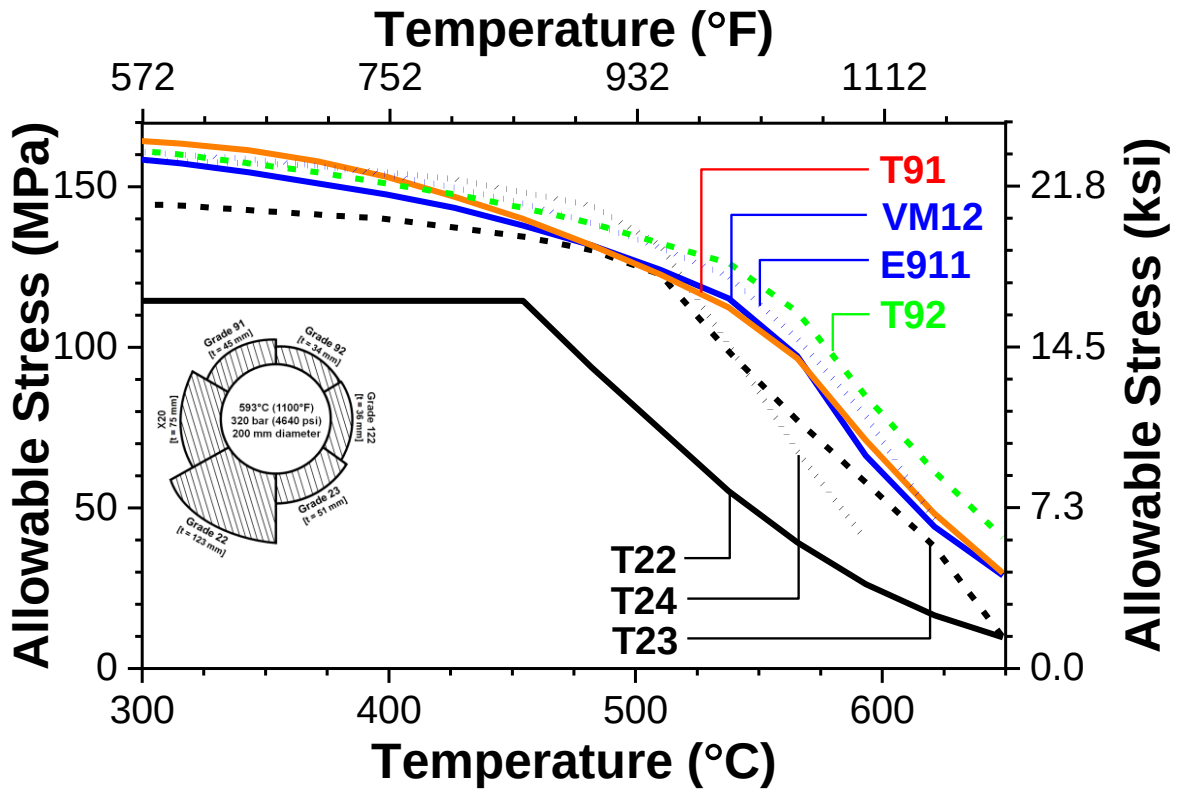

Figure 1-3. Allowable stress values for selected creep strength enhanced ferritic steels (ASME 2017, ASME Code Cases) and (inset image) comparison of the required wall thicknesses for selected creep strength enhanced ferritic steels and as compared to grade 22 for a steam condition of 593°C and 320 barg and an inside diameter of 200 mm. Adapted from (David et al. 2013).
Note: *T24 is limited to 575°C (1067°F).*

1.2 Grade 91 Standard Composition and Product Forms

Within the class of martensitic 9 to 12 wt. % Cr CSEF steels, Grade 91 steel is unique compared to the other steels in this family as it is the most widely researched steel, owing to its long development phase including no less than 35 collaborators across North America, Europe and Asia over more than a decade (ORNL 1986a), and its early introduction to the power generation industry (e.g. more than a decade sooner than Grade 92, for example). The collaboration among several leading institutes around the world led to the assessment of many types of Grade 91 steel product forms, such as those incorporated into ASME B&PV Code and highlighted in Table 1-2. Most codes and standards around the world specify the composition control for at least fourteen specific elements in Grade 91 steel product forms listed in Table 1-2. The purpose of

these main alloying elements is to impart a combination of an expected minimum creep strength, an acceptable creep ductility, and an adequate corrosion resistance in a normalized and tempered martensitic matrix that is devoid of ferrite. The creep strength of the steel is principally obtained from dislocation hardening (such as obtained through 'proper' heat treatment and processing) and the stabilization of the dislocation and network of grain boundaries through the precipitation of $M_{23}C_6$ and MX carbides (such as from a combination of C, Cr, Nb, N and V) (Cipolla et al. 2004). The combination of these basic principles in combination with an optimized compositional range helps to ensure that the material possesses acceptable long-term performance in a component that is expected to operate beyond 150,000 hours[1].

Table 1-2. Chemical composition requirements (given in weight percent) for common Grade 91 steel product forms (ASME 2017)

Product Form	SA-182	SA-213	SA-217	SA-234	SA-335	SA-336	ASME SA-387 Notes 1,2	
	Forging	Tubing	Casting	Fittings	Piping	Forging	Plate	
							Heat analysis	Product analysis
Marking Symbol	F91	T91	C12A	WP91	P91	F91	Grade 91	Grade 91
C	0.08-0.12	0.07-0.14	0.08-0.12	0.08-0.12	0.08-0.12	0.08-0.12	0.08-0.12	0.06-0.15
Mn	0.30-0.60	0.30-0.60	0.30-0.60	0.30-0.60	0.30-0.60	0.30-0.60	0.30-0.60	0.25-0.66
P	0.020	0.020	0.030	0.020	0.020	0.025	0.020	0.025
S	0.010	0.010	0.010	0.010	0.010	0.025	0.010	0.012
Si	0.20-0.50	0.20-0.50	0.20-0.50	0.20-0.50	0.20-0.50	0.20-0.50	0.20-0.50	0.18-0.56
Cr	8.0-9.5	8.0-9.5	8.0-9.50	8.0-9.5	8.0-9.5	8.0-9.5	8.0-9.5	7.90-9.6
Mo	0.85-1.05	0.85-1.05	0.85-1.05	0.85-1.05	0.85-1.05	0.85-1.05	0.85-1.05	0.80-1.10
V	0.18-0.25	0.18-0.25	0.18-0.25	0.18-0.25	0.18-0.25	0.18-0.25	0.18-0.25	0.16-0.27
Nb	0.06-0.10	0.06-0.10	0.06-0.10	0.06-0.10	0.06-0.10	0.06-0.10	0.06-0.10	0.05-0.11
N	0.03 - 0.07	0.030 - 0.070	0.030 - 0.070	0.03 - 0.07	0.030 - 0.070	0.030 - 0.070	0.030 - 0.070	0.025 - 0.080
Ni	0.40	0.40	0.40	0.40	0.40	0.40	0.40	0.43
Al	0.02	0.02	0.02	0.02	0.02	0.02	0.02	0.02
Ti	0.01	0.01	0.01	0.01	0.01	0.01	0.01	0.01
Zr	0.01	0.01	0.01	0.01	0.01	0.01	0.01	0.01

In addition to the key alloying elements, there are many impurities that may also be introduced into the melt because of the quality of scrap or iron ore that is utilized. The increased use of scrap and potential introduction of higher levels of impurities is a

[1]150,000 hours of operation was a typical design life specified by former British Standard (BS) Codes and now commonly applied in Euronorm (EN) Codes. However, many regions of the world do not institute formal minimum component lives as a part of design and the expectation is for components to operate until the end of the life for the entire power plant which may significantly exceed 150,000 hours.

direct consequence of the worldwide emphasis on recycling scrap metal. The detrimental effect of the impurity elements on the performance of Grade 91 steel has been detailed in (EPRI 2014a) and the impact of the major processing steps on the final product is provided in (EPRI 2014b). The consequence of tramp elements in the context of both creep strength and creep ductility will be highlighted in greater detail in later sections of this review.

1.2.1 Standard Product Forms

The incorporation of Grade 91 steel into the variety of product forms is unique for the approved CSEF steels. Its application is greatly emphasized since there are fewer issues in sourcing materials for both new construction or replacement components as Grade 91 can be sourced in all essential product forms. Using the fabrication of a header as an example in Figure 1-4, there is a need to procure no less than five types of product forms such as piping, tubing, plate, forgings and castings. In most cases, other CSEF steels allowed for pressure vessel construction will not be available in all the desired product forms, necessitating key substitutions of comparable materials or over-matching scenarios, thus introducing the potential for dissimilar metal welds (DMWs).

As indicated in Figure 1-4, most of the required product form to fabricate a header is piping or tubing. However, many additional types are needed such as: forgings to transport steam from the header to the outlet piping (as in tees) or to fabricate valve bodies; plate is typically utilized to fabricate end plates or attachments to support the header when it is installed in the plant; fittings where thickness transitions are required; or castings such as for valve bodies or large casings. It is thus the case that one of the unique attributes for Grade 91 steel is the multiple types of product forms in which the material can be obtained to construct complex components for today's state-of-the-art plants. This attribute is likely to guarantee the specification of Grade 91 steel for decades to come.

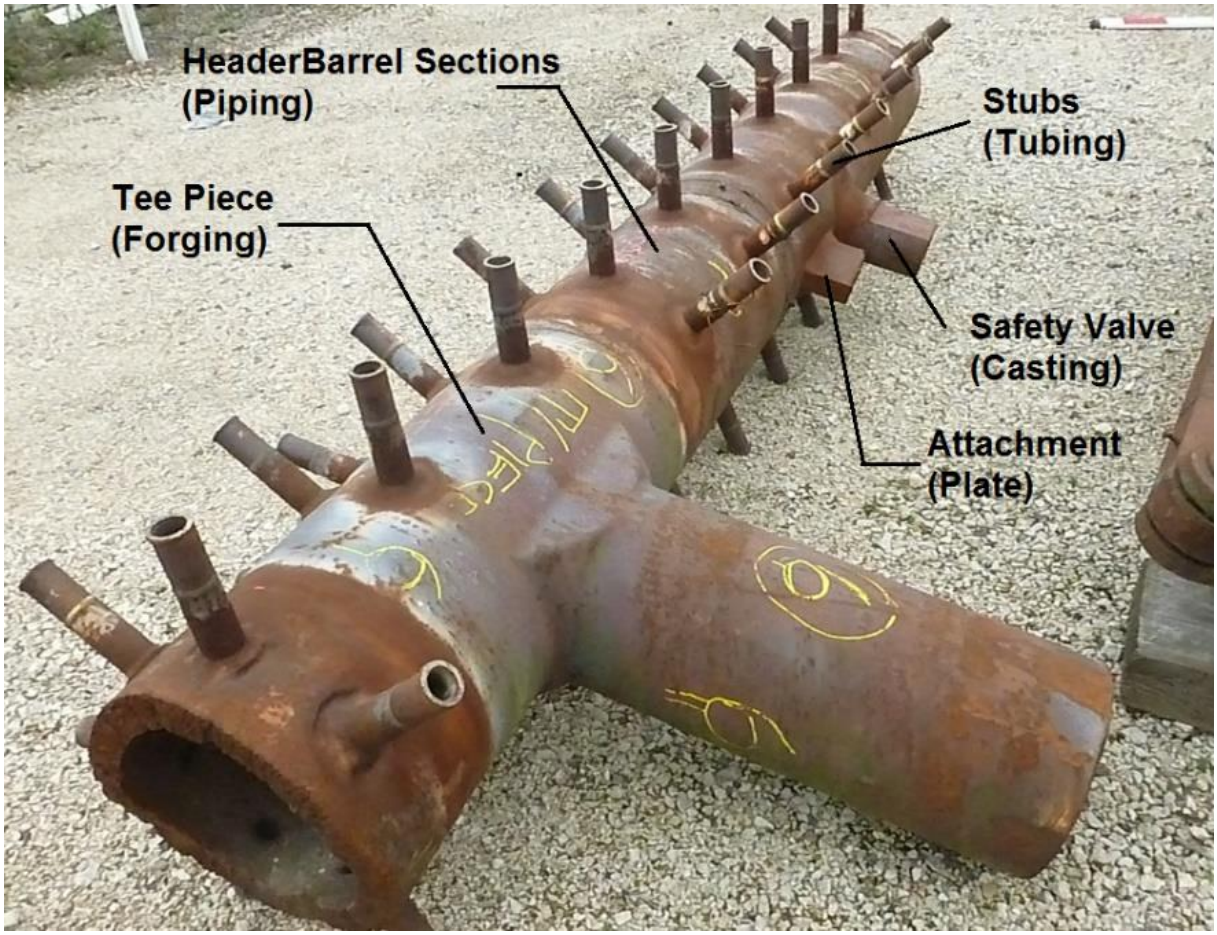

Figure 1-4. Ex-service section of a superheat outlet header illustrating the different product forms required to construct the final, installed component

1.2.2 Role of Alloying Additions

The role of each of the elements listed in Table 1-2 for Grade 91 steel is provided below:

- **Carbon and nitrogen.** Carbon and nitrogen are interstitial, austenite-stabilizing elements added for hardenability and formation of carbonitrides. These two elements have low solubility in ferrite leading to the formation of carbonitrides, such as $M_{23}C_6$ or an MX-type. To ensure materials have sufficient hardenability and weldability, the carbon level in CSEF steels has been limited to ~0.10 wt. %. Where the aluminum content is elevated, nitrogen may form AlN and reduce the available nitrogen for formation of MX-type nitrides.
- **Manganese.** Manganese stabilizes the austenite phase to high temperature and prevents formation of delta ferrite. The addition of manganese is also critical to trap excess sulfur in the form of MnS inclusions.

- **Phosphorous and sulfur.** These are impurity elements which can be controlled to very low levels using a dephosphorization and/or desulphurization step in the steel-making process.
- **Silicon.** Silicon is a ferrite-stabilizing element added primarily for deoxidation. Silicon may positively affect the stability of the oxide layer and increase oxidation resistance.
- **Chromium.** Chromium is a ferrite-stabilizing element added for corrosion-resistance in fire-side or steam-side environments. Chromium forms second-phase particles such as carbides (principally $M_{23}C_6$ [$Cr_{23}C_6$]) or Z-phase [(Fe, Cr), (Nb, V)N].
- **Molybdenum.** A ferrite-stabilizing element added for solid solution strengthening. Upon elevated temperature exposure, molybdenum can lead to the formation of Laves phase [Fe_2(Mo, W)].
- **Vanadium and niobium.** Vanadium and niobium are ferrite-stabilizing elements which combine with C, N or both to form MX-type carbonitrides.
- **Nickel.** Nickel stabilizes the austenite phase to high temperature and prevent the formation of delta ferrite. Excessive nickel can lead to a reduced lower critical transformation temperature (Ac_1) and accelerate the coarsening of $M_{23}C_6$ and Z-phase.
- **Aluminum.** Ferrite-stabilizing element added for deoxidation. Excessive aluminum can lead to the formation of AlN and reduce the amount of nitrogen available for the formation of MX-type precipitates.
- **Titanium and Zirconium.** Titanium and Zirconium are deoxidizing elements which may reduce the amount of free nitrogen through the formation of TiN.

Standard databases of material performance typically show wide variation, and Grade 91 steel is not an exception. Conventional comparisons for parent metal creep strength, represented in Figure 1-5 as a Larson-Miller parameter comparison, show a variability of at least a factor of 10. Traditionally there has been little consideration given to develop sufficient design rules for materials that may exhibit poor creep ductility. For Grade 91 the behavior is also highly variable, as shown in Figure 1-6. It is the observed variability and consequence of both parent metal strength and parent metal ductility on cross-weld creep performance that is the principal motivation for this research.

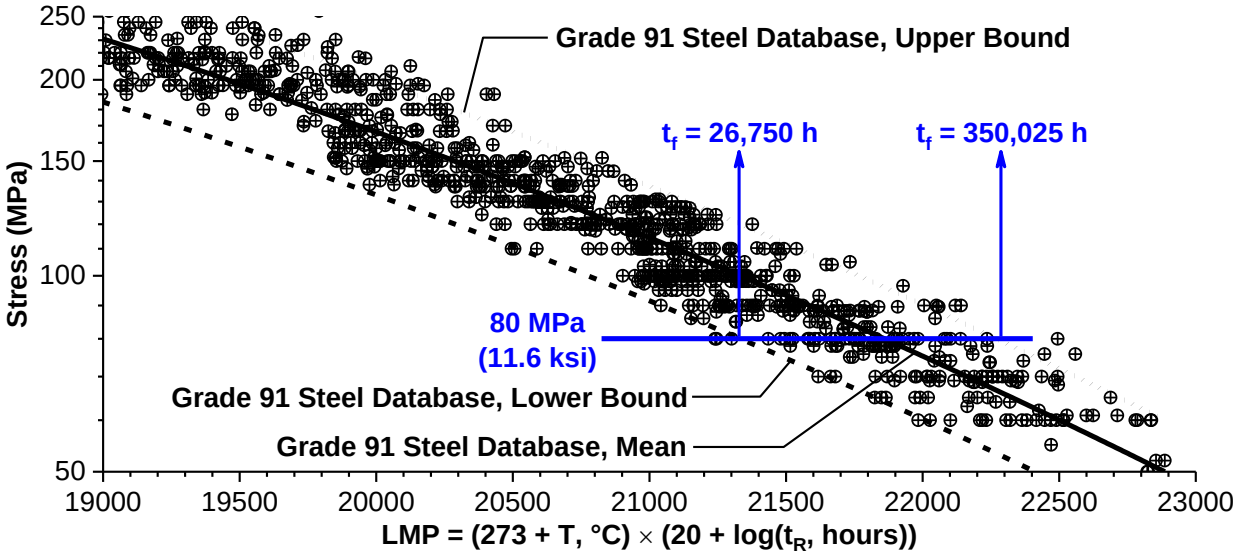

Figure 1-5. Database of Grade 91 steel parent metal creep performance represented as a Larson-Miller parameter comparison using a C value of 20 (EPRI 2018)

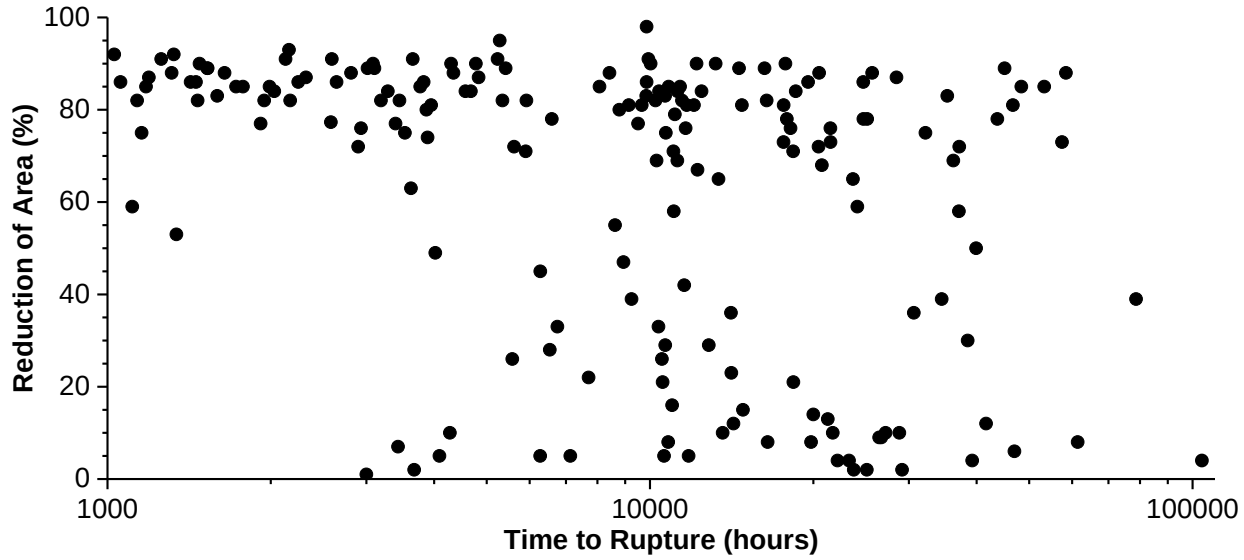

Figure 1-6. An example of the variable behavior in Grade 91 steel with respect to creep ductility for one supplier and at 550°C (1022°F) and 650°C (1202°F) (EPRI 2014a)

1.3 Welding Processes

The primary joining processes in welding Grade 91 steel for power generation or petrochemical applications involve the traditional arc welding processes such as: gas tungsten arc welding (GTAW); shielded metal arc welding (SMAW); gas metal arc welding (GMAW); flux cored arc welding (FCAW) and submerged arc welding (SAW). Specifically, the GTAW and SMAW processes have been utilized to fabricate the installed piping components currently operating in power generation systems. The emphasis on traditional arc welding processes is a direct result of legacy technology that is still utilized in preferred, low-cost fabrication shops in regions of the world where

cheap labor is widely accessible, as well as the ease of direct, field application of these processes. Although there have been studies looking at the applicability of other welding processes such as reduced pressure electron beam (RPEB) welding or friction stir welding (FSW), there is no current commercial pressure to commercialize these processes on a larger scale (Punshon 2004, Grant et al. 2015).

An example of the amount of welding required to make a single superheat outlet header component in Figure 1-4, detailed in (Parker and Brett 2013) and illustrated in Figure 1-7 is provided below:

- 408 stub to header welds
- 11 thick-section girth welds joining the forged tee pieces, pipe barrel sections and forged hemispherical end caps;
- 10 attachments, fillet-type welds joining plate to the pipe barrel sections
- 7 penetration welds to join the safety valves, pressure gauge, pressure transmitter and atmospheric pass out connections;
- 4 thick-section dissimilar metal welds to join the fabricated header to the existing Grade 22 pipe work in the field
- 408 dissimilar metal welds joining the T91 stubs to the 316H stainless steel superheater tubing

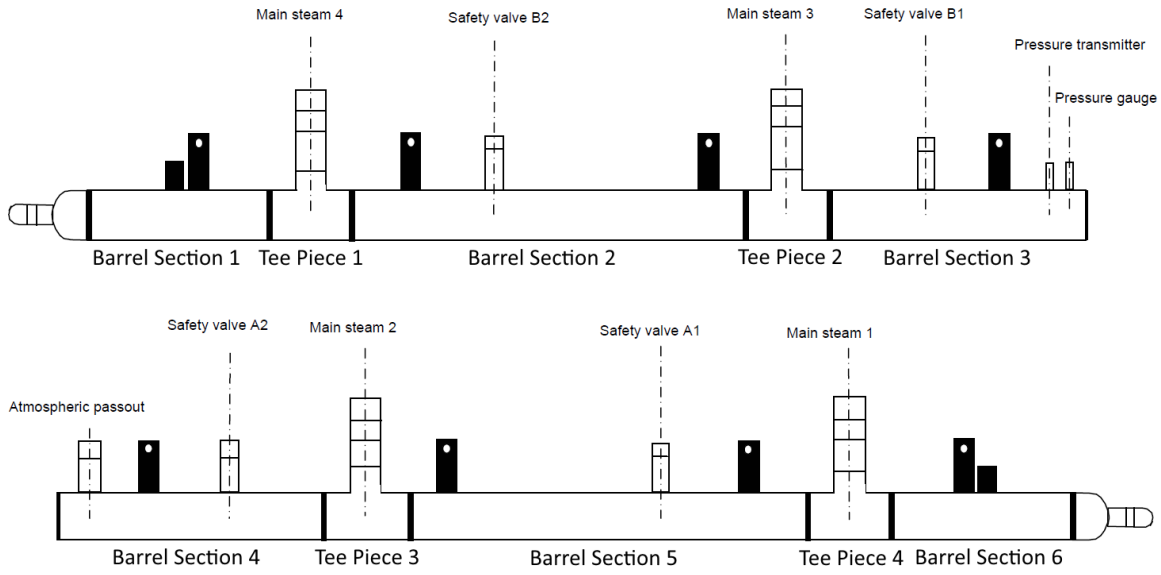

Figure 1-7. Schematic diagram of the Aberthaw Power Station Grade 91 header showing the various components and welds (Parker and Brett 2013)

Most of the welds would have been completed using GTAW or SMAW or a combination of these processes. For some of the thick-section girth welds to join pipe to pipe or pipe to forging components and made in the fabrication shop, the SAW process would have also been utilized in combination with these two processes.

1.4 Influence of Welding and Fabrication on Performance

1.4.1 Regions of a fusion weld

The fundamental regions of a fusion weld are provided in Figure 1-8 and Table 1-3. The subdivision of the HAZ into relevant descriptions is provided in section 1.4.2. The division of a conventional fusion weld are recently described by Lippold (2015) and compared in Figure 1-8 to the classical definition provided by the American Welding Society (Savage et al. 1976). Both examples present an evolved set of material zones and designations from the original description proposed by Nippes (1959).

A key differentiation in Figure 1-8A and Figure 1-8B is the introduction of a transition zone (TZ), also known as a partially mixed zone, in the weld metal-side of the fusion line. These definitions will be important later in the thesis to separate the exact location of fusion line damage that is documented in a weldment made in Grade 91 steel using a Ni-base filler metal.

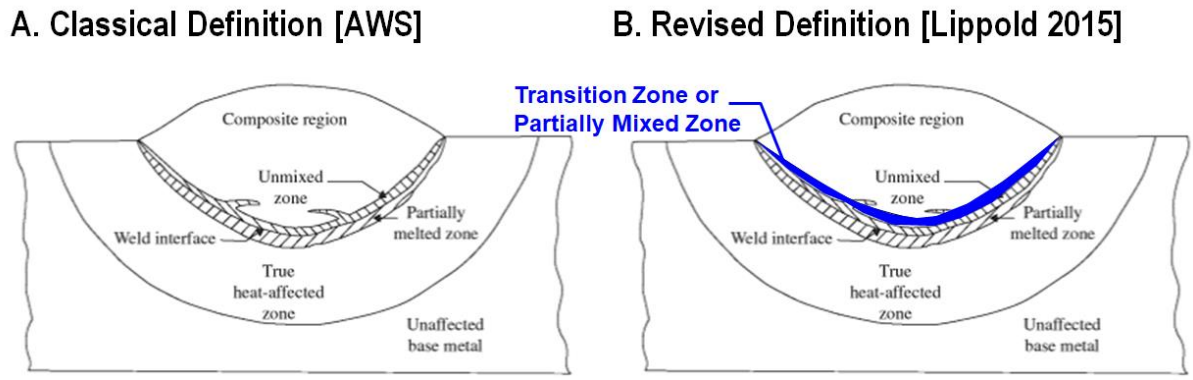

Figure 1-8. Location of distinct regions in a fusion weld to the classical definition in the American Welding Society (A) [Savage et al. 1976] and the revised definition proposed in (B) [Lippold 2015]

Table 1-3. Definitions for the distinct regions in a fusion weld (Lippold 2015)

Zone	Designation	Description
Unaffected Parent Metal		In the context of this description, the unaffected parent metal is a 9 wt. % Cr creep strength enhanced ferritic (CSEF) steel where the substructure or carbonitride distribution and size is not altered because of the peak temperature experienced by the welding thermal cycle. Broadly defined as a T_{peak} <800°C or ~A_1
Heat Affected Zone	HAZ	The region which does not experience melting but significant alteration or
Partially Melted Zone	PMZ	*This zone exists in all fusion welds since a transition from 100% liquid to 100% solid must occur across the fusion boundary*
Fusion Line		Defined as the boundary between the PMZ and UMZ regions
Unmixed Zone	UMZ	*Consists of melted and re-solidified base metal that does not mix with the filler metal*
Partially Mixed or Transition Zone	TZ	*In dissimilar metal welds, where the filler metal is of different composition from the base metal, this would represent a composition transition from the [fusion zone] to the UMZ. In welds between stainless steels and low-alloy steels, martensitic structure may form in the transition region that does not occur elsewhere in the weld.*
Fully Fusion Zone		The fully fusion zone shows a minimally diluted composition from the parent metal and is consistent with a nickel-base filler metal

1.4.2 Regions of the heat affected zone

A welding thermal cycle in Grade 91 steel creates a thermally affected region immediately adjacent to the fusion zone that is known as the HAZ. Historically in Grade 91 steel and other power generation steels, the HAZ is divided into distinct regions and commonly described as a function of the peak temperature and grain size in relationship to the iron-carbon binary phase diagram, as shown in Figure 1-9 (Easterling 1992). It is emphasized that the approach in Figure 1-9 is linked to an equilibrium diagram for chemical composition and an idealistic description that is not directly representative of non-equilibrium heating and cooling characteristic of welding thermal cycles.

More recent attempts have been made to better characterize the HAZ regions in 9 wt. % Cr CSEF steels relying on quantitative, electron microscopy methods such as electron backscatter diffraction (EBSD). The output of such efforts is a newly proposed description for the HAZ regions in martensitic CSEF steels given in Table 1-4 (Xu et al. 2017). These descriptions more closely match the original regions described in the documentation from ORNL in (ORNL 1986b).

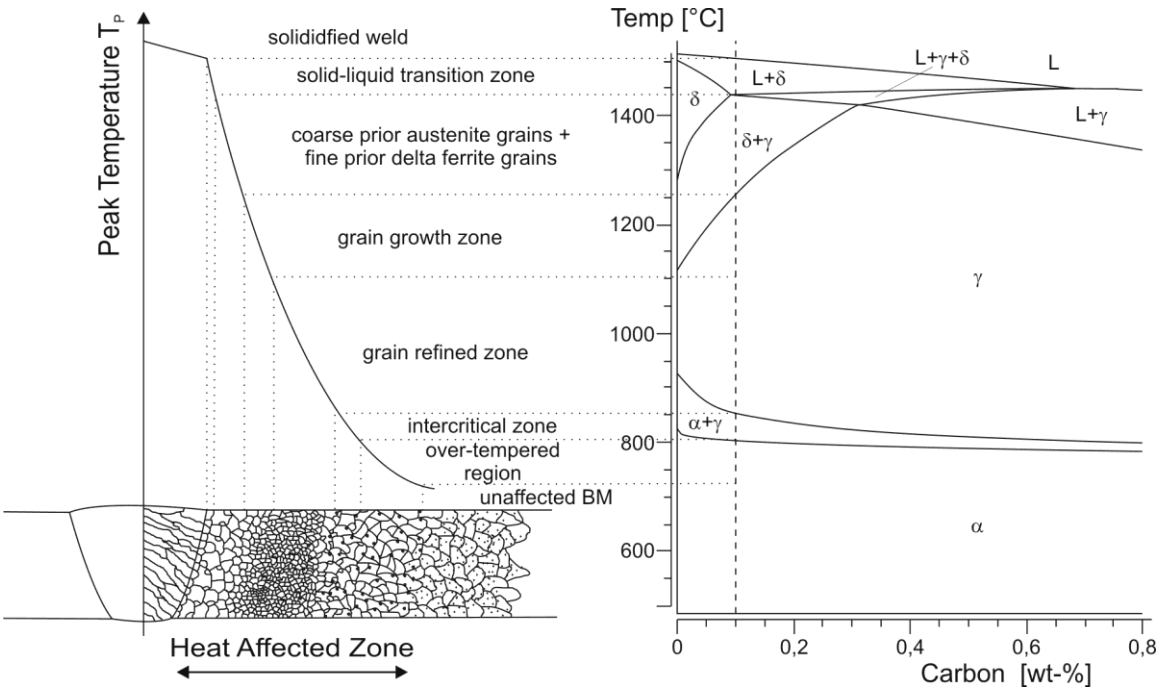

Figure 1-9. Heat Affected Zone Regions as a Function of Peak Temperature for a 0.10 weight percent Carbon Content in a Fe-base Steel (Easterling 1992)

Table 1-4. Descriptions for the heat affected zone regions in martensitic creep strength enhanced ferritic steels (Xu et al. 2017)

Region	Characteristics
CTZ (**C**ompletely **T**ransformed **Z**one)	The original matrix of the parent metal is fully re-austenitized with a complete dissolution of the pre-existing secondary precipitate particles;
PTZ (**P**artially **T**ransformed **Z**one)	The original matrix is only partially re-austenitized along with a partial dissolution of the pre-existing precipitate particles;
OTZ (**O**ver **T**empered **Z**one)	The grain structure remains similar to original matrix in the parent metal, but pre-existing secondary precipitate particles coarsen during welding.

Over the last 20 years there has been continued assessment and debate regarding best practice for the design and fabrication of welds in Grade 91 steel. It is now well established that the thermal cycles during welding can make the microstructure in the HAZ susceptible to creep damage. However, it is appreciated that while the time/temperature of the welding thermal cycles are important, the composition and microstructure of the base metal at the time of welding are also important.

A comparison of the mean and minimum bounds for Grade 91 unaffected parent metal to a cross-weld creep database is given in Figure 1-10. The observed reduction in performance associated with the HAZ in CSEF steels is commonly represented by a weld strength reduction factor (WSRF), as illustrated in Table 1-5 (Yaguchi et al. 2012)

and Figure 1-11. The provided WSRF data are notable in that there is a considerable effect of operating temperature on performance for weldments, and for two independent databases including data from Japanese (Table 1-5) or European (Figure 1-11) sources. For components operating ≤550°C, there is a minimal WRSF effectively allowing component design to the parent metal properties. For components operating >550°C, consideration may be warranted in the design phase to properly accommodate the more dramatic influence of the HAZ properties on performance. For state-of-the-art designs where components are routinely designed to operate at ~600°C, there exists at least a 30 to 35% reduction in performance when comparing the HAZ and the parent metal.

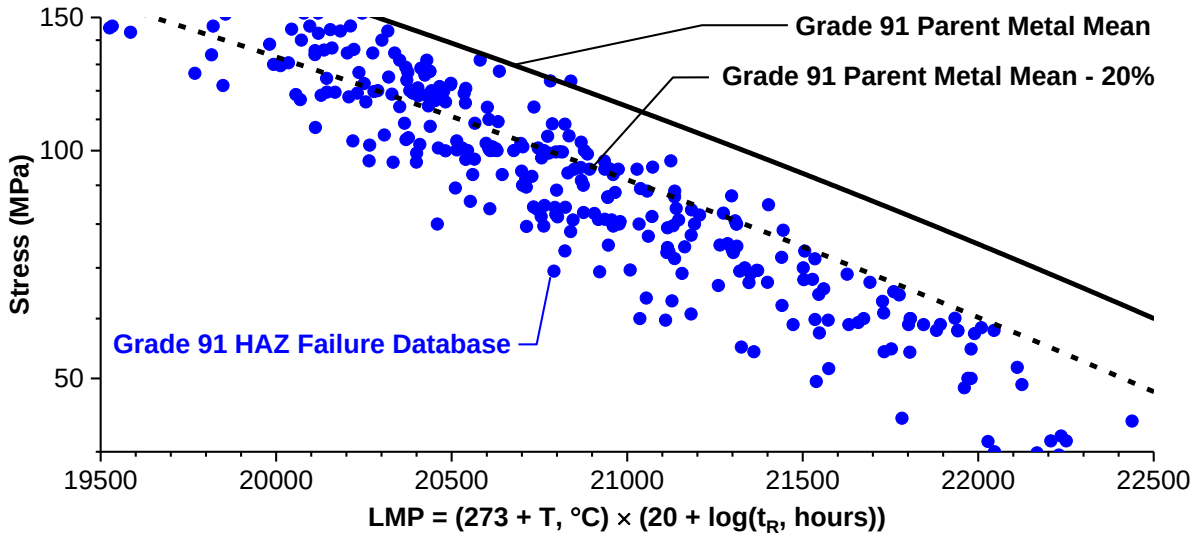

Figure 1-10. Comparison of Grade 91 steel parent metal behavior (mean and minimum bounds; minimum represented as the mean-20%) to cross-weld creep behavior (e.g. reported cross-weld creep failures in the heat affected zone) (EPRI 2018)

Table 1-5. Weld Strength Reduction Factors (WRSFs) for Grade 91 Steel Weldments based on Thickness and Product Forms (Yaguchi 2012 et. al)

Material	Weld Strength Reduction Factor					
	525°C (977°F)	550°C (1022°F)	575°C (1067°F)	600°C (1112°F)	625°C (1157°F)	650°C (1202°F)
T91	1.00	0.90	0.82	0.79	0.79	0.79
P91 (t ≤ 76 mm)	1.00	0.90	0.74	0.67	0.65	0.65
P91 (t > 76 mm)	1.00	0.90	0.74	0.68	0.65	0.65

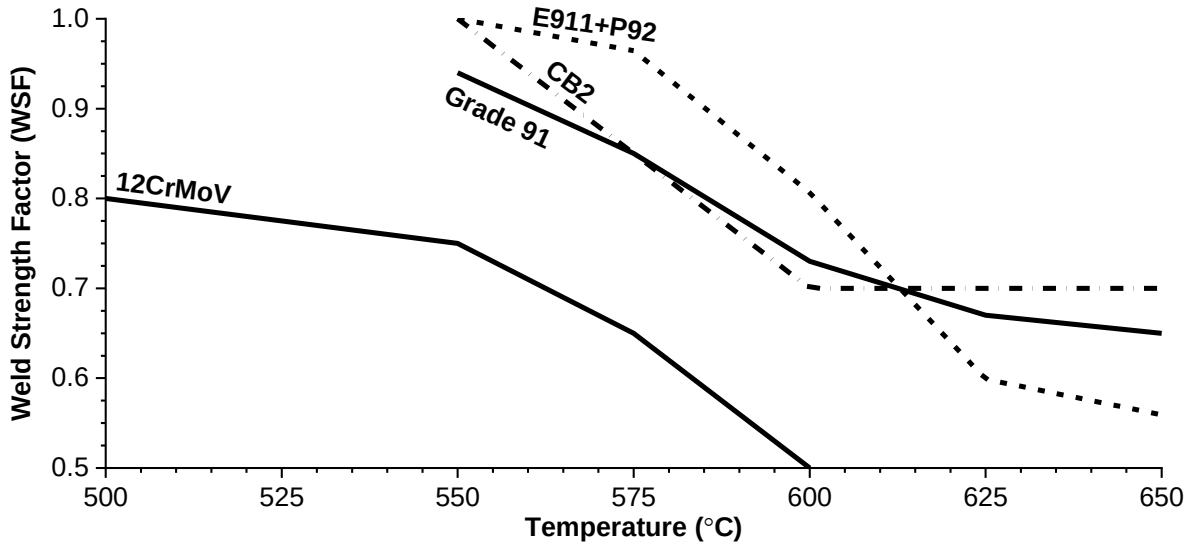

Figure 1-11. Recent Determination of Weld Strength Reduction Factors for Martensitic Creep Strength Enhanced Ferritic Steels after Testing at 100,000 hours (Krein et al. 2017)
Note: $WSF = \frac{R_{u\,min,100kh,T\,(weld)}}{0.8 \times R_{u\,,100kh,T\,(base\,material)}}$

The very large range of behavior observed in Grade 91 steel welded components introduces many risks for life management and assessment. For material which exhibits poor creep ductility, there is a concern that the material will exhibit an increased sensitivity to the evolution of damage in the presence of a metallurgical or mechanical notch. One of the principal concerns in design and life management is whether a welded component can be expected to exhibit leak-before-break behavior. Weldments provide the necessary metallurgical notch condition and can promote a non-uniform development of damage. Depending on the weldment design and orientation relative to the dominant tress there exists a risk to crack propagation through a field of creep damage, thereby increasing the rate of crack growth and reducing the integrity of the component. An example of catastrophic failure in a welded Grade 91 steel component is illustrated in Figure 1-12 where a welded, flat end cap was ejected from a superheat outlet header in a HRSG in the UK.

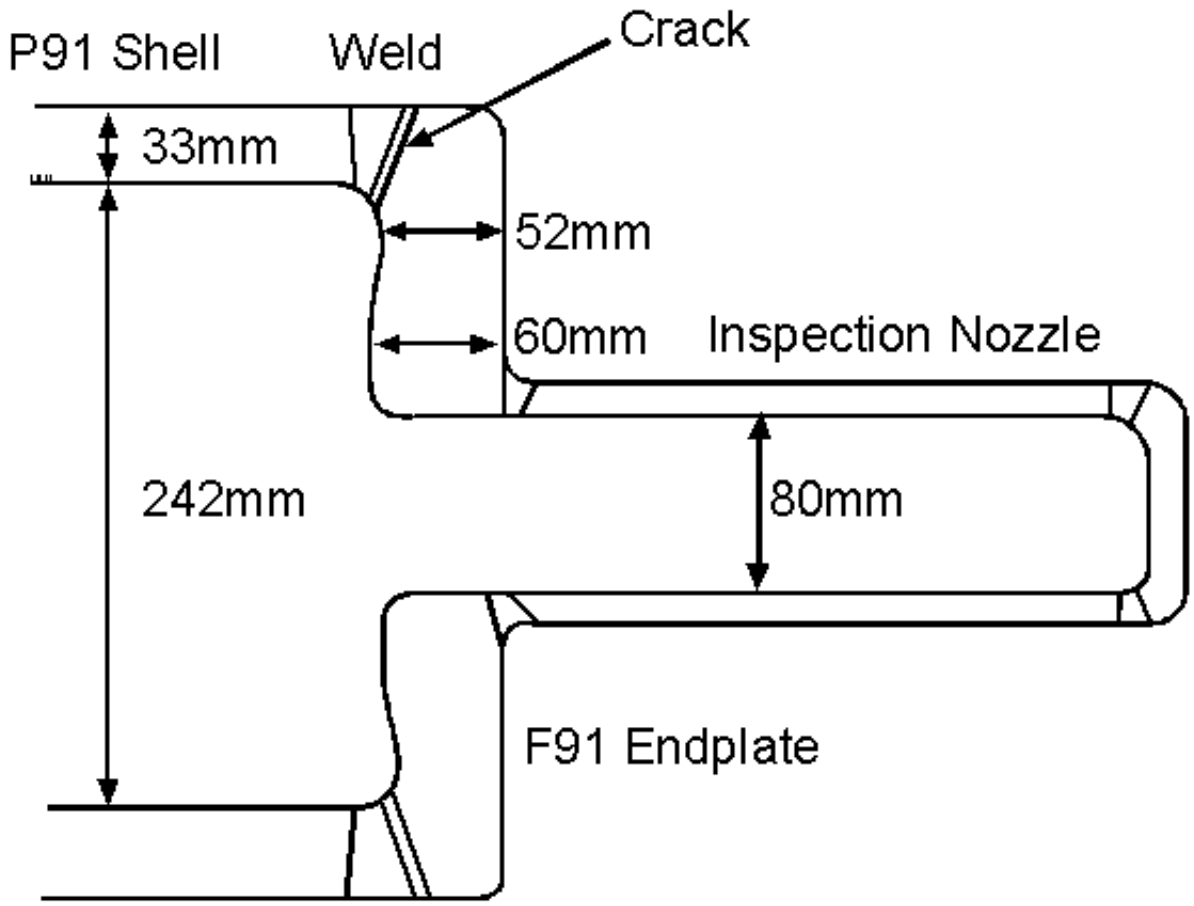

Figure 1-12. Formation of damage in the heat affected zone between the P91 shell and F91 endplate resulted in a catastrophic failure in this configuration (Brett et al. 1999).
Note: *that the geometry of the HAZ and its placement in a high stress location resulted in the uniform development of creep damage.*

1.5 Layout and Objectives of the Thesis

This thesis contains a total of 11 chapters including the introduction and references. The nine main body chapters address three key objectives:

- To evaluate the influence of parent metal creep strength (deformation) and parent metal creep ductility (damage) on the cross-weld creep response using a feature-type test geometry;
- To establish the influence of the welding process on the macro-distribution of damage through the HAZ;
- To investigate the association of damage with particles or features in the HAZ.

Chapter 2 provides a literature review covering information on creep, creep in CSEF steels, CSEF steel microstructure and performance, and details on the HAZ behavior. Chapter 3 details the experimental procedures required for the fabrication of

weldments, pre-test characterization, cross-weld creep testing and post-test assessment. The relevance of the parent metal selected for fabrication of the weldments, the utilized cross-weld creep test geometry and the test conditions are described in Chapter 4.

The results are summarized in Chapters 5 to 9. The pre-test assessment of each weldment is provided in Chapter 5, including baseline data obtained for hardness mapping and electron microscopy. The cross-weld creep test results for each evaluated weldment are included in Chapter 6. Chapter 7 provides the macro-damage characterization through the HAZ for selected cross-weld creep samples. The association of damage with features including grain boundary features and/or particles is detailed in Chapter 8. To provide a balanced assessment of association of damage on a microstructural level with specific features in the HAZ, an interrupted cross-weld creep sample in a susceptible heat of Grade 91 steel is assessed in Chapter 9. Chapter 10 provides a summary of important findings, key conclusions and recommended future work. The references are provided in Chapter 11.

2 Literature Review

The present chapter reviews the literature relevant to creep strength enhanced ferritic (CSEF) steels and emphasizes findings specific to Grade 91 steel. The influence of the parent metal deformation and damage resistance on cross-weld creep resistance is a central theme in this PhD thesis. For convenience, the parent metal behavior can be broadly binned into the matrix presented in Figure 2-1. The resistance to damage can be evaluated from standard uniaxial creep tests through a measurement of the reduction of area or elongation to failure. Alternatively, the parent metal may be assessed through the determination of the type, size and distribution of microstructural features. Similarly, the resistance to deformation can be appraised using the time to failure from a standard uniaxial creep test or resolving the type, size and distribution of strengthening and/or intermetallic phases which may contribute or decrease the deformation resistance. The resistance to deformation axis includes a 'very low' classification to incorporate material which may have been improperly heat treated resulting in a largely ferritic (as opposed to martensitic) matrix. Although the processing and heat treatment of Grade 91 steel should not result in such a microstructure, the fabrication and construction (field or shop) of complex components may produce localized regions which exhibit a ferritic microstructure.

Although not represented in Figure 2-1, it must be emphasized that stress-state plays a significant role in evaluating a given material's response. For example, the introduction of a notch into the specimen through a mechanical (such as notch-bar type tests) or a metallurgical (such as cross-weld creep tests) process can enhance the development of creep cavities in materials which exhibit 'low' resistance to damage.

In the following sections key aspects of creep processes in CSEF steels will be reviewed. The material attributes which contribute to deformation and damage will be discussed as well as how these key attributes can affect void nucleation, growth and fracture. The influence of stress state (e.g. multiaxiality) will be reviewed and discussed in terms of its potential impact on cavity nucleation and growth. Lastly, the available fundamental research in these topics will be placed into context for 9 wt. % Cr CSEF steels.

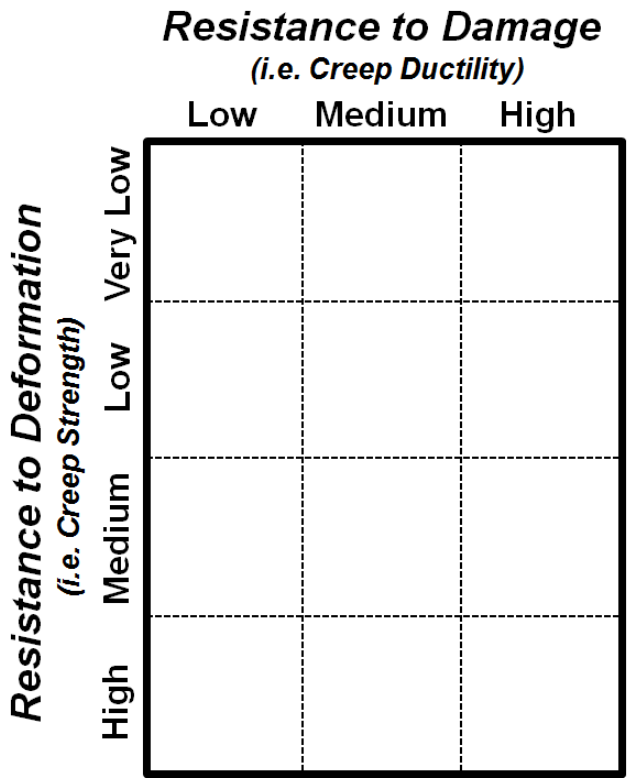

Figure 2-1. General matrix of parent metal performance for 9 wt. % Cr steels where behavior is segmented into a matrix classification scheme for the resistance to damage and the resistance to deformation.
Note: *There is no consideration in this matrix for stress-state which can play a significant role in the evolution of damage or promote accelerated deformation*

2.1 The Creep Curve

When a metal is stressed above ~0.3T_m, the metal can deform plastically with time by a mechanism known as creep (Cocks 1985). This approximate threshold in the context of 9 wt. % Cr steels corresponds to ~500°C and is in reasonable agreement with the formal recognition of the transition of material time-independent to time-dependent stress allowable values at 550°C in the world's construction codes for Grade 91 steel (ASME 2017).

The creep curve, e.g. a plot of strain versus time, is presented in Figure 2-2. The regions in this data are attributed to the classification scheme developed by da Costa Andrade in 1910 in which he divided the curve into primary, secondary and tertiary regimes (Odqvist 1981). More than a century of research in metals subjected to creep conditions has been conducted since this seminal discovery. The basis defined by da Costa Andrade and others who identified key details in the creep process provided the framework in which future researchers began to classify the fundamental material attributes that contribute to in-service performance.

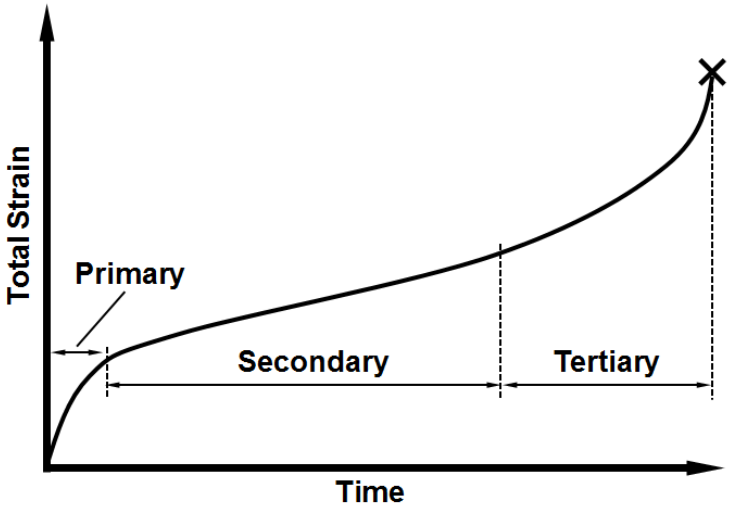

Figure 2-2. Description of the creep curve for a constant temperature and stress and including approximate regions described as the primary, secondary and tertiary regions, after da Costa Andrade (Odqvist 1981).

2.2 Fundamentals of Creep

Creep mechanisms can be divided into two basic types: diffusional creep or dislocation creep. At applied stresses near the yield strength, material deformation is by plastic flow (dislocation glide). Although the generalities provided in the deformation map in Figure 2-3A and derivation of this approach using a log ε – log σ plot in Figure 2-3B are commonly used, the specifics of the active creep mechanism(s) are a function of stress state, temperature and material condition.

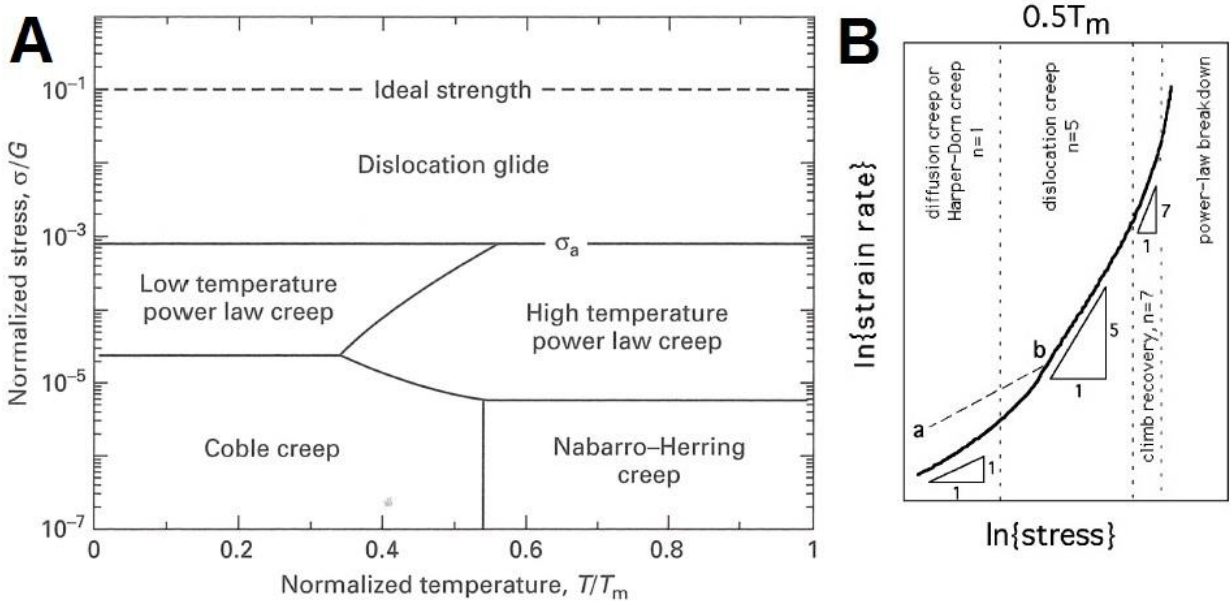

Figure 2-3. A – Schematic deformation mechanism map [4]; B – Schematic logarithmic plot of strain rate versus stress including approximate n values for the degradation mechanisms (image reprinted from Bhadeshia 2003).

Diffusional creep is classified into two types; diffusion through the volume (e.g. Nabarro-Herring creep) or grain-boundary diffusion (Coble creep). Both theories are independent of dislocation movement and are active at higher temperatures. It is typically stated that the active temperature regime for diffusional creep corresponds to values >0.5T_m. For 9 wt. % Cr steels this threshold temperature is ~750°C which is beyond the typical, maximum permissible use temperature of 650°C for these steels. In both creep processes, grains are required to slide past each other to maintain continuity and avoid cavity formation (Bhadeshia 2003), Figure 2-4. Diffusion creep is generally shown to vary linearly with stress (Figure 2-3B where n=1) and as such, the creep rate is directly proportional to the applied stress. Diffusional creep is generally not considered a dominate mechanism in 9 wt. % Cr steels although for specific test conditions there may be some suggestion that the n value is approaching 1 and some authors argue that diffusion may play a more significant role than commonly accepted (Haney et al. 2009).

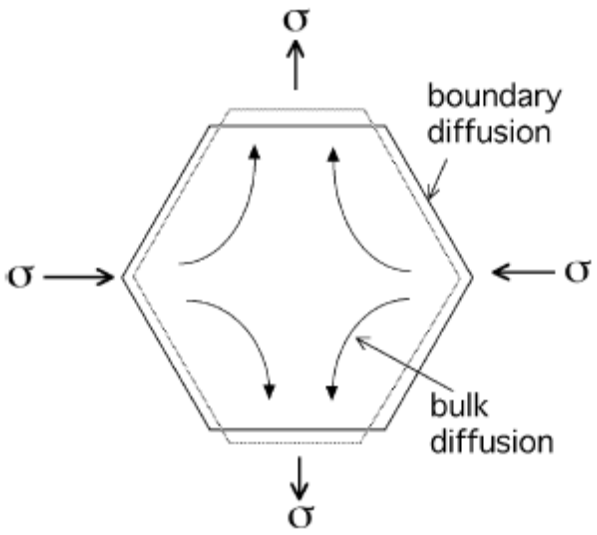

Figure 2-4. Schematic of diffusion by grain boundary (Coble creep) or bulk diffusion through the lattice (Nabarro-Herring), from (Bhadeshia 2003).

Dislocation creep is separated into two mechanisms: pipe diffusion and volume diffusion. In these mechanisms, the creep rate is shown to vary as a power or exponential function of stress. This behavior is the basis for the relationship proposed by Norton and Bailey, Equation 2.1 (Norton 1929). At higher power law 'n' values (or lower temperature), dislocation movement by pipe diffusion dominates whereas at lower 'n' values (or high temperature) the movement is by volume diffusion (Bailey 1930).

Equation 2.1. $\dot{\varepsilon} = A\sigma^n$

Where:

$\dot{\varepsilon}$ = secondary or minimum creep rate

σ = applied stress

A and n = stress-dependent constants

The interaction of dislocations with the matrix has been described by many mechanisms including: Orowan mechanism; Srolovitz mechanism; local climb and general climb. These mechanisms are illustrated schematically in Figure 2-5. Analysis and modeling of the creep behavior of CSEF steels in (Magnusson and Sandstrom 2007a) comparing Orowan looping and local climb suggests that local climb is the most representative mechanism contributing to the dislocation movement in the matrix. More recent experimental evaluation against NIMS data for Grade 91 steel suggests that at n values greater than ~12 (high stress) the dislocation movement is best described by a local climb mechanism which transitions to a general climb mechanism at reduced stress values, where n decreases to a value of ~6 (Zhao et al. 2018).

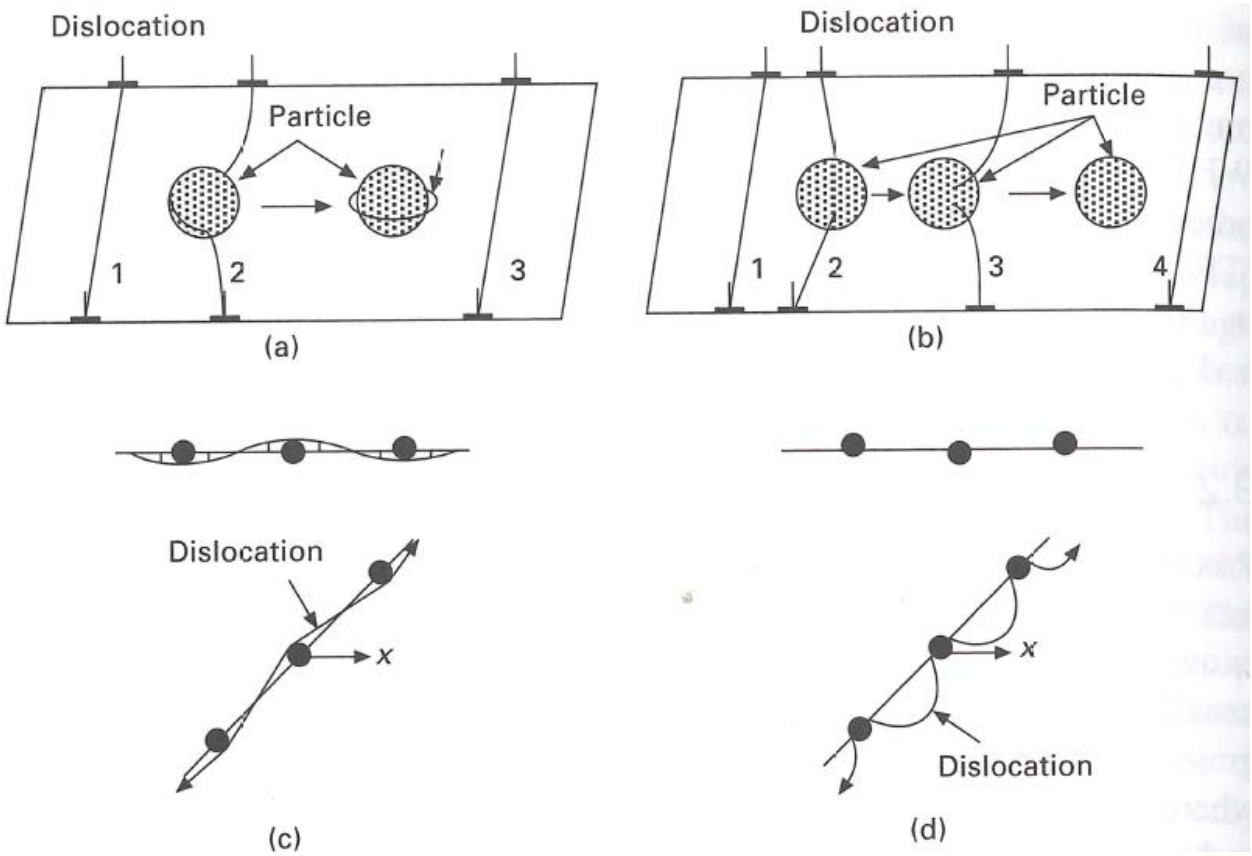

Figure 2-5. Interaction of dislocations in a precipitation strengthened material, from [4]. A – Orowan mechanism; B – Srolovitz mechanism; C – general climb; and D – local climb

Dislocations are created in bainitic or martensitic steels because of the transformation process from austenite on-cooling. Measurements of the dislocation density in martensitic CSEF steel Grade 91 and X20 clearly show a reduction in the dislocation density during creep, and particularly during the primary creep stage (Pesicka et al. 2003). Magnusson and Sandstrom have characterized dislocations in 9 to 12 wt. % Cr martensitic steels by three types (Magnusson and Sandstrom 2007b):

1. Free dislocations in the subgrain interior
2. Immobile dislocations in the subgrain interior
3. Immobile dislocations in the subgrain boundaries

Martensitic, CSEF steels are unique in that the dislocation density is very high even after tempering and by the fact that dislocations are not generated during creep. This is in stark contrast to other materials where behavior is markedly different unless comparisons are made to severely work-hardened conditions (Pesicka et al. 2003).

With respect to the potential creep mechanisms, the specifics of Coble creep (grain boundary diffusion) and dislocation movement by pipe diffusion may lend themselves to be the likely mechanisms as the activation energy for either mechanism is half that for the comparable lattice diffusion mechanism (Maruyama 2008). As creep is a temperature dependent process, Equation 2.1 can be re-written in the following form using an Arrhenius expression for the “A” term, Equation 2.2:

Equation 2.2. $$\dot{\varepsilon} = A_o \exp\left(\frac{-Q}{RT}\right)\sigma^n$$

Where:
$A_o = \text{stress-dependent constant}$
$Q = \text{activation energy}$
$R = \text{gas constant}$
$T = \text{temperature}$

Values for n (Figure 2-6) and Q (Figure 2-7A) are shown to vary for CSEF steels and with respect to the active creep mechanism for the applied stress and temperature. Similar values to those presented in Figure 2-6 have been reported in very long tests in Grade 91 steel in (Haney et al. 2009), and in the longest-term testing approach a value of 1. In analysis conducted by Maruyama, the value for Q can vary between 230 to 700 kJ/mol depending on the active mechanism (Maruyama et al. 2016). Similar values have been independently reported in the literature for grade 92 (Sakthivel et al. 2015) and 12 wt. % Cr CSEF steels (Eggeler 1989, Maruyama et al. 2015). Maruyama

has divided the creep behavior for Grade 91 steel into four distinct regions H, M, L_1 and L_2 in Figure 2-7 and are described as follows:

- The regions identified as H and M are characteristic of strain-induced (e.g. plastic) recovery. As there is insufficient test duration for diffusion to take place, thermal recovery of the substructure is not possible.
- The regions identified as L_1 and L_2 are within a time-temperature-stress regime where thermal recovery of the substructure is active and is additive to strain-induced recovery. In these regions ['long range'] diffusion is possible.

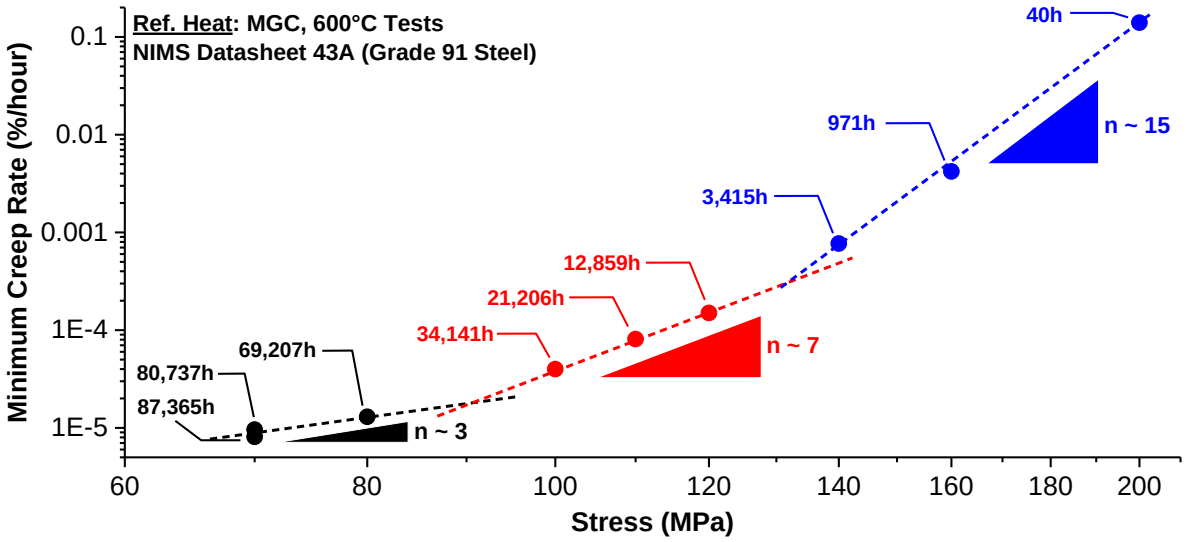

Figure 2-6. Norton plot for heat MGC Grade 91 steel from the NIMS database (NIMS 2014), adapted from (Abe 2014)

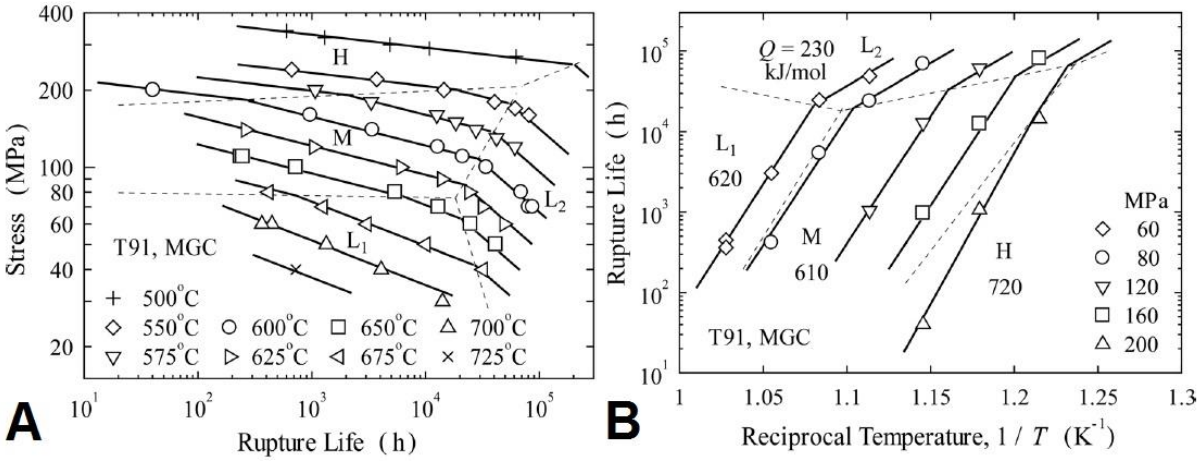

Figure 2-7. A – Stress-time to rupture plot for one heat of T91 steel (heat MGC) in the NIMS database and for the specified temperatures. Regions H, M, L_1 and L_2 refer to different creep mechanisms (and therefore activation energies), B – Activation energy values for each region in the stress-time plot, from (Maruyama et al. 2016)

In keeping with the previous discussion of creep mechanisms, Maruyama states that the activation energy of 230 kJ/mol in region L_2 is very close to that of lattice diffusion in ferritic steel (~300 kJ/mol). The values in the other regions (L_1, M and H) are at least a factor of 2 greater than this value.

2.3 Descriptions for Creep Deformation

Hollomon and Jaffe showed that tempering of steels obeyed the behavior presented in Equation 2.3 (Hollomon and Jaffe 1945). Extension of Equation 2.3 to creep behavior was first proposed by Larson and Miller and is commonly expressed in the form provided in Equation 2.4 as a 'Larson-Miller-Parameter' (LMP) relationship (Larson and Miller 1952).

Equation 2.3. $$HJP = T\ (20 + \log t)$$

Equation 2.4. $$LMP = (273 + T) \times (C + \log t)$$

Where:
HJP = Hollomon Jaffe Parameter
LMP = Larson-Miller Parameter
T = Temperature in °C
C = material specific constant; for Grade 91 steel a value between 20 and 30 is typically used and dependent on the quality of the database and material constituent (parent metal or cross-weld or tests in simulated HAZ material)
t = time to rupture in hours

There exists significant interest to evaluate methods for data interpolation and use these empirical methods to extrapolate beyond the given dataset (typically for power plant steels into regimes measured in the 100,000s of hours). This interest continues today, and in the years after the widely referenced paper by Larson and Miller resulted in numerous follow-on attempts to improve upon this approach.

Attempts to relate stress, temperature and time into a basic empirical formula are often referred to as 'time-temperature parametric (TTP) approaches' and include derivations by Orr-Sherby-Dorn (Orr et al. 1954), Manson and Haferd (Manson and Haferd 1953), Manson and Brown (Manson and Brown 1953), more recently the half-yield ($\sigma_{0.2/2}$) proposed by Kimura (Kimura 2005) and the multi-region splitting approach proposed by Maruyama (Maruyama et al. 2016). An additional set of variations to these approaches include strain-based assessment methods which attempt to incorporate a more mechanistic-based philosophy based on the shape and details of the creep curve

such as the Theta Projection Method (Evans et al. 1982) and Omega Parameter (Prager 1994).

Recent efforts have attempted to model the microstructural degradation and link this behavior to the creep curve after considering subgrain growth, dislocation movement, precipitate coarsening, etc. (Semba et al. 2008, Yadav et al. 2016, Spigarelli 2013). A review of the legacy approaches is available in (Manson and Ensign 1979) and specific to Grade 91 steel in (Abe 2014). Even today, the LMP Parameter relationship remains the most widespread approach for comparison of data in large part due to its simplistic formulation and relative agreement with creep data such as provided in Figure 2-8. In Figure 2-8 a Grade 91 parent material database is compared using the LMP as function of stress including relationships for the lower bound, mean and upper bound behavior. A detailed description for the relationship bounds, and a rationale for these including parent metal and cross-weld creep behavior will be provided in Chapter 4.

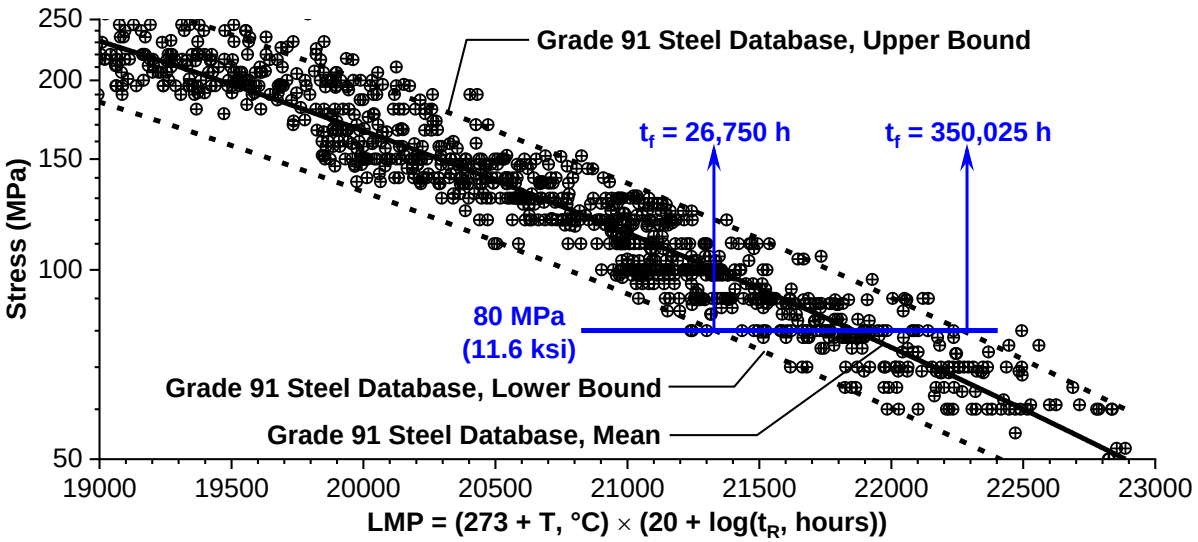

Figure 2-8. Electric Power Research Institute database for Grade 91 steel parent metal creep performance represented as a Larson-Miller parameter (LMP) comparison using a C-value of 20. The blue data represent the spread in the data for the lower and upper bounds for a given stress value of 80 MPa and a temperature of 600°C.
Note: *the variation on the estimated time to failure is more than a factor of 10*

There are inherent limitations to empirical approaches for describing creep behavior, including issues in interpolation versus extrapolation and with respect to the underlying mechanisms responsible for deformation and damage. As the relevance of the relationship is highly dependent on the database, there can be serious uncertainties and non-conservative predictions when attempts are made to extrapolate beyond the database. The issues in interpolation and extrapolation are succinctly summarized in

(Strang et al. 1999), *"The use of this approach* [parametric time-temperature relationships] *for the purposes of residual life prediction is effectively limited to interpolation within the time/temperature frame of the available dataset and cannot be reliably used for extrapolation purposes."* As pointed out in (Maruyama et al. 2016), the simple assumption of a single activation energy (such as is the case when using a Larson-Miller approach) results in non-conservative estimates of long-term behavior since there exists a bias in the data to shorter-term, higher-stress tests where the activation energy is ~≥600 kJ/mol. In some cases, the database may require filtering based on rupture life, test temperature or test stress to increase the confidence in the established relationships.

The realities of extrapolating data are reflected in continuous revisions of the C value constant in the LMP relationship. Optimization of the C parameter using the Larson Miller approach for Grade 91 steel parent material has ranged from a value of 36 or 38 (Masuyama 2005, Kimura 2005b) to more recently a refined value closer to 25 using a 3rd order lot-centered approach and filtering of rupture data >1,000 hours (Foulds 2017). For cross-weld behavior a value of 20 is commonly utilized and has been shown to be conservative and adequate for the purposes of risk-ranking and data comparison (EPRI 2013c).

2.4 Descriptions for Creep Fracture

In the prior review of TTP relationships, it should be emphasized that these approaches primarily assess the deformation behavior. As creep must accommodate descriptions not only for deformation but also fracture it is important to appreciate and review procedures which describe the fracture behavior and particularly for materials exhibiting brittle behavior (Parker and Siefert 2018). Brittle behavior can be enhanced when materials are subjected to multiaxial states of stress (such as a notch bar) and as presented schematically in Figure 2-9 or through the introduction of a metallurgical notch such as a cross-weld creep test.

Simple comparisons have been drawn on the susceptibility to fracture using either elongation at failure or the reduction of area (ROA); both descriptions are typically expressed in %. A set of examples comparing the reduction of area for grades 91 and 92 steel is provided in Figure 2-10 and Figure 2-11, respectively. As illustrated in these figures, there is a general trend to low ductility, but this trend is more apparent for

Grade 92 steel. Secondly, and for similar failure times to 100,000 hours at 650°C in Figure 2-10 the creep ductility for Grade 91 steel exhibits a range of values from near 10% to >80%.

The preferred approach to reporting creep ductility seems to be a matter of preference. However, in the evaluation of cavitation in iron, George et al. (1987) preferred ROA providing the following explanation, *"…growth of cavities by diffusion of vacancies to the cavity surface does not contribute to RA whereas such growth does contribute to total elongation. Therefore, RA is a much more sensitive measure of ductility in the case of brittle high temperature failure* (George et al. 1987)*."* Similar sentiments are provided in (Roan and Seth 1978) where a clear association was made between the impurity content (as measured through bulk chemical composition) and the decrease in ROA. Thresholds for utilizing the ROA value to screen brittle behavior have been proposed in (Viswanathan 1995) and (Bendick et al. 2001) and include values of 40, 50 or 70% ROA to screen material having either a tendency for brittle or ductile behavior.

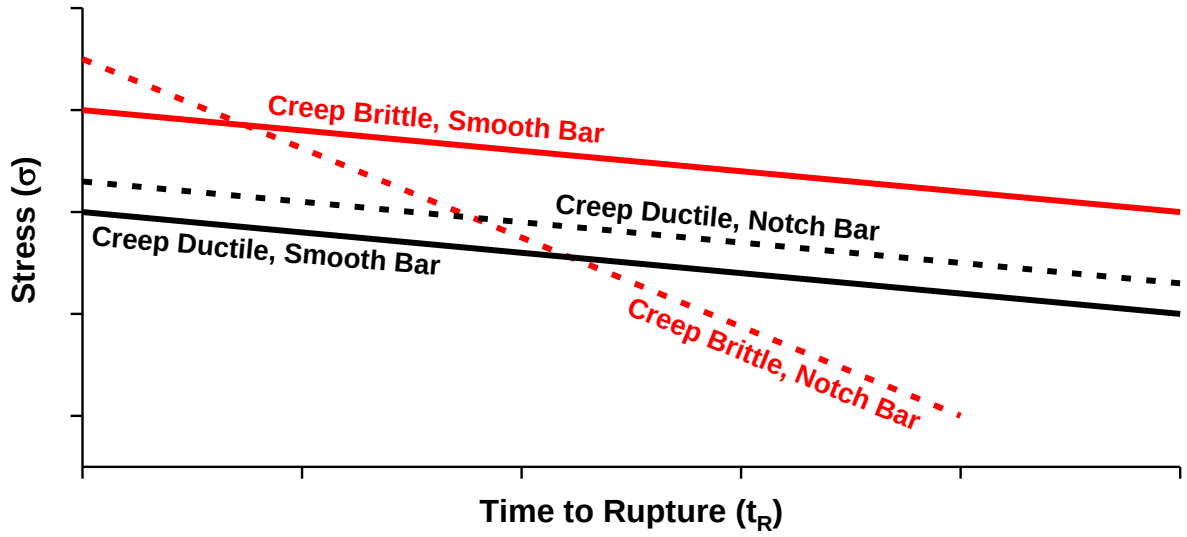

Figure 2-9. The influence of stress-state on behavior for a creep brittle and creep ductile ferritic steel. For creep brittle materials, enhancement of the maximum principal stress such as through notch bar testing will promote the evolution of damage and a reduction in performance (Viswanathan 1995).

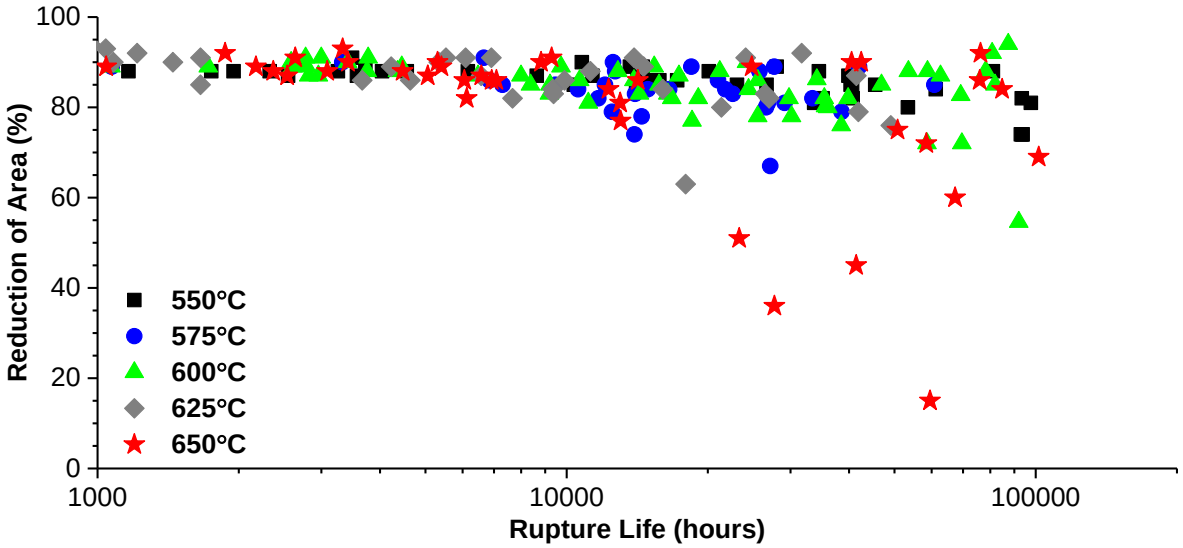

Figure 2-10. Rupture life and reduction of area for Grade 91 steel, as reported by (NIMS 2014)

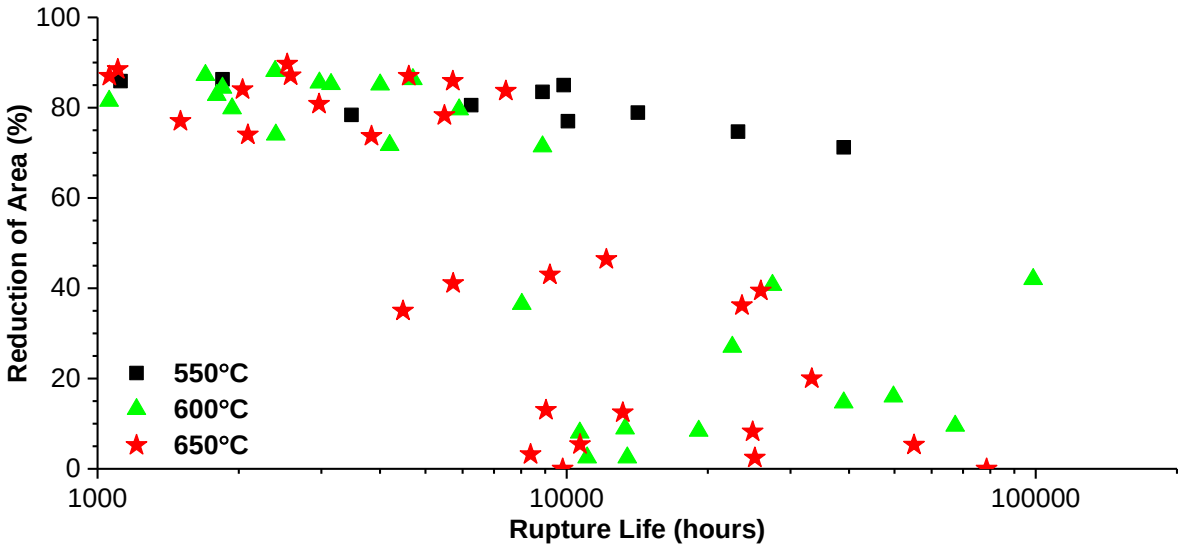

Figure 2-11. Rupture life and reduction of area for grade 92 steel, as reported by (NIMS 2012)

While the previous Norton relationship has been used to define deformation, the Monkman-Grant relationship, has been used to describe fracture, Equation 2.5. Monkman and Grant first noted that there existed a relationship between creep ductility and the product of the time to rupture and the minimum creep rate, equation 2.5 (Monkman and Grant 1956). Since the value for the constant 'm' was not observed to appreciably vary from a value of 1, equation 2.5 could be simplified in the representation given in equation 2.6. At that time, they indicated the link between Equation 2.6 and the ductility constant was not well-understood claiming, "Dimensionally the constant in this equation is some measure of elongation which is as yet not clearly understood (Monkman and Grant 1956)." This link was later examined by key researchers in the CEGB, namely Ainsworth, Chubb, Cockroft and

Goodall and a value identified by the lambda parameter, λ, was widely used as a more thorough representation of creep ductility in steels.

Equation 2.5. $\log(t_r) + mlog(\dot{\varepsilon}_{min}) = \mathrm{c}$

Where:
$\dot{\varepsilon}_{\mathrm{min}} =$ minimum creep rate
$\mathrm{t_r} =$ time to rupture
$\mathrm{c, m} =$ constants

Equation 2.6. $t_r \times \dot{\varepsilon}_{min} = \text{constant}$

The Monkman-Grant relationship for Grade 91 steel is provided in Figure 2-12. The introduction of the Monkman-Grant parameter is important as it places a constraint on creep cavitation theories discussed in following sections. A modification to the Monkman-Grant constant is given in equation 2.7 (λ_A) after Hayhurst and Leckie (Leckie and Hayhurst 1977). The need to modify the approach was presented by (Wilshire and Burt 2005) to accommodate fundamental differences in the creep curve, Figure 2-13 and Equation 2.8 (λ_B).

Equation 2.7. $\lambda_A = \frac{\varepsilon_f}{\dot{\varepsilon}_{min} \times t_f}$ [after Hayhurst and Leckie]

Equation 2.8. $\lambda_B = \frac{\varepsilon_f - \varepsilon_p}{\dot{\varepsilon}_{min} \times t_f}$ [after Wilshire and Burt]

Where:
$\lambda =$ creep damage tolerance parameter
$\varepsilon_{\mathrm{f}} =$ strain at failure
$\varepsilon_{\mathrm{p}} =$ strain at end of primary creep

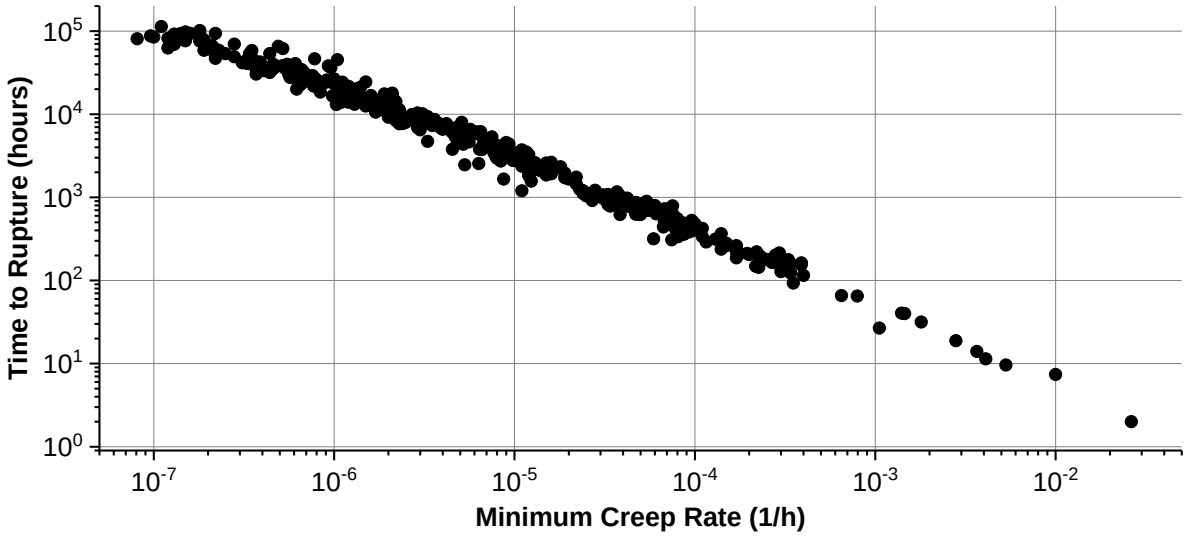

Figure 2-12. Monkman-Grant relationship for Grade 91 steel parent metal in the Electric Power Research Institute database

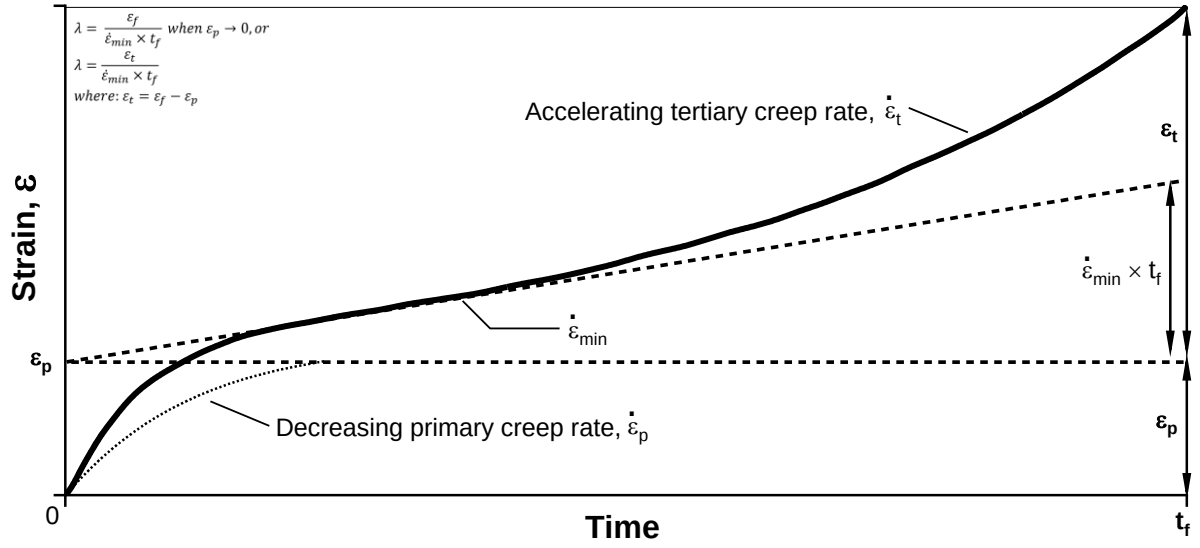

Figure 2-13. Description of the lambda parameter and as determined using the data from a uniaxial creep test in parent material (Wilshire and Burt 2005)

The use of the lambda parameter in assessment of materials for component design was proposed by (Goodall and Ainsworth 1977). This approach was eventually evolved into the requirements of R5 whereby the relationship in Equation 2.7 was applied, stating, "*the criterion used for regarding a material as creep ductile is that the average elongation or reduction of area at creep rupture must be at least five times greater than the product, at the same stress and temperature, of the average minimum creep rate and the average time to rupture. This must be demonstrated for the operational temperatures and lifetimes and for the stress levels calculated to apply during creep dwells. If this cannot be demonstrated, the material is creep brittle*" (R5). Materials meeting the requirement $\lambda_A > 5$ were deemed to be sufficiently creep ductile whereas those that did not achieve this value were categorized as creep brittle. It is important, and relevant to note that this formal requirement is the only known[2] identified criterion in mainstream construction codes for assessing whether a material is susceptible to damage. New construction codes[3], such as ASME B&PV Code, do not consider ductility in new design and have no criteria to establish whether a material should be labeled as creep ductile or creep brittle. Creep ductility is an important consideration as multiaxial stress states, such as those experience by complex components operating in plant applications, can exhibit an enhanced susceptibility to

[2]Known to the author at time of publication
[3]New construction where "new" does not imply a chronological timeframe, e.g. new construction codes can be applied at the time of fabrication of an entire plant or for a replacement component at some point well after the original commissioning of the plant

damage when exposed to a triaxial stress state (e.g. where triaxiality is often defined by one of two criteria, $\frac{\sigma_H}{\bar{\sigma}} or \frac{\sigma_I}{\bar{\sigma}}$). This is often the case for complex components or geometries such as nozzles, large branch openings or thick-section girth welds subjected to bending.

The relationship in Equation 2.7 is applied to CSEF steel Grades 91, 92 and 122 in Figure 2-14. Note that in this simple screening test, the performance of Grades 92 and 122 would lend these materials to be labelled as exhibiting the potential for brittle behavior. As the evolution of damage in a complex component is a fundamental process based on the nucleation and growth of creep cavities in a multiaxial stress field, the simplicity of the lambda parameter must be placed in a more complete context. Specifically, and while the lambda approach may be sufficient to screen the potential range of materials susceptible to brittle behavior, there are inherent difficulties in relying on reported data in the literature. This primary issue arises from the completeness of the data to calculate the lambda parameter and with regards to the pedigree of the data; e.g. do the data represent a sufficient screening of material manufacturing methods and compositions for a given 'Grade' so as to sufficiently classify it as brittle?

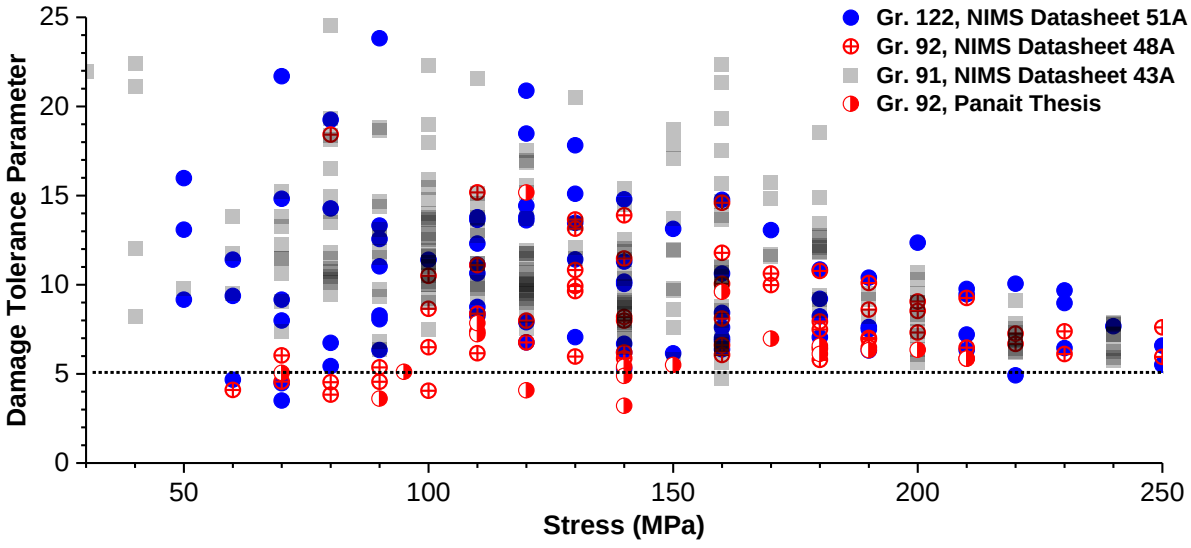

Figure 2-14. Comparison of calculated damage tolerance values (e.g. λ_A) for grades 91, 92 and 122, data filtered for test temperatures 550 to 650°C (Panait 2010, NIMS 2012, NIMS 2013, NIMS 2014)

A brief discussion is made here regarding continuum damage mechanics (CDM), which often references the classical work of Kachanov, who showed that the creep behavior (such as that shown in Figure 2-2) can be fundamentally represented by the

relationships shown in Equations 2.9 to 2.11 (Leckie and Hayhurst 1974, Riedel 1987). Whilst the emphasis of this literature review is not focused in CDM, the contribution of this relationship must be recognized as it serves as the basis for many approaches which use the concept of a single, scalar damage value that can vary from no damage (zero) to failure (one). Kachanov's approach effectively represented failure based on a loss of cross-sectional area due to the nucleation and growth of cavities. In the decades since Kachanov's contribution, many researchers have attempted to relate the observed damage through replication, for example the CEGB-developed 'A parameter', to the remnant life of the component.

Equation 2.9. $$\dot{\varepsilon} = f(\sigma, \omega), \dot{\omega} = g(\sigma, \omega)$$

Equation 2.10. $$\dot{\varepsilon} = \frac{B\sigma^n}{(1-\omega)^n}$$

Equation 2.11. $$\dot{\omega} = \frac{D\sigma^X}{(1+\varphi)\times(1-\omega)^{\varphi}}$$

Where:
$\dot{\varepsilon} =$ creep strain rate
$\omega =$ state variable providing a measurement of the damage or cracking

2.5 Influence of Deformation and Fracture on Component Behavior

Assessment of a structure operating in the creep regime must consider the material utilized to fabricate the component and whether the degradation of the material is deformation- or damage-controlled. This judgment affects the selection of the representative stress utilized to estimate remaining life, such as might be determined using finite element analysis or a reference stress solution. For the TTP relationship expressed in Equation 2.4, the relationship can be rewritten as a function of stress:

Equation 2.12. $$LMP = (273 + T) \times (C + \log t) = A_o + A_1 \log \sigma + A_2 (\log \sigma)^2 + \cdots$$

In Equation 2.12, the derivation of a best-fit line using a polynomial function for σ is based on plain bar, uniaxial test data. In plain bar, uniaxial test samples the equivalent and maximum principal stresses are equal and the hydrostatic stress is $\frac{1}{3}\sigma_I$. Thus, for materials where heat-to-heat comparison shows fundamental differences in the manifestation of damage in post-test metallographic evaluation, it is impossible to distinguish which stress is responsible for the accumulation of damage.

The relevance of stress-state is described by Cane and paraphrased here (Cane 1983). Extension of stress-state to cross-weld behavior is often an important consideration because welded structures in power generation steels possess an inherent constraint that promotes low ductility failure. Accumulation of damage is typically described in the weld as possessing intergranular cavitation and can occur during the stress relieving cycle (e.g. reheat cracking in CrMoV steels) or at elevated temperature in service (e.g. more typical of 9 wt. % Cr martensitic CSEF steels).

Use of the prior-detailed λ parameter serves a useful purpose from the perspective of stress redistribution. As the value of λ increases, the ability of the material to redistribute stress increases. This is shown schematically in Figure 2-15 where materials with low values of λ exhibit a rupture stress (σ_{RUP}) approximated by the steady state stress (σ_{SS}). However, for materials where λ>>1 and stress redistribution occurs, the value of the σ_{RUP} is less than the σ_{SS} and the value for σ_{RUP} will be approximated by the reference stress value (σ_R), equation 2.13.

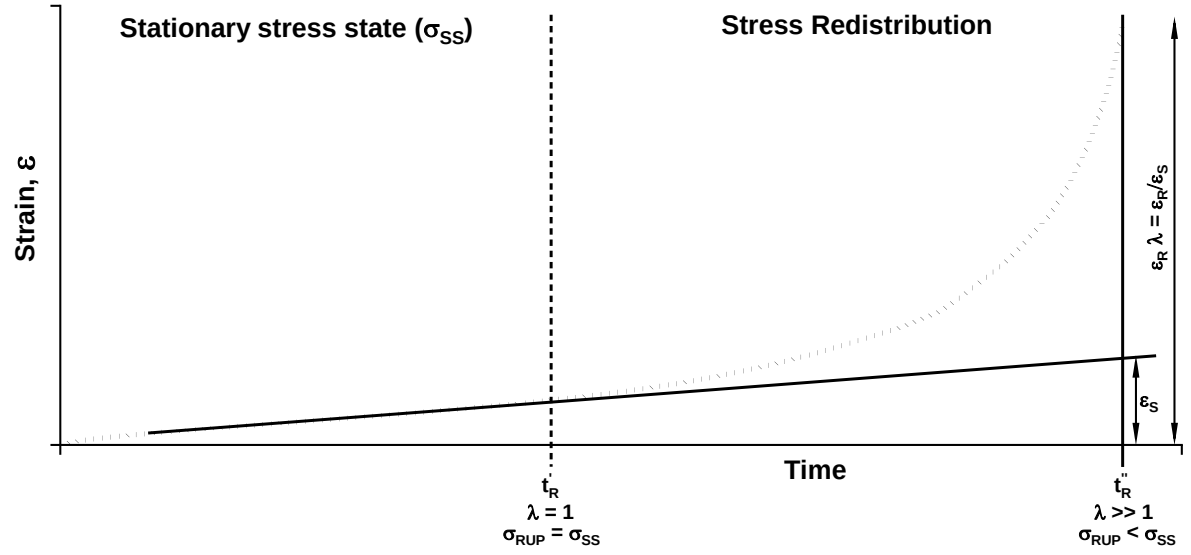

Figure 2-15. Relationship between the σ_{RUP}, σ_{SS} and λ to a representative plain bar, uniaxial creep curve plotted in the form strain versus time

Equation 2.13. $\sigma_R = P\frac{\sigma_y}{P_L}$

$Where$:
$P = operating\ pressure$
$P_L = limit\ load$
$\sigma_y = yield\ stress$

The complexity of the stress assumption in performing condition assessment necessitates the introduction of a multiaxial stress rupture criterion (MSRC). Generally, MSRC criteria are formulated based on Equation 2.14.

Equation 2.14. $\mathrm{MSRC} = \mathrm{f}(\overline{\sigma}, \sigma_1, \sigma_\mathrm{H}, \mathrm{S}_1)$

Where:

Equation 2.14A. $(\text{Von Mises equivalent stress}), \overline{\sigma} = \frac{1}{\sqrt{2}}[(\sigma_1 - \sigma_2)^2 + (\sigma_2 - \sigma_3)^2 + (\sigma_3 - \sigma_1)^2]^{0.5}$

Equation 2.14B. $(\text{Hydrostatic stress}), \sigma_\mathrm{H} = \frac{(\sigma_1+\sigma_2+\sigma_3)}{3}$

Equation 2.14C. $(\text{Maximum deviatoric stress}), \mathrm{S}_1 = \sigma_1 - \sigma_\mathrm{H}$

$And\ \sigma_1\ is\ the\ maximum\ principal\ stress$

For materials which are deformation controlled and exhibit damage resulting from structural coarsening and subsequent failure due to plastic instability, the Von-Mises equivalent stress ($\bar{\sigma}$) will control material behavior, Equation 2.14A. For material which is damage controlled, failure is dominated by the evolution of creep cavities the maximum principal stress (σ_1) or the hydrostatic stress (σ_H), Equation 2.14B. With respect to component behavior, a pipe section loaded by pressure-only will exhibit a rupture stress (σ_{RUP}) that may be approximated by σ_1 or $\bar{\sigma}$. However, most materials will exhibit a transition between these values for a given stress-state, temperature and material. An illustration of the transition between these behaviors for a set of Bridgman notch tests in a single heat of Grade 92 is shown in Figure 2-16. Here, the behavior at high stress (190 MPa) and 650°C is best described using the $\bar{\sigma}$ input in the material model while for low stress values more representative of design stresses (<100 MPa) a σ_1 criterion best estimates the time to failure. For structures, subjected to multiaxial stress states, it is important to recognize the importance that stress state will have on the initiation, growth, and distribution of damage.

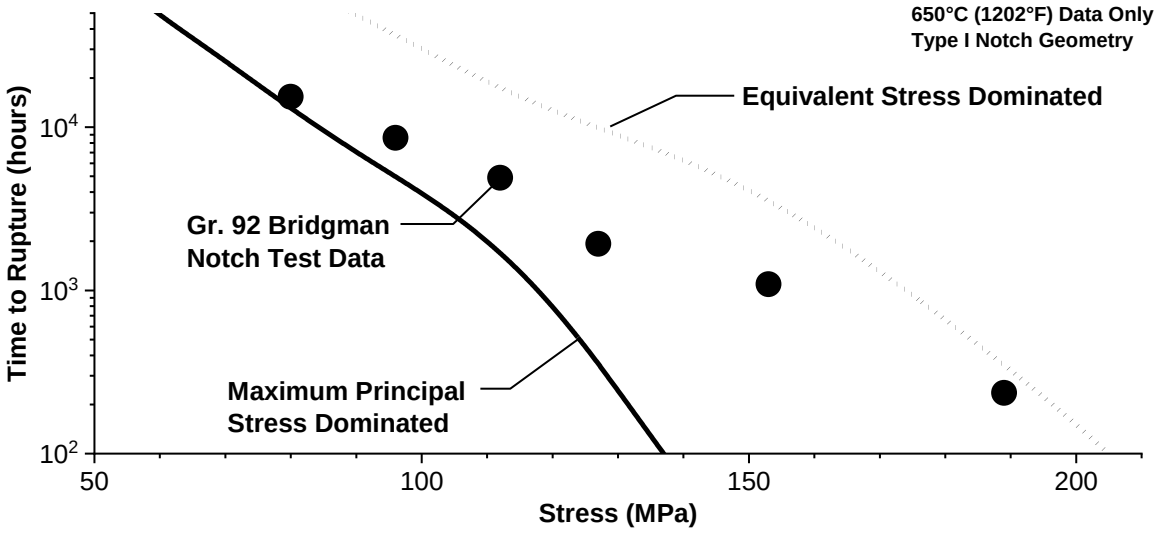

Figure 2-16. Transition in controlling stress state for Bridgman notch geometry in a commercial heat of Grade 92 parent metal, data from (Shigeyama et al. 2016).

2.6 Variability in the Creep Deformation and Creep Ductility in Grade 91 Steel

Acceptable creep strength and creep ductility of Grade 91 steel is achieved through purposeful alloying, control of impurity elements and inclusions, careful processing and proper heat treatment. An example of an acceptable tempered martensitic microstructure achieved by these variables is given in Figure 2-17A for Grade 91 steel. In the SEM image, the division of the martensitic structure into prior austenite grain boundaries (PAGBs) and substructure packet, block and lath boundaries is apparent. The fine substructure including the lath and fine carbonitride precipitates is observed in the transmission electron microscopy (TEM) bright field image in Figure 2-17B. A schematic representation of the martensite structure is provided in Figure 2-18.

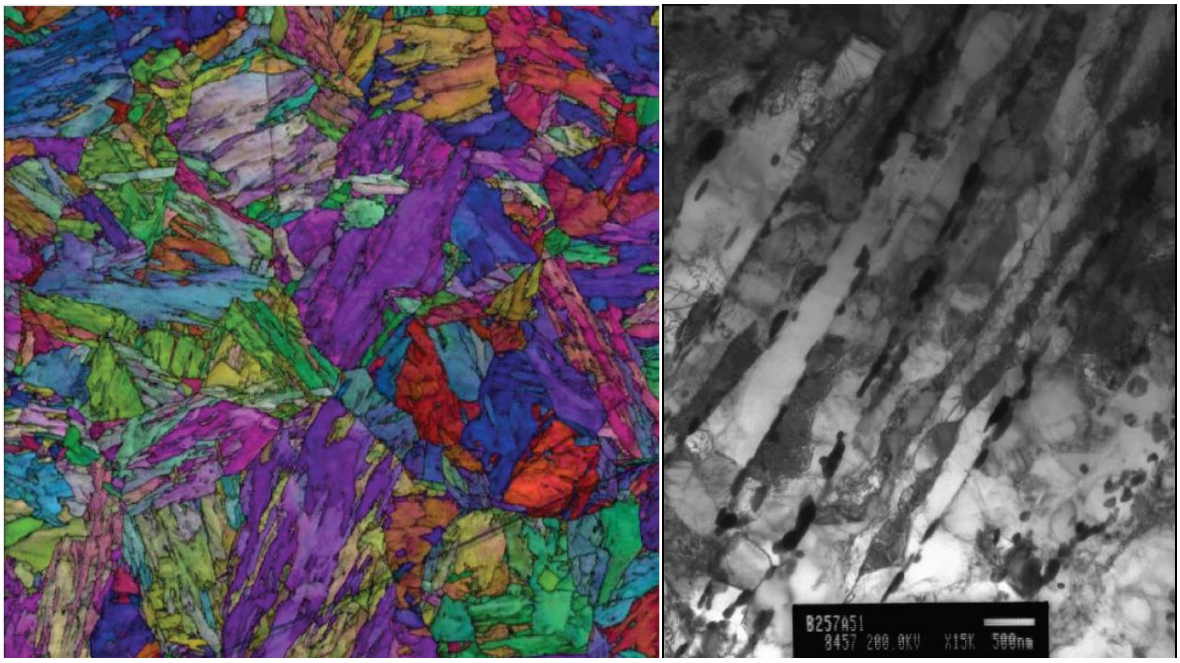

Figure 2-17. Representative images of Grade 91 steel parent metal steel in an optimum, tempered martensitic condition. Left – Scanning Electron Microscopy overlay of image quality map and inverse pole figure map; Right – transmission electron microscopy bright field image of tempered martensitic substructre (Hanton 2007)

There are numerous databases in the world which provide a comparison of acceptable creep strength on a mean and minimum basis. This behavior, such as provided in Figure 2-19 for the black data points, provides construction codes with the information necessary to set stress allowable values based on creep strength. The influence of strength is clearly important since there is a dramatic influence of mal-heat treated (i.e. “soft Grade 91”) material given in Figure 2-19 by the blue data. The minimum bound for soft Grade 91 is -45% of the strength from the mean for typical Grade 91 steel (EPRI 2013a, EPRI 2013c, EPRI 2016a). Based on Figure 2-19, and in the most extreme comparison between the absolute minimum bound for soft material and the upper bound for tempered martensitic Grade 91 steel, the influence of heat treatment can impart a variability in life that is on the order of 35X.

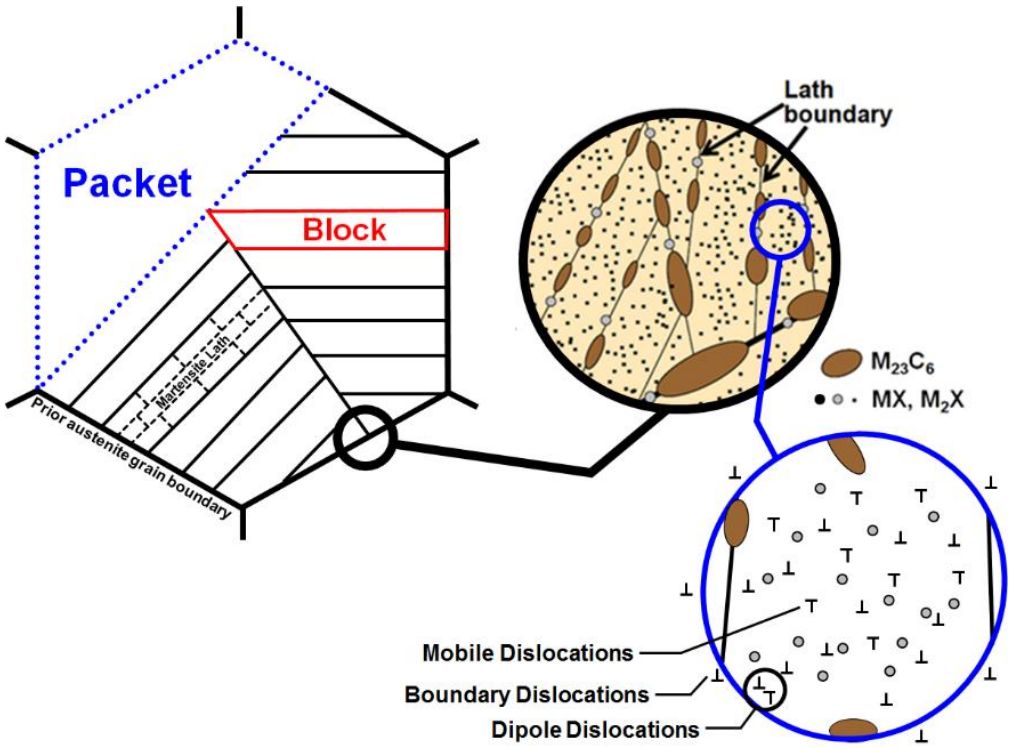

Figure 2-18. Schematic showing the types of microstructural features, boundaries and precipitates typically observed in Grade 91 Steel.
Note: *that this image does not include phases which may form in service (i.e. Laves and Z-phase), adapted from (Yadav et al. 2016, Kitahara et al. 2006, Abe 2008).*

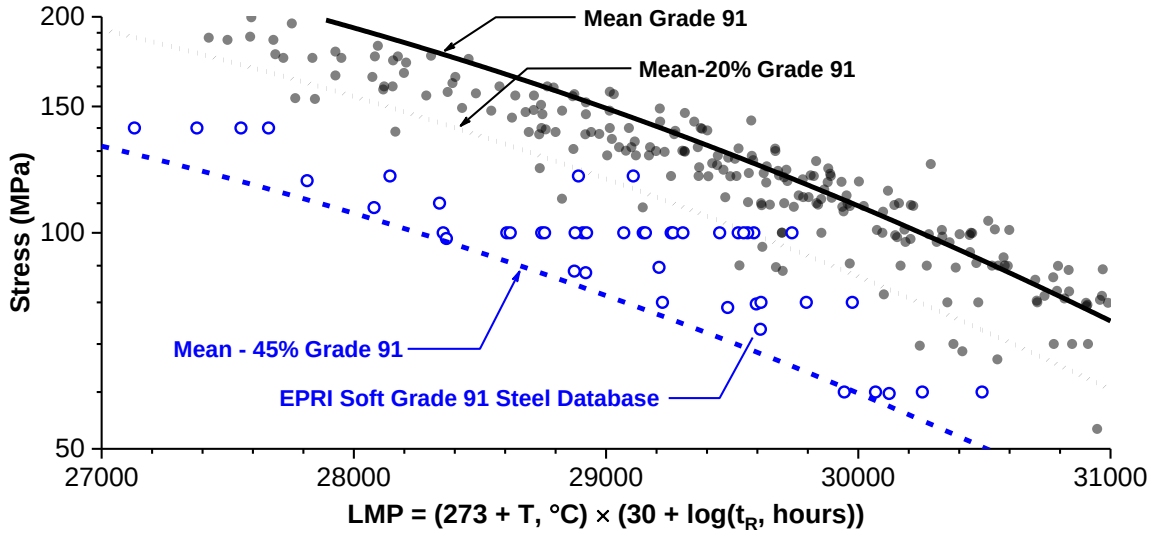

Figure 2-19. The EPRI database of creep tests in soft parent material and as compared to the EPRI database of Grade 91 of martensitic parent material ([EPRI 2013a, EPRI 2013c, EPRI 2016a)
Note: *Comparison is made using a Larson-Miller parameter (LMP) approach with a selected applied constant (C) value of 30 for Grade 91 steel.*

Less information is typically provided regarding the creep ductility and what defines "acceptable" behavior. Today, creep ductility is not given serious consideration as an engineering parameter in the world's balance of construction codes, even though this

material attribute governs the formation and evolution of damage in most engineering metals. This sentiment is highlighted by Wilshire in (Abe et al. 2008):

> *"…Compared with the emphasis placed on measurement and interpretation of the minimum creep rate and time to failure data, comparatively little attention has been devoted to the factors affecting creep ductility and the related reduction of cross-sectional area at fraction (RoA)."*

In the original Oak Ridge National Laboratory (ORNL) summary report on the development of Grade 91 steel, guidance was provided regarding acceptable performance with regard to the reduction of area (ROA) as measured in a failed, uniaxial smooth bar creep test. Specifically, it was stated that within the temperature range of 482 to 649°C the creep ductility (represented by ROA) was to be ≥70% for test durations ≥40,000 hours (ORNL 1986a).

The need for an acceptable level of creep ductility in Grade 91 steel is supported by a series of subsequent manuscripts in (Bendick et al. 2001, EPRI 2014a). Indeed, similar requirements were set in the development of Grade 92 steel, although the aim target for creep ductility (reduction of area) was 40% in 10,000 hours at 600°C (Bakker and Nath 2001). Mention of creep ductility as an important variable in material performance is routinely noted in manuscripts including an entire conference devoted to the topic (Strang 1991) and an overall appreciation in CSEF steel development through at least the mid-1990s, such as in (Pickering 1997, Nath et al. 1997). However, and more recently, the appreciation regarding the influence that creep ductility has on component performance has not been widely accepted, even though it can have very serious consequences, detailed in (Parker 2017).

The classification of creep ductility in Grade 91 steel is important because this material has been shown to have a large variation in performance. A database from a single supplier of Grade 91 steel, presented in Figure 2-20, illustrates the measured variability in ROA versus time to rupture for uniaxial creep tests at 600°C (Subanovic 2015, Panait 2010). For the highlighted data point in Figure 2-20, detailed assessment was performed on the precipitates in the post-test condition in the gauge and head sections; this information will be reviewed in later sections of this Chapter.

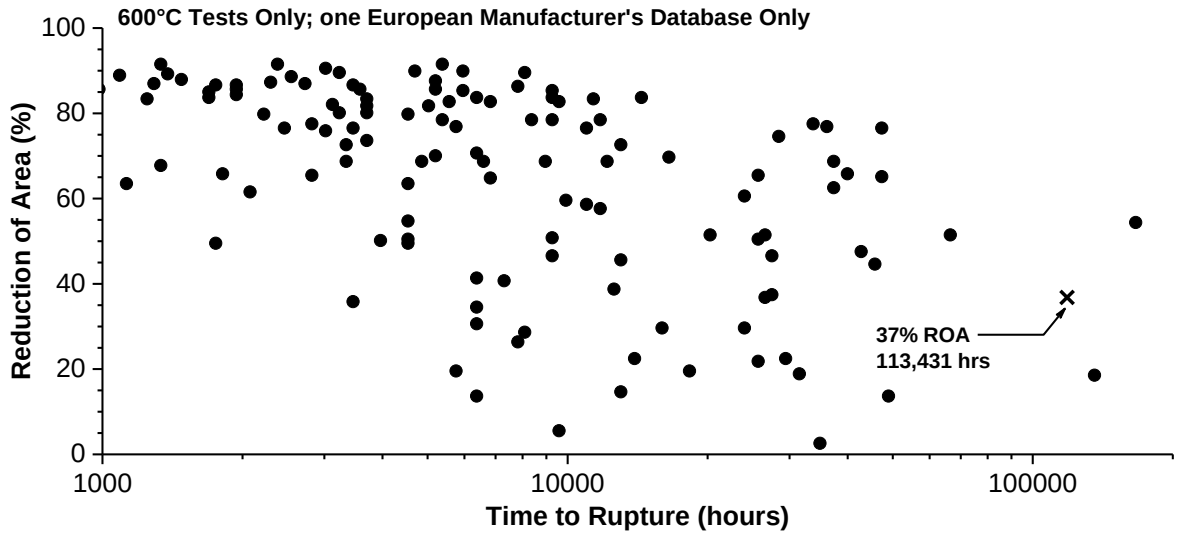

Figure 2-20. Creep ductility represented as reduction of area (%) versus time to rupture (hours) for multiple heats of Grade 91 steel parent metal tested at 600°C (Panait 2010, Subanovic 2015)

Research presented in (Bendick et al. 2001) and replotted in Figure 2-21 for uniaxial creep tests in Grade 91 steel and X20 provide three distinct classifications of behavior. The plot summarizes behavior on the basis of ROA such that for samples with >70% ROA, no creep damage was reported (except for 2 samples out of ~40 total); samples with ROA between 50 and 70% in some cases did contain damage and samples with ROA <50% creep damage was always observed. Tests which exhibit a ROA greater than 70% ROA are defined as “damage-resistant” and therefore resistant to the nucleation and/or growth of creep cavities in-service. For material with less than 70% ROA ductility, two classes emerge: a “transition” that is defined as a ROA between 50 to 70% and a “damage-susceptible” set of tests which possess a creep ductility less than 50%.

The observations in Figure 2-21 are supported in more recent assessment of the observed damage in mounted, post-test uniaxial creep samples and as given in Figure 2-22 (EPRI 2014a). The appearance and extent of damage is provided near the fracture face for a set of five Grade 91 heats which exhibit variable susceptibility to damage. For the tests labeled ‘TP1’ and ‘B1’ there is the clear appearance of elongated cavities in the direction of the applied stress (i.e. the applied stress axis is from left to right in the Figure). The damage in these two images is consistent with a deformation-dominated mechanism whereby the observed voids have formed plastic or ductile tearing at large inclusions near the end of the test. Sample ‘B3’ shows an increase in the extent of creep damage, but no apparent alignment of damage with the

applied stress. The size of the voids in the B3 material is less than that of B1 or TP1 and the balance of observations suggest that B3 exhibits characteristics of a transitional state. Lastly, heats 'B4' and 'B2' show still more creep voids which are aligned perpendicular to the applied stress. These two heats are susceptible to damage.

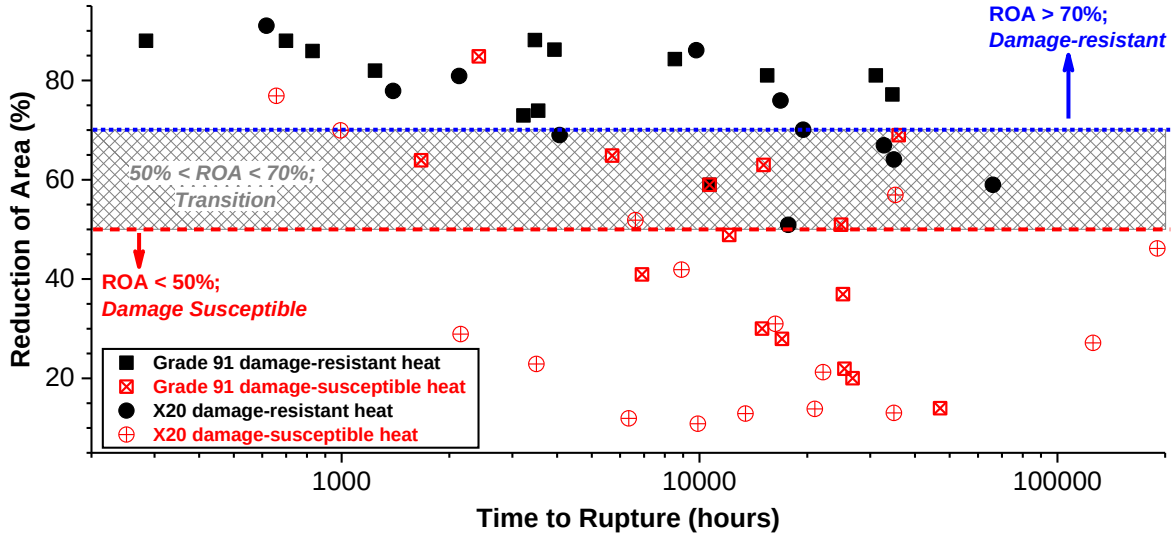

Figure 2-21. Comparison of behavior for martensitic steels X20 and Grade 91 steel and for damage tolerant and damage susceptible heats, adapted from (Bendick 2001)

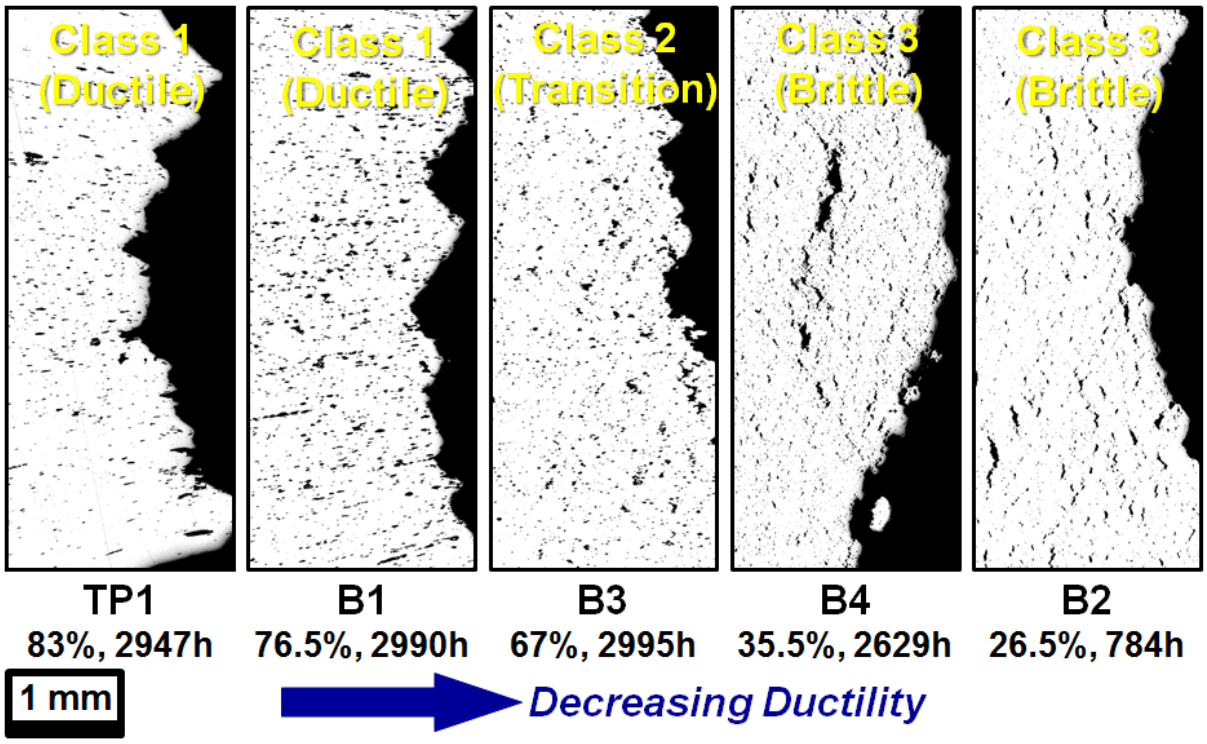

Figure 2-22. Adaptation of Figure in (EPRI 2014a) providing a classification of damage in line with observed cavitation behavior and consistent with reported behavior in Figure 2-21

The emphasis on proper analysis of both creep strength and creep ductility and how these material properties affect weldment behavior is highlighted by the fact that the service experience up to the year 2000 was primarily predicated on plant applications that only operated with steam outlet temperatures conditions up to ~540°C (1000°F), Table 2-1 (Gold et al. 2001). Furthermore, and as quoted from an additional source in the year 2004 (Rauch et al. 2004):

> "*Although components made of X10CrMoVNb9-1 (P91) installed in Germany show a service time of over 80,000h [installation in ~1994 or prior], few experiences with creep damages under service conditions exist. Among other reasons this is due to the very moderate loading conditions of first projects (e.g. P91 in power plant Tiefstack, 1992, steam parameters 540°C/240 bar).*"

Table 2-1. Application of Grade 91 steel from an original equipment manufacturer (OEM) per a conference paper from 2001 (Gold et al. 2001)

Plant	Country	MWe	SH* Steam (°C, °F)	RH** Steam (°C, °F)	Year Commissioned
Milmerran 1 & 2	Australia	400	568, 1054	596, 1105	2002
Hawthorn 5	USA	550	540, 1005	540, 1005	2001
Sidi Krir 3 & 4	Egypt	340	540, 1006	540, 1004	2002
Hinkrut 1 & 2	Thailand	700	540, 1006	540, 1004	Delayed
Saba	Pakistan	138	540, 1005	538, 1001	1999
Nantong 3 & 4	China	350	540, 1005	540, 1005	1999
Rutenberg B 3 & 4	Israel	550	540, 1006	540, 1006	2000
Yangzhou 1 & 2	China	600	540, 1006	539, 1002	1999
Taichung 5, 6, 7 & 8	Taiwan	550	542, 1008	542, 1008	1996

**SH = Superheater steam temperature*
***RH = Reheater steam temperature*

However, and more recently, most of the applications for Grade 91 steel – whether in state-of-the-art ultra-supercritical fossil fired boilers or HRSGs in gas-fired combined cycle plants – are near to or exceeding 600°C steam outlet temperatures. This includes not only thin section tubing, but thick section components such as turbine casings, valves, piping, forgings and fabricated fittings. This increase in conventional operating temperature, and within the last 15 years, has raised awareness in the power generation industry regarding life management strategies for components in which the evolution of creep damage may be controlled by deformation (von-Mises equivalent stress), damage (maximum principal stress controlled) or a transition between these extremes.

The increased awareness of Grade 91 steel performance and potential in-service implications has promoted discussion within new construction codes and standards

regarding the reduction of stress concentrations in Grade 91 steel arising from either poor design (i.e. mechanical notch) or welded fabrication (i.e. metallurgical notch). A key consideration in the metallurgy of CSEF steels is how the microstructure is affected by an imposed stress state. The material response in a complex component to multiaxial stress states is an important consideration as the evolution of creep damage in susceptible heats of 9 wt. % Cr steels can be enhanced. In controlled testing, such as through uniaxial notch bar creep tests using a Bridgman style notch (e.g. semi-circular), the effect of a multiaxial stress state (e.g. a mechanical notch) can be seen in Figure 2-23 for damage susceptible Grade 92 material whereby the reduction of area for the notch tests is consistently lower than for uniaxial tests subjected to the same applied net section stress (Shigeyama et al. 2016). This behavior is consistent with an increased notch sensitivity and ultimately may result in notch-weakening behavior consistent with the schematic provided in Figure 2-9. In fabricated components, stress concentrations are introduced not only through poor design, but are widely distributed throughout the component in the form of metallurgical notches, e.g. weld heat affected zones (HAZs).

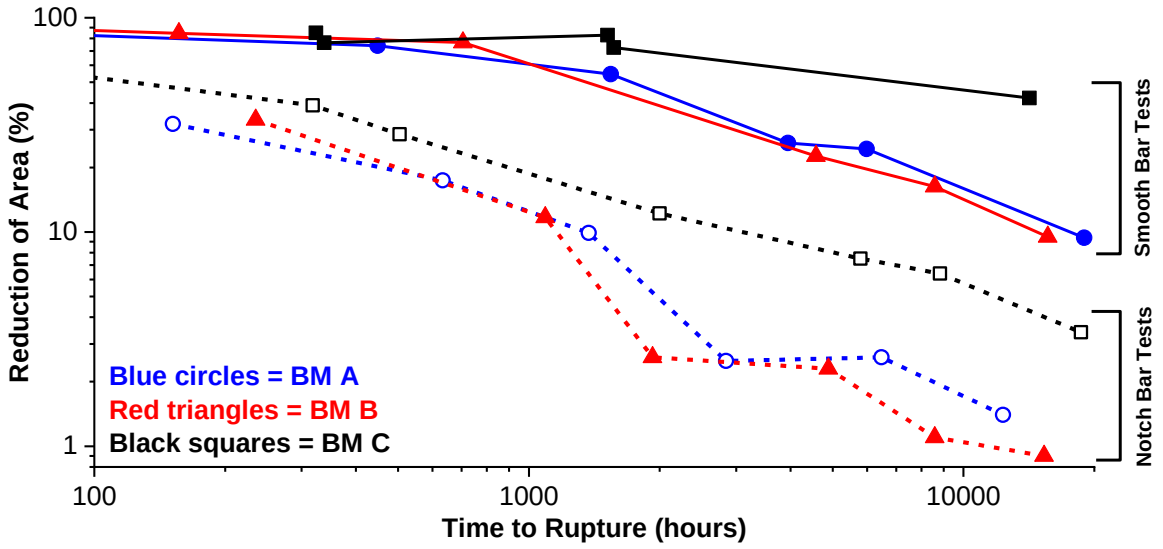

Figure 2-23. Comparison of uniaxial creep tests for three heats of grade 92 steel and for a series of smooth bar tests and notch bar tests using a Bridgman notch geometry (Shigeyama et al. 2016)

From the standpoint of conventional manufacturing routes, it is not practically possible on a universal scale to remove the metallurgical notch imposed by the under-performing HAZ in a subcritical PWHT'ed Grade 91 steel weldment. The removal of the HAZ in a 9 wt. % Cr steel would require local or complete renormalization and

tempering of the component. Thus, there has been a recent emphasis on understanding the factors which contribute to or dominate premature failures in under-performing welded components. Increasingly, the power generation industry has expressed concern that creep-dominated failures in the HAZ will be enhanced by the metallurgical condition of the material (Kimmins et al 1993).

There have been compounded influences from poor design in the presence of a weld HAZ in 9 wt. % Cr steel components. A prime example of this effect is shown in the failure of seam welded elbows, such as in (Komai 2016) and in Figure 2-24 for Grade 91 steel. In these examples, the U-groove geometry exhibits a slightly longer life (15 to 35%) and a lower maximum principal stress through the thickness of the component and as predicted using finite element analysis (Komai 2016). This assessment was verified in the measured damage, which was consistently higher for that of the X-groove geometry.

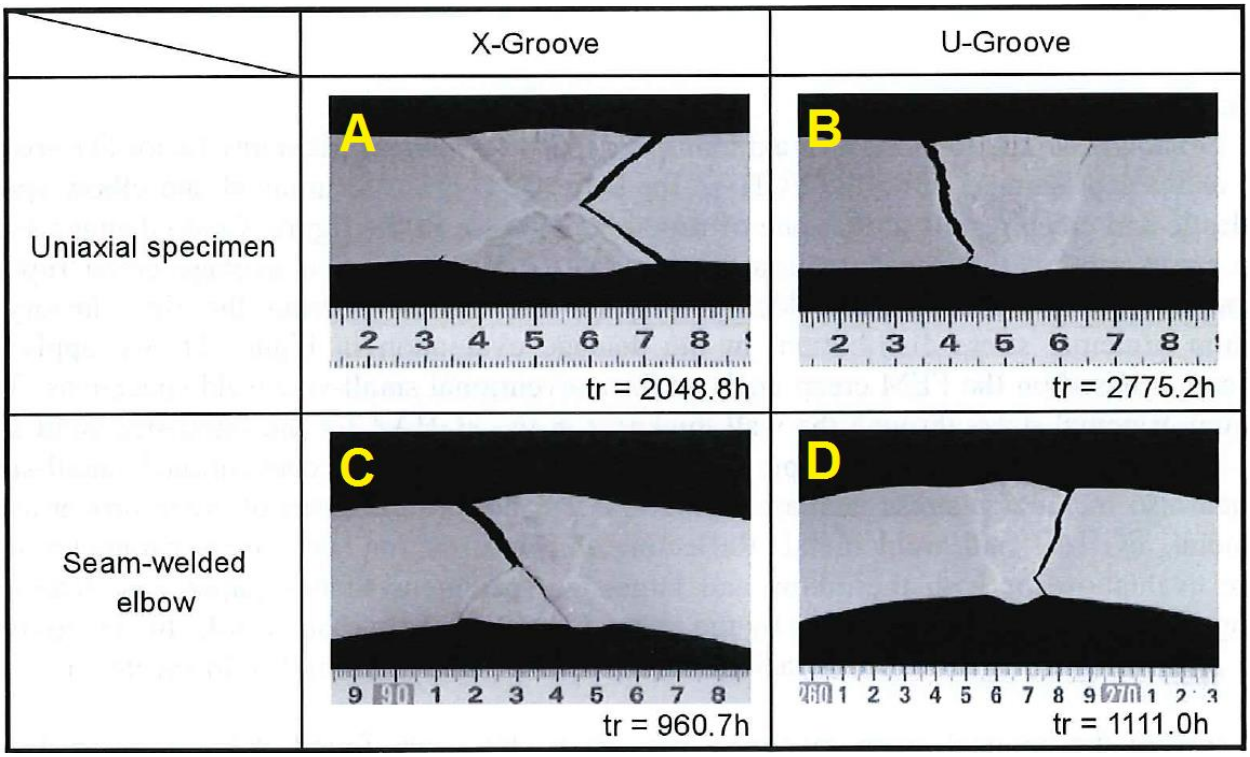

Figure 2-24. Photographs showing the cracking and fracture behavior in Grade 91 steel welds made using different weld profiles and tested as large uniaxial specimens (A and B) and as pressurized seam welded elbows (C and D) (Komai 2016)

The influence of the weld geometry (influence of bevel angle) in Grade 91 steel has been explored in (EPRI 2016b) where the steeper weld angle (e.g. a lower included angle) results in a longer life and in CrMo steels where crotch locations in the heat affected zone of seam-welds consistently developed a high level of damage

(Viswanathan and Foulds 1995). The aforementioned crotch locations (and as identified in two conventional seam-weld geometries in Figure 2-25) are a direct result of the selected weldment geometry (e.g. X-groove or a compound bevel such as in a girth weld), over-welding at the outside diameter (OD) location and/or due to back-gouging and re-welding at the inside diameter (ID) location as is commonly practiced in seam-welded construction. The influence of the welding thermal cycle, metallurgical evolution and other relevant issues will be discussed in more detail later in Chapter 2.

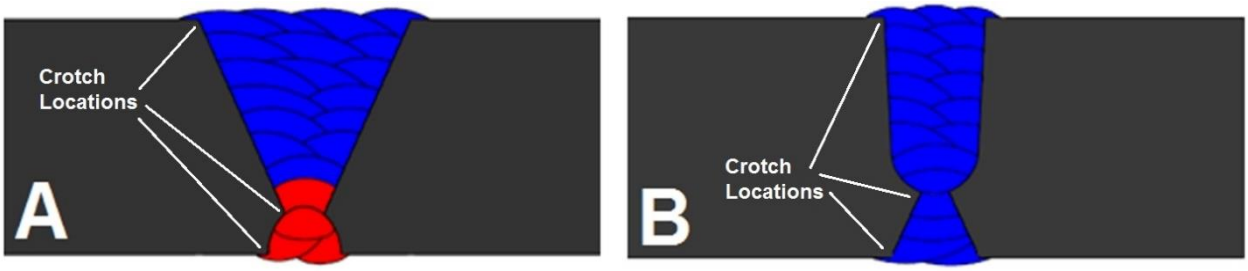

Figure 2-25. Difference in performance of seam welded Grade 91 type components have been recorded during service. Damage and cracking were found in elbows which had been made using a high bevel angle (A) rather than in straight pipe sections where the weld profile was significantly different (B) (Komai 2016)

Based on the influence of factors which contribute to strength and ductility, and the influence of a multiaxial stress state on the inherent microstructure, a balance of carefully controlled composition and optimized heat treatment is necessary. Precipitates can impose either a beneficial or deleterious effect. The formation of second phase particles can occur during the processing of the steel, final heat treatment, and/or evolve in-service. In this regard, the important parameters are not solely related to the composition alone but also to the processing temperatures and procedures, normalization temperature and quench rate, the tempering temperature, and finally the service conditions. An example of the steel making process for Grade 91 steel tube and pipe from billet is given in Figure 2-26 (Pellicani 1991). After the melting and solidification of the steel into billet form, many processing steps including the reheating of the steel to a temperature just below the stabilization range for delta ferrite (typically ~1250°C for 9 wt. % Cr steels) and subsequent hot-processing by forming, forging, rolling or extrusion are possible. In some cases, the billet may undergo several steps before achieving the final product dimensions and applying a final heat treatment. The processing steps are often specific to a given steel maker and have evolved with time. This increases the complexity in the assessment and in some cases the heat-specific variability has been linked to the evolution of steel-

making processes (Kimura 2017). The various factors relative to the performance of Grade 91 parent steel will be discussed in the following sections and in the context of composition, heat treatment, precipitate structure, and the implication of these factors on deformation and damage.

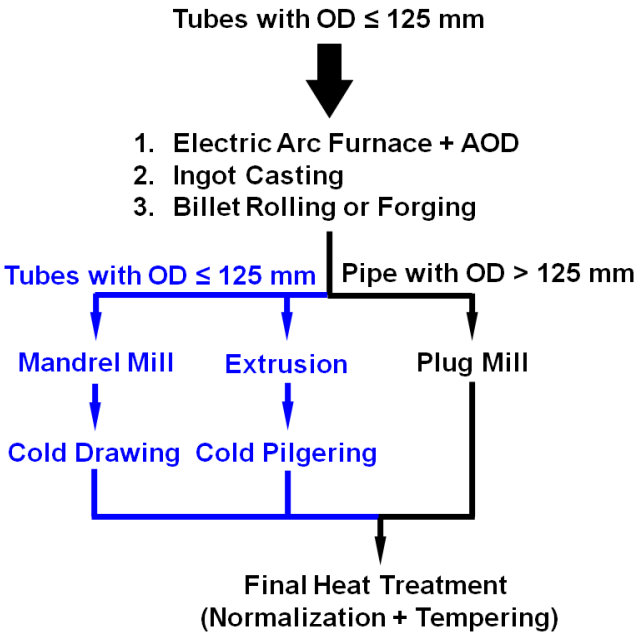

Figure 2-26. An example of the steel processing routes for making Grade 91 steel tube or pipe (Pellicani 1992)

2.7 Composition of Grade 91 Steel

Grade 91 steel possesses key alloying additions and unintentional elements that may be introduced through the recycling of scrap or because of the selected iron ore. Intentional alloying additions are aimed at having beneficial effects such as increased creep strength through optimized precipitate distribution and types. However, unintentional elemental additions can have deleterious effects in martensitic CSEF steels (primarily reduced creep ductility but also unintended consequences on strength). The potential effects that elemental additions have on Grade 91 steel are discussed below:

- **Creep Strength.** This is achieved by careful additions of C, N, V, Nb, Cr and Mo. These elements are key contributors to the formation of $M_{23}C_6$, M_2X and MX carbonitrides. The role of the specific carbonitride depends on its location in the structure. For example, $M_{23}C_6$ carbonitrides are present along prior austenite grain, packet and block boundaries (see Figure 2-18) and their inherent effect is to pin the microstructure. MX and M_2X carbonitrides are

present intragranularly and prevent dislocation movement by stabilizing the dislocation substructure. The distribution of MX in the microstructure is more uniformly distributed throughout the matrix owing to the formation and stability of this precipitate.

- **Creep Strength through Solid Solution.** Mo provides a solid solution strengthening effect in the BCC/BCT lattice. The unintended introduction of W can also provide a solid solution strengthening effect since this element is not formally controlled in common Grade 91 steel specifications. Both elements assist in the formation of Laves phase and stabilization of $M_{23}C_6$ carbides. It is thought that the solid solution strengthening of Mo and W in the BCC lattice is only a short-term effect since these elements are stabilized in $M_{23}C_6$ and Laves after relatively short times during aging or service exposure.
- **Creep Ductility.** Acceptable creep ductility is achieved by limiting both the potential formation of deleterious phases and limiting tramp elements currently not controlled by common material standards. This is addressed in (EPRI 2014a) and it is noted that the following elements must be monitored and/or controlled: As, B, Cu, Pb, Sb, Sn, W. Specifically, B and W are introduced through re-melting of grade 23, 24, 92, 122 or other CSEF steel scrap to make billet for Grade 91 steel production. Although B and W are traditionally not regarded as impurity elements, in the context of the Grade 91 composition they should be regarded as impurities and as highlighted by the original recommendations set forth by ORNL in mid-1980s, Table 2-2 (ORNL 1986a). The other impurity elements As, Cu, Pb, Sb and Sn are introduced through conventional scrap re-melting practices. Worldwide pressure to recycle metals and a universal reduction in access to raw iron ore stock has gradually increased the level of tramp elements. This is problematic because specific tramps such as Cu and Sn can be difficult to remove through conventional melting practices (Yamamoto 2013).
- **Corrosion Resistance.** This is achieved in steam-side oxidation environments by the intentional addition of Cr and potentially Si. The added Cr (e.g. an increase to ~8.5 wt. % nominal weight percent as compared to 1 to 2.25 wt. % in conventional low alloy, CrMo steels) can also marginally improve the fire-side corrosion resistance. The added benefit of Cr must be balanced against the

potential formation of Z-phase, which is stabilized by Cr. Z-phase may be further accelerated by the presence of elevated Ni (Strang 1997, Panait 2010).

- **Inclusion control and Deoxidation.** This is achieved by controlled additions of Al and Si to trap oxygen in the form of alumina (Al_2O_3) or silica (SiO_2) particles. Mn traps sulfur to form MnS stringers in the steel. It can be expected that Grade 91 steels possess these three types of precipitates because of the steel making process. Ca may also be present in these inclusions (or indeed Ca-rich inclusions) since Ca is often used to control inclusion size/shape (i.e. Ca has been shown to increase the number density and reduce the average size of inclusions) (Lind 2006). Ca is not formally controlled by common material standards and can be expected to be mostly or entirely present in inclusions where it is intentionally added to the steel. There is no guidance on a maximum limit for Ca as there has not been a systematic study assessing the impact on Ca on inclusion formation for 9 wt. % Cr steels. An example of the complexity of inclusion stringers is given in Figure 2-27 for a grade 92 steel from (Gu 2017). In this example, there is clear evidence for the co-precipitation of MnS, Al_2O_3 and Ca-rich Al_2O_3. It can be reasoned that the observed aggregation of inclusions is a result of inclusion-stability and nucleation. In this example, the stability of Al_2O_3 is higher than that of MnS and acts as a nucleation source for the formation of MnS.
- **Additional deleterious elements.** These include traditional controls on S, P, Ti, Zr and Al to prevent the formation of inclusions or potential embrittling effects associated with S and P. Martensitic steels are different from bainitic steels in that the S and P are at least partially dissolved into the $M_{23}C_6$ carbides and with respect to the formation of Laves phase. These two attributes are at least hypothesized to reduce the potential risk to intergranular cracking in-service (Gaffard 2004). This observation is further supported by research in (Middleton and Cane 1981) which mentions the avoidance of low ductility creep failures by the elimination of a boundary-deformation zone. The reduction in intergranular damage around PAGBs in Grade 91 steel is very different from the historical evidence for CrMoV bainitic steels. Research in CrMoV in (Middleton and Cane 1981) showed that cavity nucleation occurred preferentially at incoherent sulfide particles residing at PAGBs or adjacent to the PAGB in the boundary-

deformation zone. The limitation of Ti is also warranted since like Al, Ti can consume the available N and form stable, large TiN and reduce the amount of MX in the microstructure (Jara 2011). S can be particularly potent and the specifics of composition may not be entirely consumed by Mn during steel-making to form MnS. This is reflected in work by (Turkdogan and Pearson 1955) who showed that the solubility of S in an Fe-Mn matrix was ~0.0018 wt. % at 1200°C (2192°F) for a Mn content of 0.37 wt. %. Similarly, and for a temperature of 1335°C (2435°F) this solubility is increased to 0.0058 wt. %. There is the potential for excessive sulfur since most allowable specifications for 9 wt. % Cr steels allow for a maximum of 0.010 wt. %.

Table 2-2. Proposed Minimum, Maximum and Target Compositions from the Summary Oak Ridge National Lab (ORNL) Report on the Development of Grade 91 Steel (ORNL 1986a)

ORNL 6330	C	Mn	Si	P	S	Cr	Ni	Mo	Cu	V
Min	0.08	0.30	0.20			8		0.85		0.18
Max	0.12	0.50	0.50	0.02	0.01	9	0.2	1.05	0.2	0.25
Target	0.10	0.40	0.20	<0.01	<0.01	8.5	<0.10	0.95	<0.10	0.21
ORNL 6330	**Nb**	**N**	**Al**	**Ti**	**B**	**W**	**Zr**	**O**	**Sb**	
Min	0.06	0.03								
Max	0.10	0.07	0.04	0.01	0.001	0.01	0.01	0.02	0.001	
Target	0.08	0.05	<0.02	<0.01	<0.001	<0.01	<0.01	<0.02	<0.001	

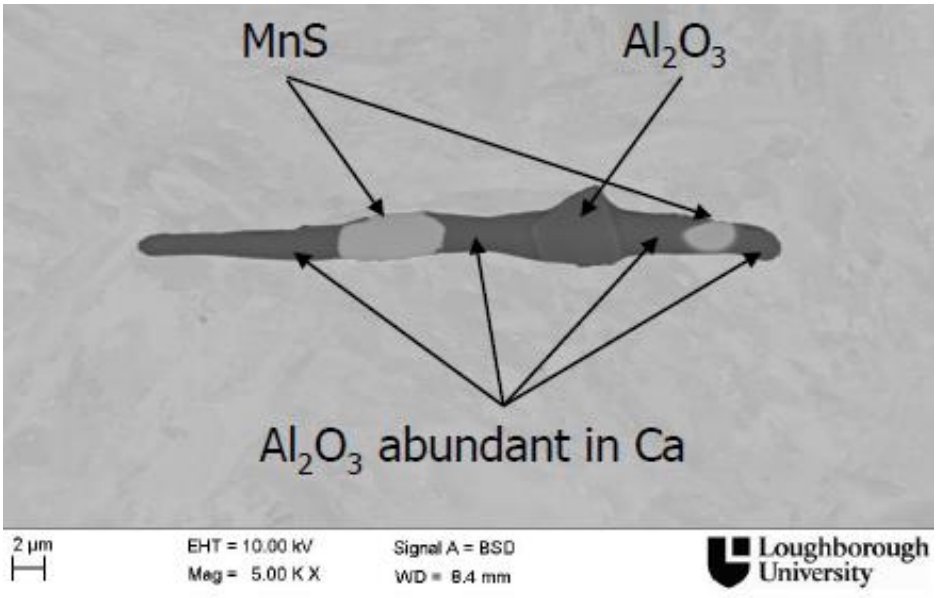

Figure 2-27. Representative inclusion cluster present in 9 wt. % Cr steels. Example taken from a grade 92 steel parent metal heat in [29].

2.8 Normalization and Tempering

Normalization and tempering can have a profound effect on the distribution and type of precipitates formed in the microstructure. The term ‘normalization or normalizing’

implies the product is cooled in still air from the austenitization temperature. However, for thick components accelerated cooling by a fan or in oil or water may be required to ensure full transformation to martensite through the product thickness, in which case the term “normalizing” is not technically appropriate. Examples of thick components which might require accelerated cooling include very-thick walled pipe, large valve bodies, steam turbine casings or forgings.

A lath martensite structure with high dislocation density in Grade 91 steel is achieved by application of an austenitization temperature >1040°C and a sufficiently fast cooling rate to avoid the formation of ferrite, Figure 2-28 (Vallourec 1992, Lundin et al. 1982). In general, Grade 91 steel will form martensite even for relatively slow cooling rates.

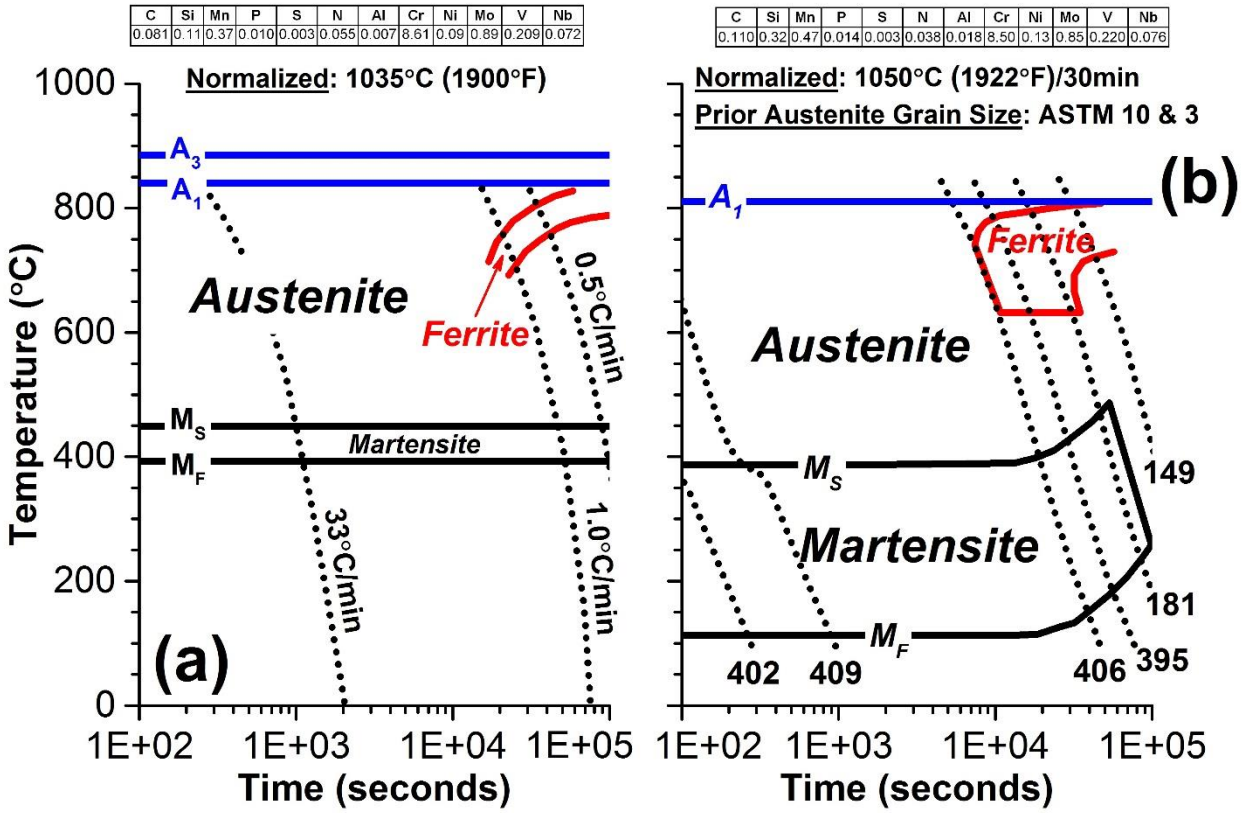

Figure 2-28. Example of published continuous cooling transformation (CCT) diagrams for Grade 91 steel, (a) adapted from (Lundin et al.) and (b) adapted from (Vallourec 1992)

The influence of austenitization time on proper homogenization is detailed in a recent article in (Kobayashi et al. 2014). The authors in (Yamada et al. 2002) have shown that the peak temperature and cooling rate can further influence the type and distribution of key precipitates in 9 wt. % Cr steels. A summary of the potential strengthening mechanisms in martensitic CSEF steels is provided below (Maruyama et al. 2001) and is a direct result of both the composition and heat treatments:

- **Dislocation hardening** at sub-boundaries and free dislocations within the subgrain structure. Dislocations are divided into mobile dislocations which can glide during creep, dipole dislocations which form dipolar or multipolar bundles and boundary dislocations which form subgrain boundaries arranged in low energy configurations (Yadav et al. 2016). The influence of dislocation hardening will be highly dependent on the service temperature and stress state. In measurements of the dislocation density in (Ennis 2000 and Ibid 2001) and Figure 2-29 has reached a steady state after ~10,000 hours at 600°C or ~3,000 hours at 650°C. Extrapolating this observation to 550°C would yield an expected steady state condition after ~300,000 to >2 million hours. A similar rate of decay in the dislocation density is reported for a CSEF 12 wt. % Cr steel in (Pesicka et al. 2010).
- **Precipitation strengthening** of the substructure by $M_{23}C_6$, MX, M_2X. The distribution of these particles in the tempered martensite matrix and their collective effects on pinning subgrain boundaries (intergranular) and pinning dislocations within the subgrains (intragranular) has been stated as the most important parameter in the consideration of resistance to deformation (Korcakova and Hald 2003). This is further demonstrated in Figure 2-29 where there is relatively little change in the substructure length even after durations of ~60,000 hours at 600°C and as compared to the achieved steady state after 10,000 hours at 600°C.
- **Solid solution strengthening** such as by Mo and W. The effect of Mo (or W in minor amounts in Grade 91 steel) is debatable from the standpoint of its effectiveness as a solid solution strengthening element. For example, and in (Korcakova and Hald 2003) the authors claim:

  > *"Solid solution strengthening is often referred to in discussions of the effect of molybdenum and tungsten on creep strength of 9-12% Cr steels but experimental evidence to demonstrate and quantify the mechanism is sparse."*

  Adding credibility to this point is data provided in (Maruyama et al. 2001) where a comparison of minimum creep rate with stress for α-Fe and α-Fe-2.3W showed a dramatic effect of the tungsten addition whilst a similar comparison for Fe-9Cr-VNbN and Fe-9Cr-2.3W-VNbN was less pronounced. Irrespective and since Laves phase is commonly observed in 9 wt. % Cr steels, it can be

concluded that the long-term solid solution strengthening effect from Mo and/or W is minimal in 9 wt. % Cr steels. The formation of Laves phase may have an intermediate beneficial effect on the precipitation strengthening (and at the expense of solid solution) and as suggested in (Di Gianfancesco et al. 1999).

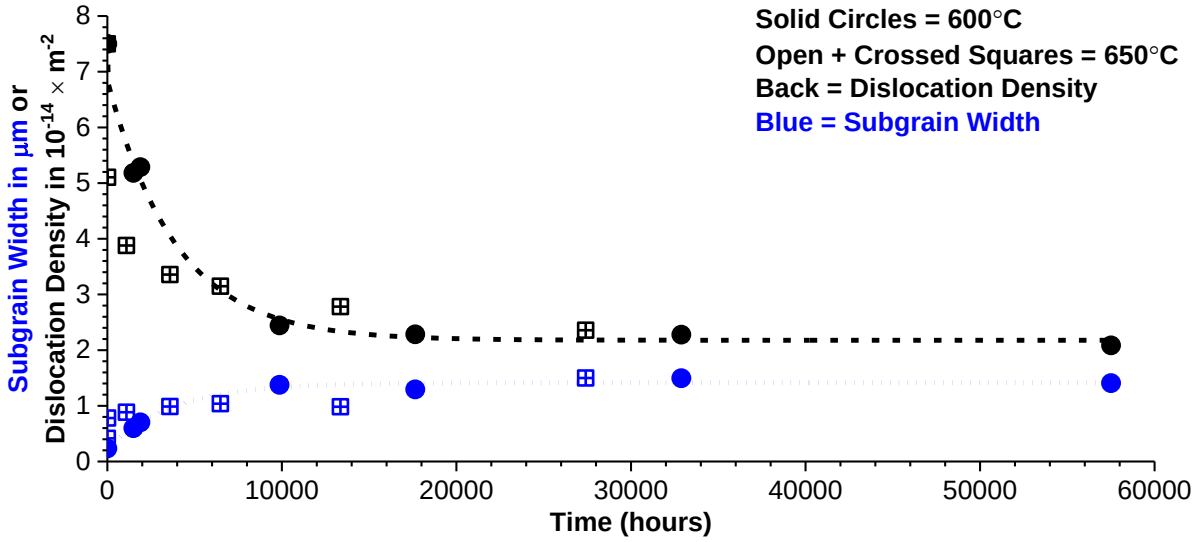

Figure 2-29. Evolution of the dislocation density and subgrain width in a grade 92 steel and for uniaxial creep tests performed at either 600 or 650°C (Ennis 2001)

2.9 Precipitates formed because of the Alloying, Processing and Heat Treatment Processes

Precipitates form as a function of the processing and final heat treatment (i.e. a combination of proper homogenization and tempering) and are dispersed along PAGBs (so-called high angle boundaries), subgrain boundaries (so called low angle boundaries or dislocation networks (Chilukuru 2009) and within subgrain boundaries (Abe et al. 2009 and Kitahara et al. 2006). The sub grain boundaries in Figure 2-18 are subdivided into block, packet and lath boundaries. The mean width of these various structures is given in (Gaffard 2004) and as follows for a Grade 91 steel with a PAGB size of ~100 µm; packets are ~20 to 50 µm in size and lath martensite of 0.5 to 2 µm in thickness. Boundaries with a misorientation of 2 to ~15 or >50 degrees are identified as subgrain boundaries such as block and lath boundaries. For boundaries possessing a misorientation of ~15 to 50 degrees these are classified as high angle boundaries (i.e. PAGBs or packet boundaries) (Kitahara et al. 2006 and Morito et al. 2006). As will be discussed in the following sections, these definitions are general such that key observations have been identified in 9 wt. % Cr steels which are not simply bounded by these relative measurements (such as the evaluation of low angle grain

boundaries down to 1° misorientation in X20 or using a threshold of 10 or 20 degrees instead of 15° to define the lower bound for low angle boundaries).

The $M_{23}C_6$ precipitate possesses a FCC crystal structure and is the principal precipitation strengthening phase considered in the original design of Grade 91 steel (ORNL 1986a). These precipitates form during tempering in the conventional range of 730 to 790°C, are seen to dissolve as the temperature approaches or exceeds the A_1 value (~800°C for Grade 91 steel) and are dependent on the balance of Cr_{eq} and Ni_{eq} stabilizing elements (Hanton 2007, Alexandrov et al. 2012). The reported complete dissolution temperature and as based on thermodynamic modeling is on the order of 870°C and close to the A_3 temperature (Hanton 2007). The general size of these particles is in most cases reported as >~100 nm in diameter in a properly tempered condition (Panait 2010). $M_{23}C_6$ carbides are observed to coarsen relatively rapidly in-service and reach a mean size of ~200 to 300 nm after 50,000 hours of exposure at 600°C (Cipolla 2007). A comparison of the size distribution for $M_{23}C_6$ is given in Figure 2-30 in the as-received condition and after >100,000 hours at 600°C (Panait 2010).

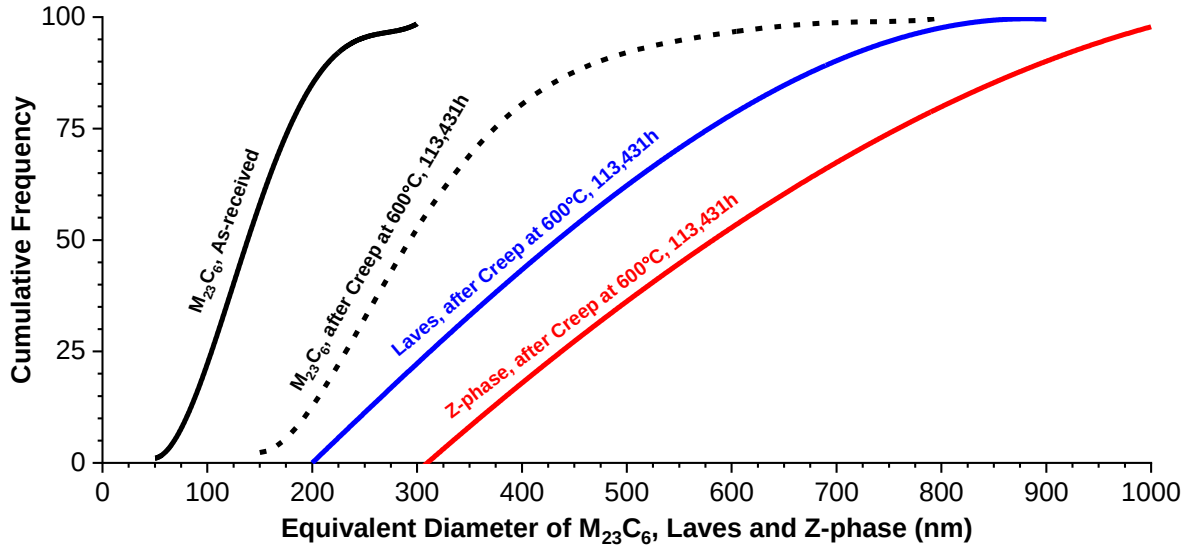

Figure 2-30. Evolution of the equivalent diameter for $M_{23}C_6$, Laves phase and Z-phase in Grade 91 steel after creep testing at 600°C and 113,431 hours (Cipolla 2007).

MX precipitates have a FCC crystal structure and are observed to have a much higher stability in creep and in service-relevant temperatures than that of $M_{23}C_6$. The dissolution temperature for VX is slightly lower than that of NbX (1100 versus 1250°C, respectively, Figure 2-31 (Tsuchida 1993)). The higher stability of the MX carbonitride and its relative size (~30 nm in diameter) and distribution compared to $M_{23}C_6$ has a number of beneficial effects inluding the pinning of grain boundaries during

normalization heat treatment, pinning the dislocation substructure in service (i.e. an intragranular effect resulting from the random distribution of MX in the microstructure) and pinning subgrain boundaries in service (i.e. an intergranular effect). Whereas the $M_{23}C_6$ has been shown to coarsen in service reducing its effectiveness in preciptiation strengthening of the matrix, MX has been observed to have significant stabiltiy even in the evaluation of long-term tests (Cipolla 2007, Panait 2010). As will be discussed, MX in combination with elevated Cr is deletrious with regard to the nucleation of Z-phase at the MX precipitate. This is particularly true for the 11 to 12 wt. % Cr martensitic steel grades, although Z-phase has been reported in Grade 91 steel where the microstructure has not been properly homogenized resulting in local increases in the Cr content (Sawada et al. 2017).

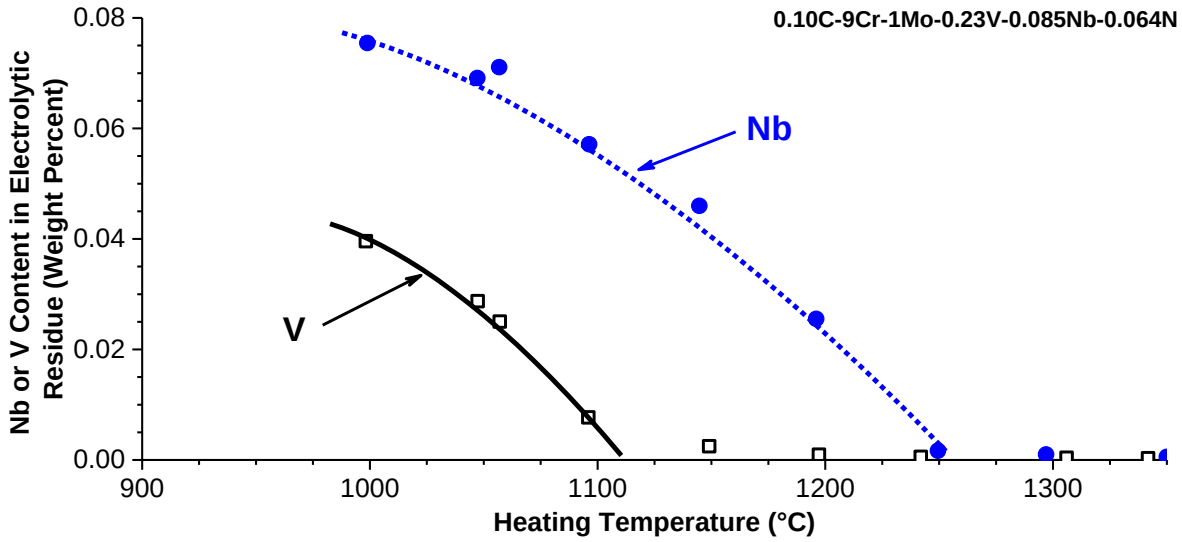

Figure 2-31. Stability of MX precipitates primarily consisting of V (black solid line) or Nb (blue dotted line) and as adapted from (Tsuchida et al. 1993)

M_2X precipitates have a hexagonal structure and although these particles are less commonly reported in Grade 91 steel, they have been observed in selected cases (Sawada et al. 2008, Kaneko et al. 2004). The formation of M_2X typically occurs where low tempering heat treatments have been investigated that are on the order of 675 to 700°C. This has been investigated for parent material in (Sawada et al. 2008) where the authors concluded that following long-term creep (i.e. >20,000 hours at 600°C) the M_2X decays into VX. There has been some association of M_2X with poor performance, namely in (Agamennone et al. 2006) and this poor performance is specific to higher Cr martensitic CSEF steels where the Cr value is >9.5 wt. %. In the opinion of the author in (Sawada et al. 2008) the presence of M_2X is beneficial to the performance

of Grade 91 steel. Further discussion in (Chilukuru et al. 2009) states, “the absence of Z-phase in heat 2A [ref. a 9 wt. % Cr heat with 9.5 wt. % Cr] may be explained by the sensitivity of Z-phase nucleation to the Cr-content which is relatively low in 2A.” This observation highlights the association of higher Cr levels with the formation of Z-phase in establishing potential risk factors in 9 to 12 wt. % Cr steels and as confirmed in (Strang and Vodarek 1997).

Many particles, classified as “deleterious” in Table 2-3 can reduce the effectiveness of the precipitation and solid solution strengthening effects. Z-phase, for example, nucleates on existing MX precipitates and through Cr-diffusion from the matrix and/or the consumed MX precipitate gradually transforms the MX into Z-phase (Hald and Danielsen 2009). Z-phase forms slowly in-service due to the diffusion of Cr and is not present in the as-produced condition. In the most extreme example, grade 122 steel has shown a dramatic loss of strength due to massive Z-phase formation (Kimura et al. 2012). Z-phase has been reported in Grade 91 steel after >80,000 hours of testing at 600°C and directly because of formation from MX precipitates, Figure 2-32 (Sawada et al. 2008). The comparison of the gauge and grip portions indicate that strain-assisted diffusion is important in the evolution of Z-phase at the expense of the existing MX precipitates.

Table 2-3. Summary of nominal composition of precipitates present in Grade 91 steel

Type of Precipitate		Stoichiometry	Composition (weight percent)					
			Cr	Fe	Mo	Nb	V	Si
Precipitation Strengthening	$M_{23}C_6$	$Cr_{23}C_6$(Fe, Mo)	54-65	28-32	7-10	0-2	0-2	2-4
	MX	V(N, C)	8-10	0-1	0-1	10-15	70-80	0-1
		Nb(N, C)	5-10	2-5	10-15	55-65	10-15	0-1
	M_2X	$(Cr, V)_2$(N, C)	70	3-4	11-13	3.5-4.5	8-11	0-1
Deleterious*	Z-phase	Cr(V, Nb)N	43	5-6		17	34	
	Laves	Fe_2Mo (+V, Nb, Si)	7-10	43-49	35-41	0.2-3	0.3-1	4-8
		$(Fe, Cr)_2Mo$ (+V, Nb, Si)	30-35	30-35	30-35	1-2	1-2	4-8

*Other deleterious phases are not listed including AlN and BN (complete compositional information is not widely reported)

In a second and third study examining Grade 91 steel which had been tested at 600°C and for >100,000 hours the number fraction of identified Z-phase precipitates for a representative and large population of analyzed particles was <1% (Cipolla et al. 2007, Ibid 2010) and <6.5% (Panait et al. 2010). Regarding the previously stated findings, this is significant since of the two heats evaluated in (Cipolla et al. 2007, Ibid 2010)

one had a relatively high Cr value for Grade 91 steel (9.12 wt. %). A comparison of the coarsening rate for Z-phase after exposure at 600°C for 100,000 hours is provided in Figure 2-32. In general, and as highlighted in (Hald 2005), “at 600°C and lower temperatures, Z-phase precipitation in the 9 wt. % Cr steels seems to be even slower and may in fact be insignificant to the long-term stability up to 300,000 hours.” As shown in (Sawada et al. 2007), the formation of Z-phase based on a time-temperature-precipitation (TTP) diagram is delayed by nearly two orders of magnitude for 9 wt. % Cr steels compared to 11 or 12 wt. % Cr steels.

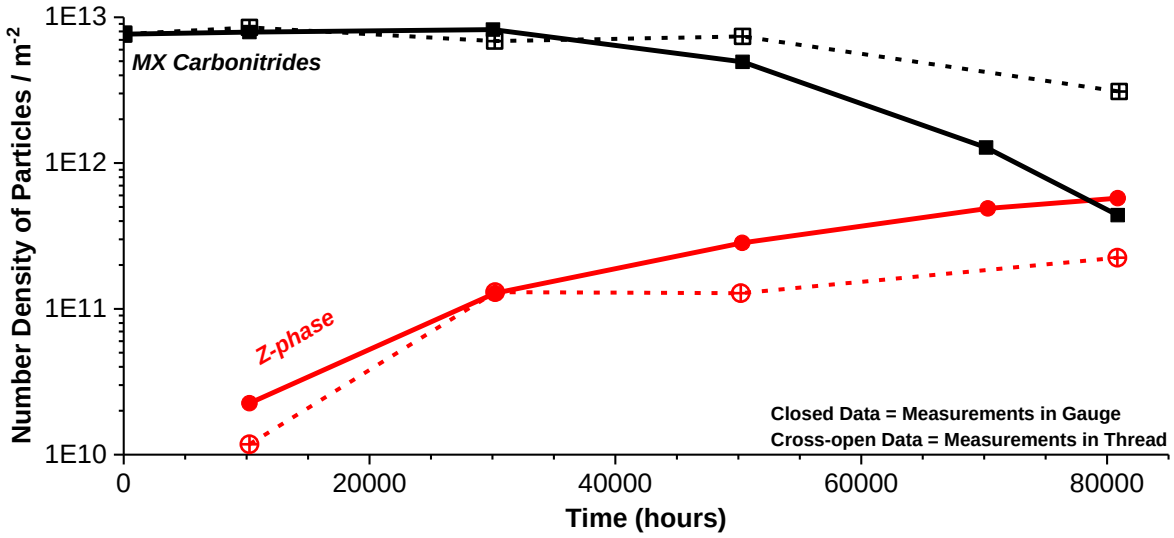

Figure 2-32. Evolution of Z-phase and MX precipitates in Grade 91 steel subjected to uniaxial creep test conditions of 600°C and 70 MPa; the provided comparison is for locations taken from the gauge and threaded sections of the sample (Sawada et al. 2014)

Laves is an intermetallic, hexagonal close packed phase that forms in-service (Panait 2010). Laves phase is seen to coarsen rapidly in Grade 91 steel to >400 nm in diameter after 50,000 hours of exposure at 600°C (Cipolla et al. 2007). The solubility of Laves phase in 9 wt. % Cr steels is generally reported to be ~675°C, Figure 2-33. This phase is stabilized by additions of Mo and especially W. Although the precipitation of Laves phase can be regarded as stabilizing the microstructure and providing a precipitation strengthening effect, its effectiveness in this role is greatly reduced as the operating temperature approaches and/or exceeds 600°C. Because Laves phase can coarsen rapidly, and increase in size to near µm values, it may act as a void nucleation site owing to its size and reported misfit in the Fe lattice (Fedorova 2014). It is seen to preferentially nucleate on high angle grain boundaries [Panait 2009, Fedorova 2014, Kipelova et al. 2011, Dudko et al. 2013] and in some reported cases Laves precipitation can be biased to high angle grain boundaries to the order of 80 to 90%.

A comparison of the coarsening rate for Laves phase after exposure at 600°C and 100,000 hours is provided in Figure 2-30 for common 9 wt. % Cr steels.

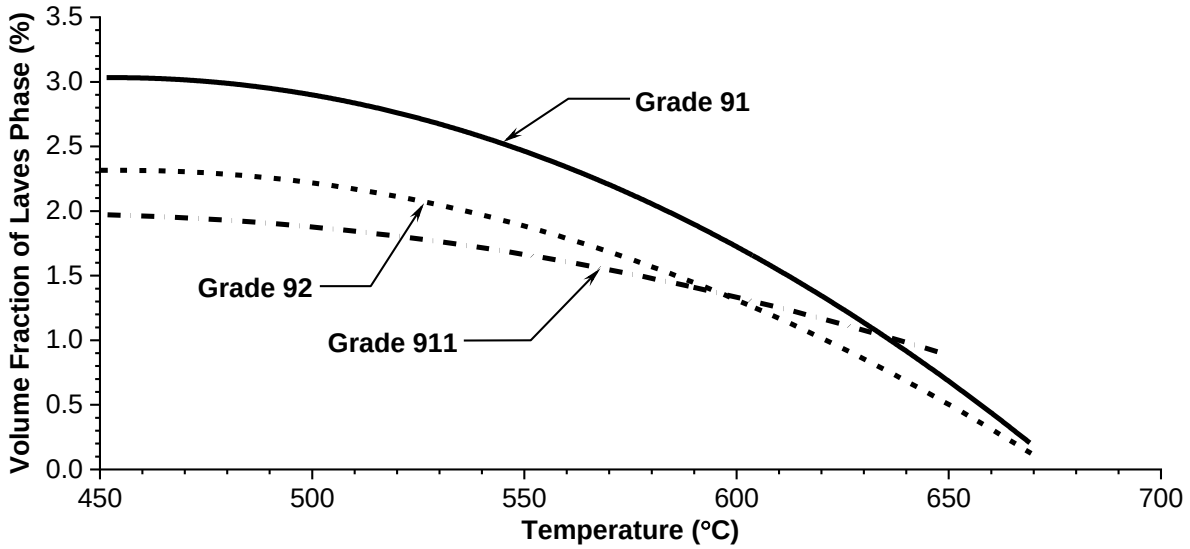

Figure 2-33. Stability of Laves phase in 9 wt. % Cr steels, adapted from (Cipolla et al. 2007)

AlN is a deleterious phase which forms during the steelmaking process. The consumption of N from the matrix prevents the formation of MX precipitates. Because the solubility temperature of AlN is on the order of ~1100°C for susceptible heats of Grade 91 steel, this precipitate cannot be dissolved during conventional normalization and tempering heat treatment of extruded tube or pipe, see Figure 2-34 (Hanton 2007). The maximum normalization temperature in SA-213 T91 or SA-335 P91 is 1080°C (ASME 2017). A similar issue occurs if BN is identified. Although B is not intentionally added to Grade 91 steel the fact that it is not deliberately controlled introduces a potential risk to BN formation. This is especially true since it has been reported that Grade 92 scrap steel is often used in Grade 91 melts (Jarrar 2016). For BN, the stability in 9 wt. % Cr steels appears to be even greater than that of AlN with a solubility temperature of around 1150 to 1200°C (Sakuraya 2006).

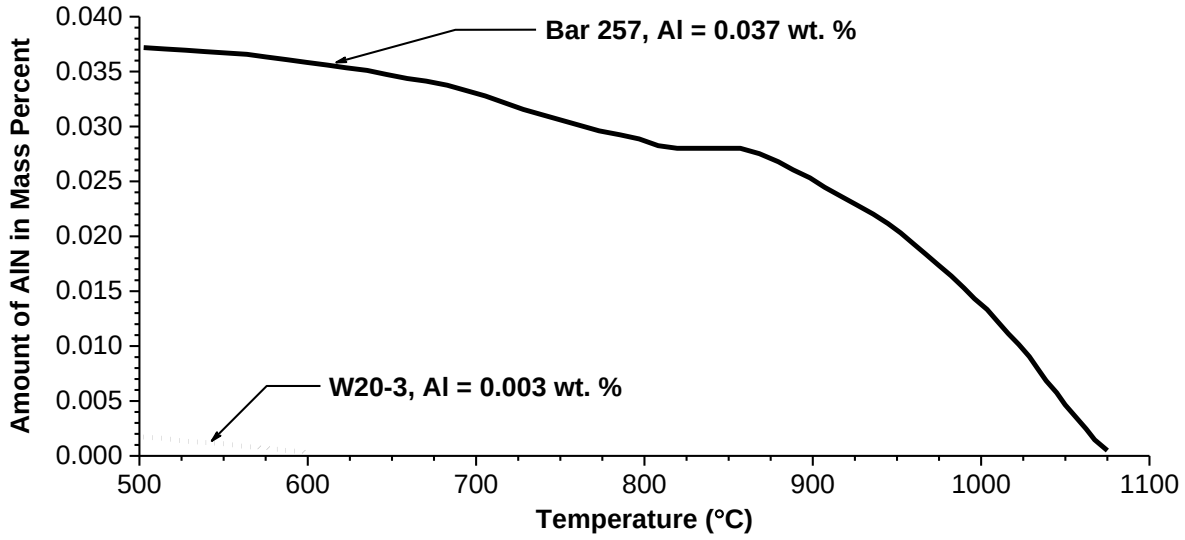

Figure 2-34. Stability of AlN in Grade 91 steel heats with high and low aluminum content (Hanton 2007)

2.10 Influence of Microstructure on Performance

As previously noted, there is a large scatter of performance for Grade 91 steel with regard to creep deformation (i.e. creep strength, Figure 2-19) and creep damage (represented as ROA, Figure 2-20). It is proposed that the general performance of Grade 91 steel parent material can be expressed as a matrix whereby the influence of both deformation (strength) and damage (ductility) are considered in the context of in-service performance, Figure 2-1. Additional information is summarized in Table 2-4 regarding the initial and coarsened size of important precipitates reported in the literature, as well as the complete dissolution temperature, the evolution of the precipitates and the potential effect on creep strength or creep ductility.

Factors controlling deformation are directly linked to the control of the subgrain structure and factors controlling damage are directly linked to inclusions or other precipitates in the microstructure which present preferential sites for cavity nucleation. Since many particles may be present in as-received material or may evolve in-service, there must exist a hierarchy of sites for void nucleation. This reality has been recognized in review articles on creep cavitation since at least 1974 (Perry 1974):

> *"Two general types of mechanism have been invoked…local break-down of adhesion associated with precipitates or impurity particles, possibly of low adhesion with the matrix, has been suggested. Local plastic deformation seems to be a requisite…, i.e. the creep strain is significant. The evidence…in the second case, association of cavities with particles in the grain boundaries has been observed by a number of authors."*

The following sections will thus describe microstructural factors which affect deformation or damage.

Table 2-4. Summary of common precipitates in Grade 91 parent material and the influence of these particles on performance. Based on information from [Gu 2017, Gaffard 2004, Maruyama 2001, Hanton 2007, Panait et al. 2010a, Panait et al. 2010b, Brookes 2015].
Note: *the "coarsened size" is a general description based on available information for Grade 91 or similar steels in test or operation at ~600°C.*

Precipitate	Initial Size (nm)	Coarsened Size (nm)	Complete Dissolution Temp. (°C)	Evolution	Effect on Performance
$M_{23}C_6$	100	200	~875°C	Present in as-received parent material. Coarsens in-service	Reduces subgrain recovery
MX	30	<70	V(C,N) ~1100°C	Resistant to in-service coarsening. May dissolve in-service due to nucleation and coarsening of Z-phase.	Reduces dislocation movement within subgrains and reduces subgrain recovery.
	50	<100	Nb(C,N) ~1250°C		
M_2X	30	<70		Resistant to in-service coarsening. May decay into MX precipitates.	Reduces dislocation movement within subgrains and reduces subgrain recovery.
Z-phase	N/A	200	~800°C	Forms from pre-existing MX precipitates.	Reduction in precipitation strengthening and potential site for nucleation of creep cavities.
Laves	N/A	≥ 400	~675°C	Forms in-service. Evidence suggests it may form in isolation or adjacent to $M_{23}C_6$	Potential degradation of strength is minimal or not existent. May act as a preferential site for nucleation of creep cavities.
AlN	300	Does not coarsen in-service	~1100°C	Forms in the steel making process either during melting (such as Al_2O_3, SIO_2 and MnS) or during processing of billet to final product (AlN and BN). These precipitates do not evolve during typical service conditions.	Consumes available N to form M_2X or MX during final heat treatment. Acts as a preferential site for nucleation of creep cavities.
BN	1,000		~1150°C		
Al_2O_3	>1,000		Stable to the melting temperature		Acts as a preferential site for nucleation of creep cavities and as a potential sink for tramp elements.
SiO_2	1,000				
MnS	>1,000				

2.10.1 Microstructural Features Which Contribute to the Evolution of Damage

The factors influencing damage are far less researched than the factors which control deformation. In many cases, this is simply due to the complex nature involving the nucleation and growth of creep voids and the length scales involved in detecting

particles or separating mutually dependent effects. In general, the nucleation and growth of cavities are simplified into five key variables:

1. Grain boundary sites for cavitation;
2. Particle sites for cavitation;
3. Segregation of tramp elements;
4. Orientation of the boundary/particle with respect to the applied stress;
5. Temperature.

Unlike bainitic steels where cavitation was observed to preferentially occur in deformation zones adjacent to the PAGB or on specific inclusions associated with sulphides such as detailed in (Middleton 1981), the cavitation in martensitic steels is more complex. Interspersed cavities characteristic of relatively low creep strain values were reported on low and high angle boundaries in (Sandstrom and Wu 1995). In the martensitic steel X20, the authors describe this reality (Eggeler et al. 1989):

> *"A characteristic feature of creep cavitation in high chromium ferritic steels is that cavities are not only found on former austenite grain boundaries but also in the interior of former austenite grains. There are additional internal surfaces such as subgrain boundaries and high angle ferrite boundaries which have formed during tempering, where segregation can occur preferentially and which will facilitate diffusion."*

Supporting this observation is the evaluation of an X20 creep test performed at 550°C whereby the conclusion was that both block and packet boundaries were associated with creep cavities (Yardley et al. 2015). In the assessment of damage in Grade 92 steel, cavities were not preferentially distributed along high angle boundaries but present throughout the martensitic structure, Figure 2-35 (Gu 2017). Based on the available research, there is sufficient evidence that not one type of boundary is susceptible to damage in martensitic steels and more generally it should be concluded that damage *can be present throughout the microstructure*.

Inclusions of the type Al_2O_3, MnS, SiO_2, or Ca-modified are likely to be present. Inclusions have been identified as key sources for void nucleation in Grade 91 steel and as highlighted in Figure 2-36 (Kobayashi et al. 2013 and Gu et al. 2013). Additional inclusions, such as TiN, AlN (in Grade 91 steel, [Yadav et al. 2015]) or BN (in grade 92 steel, [Gu et al. 2013]) and the formation of Laves phase (Panait 2010, Cipolla et al. 2010) or Z phase (Sawada et al. 2008) may also act as cavity nucleation sites.

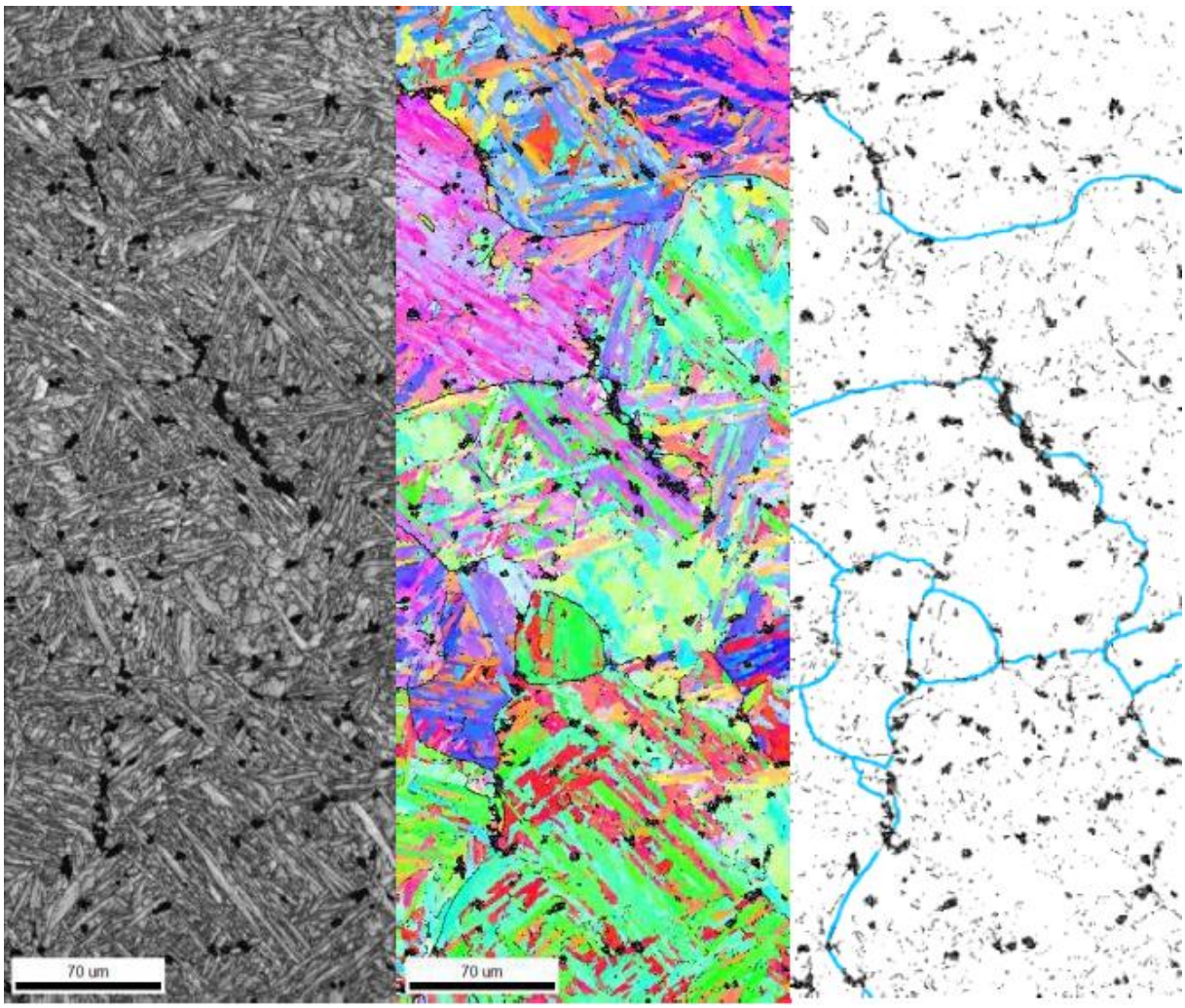

Figure 2-35. Evaluation of damage in a grade 92 notch test. The applied stress is in the horizontal orientation.
Note: *the lack of clear association of damage with the outlined high angle grain boundaries, from (Gu 2017)*

In examination of creep cavitation in Grade 91 steel tested at 650°C and 70 MPa cavities were observed to exhibit a dual distribution of coarse (mean diameter of 2.5 µm) and fine (<0.6 µm) cavities (Yadav et al. 2015). It was rationalized that the coarse cavities were pre-existing in the material and the fine cavities were formed throughout the creep test (e.g. by a continuous nucleation mechanism). In the analysis of the coarse cavities (which were reported to be the primary factor governing failure) there was an association with Al leading the authors to deduce that the particles inside the cavities were associated with AlN. Furthermore, the AlN was often reported in association with $M_{23}C_6$ carbides (i.e. potential co-precipitation effect). This co-precipitation effect was also reported in (Brookes 2015) where an example provided

in Figure 2-37 shows a creep void around a complex interaction of MnS, Al_2O_3, AlN and NbN particles.

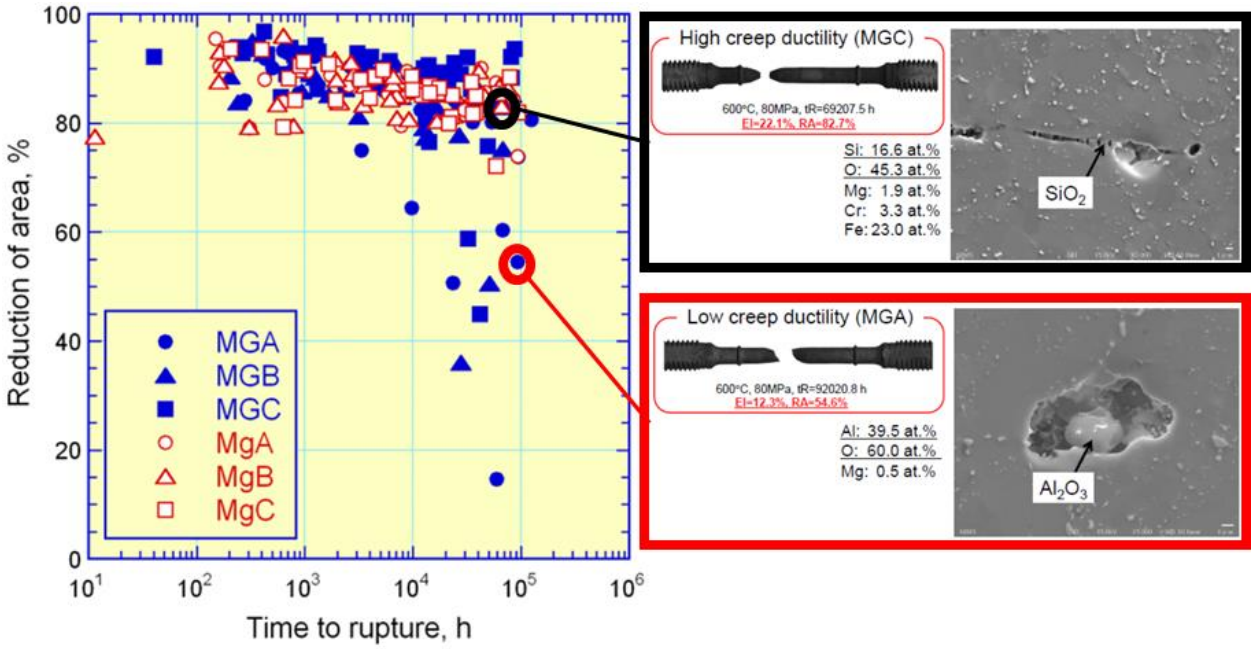

Figure 2-36. Evaluation of creep samples from the NIMS database and association of cavitation with oxide inclusions, from (Kobayashi et al. 2013)

Laves phase has been observed to act as a void nucleation site in Grade 91 steel, as shown in Figure 2-38 (Cipolla 2007). A second set of observations were made by Panait (2009) for grade 92 steel further supporting the idea that Laves phase acts as a void nucleation site. In (Panait 2009) it is suggested that while coarse Laves phase was often associated at or near a creep void, there is clear evidence in the provided images that voids were not consistently associated with Laves phase. Additional investigations in (Panait 2010) looking at the association of Laves phase with creep damage in as-received and aged grade 92 samples reached a similar conclusion in that:

> *"Small cavities are observed close to large laves phases indicating that these phases might be nucleation sites of creep damage. However, no significant change was observed in the amount of creep damage (number of cavities, size of cavities) in the thermally aged specimens compared to that in as-received T92 steel creep tested at 650°C for similar amounts of time…. Although laves phases are frequently observed in the vicinity of creep damage cavities, the precipitation of laves phases does not seem to enhance creep damage development."*

In the assessment of the creep ductility for grade 92 in the NIMS database, it is apparent that low ductility failures are reported at 700°C, a temperature that is above the stability range for Laves phase. Although it is recognized that creep voids have

been associated with Laves phase, it may not provide a dominate site for cavitation at least in the scenario where other more preferential sites exist (i.e. inclusions).

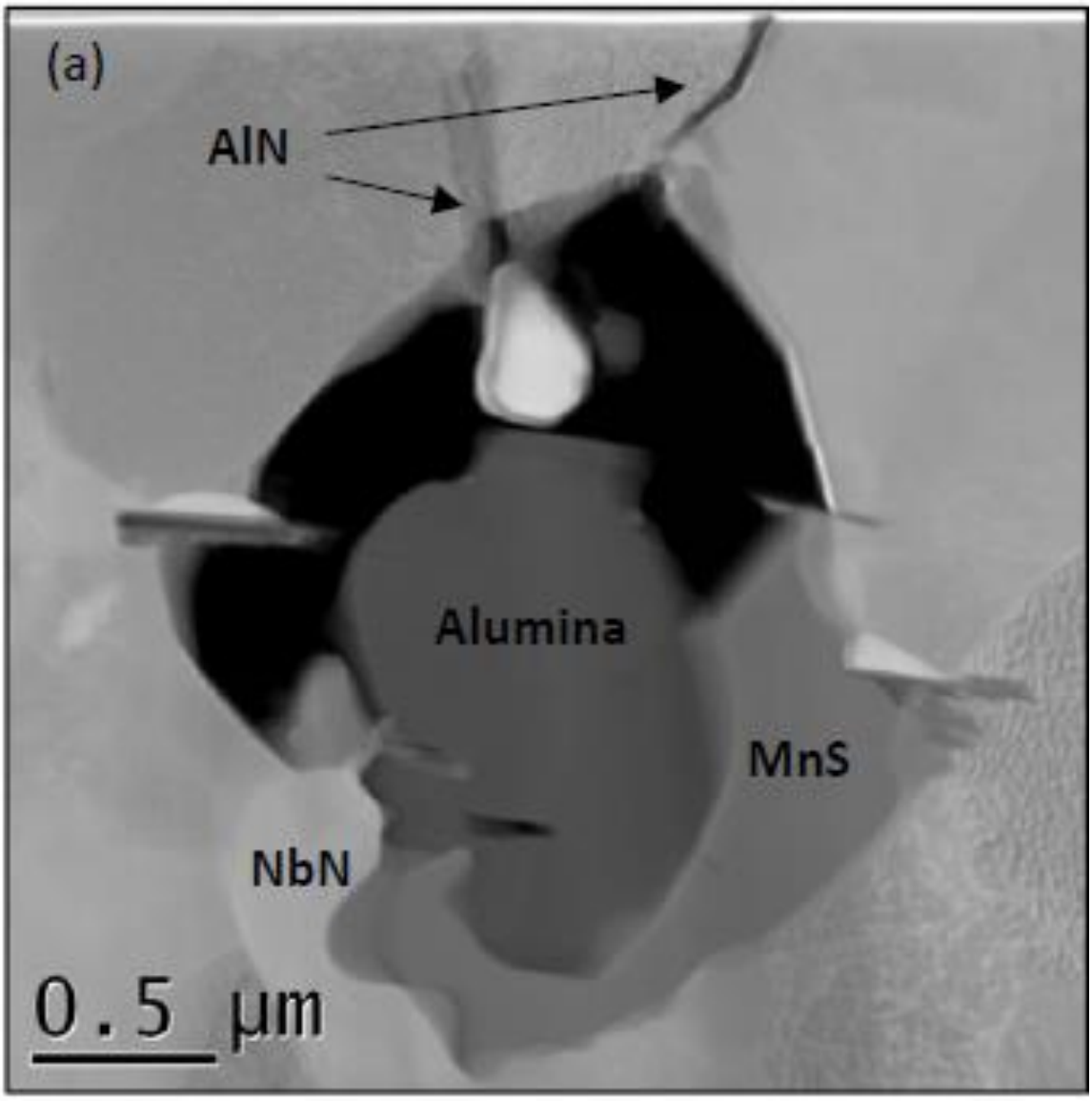

Figure 2-37. Cavitation formation around a complex cluster of particles including inclusions (MnS, Alumina, AlN) and a NbN carbonitride, from (Brookes 2015)

Although it is generally recognized that there is a clear potential for the presence of deleterious elements such as As, Cu, S, Sb and Sn (and maybe others) to increase the susceptibility to damage, traditionally little research has tried to isolate or examine these effects in martensitic steels. However, and from a variety of references specific to Fe-based studies, low alloy steels and tempered martensitic steels, these elements are clearly detrimental even if the complexities of their cumulative effects are not well-understood.

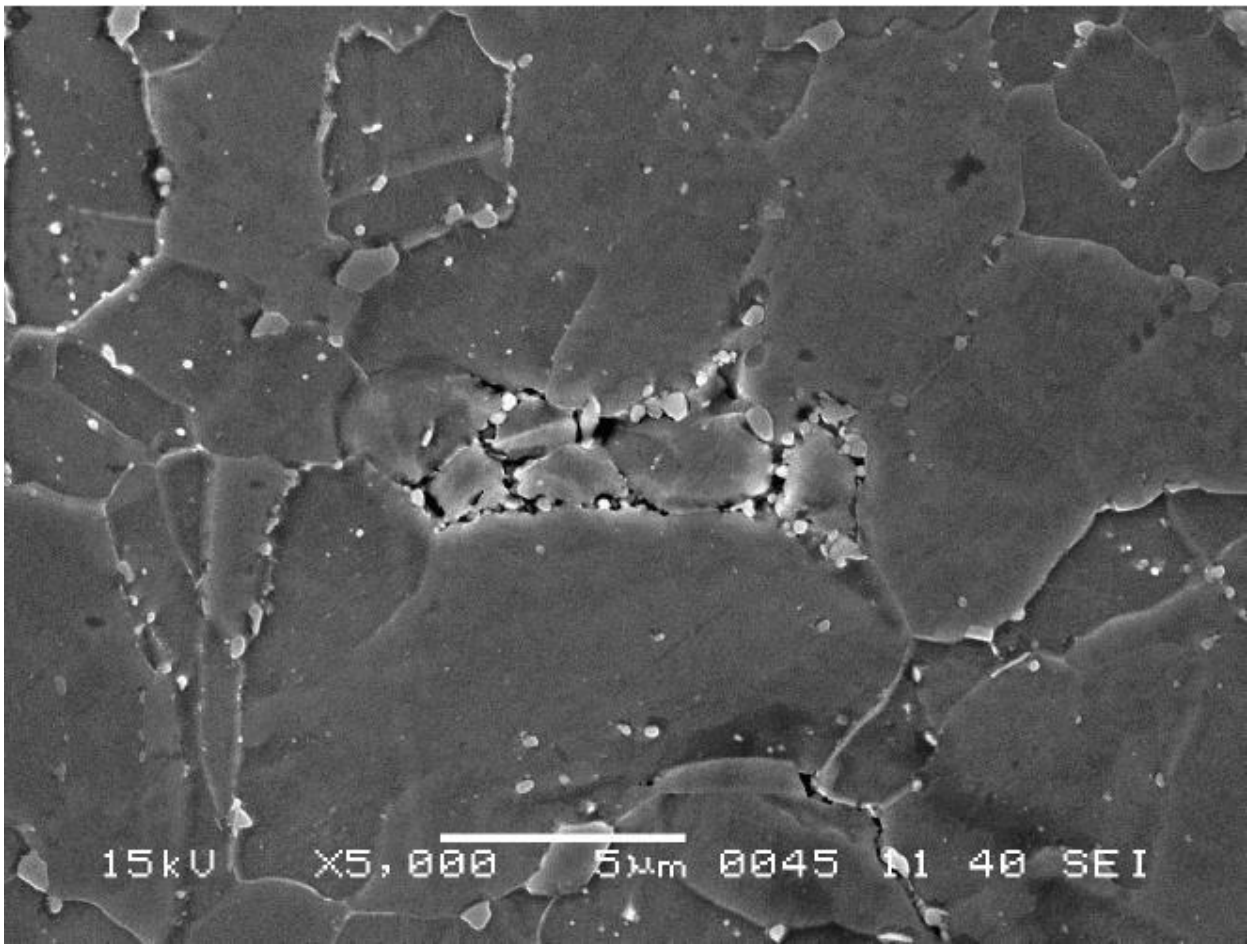

Figure 2-38. Cavitation at coarse Laves phase particles in Grade 91 steel following testing at 650°C for 20,014 hours from (Cipolla 2007).

Impurities may affect interfacial properties in steels in four ways: grain boundary and surface energies; grain boundary and surface diffusivities; grain boundary sliding; and grain boundary migration (White et al. 1984). Since in tempered martensitic steels, the effect of grain boundary sliding is negligible due to the high population of precipitation strengthening phases, the local effects of impurities can result in increased susceptibility to void nucleation. In the case of tramp elements in Fe, a plot was developed showing the effect of individual elements on grain boundary embrittlement, Figure 2-39 (Seah et al. 1980). In this analysis (and only showing elements relevant to the alloying or potential observed tramp elements in 9 to 12 wt. % Cr steels), elements like As, Sb and Sn are particularly potent.

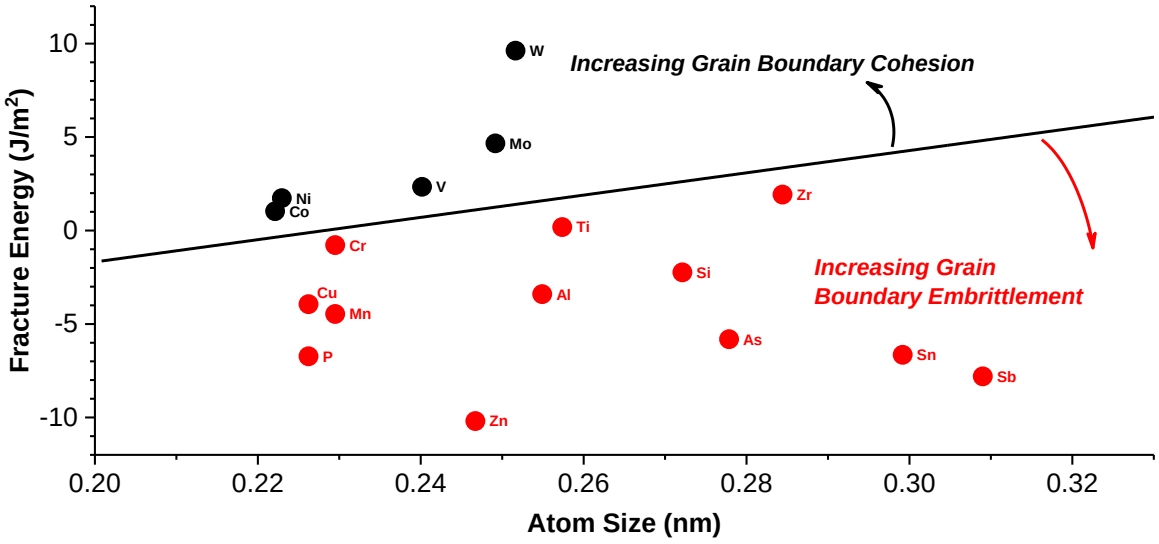

Figure 2-39. Comparison of relevant elements in 9 to 12 wt. % Cr martensitic steels and the effect of each element on cohesion or grain boundary embrittlement, adapted from (Seah et al. 1980)

There has been some suggestion, such as in the analysis performed in (George et al. 1998) for 2.25 wt. % Cr and 1 wt. % Mo steels, that elemental effects could also be cooperative. Where single additions were made of Sn and Sb, these elements were particularly deleterious to the high temperature ductility (expressed as reduction of area) whilst additions of Sn or Sb combined with an addition of P were not. Furthermore, and as reiterated in (White et al. 1984) there are potential deleterious effects of Ni on the segregation of tramp elements. Lastly, the addition of Ce in Fe increases the solubility of S in Fe effectively counter-acting the deleterious effect of S alone (George et al. 1987). Thus, the complexities involving tramp elements are not simply rationalized or explained based on a single element or factor and should consider a wider range of effects which may include compounding or counter-acting reactions.

Analysis of two heats of Grade 91 steel including a conventional heat and a Sn-doped heat (i.e. 0.004 versus 0.058 wt. %) were reported in (Song et al. 2014). Although the creep tests in this study were not markedly long (~1,000 hour maximum duration), a comparison of the heats was made using a damage tolerance parameter, λ, as calculated in Equation 2.6 using the minimum creep rate (ε_m), strain at rupture (ε_r) and time to failure (t_r).

When failure is dominated by intergranular cavitation, the value of λ is typically in the range of 1 to 2.5; the minimum value for the Sn-doped samples was calculated to be 2.39. A comparison of the gauge cavitation behavior supported this calculation – there

was dramatically more cavitation in the Sn-doped samples than in the conventional heat. To examine if Sn was segregating to subgrain boundaries in the Grade 91 steel, the authors evaluated several, precipitate-free subgrain boundaries. The focus on the subgrain boundaries was necessary because the high angle grain boundaries were nearly 100% decorated in precipitates making it impossible to perform a similar study in these locations. Their results, which are provided in Figure 2-40 showing a marked concentration in the Sn level at the subgrain boundary after creep testing at 600°C and 150 MPa for 441 hours that is at least an order of magnitude more concentrated than that in the matrix.

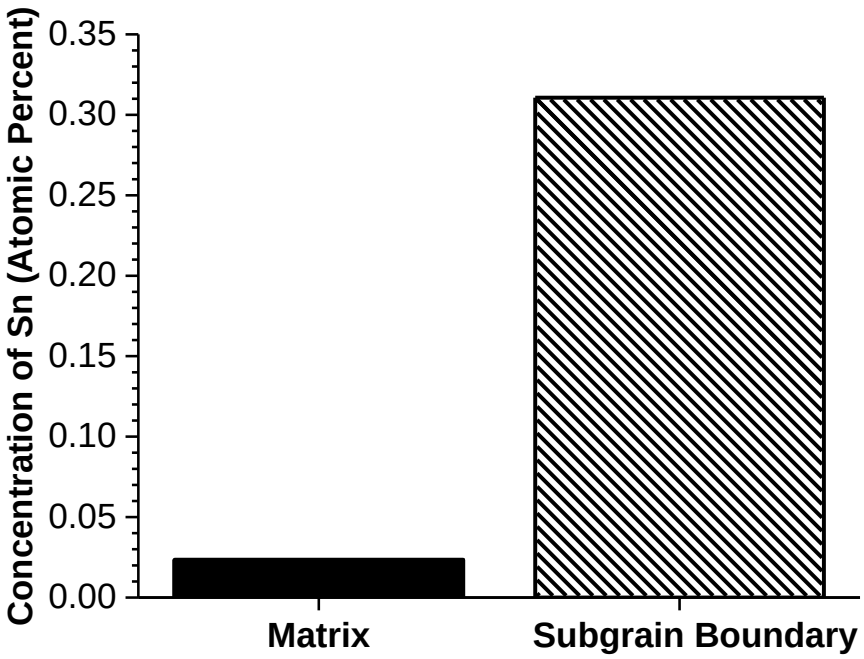

Figure 2-40. Concentration of Sn at the subgrain boundary in the post-test condition in Grade 91 steel (600°C, 150 MPa), adapted from (Song et al. 2014)

Adding to the complexity of tramp element interactions is the specific association between particles such as inclusions and carbides and increased concentration of Al, Cu, As, Sb or Sn. This is primarily true for inclusions/particles resulting from the steel making process in Grade 91 steel (specifically Al_2O_3, MnS, SiO_2 and AlN). The concentration of deleterious elements at inclusions locally reduces the interfacial energy and reduces the minimum critical strain required to nucleate a void. It has not been researched whether specific inclusions are more effective trap sites than others, but this effect is observed in a Grade 91 steel and is provided in Figure 2-41 where there is an observed “trap” effect for Cu and Al around a MnS inclusion (Brookes 2015).

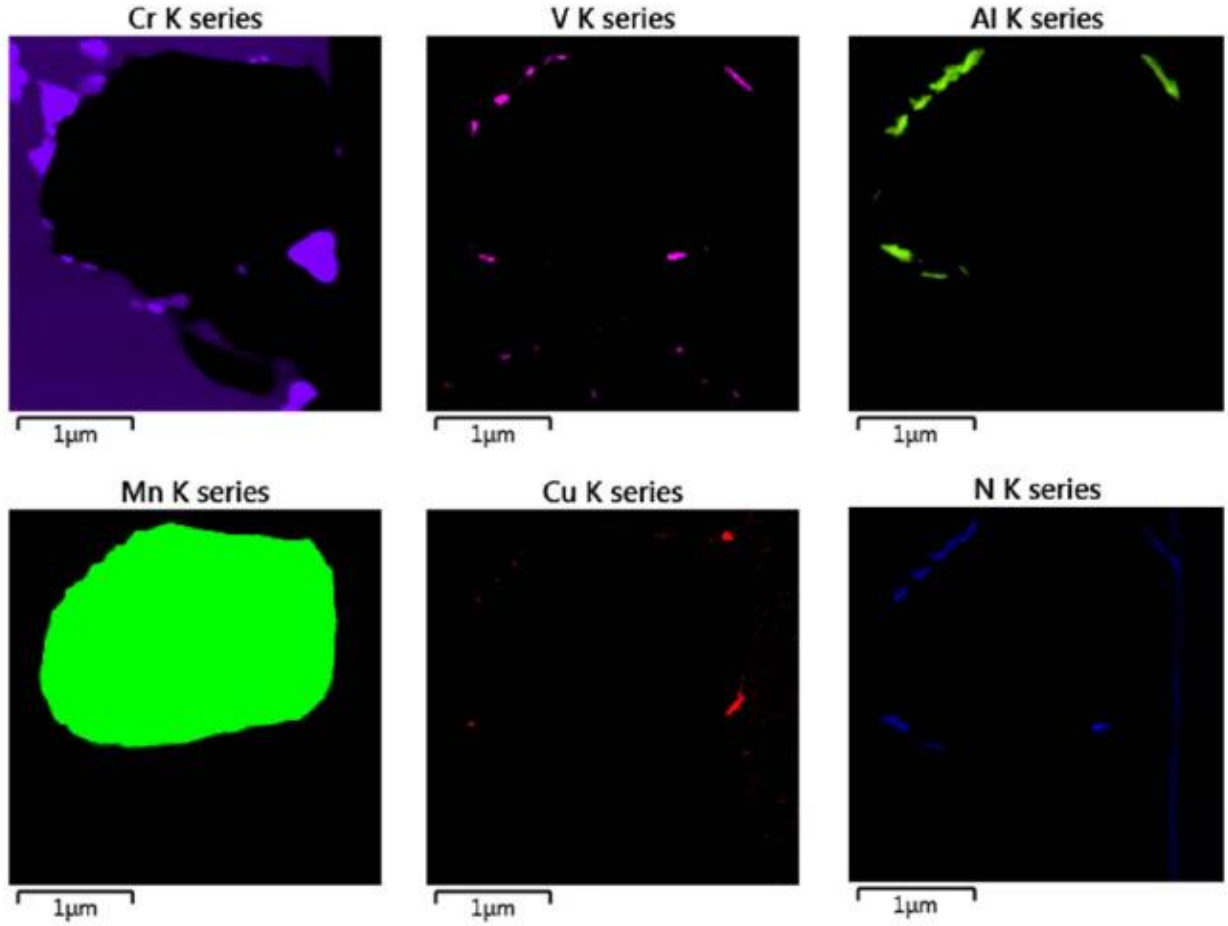

Figure 2-41. Association of a MnS inclusion as a trap site for Cu and Al in a Grade 91 steel from (Brookes 2015)

Several cooperative effects have been researched in the literature examining whether particles act as trap sites or sinks for impurity segregation. In the work in (George et al. 1987), Fe was doped with individual additions and combined additions of C, S, O, N, P and Ce. This research provided several key conclusions: cavities were not observed at carbides even in the presence of sulfur; phosphorous improved the creep ductility; and oxides were important cavity nucleation sites when sulfur was present at an intermediate level (~<0.020 wt. %). Building on these observations, the authors provided two key conclusions (George et al. 1987):

- Sulfur segregation to the oxide-matrix interface locally weakens the interface increasing the susceptibility to void nucleation. However, and based on the set of findings, it was proposed that C and P compete with S for these oxide-interface sites such that the deleterious effects of S were not readily observed at all carbide sites (i.e. not all carbides were observed to act as sites for creep voids);

- There was a clear hierarchy among particles in Fe governing the nucleation of voids. Sulfides were the most susceptible, followed by oxides (and especially where segregated sulfur was present at the oxide interface) and carbides were the least harmful. The observation of the particularly deleterious effect of sulphides is not without historical precedence since sulphides were identified as key nucleation sites in bainitic, low alloy steels (Middleton and Cane 1981).

Regarding S, auger electron spectroscopy (AES) has been used in X20 (Eggeler et al. 1989) to show that S was assisting the cavitation process. S was observed to segregate between a particle and the matrix where S is present in a weight percent > 30 ppm. Regarding X20, it was concluded that S was preferentially migrating to $M_{23}C_6$ carbides. This is an important observation since it has been stated that the solubility of S in an Fe-Mn material is very close to the stated threshold value of 30 ppm (Turkdogan and Pearson 1955).

2.10.2 Microstructural Features which affect Creep Deformation

Deformation in the context of this discussion is defined by microstructural attributes which contribute to a resistance to cavity growth. Based on the previous discussion and throughout the literature there are four potential mechanisms which reduce the deformation resistance in 9 wt. % Cr steels:

1. Localized microstructure recovery at high angle grain boundaries such as in (Kushima et al. 1999).
2. Reduction in MX by the formation of Z-phase such as reported in (Sawada et al. 2008). Z-phase has not been widely or consistently reported in grades 91 and 92 steels even after long-term creep tests.
3. Reduction of solid solution hardening by the formation of Laves phase such as suggested in (Panait et al. 2010 IJPVP, Cipolla et al. 2010). Although Laves phase has been reported, a dramatic loss in strength has not been correlated with the onset of Laves phase formation. As previously discussed, the contribution of Laves-forming elements Mo and W to solid solution strengthening in Grades 91 and 92 is not sufficient to warrant serious consideration as a deformation-weakening mechanism.
4. Recovery of the subgrain microstructure. It is proposed here that the key, controlling factor governing the resistance to deformation in tempered

martensitic steels is the resistance to subgrain recovery. Recovery can occur in two ways: strain-assisted (e.g. creep) or static (e.g. aging) and fundamentally results in a reduced pinning force by $M_{23}C_6$ which is the dominate grain boundary strengthening particle for 9 wt. % Cr steels manufactured using conventional processing routes (Abe 2014).

Tempered martensitic steels should be regarded as meta-stable (Robson and Bhadeshia 1997, Strang et al. 1999). As such, the influence of time, temperature and stress can have dramatic influences on the rate of recovery in the microstructure. Since tempered martensitic steels possess a very high density of dislocations and a fine subgrain structure, the introduction of stable particles (such as MX, M_2X and $M_{23}C_6$) can reduce or remove the driving force for recovery resulting from the dislocations in the structure (Maruyama et al. 2001). Schematics showing the location and potential effect of $M_{23}C_6$, MX, and Fe_2M (Laves phase) in the matrix are given in Figure 2-42A and Figure 2-42B. The distribution of carbides (including identified Z-phase) is provided in Figure 2-43 for different heats of Grade 91 steel. In summary, the function of carbonitrides in martensitic steels is three-fold (Kosta et al. 2007):

1. Impede knitting reactions between free dislocations and subgrain boundaries;
2. Exert Zener forces on subgrain boundaries and;
3. Prevent/delay the onset of recrystallization at large creep strains.

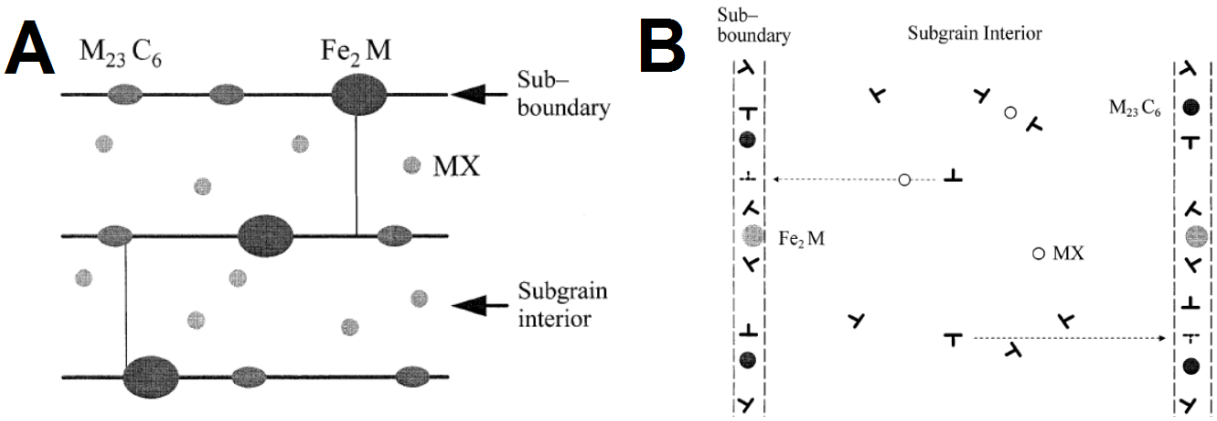

Figure 2-42. Schematic showing the location of precipitates in the substructure in Grade 91 steel. A – location of $M_{23}C_6$, MX and Laves phase (Fe_2M) relative to the sub-boundary and subgrain interior; B – effect of MX precipitates in subgrain interior on impeding dislocation movement (Maruyama et al. 2001)

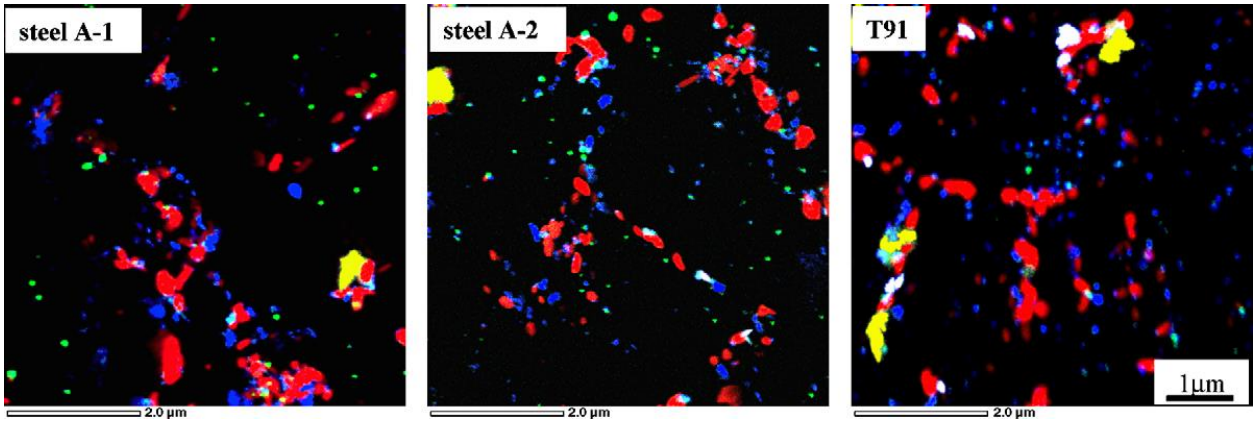

Figure 2-43. Evolution of precipitates in Grade 91 steel after creep testing at 600°C and for 20,741 hours (Steel A-1); 24,330 hours (Steel A-2) and 12,858 hours (T91).
Note: *the following: red = $M_{23}C_6$; blue = VX; green = NbX; yellow = Laves phase; white = Z-phase and the following composition and normalization + tempering of each steel: Steel A-1 = 1050°C/10 min/AC + 765°C/30 min/AC; Steel A-2 = 1050°C/30 min/AC + 680°C/30 min/AC; Steel T91 = 1050°C/30 min/AC + 730°C/30 min/AC. (Sawada et al. 2008)*

	C	Si	Mn	P	S	Ni	Cr	Mo	V	Nb	Al	N
ASME-T91	0.0900	0.29	0.35	0.009	0.002	0.28	8.70	0.90	0.22	0.072	0.001	0.044
Steel A-1, A-2	0.0870	0.30	0.45	0.002	0.001	0.03	8.89	1.06	0.22	0.08	0.001	0.049

These fundamental aspects of deformation can also be thought of in the context of a the creep curve in Figure 2-2 whereby the primary creep stage from time zero to secondary creep is governed by the movement and rearrangement of free dislocations, the time length and reduction in secondary creep is governed by the distribution of particles on subgrain boundaries, the transition to tertiary creep stage (and especially near to end of life) is governed by the resistance to plastic deformation and end of life where creep begins to dramatically escalated and is defined by dynamic recrystallization of the subgrain structure (Pesicka et al. 2003).

As a means of measuring the effectiveness of $M_{23}C_6$, MX and laves from the perspective of precipitation strengthening, calculations have been made comparing the pinning pressure using the relationship developed by Zener and detailed for a 9 wt. % Cr steel in (Kipelova et al. 2011), Equation 2.15:

Equation 2.15. $$P_Z = \frac{3\gamma F_v}{d} \text{ or } P_L = \frac{3\gamma l_o F_v}{d^2}$$

Where γ is calculated using the Read and Shockley equation given in Equation 2.16:

Equation 2.16. $$\gamma = \frac{Gb\theta \times (A - \ln\theta)}{4\pi \times (1 - \upsilon)}$$

The descriptions for each of the terms in Equations 2.15 and 2.16 are given in Table 2-5. Using Equations 2.15 and 2.16, the authors in (Kipelova et al. 2011) calculated the pinning pressure for each of the precipitates. An additional scaling factor was employed since in the investigated 9 wt. % Cr steel, the number of $M_{23}C_6$ particles per unit area at high angle boundaries were ~2X those at low angle boundaries. A similar set of observations were made for Laves phase, although in this case ~90% of the Laves phase was found to exist on high angle boundaries. The calculated pinning pressures are provided in Table 2-6.

Table 2-5. Description of terms in equation 2.15 and equation 2.16

Term	Description
γ	Surface energy of a lath boundary given by the Read and Shockley equation
F_v	Volume fraction of particles in matrix
d	Size of particle
l_o	Lath thickness
P_Z	Pinning pressure of randomly distributed MX particles
P_L	Pinning pressure of particles (such as $M_{23}C_6$ and Laves) distributed on martensitic laths
G	Shear modulus
b	Burger's vector (0.25 nm)
Θ	Misorientation of the grain boundary
A	Constant (0.45)
v	Poisson's ratio (0.30 for Grade 91 steel)
M	Taylor factor (3)
λ	Mean interparticle spacing
λ_{sg}	Lath width

Table 2-6. Calculated pinning pressure (given in MPa) for MX, $M_{23}C_6$ and Laves phase for creep tests at two conditions

Value	Particle	Calculated Pinning Pressure given in MPa for a Creep test conducted at 600°C, 200 MPa, 4,103h		Calculated Pinning Pressure given in MPa for a Creep test conducted at 650°C, 120 MPa, 4,743h	
		Thread	Gauge (Necked Location)	Thread	Gauge (Necked Location)
P_Z	MX	0.05	0.05	0.03	0.03
P_L	$M_{23}C_6$	0.50	0.21	0.27	0.09
P_L	Laves	0.02	0.02	0.01	0.01

The provided data is notable in that it suggests the pinning pressure from $M_{23}C_6$ is ~an order of magnitude greater than that of MX. The reported volume fraction of $M_{23}C_6$ in 9 wt. % Cr steels ranges from 5 to 10X greater than that of MX, and the $M_{23}C_6$ is preferentially distributed along low and high angle grain boundaries as opposed to randomly distributed (as is the case of MX). Furthermore, and as suggested in (Panait et al. 2010) following the evaluation of Grade 91 steel tests after >100,000 hours of

test duration at 600°C, the authors concluded that their results suggest that the loss in deformation resistance is mainly a result of $M_{23}C_6$ coarsening, Laves phase formation and coarsening and recovery of the matrix.

A second illustration calculating the effectiveness of precipitates on strengthening the microstructure is given in Equation 2.17 for calculation of the Orowan stress (σ_{or}), which provides a means to measure the threshold stress required for a dislocation to bypass a precipitate (Abe 2008):

Equation 2.17. $$\sigma_{or} = \frac{0.8MGb}{\lambda}$$

Consideration of this strengthening parameter is appropriate since carbonitrides at block and lath boundaries prevent the climb, redistribution and annihilation of dislocations at these boundaries. Using Equation 2.17, the effectiveness of Laves, $M_{23}C_6$ and MX is provided in Table 2-7 (Abe 2008). In addition to the individual particle calculations, a calculation for the strengthening provided by lath and block boundaries is given by Equation 2.18:

Equation 2.18. $$\sigma_{sg} = \frac{10Gb}{\lambda_{sg}}$$

Assuming a subgrain lath boundary width of 3 to 5 μm, a value of σ_{sq} = 320 to 530 MPa is obtained, Table 2-7. This value is much larger than the potential individual effects considered by fine Laves phase or $M_{23}C_6$ or MX or an additive effect of all three. The subgrain boundary hardening is enhanced by the controlled distribution of $M_{23}C_6$ and MX particles along these grains. The resistance to recovery of the subgrain structure in martensitic steels has been directly correlated to the spacing between $M_{23}C_6$ carbides, Figure 2-44 (Armaki et al. 2011). From the basis of these results the authors suggest a key relationship (Equation 2.19) linking the subgrain size ($\lambda_{S.g.}$) to the $M_{23}C_6$ carbide spacing (λ_P):

Equation 2.19. $$\lambda_{S.g.} = 0.138 \times \lambda_P^{4/3}$$

Table 2-7. Reported Orowan stress or sub-boundary hardening for major particles and subgrain features in 9 wt. % Cr martensitic steels

Particle	Volume Percent (%)	Diameter, d_p (nm)	Spacing, λ_p or Lath/Block Width, λ_{sg} (nm)	Orowan Stress, σ_{or} or Sub-boundary Hardening σ_{sq} (MPa)
Laves	1.5	70	410	95
$M_{23}C_6$	2	50	260	150
MX	0.2	20	320	120
Lath and Block Boundaries	N/A	N/A	300	320
			500	530

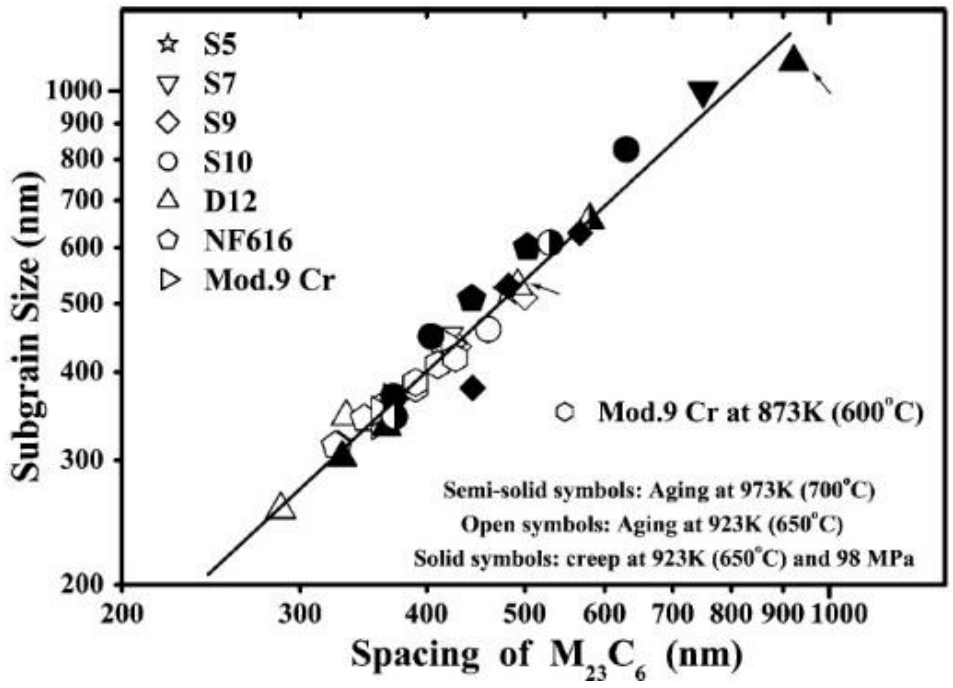

Figure 2-44. Subgrain size as a function of the spacing between $M_{23}C_6$ carbides. Data taken from aged and crept samples, from (Armaki et al. 2011)

Panait demonstrated the recovery in Grade 91 and grade 92 steels using a comparison of carefully sorted EBSD measurements for the as-received and crept conditions (Panait 2010). Consideration of the various grain boundary misorientation angles led to the conclusion that a distinct reduction in the low angle grain boundary fraction of 2-5° in the crept and/or aged conditions and balanced by a notable increase in the total grain boundary fraction >15°, Table 2-8. Additional investigations examining the recovery of the subgrain structure were investigated in (Panait et al. 2010) using TEM and verified this increase for a statistically relevant distribution of measurements, Figure 2-45.

Table 2-8. Comparison of low and high angle grain boundary fractions using electron backscatter diffraction map sizes of ~80 X 80 µm and a step size of 0.15 µm and for P91 and P92 in the as-received condition and following long-term creep testing (Panait 2010)

Material	Condition	Location	Total Length (Fraction)		
			2-5°	5-15°	15-180°
P91	As-Received		0.452	0.133	0.416
			0.410	0.128	0.462
			0.453	0.132	0.416
	113,431h at 600°C	Head	0.210	0.162	0.627
		Head	0.193	0.166	0.641
		25 mm from fracture surface	0.210	0.162	0.627
P92	As-received		0.303	0.151	0.546
	33,308h at 650°C	5 mm from fracture surface	0.190	0.137	0.672
			0.190	0.136	0.673

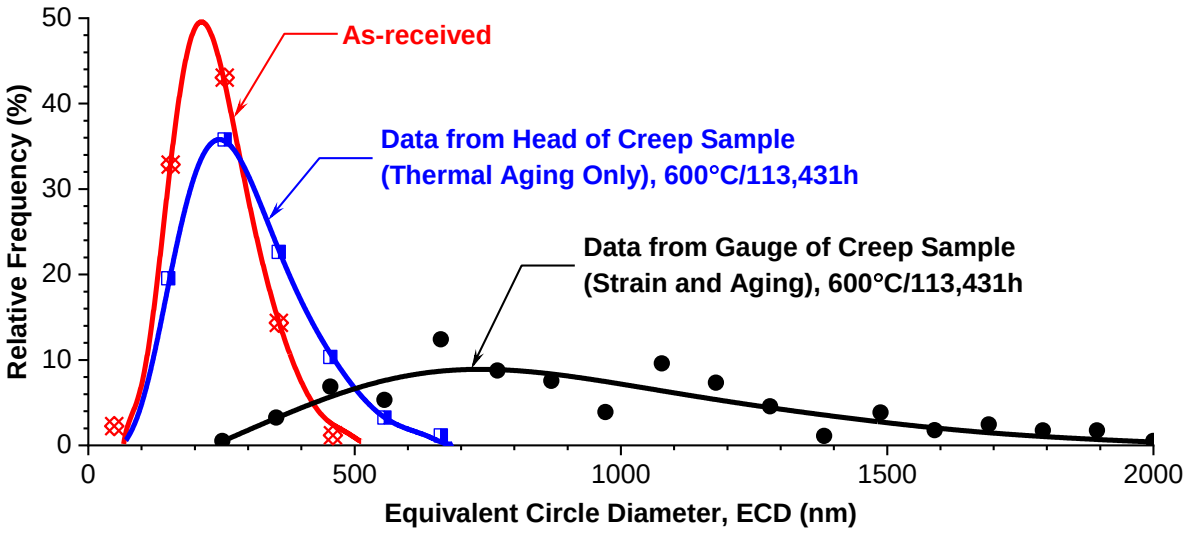

Figure 2-45. Comparison of the subgrain size represented as an equivalent circle diameter (ECD) for Grade 91 steel in the as-received condition and following a creep test at 600°C for 113,431 hours. Provided data for the equivalent circle diameter (ECD) represents a total number of ~150 measurements for each condition, adapted from (Panait et al. 2010)

The results across a large range of martensitic steels has shown that the properly termed creep strengthening mechanism in tempered martensitic steels is “carbide stabilized substructure hardening” (Kosta et al. 2007). This is reinforced in the schematic in Figure 2-46 where the room temperature hardness and decay is given as a contribution of the ferrite matrix, dislocations and precipitates/high angle boundaries (Sawada et al. 2005). The loss of deformation resistance is an important consideration in the evaluation of performance, but it is important to emphasize that the contribution of deformation to performance does not fully account for premature failure resulting from the nucleation and growth of creep cavities. In the next section,

the impact of the welding thermal cycle on the tempered martensitic matrix will be summarized.

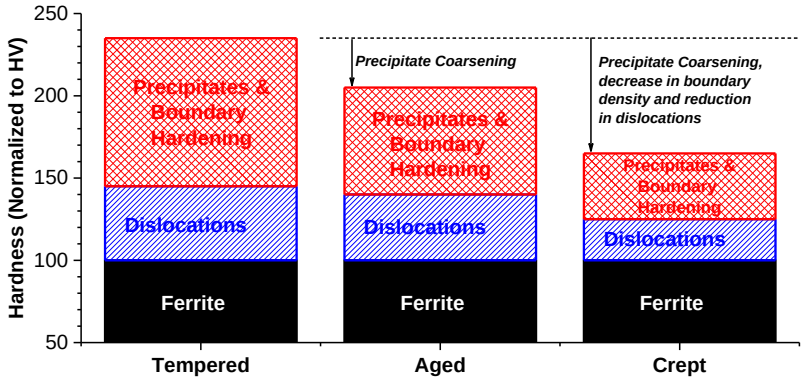

Figure 2-46. Contribution of the BCC ferrite matrix, dislocations, precipitates and subgrain hardening to measured hardness values in the tempered, aged and crept conditions, from (Sawada et al. 2005)

2.11 Weldability of 9-12 wt. % Cr Martensitic Creep Strength Enhanced Ferritic Steels

Welding processes or thermal processing exceeding the lower critical phase transformation (Ac_1) will produce a region in the fabricated component known as the HAZ. Formation of the HAZ is characteristic for all conventional welding processes utilized to join 9 wt. % Cr CSEF steels. In all cases the commonly specified arc welding processes exceed the melting temperature for this class of materials.

Martensitic 9 wt. % Cr CSEF steels are generally regarded as highly weldable materials. The countless number of new and replacement components fabricated since the late 1980s supports this assertion. Gross issues have not been widely reported for common, fabrication weld cracking mechanisms, such as:

- **Hydrogen induced cracking (HIC).** The reduction in susceptibility to HIC in 9 wt. % Cr CSEF steels compared to 12 wt. % Cr steels, such as X20, can be attributed to the reduction in nominal carbon value from 0.20 wt. % in these high Cr steels to 0.10 wt. % in Grade 91 or Grade 92. As reviewed in (EPRI 2015b), the reduction in carbon has a significant effect in reducing the hardenability and the peak hardness in the HAZ or weld metal to <425 HV for Grade 91 steel compared to <600 HV for 12 wt. % Cr steels. Where HIC has been reported in Grade 91 or Grade 92 steel the fabricator did not monitor or maintain sufficient preheat.

- **Reheat cracking (RHC).** Bainitic steels, such as vanadium-modified low alloy steels (CrMoV), are widely known to be susceptible to RHC. The increased susceptibility in low alloy steels is attributed to the bainitic phase transformation, which occurs at a higher temperature range compared to the martensite phase transformation. Figure 2-47 provides a comparison of the on-cooling phase transformation behavior for common power generation steels. For single phase materials, such as stainless-steel type 316, there is a gradual accumulation of welding residual stress on-cooling to a value at ambient temperature approximated by the yield strength. For the bainitic and martensitic steels, a more dramatic set of behavior is illustrated. Upon completion of the phase transformation, the welding residual stress is 'reset' and decays to a value near zero. In this process, the transformation strain overwhelms the effect of thermal contraction. Once the transformation is complete and the austenite has completely transformed to bainite or martensite, the thermal contraction is responsible for the buildup of welding residual stress (Francis et al. 2007). It is believed that the reduction in the welding residual stress in martensitic steels plays a large role in reducing and/or eliminating the susceptibly to RHC.
- **Hot cracking.** Filler materials matching to Grade 91 steel contain deliberate additions of C, Nb and Mo. These elements can partition to inter-dendritic regions during solidification leading to centerline cracks, crater cracks or solidification cracks. This phenomenon has been reported in open-root welding using the GTAW process due to poor bead shape or harsh extinguishing of the welding arc and secondly in high heat input processes, such as SAW, where the large bead size can promote large, internal cracking along solidification grain boundaries. Although hot cracking is sometimes noted, this is not a common issue which presents gross problems or concerns.

A brief review of common welding cracking mechanisms is provided in Table 2-9 for 9 wt. % Cr CSEF steels. Because the potential for the fabrication of a sound weld is high, the focus of the remaining sections in the review will be for cross-weld behavior with an emphasis on development and behavior of the HAZ. The WSRF values provided in Table 1-5 and Figure 1-11 emphasize the reduction in performance for cross-weld tests and point to the dramatic influence that welding has on the carefully controlled, tempered martensitic structure characteristic of the virgin parent material.

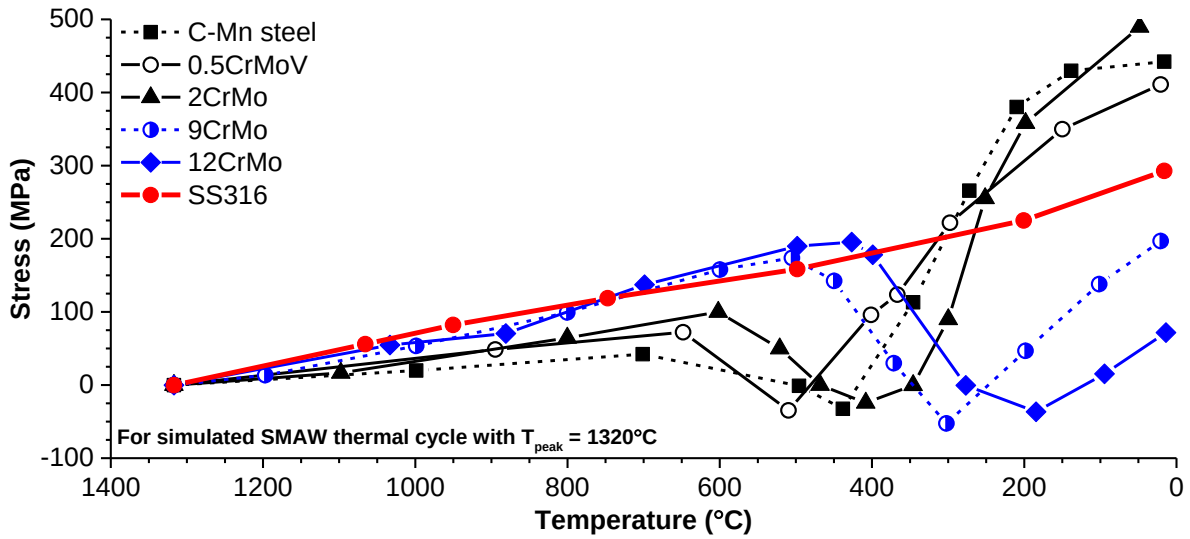

Figure 2-47. Accumulation of residual stress on-cooling for a simulated shielded metal arc welding (SMAW) thermal cycle and to a peak temperature of 1320°C (Jones and Alberry 1982).

Table 2-9. Review of common weld cracking mechanisms and the susceptibility and prevention for 9 wt. % Cr martensitic CSEF steels

Type of Cracking	Mechanism	Susceptibility	Prevention
Cold	Hydrogen induced cracking (HIC)	Yes, flux processes and/or highly restrained welds	Application of preheat
	Stress corrosion cracking (SCC)	Yes, in as-welded condition	• Post weld heat treatment as soon as possible • Maintain preheat
Warm	Reheat cracking (RHC)	No reported cases	N/A
	Ductility dip cracking (DDC)	No reported cases	N/A
	Liquid metal embrittlement (LME)	No reported cases	N/A
Hot	Weld solidification	Yes, root passes in open root welds, craters and large weld bead deposits	• Emphasizing a convex weld bead shape • Adding filler material into the solidifying crater • Optimization of weld parameters to control bead size and shape, particularly for SAW process
	Liquation cracking	No reported cases	N/A

2.12 Classification of Cracking in Weldments

The common classification scheme for identification of cracking in low alloy steels was first proposed by Schuller in 1974 (Figure 2-48). The types of cracks are detailed below using the descriptions below:

- Type I – longitudinal or transverse cracking completely contained in the weld metal. Longitudinal cracking may be linked to welding-related issues such as solidification cracking or to creep damage developed in-service. Transverse cracking may be linked to HIC developed immediately following welding or after a short period after welding (delayed).
- Type II – like Type I but damage extends into the HAZ and potentially into the base metal;
- Type III – in the HAZ very close to the fusion line, damage is concentrated in the CGHAZ and often linked to RHC;
- Type IV – in the HAZ region near the base metal developing because of in-service creep damage. Sometimes linked to a specific zone in the HAZ, for example fine-grained HAZ (FGHAZ) or inter-critical HAZ (ICHAZ).

Recently these descriptions have been extended to introduce four additional classifications as presented below:

- Type IIIa (Brett 2004) – damage concentrated in the refined HAZ grain structure near the fusion line. RHC initiates and grows fastest in the regions of coarsest grain structures and is often observed to arrest at fine grained locations. Type IIIa cracking initiates in fine grain structures and terminates at regions of coarse grains. Type IIIa cracking is reported in welds with fully refined HAZ structures in formerly CGHAZ region.
- Type V (Yamazaki et al. 2011) – damage resulting in failure through the base metal only;
- Type VI (Yamazaki et al. 2011)) – damage and/or cracking isolated to the fusion line interface.
- Type VII (Yamazaki et al. 2011) – damage and/or cracking through the dissimilar metal weld interface, HAZ and base metal;

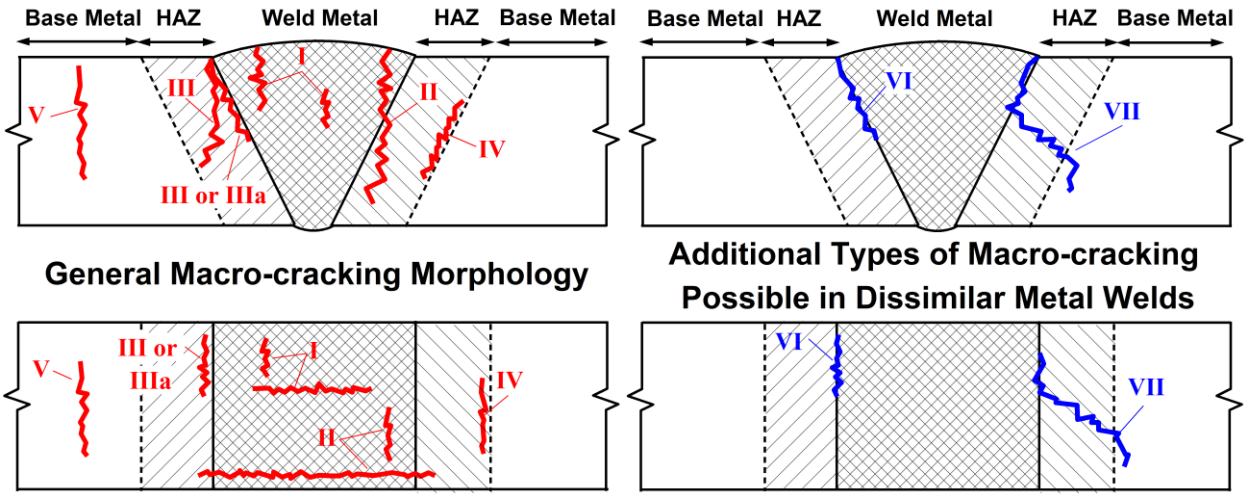

Figure 2-48. Description of failures in welded structures. Note the locations for types I, II, III or IV modes were first described by Schuller et al. (1974), type IIIa by Brett (2004) and types V, VI and VII proposed by Yamazaki et al. (2011).
Note: *the red failure modes are characteristic of 'similar' weldments and the blue failure modes for dissimilar weldments.*

The accumulation of failures in the power plant by the different modes described in Figure 2-48 has been generally described using the schematic in Figure 2-49. Curve A represents the expected performance for unaffected parent material; e.g. the observed initiation of failures in this distribution may render the plant 'life expired' and presents a best-case scenario. Due to the conservatism that is typically present in new construction code design formulae, this value might be well into the 100,000s or even 1,000,000s of hours. While some codes provide design rules incorporating a component life, others do not (for example, ASME B&PV Code Section I). This is a commonly misunderstood reality and clarification exists in the ASME B&PV Code Section I interpretation I-89-30 (ASME 1989):

> Question: *Does the ASME Boiler and Pressure Vessel Committee establish a specific design life for components designed to Section I?*
> Reply: *No*

Curve B is a distribution of failures dominated by Type III cracking. Since this mechanism can be reasonably expected to occur during PWHT or very early in the service life of the component, the bias is to the lower extreme of the overall lifetime of power plant components.

Curve C is a distribution of failures dominated by Type I or II cracking, degradation mechanisms associated with fabrication-related issues that were not found through random inspection. In conventional assessment in the fabrication shop or field, it is

common practice to inspect a selected number of welds, for example 10% of the total population and pending the identified defects, a larger percentage may be surveyed. The finding of defects in the fabrication stage is equally dependent on the methods utilized, typically a surface-based method such as visual, dye-penetrant or magnetic particle or the continued reliance on volumetric inspection by radiography.

Curve D is a distribution of failures for Type I cracking attributed to creep, Type IIIa or Type IV cracking. In the literature, the distribution represented by Curve D is sometimes called ‘mid-life cracking.’ The general population of failures in this distribution are associated with many potential factors which can generally be subclassified into four key contributors: design, fabrication, operation and metallurgical risk.

The accumulation of damage associated with Type IIIa and Type IV cracking in CrMoV piping systems has been detailed by Brett and is reviewed in Figure 2-50. In his assessment, Brett claimed at the time of reporting that of the 7,600 welds in the end-user system, ~5% of the population necessitated repair (380 welds) and of the damage mechanisms present, Type IV cracking accounted for 2/3 of the identified defects.

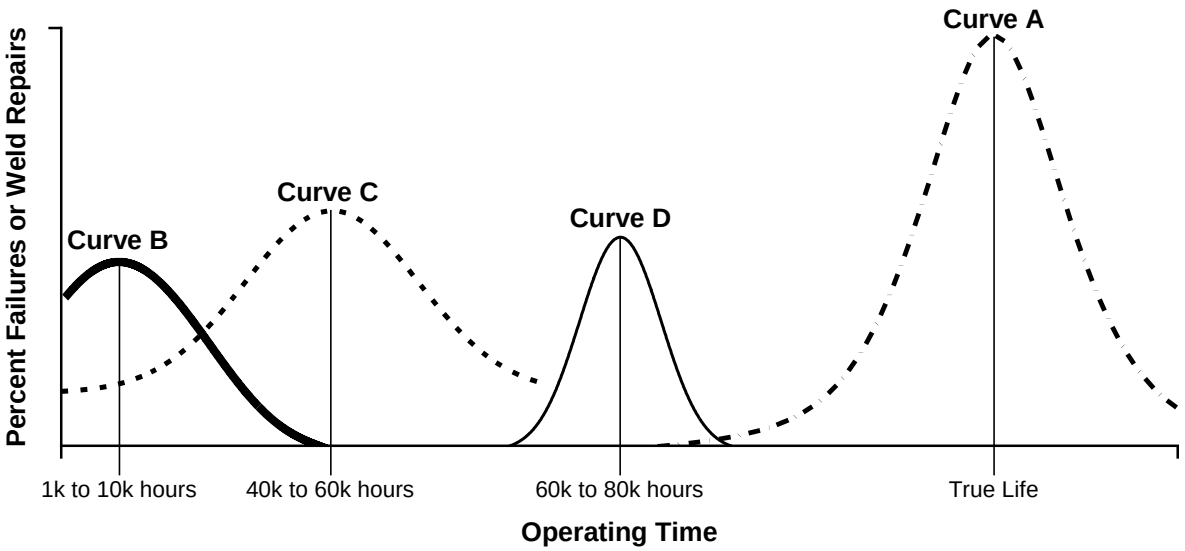

Figure 2-49. Percent failures or weld repairs as a function of operating time for commonly identified damage mechanisms in power generation steels (Williams 1982).

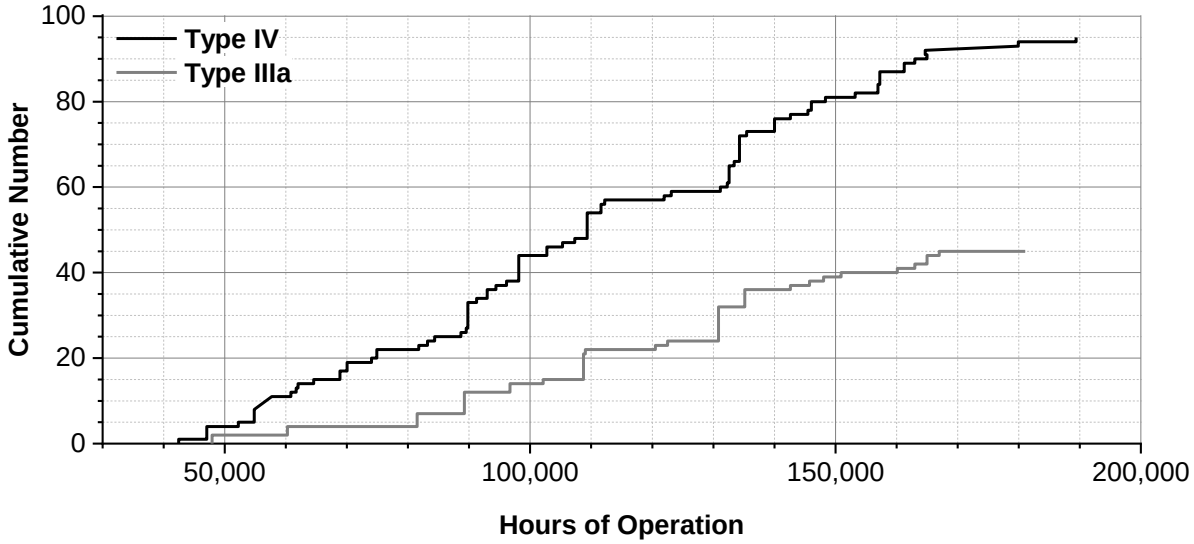

Figure 2-50. Cumulative number of failures for power piping systems fabricated from CrMoV in a European utility and attributed to either Type IV or Type IIIa cracking (Brett 2004).

2.13 The Influence of the Welding Thermal Cycle on the Tempered Martensitic Microstructure

Failure in the HAZ, otherwise known as a Type IV failure, is a primary concern in 9-12 wt. % Cr CSEF steel welded structures. Researchers have defined the local region where failure occurs in the HAZ by many terms including the ICHAZ, FGHAZ, 'soft zone', 'softened region' or 'Type IV region.' The apparent confusion in the literature regarding where failure occurs in cross-weld tests or ex-service evaluations is predicated on the reliance of the diagram utilized in Easterling's textbook (Figure 1-9) and the classification scheme developed by Schuller (Figure 2-48). This has resulted in widespread debate as to the precise location for failure and the demonstrated, overall confusion in the literature. In the following section, the formation of the partially transformed zone (PTZ) consistent with the definition from Xu will be reviewed.

One classic description for the weakest region in the HAZ susceptible to the failure mode classified as Type IV is developed from the as-fabricated hardness trace through the HAZ in the PWHT condition, Figure 2-51. In this research, the authors claim all specimens in their study "ruptured in the fine-grained part of the HAZ near the base metal and that the location of failure corresponds completely with the weakest zone of the weldment." No details are provided on how the correlation between the failure location and as-fabricated condition was realized.

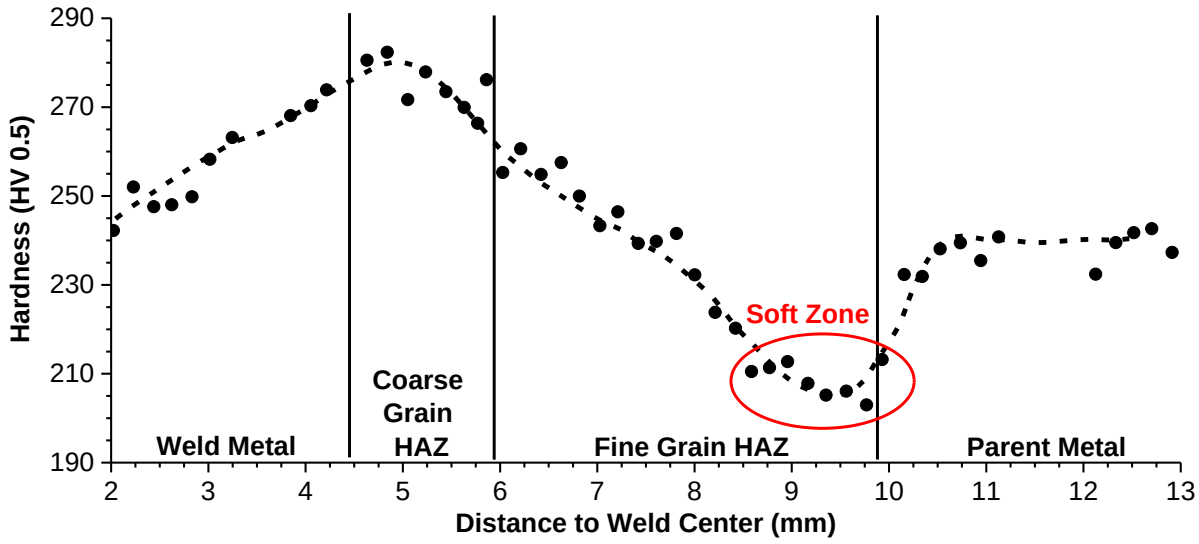

Figure 2-51. Microhardness distribution (Vickers indentation, 500g load) in a T91 similar weldment after post weld heat treatment (Arav et al. 1992)

The association of Type IV failure with the soft zone revealed by hardness testing is a common theme in many articles. However, this zone was never described by the original alloy developers of Grade 91 steel as being associated with a transformed region. In fact, the developers assessed the typical microstructure in Grade 91 steel weldments using three classifications (ORNL 1986b):

1. The weld zone (W);
2. The transformed zone (TZ) which is the region exposed to temperatures above Ac_1 (~840°C); and
3. The tempered zone (TMPZ) which is exposed to temperatures below the Ac_1 and above the typical tempering temperature (~760°C).

Furthermore, supporting documentation from ORNL-contracted research provided specific investigations of the so-called ‘soft zone’ for multiple CrMo steels. In one such report, the investigation of the location of lowest hardness was reported in a location 4 mm from the weld zone/HAZ interface and stated to coincide with the boundary between the TZ and TMPZ. The researchers concluded that the soft zone resulted from slight coarsening of carbides due to tempering by the heat generated during welding (Biss 1982).

In a second investigation performed at the former CEGB, the softening phenomenon was investigated through simulated weld thermal cycles using a Gleeble thermomechanical simulator. A key conclusion from this evaluation was identical to

the prior conclusion, namely that the softening phenomenon occurs because of a thermal cycle having a peak temperature of ~830°C, e.g. over-tempering of the base metal (Ferranti 1989). Neither the ORNL nor the CEGB work mention the association of grain refinement or other observations linked to the soft zone.

The complex series of events leading to the formation of the HAZ result in a heterogenous microstructure made more complicated by the nature of multi-pass welding. Every component fabricated and installed in a power plant can be regarded as a multi-pass weld since the traditional processes for joining components inherently require multiple weld layers. The classical definitions for the HAZ in ferritic steels was previously presented in Figure 1-9 from (Easterling 1992) and the preferred classification for martensitic steels was provided in Table 1-4 (Xu et al. 2017).

Adoption of the academic description in Easterling's book was an extension of the work of Alberry and Jones and later emphasized by the development of grain growth diagrams (Alberry and Jones 1977, Easterling and Ashby 1982). The link between grain size and the welding cycle was presented in the context of carbide/nitride dissolution; the stability of common carbides and nitrides is given in Figure 2-52 (Easterling 1992).

Partial dissolution of chromium carbide is expected to occur during the welding cycle in the PTZ where the peak temperature exceeds the Ac_1 value, and the extent of dissolution will be governed by the time duration >Ac_1 temperature. This dissolution is not important in the context of grain growth; indeed, in the PTZ region where damage originates in cross-weld creep tests in 9-12 wt. % Cr CSEF steels the grain size is typically described as having a very refined structure. However, local compositional inhomogeneity may result and this reality is supported by evaluations of local Cr enrichment in the as-welded condition (Sawada et al. 2015). Sawada et al. attributed this enrichment to several factors; a peak temperature and time sufficient to locally or partially dissolve $M_{23}C_6$ particles; the dramatic difference in diffusion rates for C and Cr in alpha iron at 877°C (1.83×10^{-10} m^2/s versus 3.31×10^{-15} m^2/s, respectively); and the cooling rate during welding which is sufficiently high to stabilize the local Cr-enriched grains (maximum of ~12 wt. % Cr compared to 8 wt. % Cr in the martensitic matrix) in alpha iron.

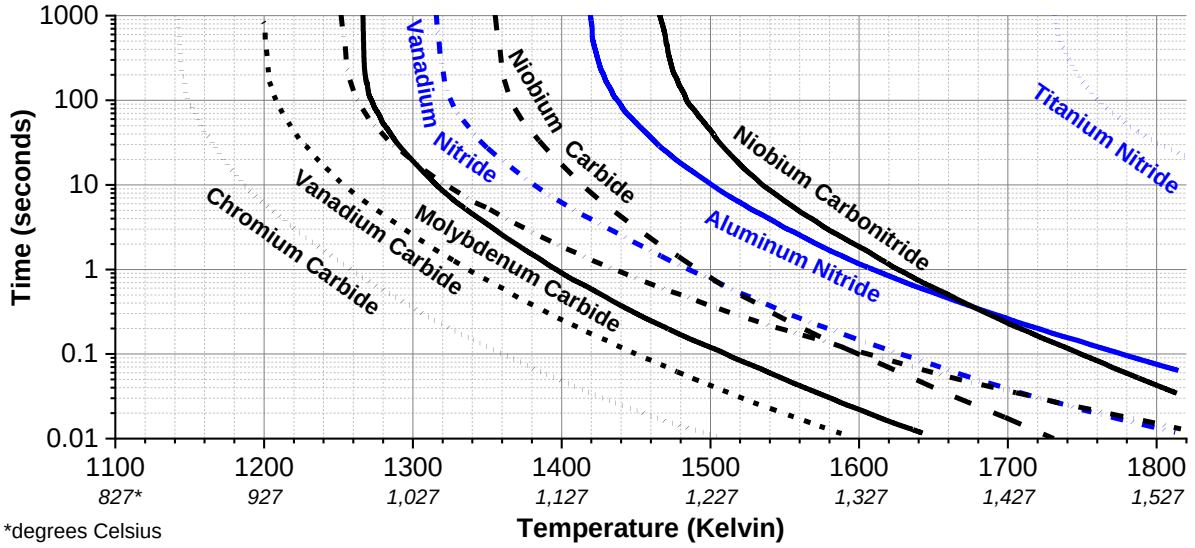

Figure 2-52. Dissolution of common carbides and nitrides in steel for a range of peak temperatures and dwell times covering the range of expected heat affected zone thermal cycles (Easterling 1992)

A comprehensive set of investigations using Grade 92 simulated HAZs was reported by (Liu et al. 2013). The systematic evolution of the HAZ was considered for three parent metal conditions and for the same heat of material, Table 2-10. A Gleeble thermomechanical simulator was utilized and the re-creation of the HAZ thermal cycle included:

- Heating and cooling rate of 100°C/s;
- Variable peak temperatures representing the range present in the HAZ; the peak temperature for the so-called Ac_3 heat treatment was 950°C;
- Hold time at peak temperature for 0.5 seconds;
- Simulated PWHT at 740°C for four hours.

The behavior of the produced microstructures was rationalized by a series of creep tests at 650°C.

Table 2-10. Condition of investigated Grade 92 parent material before simulated of the heat affected zone thermal cycle (Liu et al. 2013)

Material	Condition	Heat Treatment
Gr. 92	As-received plate	1070°C/2h/AC + 780°C/2h
Gr. 92N	Re-normalized	1070°C/2h/AC
Gr. 92NN	Re-normalized + quenched	1070°C/2h/WQ + Subzero cooling

In the microstructure evaluation of the samples generated using the Ac_3 thermal cycle, the Gr. 92 material possessed a unique distribution of precipitates. This is observed in

Figure 2-53 where a highlighted, fine prior austenite grain boundary (PAGB) is devoid of precipitates while the location of a former PAGB is still apparently decorated with precipitates. Due to the HAZ simulated thermal cycle, the former PAGB is not an actual boundary and is sometimes referred to in the literature as a 'ghost boundary.' Comparison of this behavior to the Gr. 92N and Gr. 92NN samples revealed dramatic differences. In both the Gr. 92N and Gr. 92NN after the Ac_3 simulation, the PAGB and block boundaries were highly decorated with precipitates.

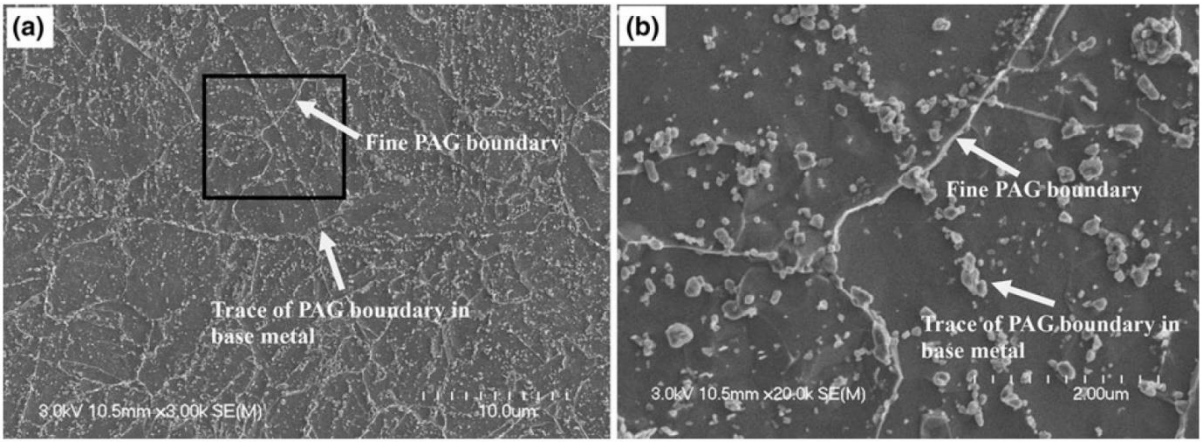

Figure 2-53. Distribution of precipitates in Gr. 92 after simulated Ac_3 heat affected zone thermal cycle (a) and the lack of precipitation at new, fine prior austenite grain boundaries (b) (Liu et al. 2013)

Comparison of the creep behavior of the Ac_3 simulated HAZ tests and a comparison of the influence of peak temperature on time to failure are summarized in Figure 2-54. The reduction in performance for the Gr. 92 Ac_3 simulated HAZ is shown in Figure 2-54A; the difference in life is about a factor of 5 compared to Gr. 92N and Gr. 92NN. The reduction in performance with peak temperature is shown in Figure 2-54B and for the Gr. 92 samples there exists a minimum in performance for simulated HAZ tests at a peak temperature of 900°C (a value approximating the Ac_3 temperature for this heat of material and for the utilized heating rate).

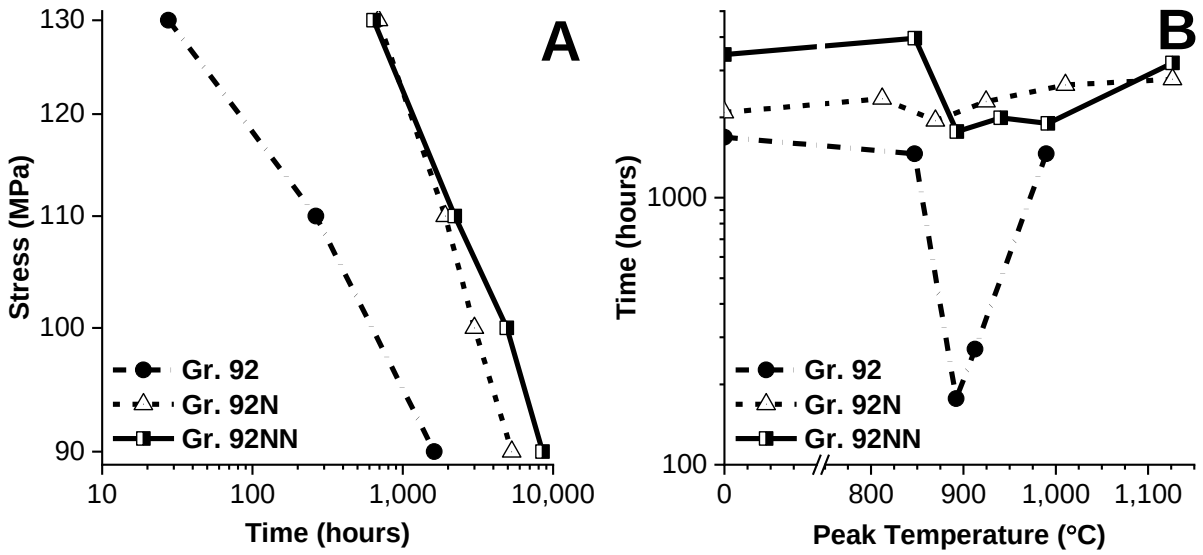

Figure 2-54. Comparison of unique Grade 92 parent material conditions after simulation of the heat affected zone peak temperature near the Ac_3 (A) and the effect of heat affected zone peak temperature on creep behavior at 650°C and 110 MPa (B) (Liu et al. 2013)

2.14 Assessment of Heat Affected Zone Damage in Power Generation Ferritic Steel Weldments

Several reviews of Type IV failure have been published over the last two decades (EPRI 1997, Francis et al. 2006, Abson and Rothwell 2013, Parker 2013). This section focuses on the nature and extent of creep damage that is reported in the HAZ for cross-weld creep tests or in the assessment of ex-service components. A brief set of literature is first reviewed for low alloy steels that will have relevance to the results in this thesis, and in the second part of this section, the literature relevant to 9-12 wt. % Cr CSEF steels including Grades 91, 92 and 122 is summarized.

2.14.1 Assessment of Heat Affected Zone Damage in Low Alloy Steels

The overview authored by (Kimmins et al. 1993) of HAZ failures in ferritic steels proposed a general link between parent metal creep ductility and the ratio between the time to failure for the parent metal to that of the HAZ, Figure 2-55. It was argued that the Type IV creep strength is independent of parent steel strength because the Type IV condition represents the weakest possible condition for any ferritic steel.

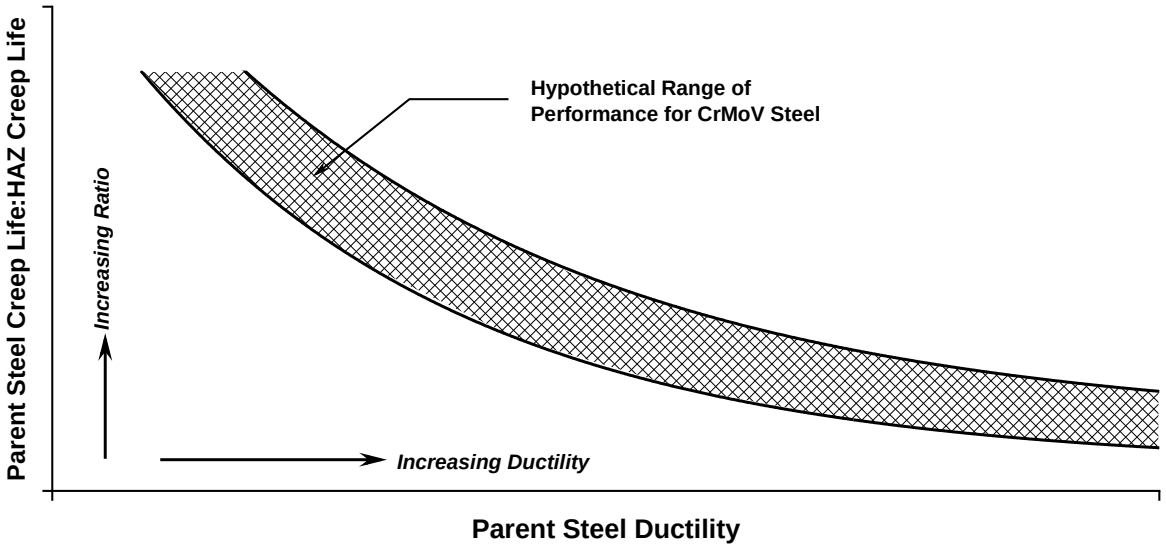

Figure 2-55. Relationship between the Parent Steel Ductility and the Ratio between the Parent Steel to Heat Affected Zone Creep Life. In this illustration, decreasing parent steel ductility leads to a higher ratio (i.e. a reduction in cross-weld creep life), adopted from (Kimmins et al. 1993)

The link between creep ductility of the parent metal and HAZ failure performance is noted in several studies including lab-based cross-weld tests and ex-service observations. Parker and Parsons evaluated an ex-service weldment where two unique heats of CrMoV were joined with a 2¼Cr-1Mo filler material (Parker and Parsons 1995). The parent metal heats were simply identified as “A” and “B” in their evaluation. It was observed that cross-weld tests which failed in the HAZ were consistently reported on the B-side of the weldment whilst no damage was observed in the HAZ evaluation of the A-side of the weldment.

Parent metal creep tests performed in the B parent metal consistently exhibited lives 30% longer than for side A, but the measured creep ductility was on the order of 10% as compared to >20% for side A. Subsequent metallographic evaluation showed a high density of grain boundary cavitation in the B material whereas the extent of damage in the A material was limited to locations very close to the fracture face. Analysis of the inclusion density in both materials yielded a similar volume fraction, but the density of fine inclusions was much higher in the B material. Because of the fine grain size in the HAZ and the presence of a high density of small inclusions, it was rationalized that the likelihood for an inclusion existing on a grain boundary was high, thereby lowering the barrier to void nucleation in the B material. The authors concluded, “the observed susceptibility for HAZ failures is directly related to the base

material ductility, rather than simply being a consequence of the microstructural modification developed during welding."

Assessment of a leak in a 1¼Cr-½Mo girth weld was reported by (Westwood et al. 1990). The leak occurred in the valve-side HAZ of a girth weld between a forged T-piece and a cast main steam boiler stop valve after 88,000 hours of operation at an estimated temperature of 538°C. The grain size for each component was similar, ~30 µm, and assessment of composition showed consistently higher values in the casting material for the elements C, S, P, As and Sn. The authors suggested there was inferential evidence that the creep strength and creep ductility in the casting were inferior to that of the forging. Comparison of hardness data determined that other factors were more important than the hardness differential approach reported by (Bissel et al. 1996). The hardness differential is defined as the ratio of the minimum to maximum hardness in different parts of the weld regardless of constituent. In conclusion, Westwood et al. argued that it is important to consider the balance in behavior between creep deformation resistance and creep damage.

In a review of cross-weld creep test procedures and databases, Parker offered perspective on the need to emphasize creep ductility of the parent material when assessing Type IV cracking (Parker 1996). His analysis showed that the available information for cross-weld behavior could not be rationalized by the specimen geometry nor test conditions. More specifically, the evolution of damage in the HAZ leading to Type IV failure was more clearly linked to the tendency for creep cavity formation, a reality that is governed by alloy type, weld procedure including PWHT, test conditions, and dimensions of the test sample and factors affecting the creep ductility of the parent material.

2.14.2 Assessment of Heat Affected Zone Damage in 9-12 wt. % Cr CSEF Steels

Early work investigating Type IV failures in Grade 91 focused on linking the specific HAZ region with the location for Type IV failure (Kojima et al. 1995). The authors noted that for tests performed at 650°C the extent of HAZ softening was enhanced and the creep rupture location shifted into the soft zone of the HAZ due to the change in strength balance. The reduction in hardness, as demonstrated by test data in Figure 2-56, was linked to the precipitation behavior of carbonitrides and matrix recovery under creep. No attempt was made to link the softening in Figure 2-56 to the

accumulation of creep damage, which might offer a second, plausible explanation for the local hardness reduction.

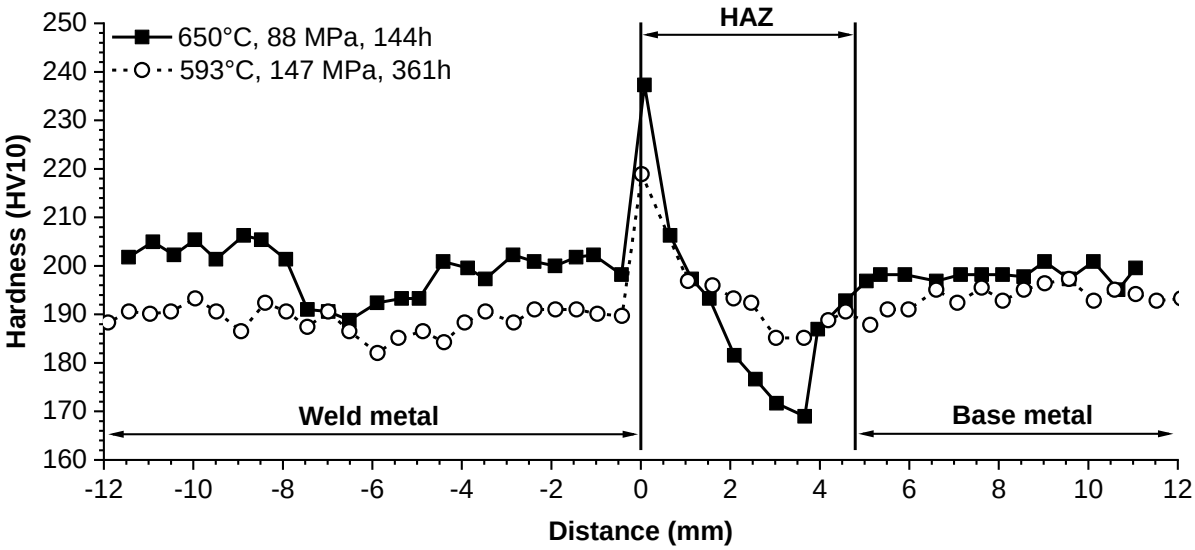

Figure 2-56. Hardness of ruptured cross-weld creep samples produced in Grade 91 steel using the submerged arc welding process after testing at 593°C, 147 MPa and 361 hours or 650°C, 88 MPa and 144 hours (Kojima et al. 1995)

Numerous papers have been authored by Laha and his colleagues over about a decade, specific to the location of failure in the HAZ of ferritic steels. Cross-weld creep tests were carried out for temperatures of 550, 600 and 650°C for an applied stress range of 40 to 280 MPa. Specific to Grade 91, Laha claims that the soft zone occurs in the ICHAZ and is caused by coarsening of the martensitic substructure, coarsening of precipitates and a reduction in the dislocation density (Laha et al. 2007). The location of failure is therefore linked to the soft zone in the HAZ, otherwise referenced in this study as the ICHAZ. Experiments for simulated HAZ tests relied on hardness and tensile test evaluations to show that the weakest region in the HAZ was biased to a region with a peak temperature closer to the Ac_1 value. The association of tensile and creep behavior is problematic, although many in the literature have attempted to provide this rationale with regard to life management or remaining life assessment (Allen and Fenton 2007 and Masuyama 2013).

Tests conducted by (Parameswaran et al. 2010) concluded that failure occurred in the ICHAZ where the peak temperature is between the Ac_1 and Ac_3. In this region, the dissolution of carbides, formation of fresh ferrite and martensite leads to a heterogenous microstructure. The stabilization of ‘soft ferrite grains’ due to carbide dissolution provides a microstructure which is susceptible to glide in creep. The soft

ferrite zone was strengthened locally by MC carbides until Z phase formed. The formation of Z phase was postulated to drastically reduce the creep strength in the HAZ.

Cross-weld creep tests evaluating weldments made using an automated GTAW process and the SMAW process support the argument that Type IV failure occurs in the soft zone in the HAZ (Sakthivel et al. 2016). The soft zone is further identified as the ICHAZ and forms because of subgrain evolution and coarsening of $M_{23}C_6$ particles. Comparison of an automated GTAW weldment and a SMAW weldment consistently showed that the performance of the GTAW weldment was better. This was attributed to the joint geometry, the bevel for the GTAW weldment was approximately normal to the applied stress axis (e.g. close to 0°). The impact of joint geometry is the focus of a later subsection in this review.

Microstructural evaluation of Type IV failure for a feature-type cross-weld creep test in Grade 91 steel conducted at 650°C and 83 MPa lasting 442 hours was reported in (Lee et al. 2005). This manuscript made the assertion that Type IV failure in Grade 91 occurs in the ICHAZ, including evidence for the nucleation of cavities at coarse $M_{23}C_6$ on grain boundaries, Figure 2-57. Although FGHAZ and ICHAZ regions have a refined grain structure, the size of $M_{23}C_6$ was larger in the ICHAZ.

Research from the early 2000s evaluated the difference between samples simulated to Ac_1 and Ac_3 peak temperatures (Matsui et al. 2001). In this work, the reduced performance for the Ac_3 simulated samples was attributed to the preferential recovery of higher density of dislocations and a relatively diffuse distribution of large $M_{23}C_6$ carbides. Furthermore, and for the Ac_1 simulated samples, the microstructure investigation did not reveal a marked recovery in the substructure and fine $M_{23}C_6$ carbides were observed in the matrix including lath boundaries.

Simulated HAZ evaluation in Grade 122 suggested the creep life reaches a minimum for samples given a peak temperature near the Ac_3 and not at the Ac_1. The authors found this outcome notable since the minima in hardness values for all simulated thermal cycles was documented for the peak temperatures near the Ac_1 temperature (Albert et al. 2002). The authors state that the development of large precipitates after PWHT in the FGHAZ or ICHAZ close to the Ac_3 temperature are the preferred sites for the nucleation of cavities. Attempting to disposition the results, the authors argue

that heating and cooling rates during welding might shift transformation temperatures and that the location of final fracture is well within the ICHAZ and not close to the Ac_3. However, the authors do recognize an important point from their study simply stating, “It appears precise identification of the location of Type IV cracking would be difficult and further studies are required in this regard.”

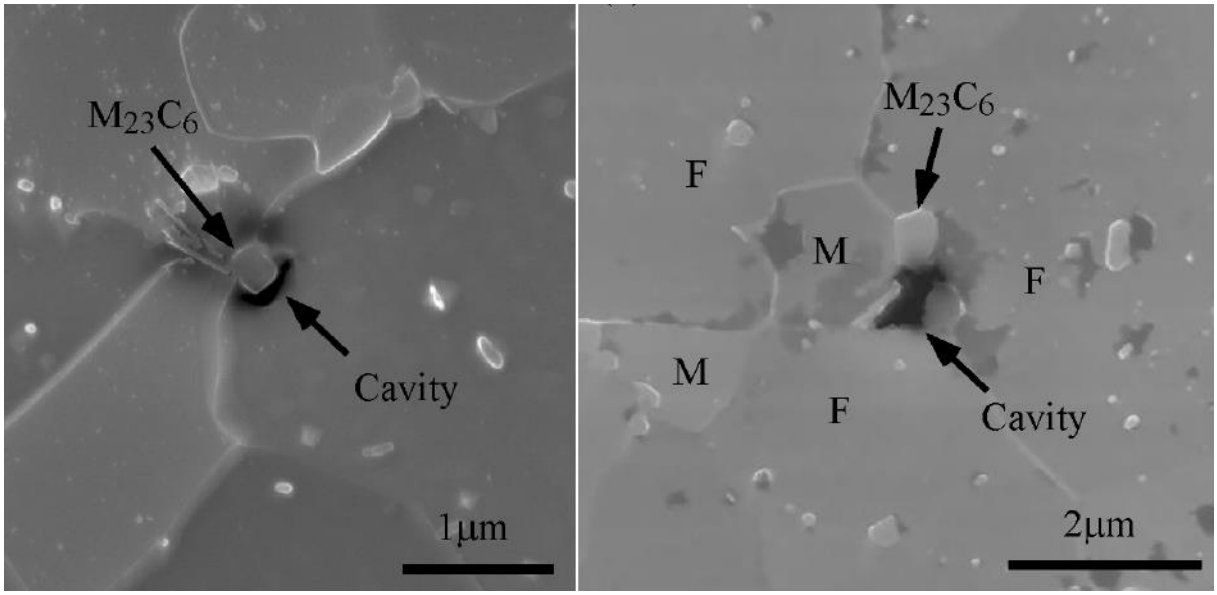

Figure 2-57. Cavity nucleation in a Grade 91 steel heat affected zone at a $M_{23}C_6$ particle after exposure in a cross-weld test at test conditions of 650°C, 83 MPa and failure in 442 hours (Lee et al. 2005)
Note: *M = martensite, F = ferrite*

Jandova and Kasl provide perspective on the evolution of damage in the weld metal and HAZ for long-term cross-weld tests in Grade 91 steel in the temperature range of 550 to 625°C and for tests up to 30,000 hours (Jandova et al. 2009, Jandova and Kasl 2010). The observed Type I cracking in the weld metal was associated with irregular clusters of Laves phase. The Laves phase precipitated on oxides in the weld metal leading to large, complex clusters. These sites served as preferred nucleation sites for damage. Z-phase was also noted in the weld metal, but was sparsely present leading the authors to conclude that the presence of Z-phase was of secondary importance.

Jandova and Kasl claim that the documented Type IV cracks in some of the test samples resulted from the interaction of soft grains or subgrains easily deformed during the creep process in the FGHAZ. The process described by the authors suggested that plastic deformation leads to the formation of steps at (sub)grain boundaries and that nucleation occurred at these sites. Secondly, they claim that a second set of interactions could occur between dislocation and particles located on

grain boundaries. Growth of nucleated cavities was accelerated by grain boundary diffusion.

(Liu et al. 2013), building on the prior summary of information in Figure 2-54 concluded that creep voids in the HAZ formed at fine PAGB. Furthermore, some PAGBs exhibited evidence of recrystallization suggesting that precipitate coarsening was not a dominate factor in Type IV failure. The observed extent of damage suggested that grain refinement in the HAZ cannot solely account for the reduced creep strength in simulated Ac_3 HAZ tests as in long-term test data the influence of grain refinement diminishes. Based on their evidence they conclude that the lack of grain boundary strengthening due to a poor distribution of precipitates at the boundaries in the HAZ plays the most important role in determining the resistance to creep deformation.

Assessments of Grade 92 observed the shortest time to failure in the simulated HAZ material given a peak temperature to the Ac_3 value (Hasegawa et al. 2009). Double thermal cycled tests showed a further reduction in performance. The balance of test data suggested that the peak temperatures responsible for the HAZ-softening phenomenon and the Ac_3 did not coincide and thus strain concentration in the HAZ softening region contributing to Type IV damage was not validated.

A detailed evaluation, including the assessment of interrupted samples, was detailed by Hongo et al (2012). In this study, the reduction in performance for simulated HAZ thermal cycles showed a consistent minimum in the time to failure at 600°C and 120 or 140 MPa near a peak temperature approximated by the Ac_3, Figure 2-58. Feature-type cross-weld tests were performed over a range of test conditions.

The simulated HAZ results were compared to the evaluation of cross-weld creep behavior in Figure 2-58 and Figure 2-59. The evolution of creep damage at life fractions of 20, 70, 80 and 90% clearly showed the initiation of damage early in the life of the test (e.g. a notable distribution of cavities was observed at 20% life) and a distribution of damage in the HAZ existed through ~1.5 mm in width.

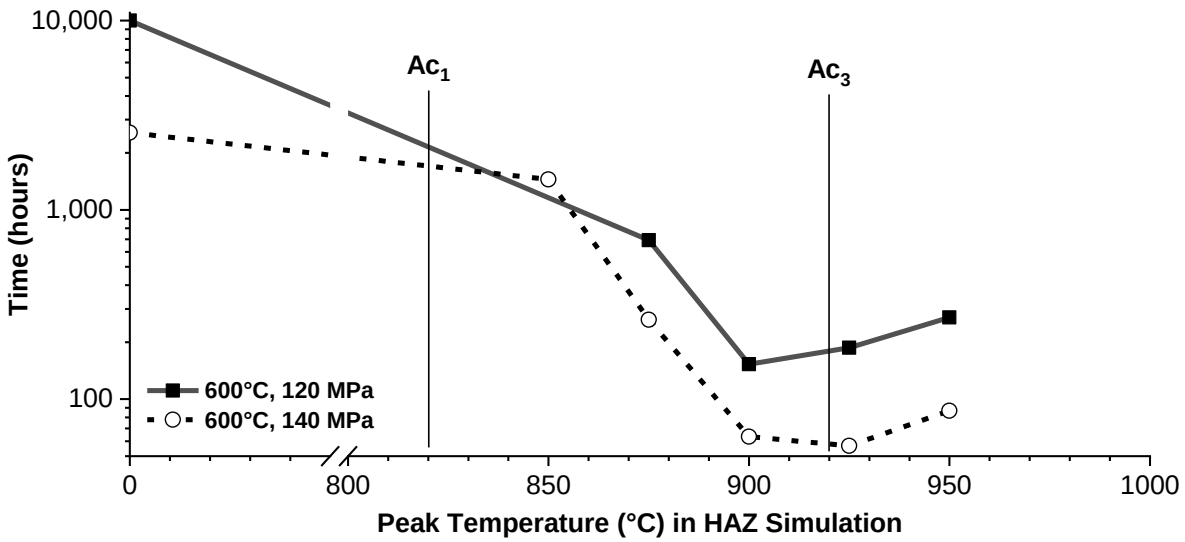

Figure 2-58. Assessment of simulated heat affected zone performance for a single heat of Grade 91 steel tested at 600°C and 120 or 140 MPa to the indicated peak temperature (Hongo et al. 2012)

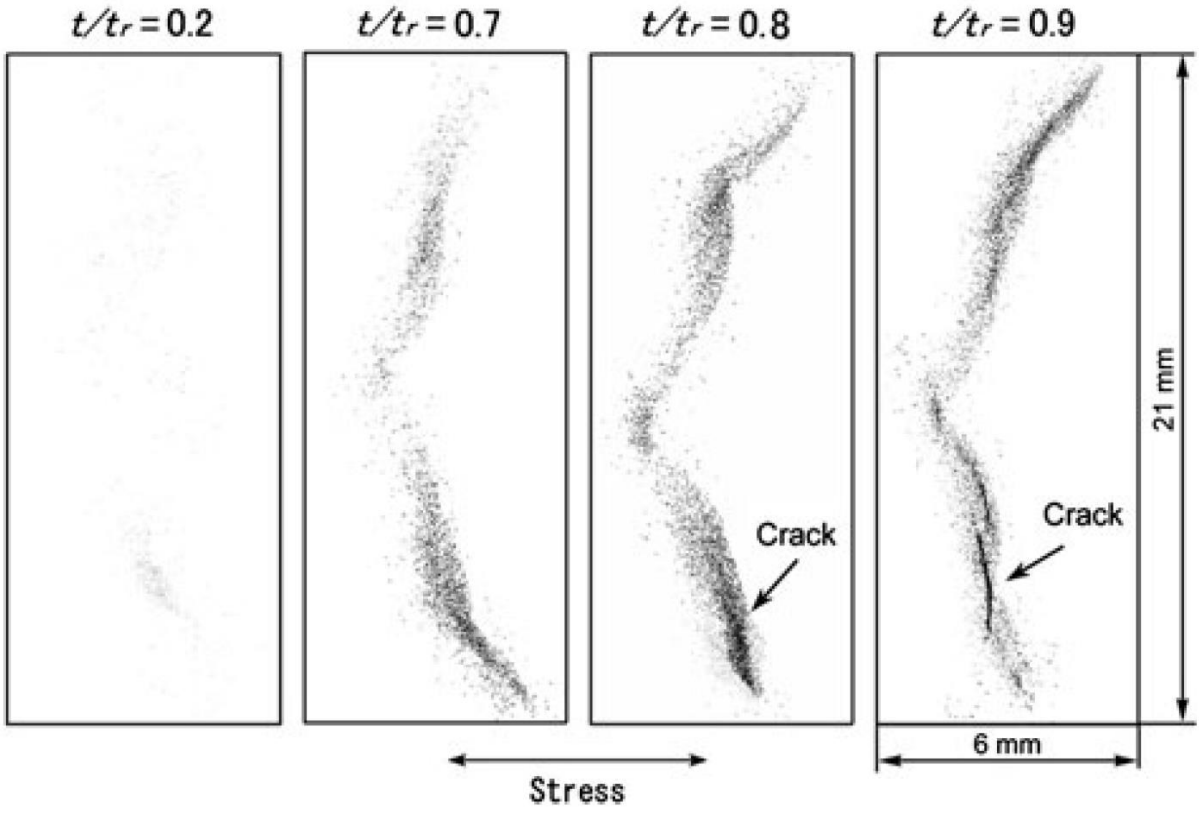

Figure 2-59. Distribution of damage through the heat affected zone for a series of interrupted tests performed at 600°C and 90 MPa
Note: *that the ultimate failure time for this weldment and stated test condition is 8,853 hours (Hongo et al. 2012).*

This observed distribution of damage in Figure 2-59 was not clearly isolated to a specific zone or region. This point is emphasized by the data plotted in Figure 2-60. A measurable amount of creep damage was observed over a 1.5 mm length through the

HAZ. This damage peaks at a local value measured in the 1,000s voids/mm^2. The trend in damage was compared to an as-fabricated hardness trace and a post-test hardness trace through the HAZ. Unlike in other studies, the authors attempted to rationalize the decrease in post-test hardness with that of the as-fabricated state and the damaged condition for a test life fraction of 90%. The data clearly showed the accumulation of damage (blue solid line) removed from the lowest hardness value in the as-fabricated hardness trace (solid black line). Furthermore, microstructural examination was performed in the as-fabricated condition at locations indicated by (a), (b), (c) and (d). In these locations, the authors noted microstructures consistent with a CGHAZ (a), a mixed microstructure at location (b) that was stated to be the FGHAZ, a mixed-grain microstructure at location (c) stated to be the ICHAZ and finally a tempered martensitic matrix in (d) that possessed a grain size identical to that in the base metal.

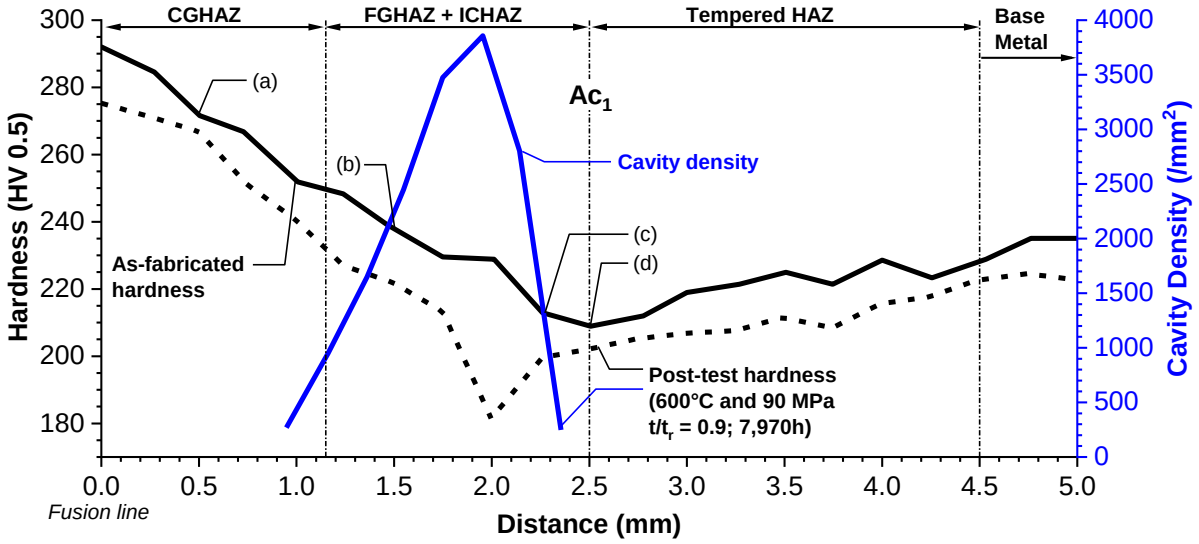

Figure 2-60. Comparison of hardness in the as-fabricated condition, hardness in the post test condition for a feature, cross-weld test performed interrupted at 90% life (at 600°C, 90 MPa and 7,970 hours) and the density of creep voids across the heat affected zone (Hongo et al. 2012)

Tabuchi et al., building on long-term test data in the reported evaluations in Hongo et al., compared the experimental test data to a calculated set of predictions for cross-weld creep behavior. In the assessment, a set of equations originally proposed by Hayhurst were utilized (Vakili-Tahami et al. 2005). These equations relate to the MSRC equation introduced in Equation 2.14, and detailed below in Equations 2.20 and 2.21.

Equation 2.20

$$\frac{d\varepsilon_c}{dt} = \frac{3}{2} A \left[\frac{\sigma_{eq}}{1-\omega}\right]^n \frac{S_{ij}}{\sigma_{eq}} t^m$$

Equation 2.21 $$\frac{d\omega}{dt} = \frac{M[\propto\sigma_1+(1-\alpha)\sigma_{eq}]^{\chi}}{(1+\emptyset)(1-\omega)^{\emptyset}}$$

Where:

$\sigma_1 =$ maximum principal stress

$\sigma_{eq} =$ equivalent stress

$A, n, m, M, \phi, \chi =$ material constants

$\alpha =$ multiaxial stress state parameter

The assessment of the computed failure time using the approach outlined in equations 2.20 and 2.21 is compared to the experimental failure time. A few interesting observations are noted. For short cross-weld creep lives, the multiaxial equation for an alpha value of either 0.3 or 0.4 clearly under predicts performance. This suggested that the multiaxial stress state parameter value should be closer to 0 in these tests, e.g. a bias to a deformation-controlled, equivalent stress mechanism. In the intermediate timeframe, the utilized values for α reasonably predict the experimental failure time showing some contribution in this intermediate regime for both the maximum principal and equivalent stresses. For the long-term test data, the opposite trend emerges, e.g. the calculated time to failure grossly over-predicts the lifetime of cross-weld samples indicating that the α value should be closer to 1, e.g. a maximum principal stress controlled condition.

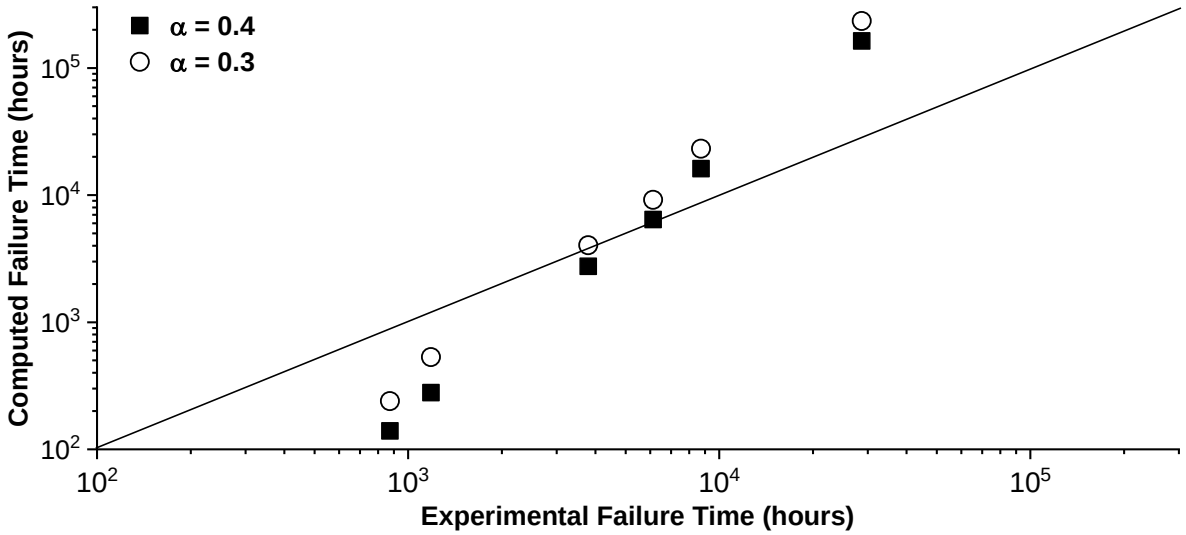

Figure 2-61. Comparison of the computed time to failure using equations 2.20 and 2.21 to the experimental failure time reported in (Tabuchi et al. 2017)

Recent evaluation of simulated HAZ, plain bar creep tests for multiple heats of Grade 91 steel are detailed in Figure 2-62. This comparison provides a set of data for an identical, simulated HAZ thermal cycle whereby the induction heating method included the following parameters: heating and cooling rate of 1°C/s, to a peak temperature of

900°C, and a simulated PWHT of 740°C/4h (Takahashi et al. 2018). Simultaneous dilatometer measurements revealed that the peak temperature of 900°C was at or just above the Ac_3 temperature for all parent materials. In this evaluation, the variability for the HAZ samples for the provided test condition of 625°C and 60 MPa is only about a factor 2 on life. Plain bar creep tests in the unaffected parent metal showed that the parent material variability is about a factor of 20. Low ductility failures in the parent material were reflected in the simulated HAZ tests, although the parent metal tests exhibited lower ductility overall. The ductility values are provided as ROA (%) above each bar in Figure 2-62.

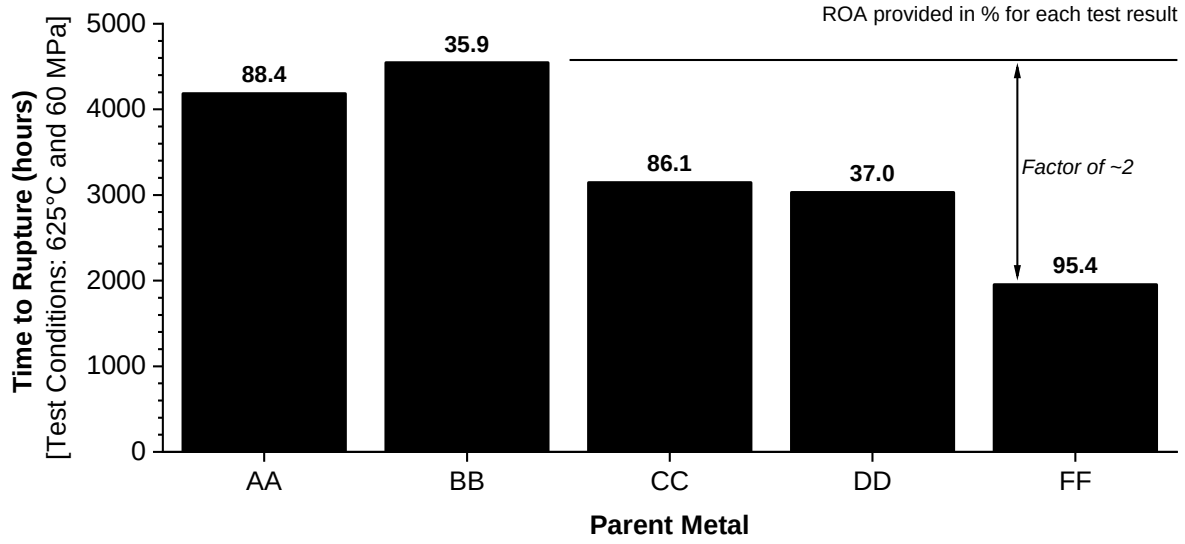

Figure 2-62. Evaluation of simulated heat affected zone performance; plain bar samples subjected to a test condition of 625°C and 60 MPa. Values above each bar are the reduction of area, reported as percent. Four unique parent metal heats are represented: AA, BB/DD, CC and FF.

2.15 The Influence of the Welding Procedure on Cross-weld Creep Performance

There are a handful of studies which have attempted to establish the effect of the welding procedure on performance including attempts to isolate specific variables concerning heat input or welding process, the preheat temperature, welding geometry (and more specifically the bevel angle), post weld heat treatment (PWHT) and filler metal. More appropriately, the research studies of interest have specifically tried to relate these variables to cross-weld creep performance. As will be discussed and for each of these potential variables, the specific influence is often masked by practical limitations in testing either regarding the chosen conditions, sample geometry or test duration.

2.15.1 The Influence of Weld Geometry

Assessment of the weld geometry has been performed for Grade 122 comparing an electron beam weld (0° bevel) to a single-vee groove and U-groove. Each of the groove welds were made using the GTAW process (Abe and Tabuchi 2004). This study showed that the electron beam weldment exhibited better performance than either a GTAW single vee groove or a GTAW U-groove weldment, Figure 2-63. The improvement in performance was directly attributed to the decrease in the width of the HAZ from 2.5 mm for the GTAW weldments to 0.5 mm for the EB weldment. The primary consequence in narrowing the HAZ is to increase the constraint in the HAZ region where damage develops, resulting in a reduction in the magnitude of the stress in the HAZ, and thereby improve performance.

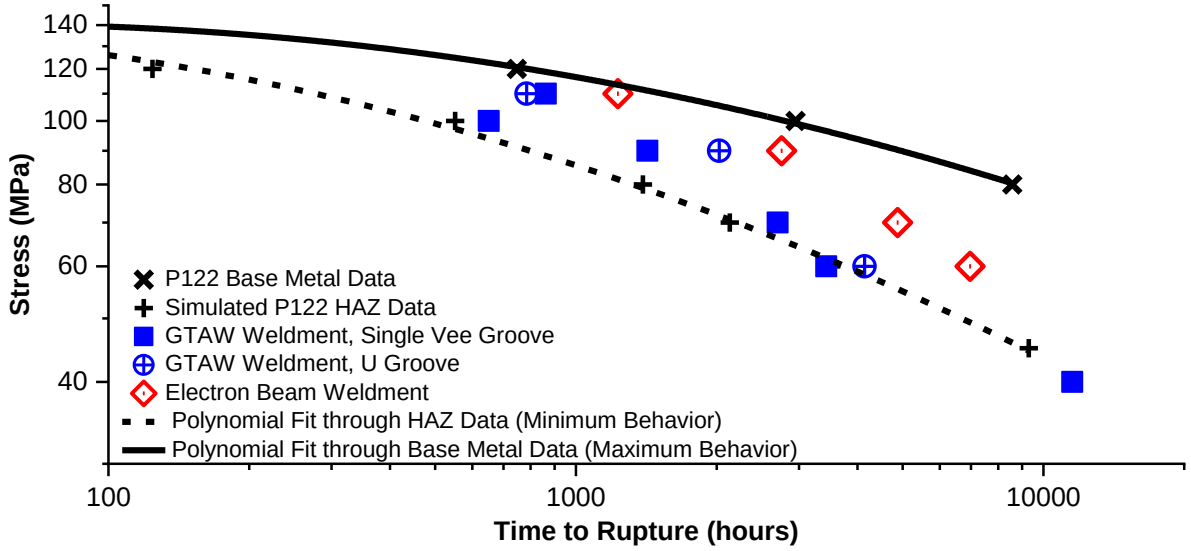

Figure 2-63. Comparison of Behavior for Cross-weld Tests in Grade 122 Steel. Comparison includes data for a Single Vee (20° bevel), a U Groove and an Electron Beam Weldment. These data are compared to a hypothetical minimum represented by data generated for simulated HAZ samples to a peak temperature of 920°C (equivalent to the A_{C3} temperature measured in this material) and the performance of virgin, as-received parent metal. All tests performed at 650°C (Abe and Tabuchi 2004).

No analysis or comment on the potential influence of the bevel angle was made on the deviation in cross-weld performance for the different welding procedures. This is an important point because for the selected test conditions and durations (<10,000 hours), the influence of the geometry may have been more critical to performance than the width of the HAZ since there is a marked difference for these two types of welds (i.e. 0° for the EB weldment and 20° for the single vee GTAW).

Although the data in Figure 2-63 clearly shows for higher stress and shorter test durations there is an apparent improvement in performance for the EB welds there is a noticeable transition to a lower bound behavior represented by the simulated HAZ samples and GTAW cross-weld tests. In the minimum, this dataset suggests a decreasing effect of the bevel angle and/or constraint on the HAZ with increased test duration.

Cross-weld data provided in (Cantin et al. 2009) was used to calibrate a continuum damage mechanics (CDM) analysis of a simulated creep test with 5° delineations of the bevel angle in the range of 0 to 45°, Figure 2-64 (Tanner et al. 2012). Although the simulations provided additional experimental evidence supporting the influence of the weld bevel angle on behavior, the simulated test conditions only represented a single temperature (650°C) and stress (70 MPa). The modeling does suggest that it is not unreasonable to see a factor of 2 improvement for bevel angles ≤15°, and as compared to a minimum life which was exhibited for a bevel of ~30°.

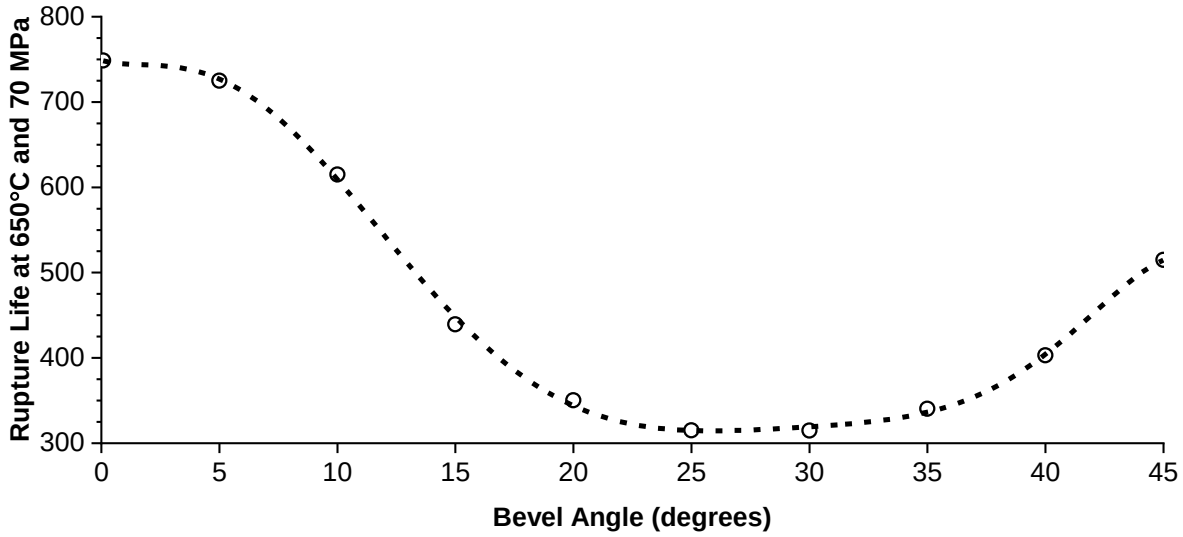

Figure 2-64. Modeling Results for a Round Bar Grade 91 Steel Cross-weld Test at 650°C and 70 MPa and for Variations in the Bevel Angle at 5° Intervals between 0 and 45° (Tanner et al. 2012)

2.15.2 The Influence of Weld Preheat

The study in (Abe and Tabuchi 2004) served as one driver for a more thorough interrogation of factors affecting cross-weld creep performance in 9-12 wt. % Cr CSEF steels reported in (Francis et al. 2006). This study assembled a database of >50 cross-weld creep data points from the literature where the material, PWHT, geometry, preheat and test conditions were well-pedigreed. In the analysis, it was suggested that

the preheat temperature may have a large effect on cross-weld creep performance even though the longest-term cross-weld test in this selected database from the literature was only ~11,000 hours.

A follow-on study, reported in (Cantin et al. 2009), attempted to isolate the variables of preheat, heat input and bevel angle on performance. The authors concluded that the heat input did not have a major effect on performance, a point highlighted in Figure 2-65. Examination of the bevel angle revealed some minor improvement in life as the bevel was decreased to a value near 0° (Figure 2-65). This result was like those for the EB weld in (Abe and Tabuchi 2004) where the life was increased by ~a factor of 2 for the reported test conditions. Lastly, the positive effect of increased preheat temperature (i.e. 350 versus 250°C) was rationalized by the results in Figure 2-66 for the 30° bevel angle. No fundamental or metallurgical explanation was provided as to the reason for the improved performance when the higher preheat was applied.

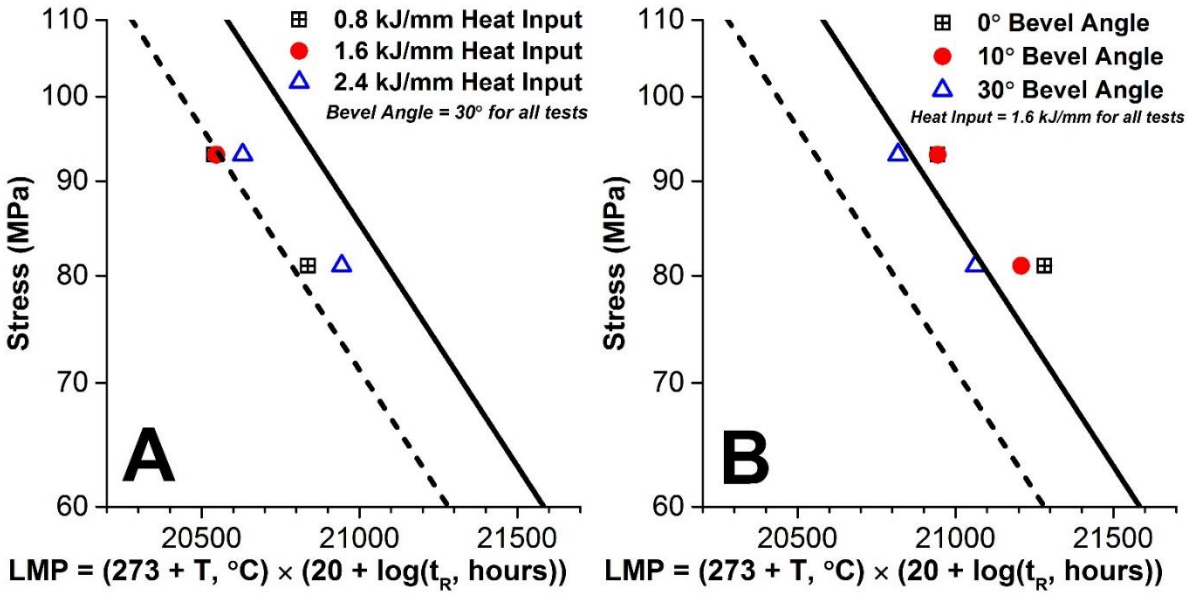

Figure 2-65. A – Influence of Heat Input on Performance for a Single of Heat of Grade 91 Steel and a Single-Vee Geometry using a 30° Bevel. The Referenced Preheat Temperature for this comparison of data is 250°C. B – Influence of Bevel angle for a Single-Vee Geometry and for a Single Heat of Grade Steel and Heat Input of 1.6 kJ/mm. The Referenced Preheat Temperature for this comparison of data is 350°C (Cantin et al. 2009).
Note: *for all reported data, a test temperature of 620°C was utilized and a stress of either 81 MPa or 93 MPa or both. Comparisons are made to the EPRI database of Grade 91 steel cross-weld creep performance for mean (solid black line) and minimum (dashed black line).*

Fundamentally, it is difficult to rationalize the results for the higher preheat in (Cantin et al. 2009) on a metallurgical basis since a susceptible region in the HAZ is created no matter the welding process or weld geometry. Furthermore, and contrary to the comment in (Abe and Tabuchi 2004) where the narrowed HAZ increased the restraint

on the HAZ, a higher preheat is expected to increase the width of the HAZ and decrease the restraint on the HAZ.

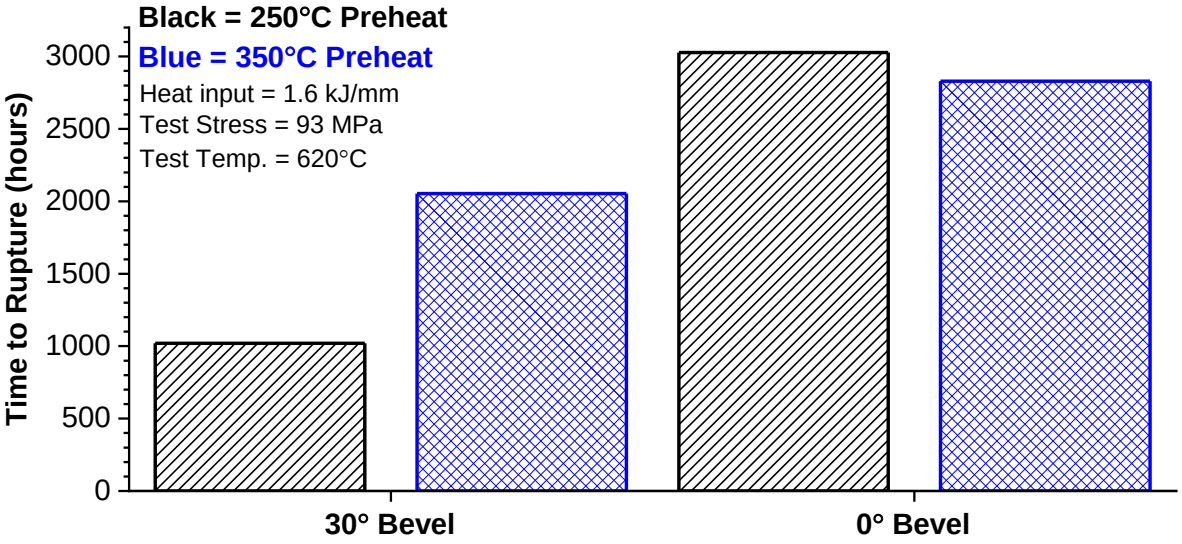

Figure 2-66. Influence of Preheat and Bevel Angle for a Single Heat of Grade 91 Steel, a Single Vee Geometry and for a Heat Input of 1.6 kJ/mm (Cantin et al. 2009).
Note: *for reported data, a test temperature of 620°C was utilized and a stress of 93 MPa.*

The improvement in performance for weldments made with a higher preheat was investigated in (EPRI 2013a) for a single heat of Grade 91 steel machined with a single vee 10° bevel, using a preheat of 204 or 482°C, the SMAW process with matching filler metal (i.e. E9015-B9) and a PWHT of 760°C/3 hours. For hardness maps in Figure 2-67, the effect of the higher preheat temperature is clear and is observed to increase the width of the HAZ by ~50%. However, and as shown in Figure 2-68, there did not appear to be a noticeable effect on performance for identical tests performed at 625°C and 80 MPa. In this evaluation, the rupture lives for both preheat temperatures were nearly identical.

A second set of studies detailed in (EPRI 2013a, EPRI 2015a), and using the same heat of Grade 91 steel were conducted to validate the influence of the bevel angle on performance. In this examination, the difference in a single vee geometry where both a 10° and 35° were evaluated at 625°C and 100, 80 and 60 MPa. The data in Figure 2-68 shows a noticeable difference in performance at 80 MPa (i.e. a Factor of 2 on life and like the previously detailed studies) whilst performance at 60 MPa is not as definitive (i.e. only a Factor of 1.5 on life). This decrease in performance further supports the trend detailed earlier in (Abe and Tabuchi 2004) – namely that for lower

stress at relevant test temperatures, the data begins to converge and the initial improvement in performance becomes less dramatic with decreasing test stress and/or increased test duration.

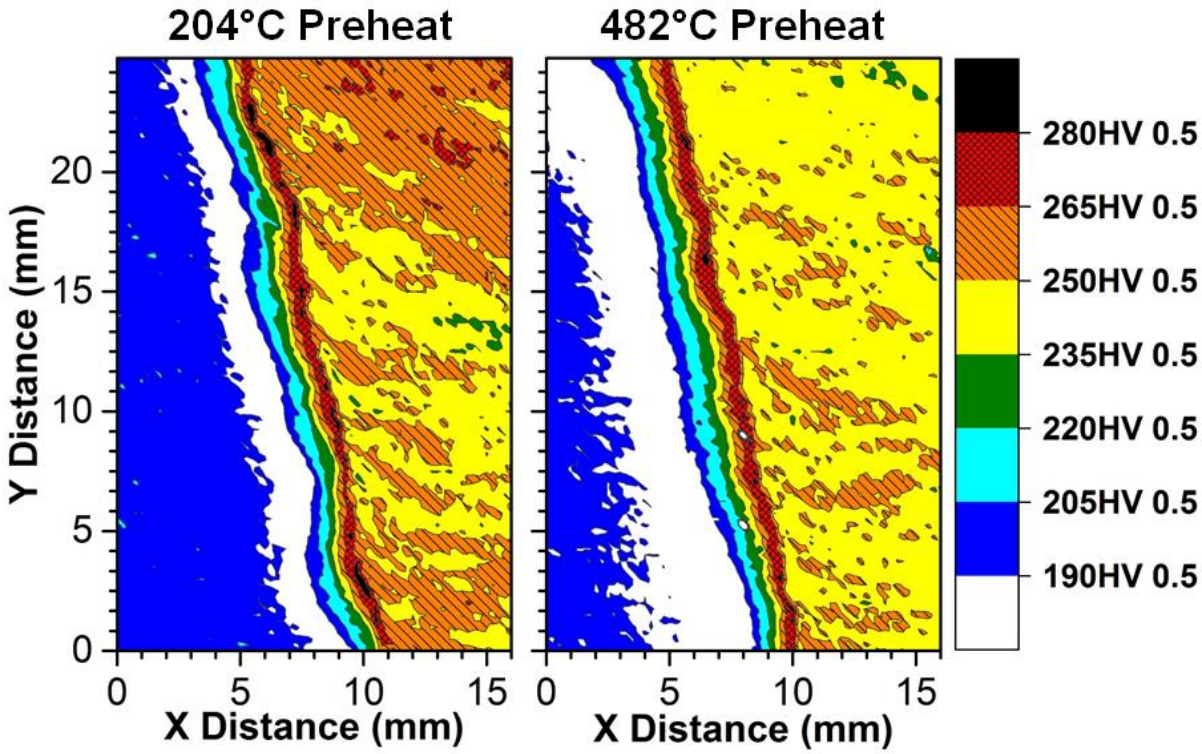

Figure 2-67. Color Hardness Maps Generated through a Large Portion of the Center of Each Weldment Produced with the Stated Preheat Temperature
Note: *Hardness map data produced using a Vickers indenter, 0.25 mm spacing, 25 mm tall X 16 mm wide (6400 total indents) and following a PWHT of 760°C/3h.*

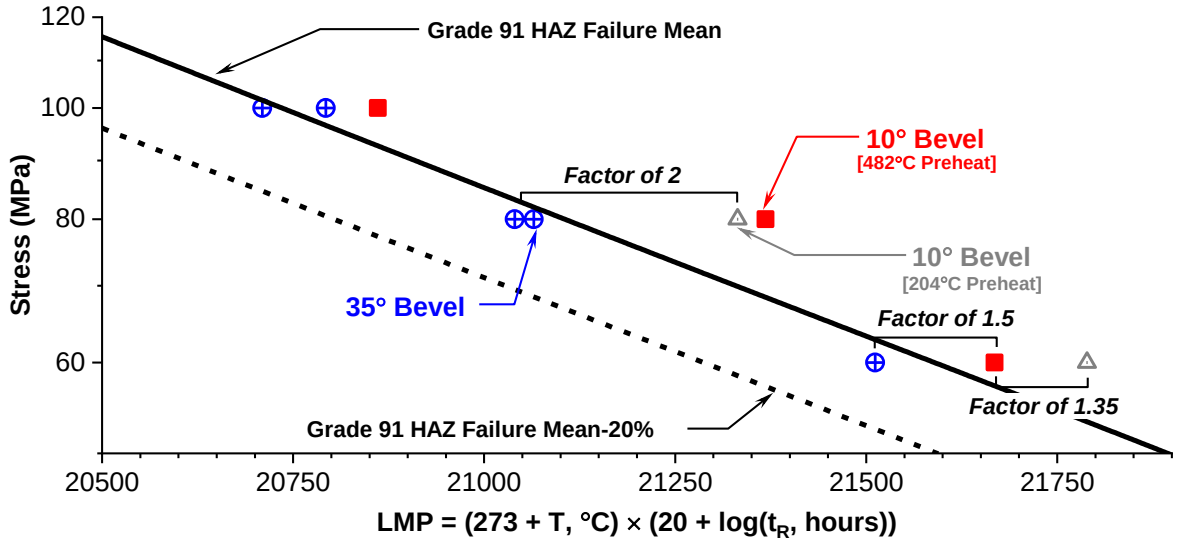

Figure 2-68. The Influence of Preheat and Bevel Angle on Performance of Large, Feature-Type Cross-weld Creep Tests in Grade 91 Steel and as Reported in (EPRI 2013a, EPRI 2015a).
Note: *There is no observed effect of preheat for a bevel angle of 10° and the observed, potential effect of bevel angle at 80 MPa is not as definitive at 60 MPa and for tests that approached or exceeded 10,000 hours in duration.*

2.15.3 The Influence of Heat Input and Post Weld Heat Treatment

Evaluation of heat input and PWHT was examined in Grade 91 steel in two studies (Rahman et al. 2013a, Ibid 2013b). Weldments using the SMAW process for three heat inputs (1.15, 2.28 and 3.16 kJ/mm; assuming arc efficiency of 0.8), a preheat of 200 to 250°C and PWHT of 760°C/3.5 hours were evaluated in cross-weld creep. Although representative welds were fabricated, the chosen test conditions produced results that may have been improperly assessed. In this study, a test stress of 135 MPa was selected and in a temperature range of 630 to 677°C (including two test temperatures >650°C; 665 and 677°C). The longest duration test using these conditions was 559 hours with most test results <100 hours. No comment was made regarding the failure location. The absence of any reference to the failure location in the cross-weld creep tests makes it impossible to draw any serious conclusion regarding the influence of heat input and PWHT on performance from this set of studies.

Few studies have been performed which examine the influence of PWHT on the cross-weld creep behavior of Grade 91 steel. This is because the balance of the world's Codes has mandated PWHT (typically in range of 730 to 790°C) for 9-12 wt. % Cr CSEF steels and for all product forms independent of thickness (ASME 2017, ASME Code Cases). In (Rothwell and Abson 2012), weldments were made in Grade 91 steel using the reduced pressure electron beam (RPEB) welding process. Cross-weld creep testing was conducted for five unique scenarios including:

1. As-welded;
2. Parent metal tempered at 760°C/6hrs, and left in as-welded condition;
3. Welded and given a PWHT at 760°C/3hrs;
4. Parent metal tempered at 760°C/6hrs, welded and PWHT @ 760°C/3hrs;
5. PWHT X 2 @ 760°C/3hrs.

The heating and cooling rates for these examined scenarios was controlled to 150°C/hr. The results did not provide a distinct result leading the authors to state that the "cross-weld creep rupture strength is not significantly influenced by sub-critical or post-weld heat treatments within the time and temperature ranges investigated, which are valid for most fabrication and repair purposes." Furthermore, and for the test

conditions that were utilized for screening these variables (630°C and 130, 110, 90, 80, 70 and 60 MPa) HAZ failures were reported for applied stress values ≤110 MPa.

2.15.4 The Influence of Filler Metal Strength

The effect of the filler metal strength on performance has been examined in (Mayr et al. 2013, EPRI 2014c, EPRI 2014d, Parker and Siefert 2016a]. In the approach in (Mayr et al. 2011), E911 was utilized as the parent metal since it nominally possesses a strength that is between that of Grade 91 and Grade 92. For the reported values in (Mayr et al. 2013), the 10^5 strength values according to ECCC and at 600°C for Grade 91, 911 and 92 steels are 86, 98 and 113 MPa, respectively. Based on these allowable values, using E911 allowed for an identical set of weldments to be made while only changing the filler material from slightly undermatching (Grade 91) to matching (E911) to slightly overmatching (Grade 92). All weldments were given an identical subcritical PWHT of 760°C/2hrs. This study is particularly relevant because of the identical test conditions for the three weldments with some durations approaching 50,000 hours.

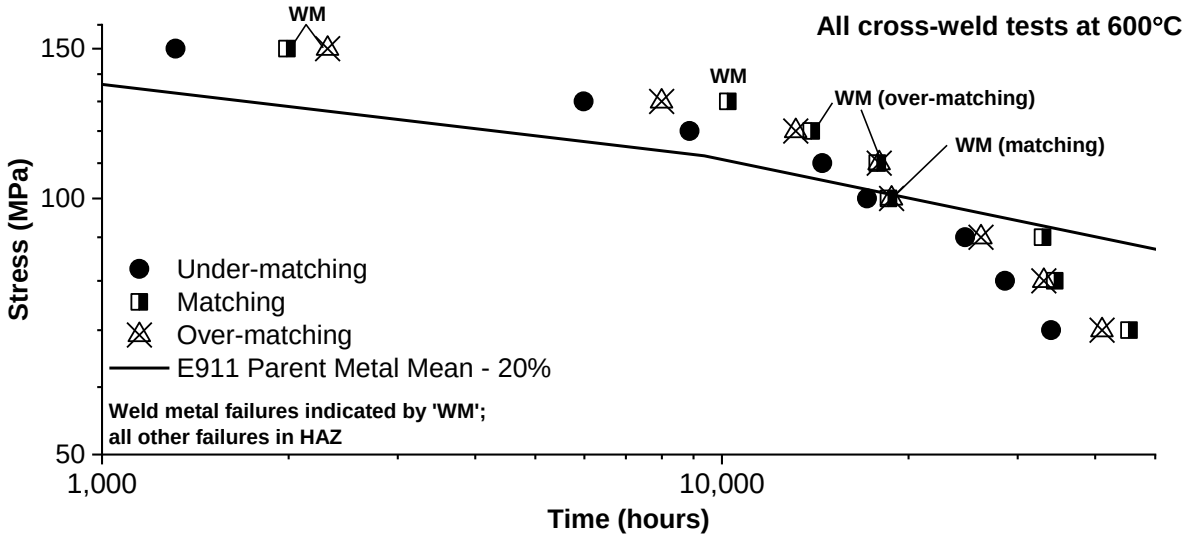

Figure 2-69. Larson miller parameter comparison for weldments fabricated in E911 steel using under-matching (Grade 91), matching (E911) and over-matching (Grade 92) filler metals.
Note: *all failures in the heat affected zone unless otherwise identified with 'WM', e.g. a weld metal failure (Mayr et al. 2011)*

From the data in Figure 2-69 and for tests ≤100 MPa there is a trend in that increasing constraint on the HAZ does increase the life. For all tests <100 MPa, the failure location was reported in the HAZ; the noted improvement in performance is only a about a factor of 1.3. For the matching and over-matching filler material, there is not a marked difference in behavior clearly suggesting that the matching filler material

sufficiently over-matches the E911 HAZ to provide a similar constraint to that of the over-matching filler material.

2.15.5 The Influence of Welding Procedure

In (EPRI 2014c), the influence of as-welded, simulated weld repair procedures with and without proper controls were compared to typical welding procedures given a low PWHT at 675°C/2h. All failures were reported to be in the HAZ, and as a result, there is not significant scatter in the data except for one data point, highlighted by the star in Figure 2-70. This data point represents a weldment that was tested with a single vee bevel at 25° whereas the others were tested with a single vee bevel of 10 or 15°. This test data was interesting when previously detailed results are considered (Abe and Tabuchi 2004, Cantin et al. 2009). Furthermore, two weld procedures examined the quality of the welding procedure on behavior. For the 'poor practice' welding procedure, weld beads were deposited in the weld joint such that an aligned region in the center of the weld contained refined weld metal. The lives for this weld were comparable to a cross-weld test for a weld procedure using a more acceptable bead placement. The results highlight the sensitivity of the material to HAZ failure.

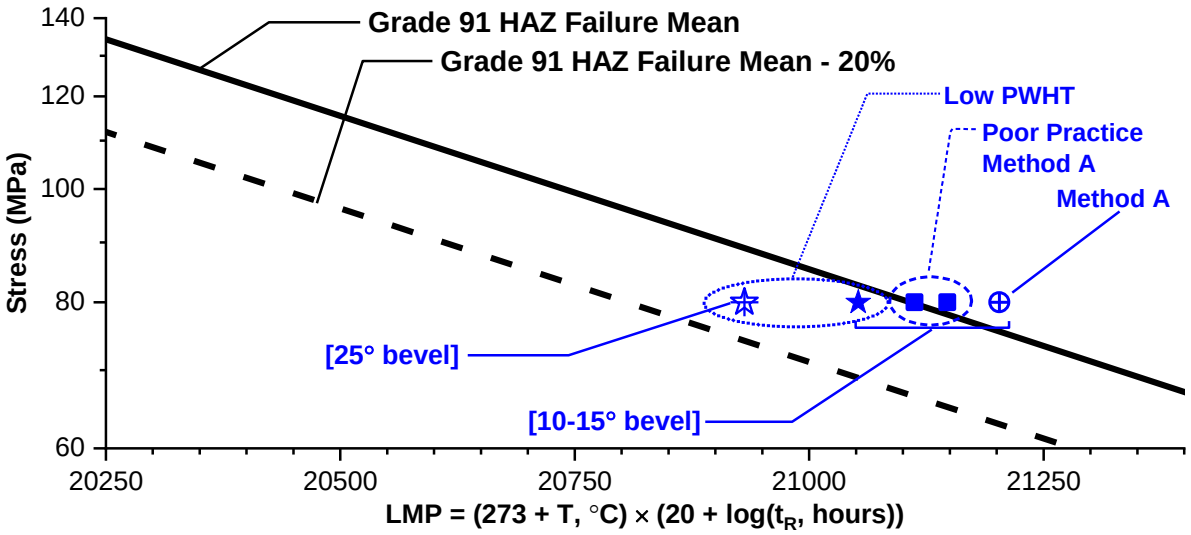

Figure 2-70. Influence of Welding Procedure on Performance of Simulated Weld Repairs in Grade 91 Steel including Procedures with and without PWHT
Note: *All welds made in the same parent material. Method A procedures made without PWHT. Those identified as having received a "Low PWHT" were given a subcritical PWHT of 675C/2h. All failures in the HAZ regardless of the welding procedure. Adapted from [14]*

2.16 Summary of Parent Metal Behavior

The observations of microstructural change on performance is critical in the evaluation of performance for 9 to 12 wt. % Cr steels because the in-service performance has

been observed to be variable, including failures well before the intended design life of the component (Brett et al. 1999, EPRI 2009, Brett and Parker 2013, EPRI 2015e, Nitsche et al. 2015). The application of conventional non-destructive evaluation (NDE) techniques have not been fully proven to detect damage until at least 90 to 95% of consumed life in martensitic steels (EPRI 2015d, Parker et al. 2012). This fact emphasizes the need for better predictive assessments using constitutive models sufficient to not only accurately interpolate a given database, but also allow for physically-sensible extrapolation beyond the bounds of the database. Achieving this objective is only possible using mechanistic and physics-based, materials models which incorporate multiaxial affects representative of component behavior.

Analysis of an available, representative set of research studies in the literature provide perspective on a few trends that should be considered in the analysis of parent metal behavior. The factors summarized below are specific to the deformation resistance of 9 to 12 wt. % Cr martensitic steels:

- The resistance to deformation is controlled by the subgrain boundary.
- The subgrain boundary structure is stabilized by the controlled distribution of precipitates which pin these boundaries and in Grade 91 steel, the stabilization is linked to the distribution of $M_{23}C_6$ carbides (and perhaps more specifically the inter-particle spacing).
- MX carbonitrides are observed to effectively impede dislocation motion inside subgrain boundaries, but the random distribution of MX carbonitrides has not proven to be dominant regarding subgrain boundary stabilization due to the differences in volume fraction (i.e. $M_{23}C_6$ exists in a volume fraction that is ~5 to 10X greater and $M_{23}C_6$ partitions to the grain boundary as opposed to the random distribution of MX throughout the matrix)

Important considerations governing the evolution of creep damage are highlighted below in the context of martensitic CSEF steels:

- Where a high density of cavities is observed to contribute to low ductility creep failures, there must be many nucleation sites;
- The nucleation sites in 9 wt. % Cr steels may consist of one of the following combinations based on the available research:

- Inclusions of the basic forms MnS, Al_2O_3, SiO_2, AlN or BN or complex variations which can include additional elements such as Ca or Mg.
- Subgrain boundaries that may possess segregated tramp elements such as Sn;
- Evolution of deleterious particles which coarsen rapidly and beyond a critical radius resulting in sufficient incoherency with the matrix to nucleate voids. These particles may include Laves or Z-phase and are generally seen to be dependent on the composition and operating temperature of the steel. In 9 wt. % Cr steels it has not been definitively shown that either phase is a dominate contributor to damage on a consistent heat to heat basis;

- Based on the available literature and historical precedence there clearly exists a hierarchy of susceptible particles to the nucleation of damage:
  - There does not appear to be a dominant high or low angle boundary which consistently nucleates creep voids. Thus, the distribution of damage in martensitic CSEF steels can be regarded as random in nature with respect to the grain/subgrain boundary distribution;
  - The most susceptible particles to creep void nucleation are inclusions since these can exist in large populations and with a diameter that is on the order of 1,000 nm at the time the steel enters service. This is problematic since inclusions are at least 10X greater in diameter than the nearest, comparably sized carbonitride for a component entering service (i.e. $M_{23}C_6$ or Laves phase which is ~100 nm in diameter in the as-manufactured condition).
  - The modern practice of inclusion optimization includes the introduction of Ca to create a larger population of more widely dispersed fine inclusions to increase the fracture toughness. However, this method of inclusion optimization is potentially detrimental to the creep ductility since relatively “small” inclusions on the order of ≤1,000 nm still represent ideal sites for cavity nucleation.
  - The modern steel practice of continuous casting billet may present additional complexities regarding damage since inclusions can agglomerate and/or act as ideal segregation trap sites. Because of the continuous casting process and its potential for segregation, the

production of continuous cast billet must include slow cooling from melting to prevent cracking of the billet. In some cases, hot forging steps of the billet are deliberating introduced to sufficiently “break up” the segregated microstructure whilst in other steel making routes these practices are not utilized. Thus, there is a potential large range in steel making practices around the world which may inadvertently increase the risk to damage in martensitic CSEF steels.

- Because inclusions exist in the steel from the initial melting process of the billet, they are likely to represent ideal trap sites for steels which have appreciable levels of tramp/impurity elements such as Al, As, Cu, Pb, S, Sb, Sn, etc. These elements locally reduce the boundary resistance to fracture and therefore increase the susceptibility to void nucleation. Where excessive levels of these impurities exist, they may be more uniformly distributed throughout the microstructure and along grain boundaries.

The implications of the factors which contribute to deformation and damage must be properly accommodated in models used to assess and/or predict component integrity. Since many models aim to fit creep curves as opposed to address the underlying physics of the material, it is vital that the descriptions used in constitutive models be grounded in a combination of component performance and underlying material behavior. The goal, therefore, in modeling simulations cannot be to merely assess a given creep curve, but to provide a rational approach which aims to firstly predict where damage may occur in a component and secondly within a reasonably accurate timeframe in which to begin inspections. Too often this is not achieved because the developed relationships are only validated using available creep curves produced from uniaxial creep tests and in some cases from a single heat of material or a pre-selected, minimal set of heats. This paradigm must change if the paramount issue of when and where to inspect for damage is to be sufficiently addressed for the end-user of 9 to 12 wt. % Cr CSEF steels.

2.17 Summary of Cross-weld Creep Behavior

Cross-weld creep performance is often assessed for a single heat or limited set of variables. Few studies have simultaneously examined behavior where multiple

welding variables were systematically altered. Additional context for this observation is summarized below:

- Assessment of cross-weld performance is often reported using small diameter samples which include a single HAZ convoluting the assessment of damage in the post-test condition. This is problematic since the immediate sequence leading to failure can promote local plasticity and mask the underlying features responsible for the development of damage, resulting in the formation of micro-cracks which might rapidly link to form a dominant macro crack and result in rapid crack propagation.
- Unlike parent metal tests, which often report failure times in the 10,000s of hours, cross-weld creep tests are generally tested for shorter durations due to the observed reduction in performance. There is little, general consideration or consensus of what constitutes a relevant set of test conditions and/or test geometries for 9-12 wt. % Cr CSEF steels.
- Although the influence of filler metal strength on HAZ performance for a 9 wt. % Cr CSEF steel (E911) was the focus of the study in (Mayr et al. 2011), the strength of the deposited weld metal relative strength to the HAZ may not have been sufficiently extreme. For example, the development of damage was consistently reported in the HAZ and particularly for test conditions within relevant stress ranges for the steel of interest. Examples exist for investigation of relative extremes in weld metal strength providing highly beneficial perspective on component performance in CrMoV steel and should be duplicated for Grade 91 steel (Hyde et al. 2001).
- Most studies do not investigate interrupted samples. Where small diameter samples which might only contain a single HAZ for investigation, the value of interrupted samples should not be underestimated.
- Evaluation of damage using SEM-based imaging or quantifiable techniques is frequently performed in the etched condition although equipment and procedures exist to facilitate evaluation in the unaltered, as-polished condition.
- Research studies often do not provide a detailed set of evaluations in the as-fabricated condition to link to the post-test condition. Available information in the literature, particularly for low alloy steel testing, recognized the potential importance of parent metal creep ductility on cross-weld creep performance.

This assertion was not recognized in the studies, neither early nor even recently, with respect to 9 to 12 wt. % Cr martensitic CSEF steels.

- There exists widespread disagreement on which HAZ region is responsible for the development of damage and resulting Type IV macro-failure classification. A similar number of studies claim that the region responsible for failure is the soft zone, the ICHAZ or the FGHAZ. Ultimately, it should be recognized that the classification of HAZ regions to the diagram proposed by Easterling may not be appropriate for 9-12 wt. % Cr martensitic, CSEF steels. More recently, the HAZ for this class of martensitic steels has been proposed using a more simplistic classification scheme developed by Xu et al. (2017). This approach is consistent with the assessment developed by the original alloy manufacturers for Grade 91 steel.
- Researchers often attempt to link the soft zone in the post-test condition to the soft zone in the as-fabricated condition without a clear set of well-defined evaluations which support this approach. For example, the hardness reduction observed in the HAZ following creep testing could be linked to the evolution of creep voids and simultaneous microstructural effects complicating the interpretation of the result.
- Few investigations evaluate ex-service parent material behavior. This point was commonly addressed as part of routine failure examinations in low alloy steels, see examples provided in (Ellis et al. 1982 and Westwood et al. 1990).
- On a microstructural level, there is little agreement regarding the responsible feature(s) for the nucleation of creep damage. There are manuscripts which suggest that the responsible particle is coarse $M_{23}C_6$, Laves phase, or Z-phase, or local interactions between martensitic and ferritic grains, or local subgrain recovery among others. Very few studies have attempted to evaluate the manifestation of damage in CSEF steels, one such evaluation has been recently detailed for an advanced 9 wt. % Cr CSEF steel in (Schlacher et al. 2015).

The overall set of available information, including reporting on Grade 91 steel since the early 1980s, still contains significant gaps and particularly for cross-weld assessment. This statement, on the surface, is perhaps hard to fathom but is indeed a reality. A continued emphasis on easy-to-use methods like light microscopy or

hardness testing as opposed to relevant methods for assessing martensitic, CSEF steels continue to result in questionable interpretations. Today's access to advanced microscopy, let alone to routinely utilized characterization methods like hardness (e.g. mapping hardness), are far superior to the available tools/methods in the original development of Grade 91 steel. Additionally, it is demonstrated there does not exist a comprehensive study where extremes in parent metal deformation and damage resistance are evaluated in the context of cross-weld creep behavior. This is a vital need for the power generation industry since material in the plant is expected to exhibit large variability due to several complicating factors such as global material procurement, lack of QA/QC oversight during fabrication, complications associated with field PWHT, and the like. Such deficiencies have necessitated best practice documents to provide safeguards against gross errors in the fabrication and erection of Grade 91 steel comments (EPRI 2015f).

It is often the case that an at-risk component or system will not experience a simultaneous failure in an extensive manner. For example, In the catastrophic failure of long seam-welds in low alloy steels installed in the well-documented cases in the USA (EPRI 2017), a systematic failure of the entire system was never documented. The failure of a large section of piping was indeed catastrophic, but it is equally remarkable that the balance of the system was often inspected and deemed to be fit for service. It is the reality that assessment of fabricated, power generation components needs to locate and identify such at-risk locations accounting for key factors in the design, fabrication, operation and metallurgical risk of such components. This is only possible if the variability in material performance is sufficiently evaluated under well-controlled conditions, and for 9 to 12 wt. % Cr CSEF steels this must include an assessment of cross-weld behavior.

3 Experimental Procedure

The series of microstructural assessments in this research are focused on linking observations in the as-fabricated, pre-test condition to the observed damage in selected cross-weld creep test samples. Historically, for power plant components a reliance has been placed on simplistic approaches for evaluation including hardness traces, light microscopy and basic scanning electron microscopy (SEM) imaging. An attempt is made in this chapter to provide a standard set of procedures beyond the historical, basic methods. The aim in using this set of methods is to provide a balance of quantitative assessment in subsequent chapters and illustrate the value of these procedures when coupled with well-controlled, feature-type cross-weld creep tests. The set of procedures addresses the series of questions and methods listed in Figure 3-1.

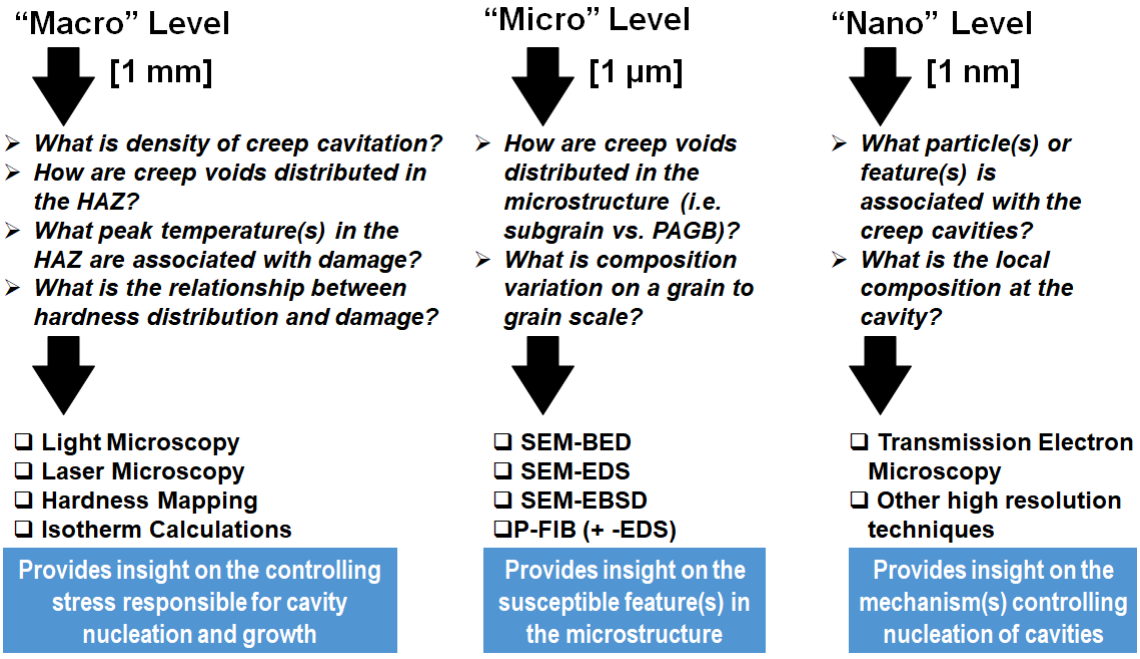

Figure 3-1. A common set of questions and techniques that can be used to address assessment of 9 wt. % Cr creep strength enhanced ferritic (CSEF) steels

As suggested in Figure 3-1 the detailed procedures used to evaluate cross-welds in the as-fabricated and post-test condition are often classified based on length scale. The objectives of this evaluation are to provide comparable information for six total weldments using an identical set of procedures and to link these results to the post-test condition. In the first section of the experimental procedure, the procedures for macro-characterization are detailed. The objective in these macro-based procedures

is to evaluate the effect that the welding thermal cycle has on the distribution of damage through the heat affected zone (HAZ); e.g. with respect to damage as a function of distance from the fusion line, Figure 3-2.

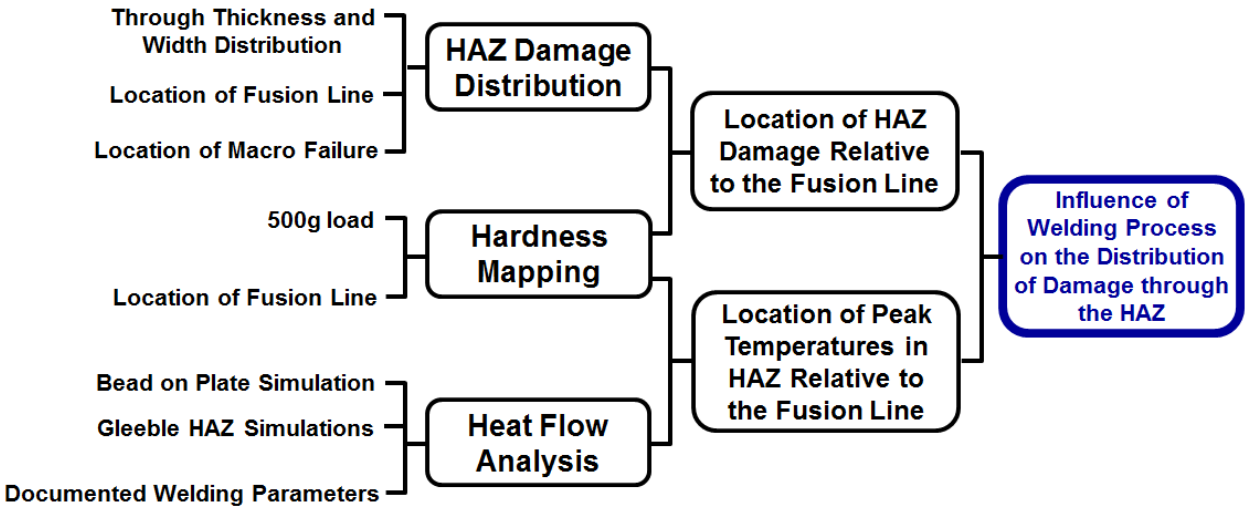

Figure 3-2. Documentation of the experimental procedures described in this manuscript as linked to the results needed to answer the objective (blue box) for the macro-based analysis

Regarding the micro-based analysis, SEM-based techniques are used to collect key results which are summarized in Figure 3-3. As indicated, the objective (given in blue outlined box) in this set of analysis is to identify susceptible features in the HAZ responsible for damage. In the following sections, each of the highlighted analyses are presented to provide supporting information to achieve the objective.

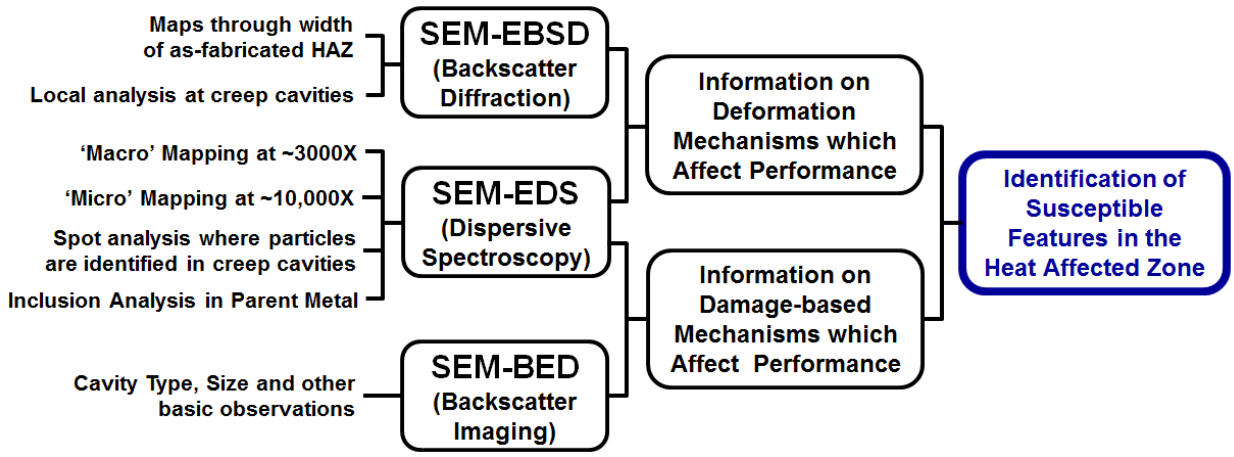

Figure 3-3. Documentation of the experimental procedures described in this manuscript as linked to the results needed to answer the objective (blue box) for the micro-based analysis

3.1 Parent Metal Selection

3.1.1 Condition

The two parent materials of interest in this study, Tee Piece 1 (TP1) and Barrel 2 (B2), were removed from an ex-service header that was designed to conditions of 580°C and 17.6 MPa and operated in-service for 79,000 hours before replacement. Detailed information in Chapter 4 provides a rationale for the condition of these materials as well as salient background information on operating history.

3.1.2 Chemical Composition

It is important to obtain a complete, chemical composition for Grade 91 steel base material. As highlighted in [EPRI 2014a, Siefert et al. 2016], there is concern that the influence of tramp elements such as, As, S, Sn, Sb and Cu has been underappreciated and that these elements are playing a role in the reduction in creep ductility in martensitic CSEF steels. In general, the analysis of elements can be grouped into elements required by common specifications for Grade 91 steel (14 total elements) [Table 1-2] and elements for informational purposes (typically 10+ additional elements), Table 3-1.

Table 3-1. Elements which should be considered for analysis in 9 wt. % Cr Steels

Elements required by conventional specifications for Grade 91 steel product forms [e.g. SA-182 F91, SA-213 T91, SA-335 P91]	Al, C, Cr, Mn, Mo, N, Nb, Ni, P, S, Si, Ti, V, Zr
Suggested minimum list of additional elements, even if for informational purposes	As, B, Cu, O, Pb, Sb, Sn
Additional list of elements for analysis where specified and/or required	Bi, Ca, Co, La, Ta, W

The following approaches were utilized to determine the quantity (or weight percent) of each of the elements. Inductively coupled plasma optical emission spectrometry (ICP-OES) was utilized to determine the values for: Al, B, Ca, Co, Cr, Cu, La, Mn, Mo, Nb, Ni, P, Si, Ta, Ti, V, W, Zr. Inductively coupled plasma mass spectrometry (ICP-MS) was used to determine the amounts of As, Bi, Pb, Sb, Sn. Finally, a combustion method was necessary to determine the C, S levels while insert gas fusion (IGF) was used to assess the amount of O and N in the steel. It should be noted that, to ensure sufficient information is provided for each of the requested elements, the number of

required significant digits should also be specified in any instructions to the laboratory performing the analysis.

3.1.3 Inclusion Analysis

The number density and type of inclusions in the parent material were evaluated to provide a 'fingerprint' of the parent metal condition. As reviewed in Chapter 2, prior research has indicated some association of poor performance in the HAZ with an increased inclusion density (Parker and Parsons 1995). Inclusion analysis was conducted in this research using an automated scanning electron microscope coupled with energy dispersive spectroscopy (SEM-EDS) using a tungsten source. The system used was FEI's Aspex Explorer model. Analysis was performed using the Automated Feature Analysis (AFA) and reports created using the Metals Quality Analysis (MQA) software. The following parameters were utilized: an accelerating voltage of 20 kV, a working distance of ~17 mm, a minimum EDS scan time of 1 second, a maximum EDS scan time of 2 seconds and in an area measuring 7.2 X 7.2 mm (51.5 mm^2). The minimum identified particle threshold was set to 1 µm and the maximum to 228 µm.

The inclusion index is a value provided by the MQA standard documentation and is calculated from the area of scanned inclusions divided by the total area scanned. The discrepancy between 'total features' and 'characterized inclusions' is explained by three potential observations:

- The identified potential inclusion sites may not have had a particle inside the feature; or
- The particle was below the specified threshold for diameter and contained an inclusion that could not be sufficiently indexed against the inclusion database; or
- The particle was near the specified threshold size and contained a complex inclusion which was not able to be definitively indexed against the inclusion database.

3.1.4 Heat Treatment of Parent Material

The two parent materials of interest in this study, Tee Piece 1 (TP1) and Barrel 2 (B2), were given selected heat treatments to 'restore' the material to a 'like-new' state (e.g. renormalization and tempering in black) or to deliberately produce a ferritic

microstructure (blue), Figure 3-4. Combined with evaluation in the as-received, ex-service state, there were a total of four parent metal conditions. TP1 was heat treated to produce a ferritic microstructure and B2 was heat treated to produce an optimized microstructure that would be representative of the as-received condition and using the specified procedures in Table 3-2.

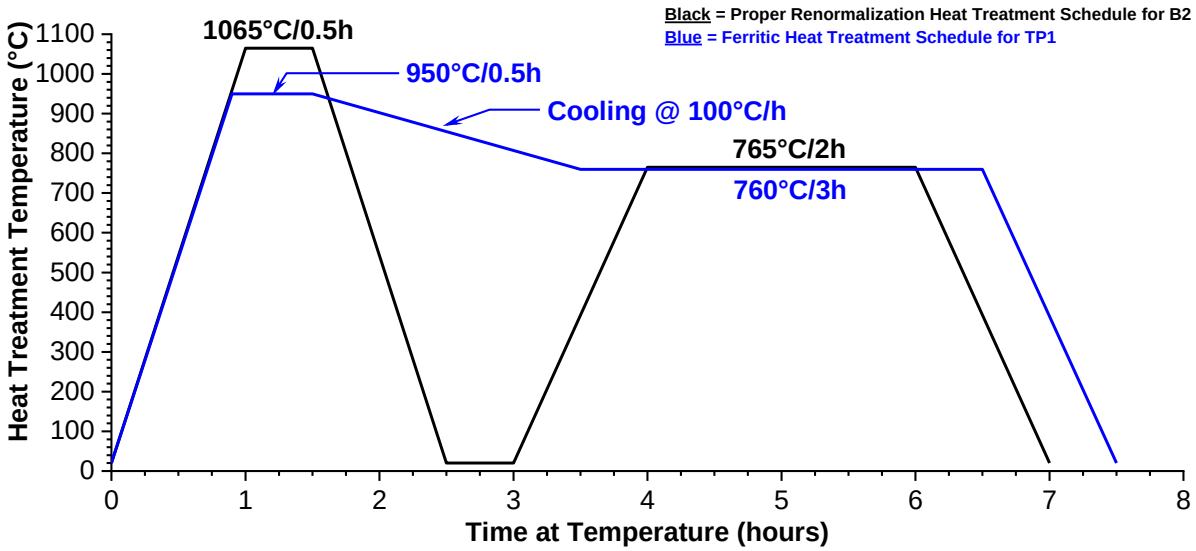

Figure 3-4. Heat treatment schedule for the renormalized and tempered B2 and the ferritic TP1

Table 3-2. Heat treatment procedures for the parent material prior to fabricating weldments.

Condition		Heat Treatment	Notes
1	As-received (AR)	Service-exposed at 570°C for 79,000 hours	TP1 and B2 material; designated as TP1 or AR-B2
2	Ferritic (F)	950°C/0.5h cool at 100°C/h to 760°C/2h/AC	Applied only to TP1 material; designated as F-TP1
3	Renormalization and tempering (RNT)	1065°C/0.5h/AC 765°C/2h/AC	Applied only to B2 material; designated as RNT-B2

3.2 Fabrication of Weldments

In total, six weldments were produced using an identical weld geometry in a total of four parent metal conditions. Weldments were fabricated with a machined U-groove or single-vee with a backing bar including a 15° bevel and using best practice guidance for the shielded metal arc welding (SMAW) process as detailed in (EPRI 2015b). This procedure included a minimum preheat temperature of 150°C (300°F), a maximum interpass temperature of 315°C (600°F), stringer beads only (e.g. no weaving was permitted), and removal of slag after each weld layer through light grinding. The

fabrication details for each weldment are provided in Table 3-3 and the filler materials used to fabricate the weldments are listed in Table 3-4.

Table 3-3. Details for the welding procedures used to fabricate the weldments in this study

Weld	Filler Metal	Diameter	Filler Metal Strength Relative to Parent Metal	PWHT
7C (TP1)	E9015-B9	• 3.2 mm (0.125 inch) for all fill passes	Matching	675°C (1250°F) for 2 hours
8C (TP1)	E8015-B8	• 2.5 mm (0.093 inch) for fill passes in contact with machined excavation and • 3.2 mm (0.125 inch) for the balance of the fill passes	Under-matching	None
9C (TP1)	EPRI P87	• 3.2 mm (0.125 inch) for fill passes in contact with machined excavation and • 4.0 mm (0.157 inch) for the balance of the fill passes	Over-matching	None
AR-B2 RNT- B2 F-TP1	E9015-B9	• 3.2 mm (0.125 inch) for all fill passes	Matching	675°C (1250°F) for 2 hours

Table 3-4. Filler material compositions, as reported by the material certification (values given in weight percent) and balance Fe

Material	Dia. (mm)	C	Mn	Si	S	P	Cr	Ni	Mo	Nb	Cu	Others
E9015-B9	3.2	0.10	0.52	0.26	0.008	0.010	8.4	0.3	0.96	0.04	0.06	V: 0.17 Al: 0.010 N: 0.040
E8015-B8	2.5	0.096	0.80	0.33	0.0059	0.0047	8.8	0.38	1.01			
E8015-B8	3.2	0.061	0.73	0.49	0.005	0.0026	8.8	0.29	0.88			
EPRI P87	3.2	0.09	1.6	0.43	0.009	0.010	9.0	Bal.	2.2	1.12	0.03	Fe: 39.9 B: 0.0009
EPRI P87	4.0	0.09	1.3	0.21	0.010	0.010	8.4	Bal.	1.7	1.31	0.02	Fe: 38.3 B: 0.001

The completed weldment including a macro sample, documented fill sequence, and the recorded data for current, voltage, travel speed and interpass temperature is provided in a later summary table (Table 3-5). In general, each weldment required about 200 weld passes to completely fill the excavation. Following welding, the weldment was slowly cooled to room temperature. Post weld heat treatment (PWHT) was performed at 675°C (1250°F) and for 2 hours for welds 7C, AR-B2, RNT-B2 and

F-TP1, consistent with the recommendations in (EPRI 2015c). Welds 8C and 9C were left in the as-welded condition.

3.3 Evaluation of the As-fabricated Condition

Macro-characterization of each weldment in the pre-test condition is summarized in Figure 3-2. Key assessments include the preparation of the sample for hardness mapping and the evaluation of the welding thermal cycle to link the isotherms through the HAZ to the distribution of damage following post-test evaluation of feature, cross-weld creep tests.

3.3.1 Sample Preparation

Macro samples prior to hardness mapping in the as-fabricated condition or performing post-test assessment for the macro-failure location or cavitation analysis were prepared using the following polishing procedure:

- **Grinding**. Sequential grinding using a silicon carbide abrasive with water and for grits of 120, 320 and 600.
- **Polishing**. 3 µm high performance finish using an abrasive pad imbedded with monocrystalline diamonds followed by a 1 µm high performance diamond polish. Hardness mapping and cavitation analysis were performed in the as-polished condition.
- **Etching**. After the hardness mapping was completed, the weldments made with Fe-base filler metals were etched in Villella's reagent containing: 45 ml glycerol, 15 ml nitric acid, 30ml hydrochloric acid. For the weldment made with Ni-base filler metal, aqua regia etchant was utilized ($HCl:HNO_3$ in a 3:1 ratio).

3.3.2 Hardness Mapping

The equipment utilized for the hardness mapping characterization was a LECO Automatic Hardness Tester, Model AMH-43. Hardness mapping was conducted so that the requirements in both ASTM E384-11 (ASTM 2011) and ISO 6507 (ISO 2005) were met. One of the key requirements in these two standards is that for a given hardness load (e.g. for this study 0.5 kgf), the indents should be at least 2.5d apart (where d = mean diagonal distance of the measured Vickers indent in the material being examined).

To validate the procedure using the stated 0.5 kgf load, an indent-to-indent spacing of 250 µm was chosen to prevent the potential for interference in the measurements. This spacing was utilized uniformly in both the X and Y orientations. The selected spacing between indents met the criterion in ISO 6507 and ASTM E384-11, and as validated using the relationship in Equation 3.1. Assuming a diagonal value of 100 µm (i.e. 250 µm spacing divided by the indent-to-indent minimum spacing of 2.5) the lowest theoretical hardness value that could be measured and still meet the requirements in each of the standards was 93 HV 0.5. This value is not likely to be observed in the examined material constituents in Grade 91 steel (parent, HAZ or weld). This statement is true regardless of the state of examined material (i.e. whether in the properly fabricated condition or in the ferritic condition).

Equation 3.1: $$\mathrm{HV} = \frac{1.8544\mathrm{F}}{\mathrm{d}^2}$$

Where:

$\mathrm{F} = \text{Force of Vickers indenter in kgf (i.e. 0.5 kgf)}$

$\mathrm{d} = \text{mean diagonal measurement of the pyramid Vickers indenter in material of interest in mm}$

$\mathrm{HV} = \text{Vickers hardness}$

The 0.5 kgf load for the Vickers hardness mapping was selected to minimize the standard deviation in the data. This effect has been previously investigated in (Siefert et al. 2013) where the standard deviation was seen to increase dramatically for lower loads of 0.10 or 0.20 kgf. This deviation is possibly due to a few potential sources of error, namely due to the sharpness of the indenter or the quality of optics used to measure each of the indents.

To ensure that sufficient resolution in the data was obtained, i.e. is to achieve enough indents in the heat affected zone, a very large area was analyzed so that a portion of the base metal, heat affected zone (HAZ) and deposited filler metal were captured in the hardness map. This approach resulted in a final hardness map size that was 25 X 25 mm and included a total of 10,000 indents, Figure 3-5.

If a conservative assumption is made regarding the width of the HAZ of 2.0 mm for the SMAW process, then it can be reasoned that at least 250 indents are obtained within the confines (through the width and along the length) of the analyzed region in the HAZ. Although this sounds insufficient based on the total number of indents captured in the hardness map, a conventional analysis of the HAZ region in Grade 91 steel

normally involves a single line trace or triplicate line traces at the root, mid-wall and cap regions. In the case of a triplicate line trace and using an identical procedure to that detailed here for an indent-to-indent spacing of 250 µm and indent load (0.5 kgf) the resulting scan would only produce a total of ~25 indents in the HAZ. In this regard, using a mapping procedure ensures at least an order of magnitude better resolution through the HAZ of the weldment and allows for a meaningful statistical analysis of the obtained data.

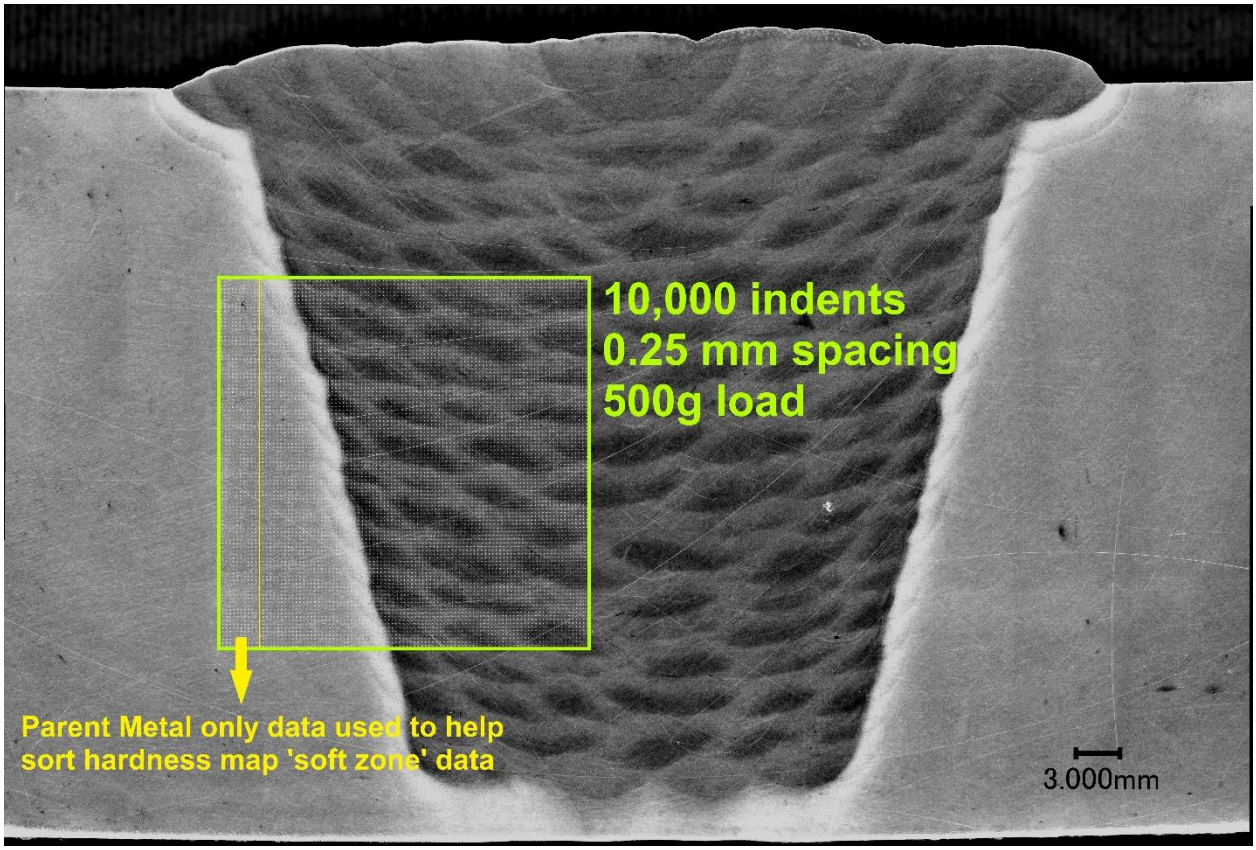

Figure 3-5. Location of the hardness map in the weldment of interest; hardness map contained a total of 10,000 Indents with the same spatial resolution in the X and Y orientations of 0.25 mm, Vickers indenter, a 0.5 kgf load and an area scanned that measured 25 X 25 mm

Color hardness maps were produced using the software package Origin. The hardness map data were sorted using obtained data from the parent metal hardness as reference. 1,000 data points in the unaffected parent material (shown in Figure 3-5) were used for the reference data. Using this data, a simple boxplot was created, Figure 3-6A.

An example of the filtering process required to set the ‘color’ thresholds for the hardness map plots is detailed in this section. An exemplar dataset is given in Figure 3-6A for TP1. The minimum threshold value for the color scheme for a given weldment

was set by the 10th percentile value. Analysis of each dataset on an independent basis was necessary as each parent metal condition (four total): AR-B2, TP1, RNT-B2 and F-TP1 possessed unique hardness distributions. Data below the 10th percentile were potentially flagged as being in the over-tempered zone (OTZ) in the HAZ and given the color white. For all other data, the color scheme was scaled to minimize the number of color variations in the plot to provide an easier interpretation of the data.

Subsequent analysis of the data ≤10th percentile was performed, such as the exemplar data provided in Figure 3-6B. For all data ≤10th percentile, the location of each hardness value was referenced with respect to the fusion line. The location of the fusion line was determined after etching the exact region for which the hardness map had been carried out. In the boxplot provided in Figure 3-6B, the data are plotted as the location of each hardness indent ≤10th percentile as a function of distance from the fusion line. The OTZ was considered to exist in the regime represented by the 5th to the 75th percentiles, as indicated in Figure 3-6B. This value was then compared to the macro failure location and to the distribution of damage in the HAZ for the given weldment.

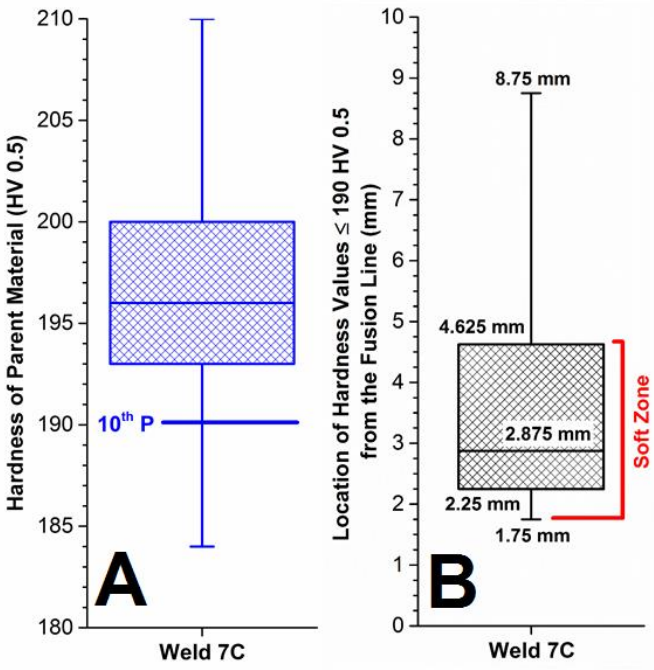

Figure 3-6. A – Boxplot analysis of the parent metal hardness values as shown in Figure 3-5. In this plot the whisker lengths represent the minimum and maximum of the dataset, while the box values are the 25th, 50th and 75th percentiles.
Note: *that the 10th percentile is provided for reference, i.e. 190 HV 0.5. B – Boxplot Analysis of the Location from the Fusion Line of all Hardness Values ≤190 HV 0.5. In this plot the whisker lengths represent the 5th and 95th percentiles of the dataset, while the box values are the 25th, 50th and 75th percentiles. Note that the so-called 'Soft Zone' (i.e. Over Tempered Zone) is shown as being located from ~5th to 75th percentiles, i.e. from 1.75 to 4.625 mm from the fusion line.*

3.3.3 Micro-XRF Mapping

The equipment utilized for the micro-XRF mapping was an EDAX Orbis PC. This equipment uses a rhodium x-ray source and contains a high precision, automated stage to facilitate mapping. An area in the center of the as-welded sample was scanned using an accelerating voltage of 25 kV, a 10 mm working distance, dwell time of 2,000 ms over an area ~10 mm tall by ~20 mm wide at a resolution of 30 µm. The number of measurements collected in the area were 760 X 431 yielding a total of ~325,000 measurements. One weld was mapped using this process, the under-matching weld 8C which was welded with AWS type -B8 filler metal. The collected data were post-processed using the software package Origin Lab. Data were collected for Cr, Ni, Fe, Al, Mn, Mo, Nb, S, Si and V. Only the data for Cr, V and Mn are reported to illustrate this variability as the objective of this evaluation was to examine the heterogeneity of the weld.

3.3.4 Evaluation of As-fabricated Welding Thermal Cycle

Solutions for thick-plate thermal heat flow have been investigated and evolved since Rosenthal introduced solutions in the early 1940s (Rosenthal 1941, Ibid 1946). Available solutions exist for an approximate determination of the calculated peak temperature with respect to the fusion line using a range of potential solutions. The selected solution is provided as an example problem in (e.g. in Grong 1997) and for a 3D thick plate solution, as justified by plotting the general welding conditions for the stated weldments in Figure 3-7.

With regards to any simplified solution, it is imperative that reasonable assumptions, and more ideally actual measurements, be utilized to reduce the uncertainty in the calculation. The selected solution requires a series of five basic calculations shown below in Equations 3-2 to 3-6 and requires the use of Figure 3-8. The indicated region in Figure 3-8 was fit with a polynomial function to avoid estimating the value directly from the chart. The terms used in the calculation are defined in Table 3-5 and Figure 3-8:

Equation 3-2: $$\frac{\theta}{n_3} = \frac{4\pi a^2 \times \Delta H}{I \times U \times \nu \times \eta}$$

Equation 3-3: $$\frac{n_3}{\theta_p} = \frac{1}{\frac{\theta}{n_3}}$$ *used to estimate Λ_1 from Figure 3-8*

Equation 3-4: $\frac{n_3}{\theta_p} = \frac{1}{\frac{\theta}{n_3}} \times \frac{(T_m - T_o)}{(T_{peak} - T_o)}$ *used to estimate* ψ_m *from Figure 3-8*

Equation 3-5: $\Delta\psi_m = \psi_m - \sqrt{\frac{2}{\pi} \times \Lambda_1}$

Equation 3-6: $\Delta y_m = \frac{2a \times \Delta\psi_m}{v}$

Table 3-5. Definitions and values used in the simplified calculation of the distribution of peak temperatures through the width of the heat affected zone (i.e. as a function of distance from the fusion line)
Note: *F-TP1 not shown as damage was consistently observed in the parent metal and not in the heat affected zone. Thus, the F-TP1 weldment was not considered in the weld thermal cycle analysis*

Variable	Definition	7C	8C	9C	AR-B2	RNT-B2	Units
T_o	Interpass temperature [mean value from Figure 4]	205	188	170	178	178	°C
I	Amperage [mean value from Figure 4]	115	89	100	120	122	A
U	Voltage [mean value from Figure 4]	23.3	23.4	22.7	23.5	24.0	V
v	Travel Speed [mean value from Figure 4]	2.34	3.54	3.68	2.96	2.96	mm/s
η	Arc Efficiency (SmartWeld 2016)	0.75	0.75	0.75	0.75	0.75	N/A
a	Thermal Diffusivity (Swindeman 2015)	6.1	6.1	6.1	6.1	6.1	mm^2/s
T_m	Melting Temperature [Figure 8]	1500	1500	1395	1500	1500	°C
ΔH	Enthalpy Increment (Grong 1997)	7.5	7.5	7.5	7.5	7.5	J/mm^3
y_m	Maximum width of isotherms	See equations 3-2 to 3-6 and Figure 3-8					mm
θ	Dimensionless temperature	See equations 3-2 to 3-6 and Figure 3-8					None
θ_p	Dimensionless peak temperature	See equations 3-2 to 3-6 and Figure 3-8					None
Ψ_m	Dimensionless maximum width of isotherms	See equations 3-2 to 3-6 and Figure 3-8					None
Λ_1	Dimensionless cross-sectional area	See equations 3-2 to 3-6 and Figure 3-8					None

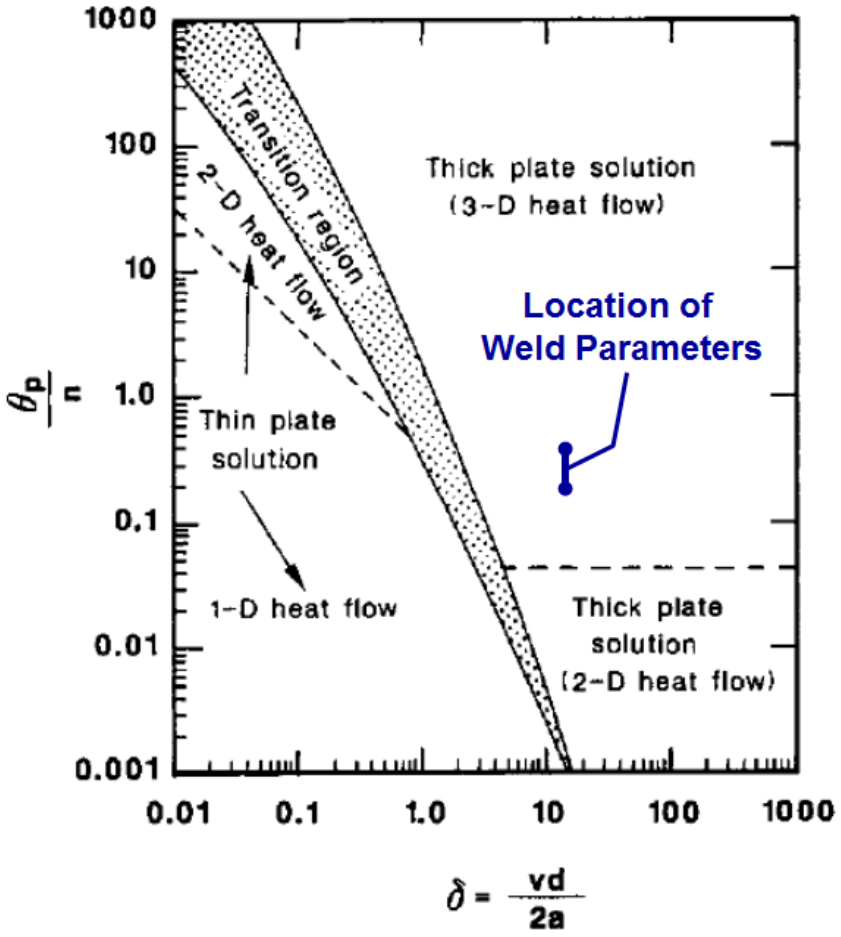

Figure 3-7. Validation of selected, simplified solution for available heat flow models and the utilized welding parameters, plotted against figure in (Myhr and Grong 1990)

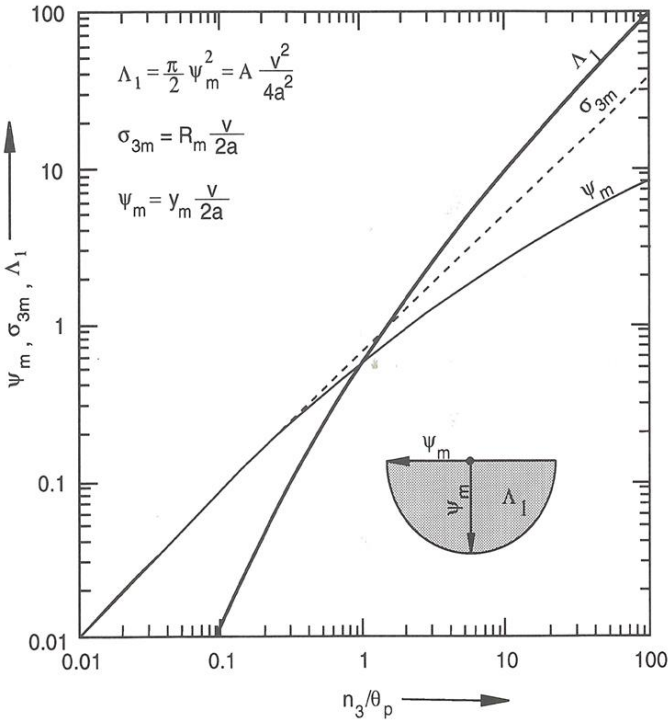

Figure 3-8. Dimensionless distance σ_{3m}, half width ψ_m and cross-sectional area Λ_1 vs n_3/θ_p; from (Grong 1997)

As the melting temperature for Grade 91 steel and EPRI P87 Ni-base filler metal is not widely reported in the open literature, a simulation was performed in ThermoCalc using the TCFe5 database to calculate this temperature, Figure 3-9 (ThermoCalc). The reference compositions are given in each of the Figures. As provided in Table 3-5 and Figure 3-9, the melting temperature was determined to be 1500°C for Grade 91 steel and 1395°C for EPRI P87. These results are in good agreement with the general, stated melting temperatures for unalloyed steel, 1525°C or the Ni-base alloy 600, 1400°C (Easterling 1992).

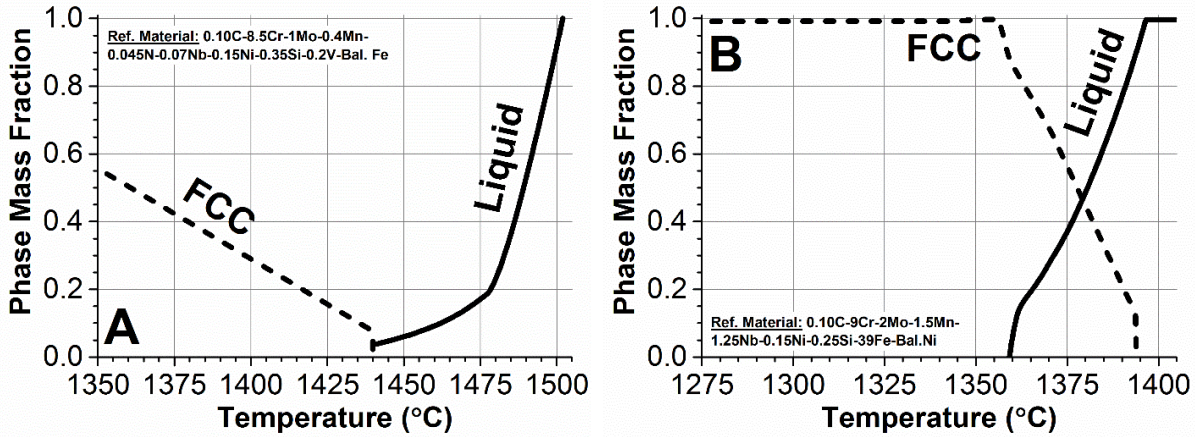

Figure 3-9. Calculation of the melting temperature using the ThermoCalc database TCFe5 and for A – Grade 91 reference composition (given in weight percent) and B – EPRI P87 reference composition (given in weight percent)

To ensure that the simplified, isotherm calculation was valid with respect to the Grade 91 welded with an Fe-base filler metal, an assessment against documented thermocouple data was performed. This validation compared the calculation in Equations 3-2 to 3-6 to actual thermocouple measurements in a 9 wt. % Cr CSEF steel thick pipe weldment, Figure 3-10 (Bauer et al. 2010). In these two figures, it is shown that the calculated data using the simplified solution is in very good agreement with the elevated temperature portion of the measured HAZ isotherms (i.e. for the measurements where the T_{peak} >875°C). Since failure in the HAZ occurs in a region that is approximate to or greater than this value (and will be shown in Chapter 7), the most critical portion of the reported data in (Bauer et al. 2010) is the portion >875°C. Reasons for the observed deviations in the discrepancy below this temperature are a result of the latent heat of the γ→α transformation. This will be elaborated in Chapter 5.

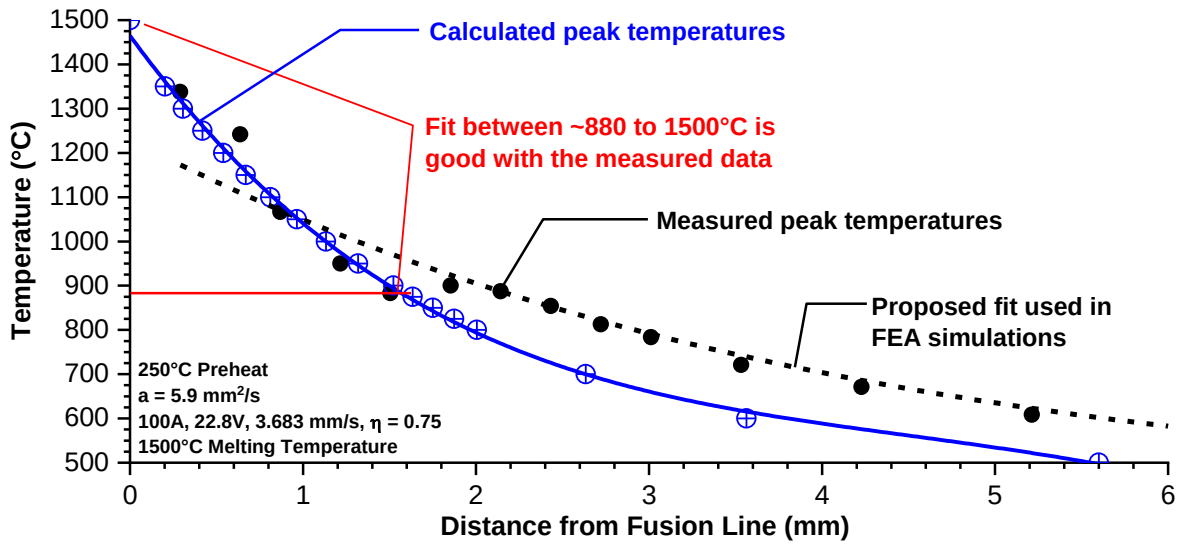

Figure 3-10. Comparison of results for the procedure in section 3.3.4 (blue data) for the measured peak temperatures to a series of embedded thermocouples in a thick-section pipe weldment (black solid circles) and a proposed finite element analysis fit in the literature
Note: *the fit between the proposed procedure and the actual measurements is excellent within the range of ~880°C (1615°F) to the melting temperature (~1500°C, 2730°F). The black data are from (Bauer et al. 2010)*

Sensitivity measurements for the simplified heat flow solution were conducted to determine the impact of the inputs on the calculation. Although not detailed in this section, the following variables can affect calculations, and are listed in order of highest to lowest impact on the calculated isotherms: arc efficiency and/or heat input (high impact); melting temperature (medium impact) and thermal diffusivity (low impact). In summary, it is particularly important to have an accurate set of measurements for the welding parameters such as those given in previous sections and for multiple passes to confirm consistency in the weld procedure and provide sufficient confidence in the calculation.

3.4 Cross-weld Creep Testing

Creep specimens were subsequently machined from the completed weldment. These specimens had a gauge cross-section of nominally 50 mm through the thickness of the weld, and 15.2 mm through the width of the weld, Figure 3-11. The gauge length was sufficient to include both fusion lines and both HAZs and was nominally 125 mm and provided the opportunity for metallographic analysis of the failure location as well as damage assessment of damage in the unfailed HAZ. The total area of the gauge cross-section in the feature test samples was ~635 mm^2; typical round bar creep specimens only have a gauge cross sectional area of 30 to 80 mm^2.

All testing was conducted using constant load (dead weight) machines under a set of standard test conditions for applied temperatures of 600 or 625°C monitored using three thermocouples attached at equal distances in the gauge length (3 total thermocouples). An additional test temperature of 575°C was included for Weld 8C. The test stresses were in the range of 50 to 90 MPa. These test parameters were selected based on the desire to develop HAZ-dominated failures.

Three thermocouples were distributed along the gauge length to monitor the temperature. The central 'hot zone' where the test temperature was recorded was within ± 2°C over the entire 125 mm gauge length. Samples were taken to either 100% rupture or terminated at a life fraction near rupture. For samples that did not completely rupture, testing was generally terminated upon indication of tertiary creep as the strain was continuously monitored during testing. There were two exceptions to this procedure:

- The weldment fabricated with an under-matching filler metal (e.g. Weld 8C) because the AWS type -B8 filler metal exhibited high creep ductility and reduced the triaxiality in the HAZ. Therefore, the '8C-X' tests featured a well-developed tertiary creep portion.
- The weldment fabricated with a low deformation resistant but creep ductile parent metal (e.g. Weld F-TP1) exhibited high creep ductility. These tests proceeded well into an observed tertiary regime.

For the balance of the weldments, and because failure often occurs with little macro tertiary creep in cross-weld samples in 9 wt. % Cr steels, it was sometimes not possible to interrupt the test immediately before failure. Whenever possible, the cross-weld creep test was always interrupted to preserve advanced stages of damage that otherwise might be difficult to assess due to macro tearing and local plasticity in the immediate sequence of events leading to final fracture. This is true for the tested weldments AR-B2, RNT-B2, Weld 7C (fabricated in TP1) and Weld 9C (fabricated in TP1).

Data recorded during each creep test included extension from two sides of an extensometer that extended over the total sample length, a calculated average extension, time to rupture, and temperature. Initially, the average extension was used to calculate creep strain based on the full original gauge length. However, this strain

is only representative of the nominal deformation of the sample. Local deformations that occur in the HAZ of matching cross-weld samples and the weld metal and HAZ of undermatching cross-weld samples are known to be underestimated by this approach.

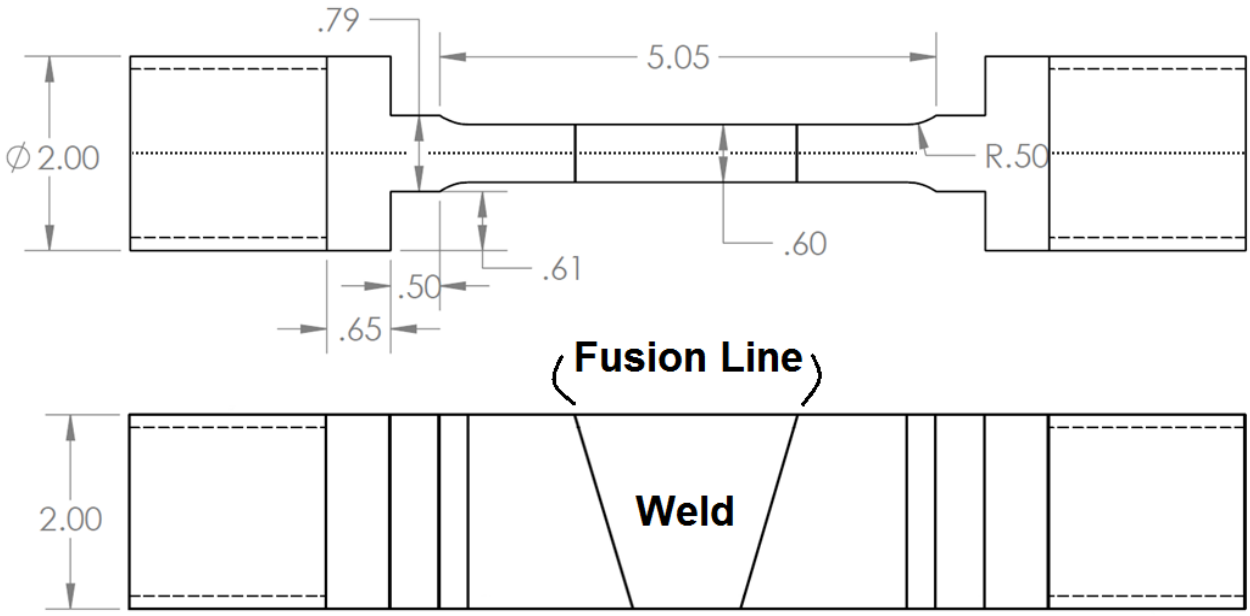

Figure 3-11. Feature, cross-weld creep test dimensions. Weld is indicated by the outlined location of the fusion line and as centered in the gauge length.
Note: *dimensions provided are in, inches; 25.4 mm = 1 inch*

3.5 Damage Evaluation

3.5.1 Post-test Sample Preparation

After creep failure or termination of the creep test, a macro sample was removed from the post-test feature creep test using fine wire, electrostatic discharge machining (EDM). All specimens were removed from the approximate center (dotted line in the top image in Figure 3-11) to analyze the most representative distribution of damage in the sample, Figure 3-12. Previous studies have highlighted the need to examine this center plane (EPRI 2013b, EPRI 2015d) as damage in materials susceptible to HAZ failure generally occurs subsurface. Creep damage is typically not surface-connected because the free surfaces do not experience a multiaxial stress state and are effectively at a zero or very low stress state. Subsequent preparation of each sample involved the previously detailed procedure for grinding and polishing.

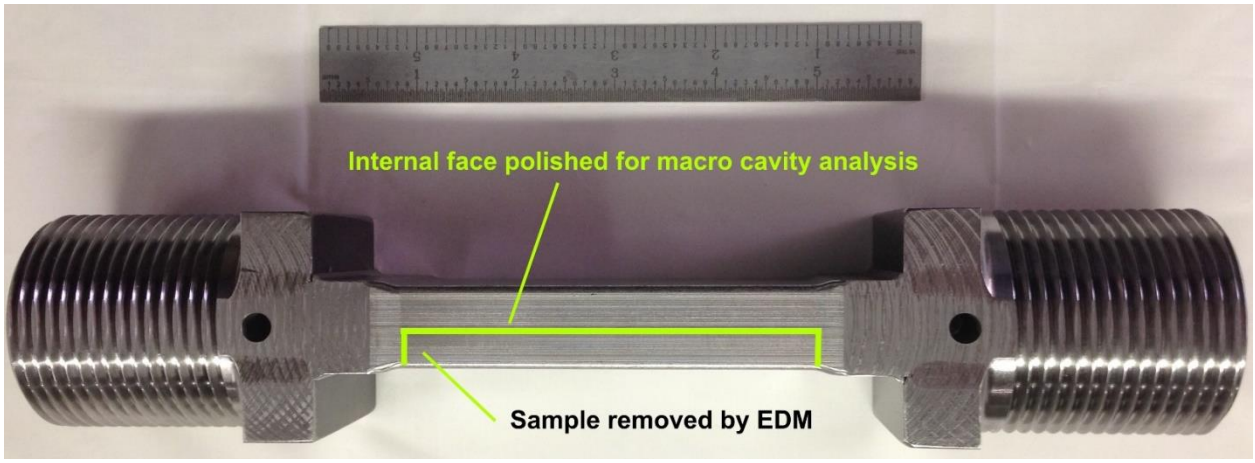

Figure 3-12. Details for the extraction of a sample for macro-evaluation following cross-weld creep testing

3.5.2 Evaluation of Macro-Failure Location

A Keyence VK-105 confocal laser microscope and a 5X objective was utilized to obtain through-thickness images for the failed and interrupted samples. Figure 3-13A details the procedure for evaluation where complete failure occurs through the HAZ whereas Figure 3-13B details the procedure for evaluation where the sample is terminated prior to complete failure but possesses large macro-crack(s) in the HAZ. Data were collected which included the failure, HAZ and a portion of the weld metal to identify the location of the fusion line.

Calculation of the mean distance between the fracture and the fusion line is provided in Figure 3-13. To identify the location of the fusion line, the image can either be adjusted using the VK Image Analyzer Software or etched prior to evaluation. The area, as identified in Figure 3-13 by the blue cross-hash marks, was obtained through measurement using the “area function” in the VK Image Analyzer Software. Similarly, the through-thickness distance “D” was measured using a “line measurement” function in the VK Image Analyzer Software.

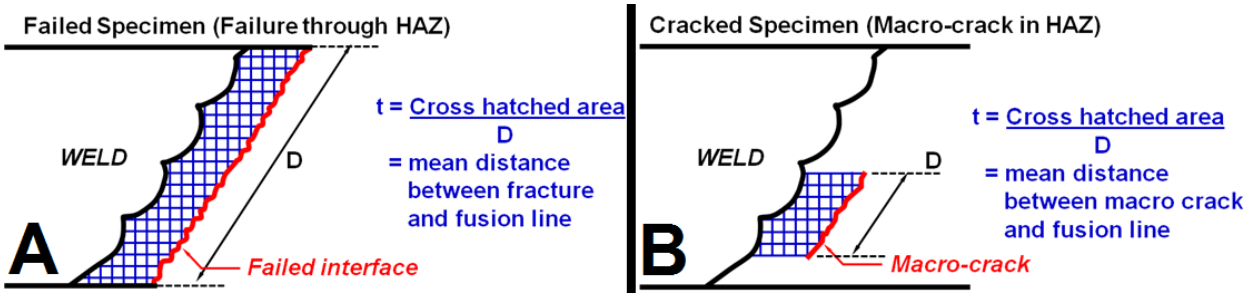

Figure 3-13. Evaluation of the macro-damage location in the heat affected zone and for samples taken to 100% failure (A) or terminated prior to complete failure (B)

3.5.3 Characterization of Macro-Damage through the Heat Affected Zone

The procedure provided in this section presents an evolved procedure beyond the one detailed in (Parker and Siefert 2016b). In the procedure described herein, an emphasis was placed on the development of a method to scan a larger area than in (Parker and Siefert 2016b) and to evaluate the collected data in its full resolution. This was made possible using a 'teaching function' in the VK-105 software that requires an additional level of expertise and the writing of additional software to assist in post-processing of the data.

A Keyence VK-105 confocal laser microscope and a 20X objective was utilized to collect images in the HAZ. The selected objective provides a magnification on a standard monitor that is ~400X magnification. However, and more importantly, due to the standard collection size of each image (695 X 522 µm) and the resolution (1024 X 768 pixels), the theoretical minimum cavity size that can be analyzed is 0.70 µm (1 pixel) in diameter. Due to the need for data filtering, the use of the stated 20X objective provides a more realistic analysis of the large dataset, where the minimum cavity size is on the order of ~3.5 µm (5 pixels) in diameter.

In the example shown in Figure 3-14 and Figure 3-15, a total of 270 images (6 images through the width X 45 images through the thickness) were collected in the HAZ for the failed creep test sample 7C-2 (625°C, 60 MPa). To reduce the number of required images (reduction by ~factor of 3), the sample was rotated such that the 15° plane created by the machined bevel and subsequent welding was adjusted to 0°. This procedure yielded an area of ~6,150 X 33,000 pixels for a total of ~207 million pixels. An overlap of ~1.5% was used such that the effective area captured was 685 X 515 µm (1010 X 755 pixels) and to facilitate meshing of the entire captured area in the VK Assembly software. Accurate spatial position was maintained by an automated stage that has a maximum travel distance of 100 mm in both the X and Y direction.

The data collection and post-processing sequence is detailed below:

1. Images were obtained using a Keyence VK-105 confocal laser microscope. A total of 270 images were obtained in a .vk4 format;
2. A custom-built program (Java-based routine) converted each individual .vk4 laser file into a .bmp file [for ~270 images this process takes <60 seconds];

3. MatLab was utilized to count and locate each cavity in X-Y space. A custom routine written by the Ohio State University (OSU 2015) analyzed the individual .bmp files by interfacing with the free, open source software FIJI and combined the data into a “damage map.” The MatLab routine provided many data outputs, but only the X location, Y location and area of each cavity was used. The location of each cavity was referenced with respect to the location of the fusion line, a process described in the next series of steps.

4. Locating the fusion line in space required an additional sequence of steps, provided below and in more detail with examples in [24]:

    a. The collected images were stitched together using the Keyence VK Assembly software;

    b. The contrast/brightness/laser intensity were modified for the stitched image to reveal the fusion line;

    c. The fusion line was traced in free open source image-editing software Paint.net;

    d. The location of the fusion line was digitized using the free open source software Engauge.

5. Once the X and Y location for each individual cavity was established, the location of each cavity with respect to the fusion line location was calculated in Excel using the function “LOOKUP”;

6. The balance of the data was post-processed in Origin because Excel cannot easily post-process the amount of provided data [in the provided example, there were initially ~50,000 lines of data but in some analysis, there can be >100,000 lines of data].

7. After the initial dataset was obtained, the data were evaluated as a function of the initial data, Figure 3-16A and for a series of threshold sizes as shown in Figure 3-16B and Figure 3-17. To remove the false cavities that can be seen in in Figure 3-16A (shown as large cavity populations in the form of apparent ‘black boxes’) the data are evaluated as a boxplot for multiple threshold cavity sizes, Figure 3-17. Of importance is to remove the long tail in the data which

extended well below zero (in this case values <0 are into the weld metal). Applying a 5-pixel threshold for this dataset was effective in this regard, and a reasonable damage map was created for analysis (as shown in Figure 3-16B). As seen in the provided analysis, the important statistical measurements for the 25th, 50th and 75th percentiles (i.e. the location of 'peak damage') were not dramatically changing in Figure 3-17 once a threshold of 5 pixels was applied.

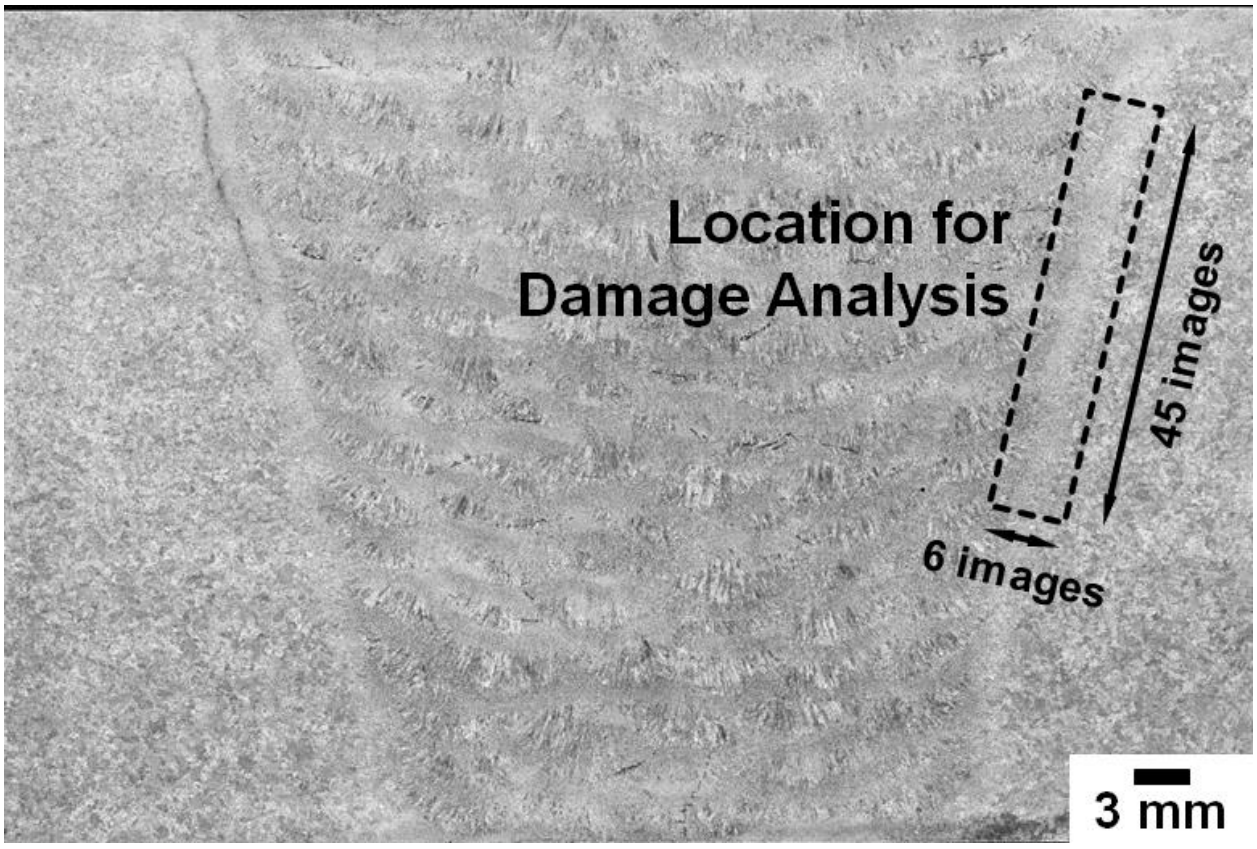

Figure 3-14. Location of the damage analysis performed using the laser microscope
Note: *cross-weld sample 7C-2 (625°C and 60 MPa) shown*

For the selected sample 7C-2, a total of ~50,000 'features' were documented in the initial dataset. After post-processing and filtering the total number of features associated with creep voids were ~11,000. The primary objective in mapping the damage was to provide a set of data which was sufficient to analyze for trends and to determine the location in the HAZ where damage was observed.

Once the data were filtered, the data were presented as a damage plot or more simplistically as a normalized 1D histogram which presented the entirety of the dataset as a function of distance from the fusion line. The histogram analysis allowed for more straightforward comparisons to the hardness map results (specifically the location of the OTZ) and the calculated peak temperatures through the width of the HAZ.

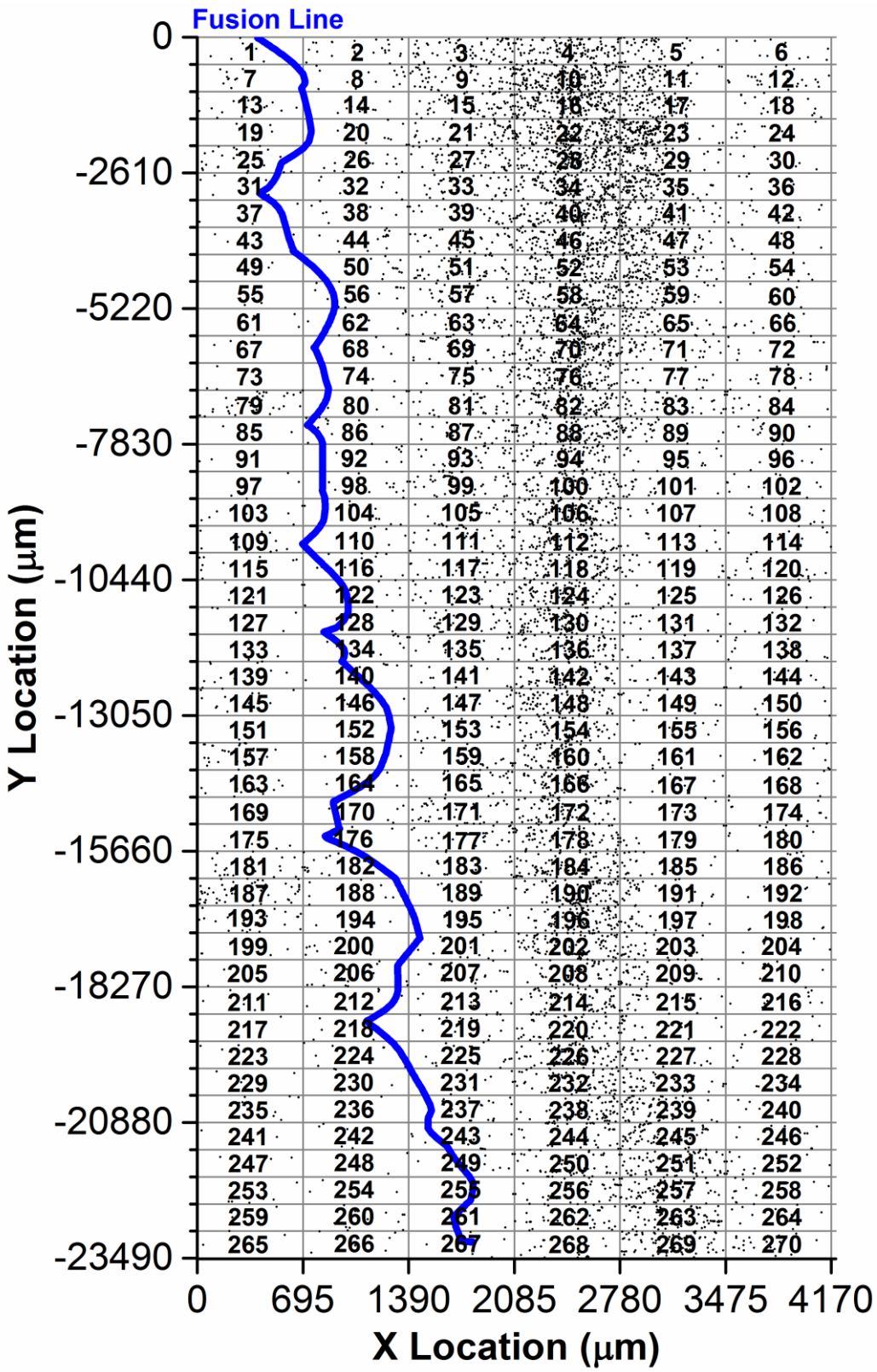

Figure 3-15. Routine used for data collection using the Keyence VK-105 confocal laser microscope and a 20X objective; location of the fusion line provided as a solid blue line for reference

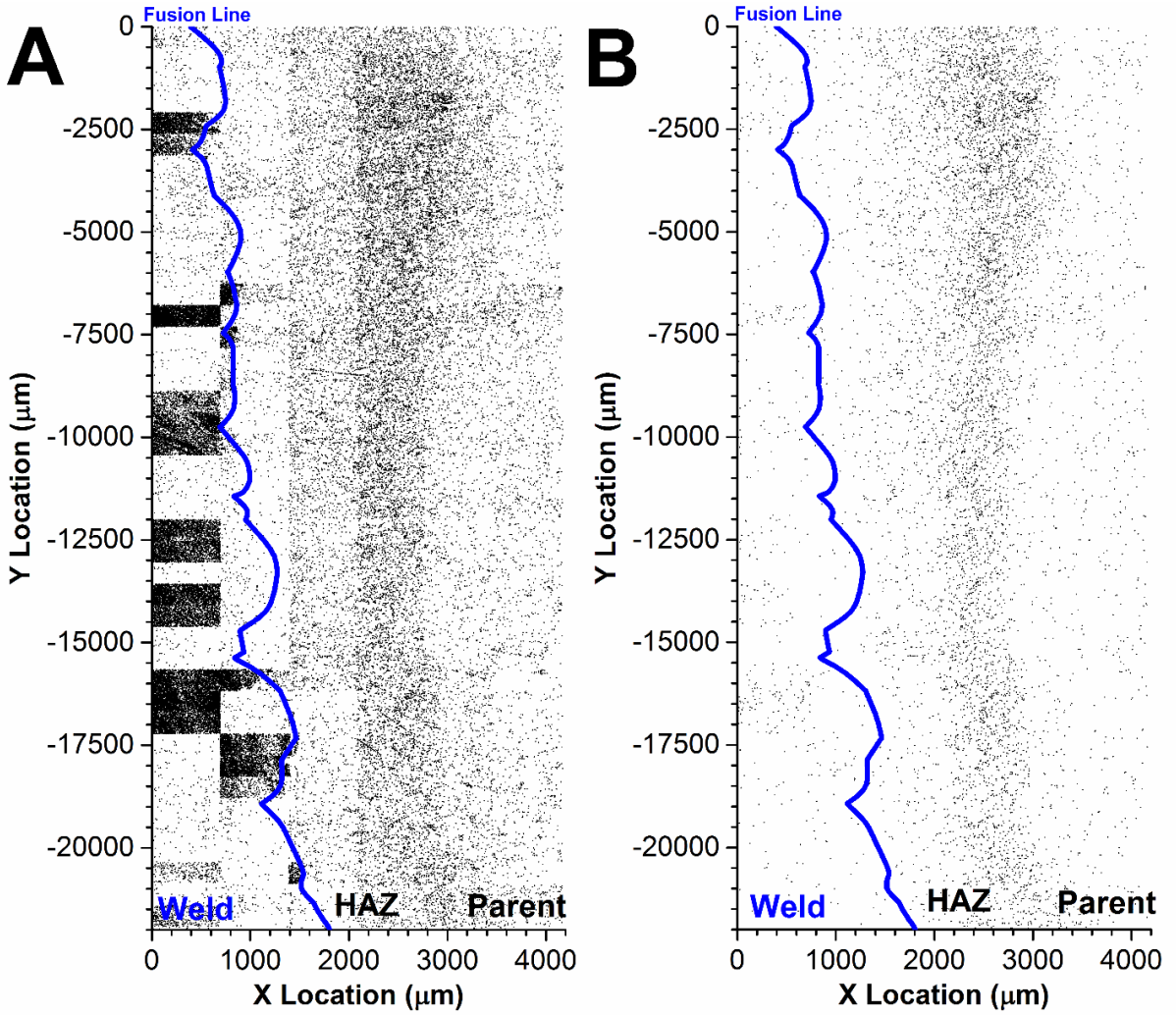

Figure 3-16. Comparison of damage maps for the entirety of the dataset (A) and a filtered dataset to a 5-pixel threshold (B)

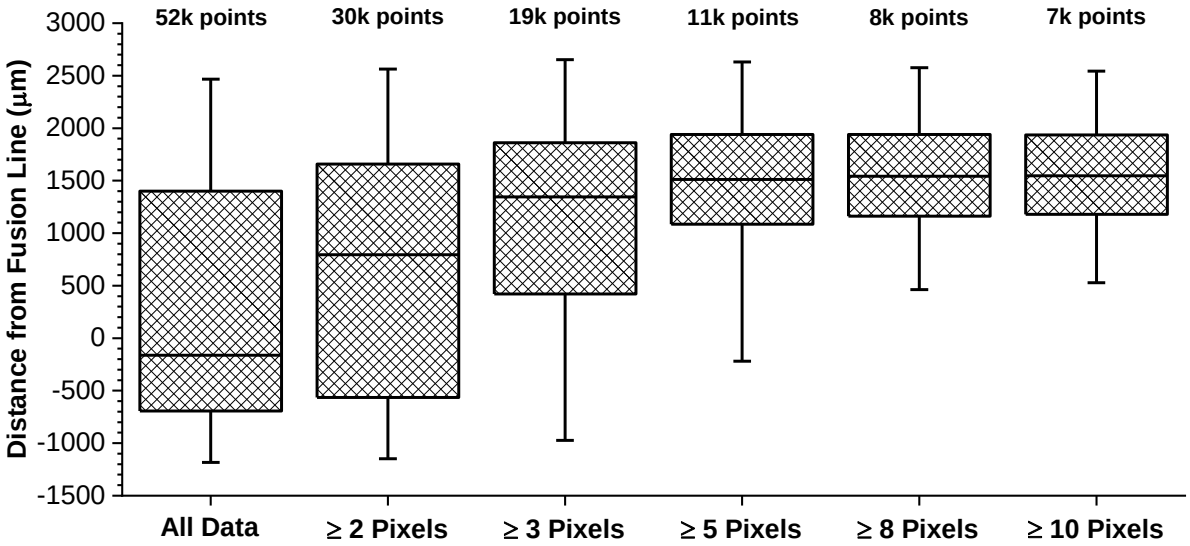

Figure 3-17. Data filtering of the counted 'cavities' by pixel size

3.6 Scanning Electron Microscopy

Micro-characterization of each weldment in the pre- or post-test condition is summarized in Figure 3-3. Samples were prepared for evaluation in the as-polished condition; no sample received etching prior to assessment using an SEM-based technique. Key assessments include the evaluation of the HAZ microstructure in the as-fabricated condition using backscatter electron imaging, electron backscatter diffraction or energy dispersive x-ray spectroscopy. In the post-test condition, feature cross-weld creep samples were evaluated using a similar set of methods with the objective of linking the pre-test condition to the present damage in the post-test sample.

3.6.1 Preparation of Samples for Scanning Electron Microscopy (SEM)

The preparation of samples for evaluation using SEM-based techniques often involves the etching of samples to reveal the grain boundaries and precipitates within the microstructure. When adequate polishing techniques are utilized, 9 wt. % Cr CSEF steel samples should not require etching. In this work the samples have been characterized in the as-polished condition to avoid any artifacts introduced by the etching process (e.g. in some instances the etching can remove an excessive amount of material and/or attack phases that might otherwise be better characterized in the as-polished condition).

A region measuring approximately 25 X 25 mm was machined (such as shown in Figure 3-18) from the mid-wall location in both the as-fabricated and post-test condition. The samples were subsequently mounted in conductive Bakelite, followed by grinding using 240 to 1200 grit SiC in a resin bond. The polishing process consisted of polishing the samples using standard cloths with polycrystalline diamond suspensions with particle sizes of 9 µm, 3 µm and 1 µm. In the final step the samples were polished using a 0.02 or 0.04 µm colloidal silica. In some cases, an additional step using an automated vibratory polisher system for 2-4 hours was utilized. If scratches were observed after a polishing stage which would not be removed by the next polishing stage the step was repeated. At the end of the final polishing stage the pad was rinsed thoroughly with water for an additional two minutes to avoid the colloidal silica crystallizing on the samples. The surface of the sample was then

rubbed with cotton wool and water before final cleaning using methanol. The sequential polishing steps are provided in Table 3-6 for reference.

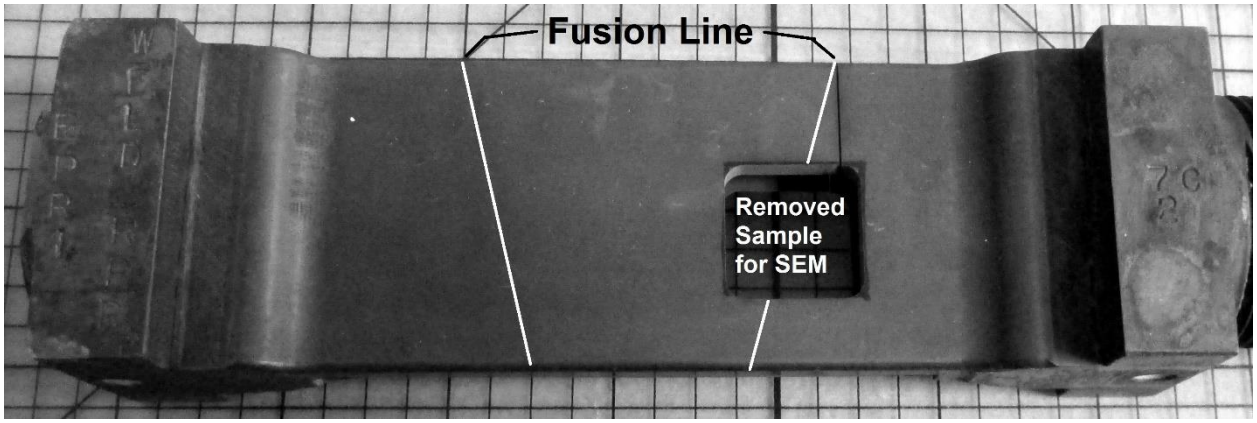

Figure 3-18. Details for the extraction of a sample for micro-evaluation following cross-weld creep testing

Table 3-6. Polishing parameters used in the preparation of metallographic samples in this study

Polishing Stage	Force	Rotation Speed	Time
9 µm	20 N	120 rpm	4 – 5 minutes
3 µm	15 N	120 rpm	5 – 6 minutes
1 µm	15 N	120 rpm	5 – 6 minutes
0.020 µm Colloidal Silica*	10 N	40 rpm	10 – 15 minutes

*In lieu of a final polishing step using colloidal silica, samples were polished on a vibromet automated system for a minimum of 2 hours

3.6.2 Identification of Reference Locations in the As-fabricated Condition

A hardness trace was applied at the mid-wall location following the sample preparation using a Struers Durascan 70 with a load of 0.5 kgf load and a dwell time of 15 seconds. The indents had a spacing of 0.20 mm. These indents were used as reference locations for backscatter imaging, EBSD and EDS mapping in the as-fabricated condition.

3.6.3 Evaluation of the As-fabricated and Post-test Heat Affected Zone using SEM-BED

Scanning electron microscopy images were captured using a JEOL 7100 field emission gun system (FEG-SEM) in the as-polished condition using the backscatter electron detector (BED) mode, a working distance of ~6 to 9 mm, 10.0 kV accelerating current and multiple magnifications (generally 500 to 5000X). In the weldment of interest, images were captured in the immediate vicinity above or below each

reference hardness indent starting at the fusion line and moving through the HAZ and into the parent material across a total distance of up to ~4.0 mm from the fusion line in the as-fabricated condition (weldment dependent). With respect to the evaluation in the post-test condition, images were taken at various magnifications throughout the HAZ to document the observed damage.

3.6.4 Evaluation of the As-fabricated Heat Affected Zone using Electron Backscatter Diffraction (EBSD)

Scanning electron microscopy was carried out in a JEOL 7100 field emission gun system (FEG-SEM) using an electron backscatter detector. An accelerating voltage of 10 kV was used in conjunction with an aperture of 30 µm and a working distance of ~5 mm. Electron back scatter diffraction (EBSD) was used for quantification of the grain size and orientation and was carried out using an EDAX Hikari camera. The data was acquired using a step size of 0.20 µm, an accelerating voltage of 20 kV and an aperture of 50 µm. Maps were acquired with a field of view of 150 X 150 µm and in the general distance 0.20 to 3.8 mm from the fusion line.

The EBSD data were post-processed in EDAX OIM Analysis™ Version 7 and involved three refinement steps. First, the data were partitioned using the image quality value ≥10% to remove any voids or inclusions. In the second step, the data were 'cleaned' such that the indexed points with a confidence index of lower than 0.2 were excluded using a 'neighbor CI correlation' method imbedded in the software. Lastly, a misorientation tolerance angle of 2° and a minimum size limitation of three points were used to define an individual grain. The grains that were of less than three points in size were excluded using a 'grain dilation' method by using an available tool imbedded in the software.

In this manuscript, the following misorientation definitions were used to define the different grain boundary types:

- 2 to 20° ➔ Low angle grain boundaries and consistent with the subgrain boundary structure defined by block, packet and lath boundaries;
- 20 to 50° ➔ High angle grain boundaries, sometimes defined as 'prior austenite grain boundaries' although in the context of non-homogeneous heating such as with a welding thermal cycle the exact definition for grain boundaries in this measured regime has not been properly assessed;

- 50 to 60° ➔ Low angle grain boundaries and consistent with the subgrain boundary structure defined by block, packet and lath boundaries. These boundaries follow a similar trend as the data for 2 to 20° and so the data will be reported as a 'combined' 2 to 20 + 50 to 60° value when assessed against several different quantitative comparisons in the results section.

3.6.5 Evaluation of the As-fabricated Heat Affected Zone using Energy Dispersive X-ray Spectroscopy (EDS) Mapping

Scanning electron microscopy images were captured using a JEOL 7100 field emission gun system (FEG-SEM) in the as-polished condition using the energy dispersive x-ray spectroscopy (EDS) mode. EDS maps were captured in the as-fabricated condition at low or high magnifications, generally 3,000X or 10,000X. A working distance of ~12 mm and an accelerating voltage of 15 kV were required to achieve ~75,000 to 100,000 counts per second (cps). The resolution of each image was 512 X 400, the dwell time was 5,000 µs and 1 frame per map was collected to compare the as-fabricated inhomogeneity in the HAZ. Data were first reviewed using EDAX TEAM software, and exported into .csv files for replotting in Origin for each of: Cr, C, Mo and Fe. The location of the collected maps was selected in the HAZ where there was clear evidence of local inhomogeneity in the HAZ structure, where a clear dispersion of apparent ferrite and martensitic grains co-exist.

3.6.6 Evaluation of Damage in the Heat Affected Zone

For this set of analyses, a FEI Teneo FEG-SEM was utilized with an EDAX Hikari Octane Elite Plus (30 mm^2 chip and silicon nitride window) detector. The general procedure included the basic parameters: 20 kV; 26.0 mm working distance; spot size 14 (6.4 nA); and the 'reduced noise' setting imbedded in the EDAX Team software version 4.5. The area analyzed was a 'larger' zone in the HAZ consisting of 141 X 106 µm, 1,500X magnification, and a 0.15 µm step size. Following data acquisition, the data were post-processed in EDAX OIM Analysis™ Version 8 using a grain dilation which altered some data in each map. The amount of data altered using this process is 2.0% (15,686 total points).

3.6.7 Evaluation of Local Strain Accumulation at Heat Affected Zone Cavities

For this set of analyses, a FEI Teneo FEG-SEM was utilized with an EDAX Hikari Octane Elite Plus (30 mm^2 chip and silicon nitride window) detector. A refined set of

procedures (namely a reduced step size) were utilized to assess the potential for strain accumulation and to identify if grain recrystallization was present in selected locations in sample AR-B2-5. The general procedure included the basic parameters: 20 kV; 26.0 mm working distance; spot size 14 (6.4 nA); and the 'reduced noise' setting imbedded in the EDAX Team software version 4.5.

Following data acquisition, the data were post-processed in EDAX OIM Analysis™ Version 8 using a grain dilation which altered some data in each map. The amount of data altered using this process are indicated in the following information. The procedure utilized for this process included the assessment of three locations with slightly different procedures:

- Location 1; 25,000X magnification, 0.03 µm step size, area evaluated 8 X 6 µm, and 1.9% total data (1,314 total points) changed using post-processing procedure;
- Location 2; 20,000X magnification, 0.05 µm step size, area evaluated 11 X 8 µm, and 1.5% total data (585 total points) changed using post-processing procedure;
- Location 3; 12,000X magnification, 0.05 µm step size, area evaluated 18 X 13 µm, and 2.8% total data (3,001 total points) changed using post-processing procedure.

For locations 1 and 2, particles were identified inside the cavity. This assessment utilized the basic parameters: 20 kV; 10.3 mm working distance; and spot size 14 (6.4 nA). This set of parameters achieved about 125,000 cps.

3.7 Fractography

A sample was extracted from the interrupted feature, cross-weld creep test sample AR-B2-5 to allow for assessment of a fracture sample with a fractured plane through the HAZ. Removal of the sample is shown in Figure 3-19. To minimize wastage, the EDM process was utilized. Notches were machined in each of the four planes, more clearly shown in the broken sample in Figure 3-20 as the 'notch' or 'scored edges.' Following removal, the sample was quenched in liquid nitrogen for 30 minutes upon which it was placed in a vise and broken with a controlled blow from a hammer. The sample was placed in the SEM for assessment following this procedure. Due to the

nature of the sample removal, machining and alignment of HAZ, it was not possible to obtain a 'perfect' plane of HAZ damage. This is noted in Figure 3-20 where a relatively flat surface with clear voids was noted and associated with the region of highest damage concentration in the HAZ, whereas regions above and below this region deviated outside of this zone during the fracture process. Although the approach for performing this assessment is straightforward, subsequent attempts to fracture samples using this procedure were variable, e.g. there merits some additional work to optimize the approach.

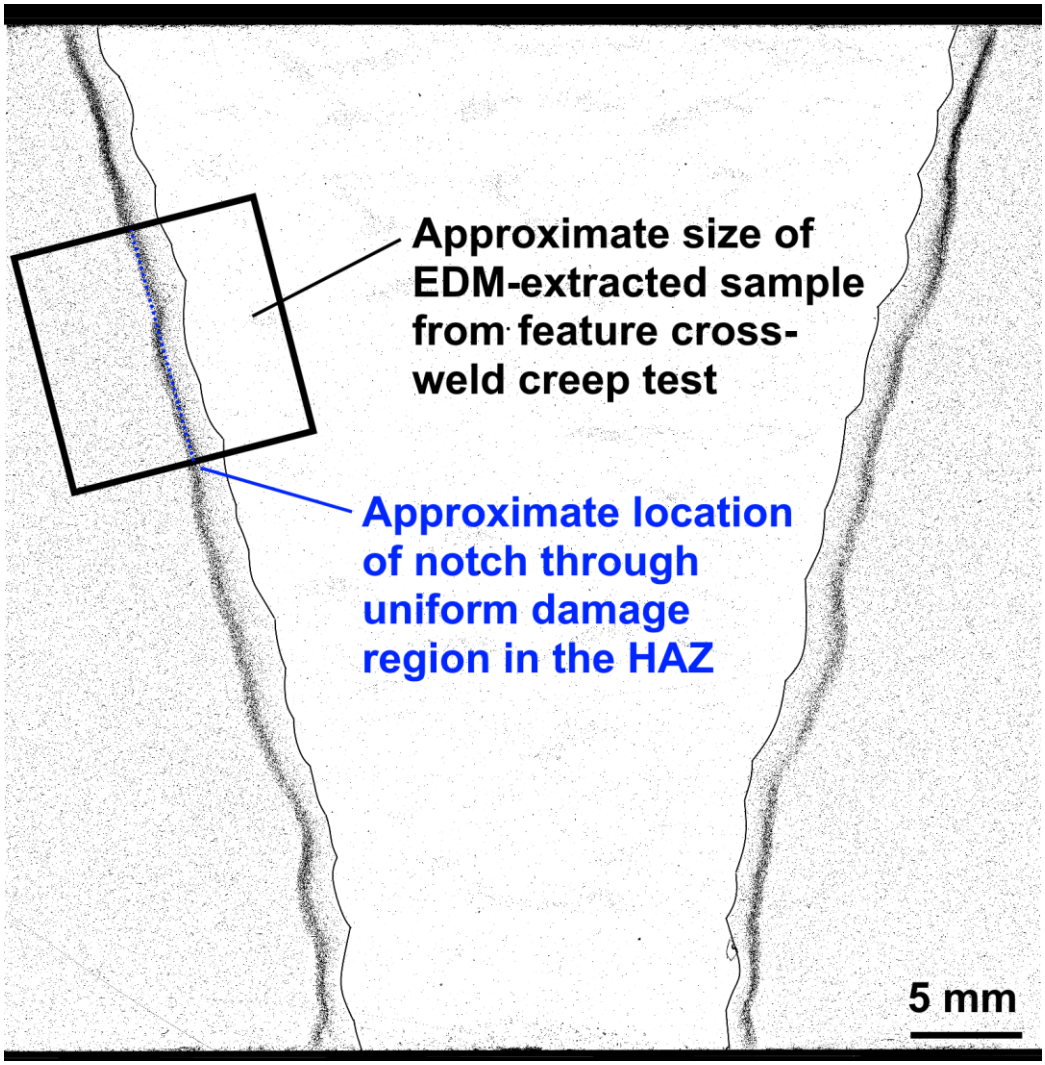

Figure 3-19. Removal of sample from a feature cross-weld creep test for fractographic evaluation

The sample was analyzed in a FEI Teneo FEG-SEM and an EDAX Octane Elite 25 detector or a JEOL 7800F FEG-SEM and an Oxford X-Max^{N}150 SDD EDS detector using a general set of conditions: 10kV; working distance of ~10 mm; SE or BED mode for imaging; EDS settings obtained ~10,000 to 100,000 cps (orientation of area of

interest relative to detector dictated the absolute number of cps); a dwell time of 30 to 45 seconds and either spot or area mode depending on the size of the particle inside the cavity. Regarding the S-Kα and Mo-Lα overlap; it is difficult to determine whether S peaks are real, particularly when the signal is not very strong. Where Al-K peak is noted, there may exist a N or O peak as well.

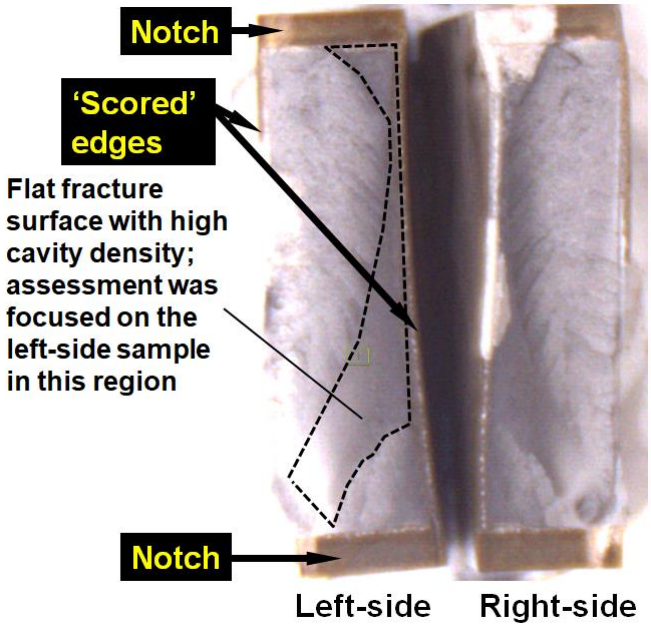

Figure 3-20. Fractured sample for SEM-based assessment of damage in the heat affected zone using a fractographic-based approach

3.8 Focused Ion Beam Milling

Focused ion beam (FIB) milling is an SEM-based technique in which a beam of ions, usually from a gallium (Ga) source, are used to bombard the sample to facilitate material removal in situ. This process therefore has the advantage of minimizing any influence of sample preparation artifacts and is particularly suitable for the examination of features such as cavities or, in combination with EDX analysis, the composition and morphology of fine second phase particles in 3D.

In this research, dual beam microscopy was performed in sample AR-B2-5 for multiple experiments. A conventional Ga, Scios (FEI) dual beam FIB/FEG-SEM was utilized for the first series of evaluations to provide a plane in the HAZ for evaluation after new cavities were revealed by serial sectioning. In the second investigation, a high rate of removal process using a xenon gas plasma source in an FEI Helios PFIB was utilized.

3.8.1 Dual Beam Focused Ion Beam Milling

A Scios (FEI) dual beam FIB/FEG-SEM with an X-Max^{N}150 SDD EDS detector was utilized to prepare a plane for serial sectioning given in Figure 3-21 with dimensions of 28 µm (y-axis) and 50 µm (x-axis). Trenches were machined on each side of the plane with approximate dimensions of 20 µm wide, 75 µm long and 40 µm in depth using the highest available current, nominally 65 nA. A stair-cased trench was dug immediately in front of the plane-of-interest to facilitate interruption of the serial-sectioning process with EDS analysis. The exposed surface was preserved with a thin platinum (Pt) layer.

Approximately 100 sections with an average slice thickness (z-axis) of 100 nm were collected. As new cavities were opened, the process was interrupted to perform EDS in the serial-sectioning plane. This was done using the same electron beam conditions used during the 3D acquisition (10 kV) which had a high enough current to generate EDS data with good statistics (70,000 cps, ~20-30% dead time, current of ~3 nA). EDS data was collected in spot and/or map format depending on the complexity of the feature. A total of 30 cavities were opened by the FIB process and chemically analyzed in this way.

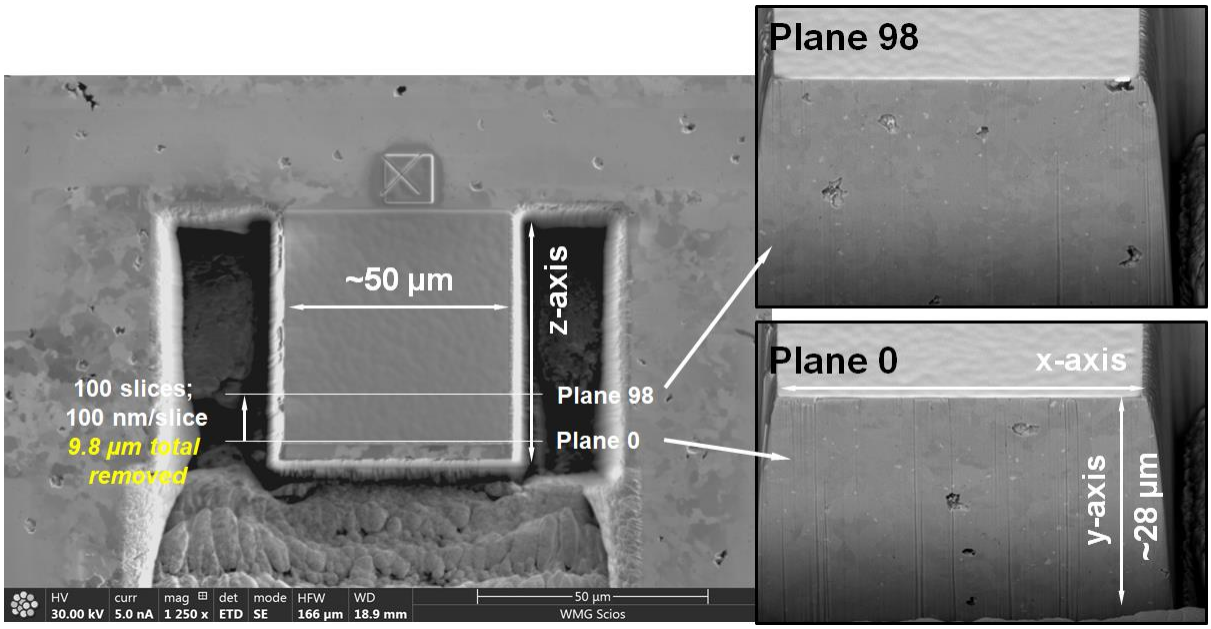

Figure 3-21. Overview of the location in the heat affected zone evaluated with focused ion beam milling and interrupted periodically to conduct assessment of cavities using SEM-EDS

3.8.2 Plasma Focused Ion Beam Milling

A xenon gas plasma source in an FEI Helios PFIB was utilized to allow serial sectioning of larger HAZ area than possible by the prior procedure detailed in section 3.8.1. To perform large-area EDS mapping, a volume of material extracted from the HAZ was removed and placed onto a silicon wafer. This volume measured ~190 µm wide, ~105 µm tall with a depth of at least 45 µm. The thickness of each slice removed from this plane was ~50 nm. A total of 812 slices were sequentially removed from the volume.

EDS mapping, secondary electron imaging and backscatter electron imaging were performed after the removal of each set of four consecutive slices resulting in 203 frames for assessment (and the first 'slice', e.g. 204 in total). Collection of the EDS maps was performed using an accelerating voltage of 10 kV.

3.9 Transmission Electron Microscopy

A suitable, subsurface cavity was identified on the polished surface in the SEM using a high accelerating voltage of 30 kV in backscattered electron mode using a solid state backscattered electron detector. These conditions increase the interaction volume of the incident electron beam and allow subsurface cavities such as that shown in Figure 3-22 to be revealed. In this example the subsurface cavity was ~200 nm from the surface and extraction of the thin foil was aligned to capture a portion of this cavity in the foil.

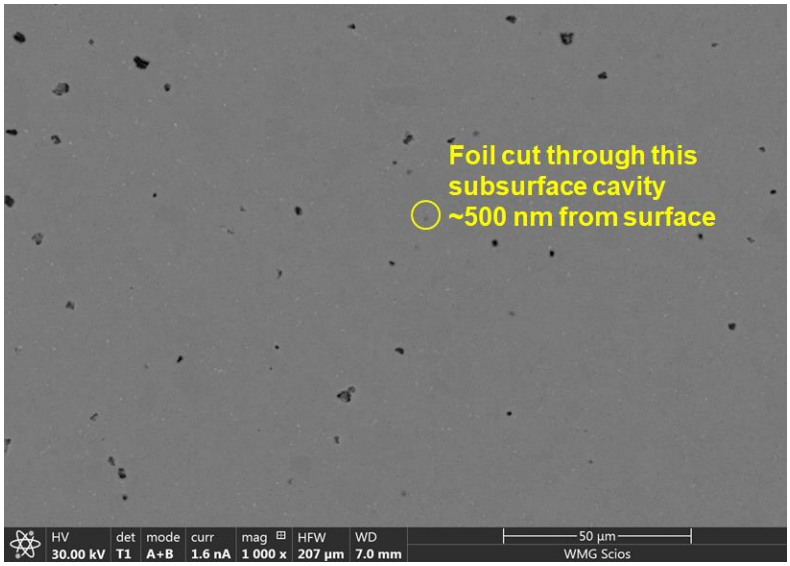

Figure 3-22. A high kV backscattered electron image showing the location of the sub-surface cavity lifted-out for subsequent analysis using TEM/STEM

A TEM sample was prepared from site specific feature by a standard in-situ lift out procedure using a Versa (FEI) dual beam FIB/FEG-SEM with an Easylift micromanipulator. The preparation procedure involved depositing a 20 X 2.0 X 1.5 µm thick layer of platinum on top of the feature of interest using the ion beam and the platinum (Pt) gas injection system with the plane of the sample surface perpendicular to the ion beam (stage tilted to 52°).

Staircase shaped trenches were dug on each side of this strip with approximate dimensions of 30 X 15 X 10 µm with the highest available current, nominally 65 nA. The cross-section on both sides of the Pt strip was then cleaned using a lower current (nominally 15 nA) and the 'cleaning cross-section' setting which moves the beam line by line towards the cross-section. A U-shaped cut was performed at 5 nA at a tilt of 7°. This cut was made to produce a lamellar with an approximate length of 20 µm and a depth of around 7 µm. A small ligament was left attached at one side to prevent it from falling.

The Easy Lift micromanipulator was then inserted, positioned so that it touched the end of the lamellar and then welded onto the lamellar using Pt. The ligament attaching the lamella to the bulk sample was cut away using the FIB and the lamellar was lifted free by moving the Easy Lift in the Z direction. The stage was then moved to the TEM grid position and the Easy Lift micromanipulator positioned so that the lamellar can be detached to the desired location on a Cu Omniprobe 3 prong half-grid. For samples in this research a V-position was chosen for attachment as it allows specific features across the entire lifted-out section (e.g. a cavity) to be thinned to electron transparency. The lamella was welded onto the grid using Pt and then detached from the probe using the FIB. Great care was taken during final thinning to electron transparency to produce a sample of uniform thickness as this is a mandatory requirement for compositional mapping in STEM. To achieve acceptable transparency, both sides of the lamellar were thinned using sequentially lower beam currents of 1, 0.5, and 0.3 nA with a tilt angle of 1.5° from edge on. A final clean-up process that involved using a FIB voltage of 5 kV, an inclination angle of 5° and a beam current of approximately 80 pA using a rectangular pattern for approximately 60 seconds. To reduce Cu-interaction, a Be spacer was utilized to ensure that the particle- or cavity-association with Cu was not an artifact.

Samples were analyzed in a Talos F200X FEG TEM (FEI) equipped with super X EDS detectors that allow high sensitivity chemical analysis. The system was operated at 200 kV in STEM mode and images were collected using both bright field (BF) and High Angular Annular Dark Field (HAADF) detectors. EDS maps were collected with an input count rate of approximately 150,000 cps in about 30 minutes using Velox software.

3.10 Summary

A series of procedures were detailed for the experimental methodologies that will be employed for a series of samples in the pre- and post-test conditions. An important set of evaluations involve firstly investigating each weldment after the specified fabrication steps and then following the execution of a well-controlled cross-weld creep test program. The combined set of results provide an understanding of the relationship between the microstructure in the pre- and post-test condition to highlight microstructural features responsible for the evolution of damage in the feature cross-weld tests conducted in Grade 91 steel.

A wide range of characterization techniques have been detailed for the systematic investigation of the microstructures in the HAZ. Hardness mapping has been utilized to evaluate the present heterogeneity in the HAZ and weld metal. Confocal laser microscopy is used to measure and document the extent of damage in the HAZ for selected cross-weld creep test samples. SEM-based techniques such as qualitative imaging and quantitative EBSD or EDS measurements have been employed to provide insight regarding the microstructural characteristics responsible for cross-weld creep behavior. Three-dimensional serial sectioning with coupled EBSD and EDS has been used to detail the association of creep cavities to second phase particles such as $M_{23}C_6$, Laves or inclusions. Perspective regarding the selection of the feature test geometry, the carefully selected test parameters, well-pedigreed parent materials and the identical weld geometry and weld procedure is the focus of the next Chapter.

4 Background for the Selected Parent Metal and Influence of Sample Geometry on Cross-weld Creep Performance

4.1 Introduction

In this chapter, a rationale for the selection of the parent materials, the cross-weld sample test geometry and the cross-weld test conditions is provided. An emphasis is placed on the relevance of these important factors and the contribution each has on the assessment of creep damage in the post-test coupons. The assessment of the creep damage in the post-test condition is the subject of the results provided in subsequent chapters and constitutes the central task in this thesis.

4.2 Selection of Parent Materials

The parent materials utilized in this research are taken from an ex-service, final superheat outlet header which operated in the Aberthaw power station Unit 8 for 79,000 hours at a nominal steam outlet temperature of 570°C and pressure of 16.5 MPa. It is noted that an identical header (albeit different heats of material) is still operating in Aberthaw power station Unit 9 for a duration that is now well above 100,000 hours.

For the remaining thesis, reference to the ‘Aberthaw header’ specifically refers to the Unit 8 header material from which the selected parent material was utilized for the fabrication of weldments in this research. The service history of the Aberthaw power station Unit 8 header is well-detailed in several publications from Brett et. al. (Brett et al. 2004, Brett 2007, Brett et al. 2007, Brett 2008, Brett 2010, Parker and Brett 2013). The location of the material utilized to fabricate the weldments is detailed in Figure 4-1 and these materials are identified as Tee Piece 1 (TP1) and Barrel Section 2 (B2). Similar nomenclature will be utilized for the other sections of the header.

The operating temperature of any installed header is expected to vary along the length of the header and the distribution of temperatures is dependent on the design. Indeed, this is documented for the final superheat outlet header installed in the Aberthaw power station, Figure 4-2. The temperature is generally lowest in B1 and B6; where the hemispherical end caps are located. The nominal steam temperature is documented at each of the four outlet TP1, TP2, TP3 and TP4. As the header was designed to provide steam to the turbine at a nominal temperature of ~570°C it is not surprising that the tee sections operated at a relative temperature of 1.00. Local

increases in temperature are noted near the center-sections of B2, the center girth weld between B3 and B4, and B5. The material from B2 is taken near stub row 22 where the operating temperature was consistent with that of TP1; e.g. a relative temperature of 1.00.

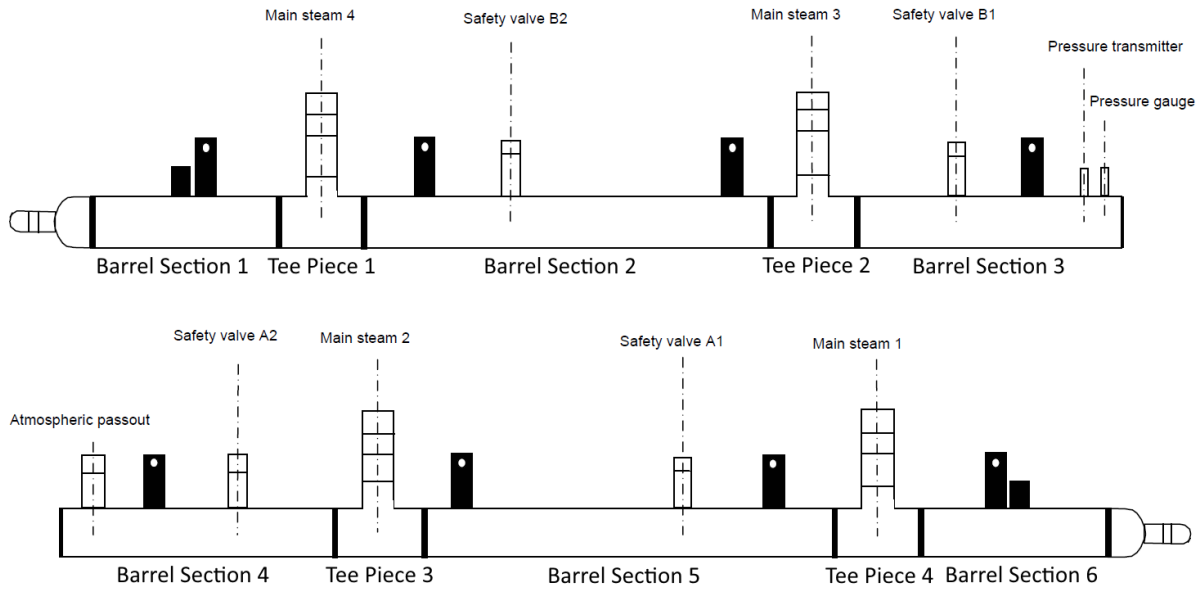

Figure 4-1. Fabricated final superheat outlet header removed from Aberthaw power station after 79,000 hours of operation at a nominal steam outlet temperature of 570°C.
Note: *that the material utilized in this study was removed from the locations labeled Tee Piece 1 (TP1) and Barrel Section 2 (AR-B2).*

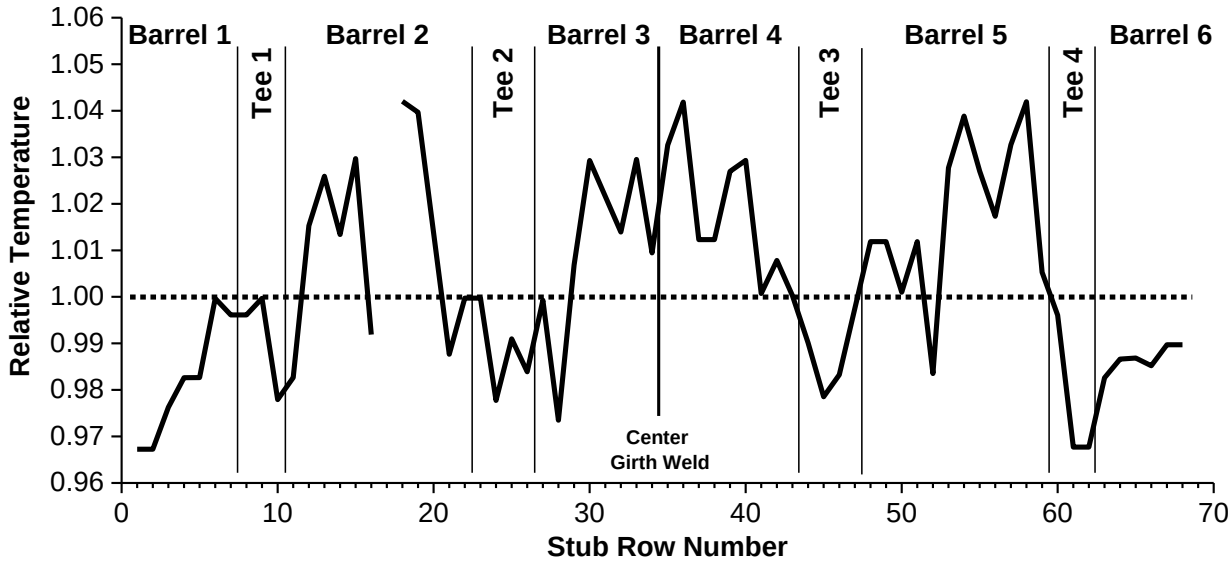

Figure 4-2. Reported temperature distribution along the length of the final superheat outlet header (Brett 2008)
Note: *'tee 1' and 'Barrel 2' are analogous to 'TP1' and 'AR-B2'. The removed material for fabrication of weldments for the AR-B2 and RNT-B2 weldments is taken from the section between Row 22 and Tee 2. The term 'relative' refers to the nominal operating outlet condition of ~570°C.*

The operating history of the Aberthaw final superheat outlet header is characterized by extensive damage in specific heats of material and weld geometries such as in the stub to header welds, Figure 4-3. The B2 and B5 sections exhibited extensive damage whilst B1 and B6 contained no documented damage. The temperature distribution, in part, can explain this difference as the observed damage in the header is consistent with time-dependent, creep damage. However, as elevated temperature is noted in multiple locations in the header, the temperature distribution alone cannot account for the variability in damage.

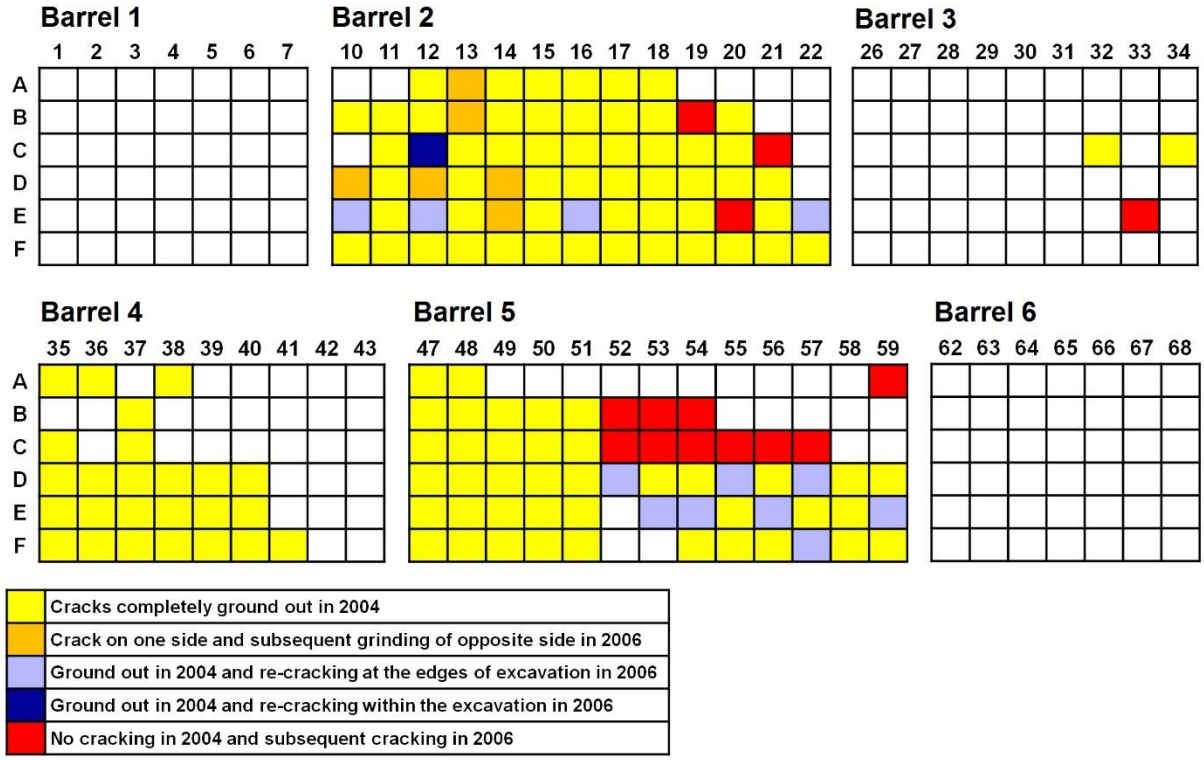

Figure 4-3. Distribution of damage in the final superheat outlet header in Aberthaw power station through its life (Brett 2007)
Note: *A-F refers to the individual stub in the row. The rows along the length of the header are identified by numerical values 1-68.*

In the original assessment by Brett et. al. (2004), a metallurgical risk factor linked to the N:Al ratio is utilized to more fully explain the differences in the accumulated damage in the Aberthaw header. This metallurgical risk is shown to scale with the amount of Al, which increases the number density of AlN. The observations regarding the presence of elevated AlN in some heats of material may thus partially explain the additional damage that was noted in the Aberthaw header. The morphology of AlN in 9 wt. % Cr CSEF steels is a needle or rod shaped and is randomly distributed in the matrix. Examples of AlN particles identified in transmission electron microscopy (TEM)

thin foils, and as reported by Brett et. al., are illustrated in Figure 4-4. The AlN can also be observed as clusters exhibiting a more complex, local geometry.

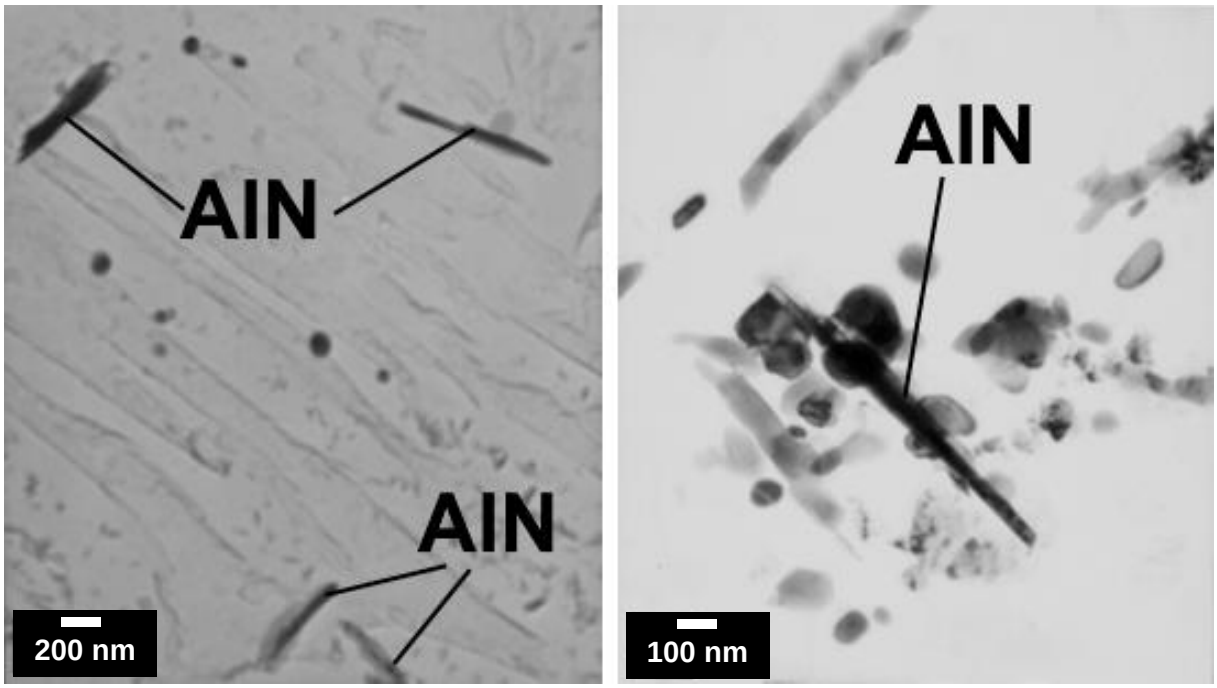

Figure 4-4. Examples of AlN in Grade 91 steel, as reported by Brett and Hanton (Brett 2010, Hanton 2007)

To assess whether AlN is dominating the evolution of damage, the comparison of the B2 and TP1 materials is relevant as the N:Al content in both heats is less than desirable, e.g. for B2 the ratio is ~1 while for the TP1 the ratio is ~2. It has been explained by Brett that the N:Al ratio should be ideally >4, Figure 4-5. A comparison of the extent of damage in the barrel sections is provided in Figure 4-3 and Figure 4-6. While low N:Al heats clearly exhibit extensive damage, there is a high, observed extent of damage in the stub to header population for the B4 section which possesses a N:Al ratio of 3.7, Figure 4-6. Thus, from this summary, there appears to be a trend with N:Al ratio but it is not clear if other metallurgical risk factors are present. The relationship between damage in the HAZ and the parent metal composition and/or presence of metallurgical risk factors is a key objective in the present research.

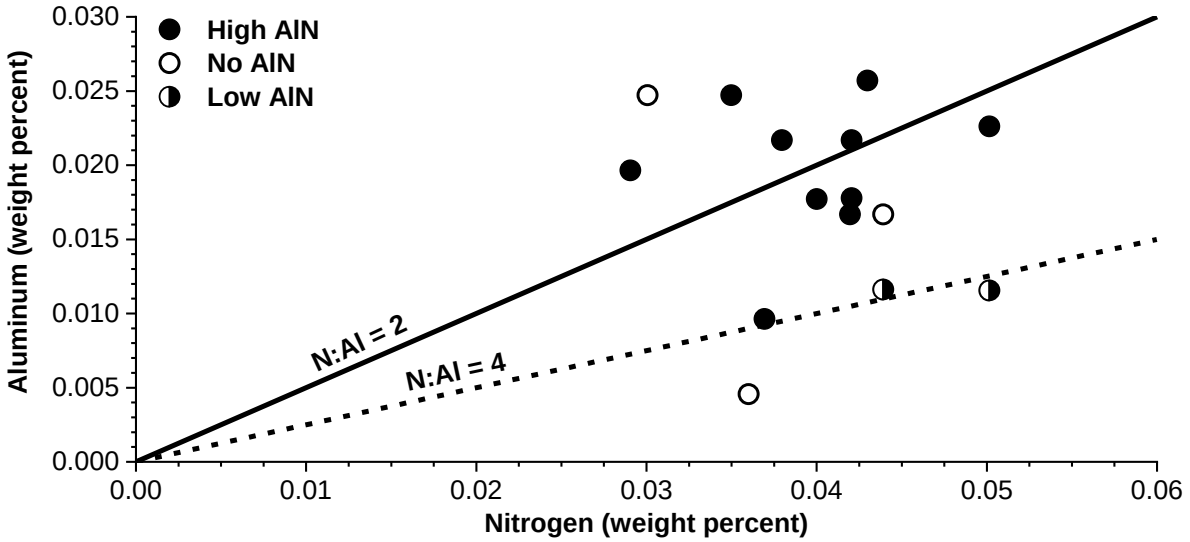

Figure 4-5. Relationship of no, low or high AlN content with the N:Al ratio for evaluated heats of Grade 91 steel in the Aberthaw headers

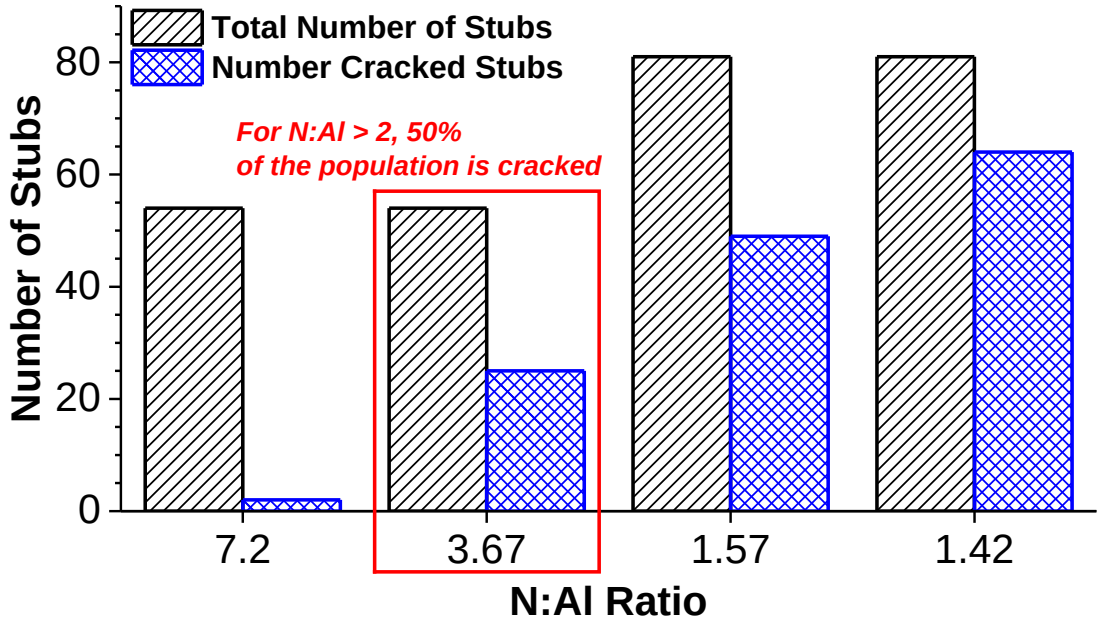

Figure 4-6. Distribution of damage relative to the N:Al ratio in selected heats.
Note: *the N:Al ratios of 1.42, 1.57, 3.67 and 7.2 correspond to Barrel 2, Barrel 5, Barrel 4 and Barrel 3, respectively. The N:Al ratio for TP1 is ~2 and no damage was reported.*

Using the stated operating pressure of 16.5 MPa, the maximum principal stress (assuming it is equal to the hoop stress) can be calculated using the Tresca reference stress solution given in Equation 4.1 (ASME 2017);

Equation 4.1 $$\sigma = \frac{P}{ln(\frac{OD}{OD - 2WT})}$$

P = Pressure in MPa
D = Outside diameter in mm
WT = wall thickness in mm

Using the provided operating temperature and calculated hoop stress, the expected extent of damage in the utilized parent material can be assessed. This is an important consideration since the presence of prior damage from in-service operation can affect the test results. The data provided in Table 4-1 presents a set of calculations using the relationships for parent metal given by Equation 4.2 (EPRI 2006b) and for cross-weld behavior given by Equation 4.3 (Abson and Rothwell 2013, EPRI 2014e). To calculate the minimum predicted life, the hoop stress is multiplied by a factor of 1.2 (e.g. to develop a -20% minimum bound). No attempt was made to develop new correlations as the utilized expressions in Equations 4.2 and 4.3 have been shown in prior assessments to provide reasonable bounds on Grade 91 steel behavior for the purposes of risk-ranking and screening parent material and welded components (EPRI 2014e).

Equation 4.2. (Parent metal)

$$\frac{T+460}{1000} \times [28 + \log t_R] = 57.17 + 2.05 \times (\log \sigma) - 6.163 \times (\log \sigma)^2$$

$T = \text{temperature in Fahrenheit}$
$t_R = \text{time to rupture in hours}$
$\sigma = \text{stress in ksi}$

Equation 4.3. (cross-weld) $\log t_R = 12.3 + [0.7 - 16 \times (\log \sigma)] \times \frac{(T+273-600)}{1000}$

$T = \text{temperature in Celsius}$
$t_R = \text{time to rupture in hours}$
$\sigma = \text{stress in MPa}$
Note: this relationship is normalized to 600°C

Table 4-1. Estimated lives for the Aberthaw header parent metal and weldment and for minimum and mean material

Constituent	Condition	Calculated Hoop Stress (MPa)	Temperature (°C)	Predicted Life (hours)
Parent Metal	Minimum	65.5	570 (Operation)	3,500,000
	Mean			12,000,000
	Minimum		580 (Design)	1,500,000
	Mean			5,000,000
Weldment	Minimum		570 (Operation)	107,589
	Mean			256,185

The parent metal should not exhibit any appreciable damage as the predicted life, even for minimum bound material, at the stated operating parameters is >>1,000,000 hours. On a time-fraction basis, this would mean that the material removed from service exhibited a consumed life fraction of <1 to at most 5%. For reference, the

predicted cross-weld performance is also provided in Table 4-1. The estimated life indicates that for minimum bound cross-weld behavior, the observation of creep damage in the original assessment by Brett is not surprising, e.g. the predicted minimum life of ~108,000 hours is within 25% of the total operating time of the actual header at the time of replacement. To accommodate this observation, the parent material utilized for the fabricated weldments is sufficiently removed from welded locations in the header which include large attachments, girth welds or stub to header welds.

4.3 Equilibrium Assessment of Parent Materials

The complete composition for the evaluated parent materials TP1 and B2 is given in Table 4-2. The analyzed elements include those explicitly required by common piping specification ASTM A-335 P91 or ASME SA-335 P91 as well as additional elements which may influence creep behavior but are not required for analysis by these specifications (As, B, Cu, O, Pb, Sb, Sn). The procedure utilized to determine these values is provided in section 3.1.2.

Table 4-2. Measured chemical composition for the investigation parent materials, given in wt. % and balance Fe

Material	C	Cr	Mn	Mo	Ni	Si	Al
SA-335 P91	0.08	8.0	0.30	0.85	0.40 max	0.20	0.02 max
	0.12	9.5	0.60	1.05		0.50	
B2	0.10	8.77	0.41	0.94	0.12	0.41	0.040
TP1	0.10	8.30	0.40	0.94	0.19	0.33	0.020
Material	**P**	**S**	**N**	**Nb**	**V**	**Ti**	**Zr**
SA-335 P91	0.020 max	0.010 max	0.030	0.06	0.18	0.01 max	0.01 max
			0.070	0.10	0.25		
B2	0.009	0.010	0.0454	0.071	0.21	<0.002	<0.002
TP1	0.012	0.002	0.0424	0.070	0.21	<0.002	<0.002
Material	**Cu**	**Pb**	**As**	**Sn**	**Sb**	**B**	**O**
SA-335 P91	N/A	N/A	N/A	N/A	N/A	N/A	N/A
B2	0.19	0.00075	0.0128	0.008	0.0023	<0.0003	0.003
TP1	0.05	0.00003	0.0042	0.003	0.00063	<0.0003	0.0024

Assessment of the equilibrium phases present in the TP1 and B2 materials is provided in Figure 4-7 to Figure 4-9 using the simplified compositions detailed in Table 4-3. Note that for the remaining study the B2 material is either referred to as ‘AR-B2’ or ‘RNT-B2’ to identify whether a weldment is tested in the ‘as-received’ or ‘renormalized and tempered’ condition. The provided simulations include a few details below:

- Database ThermoCalc TCFe7;
- Impurity elements such as Cu, As, Sn, Sb and Pb are not included in the assessment. The utilized database is not sufficiently well-developed to accommodate the potential influence of these elements in the simulation (ThermoCalc);
- Several phases were eliminated from the analysis including: Gas and M_3P (Phosphorous-rich);
- The included phases are representative of identified and verified phases in 9 wt. % Cr CSEF steels and include: liquid, delta-ferrite, austenite, alpha-ferrite, $M_{23}C_6$, MX, AlN, MnS and Z-phase;
- The simulation represents a temperature range from melting, through solidification and to a thermally stable temperature, e.g. 1600 to 500°C;
- There exist subtle, yet significant differences in the phase stability. Note that for the compositions provided in Table 4-3 there is relatively little difference in the main alloying elements. Significant deviations exist primarily for the Al and S content and to a less extent for Cr and Si;
- The influence of the Al and S content, particularly regarding the formation of AlN and MnS, respectively, is reflected in the comparison in Figure 4-9. The higher content of Al and S in the AR-B2 material stabilizes more AlN and MnS as well as to a higher temperature. With respect to the AR-B2 material, a renormalization at 1065°C, and as performed for the RNT-B2 material, is not expected to resolutionize the AlN as the stability is >1100°C.

A second observation is specific to the formation of MnS in the AR-B2 heat which overlaps with the liquid phase. As deleterious elements with low temperature melting points such as, As, Cu, Sb and Sn can be expected to segregate to the liquid during solidification, it is expected that the liquid phase may be present to even lower temperatures than the simulation suggests. The simultaneous formation of MnS in this regime may increase the likelihood of local enrichment of As, Cu, Sn and Sn at these inclusions. Prior analysis in (Brookes 2015) did suggest an enriched Cu phase around MnS in the AR-B2 material, Figure 4-10.

Table 4-3. Composition for AR-B2 and TP1 utilized in the equilibrium simulations

Material	C	Cr	Mn	Mo	Ni	Si	Al	P	S	N	Nb	V
AR-B2	0.10	8.77	0.41	0.94	0.12	0.41	0.040	0.009	0.010	0.0454	0.071	0.21
TP1	0.10	8.30	0.40	0.94	0.19	0.33	0.020	0.012	0.002	0.0424	0.070	0.21

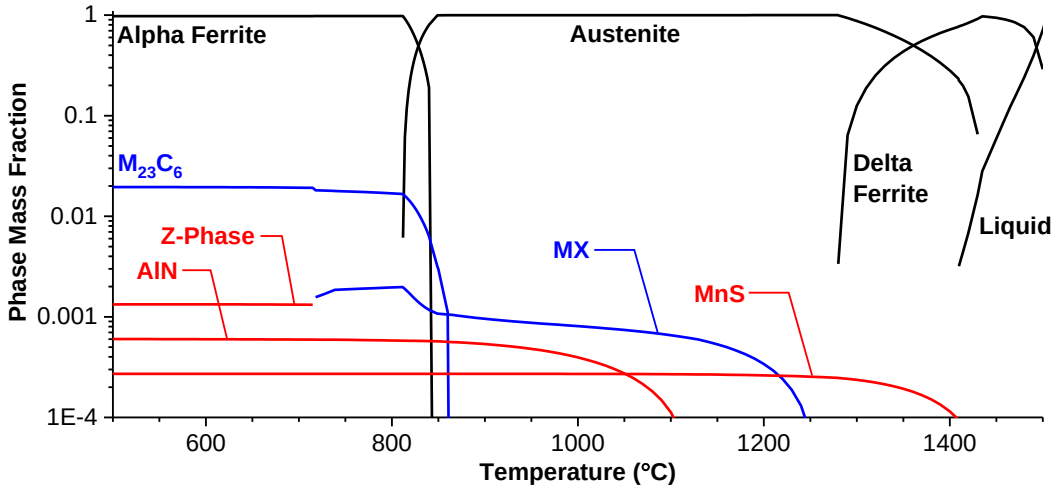

Figure 4-7. Equilibrium simulation for parent metal AR-B2. Black = matrix phase; Blue = carbonitride phase; red = deleterious phase

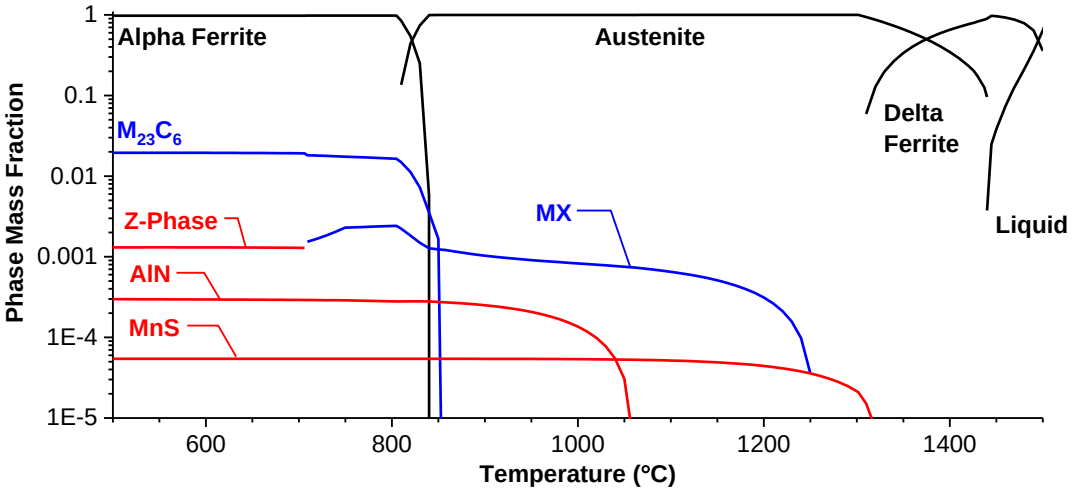

Figure 4-8. Equilibrium simulation for parent metal TP1. Black = matrix phase; Blue = carbonitride phase; red = deleterious phase

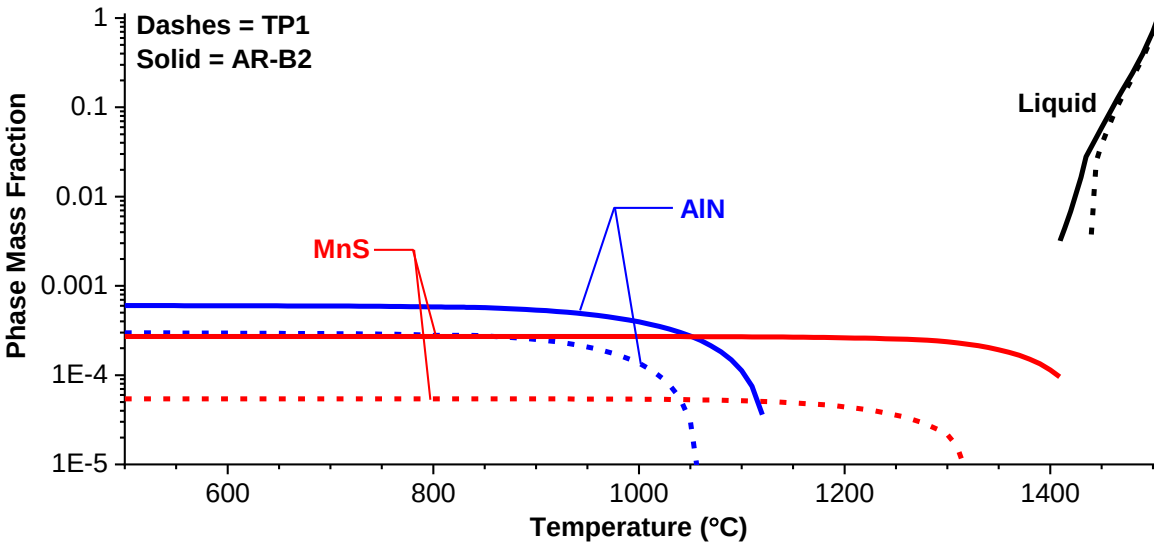

Figure 4-9. Comparison of phase stability for AlN and MnS in AR-B2 (solid lines) and TP1 (dotted lines)

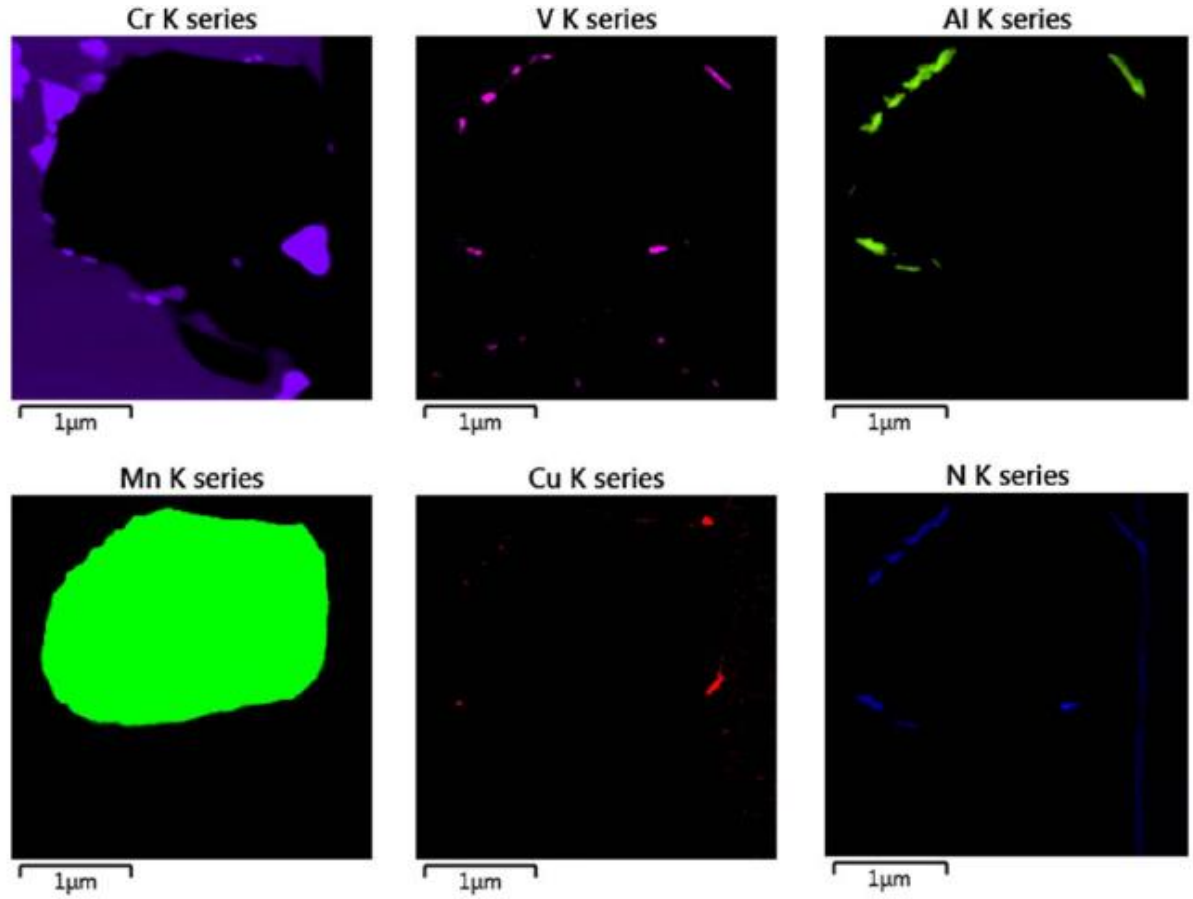

Figure 4-10. Association of a MnS Inclusion as a Trap Site for Cu and Al in the AR-B2 material, from (Brookes 2015)

4.4 Particle Analysis of Parent Materials

Assessment of the area density of particles in the as-received material AR-B2 and TP1, for example $M_{23}C_6$, Laves, AlN, MnS and the inclusion content which have been

observed to be present in these types of steels, is provided in this section. The determination of particle density is provided using a set of SEM-based procedures relying on image processing of backscatter image maps or energy dispersive spectroscopy (EDS). The procedures are briefly summarized below:

- **$M_{23}C_6$, AlN and Laves phase.** These particles were analyzed using the procedures provided in Table 4-4; an example of each particle is highlighted in a representative backscatter image in Figure 4-11. For the assessment of AlN, five areas were averaged including 196 images in each location. 20 images were processed for Laves and $M_{23}C_6$. The images were post-processed using ImageJ to highlight, count and size the particle population of interest.

- **Inclusions.** The database for the inclusion analysis was specific to the type of equipment utilized (FEI Aspex Explorer microanalysis system) and includes ~45 types of inclusions. To facilitate comparison, the inclusions are grouped into basic types: Al-type; S-rich; MnSi-type; Nb-type; Ti-type; Ca-type; Mg-type; high Si; complex spinel; and unclassified. The reported analysis was obtained from a service-provider offering inclusion analysis as a routine service. An example of identified inclusions in an inclusion cluster is provided in Figure 4-12. It should be noted that inclusions present as clusters may complicate the assessment since the procedure for 'counting' the clusters as a single or inclusion cluster was not clearly prescribed by the service provider in the software routine.

- **MnS.** Assessment of MnS included an alternative procedure to assess particles which may have been below the threshold size for the standard inclusion analysis. The assessment for MnS is given in Table 4-4. MnS possesses a darker contrast in BSE imaging compared to steel matrix. The analysis was configured such that the association of Cu with MnS was also measured using EDS analysis at each MnS feature. An example of the association of Cu with MnS is given in Figure 4-13 for the AR-B2 material.

Table 4-4. Scanning electron microscope parameters used in the collection of data to characterize each indicated particle

Parameter	$M_{23}C_6$	AlN	Laves	MnS	Inclusions
Scanning electron microscopy method	Backscatter imaging	Backscatter imaging	Backscatter imaging	Energy dispersive spectroscopy	Energy dispersive spectroscopy
Accelerating Voltage	2 kV	2 kV	2 kV	5 kV	20 kV
Horizontal field width (HFW)	20.7	41.1	20.7	50.0	
Magnification	10,000X	5,000X	10,000X	8,000X	
Pixels	3072 X 2207	3072 X 2207	3072 X 2207	1024 X 704	
Counts per second	N/A	N/A	N/A	150,000 to 200,000	
Acquisition time	N/A	N/A	N/A	0.50 seconds	1.0 second
Area sampled	0.00616 mm^2 (20 images)	1.43 mm^2 (980 images)	0.00616 mm^2 (20 images)	1 mm^2 (580 images)	51.5 mm^2

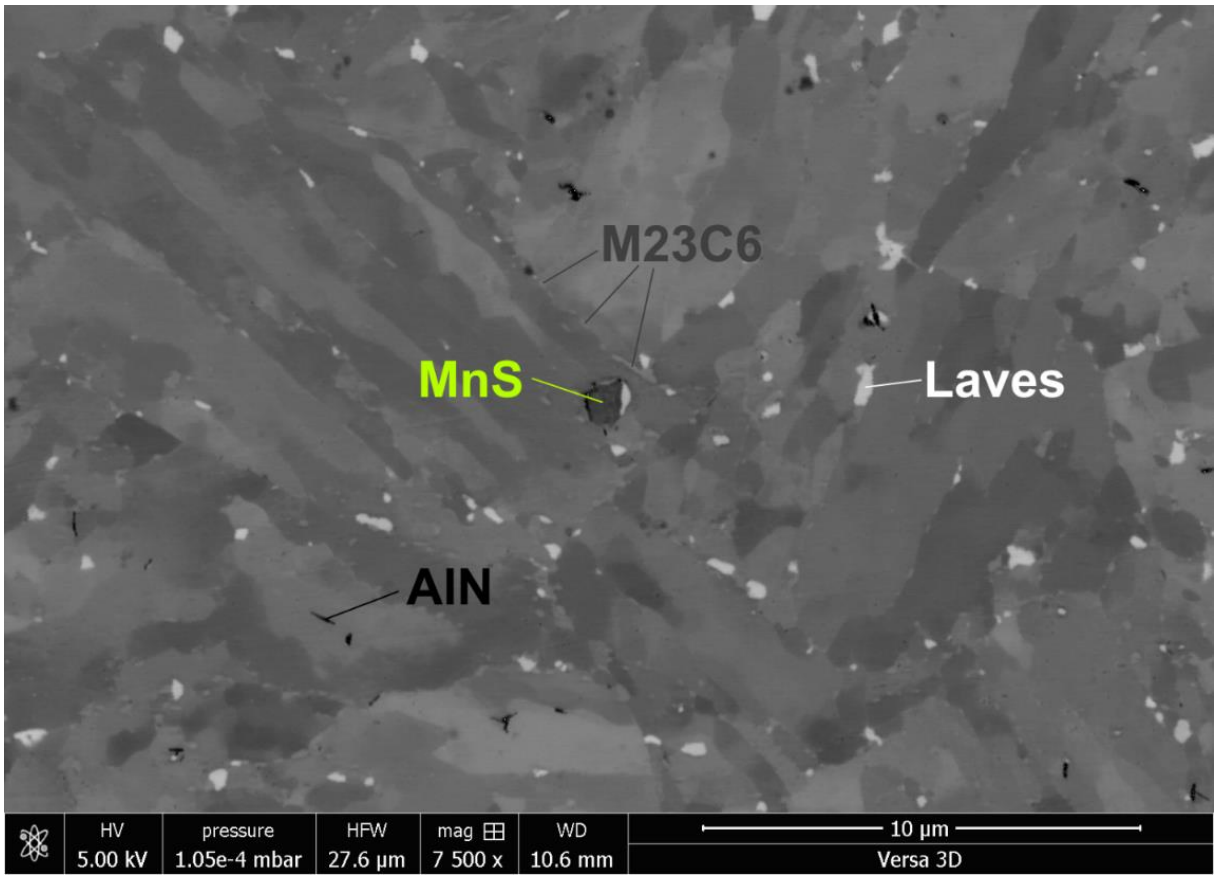

Figure 4-11. Example of assessed particles (sample AR-B2 parent metal shown)

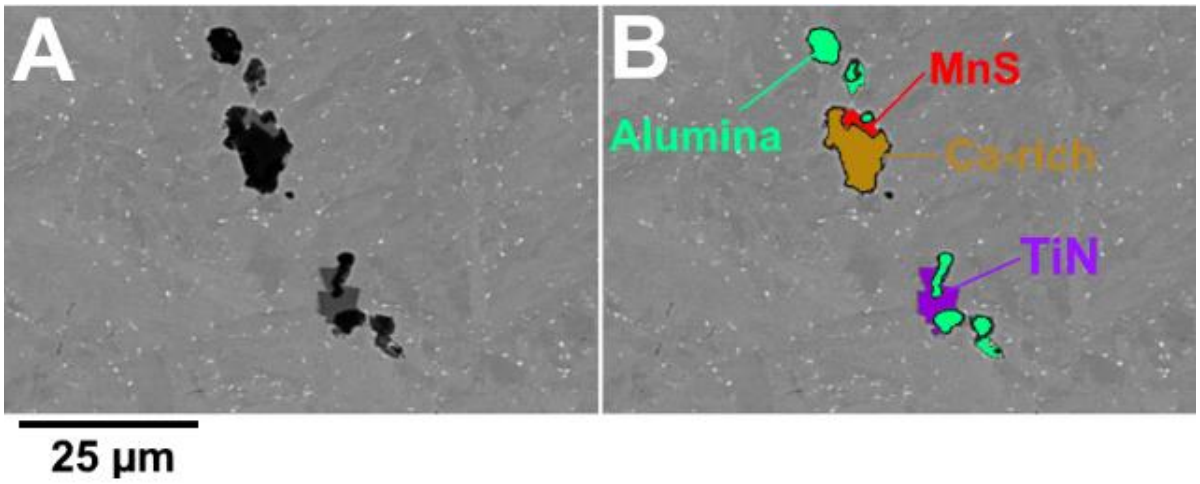

Figure 4-12. Example of inclusion cluster (sample TP1 parent metal shown)
A – electron backscatter image of inclusion cluster
B – inclusion cluster with classification

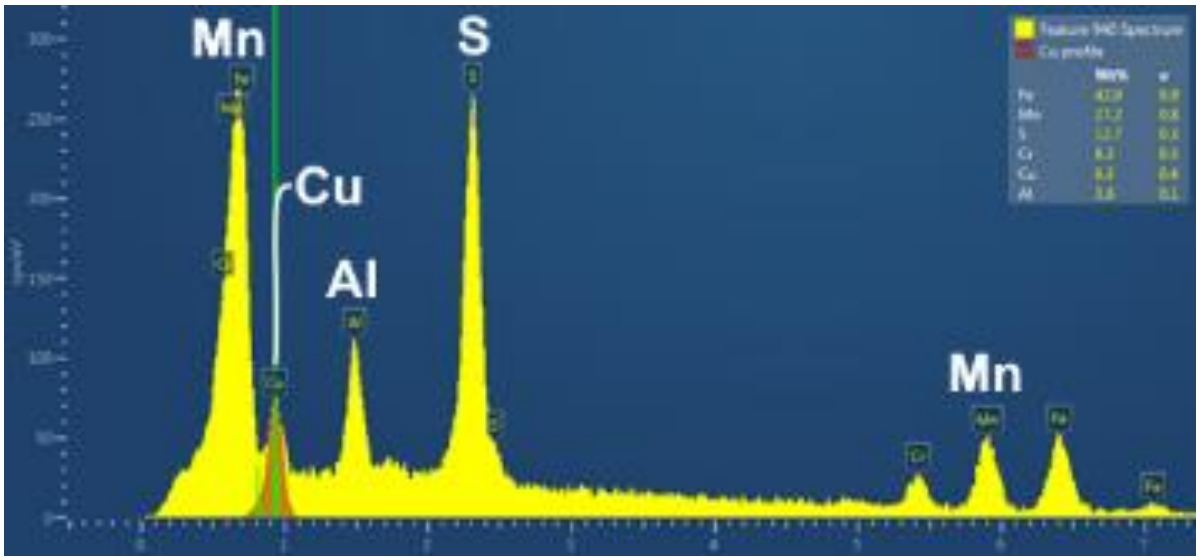

Figure 4-13. Association of Cu with MnS particle in the AR-B2 parent material

Confirmation of the particles in Figure 4-11 is provided using SEM-EDS evaluations in Figure 4-14 to Figure 4-17. The EDS maps provided in Figure 4-14 show general depletion or enrichment for the elements Fe, Cr, Mo, Si, Nb, Al, and V. It is shown for the phases of interest that:

- $M_{23}C_6$ shows depletion in Fe and enrichment in Cr;
- Laves exhibits depletion in Fe, enrichment in Mo and Si, and slight enrichment in Nb;
- AlN is enriched in Al.

For the documented elemental maps, there was subsequent evidence for MX carbonitrides present as Nb or V enrichment in locations removed from Laves or $M_{23}C_6$ particles.

Individual particles were analyzed in the parent metal (Figure 4-15) and the HAZ (Figure 4-16 and Figure 4-17) for a representative sample to assess the composition for the dominate phases and as linked to the appearance of the particle using imaging alone (for example in Figure 4-11). This information provides a context to link the contrast of the particle for an image to a distinct composition.

A summary of the particle densities for each parent metal are provided in Table 4-5. The variations in specific populations are in most cases linked to the composition of the parent material. The inclusion analysis results are given in Table 4-6 using the screening-based procedure. It is clear from these two tables that the AR-B2 material has a higher density of MnS and AlN; both populations of which are likely to be deleterious to cross-weld creep behavior.

The AR-B2 material is compared to the RNT-B2 material in Figure 4-18. The distribution of AlN is very similar in the provided comparison whilst the Laves phase is notably absent in the RNT-B2. As previously noted, the stability of AlN is greater than that of the renormalization temperature for the RNT-B2 material (e.g. 1065°C). Although Laves phase is not included in Figure 4-7 and Figure 4-8, prior research presented in (Cipolla 2007) suggests the stability of Laves phase in Grade 91 steel is such that it is present <700°C. This is supported in these images as no Laves appears to be present in the RNT-B2 material.

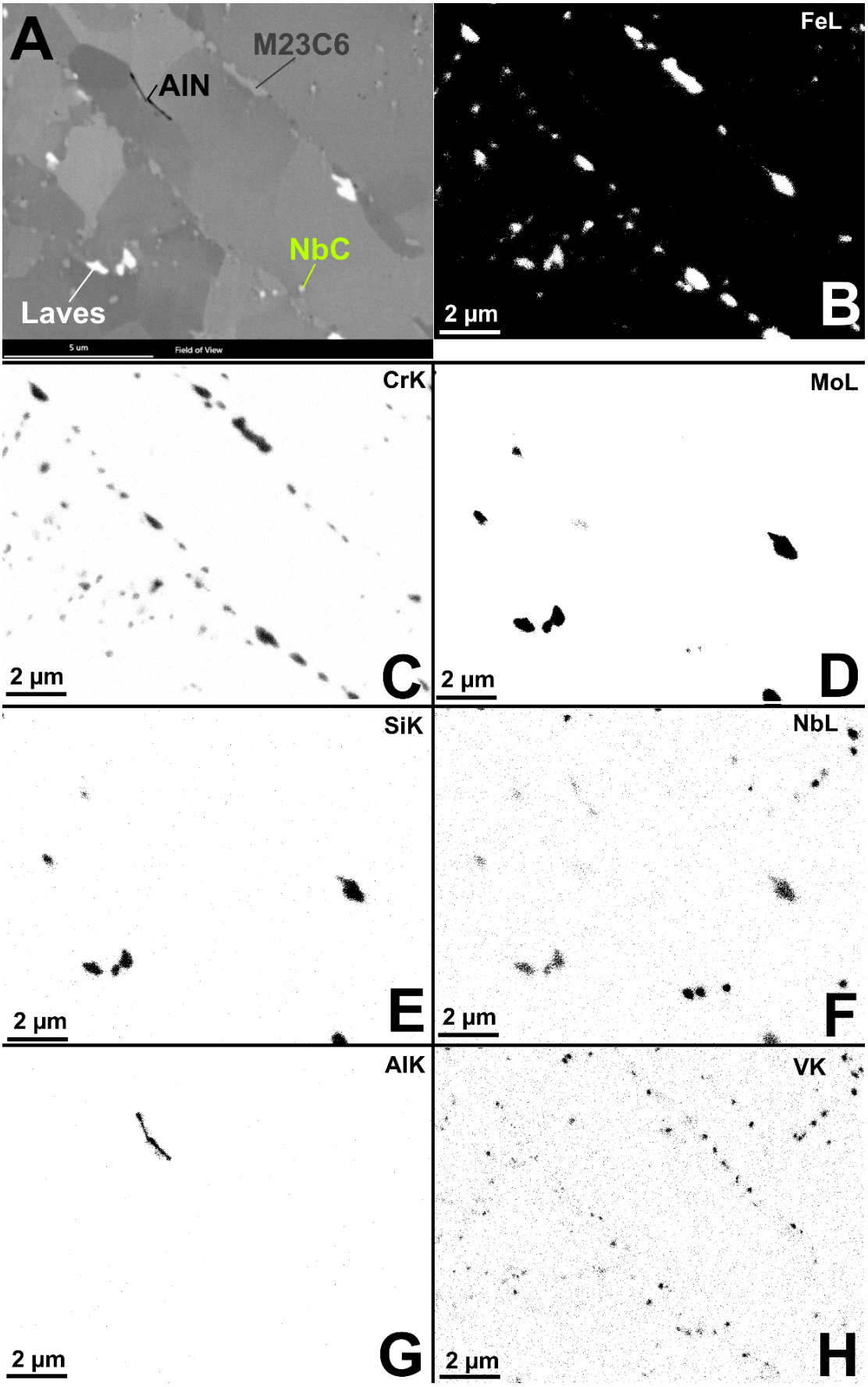

Figure 4-14. Representative elemental maps produced using SEM-EDS in Grade 91 steel (TP1 material) for an area of interest (A), Fe (B), Cr (C), Mo (D), Si (E), Nb (F), Al (G) and V (H)

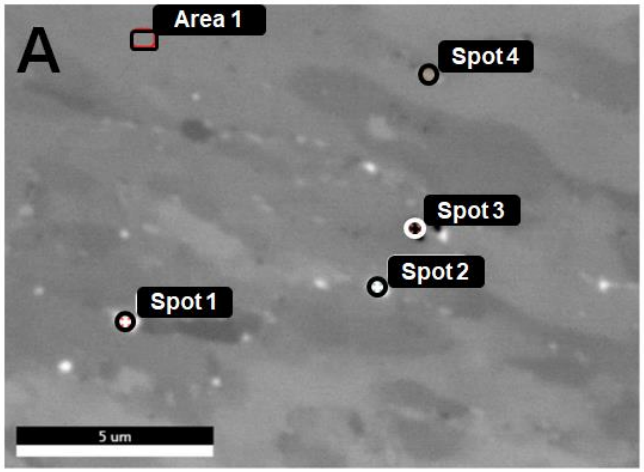

B

Element	1	2	3	4	Area 1
C (K)			12.28	10.59	
N (K)					
O (K)					
Cr (L)	9.97	9.61		34.01	18.70
Fe (L)	33.75	34.14	44.40	43.71	81.30
Al (K)			36.95		
Nb (L)			6.38		
Mo (L)	50.79	50.74		11.69	
Si (K)	5.50	5.50			

Figure 4-15. SEM-EDS for five locations in Grade 91 steel (sample 9C-3; parent metal TP1); locations given in (A) and values in weight percent given in (B)

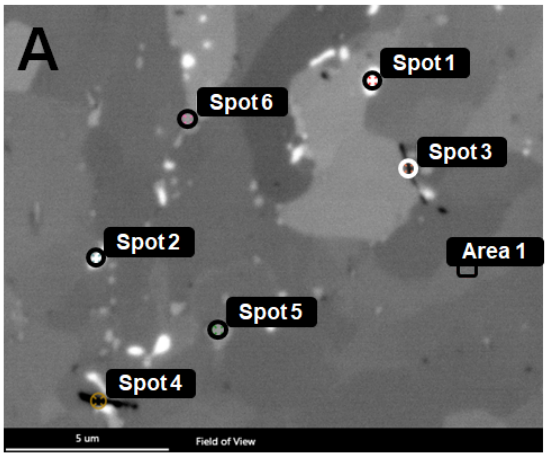

B

Element	1	2	3	4	5	6	Area 1
C (K)					7.25	5.61	
N (K)			4.05	11.80			
O (K)				5.37			
Cr (L)	7.95	8.58	11.89		43.77	36.27	16.49
Fe (L)	30.28	32.72	72.87	30.95	29.14	42.23	83.51
Al (K)			11.18	34.52			
Nb (L)				8.24			
Mo (L)	55.54	52.63		9.13	19.84	15.90	
Si (K)	6.23	6.08					

Figure 4-16. SEM-EDS for seven locations in Grade 91 steel (sample 9C-3; heat affected zone); locations given in (A) and values in weight percent given in (B)

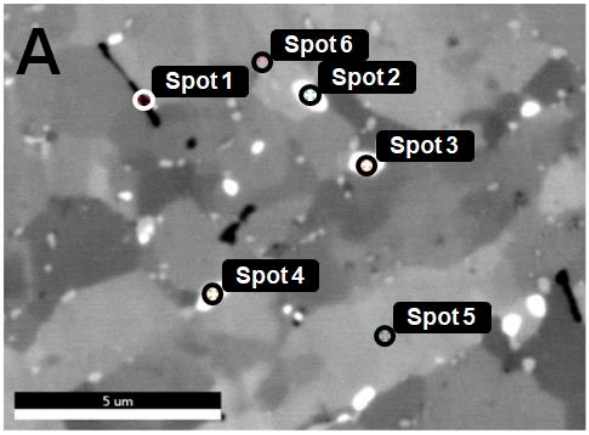

B

Element	1	2	3	4	5	6
C (K)						6.47
N (K)	18.20					
Cr (L)	11.44	9.82	7.97	8.44	18.88	40.40
Fe (L)	40.01	27.05	27.05	28.82	81.12	36.24
Al (K)	19.57					
Nb (L)	10.77					
Mo (L)		55.76	57.33	55.38		16.89
Si (K)		7.37	7.65	7.36		

Figure 4-17. SEM-EDS for six locations in Grade 91 steel (sample 9C-3; heat affected zone); locations given in (A) and values in weight percent given in (B)

Table 4-5. Particle density (/mm^2) for the parent materials utilized in this research

Particle	AR-B2	TP1
$M_{23}C_6$	1,220,000	1,000,000
Laves	851,000	382,000
AlN	58,065	7,745
Inclusions	142	18
MnS	715	295

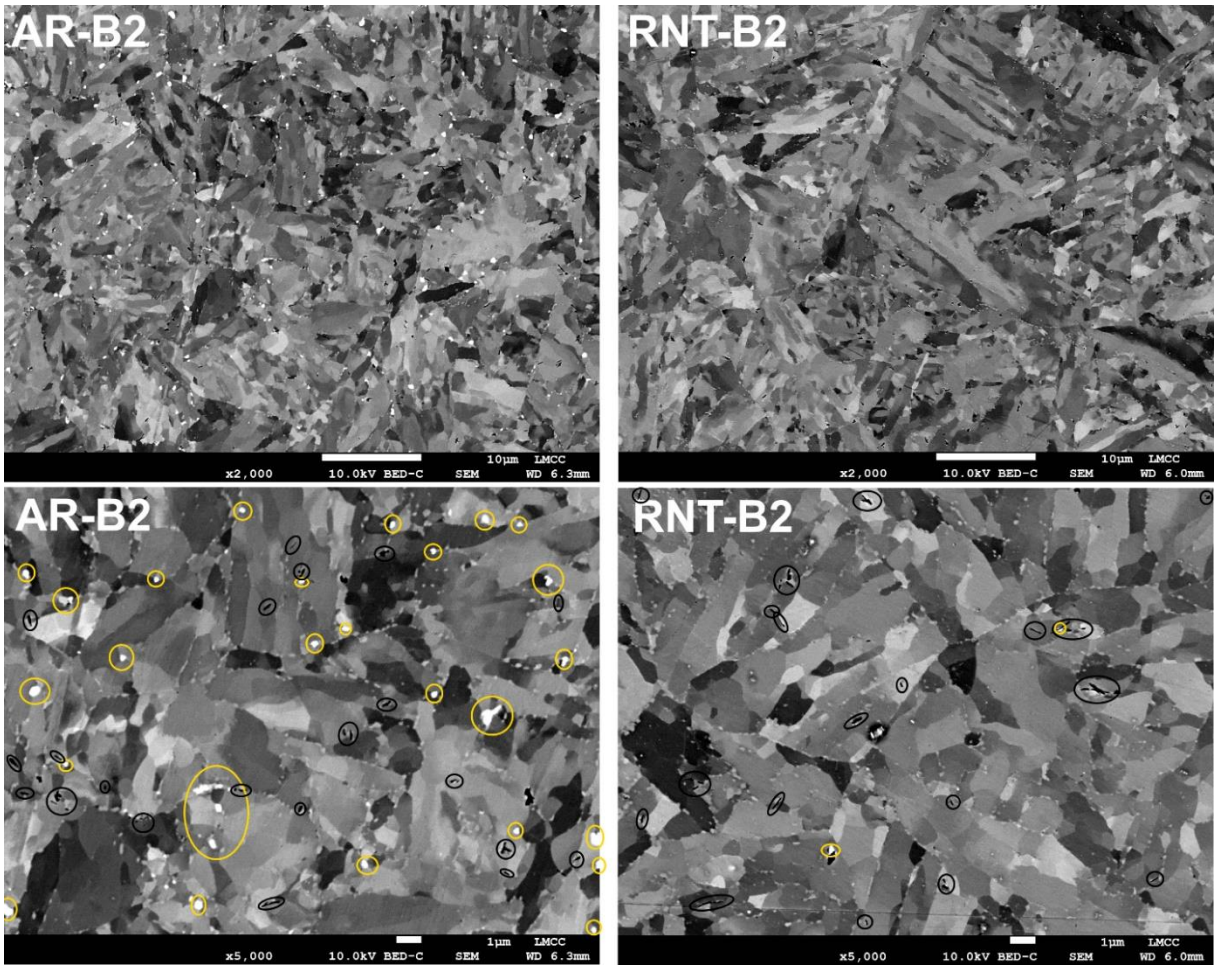

Figure 4-18. Comparison of AR-B2 and RNT-B2 for presence of Laves phase and AlN. The top images were taken at 2,000X magnification (scale marker = 10 µm) and the bottom images taken at 5,000X magnification (scale marker = 1 µm)
Note: *Laves phase is highlighted in yellow and AlN is highlighted in black.*

Table 4-6. Comparison of analyzed inclusions in the parent materials utilized in this research

Type	AR-B2	TP1
Al-type	251	252
S-rich	5,481	448
MnSi-type	1	1
Nb-type	11	25
Ti-type	0	0
Ca-type	191	41
Mg-type	1	0
High Si	0	0
Complex Spinel	10	91
Unclassified	4	19
Features which were unable to be assessed	1,343	39
Total (classified inclusions)	5,950	877
Total features	7,293	916
Inclusion density	141.6	17.8
Feature density	115.5	17.0

A comparison of the MnS assessments is provided in Table 4-7 and Figure 4-19. Based on the stated threshold particle size for the screening assessment (e.g. 1 µm) there exists a concern that the real MnS particle density is not documented. To assess this, the results for the refined (image-based and EDS-analysis) procedure are detailed in Table 4-7. The screening assessment (Table 4-6) clearly underestimates the content of MnS in each parent metal as the distribution of the MnS particle diameters in Figure 4-19 and calculated using the equivalent circle diameter (Equation 4.4) is <1 µm. The same may also be true for other inclusions which are expected to show a distribution in size. The result for MnS is used as an illustration of the potential differences which exist in screening methods for inclusion type versus detailed assessment which may be required to establish a 'true inclusion density'. As highlighted earlier, a focus is made for MnS as the formation of this particle overlaps the solidification temperature range for the ferrous matrix.

Equation 4.4 $$x_A = \sqrt{\frac{4A}{\pi}}$$

Where:
$A = \text{recorded area of the inclusion}$
$x_A = \text{circular equivalent diameter}$

Table 4-7. Comparison of MnS content in the parent materials utilized in this research

Material	Bulk assessment (MnS/mm^2)	Optimized, Location 1 (MnS/mm^2)	Optimized, Location 2 (MnS/mm^2)
AR-B2	131	708	727
TP1	9	311	280

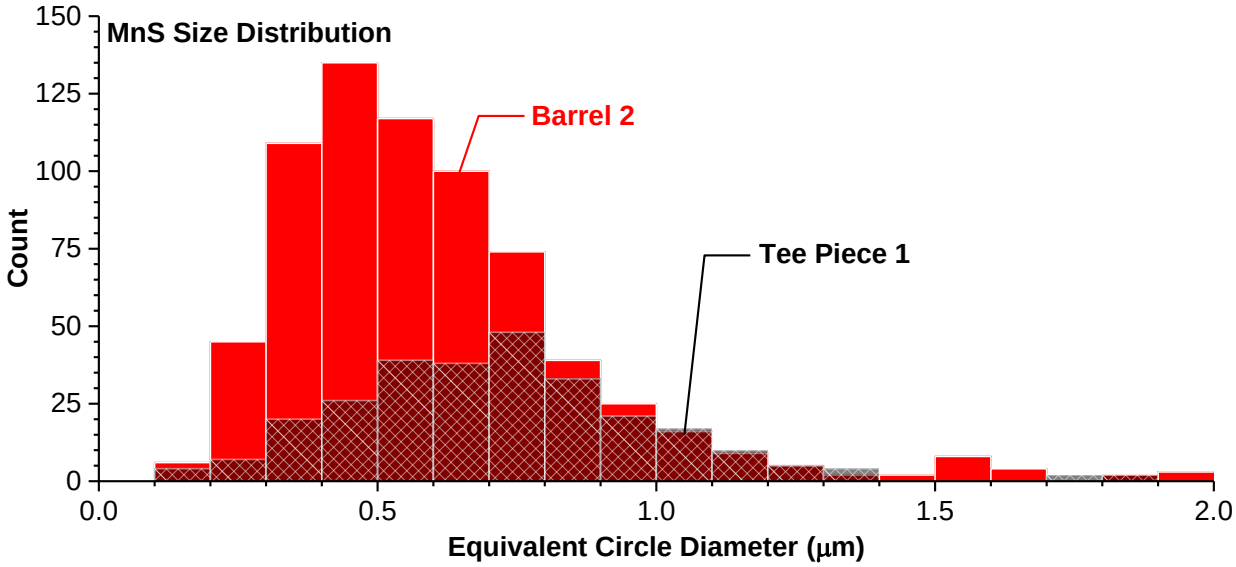

Figure 4-19. Comparison of MnS content in the AR-B2 and TP1 materials

4.5 Selection of Sample Geometry

Few studies exist on the effect of sample geometry on the evolution of creep damage in the HAZ of cross-weld creep tests, indeed in the clear majority of research little or no thought is given to the influence that specimen geometry has on results. Moreover because of the paucity of knowledge Codes and Standards offer little advice on how to ensure that test results from laboratory are relevant. In cases where geometry is considered too often the test conditions are selected to give rupture in ≤1,000 hours so the data trends obtained cannot be properly assessed for long term performance.

As noted earlier running creep tests to rupture makes informed assessment of damage formation and development difficult if not impossible. Yet, researchers rarely include evaluation of test samples prior to fracture. In general, this key omission is directly the result of performing only stress rupture tests. The current research has included detail measurement of strain:time. Importantly, this allows for the evaluation regarding the reproducibility of results from different tests and offer both a displacement fraction and time fraction opportunity for consideration in interrupted tests. The greater analysis possible combined with the results of meticulous characterization of the location, size,

nature and distribution of damage is unique research in CSEF steels and Grade 91 in particular.

In this section, details are provided for variations in the sample geometry which include round bar and feature-type sample geometries, Figure 4-20. A description of the evaluated tests is provided below:

- Standard round bar test with a diameter of 6.35 mm and a gauge length four times the diameter. Note that the gauge length is only sufficient to include one HAZ. Two samples are evaluated; an interrupted test to examine the evolution of creep damage and a second test taken to failure.
- Standard round bar test with a diameter of 12.7 mm and a gauge length four times the diameter. Note that the gauge length is only sufficient to include one HAZ. One sample is evaluated; an interrupted test to examine the evolution of creep damage.
- Feature cross-weld creep tests consistent with the prior descriptions for testing in the experimental procedure and included a cross-sectional area of 12.7 X 59 mm and a gauge length of 125 mm.
- For all tests, simultaneous strain measurements are recorded to allow for an informed interruption of the sample before final fracture where this is an important detail of the test. The selected test condition for all tests is 625°C and 60 MPa. A rationale for this (and other) test conditions utilized in this research to explore cross-weld creep behavior is explained in the following section. An attempt was made to terminate the 'interrupted tests' at a similar or identical interval to facilitate a reasonable comparison.

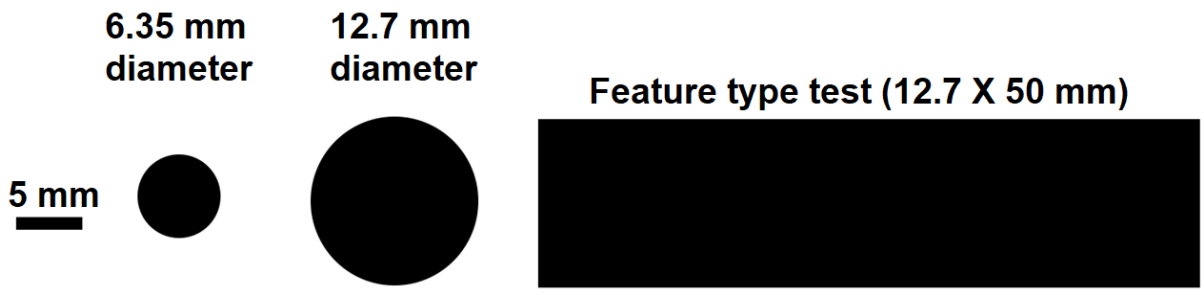

Figure 4-20. Comparison of the cross-sectional area for each type of sample evaluated in the AR-B2 material
Note: *The total area varies from 31.7 mm^2 (6.35 mm dia.) to 127 mm^2 (12.7 mm dia.) to 645 mm^2 (feature test)*

The results for each of the cross-weld test geometries including samples taken to failure and interrupted are given in Table 4-8. In this table, the estimated life fraction, expressed as a time or strain fraction, is calculated from the failed test samples. The procedure for making this determination is given in Figure 4-21 and Figure 4-22. In the failed test samples AR-B2-2 and RND-B2-2 there is a slight increase in the strain rate near the end of the test associated with plastic tearing. This increase is more extreme for the round bar sample (RND-B2-2) than for the feature test (AR-B2-2). This strain is not considered in the estimated strain fraction calculation.

Table 4-8. Assessment of cross-weld creep performance at 625°C and 60 MPa as a function of sample geometry and interrupted tests to assess the evolution of damage in the heat affected zone

Test Sample	Type of Sample	Time (hours)	Estimated Life Fraction (%)	
			Time	Strain
RND-B2-1	Round bar, 12.7 mm	1,347	64	85
RND-B2-2	Round bar, 6.35 mm	2,195	100	100
RND-B2-3		1,250	61	83
AR-B2-2	Feature-type cross-weld test	1.635	100	100
AR-B2-5		1,006	61	72

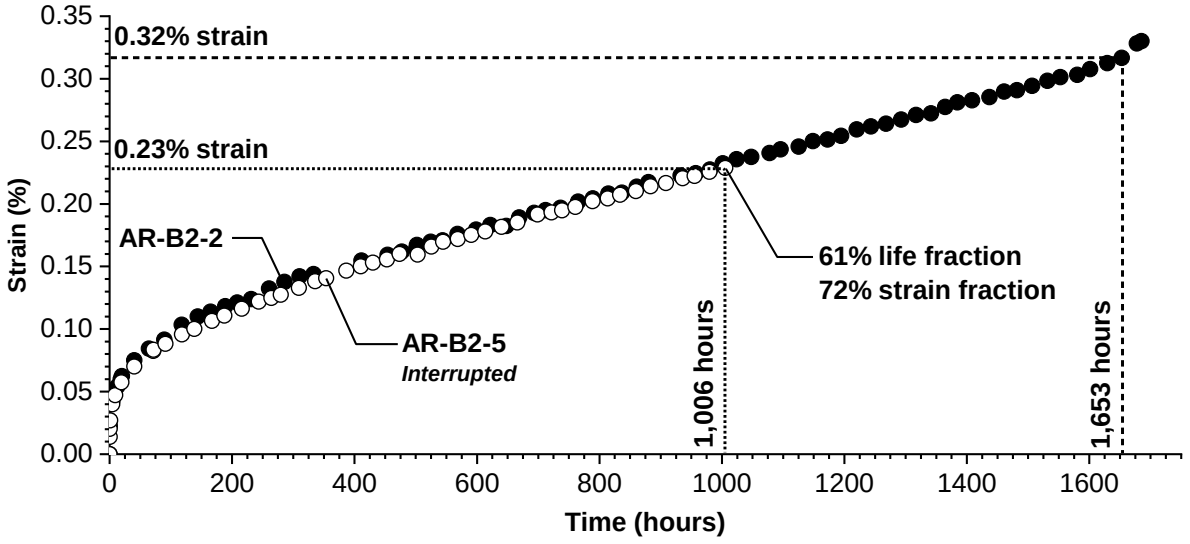

Figure 4-21. Comparison of the strain versus time data for the interrupted test AR-B2-5 to the failed test AR-B2-2. Based on the analyzed creep tests the AR-B2-5 was interrupted at a time or strain fraction of 61 or 72%, respectively

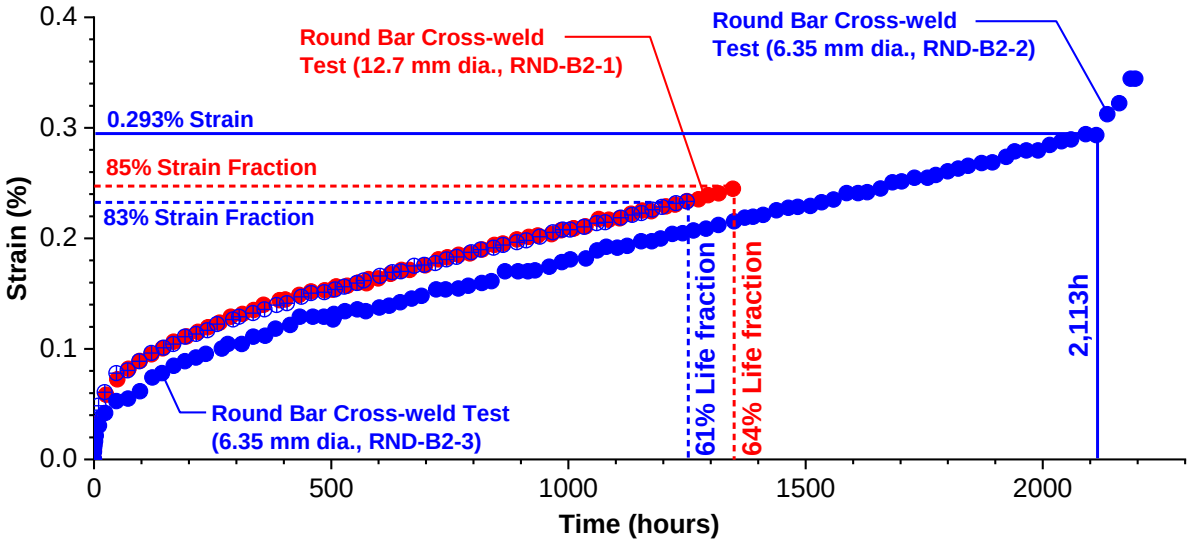

Figure 4-22. Comparison of the strain versus time data for the interrupted tests RND-B2-1 and RND-B2-3 to the failed test RND-B2-2. Based on the analyzed creep tests the RND-B2-1 test was interrupted at a time or strain fraction of 64 or 85%, respectively. Similarly, for RND-B2-3 this interruption occurred at a time or strain fraction of 61 or 83%, respectively.

Evaluation of the damage in the cross-sections for each cross-weld test are documented in Figure 4-23 to Figure 4-29. A comparison of a local area of damage in the HAZ is provided in Figure 4-30 for each of the interrupted test sample geometries (e.g. 6.35 mm, 12.7 mm and feature test). As the sample cross-sectional area increases, the extent of damage is observed to increase for the large test samples. The level of damage in the 6.35 or 12.7 mm diameter samples compared to the feature cross-weld creep test is notably lower.

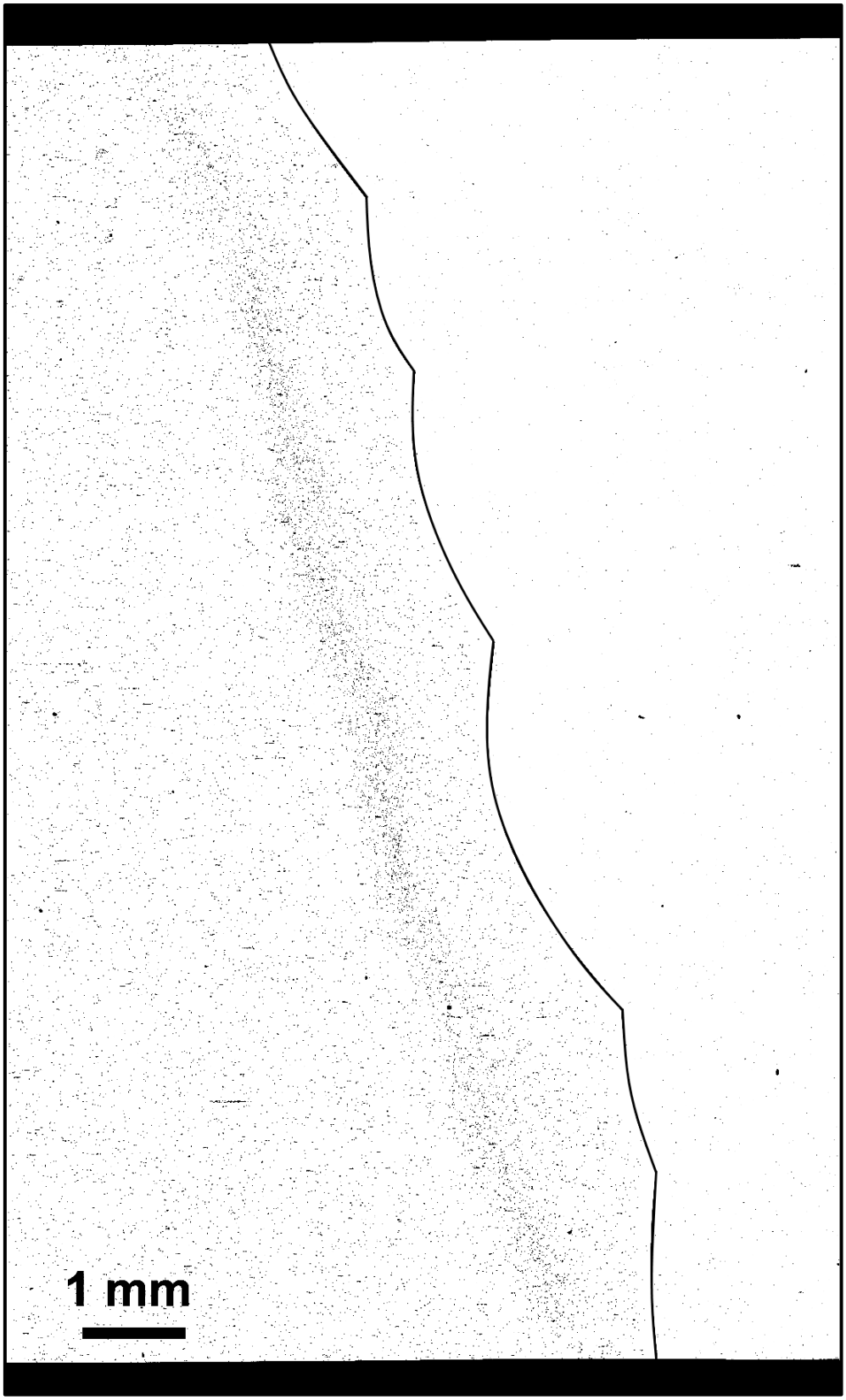

Figure 4-23. The distribution of damage through the heat affected zone in the interrupted sample RND-B2-1 (12.7 mm diameter, 1,347 hours to termination, 64% time fraction, 85% strain fraction).
Note: *The weld is on the right of the image, fusion line is indicated as a continuous black line and the heat affected zone damage can be observed as a broad distribution near the center of the image*

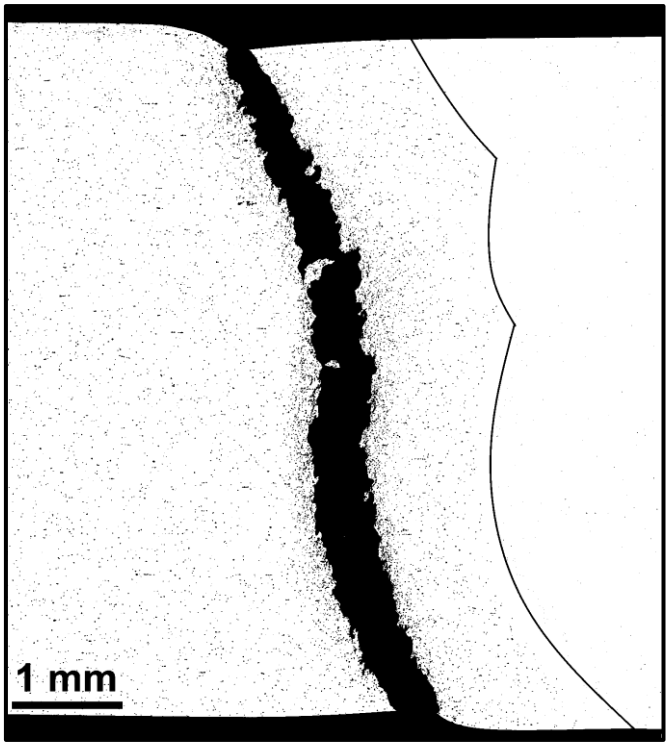

Figure 4-24. The distribution of damage through the heat affected zone in the failed sample RND-B2-2 (6.35 mm diameter, 2,195 hours to failure).
Note: *The weld is on the right of the image, fusion line is indicated as a continuous black line and the heat affected zone damage can be observed as a broad distribution near the center of the image*

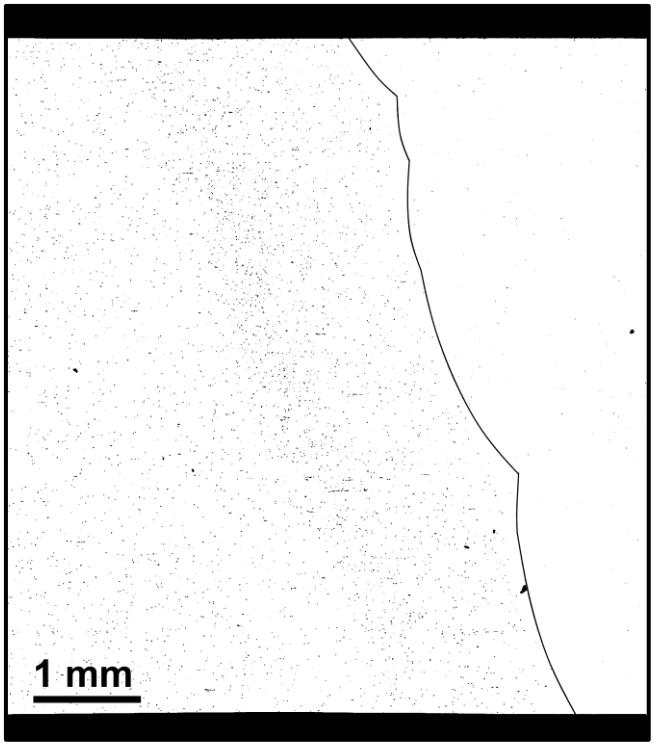

Figure 4-25. The distribution of damage through the heat affected zone in the interrupted sample RND-B2-3 (6.35 mm diameter, 1,250 hours to termination, 61% time fraction, 83% strain fraction).
Note: *The weld is on the right of the image, fusion line is indicated as a continuous black line and the heat affected zone damage can be observed as a broad distribution near the center of the image*

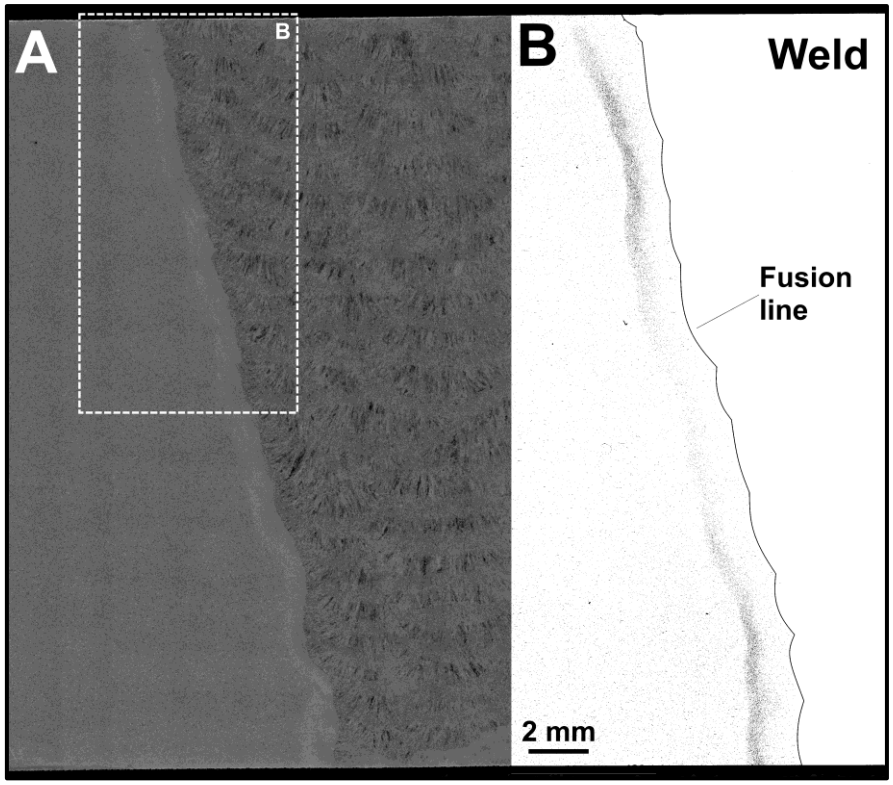

Figure 4-26. The distribution of damage through the heat affected zone region in the top left region of the sample indicated in (A) and provided in (B) for the interrupted sample AR-B2-5 (feature cross-weld test geometry, 1,006 hours to termination, 61% time fraction, 72% strain fraction).

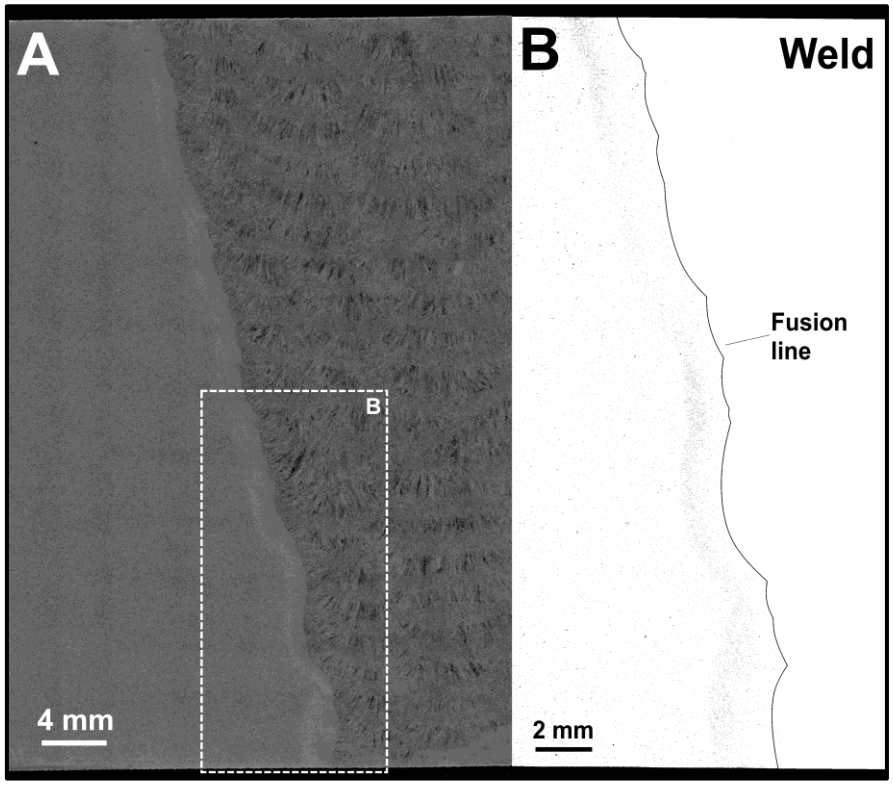

Figure 4-27. The distribution of damage through the heat affected zone region in the bottom left region of the sample indicated in (A) and provided in (B) for the interrupted sample AR-B2-5 (feature cross-weld test geometry, 1,006 hours to termination, 61% time fraction, 72% strain fraction).

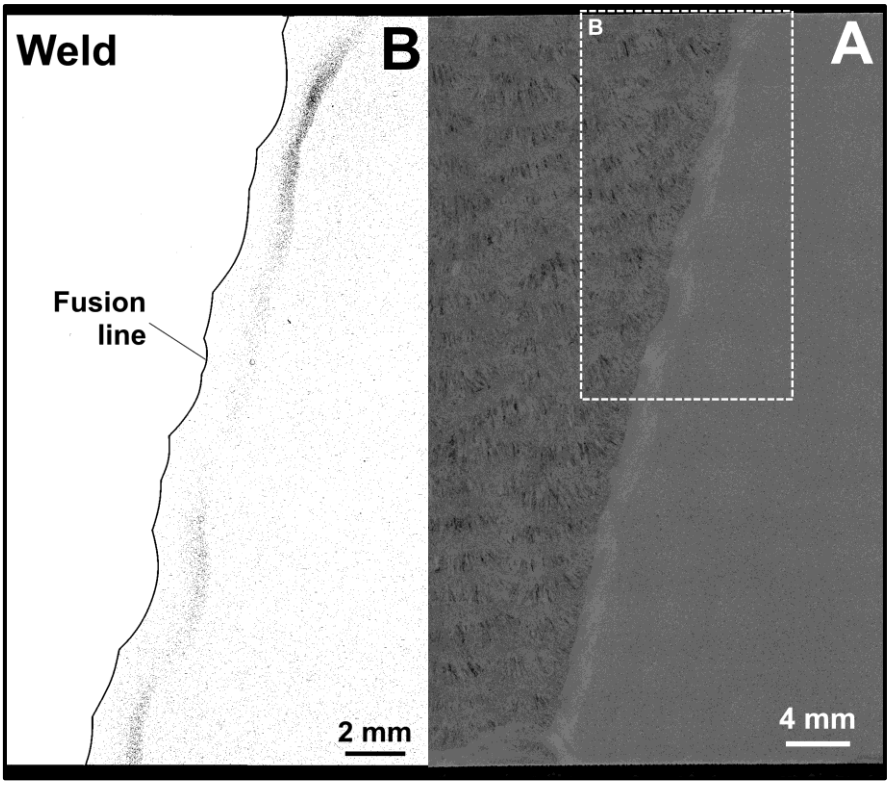

Figure 4-28. The distribution of damage through the heat affected zone region in the top right region of the sample indicated in (A) and provided in (B) for the interrupted sample AR-B2-5 (feature cross-weld test geometry, 1,006 hours to termination, 61% time fraction, 72% strain fraction).

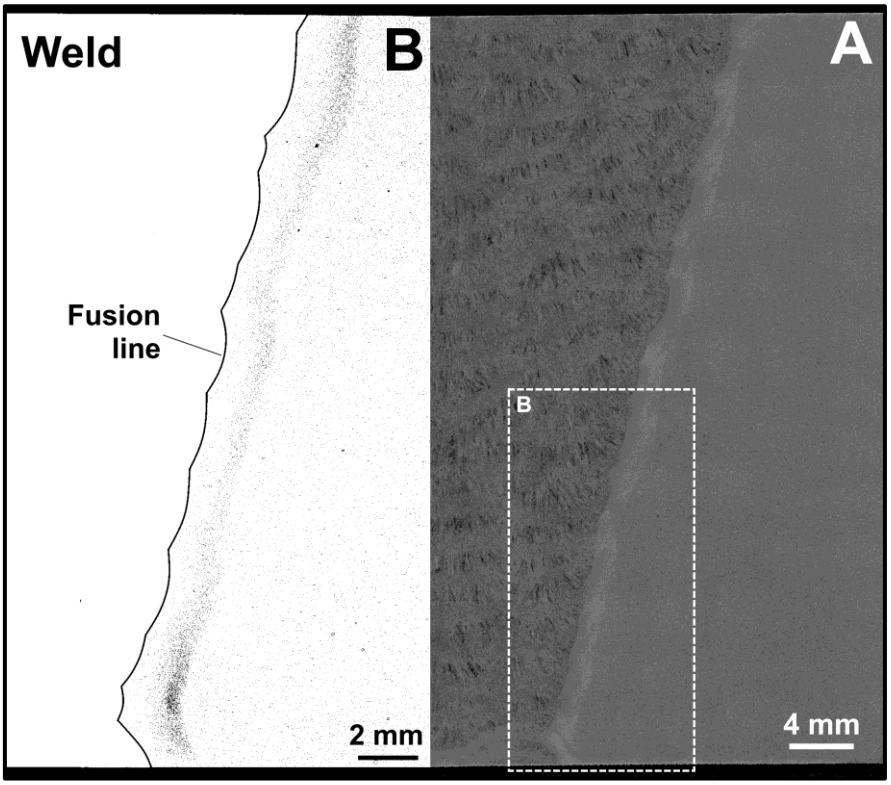

Figure 4-29. The distribution of damage through the heat affected zone region in the bottom right region of the sample indicated in (A) and provided in (B) for the interrupted sample AR-B2-5 (feature cross-weld test geometry, 1,006 hours to termination, 61% time fraction, 72% strain fraction).

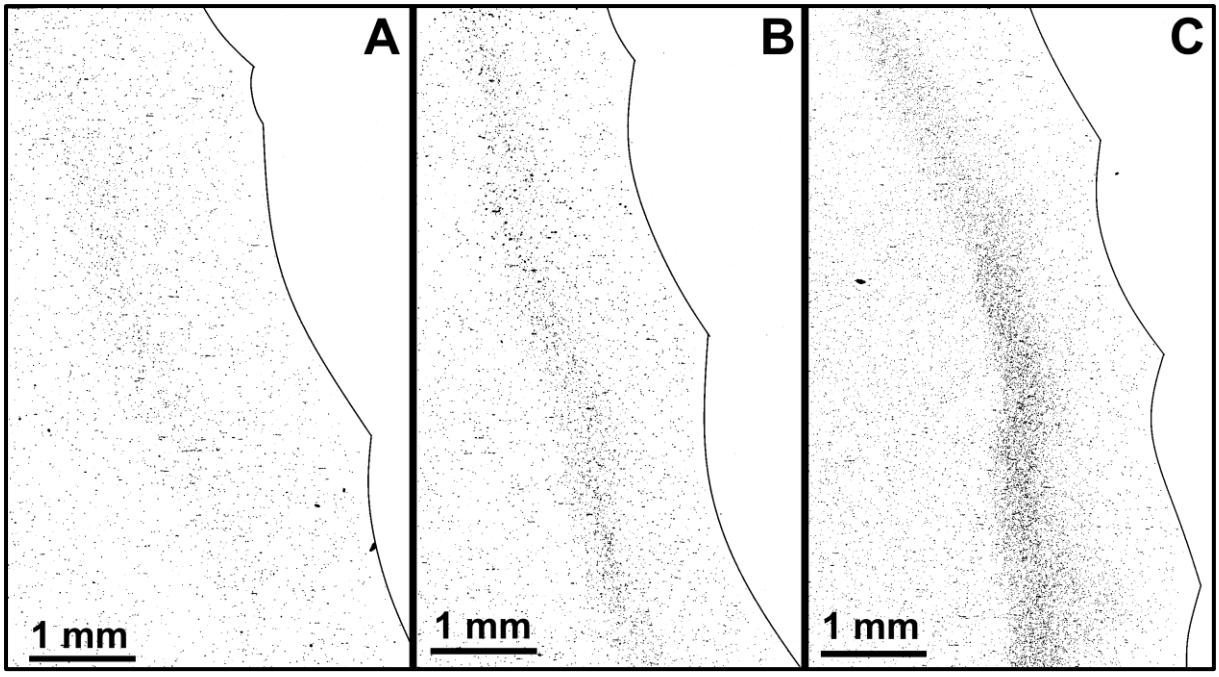

Figure 4-30. Comparison of the cavity density for each of the interrupted cross-weld creep test samples in the 6.35 mm diameter (A), 12.7 mm diameter (B) and the feature test geometry (C)

4.6 Selection of Test Conditions

In general, researchers should balance the following when developing a creep test program:

- Accelerated testing in which a relevant distribution of damage is developed in the HAZ. As most studies are conducted over a time scale that is characterized as a fraction of expected in-service exposure there is a need to evaluate the factors that affect the accumulation of representative damage in a reasonable timeframe;
- The test temperature should be as close to operation as possible;
- The test stress should be as close to operation as possible.

These ideal scenarios are not easily accommodated, e.g. development of damage in the original Aberthaw header is only documented after more than 50,000 hours of operation at a mean steam outlet temperature of ~570°C, and therefore there exists a need to accelerate the development of damage through increasing the temperature and/or stress. Prior assessments for low alloy steels typically relied on iso-stress tests where a stress very close to operation was chosen and the temperature increased over a suitable range to induce failures in an accelerated time (Viswanathan 1995).

This approach is not favorable for 9 wt. % Cr steels as acceleration of the temperature >650°C (1202°F) will include microstructural changes that complicate the test results, such as the dissolution of Laves or Z-phase, Figure 4-7 and Figure 4-8. Because of this, there is a need to carefully consider the testing conditions whenever a 9 wt. % Cr steel is assessed for creep behavior (cross-weld or otherwise). For the Aberthaw header, the following is summarized from the previous details:

- The calculated hoop stress in the header body is 65.5 MPa;
- The nominal operating temperature is 570°C (1058°F) and
- A maximum temperature of ~593°C (1100°F; e.g. 570°C × 1.04) is documented.

With respect to the applied test stress for minimum-bound parent metal and minimum-bound cross-weld behavior, there is a cross-over at an applied stress of 125 MPa in the parent material and cross-weld relationships in Equations 4.2 and 4.3, Figure 4-31. If the generation of HAZ failures is paramount, then the maximum applied stress should be below this value to ensure a relevant failure mode is generated. To achieve this objective, it is preferable to utilize a test stress ≤100 MPa as the cross-weld and parent metal behavior is clearly offset at this applied stress value. Applied stress values ≤100 MPa have been shown by Brett to be reasonable for assessing the cross-weld behavior of minimum bound Grade 91 steel (Brett 2010).

The recommendation for the assessment of behavior is highlighted in Table 4-9 using Equation 4.3 and includes the following test conditions: 625°C and 80 MPa; 625°C and 60 MPa; and 600°C and 80 MPa. Using a similar temperature and a similar stress provides a reasonable comparison for behavior; using a Larson-Miller parameter comparison at 80 MPa the results at 600 and 625°C should be very similar.

Table 4-9. Minimum and mean life calculations for Grade 91 steel cross-weld creep performance.
Note: *the selected cross-weld creep test conditions for this research are highlighted in black.*

Temperature (°C, °F)	Stress (MPa, ksi)	Minimum Life (hours)	Mean Life (hours)
600, 1112	120, 17.4	950	2,500
600, 1112	100, 14.5	2,150	5,700
600, 1112	**80, 11.6**	**5,700**	**15,000**
600, 1112	60, 8.7	20,000	53,000
625, 1157	120, 17.4	135	400
625, 1157	100, 14.5	325	940
625, 1157	**80, 11.6**	**940**	**2,700**
625, 1157	**60, 8.7**	**3,700**	**10,725**
650, 1202	80, 11.6	155	490
650, 1202	60, 8.7	685	2,170
650, 1202	40, 5.8	5,570	17,650

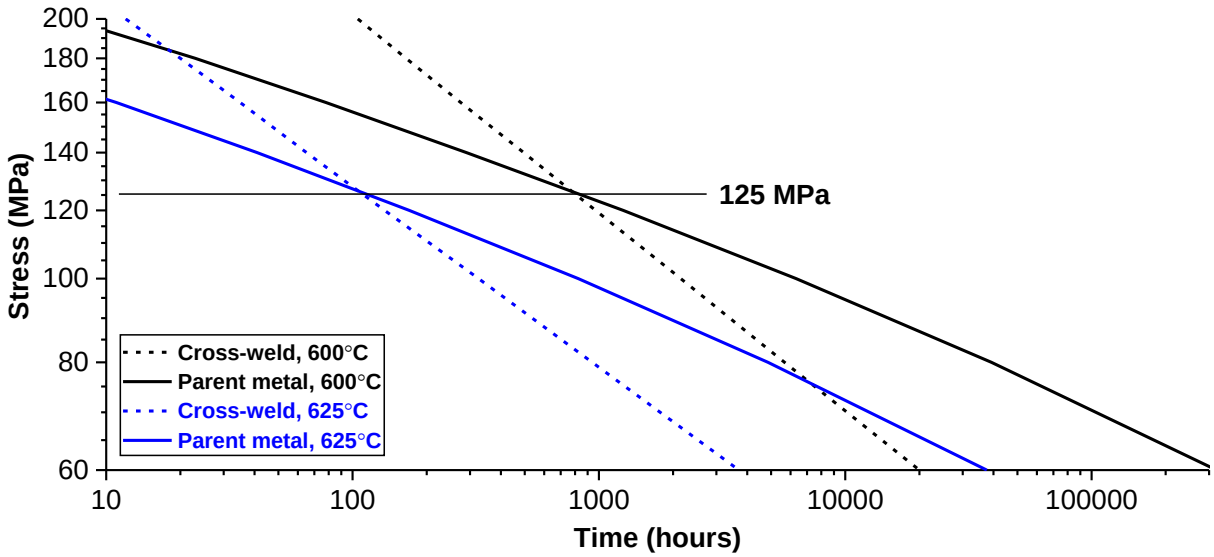

Figure 4-31. Comparison of the minimum test data for parent and cross-weld behavior given in equations 4.2 and 4.3 for Grade 91 steel
Note: *the cross-over in the potential for parent metal or cross-weld failure occurs at 125 MPa. This suggests that the applied stress for cross-weld tests where failure should be generated in the heat affected zone should be <125 MPa.*

4.7 Discussion

The selected parent materials for the cross-weld creep evaluation have been shown to exhibit similar amounts of $M_{23}C_6$ and Laves phase after service exposure at ~570°C and 79,000 hours of operation. For each parent metal there exists a real and significant difference in the AlN and inclusion content. Specifically, the AR-B2 material has about 5X more AlN and 3X more inclusions than the TP1 material. Calculations based on the reported service conditions demonstrated that these two materials should possess <5% life consumption and more realistically a consumed life that is ~1%. Thus, there

is not believed to be a relevant distribution of creep damage in the post-service parent material which might adversely affect the cross-weld creep test results.

The influence of test sample geometry in Figure 4-32 is compared for unique test geometries including two round bar geometries and a feature cross-weld test geometry. These test samples, which are very close in configuration to those detailed earlier for the microstructural evaluation, explore the effect of the variability in the cross-sectional area of ~20X. A creep redistributed stress analysis was performed using the software package ABAQUS, partitioning of the model to include parent metal, PTZ (1.0 mm wide), CTZ (1.5 mm wide) and weld regions. The parent metal, CTZ and filler material were given similar properties while the PTZ was assigned a unique set of properties. The utilized approach is consistent with a recent publication, which details the form of the constitutive models and values for the constants in the model (Pritchard et al. 2018), and summarized in Equations 4.5 to 4.12 and Table 4-12. The parent metal, weld metal and CTZ were assumed to exhibit the same behavior, Equation 4.5 and hence the same values for each of the material constants were assumed in these three regions (Table 4-12). Although the PTZ followed a similar approach, Equation 4.6, the strength factor F (Equation 4.7) was introduced to account for the reduction in strength in the PTZ with increasing temperature ~≥550°C. The strength factor follows an Arrhenius temperature dependence as the variation in the performance for the PTZ is temperature-dependent and it should be noted that the activation energy Q_F is not linked to a specific metallurgical phenomenon.

Equation 4.5 (Base metal, weld metal, CTZ) $\dot{\varepsilon}_{ij}^{c} = \frac{3s_{ij}}{2\sigma_e}\left(A_{HT}{\sigma_e}^{n_H} + A_{MT}\left(\frac{\sigma_e}{(1-\omega)(1-G)}\right)^{n_M}\right)$

Equation 4.6 (PTZ) $\dot{\varepsilon}_{ij}^{c} = \frac{3s_{ij}}{2\sigma_e}\left(A_{HT}\left(\frac{\sigma_e}{F}\right)^{n_H} + A_{MT}\left(\frac{\sigma_e}{F(1-\omega)(1-G)}\right)^{n_M}\right)$

Equation 4.7 $F = 1 - F_o exp\left(\frac{-Q_F}{RT}\right)$

Equation 4.8 $\dot{\omega} = \frac{A_{DT}{\sigma_I}^{x}}{(1-\omega)^{\varphi}}$

Equation 4.9 $\dot{G} = k\dot{\varepsilon}_{e}$

Equation 4.10 $A_{HT} = A_H exp(-Q_H/RT)$

Equation 4.11 $A_{MT} = A_M exp(-Q_M/RT)$

Equation 4.12 $A_{DT} = A_D exp(-Q_D/RT)$

Table 4-10. Model parameters for the creep continuum damage mechanics model described in Equations 4.5 to 4.12

Parameter	Symbol	Units	Value	
			Parent metal, weld metal, CTZ	PTZ
High stress deformation multiplier	A_H	abs./(MPa)^{nH}/hr	1.8x10^8	1.8x10^8
High stress activation energy	Q_H	J/mol	825,000	825,000
High stress creep exponent	n_H		17	17
Mid stress deformation multiplier	A_M	abs./(MPa)^{nM}/hr	4.2x10^{16}	4.2x10^{16}
Mid stress activation energy	Q_M	J/mol	617,000	617,000
Mid stress creep exponent	n_M		7	7
Strain softening coefficient	k	hr	6.25	6.25
Damage rate multiplier	A_D	abs./(MPa)^x/hr	TBD	1.2x10^{14}
Damage activation energy	Q_D	J/mol	TBD	487,000
Damage stress exponent	x		TBD	5
Damage tolerance exponent	φ		TBD	10
Strength factor multiplier	F_0		0	143
Strength factor activation energy	Q_F	J/mol	0	45,900

In each case, the stress distribution is plotted after 95% of the time to crack initiation and as a function of the distance (r) from the center of the sample to the edge (total radius, R), Figure 4-32. The Von-Mises equivalent stress (Figure 4-33) and the maximum principal stress (Figure 4-34) are plotted as a function of r/R (e.g. distance from the center of the sample, which is ‘0’). It should be emphasized that although the Von-Mises stress is highest very near to the free surface the lowest level of damage in all samples is near the free surface. On the contrary the maximum principal stress shows the highest value near the center of the sample.

As the sample diameter or section size decreases, there is a more extreme variation from the center of the sample. This variation in stress, and thus modification of the stress-state in each sample, may account for the difference in damage distribution highlighted in Figure 4-30. Since the samples were taken from the same weldment, the same location in the weld, and the same test parameters, it is difficult to explain the variation in the damage based on variables in the welding procedure. Stress-state, and the constraint imposed by the larger diameter samples, are thus believed to play a potentially significant role in the evolution of damage highlighting the importance of cross-weld sample geometry.

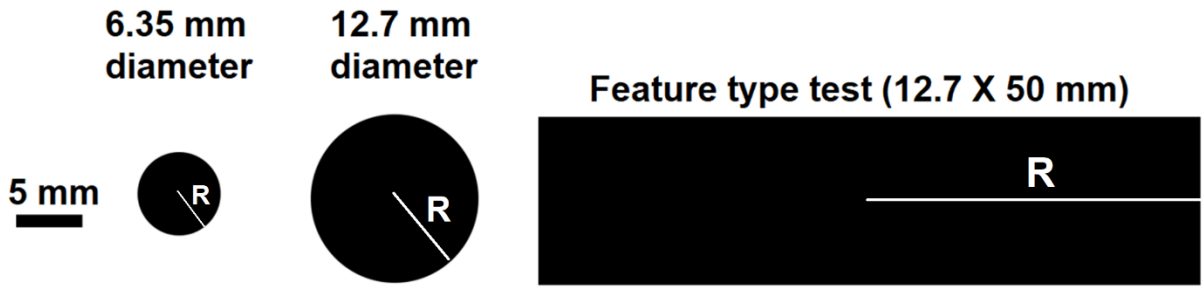

Figure 4-32. Definition of the value R for each evaluated test sample geometry

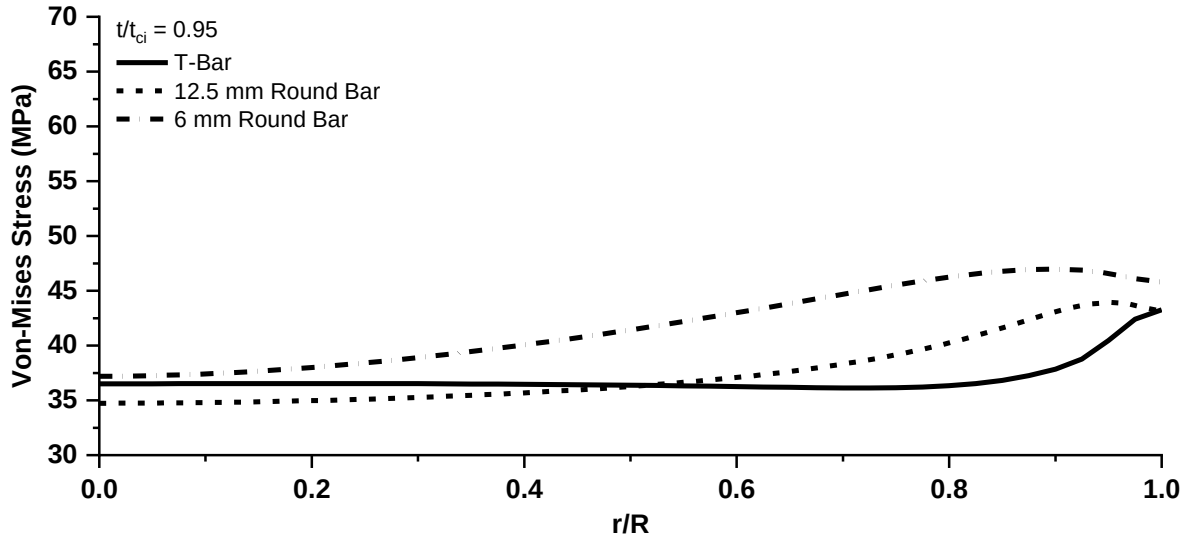

Figure 4-33. Comparison of the distribution of the equivalent stress through the length of the heat affected zone as a function of the sample geometry

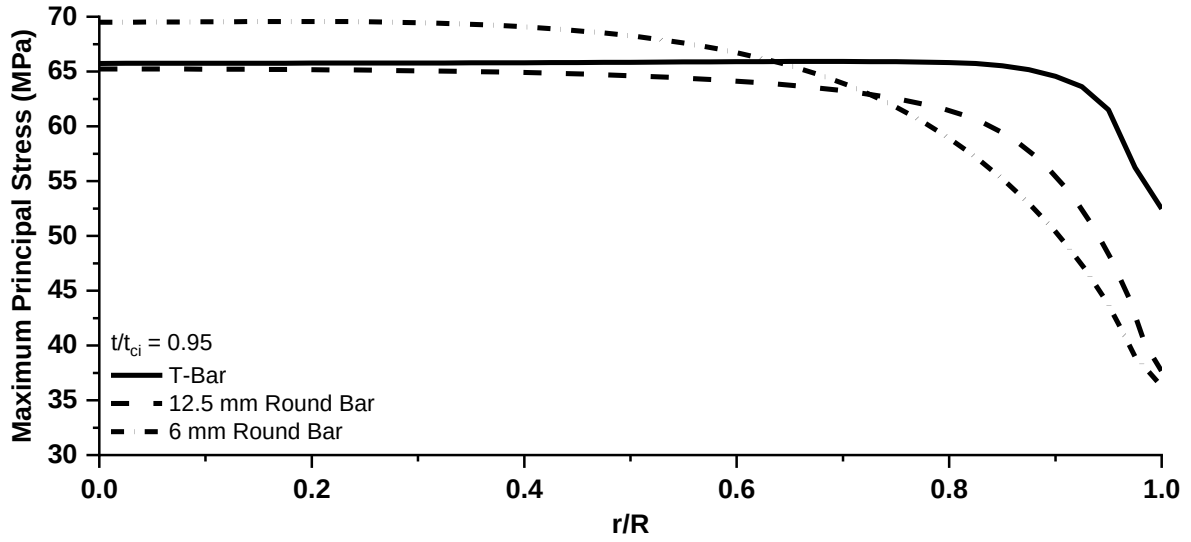

Figure 4-34. Comparison of the distribution of the maximum principal stress through the length of the heat affected zone for investigated sample geometries

The selection of test parameters includes a standard test condition of 625°C and 80 MPa and two additional conditions of 625°C and 60 MPa and 600°C and 80 MPa. The bracketing of the test conditions for two similar stresses and temperatures is useful in

the comparison of the damage accumulation. For perspective, the allowable stress value for Grade 91 steel according to ASME B&PV Code Section IID is provided in Figure 4-35. The use of a test stress of 80 MPa at 600 or 625°C is about 25 to 50% greater than the allowable stress at this same temperature. By comparison, a stress value of 100 MPa (e.g. an 80 to 100% increase) is commonly utilized. A 60 MPa applied stress value at 625°C is similarly ~50% greater than the allowable stress value.

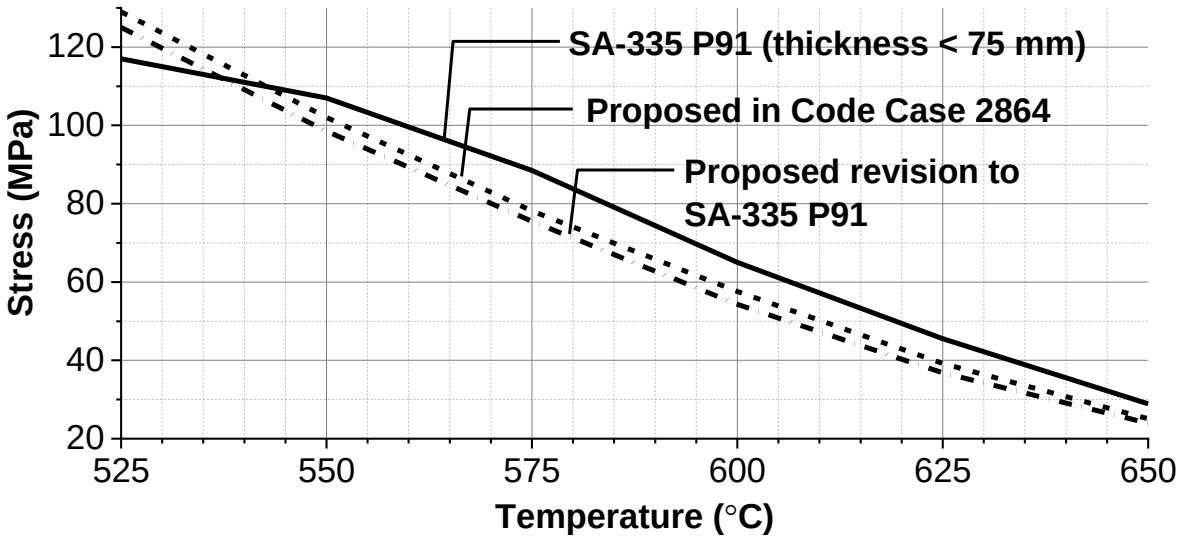

Figure 4-35. Comparison of allowable stress values for Grade 91 steel in the ASME B&PV Code Section IID and proposed revisions to these values

In summary, there has been a methodical evaluation for the selected parent materials, feature-test geometry and test conditions utilized in the cross-weld creep evaluation which is reported in Chapter 6. There is reason to believe that the combination of factors described in Chapter 4 are essential for ensuring the assessment of damage in the test samples is relevant to in-service component behavior with respect to maximum densities and distributions of damage in the HAZ.

4.8 Summary

The selected parent materials and weld details are provided for each of the unique weld IDs utilized in this thesis are provided in Table 4-11. The selection of the weldments is carefully planned and executed to assess two primary aspects of cross-weld behavior:

- Influence of parent metal condition on cross-weld behavior: AR-B2; RNT-B2, 7C and F-TP1 and using a single heat of AWS type -B9 filler material;

- Influence of filler metal strength and PWHT on cross-weld behavior: 7C, 8C and 9C.

Each weldment was fabricated using identical set of considerations for the welding process (SMAW), preheat, and interpass temperature. The variation of PWHT in welds 7C, 8C and 9C was examined, in part, to support the evaluation of alternative weld repair procedures for Grade 91 steel. Consequently, these welds also provide a means to evaluate the influence of PWHT on cross-weld creep behavior.

Table 4-11. Parent materials and fabricated weldments investigated for cross-weld creep performance using feature cross-weld tests and identical weld geometries

Parent metal	Condition	Weld ID	Weld Details	
			Filler metal	PWHT
B2	As-received	AR-B2	E9015-B9	675°C/2h
	Renormalized and tempered	RNT-B2	E9015-B9	675°C/2h
TP1	Ferritic	F-TP1	E9015-B9	675°C/2h
	As-received	7C	E9015-B9	675°C/2h
		8C	E8015-B8	None
		9C	EPRI P87	None

The selected test geometry includes a 15° bevel on either side of the weldment resulting in a 30° included angle. This machined geometry approximates the utilized bevel angle for a compound bevel geometry where the upper half (or more depending on the section thickness) of the weld is typically 10 to 15°, Figure 4-36. The use of a single bevel angle, as opposed to the depicted compound bevel, removes the stress concentration that can sometimes accelerate the formation of damage at the transition between bevel angles.

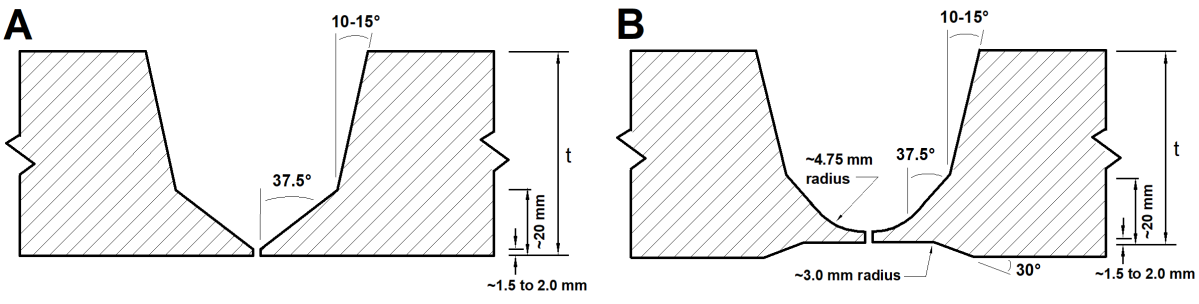

Figure 4-36. Comparison of common weld geometries for thick-section girth welds in piping systems and headers, a compound bevel without ID-matching (A) and a compound bevel combined with a J-prep where ID-matching is specified (B)

The selection of test conditions for each weldment are provided in Table 4-12. The standard conditions of 625°C and either 60 or 80 MPa are utilized for all fabricated

welds. Except for weld 7C, a third, standard test condition of 600°C and 80 MPa is used to provide a set of temperature and stress values for comparison. The investigation of behavior for the under-matching weld 8C includes a larger range of test conditions since it is expected that this weldment will exhibit variable behavior with respect to failure location. For welds in the low deformation resistant material (F-TP1) or damage intolerant (AR-B2 and RNT-B2) parent metal, an additional test condition of 625°C and 50 MPa is specified to ensure the trends at representative, hoop stress values (e.g. ~60 MPa) for conventionally designed components are sufficiently evaluated.

Table 4-12. Selected test conditions for the investigated weldments in Table 4-11

Test Conditions		7C	8C	9C	AR-B2	RNT-B2	F-TP1
°C	MPa						
575	90		8C-7				
600	80		8C-2	9C-2	AR-B2-3	RNT-B2-3	F-TP1-3
600	70		8C-5				
600	60		8C-6				
625	80	7C-1	8C-1	9C-1	AR-B2-1	RNT-B2-1	F-TP1-1
625	60	7C-2	8C-3	9C-3	AR-B2-2 AR-B2-5	RNT-B2-2	F-TP1-2
625	50		8C-4		AR-B2-4	RNT-B2-4	F-TP1-4

The difference in the selected parent materials is clear whether based on the fundamental, thermodynamic assessment using the main alloying elements or the results for the assessment of the present inclusions and second phase particles (such as Laves, $M_{23}C_6$, AlN). Each parent metal has an elevated Al content leading to the formation of AlN, although the amount present in the B2 material exceeds that of the TP1 material. The inclusion content for the B2 is notably greater as compared to the TP1 material. The noted S content in the B2 is about 5X greater resulting in a larger number of MnS whether assessed by a ‘conventional’ method or a refined image-based method using SEM. The documented variability in the selected parent materials, particularly for the inclusion content, is expected to be an important factor in the subsequent evaluation of mechanical performance and association of damage in the HAZ.

5 Characterization of Microstructure in As-fabricated Weldments

5.1 Introduction

Linking features in the heat affected zone (HAZ) to the observed damage in cross-weld test samples requires that the pre-test condition be assessed using a set of comparable procedures. This is needed since a secondary set of objectives are focused around weld-to-weld comparisons for the present damage. This chapter provides an evaluation of the six weldments detailed in Table 5-1 in the as-fabricated condition prior to cross-weld creep testing. Additional details for the fabrication of each weldment can be found in section 3.2. It is reiterated that the term 'as-fabricated condition' may refer to weldments in the as-welded condition (welds 8C and 9C) or after a subcritical post weld heat treatment (PWHT) at 675°C for 2 hours (7C, AR-B2, RNT-B2 and F-TP1). Additionally, there exists variability in the selection of filler material; the important details for each weldment are included in Table 3-3. Definitions or association of microstructural features rely on the preferred terminology detailed in Table 1-4 for the regions denoted as the completely transformed zone (CTZ), partially transformed zone (PTZ) or over-tempered zone (OTZ).

Table 5-1. Details for the welding procedures used to fabricate the weldments in this study

Weld	Parent Metal	Filler Metal	Filler Metal Strength Relative to Parent Metal	Post Weld Heat Treatment
7C	TP1	E9015-B9	Matching	675°C (1250°F) for 2 hours
8C	TP1	AWS type -B8	Under-matching	None
9C	TP1	EPRI P87	Over-matching	None
AR-B2	B2	E9015-B9	Matching	675°C (1250°F) for 2 hours
RNT- B2	B2			
F-TP1	TP1			

The evaluation that serves as the basis for this Chapter utilizes a consistent set of procedures including: macro-assessment using hardness mapping, micro-assessment using scanning electron microscopy (SEM) based techniques including qualitative and quantitative methods and finally linking the data to the distribution of calculated peak temperatures through the HAZ. The mechanical behavior of these weldments in the as-fabricated state is detailed in Chapter 6. The macro-distribution of damage in the weldment is presented in Chapter 7, whilst an assessment of the association of damage with specific features in the microstructure is provided in Chapters 8 and 9, respectively.

5.2 Hardness Mapping

Color hardness maps are provided in Figure 5-1 through Figure 5-6 for each of the weldments in the as-fabricated condition. In all cases, the referenced hardness scale is optimized using the procedures detailed in section 3.3.2. The location of the fusion line, as highlighted by a solid white line, is provided after overlaying an etched macrograph produced on the hardness map data.

For all welds, the hardest region in the HAZ is immediately adjacent to the fusion line in a region consistent with the definition for the CTZ. In the welds fabricated with Fe-base filler materials (e.g. AWS type -B8 or -B9), general peak hardness values are observed in the weld metal and CTZ. The observed peak values in the Fe-base weld metal for weld 8C are linked to coarse, columnar regions which did not experience a refinement process from adjacent weld thermal cycles. For the weldment 9C, fabricated with a Ni-base filler material, the austenitic weld metal possesses a similar hardness to that of the parent material (e.g. ~190 to 230 HV 0.5).

For weld 8C, there is a notable tempering effect even in the as-welded condition. This is attributed to the reduced resistance to tempering that is characteristic of the AWS type -B8 weld metal as it does not possess the same alloying content as for Grade 91 steel. Specifically, AWS type -B8 filler material does not contain intentional additions of N, Nb or V. N, Nb and V will form and stabilize a distribution of MX-type carbides which increase hardenability. The reduction in hardness in the as-welded condition for the AWS type -B8 weld metal is notable as the local minimum values in the locations of bead-to-bead tempering are ≤240 HV 0.5.

After PWHT, the welds 7C, AR-B2 and RNT-B2 exhibit a hardness value that is <350 HV 0.5. The observed maximum value is higher than for typical weldment manufacturing where the hardness values are reduced to ~<300 HV 0.5. The difference is attributed to the specified PWHT in this study (675°C for 2 hours), which is consistent with the recognized minimum in the National Board Inspection Code Part 3 Repairs and Alterations Supplement 8 (NBIC 2017). This Code provides post construction repair requirements for power generation components and materials including Grade 91 steel, and is commonly utilized in North America and in some southern European countries.

More recently, ASME B&PV Code Section I reduced its minimum PWHT requirements to a value of 705°C (1300°F) for weld thickness > 13 mm (0.50 inches) or to a value of 675°C (1250°F) for weld thickness ≤ 13 mm (0.50 inches) (ASME 2017). The minimum value of 705°C (1300°F) is in line with the requirements in earlier editions of ASME B&PV Code Section I and B31.1 before ~2007. The change in the minimum value after 2007 was argued based on Charpy v-notch impact values which did not meet the commonly referenced Euro-Norm (EN) requirement of 27J (20 ft-lbs).

In the context of PWHT in the field, which would typically be required to fabricate ~1/2 of the total welds in piping system, the use of ceramic heating resistance pads is most often utilized to perform the PWHT. This necessitates heating from the outside surface, and the inside diameter of the weldment is not expected to reach the target temperature due to heat conduction. Thus, the utilized PWHT temperature of 675°C (1250°F) is within reason for the evaluation of ‘lower bound’ in the context of field PWHT and in consideration of prior and current editions of new construction and repair Codes (ASME 2017, NBIC 2017).

Through the width of the HAZ there exists a gradient of hardness, including the presence of a ‘soft zone’ often referenced in the literature. This soft zone is observed in the as-welded condition (welds 8C and 9C) as a discontinuous region that would normally be difficult to consistently identify if the hardness evaluation is performed using a randomly placed hardness line trace. The soft zone becomes more consistent and wider in each of the weldments, which were given the PWHT. Aside from the trends noted previously, the hardness mapping is a useful tool to:

- Provide confidence in the welding procedure. For example, note the consistency of bead size and placement in Figure 5-2, and the application of PWHT is apparent for the welds which specified this step in fabrication (e.g. Figure 5-1, Figure 5-4 to Figure 5-6);
- Evaluate the heterogeneity of the microstructure, which is most obvious in the hardness maps provided for weld 8C (Figure 5-2);
- Identify the location and extent of the soft zone in the microstructure, which is more obvious in the hardness maps for the samples which had a PWHT, such as for weld 7C (Figure 5-1).

The following sections will link the as-fabricated hardness to important observations for the calculated peak temperature and the quantified distribution of low or high angle grain boundaries assessed using SEM-EBSD.

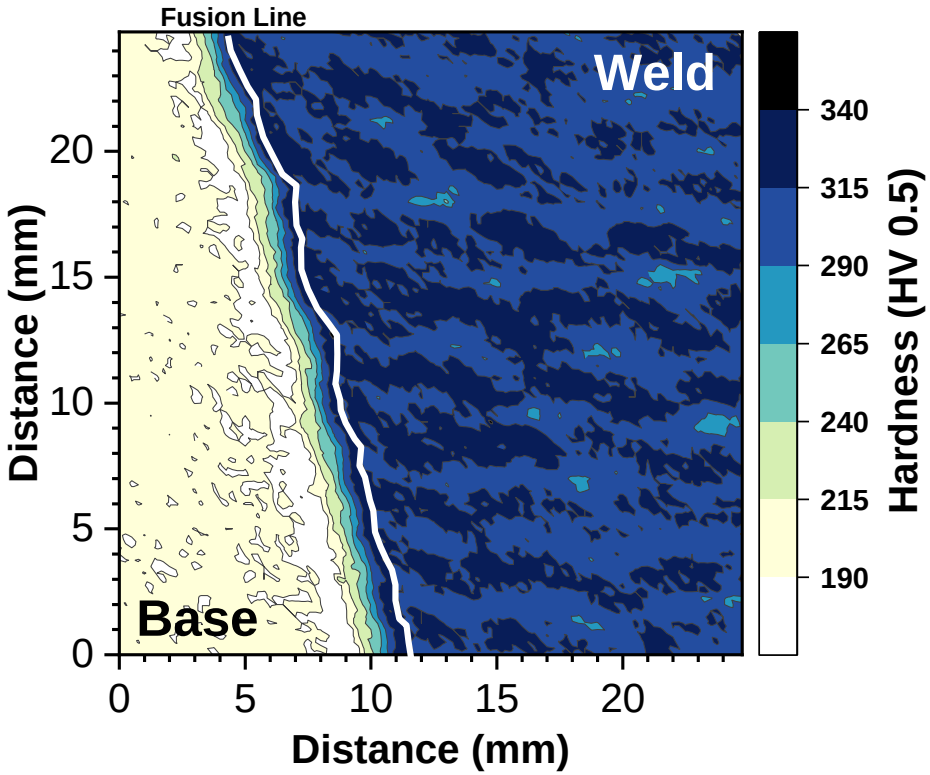

Figure 5-1. Color hardness map through the base metal (left), heat affected zone (middle) and deposited weld metal for weld 7C (E9015-B9 matching filler metal, PWHT at 675°C for 2 hours, and martensitic parent metal TP1);
Note: *position of fusion line provided from etched macrograph and data reported after post weld heat treatment*

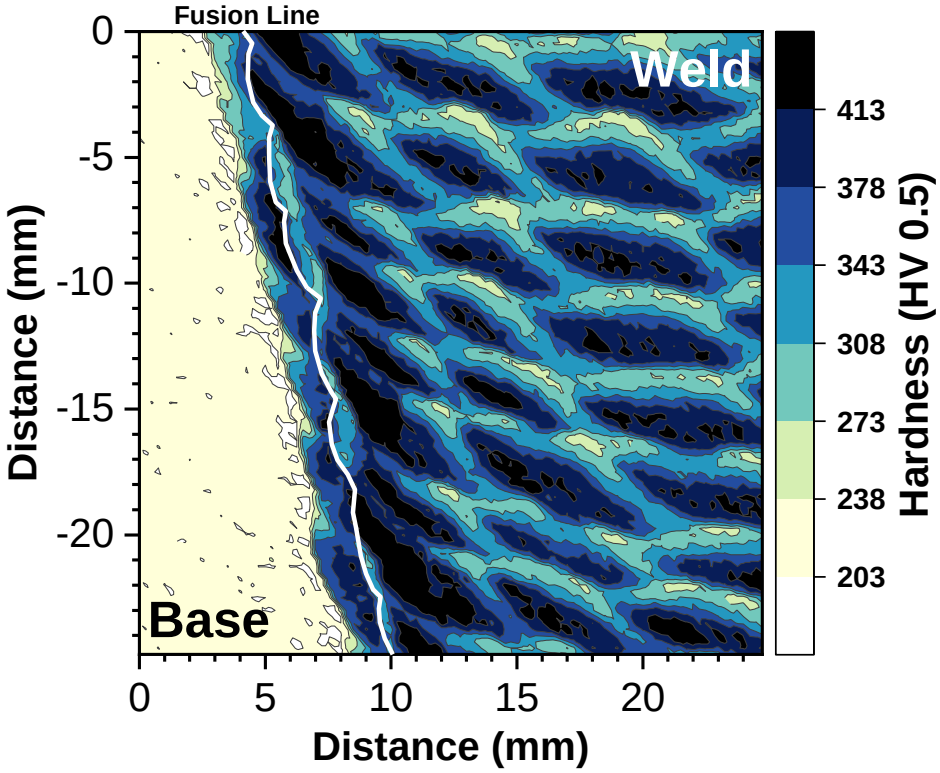

Figure 5-2. Color hardness map through the base metal (left), heat affected zone (middle) and deposited weld metal for weld 8C (AWS type -B8 under-matching filler metal, as-welded condition, and martensitic parent metal TP1);
Note: *position of fusion line provided from etched macrograph and data reported in the as-welded condition*

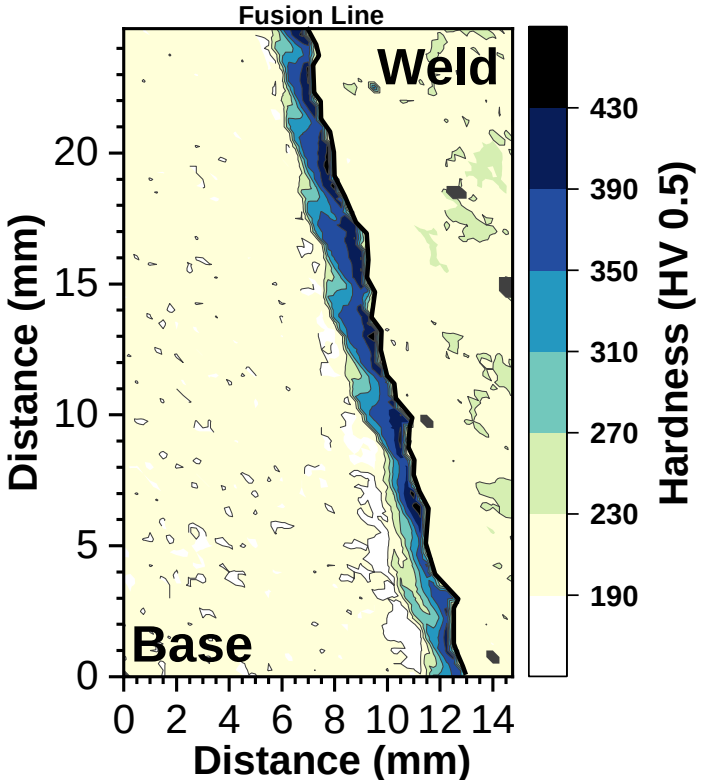

Figure 5-3. Color hardness map through the base metal (left), heat affected zone (middle) and deposited weld metal for weld 9C (EPRI P87 over-matching filler metal, as-welded condition, and martensitic parent metal TP1);
Note: *position of fusion line provided from etched macrograph and data reported in the as-welded condition. There is less reported data for weld metal (as compared to the other evaluated weldments) due to consistency of hardness in the as-deposited condition.*

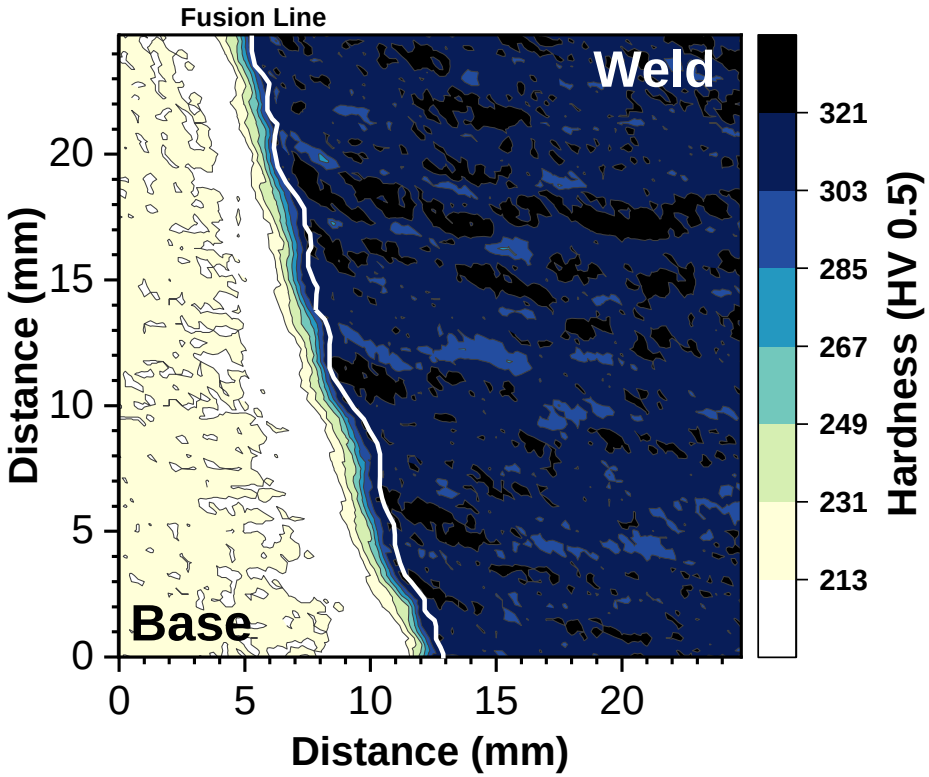

Figure 5-4. Color hardness map through the base metal (left), heat affected zone (middle) and deposited weld metal for weld AR-B2 (E9015-B9 matching filler metal, PWHT at 675°C for 2 hours, and martensitic parent metal B2);
Note: *position of fusion line provided from etched macrograph and data reported after post weld heat treatment*

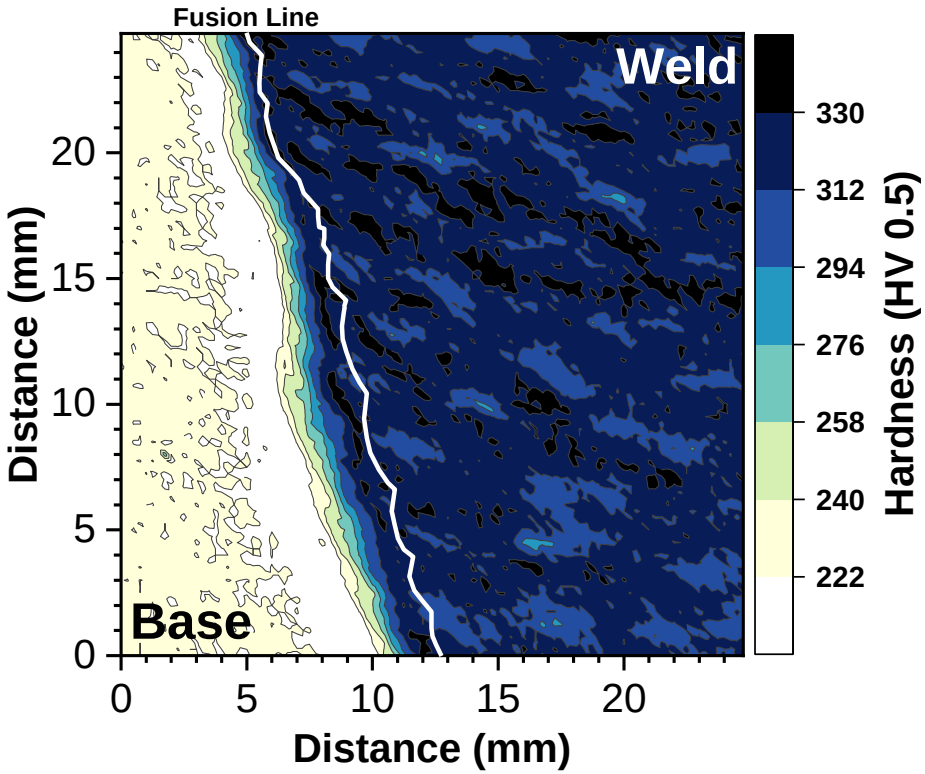

Figure 5-5. Color hardness map through the base metal (left), heat affected zone (middle) and deposited weld metal for weld RNT-B2 (E9015-B9 matching filler metal, PWHT at 675°C for 2 hours, and re-normalized and tempered, martensitic parent metal B2);
Note: *position of fusion line provided from etched macrograph and data reported after post weld heat treatment*

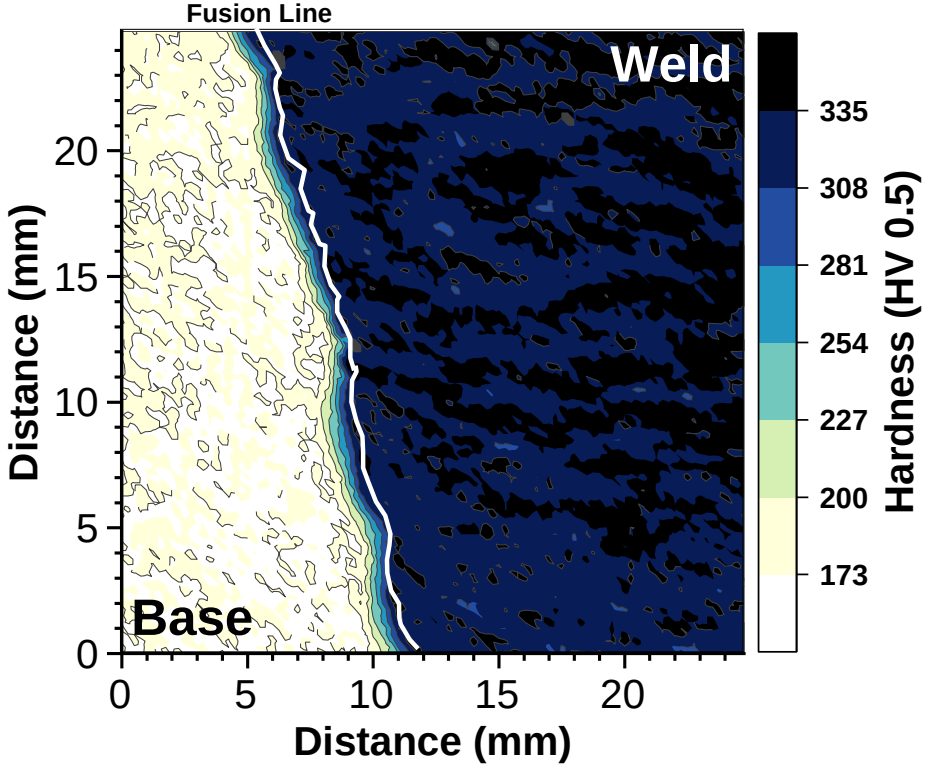

Figure 5-6. Color hardness map through the base metal (left), heat affected zone (middle) and deposited weld metal for weld F-TP1 (E9015-B9 matching filler metal, PWHT at 675°C for 2 hours, and ferritic parent metal TP1);
Note: *position of fusion line provided from etched macrograph and data reported after post weld heat treatment*

5.3 Analysis of Macro-Composition Heterogeneity in Under-Matching Weld Metal

Initially, it was not well-established how the under-matching cross-weld tests would fail. Thus, compositional mapping was performed in a mid-wall location since the AWS type -B8 weld metal in Table 3-4 possesses notable deviations in the elements Cr, V and Mn. Should the cross-weld tests exhibit failure in the fusion line or first weld bead deposited along the machined groove, it would be important to document the composition heterogeneity that exists as a consequent of the welding process. Note that the additional weldments were not compositionally mapped using micro-XRF.

The results for the compositional mapping (procedure in section 3.3.3) are provided in Figure 5-7 to Figure 5-9 for Cr, V and Mn, respectively. The results show the heterogeneity present in the parent material (left side of each image), first weld layer deposited along the machined groove (approximately centered at the 32 mm position), and the weld metal (right side of each image). For the first layer of weld metal, there is notable dilution from the parent material, particularly in the V-map. However, for the bulk of the weld metal deposit, there exists little additional dilution. This is attributed to the number of weld beads required to finish the weldment and it can be expected that the bulk of the weld metal deposit is thus very close to the reported material certification values in Table 3-4.

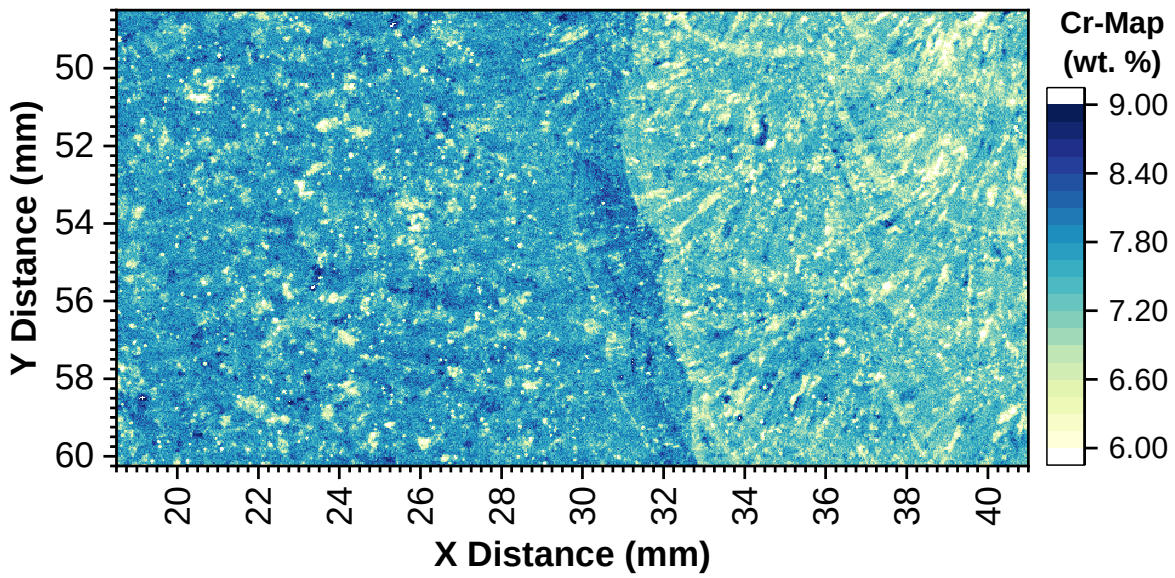

Figure 5-7. Chromium (Cr, wt. %) micro-XRF mapping results for weld 8C (AWS type -B8 under-matching filler metal, as-welded condition, and martensitic parent metal TP1)
Note: *parent metal on left and weld metal on right of the image*

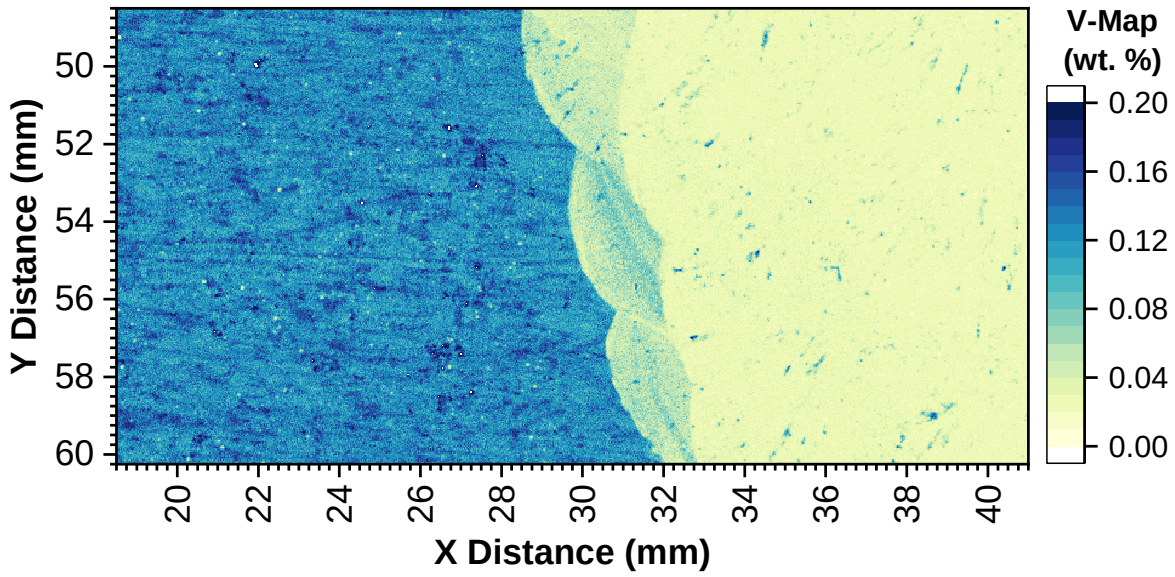

Figure 5-8. Vanadium (V, wt. %) micro-XRF mapping results for weld 8C (AWS type -B8 under-matching filler metal, as-welded condition, and martensitic parent metal TP1)
Note: *parent metal on left and weld metal on right of the image*

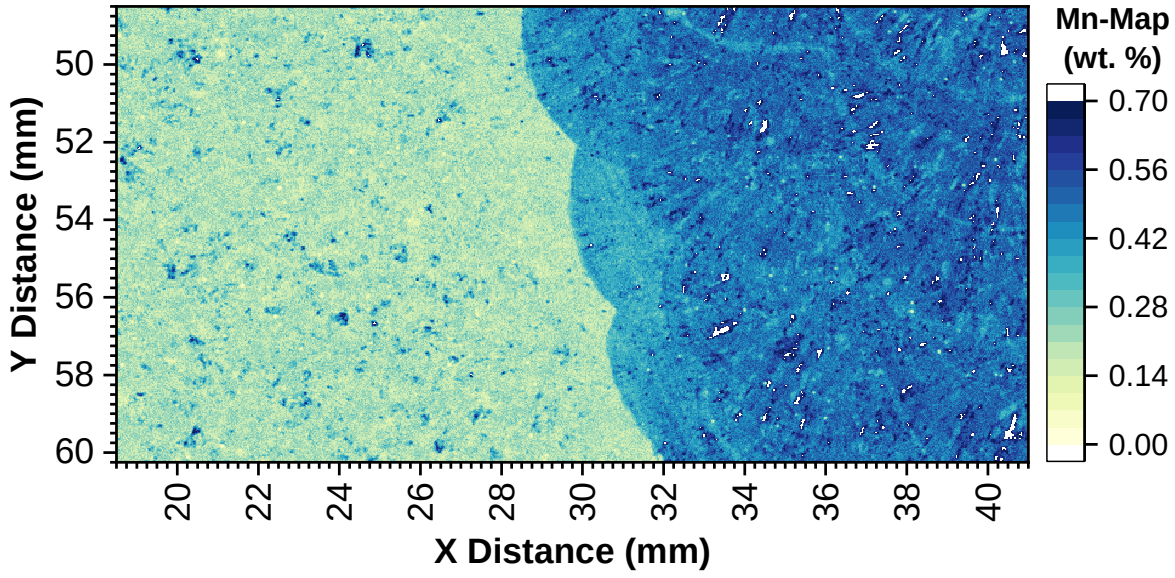

Figure 5-9. Manganese (Mn, wt. %) micro-XRF mapping results for weld 8C (AWS type -B8 under-matching filler metal, as-welded condition, and martensitic parent metal TP1)
Note: *parent metal on left and weld metal on right of the image*

5.4 Calculated Peak Temperatures through the Heat Affected Zone

The calculated peak temperatures using the assumptions provided in Chapter 3 and for each weldment are provided in Figure 5-10 to Figure 5-15. The black data indicate the position of hardness indents (used as reference locations) as a function of distance from the fusion line. Closed data points provide the locations where electron back scatter diffraction (EBSD) data were collected. The blue data provide the calculated peak temperature through the HAZ.

The peak temperature data follow a similar profile for each investigated weldment as the utilized welding procedure did not vary significantly, e.g. only the SMAW process was utilized and either a 2.5 or 3.2 mm diameter electrode for weld beads placed in immediate contact with the machined groove. The hardness profiles for each weld show a significant variability and reflect the general trends in the hardness map data presented in section 5.2.

For the welds in the as-welded condition (Weld 8C and Weld 9C), the hardness values in the HAZ are observed to reach a maximum value of ~380 HV 0.5 and decrease to values which stabilize near the parent metal mean value. For the welds given a subcritical PWHT (Weld 7C, AR-B2 and RNT-B2), the hardness is observed to decrease from a maximum near or at the fusion line (FL) to a local minimum value that is located within or adjacent to the HAZ and increase slightly to values characteristic of the unaffected parent material. For the F-TP1 weld (also given a subcritical PWHT), the hardness does not pass through a local minimum as the ferritic parent material is already in its softest state.

It should be emphasized that the reported hardness data (and subsequent EBSD data) are believed to be representative of the weldment, but are unable to entirely characterize the heterogeneity that exists. The area of each collected EBSD map is 150 X 150 microns, which only constitutes about 1/500th of the through-thickness area. Similarly, and with respect to hardness, a single indent measuring about 60 microns in width (250 HV 0.5) only characterizes about 1/33rd of the through-thickness width. This reality presents valid concerns regarding the representation of data, particularly in the literature, which is often used to ‘characterize the weldment’. Since the weldments in this study constitute thick-section, multi-pass welds, the information provided should be interpreted accordingly.

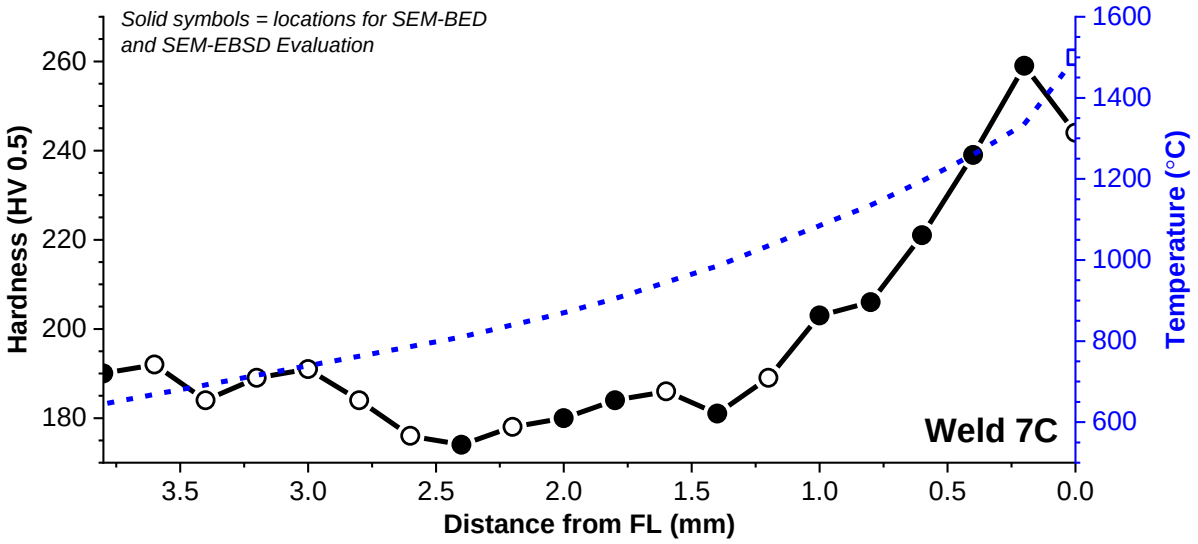

Figure 5-10. Hardness trace through the heat affected zone (black data) and the calculated peak temperature in the heat affected zone (blue data) for weld 7C (E9015-B9 matching filler metal, PWHT at 675°C for 2 hours, and martensitic parent metal TP1);
Note: *solid symbols indicate locations where electron backscatter diffraction (EBSD) data and BED images were collected*

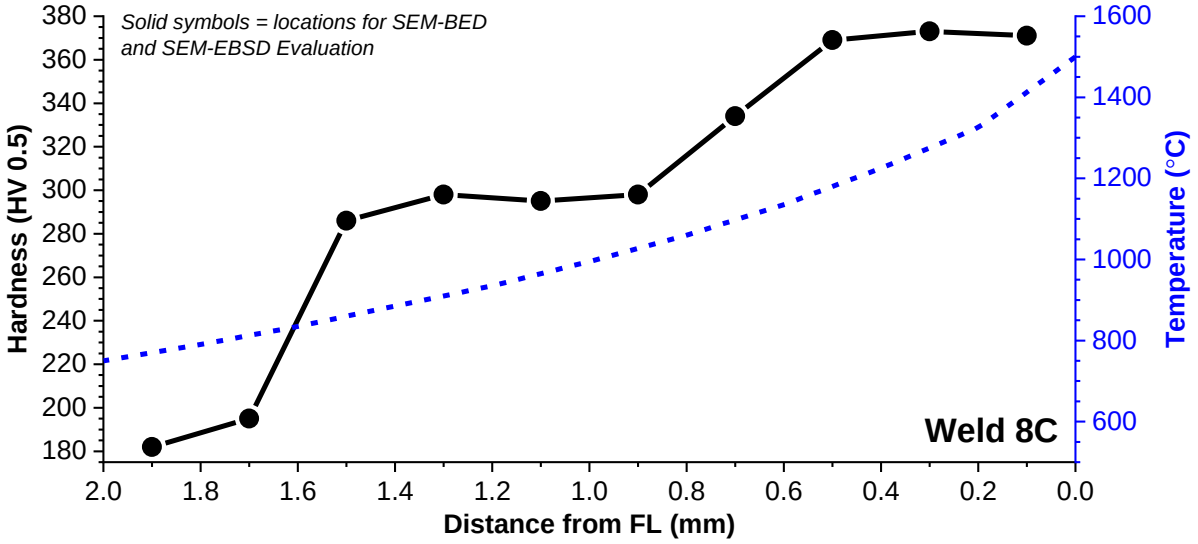

Figure 5-11. Hardness trace through the heat affected zone (black data) and the calculated peak temperature in the heat affected zone (blue data) for weld 8C (AWS type -B8 under-matching filler metal, as-welded condition, and martensitic parent metal TP1);
Note: *solid symbols indicate locations where electron backscatter diffraction (EBSD) data and BED images were collected*

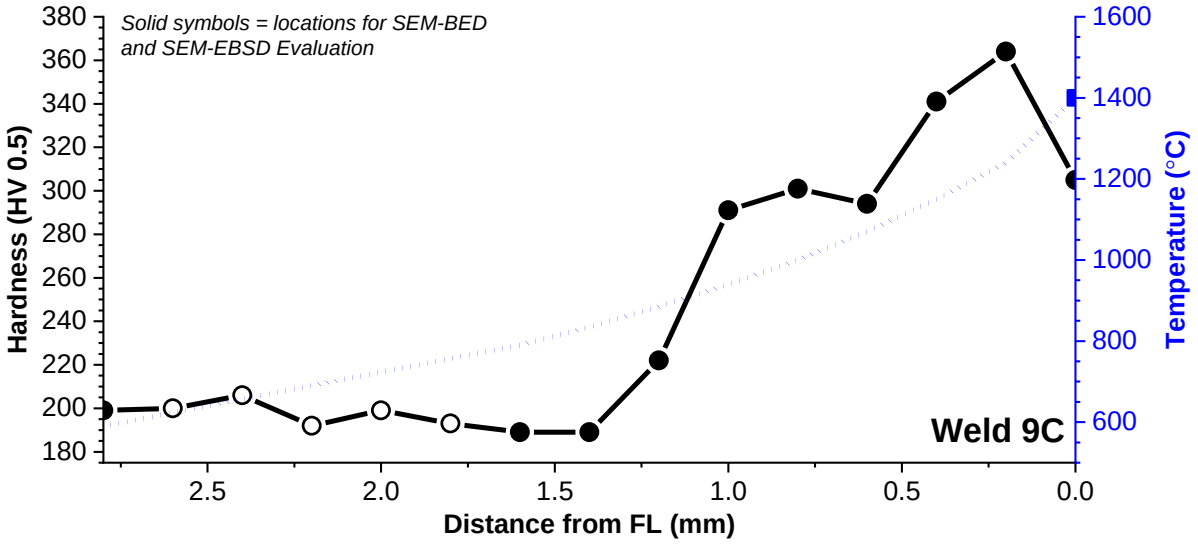

Figure 5-12. Hardness trace through the heat affected zone (black data) and the calculated peak temperature in the heat affected zone (blue data) for weld 9C (EPRI P87 over-matching filler metal, as-welded condition, and martensitic parent metal TP1);
Note: *solid symbols indicate locations where electron backscatter diffraction (EBSD) data and BED images were collected*

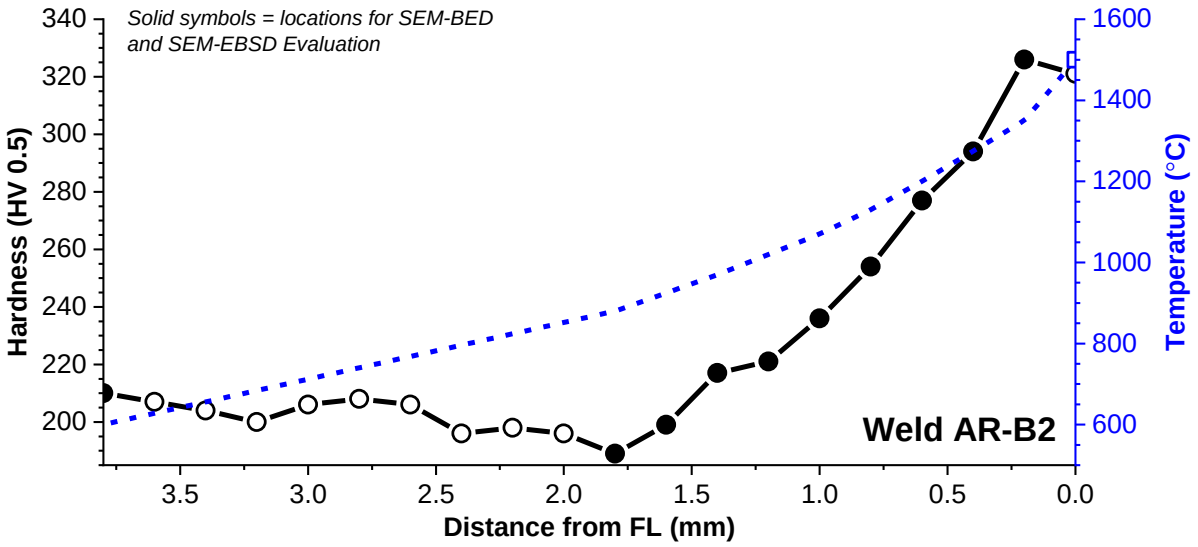

Figure 5-13. Hardness trace through the heat affected zone (black data) and the calculated peak temperature in the heat affected zone (blue data) for weld AR-B2 (E9015-B9 matching filler metal, PWHT at 675°C for 2 hours, and martensitic parent metal B2);
Note: *solid symbols indicate locations where electron backscatter diffraction (EBSD) data and BED images were collected*

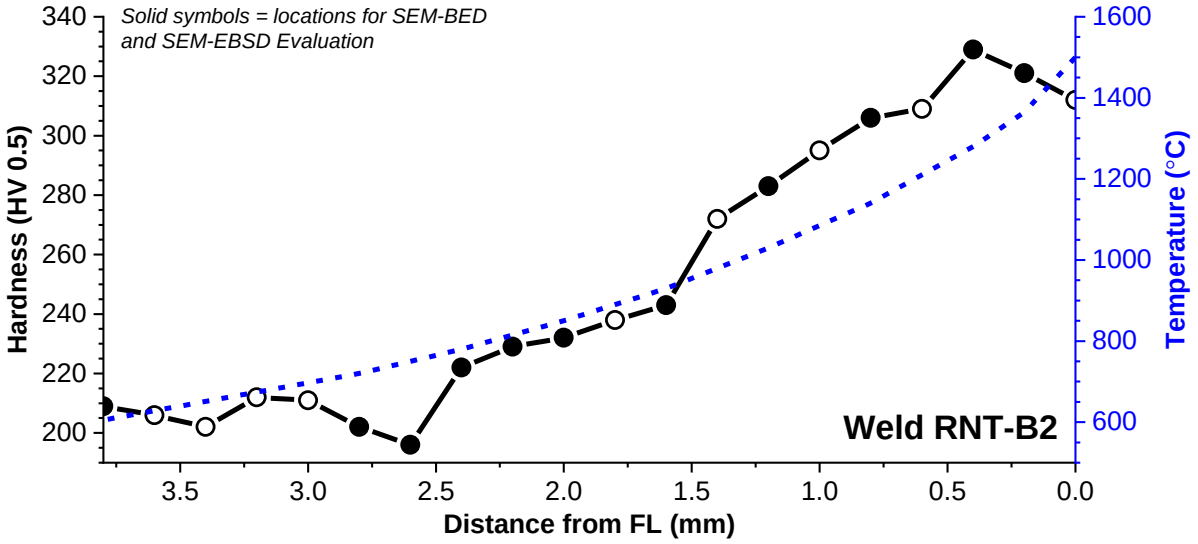

Figure 5-14. Hardness trace through the heat affected zone (black data) and the calculated peak temperature in the heat affected zone (blue data) for weld RNT-B2 (E9015-B9 matching filler metal, PWHT at 675°C for 2 hours, and re-normalized and tempered, martensitic parent metal B2);
Note: *solid symbols indicate locations where electron backscatter diffraction (EBSD) data and BED images were collected*

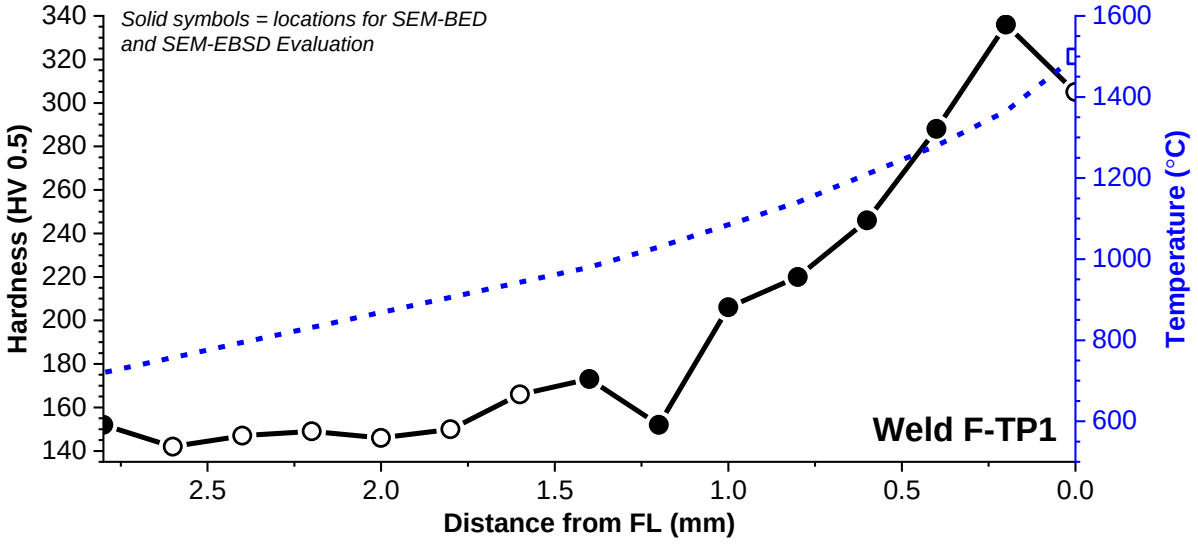

Figure 5-15. Hardness trace through the heat affected zone (black data) and the calculated peak temperature in the heat affected zone (blue data) for weld F-TP1 (E9015-B9 matching filler metal, PWHT at 675°C for 2 hours, and ferritic parent metal TP1);
Note: *solid symbols indicate locations where electron backscatter diffraction (EBSD) data and BED images were collected*

5.5 Scanning Electron Microscopy (SEM) Imaging

Backscatter electron (BED) images were collected at multiple magnifications (e.g. a microscope setting of 2000X or 5000X was utilized) for each weldment in the locations indicated in Figure 5-10 to Figure 5-15 (e.g. the solid black circles); these images are illustrated in Figure 5-16 to Figure 5-21. It is difficult to compare each weldment on the

same scale due to the variation in grain size and microstructure features. For example, the F-TP1 weld was purposefully heat treated to create a ferritic microstructure and the weldments in the TP1 martensitic parent material possess a prior austenite grain (PAG) size larger than the B2 material by about a factor of 10. The position of each image is indicated and includes the calculated peak temperature (see section 5.3) for the position where the images were collected.

The observed microstructure through the HAZ changes extensively, starting in the parent material and moving to the fusion line. The martensitic (or ferritic) matrix of the parent metal is observed to gradually disappear, transitioning to a microstructure with a reduced area fraction of subgrain boundaries and characterized by a distribution of fine grains. Very close to the fusion line, a microstructure with an increased area fraction of substructure is observed; this substructure is characteristic of martensite including a quantifiable amount of block and lath boundaries.

In the HAZ for weldments given a PWHT there exists a distribution of particles that are readily observed, while for the weldments left in the as-welded condition, the HAZ is devoid of such precipitates. The bright particles observed in several figures and most clearly Figure 5-17 are Laves phase which formed during service exposure, but did not completely dissolve during the welding thermal cycle until a calculated peak temperature of ~935 to 995°C was reached. The black, needle-like particles observed in the weldments are AlN (most clearly observed for weldments AR-B2 or RNT-B2), which is stable in non-equilibrium conditions until ~1200°C. The dissolution of AlN matches well with the diagram detailed by Easterling (Figure 2-52, Easterling 1992) where AlN is predicted to dissolve at 1227°C after 10 seconds or 1327°C after 1 second. Identification of these phases was previously detailed in section 4.4.

For the F-TP1 weldment where the parent material was welded in the ferritic condition (Figure 5-21), there is widespread carbide-necklacing around local grains. This is observed in isolated cases in the other weldments, for example in Figure 5-16 (T_{peak} = 1195 or 1260°C). This observation suggests that isolated decomposition of $M_{23}C_6$ or MX is leading to local, heterogeneous enrichment of Cr and upon re-heating to PWHT, the precipitation of carbides occurs around these grains boundaries.

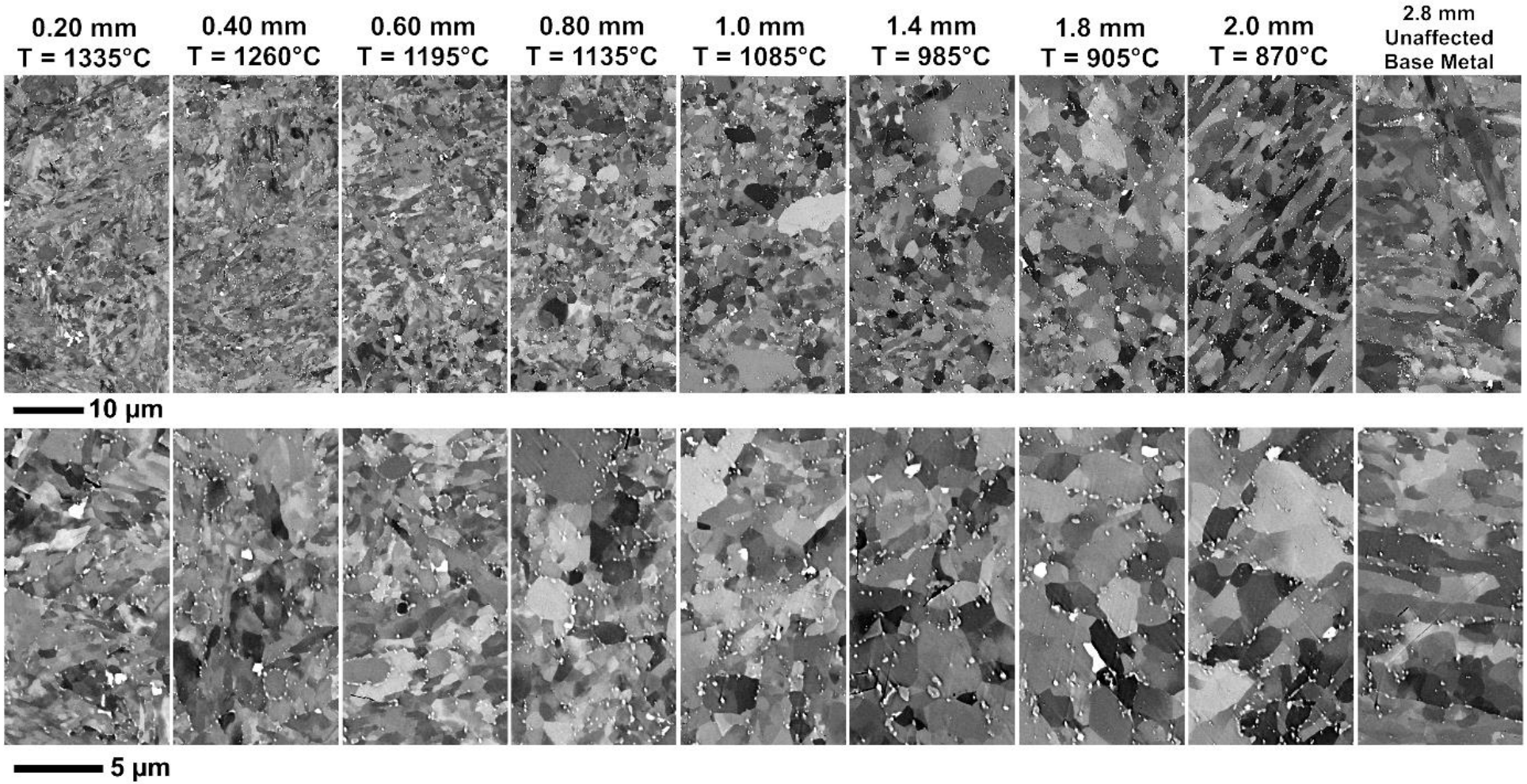

Figure 5-16. Backscatter electron imaging through the heat affected zone for weld 7C (E9015-B9 matching filler metal, PWHT at 675°C for 2 hours, and martensitic parent metal TP1);
Note: *for each location the indicated values give in millimeters (mm) refer to the distance from the fusion line and the calculated peak temperature is provided from Figure 5-10.*

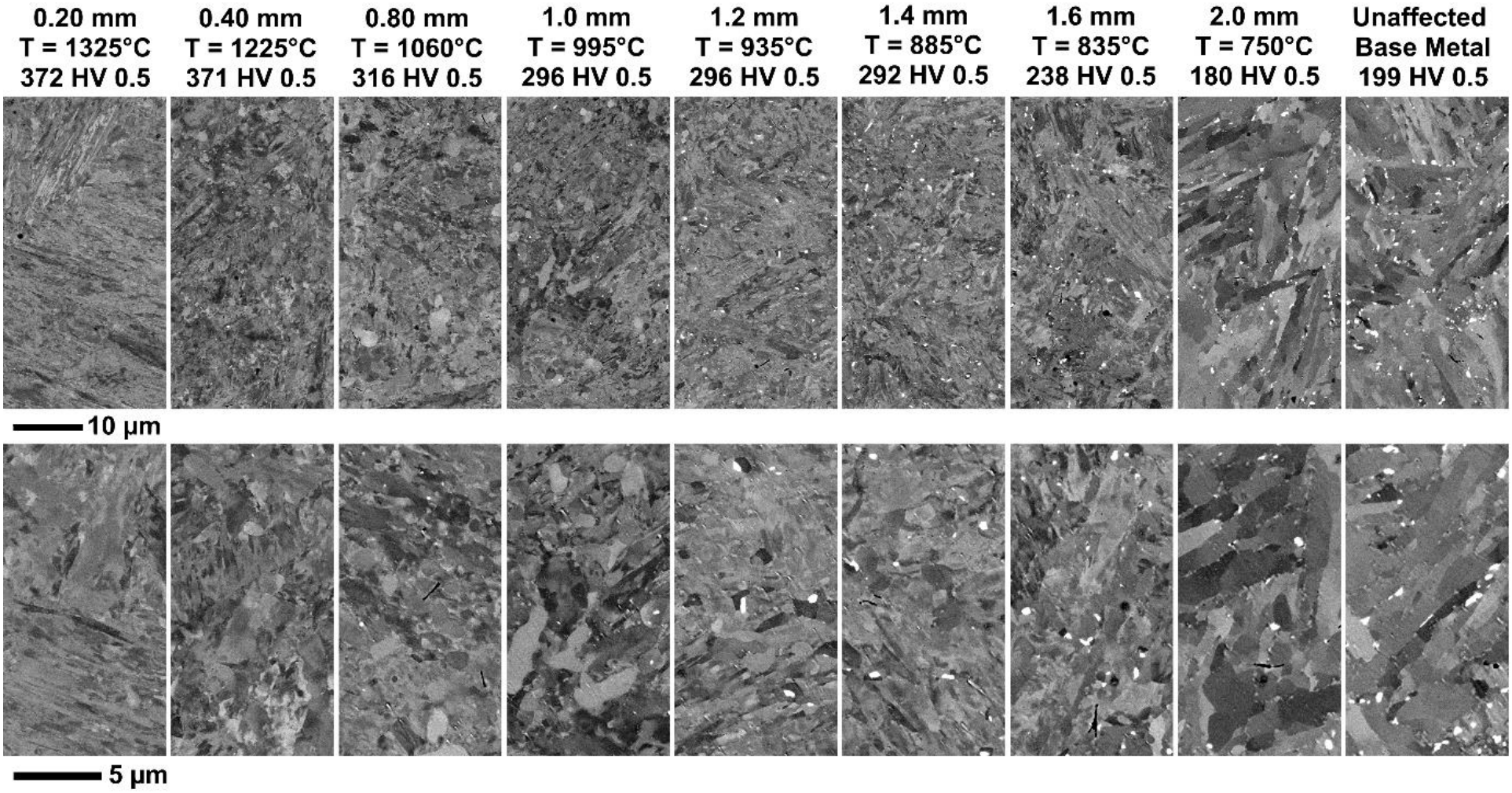

Figure 5-17. Backscatter electron imaging through the heat affected zone for weld 8C (AWS type -B8 under-matching filler metal, as-welded condition and martensitic parent metal TP1);
Note: *for each location the indicated values give in millimeters (mm) refer to the distance from the fusion line and the calculated peak temperature is provided from Figure 5-11.*

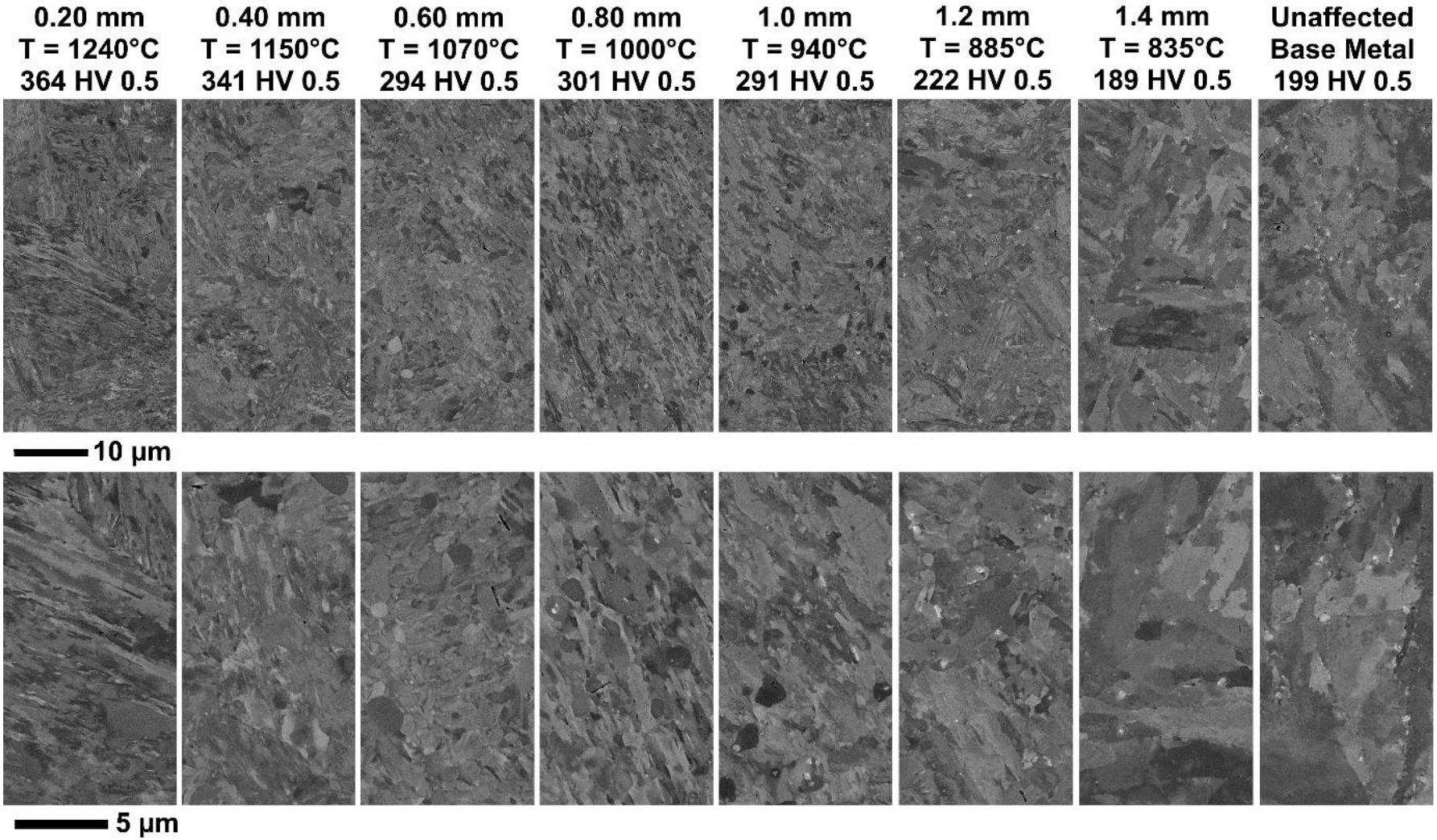

Figure 5-18. Backscatter electron imaging through the heat affected zone for weld 9C (EPRI P87 over-matching filler metal, as-welded condition, and martensitic parent metal TP1);
Note: *for each location the indicated values give in millimeters (mm) refer to the distance from the fusion line and the calculated peak temperature is provided from Figure 5-12.*

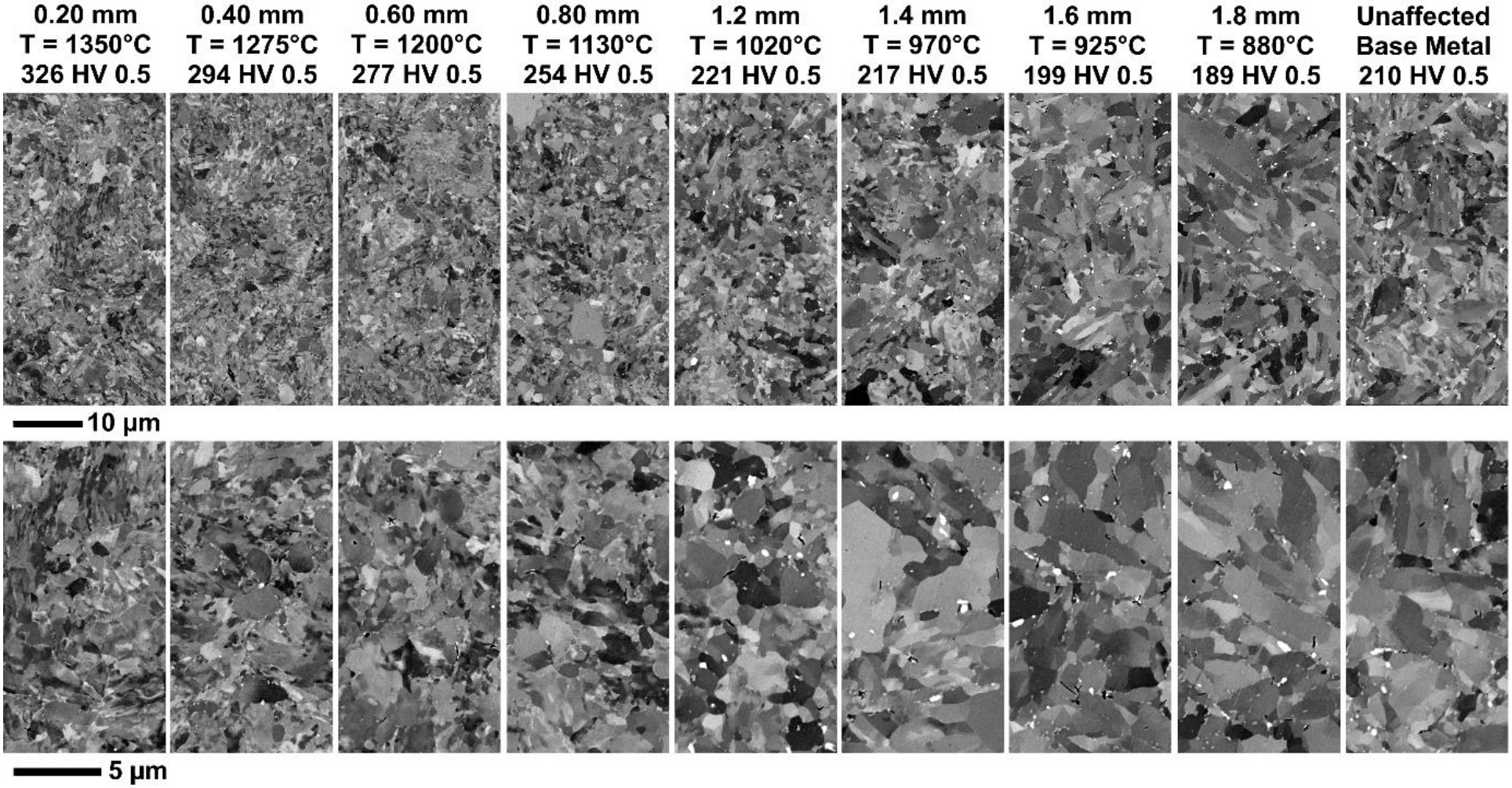

Figure 5-19. Backscatter electron imaging through the heat affected zone for weld AR-B2 (E9015-B9 matching filler metal, PWHT at 675°C for 2 hours, and martensitic parent metal B2);
Note: *for each location the indicated values give in millimeters (mm) refer to the distance from the fusion line and the calculated peak temperature is provided from Figure 5-13.*

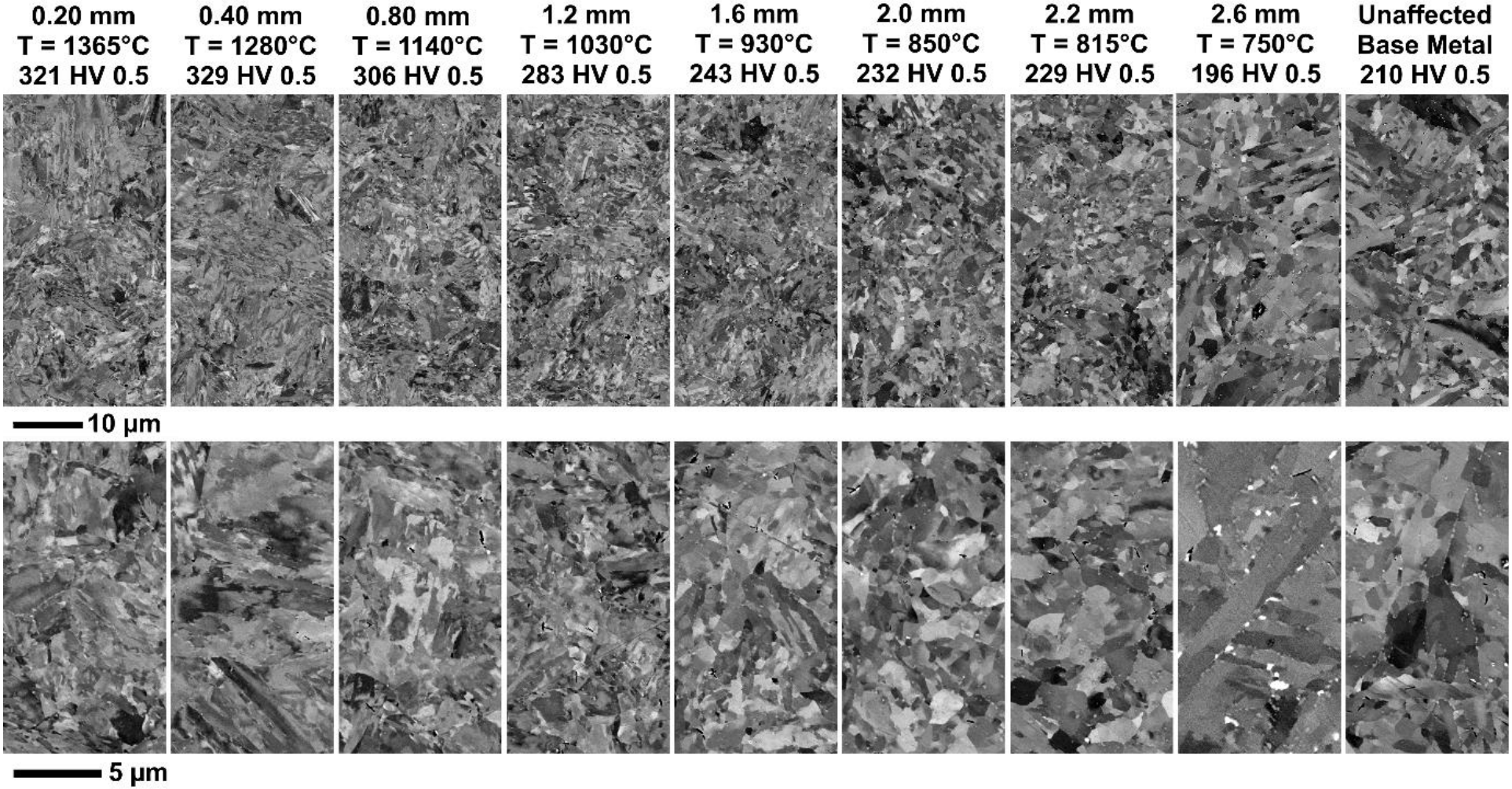

Figure 5-20. Backscatter electron imaging through the heat affected zone for weld RNT-B2 E9015-B9 matching filler metal, PWHT at 675°C for 2 hours, and tempered, martensitic parent metal B2);
Note: *for each location the indicated values give in millimeters (mm) refer to the distance from the fusion line and the calculated peak temperature is provided from Figure 5-14.*

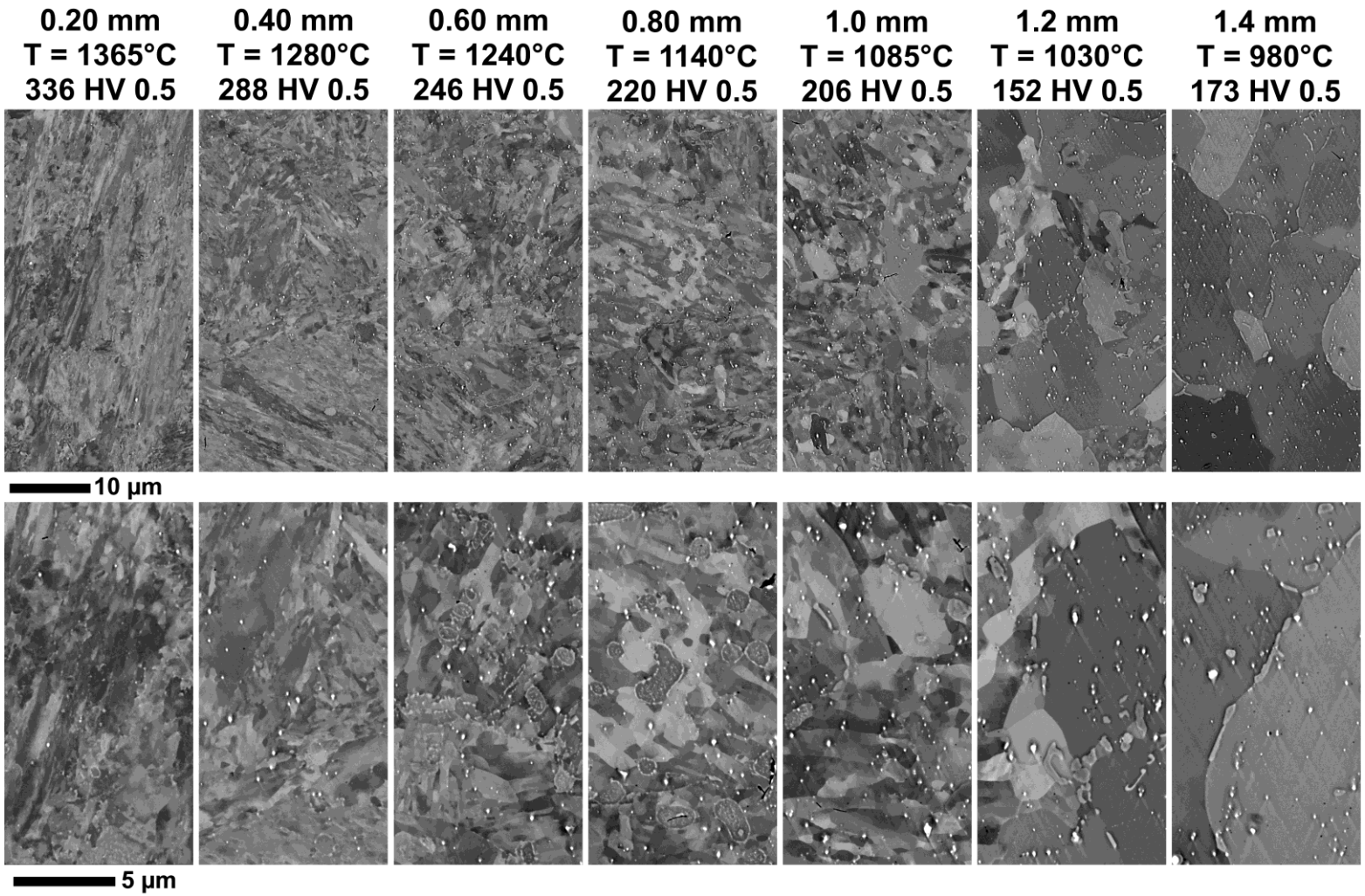

Figure 5-21. Backscatter electron imaging through the heat affected zone for weld F-TP1 (E9015-B9 matching filler metal, PWHT at 675°C for 2 hours, and ferritic parent metal TP1);
Note: *for each location the indicated values give in millimeters (mm) refer to the distance from the fusion line and the calculated peak temperature is provided from Figure 5-15. The apparent 'streaking' in selected images is a polishing artefact from the final polishing step using colloidal silica.*

The difficulty in quantifying observations from SEM imaging alone is a motivating factor for employing EBSD in the following section. It is also clear from the images that visual documentation of the observed microstructures can be variable. This variability is a result of the selected brightness, contrast and operating parameters for a given SEM (most notably, accelerating voltage, working distance and detector [in this example backscatter detector]). These settings are highly dependent on the user, the equipment and/or the surface quality of the sample (note that no etching was utilized in this study in conjunction with SEM-based evaluation).

It is necessary to better identify where the microstructural change is initiated on a global scale in the HAZ. The following section will attempt to link the thermal cycle and hardness mapping results to the grain boundary length for low and high angle boundaries. This will serve to clarify the delineation between the OTZ and the PTZ. The hardness map data will provide perspective on the location of the OTZ with respect to the unaffected parent metal for each of the evaluated weldments.

5.6 Electron Backscatter Diffraction (EBSD) through the Heat Affected Zone

Assessment of the distribution of the low angle, subgrain boundary (SGB) and high angle, prior austenite grain boundary (PAGB) length is compared to the peak temperature and hardness values measured in Figure 5-22 to Figure 5-27. For this assessment, the grain boundary length is reported for images collected in an area of 150 X 150 µm. Assessment of the boundaries based on 2-20° and 50-60° (low angle, SGBs) and 20-50° (high angle, PAGBs) follows a similar analysis detailed in (Xu 2017). The documented locations in Figure 5-28 to Figure 5-33 provide a selected area of ~50 X 150 µm from each image to facilitate comparison across the image for the analyzed locations through the width of the HAZ.

For the data in Figure 5-22 to Figure 5-26 the local minimum hardness does not correspond to a marked reduction in the low angle, SGBs or increase in the high angle, PAGBs. For the weld 7C, the local reduction in hardness is ~400 µm removed from the initiation of a local deviation in the measured grain boundary length fractions for either the SGB or PAGBs. For welds 9C, AR-B2 and RNT-B2 the onset of the local deviation in grain boundary length fraction is approximated by the local minimum in hardness. For weld 8C (the first weld analyzed), the number of analyzed locations was

insufficient beyond the total width of the HAZ (a point that was corrected for the balanced of the analyzed five weldments).

As mentioned previously, the assessment of F-TP1 provides a unique case study since the parent metal contains a very coarse grain structure resulting from the purposeful heat treatment prior to welding to create a ferritic matrix. In the analyzed F-TP1 material, there exists a more gradual trend in the grain boundary length fraction, suggesting more complete transformation to martensite as the thermal cycle extends closer to the fusion line. Review of the images provided in Figure 5-33 supports this assessment and the incomplete dissolution of the mixed microstructure is observed for the T_{peak} = 1030 or 1085°C while for T_{peak} = 1365°C is best described as having a very fine, martensitic substructure.

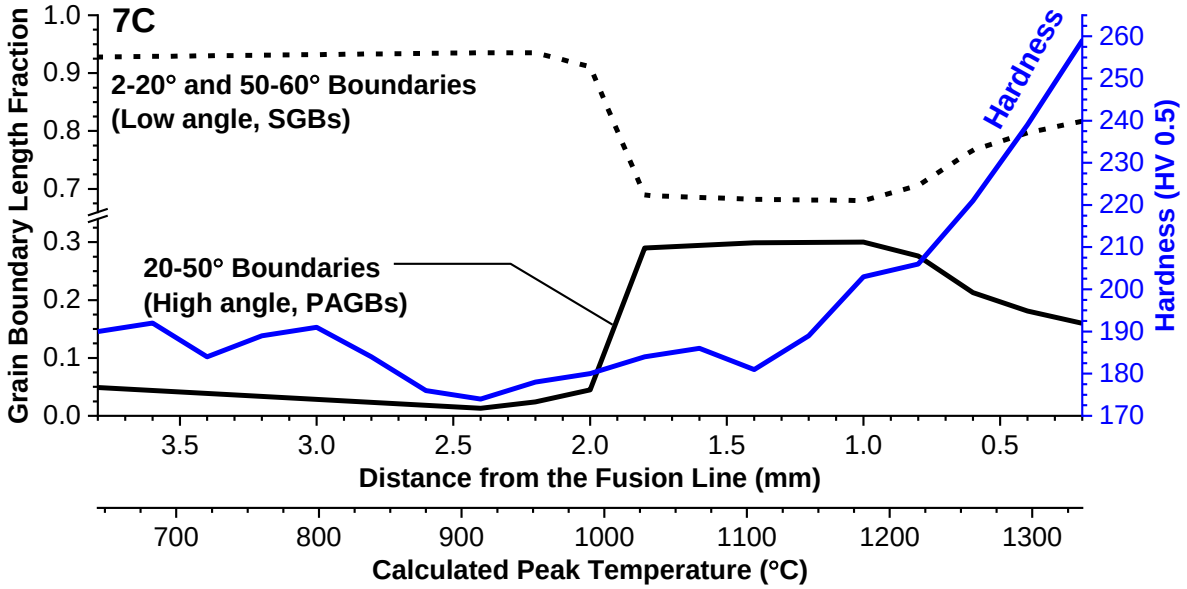

Figure 5-22. Distribution of low angle subgrain boundaries (SGBs) and high angle prior austenite grain boundaries (PAGBs) as a function of distance from the fusion line or calculated peak temperature for weld 7C (E9015-B9 matching filler metal, PWHT at 675°C for 2 hours, and martensitic parent metal TP1)

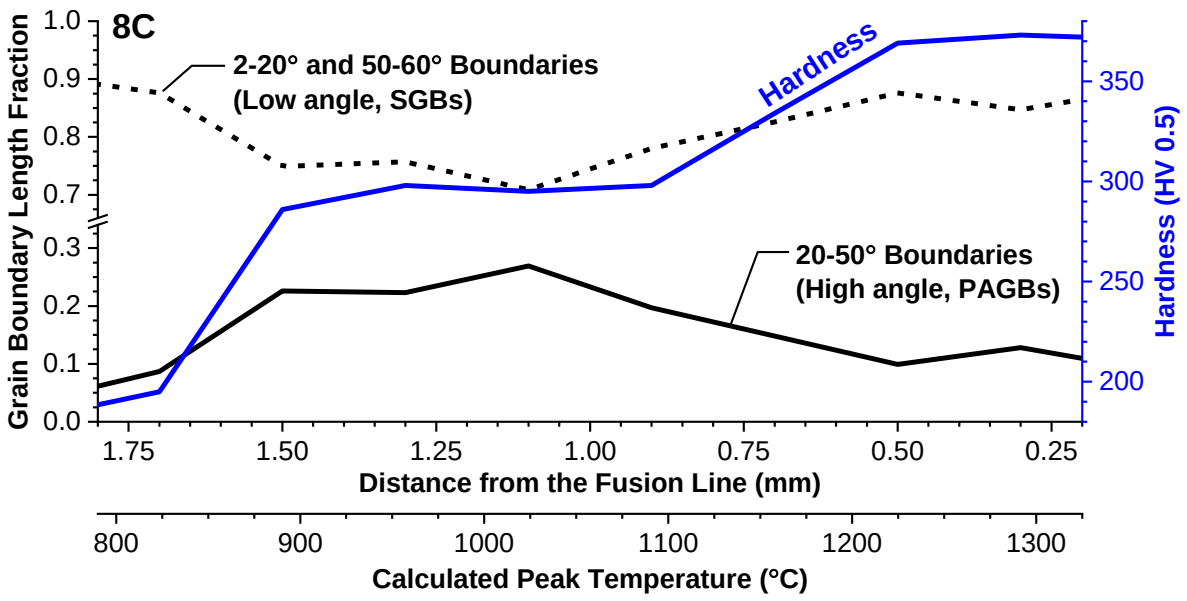

Figure 5-23. Distribution of low angle subgrain boundaries (SGBs) and high angle prior austenite grain boundaries (PAGBs) as a function of distance from the fusion line or calculated peak temperature for weld 8C (AWS type -B8 under-matching filler metal, as-welded condition, and martensitic parent metal TP1)

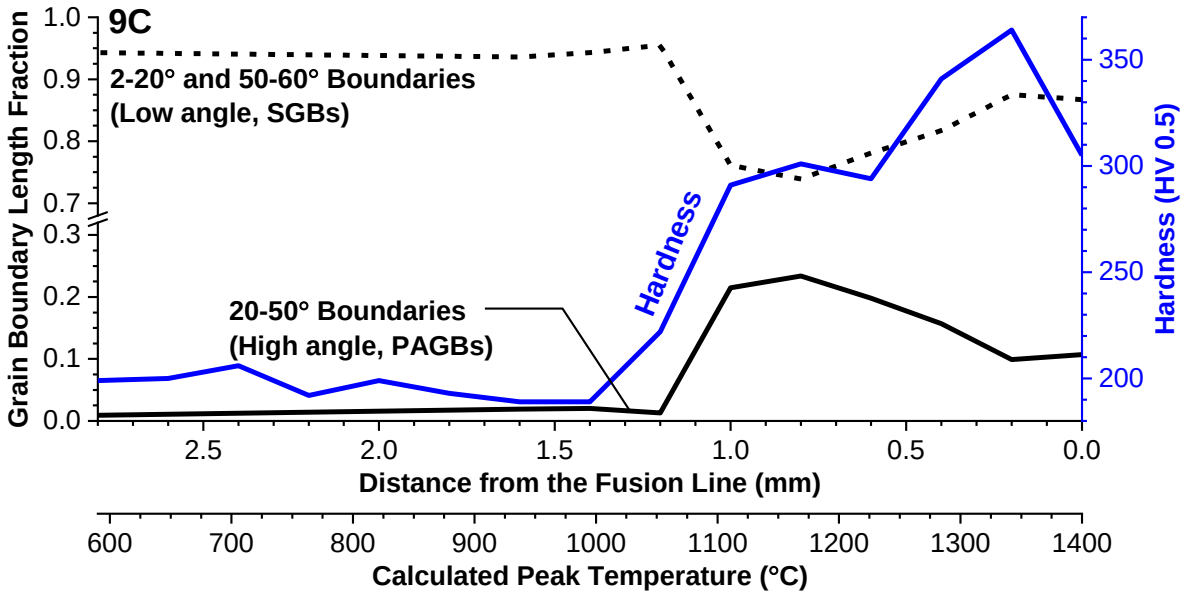

Figure 5-24. Distribution of low angle subgrain boundaries (SGBs) and high angle prior austenite grain boundaries (PAGBs) as a function of distance from the fusion line or calculated peak temperature for weld 9C (EPRI P87 over-matching filler metal, as-welded condition, and martensitic parent metal TP1)

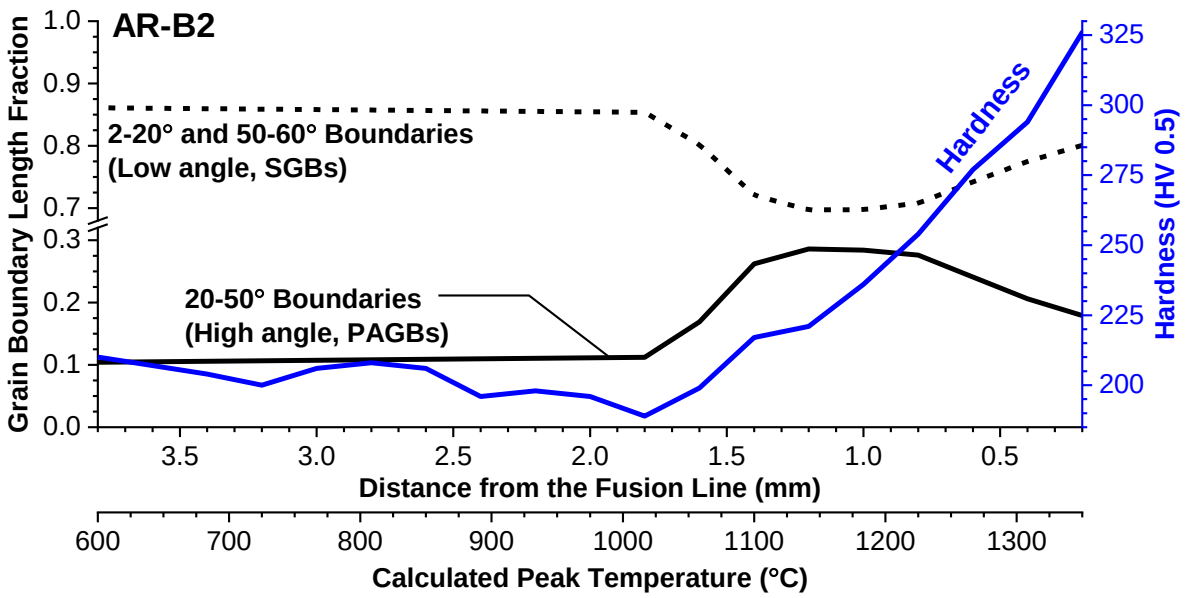

Figure 5-25. Distribution of low angle subgrain boundaries (SGBs) and high angle prior austenite grain boundaries (PAGBs) as a function of distance from the fusion line or calculated peak temperature for weld AR-B2 (E9015-B9 matching filler metal, PWHT at 675°C for 2 hours, and martensitic parent metal B2);

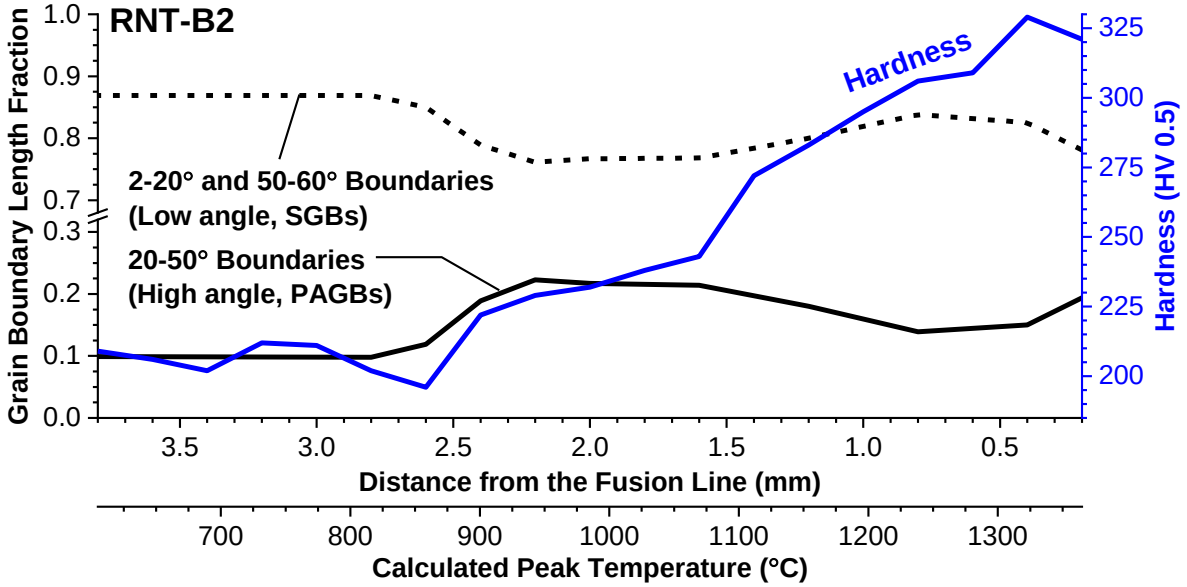

Figure 5-26. Distribution of low angle subgrain boundaries (SGBs) and high angle prior austenite grain boundaries (PAGBs) as a function of distance from the fusion line or calculated peak temperature for weld RNT-B2 (E9015-B9 matching filler metal, PWHT at 675°C for 2 hours, and re-normalized and tempered, martensitic parent metal B2)

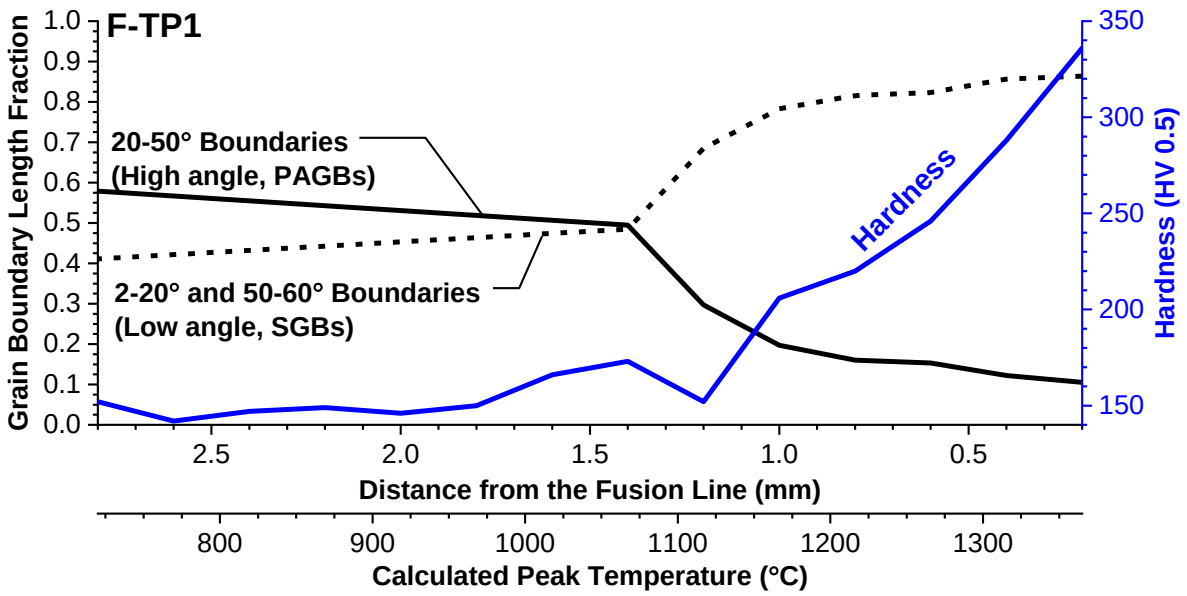

Figure 5-27. Distribution of low angle subgrain boundaries (SGBs) and high angle prior austenite grain boundaries (PAGBs) as a function of distance from the fusion line or calculated peak temperature for weld F-TP1 (E9015-B9 matching filler metal, PWHT at 675°C for 2 hours, and ferritic parent metal TP1)

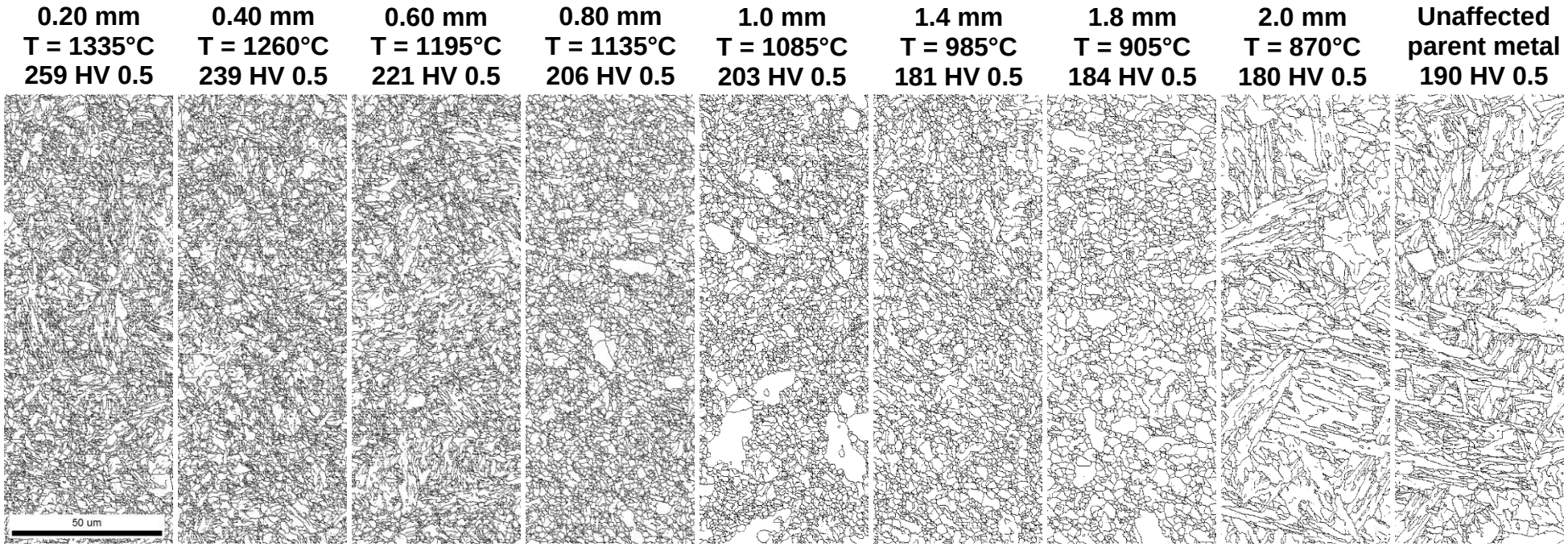

Figure 5-28. Electron backscatter diffraction (EBSD) images for all boundaries with misorientation of 2-180 degrees in weld 7C (E9015-B9, matching filler metal, PWHT at 675°C for 2 hours, and martensitic parent metal TP1); scale length = 50 μm
Note: *for each location the indicated values give in millimeters (mm) refer to the distance from the fusion line and the calculated peak temperature is provided from Figure 5-10.*

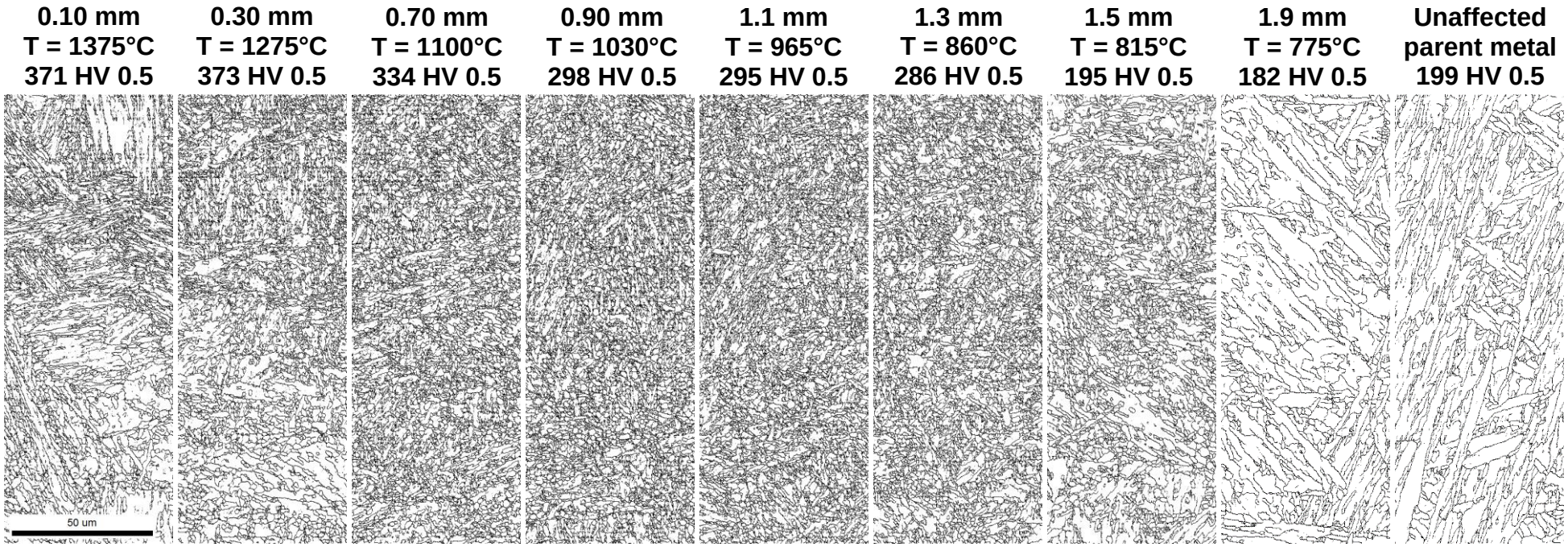

Figure 5-29. Electron backscatter diffraction (EBSD) images for all boundaries with misorientation of 2-180 degrees in weld 8C (AWS type -B8, under-matching filler metal, as-welded condition, and martensitic parent metal TP1); scale length = 50 µm
Note: *for each location the indicated values give in millimeters (mm) refer to the distance from the fusion line and the calculated peak temperature is provided from Figure 5-11.*

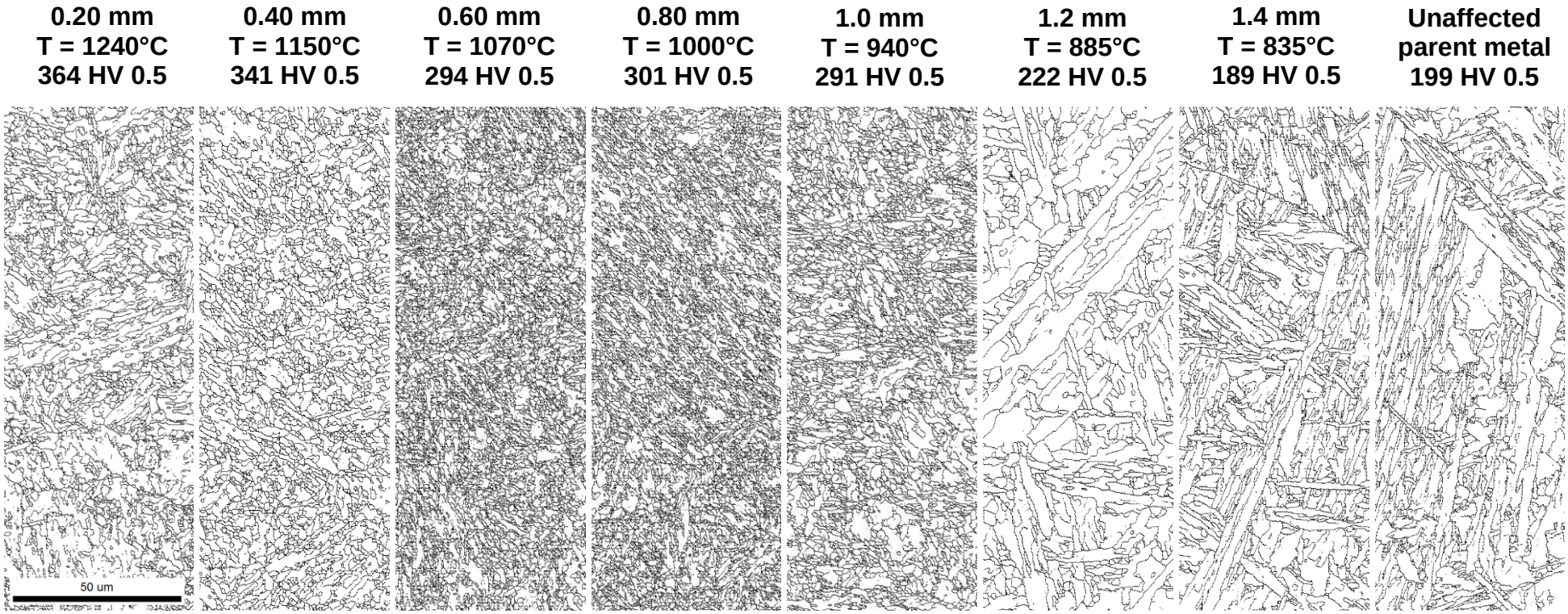

Figure 5-30. Electron backscatter diffraction (EBSD) images for all boundaries with misorientation of 2-180 degrees in weld 9C (EPRI P87, over-matching filler metal, as-welded condition, and martensitic parent metal TP1); scale length = 50 μm
Note: *for each location the indicated values give in millimeters (mm) refer to the distance from the fusion line and the calculated peak temperature is provided from Figure 5-12.*

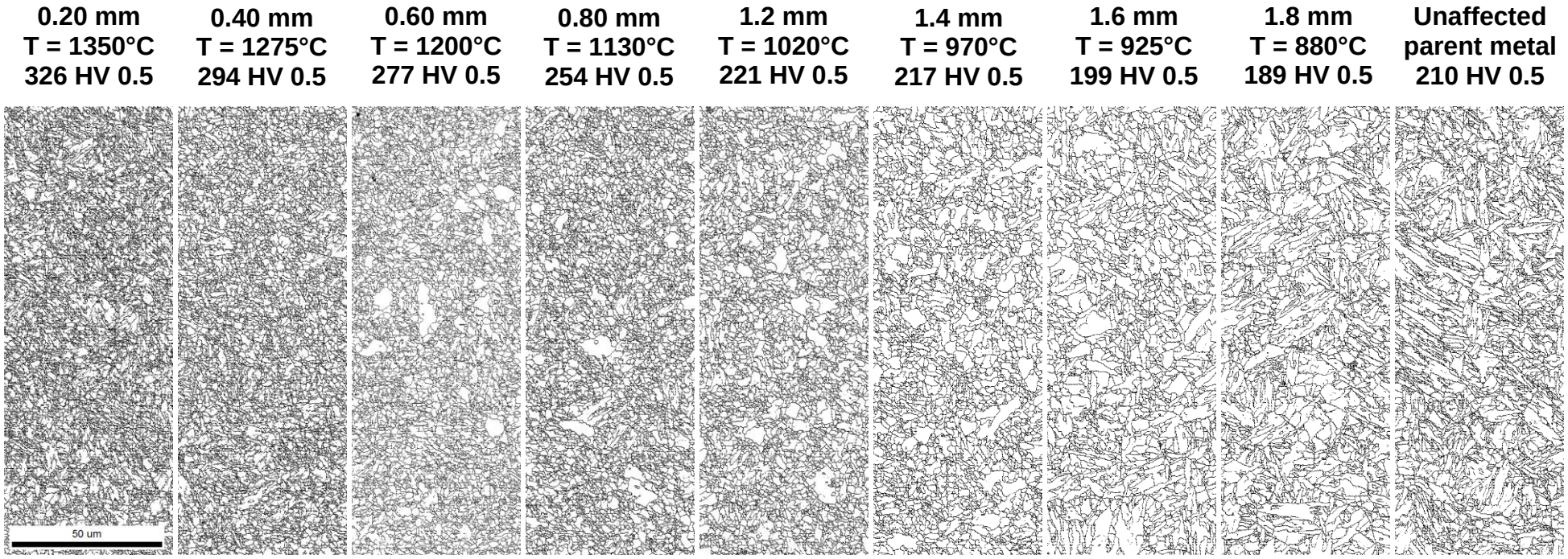

Figure 5-31. Electron backscatter diffraction (EBSD) images for all boundaries with misorientation of 2-180 degrees in weld AR-B2 (E9015-B9, matching filler metal, PWHT at 675°C for 2 hours, and martensitic parent metal B2); scale length = 50 μm
Note: *for each location the indicated values give in millimeters (mm) refer to the distance from the fusion line and the calculated peak temperature is provided from Figure 5-13.*

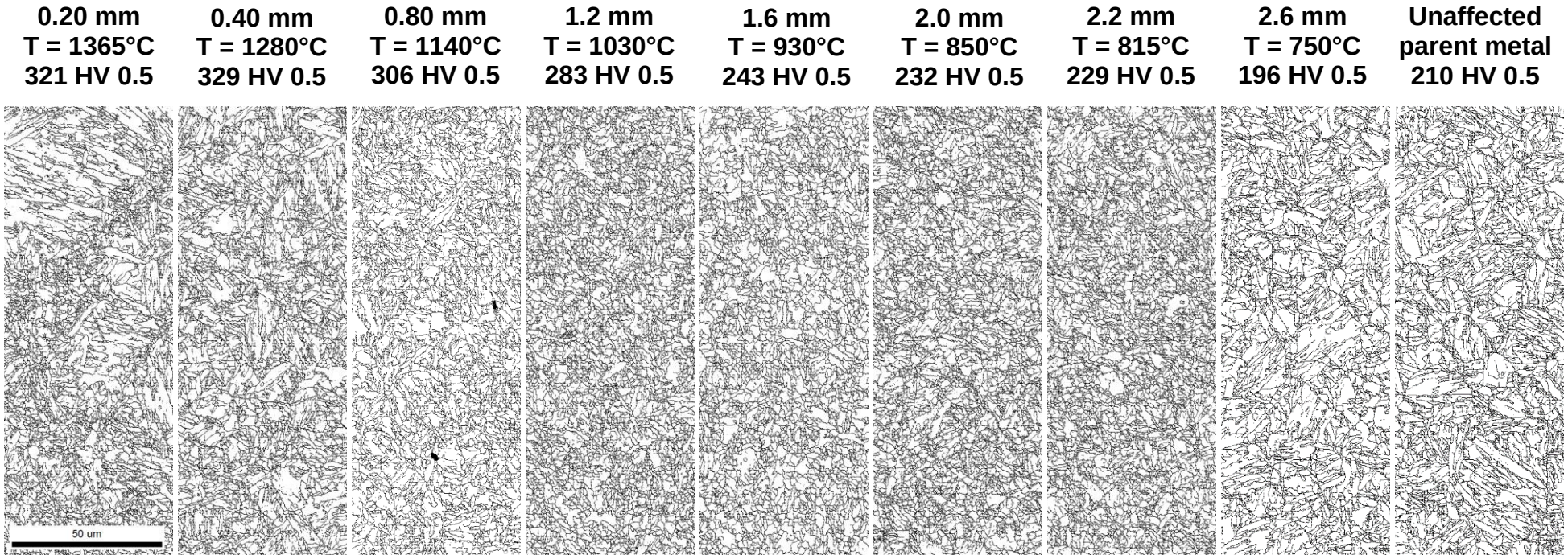

Figure 5-32. Electron backscatter diffraction (EBSD) images for all boundaries with misorientation of 2-180 degrees in weld RNT-B2 (E9015-B9, matching filler metal, PWHT at 675°C for 2 hours, and re-normalized and tempered, martensitic parent metal B2); scale length = 50 µm
Note: *for each location the indicated values give in millimeters (mm) refer to the distance from the fusion line and the calculated peak temperature is provided from calculated peak temperature from Figure 5-14.*

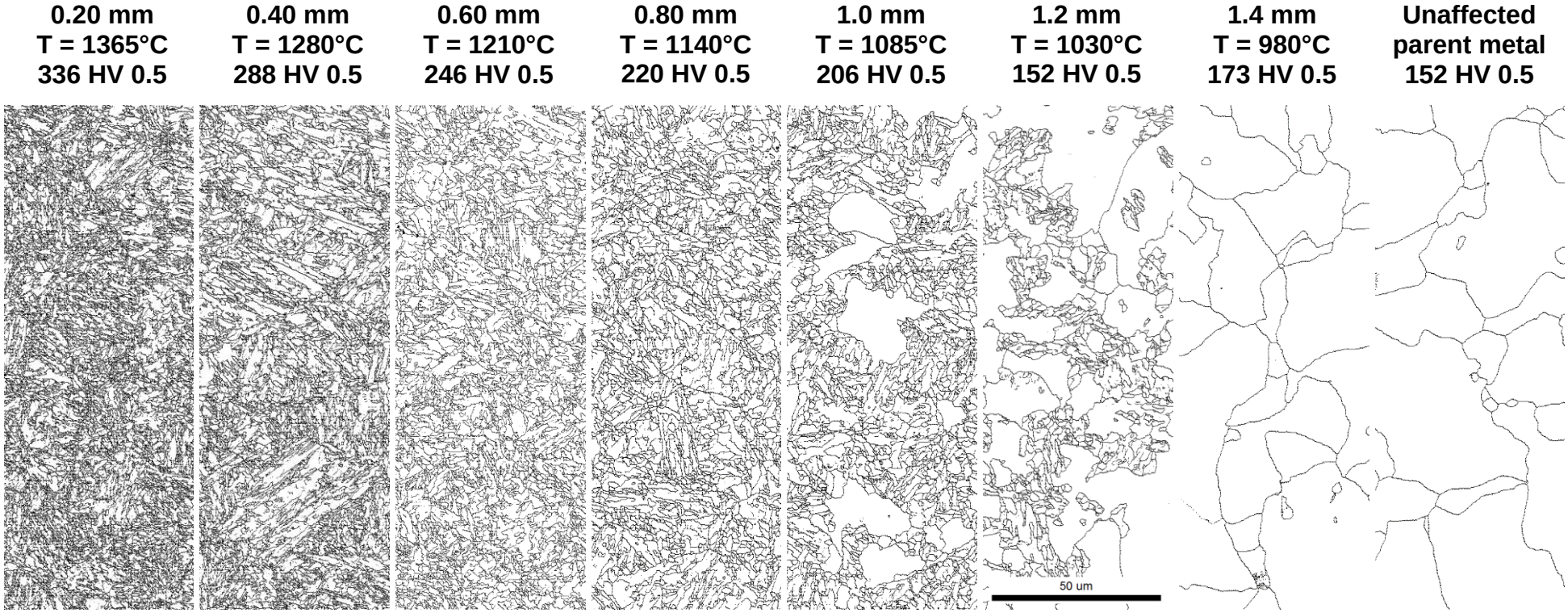

Figure 5-33. Electron backscatter diffraction (EBSD) images for all boundaries with misorientation of 2-180 degrees in weld F-TP1 (E9015-B9, matching filler metal, PWHT at 675°C for 2 hours, and ferritic parent metal TP1); scale length = 50 μm
Note: *for each location the indicated values give in millimeters (mm) refer to the distance from the fusion line and the calculated peak temperature is provided from Figure 5-15.*

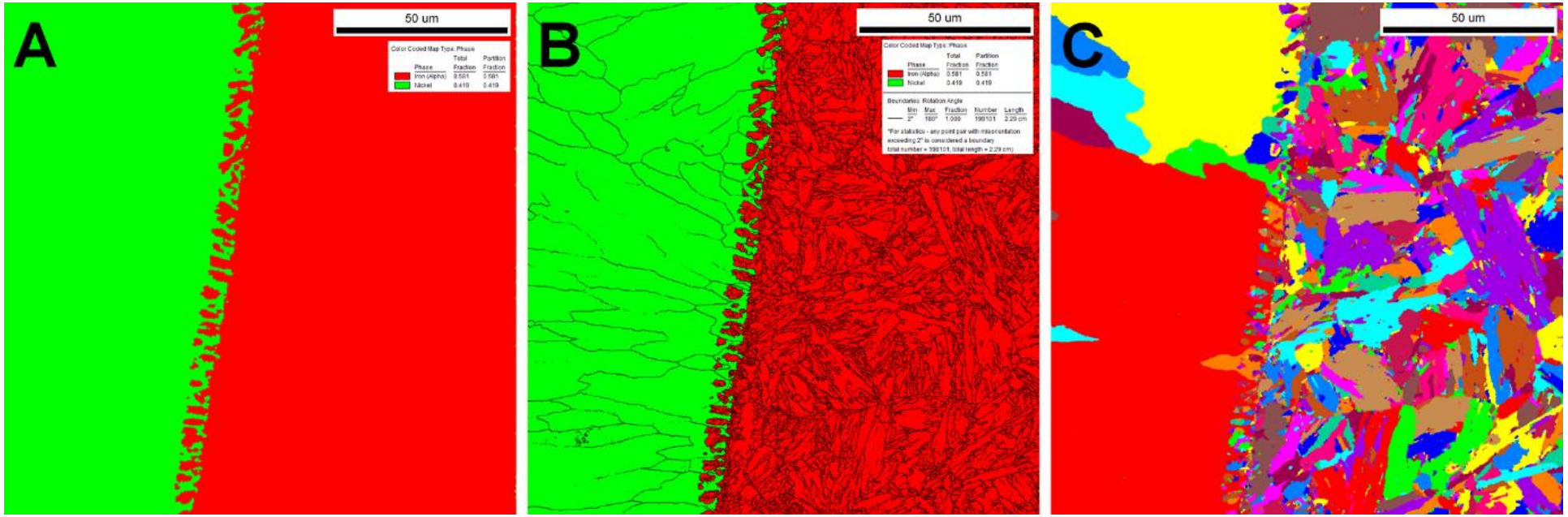

Figure 5-34. Results for SEM-EBSD at the fusion line in the as-fabricated condition for weld 9C (EPRI P87 weld metal on left-hand side and Grade 91 on the right-hand side of each image); phase map where green is FCC and red is BCC (A); phase map and image quality overlay where the boundaries are for a misorientation of 2 to 180 degrees (B); and a color grain map (C); scale length = 50 µm

5.7 Energy Dispersive X-ray Spectroscopy (EDS) Mapping

5.7.1 Analysis of local regions in the heat affected zone

Compositional mapping for locations in the HAZ defined by a relative increase in the PAGB length or decrease in the SGB length is provided in Figure 5-35 to Figure 5-41. The purpose of these evaluations is to assess the local variability in main alloying elements (such as Fe, Cr and Mo) in the HAZ and evaluate the potential for local dissolution of $M_{23}C_6$ or Laves phase. In each set of HAZ results, the examined area is given in the "A" image, while the segregation of elements Fe ("B" image), Cr ("C" image) or Mo ("D" image) is provided with respect to the measured, local intensity. Evaluation of the dissolution and/or reprecipitation of $M_{23}C_6$ will show local variability in composition when compared to the matrix for Cr, Mo and Fe. It is noted that Laves phase shares a similar overlap in composition to $M_{23}C_6$; Laves phases is likely to be observed in these steels since they were utilized in the ex-service condition. The composition of these phases is reviewed in Table 5-2 and compared to published data by Gaffard (2004) and Panait (2010). The data show there exists a considerable variation in Cr and Mo when comparing these precipitates allowing for a clear distinction between the matrix, $M_{23}C_6$ or Laves phase.

Table 5-2. Reported composition for $M_{23}C_6$ and Laves phase in Grade 91 steel, given in weight percent and as determined using SEM-EDS measurements in Figure 4-15 to Figure 4-17

Precipitate	Cr	Fe	Mo	Nb	V	Si	Mn
$M_{23}C_6$ (Panait 2010)*	57.4	27.9	9.9		0.1		4.8
$M_{23}C_6$ (Panait 2010)**	65.9	17.1	11.7		0.1		5.2
$M_{23}C_6$ (Gaffard 2004)	54-65	28-32	7-10	0-2	0-2	2-4	
Laves (Panait 2010)***	7.8	32.8	55.5			2.9	1.1
Laves (Gaffard 2004)	7-10	43-49	35-41	0.2-3	0.3-1	4-8	
Laves (current study)	8.9	30.5	54.0			6.5	

*Average of 128 particles in the as-received condition
**Average of 120 particles following creep test at 600°C for 113,431 hours
***Average of 4 particles following creep test at 600°C for 113,431 hours

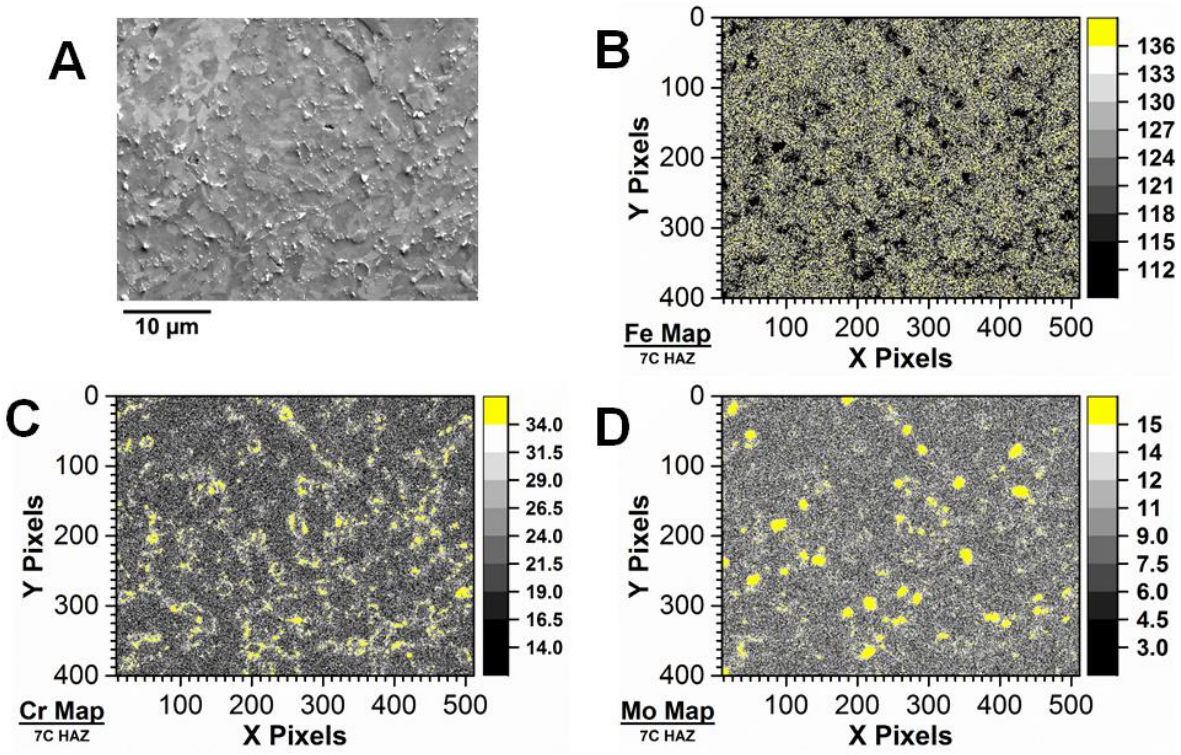

Figure 5-35. SEM-EDS map for the location where the map was collected (A), Fe (B), Cr (C) and Mo (D); E9015-B9 matching filler metal, PWHT at 675°C for 2 hours, and martensitic parent metal TP1

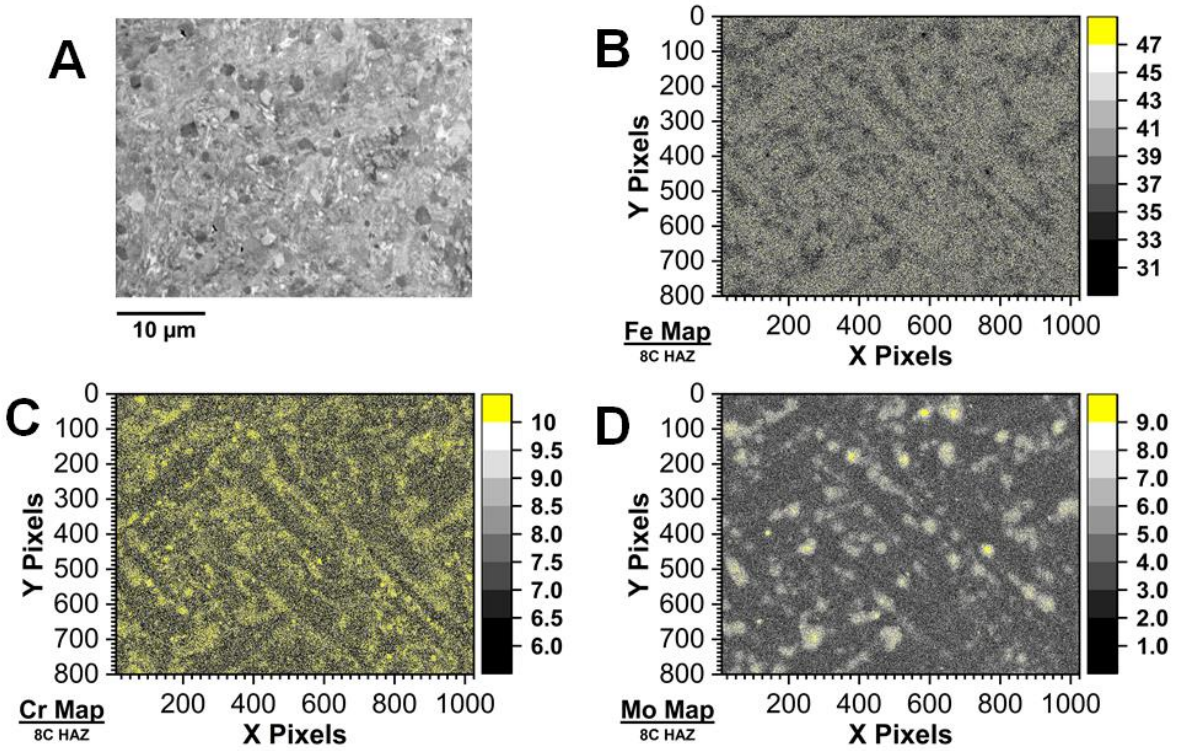

Figure 5-36. SEM-EDS map for the location where the map was collected (A), Fe (B), Cr (C) and Mo (D); AWS type -B8 under-matching filler metal, as-welded condition, and martensitic parent metal TP1

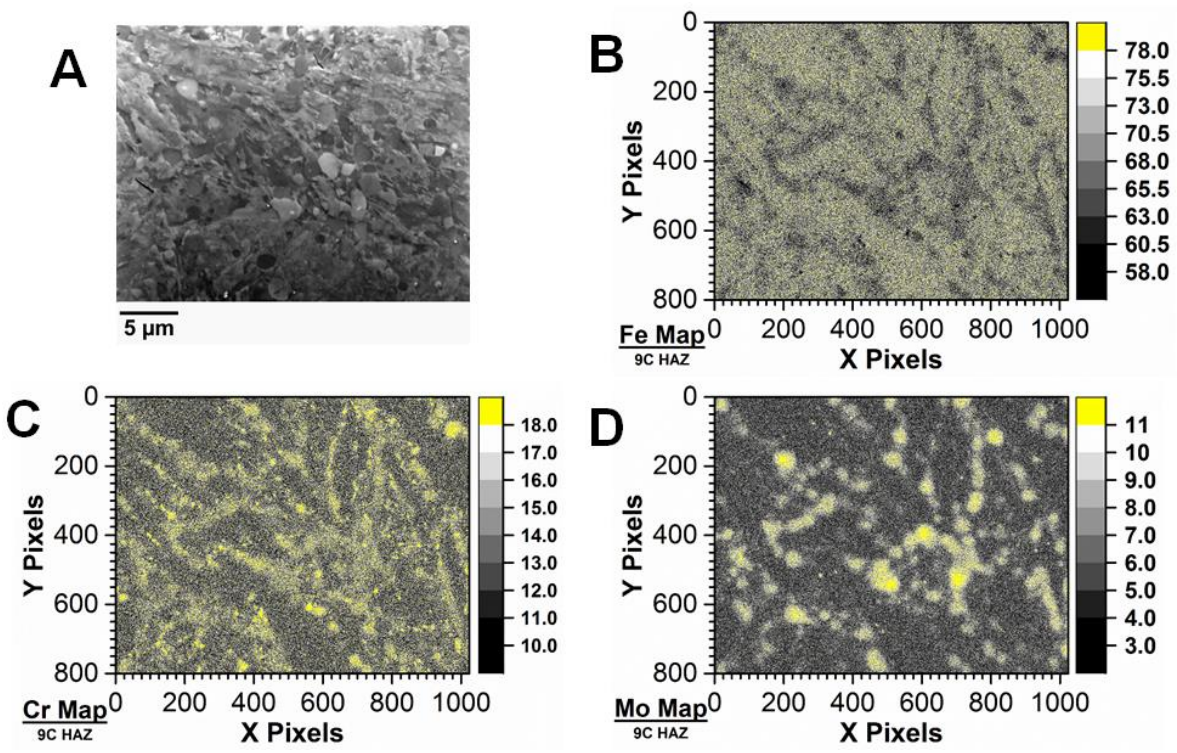

Figure 5-37. SEM-EDS map for the location where the map was collected (A), Fe (B), Cr (C) and Mo (D); EPRI P87 over-matching filler metal, as-welded condition, and martensitic parent metal TP1

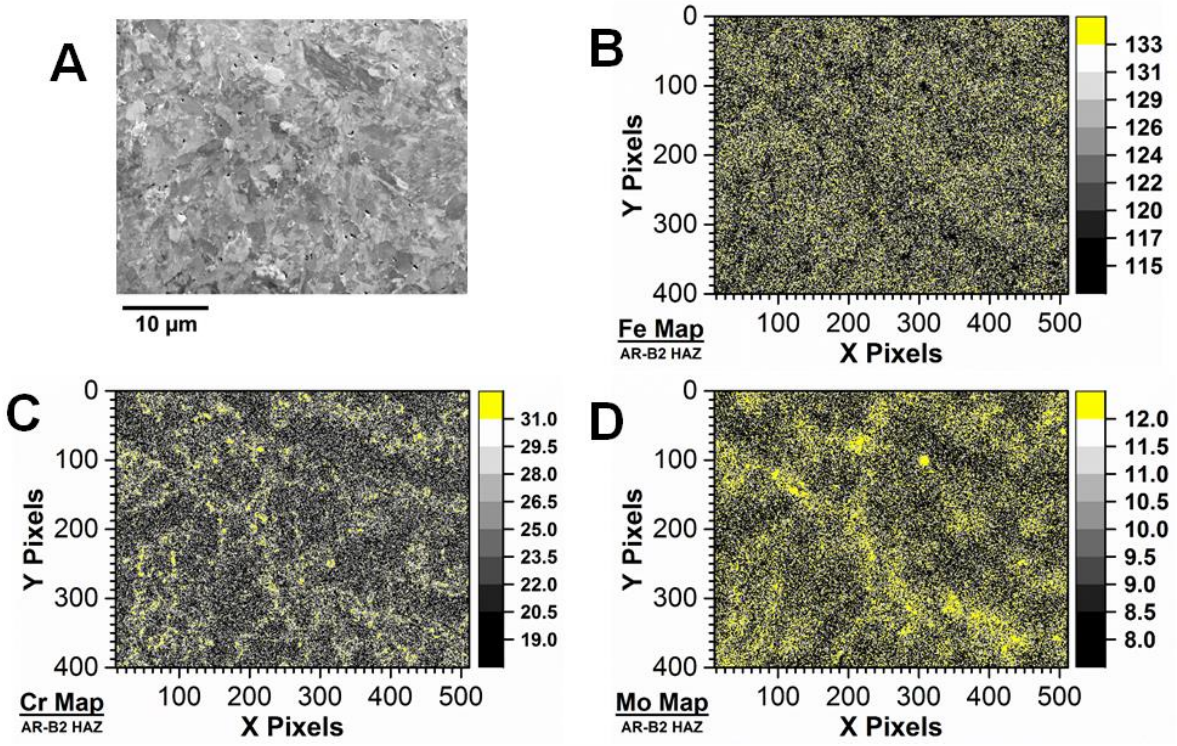

Figure 5-38. SEM-EDS map for the location where the map was collected (A), Fe (B), Cr (C) and Mo (D); E9015-B9 matching filler metal, PWHT at 675°C for 2 hours, and martensitic parent metal B2

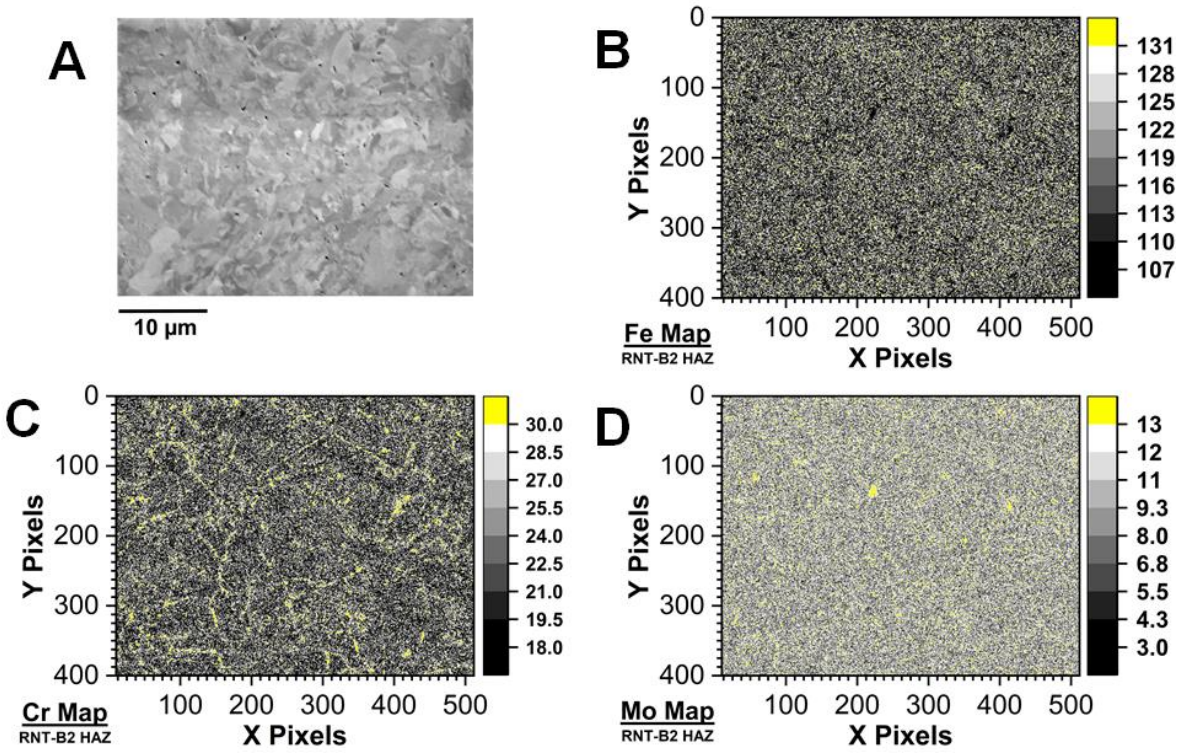

Figure 5-39. SEM-EDS map for the location where the map was collected (A), Fe (B), Cr (C) and Mo (D); E9015-B9 matching filler metal, PWHT at 675°C for 2 hours, and re-normalized and tempered, martensitic parent metal B2

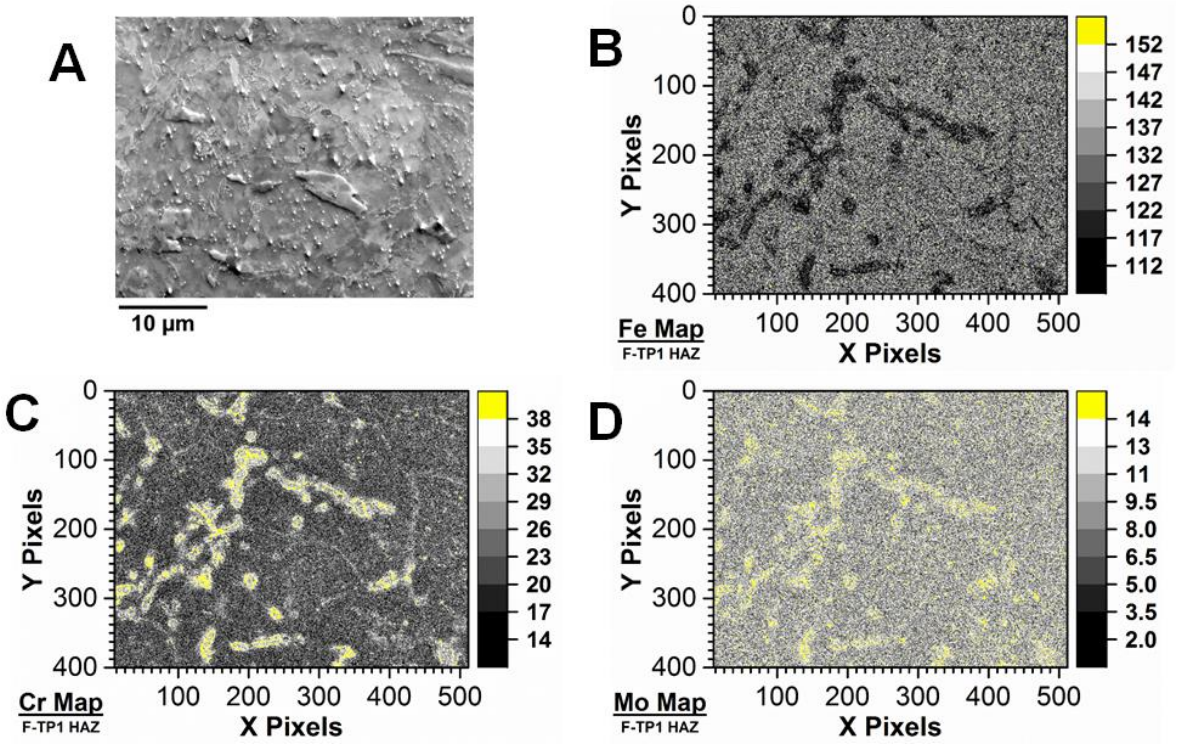

Figure 5-40. SEM-EDS map for the location where the map was collected (A), Fe (B), Cr (C) and Mo (D); E9015-B9 matching filler metal, PWHT at 675°C for 2 hours, and ferritic parent metal TP1

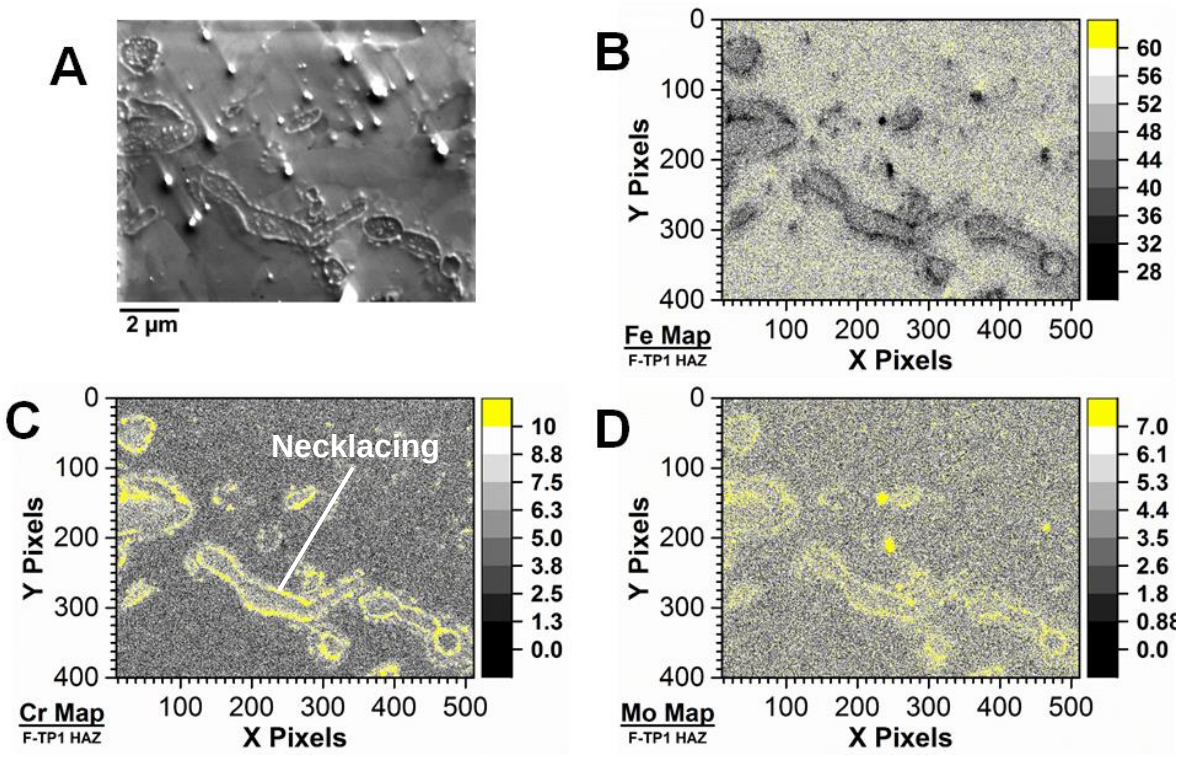

Figure 5-41. SEM-EDS map for the location where the map was collected (A), Fe (B), Cr (C) and Mo (D); E9015-B9 matching filler metal, PWHT at 675°C for 2 hours, and ferritic parent metal TP1

In the HAZs assessed, there is evidence in the EDS maps in the as-welded condition (Figure 5-36 and Figure 5-37) for the local enrichment of both Mo and Cr. The stabilization of ferrite observed in the SEM-BED images is clearly shown in Figure 5-42 and Figure 5-43 for Weld 8C in a location 1.0 mm from the fusion line (e.g. calculated T_{peak} = 995°C). The ferrite grains in the 2D plane are not continuous, although they may be linked in 3D (e.g. in or out of the observed plane) appear to have a characteristic rounded morphology. It is rationalized by Sawada et al. (2015) who claimed that the simultaneous effect of $M_{23}C_6$ dissolution and C diffusion away from the location assists in stabilizing ferrite.

Carbide necklacing is clearly observed following PWHT in Figure 5-35C for weld 7C and Figure 5-40 for weld F-TP1. For the F-TP1 weldment, widespread development of this microstructure is documented and a higher magnification map shows this in more detail in Figure 5-41. A lesser extent of necklacing is evident in Figure 5-38 and none is apparent in Figure 5-39. In Figure 5-39 there appears to be a more uniform distribution of Fe and Mo compared to the other elements as well as a finer distribution of Cr, which appears to be more evenly concentrated along boundaries. This observation suggests that the renormalized and tempered heat treatment prior to

welding was sufficient to resolutionize Laves phase and reduce the propensity for localization of Cr *and* Mo in the matrix after welding. Nevertheless, extensive welding does take place in the form of repair or replacement of in-service material and the interesting observations in this set of weldments with respect to apparent stabilization of ferrite grains in the as-welded condition, is not without relevance.

The microstructures in a HAZ region ~1 mm from the fusion line where ferrite formation is observed is documented in Figure 5-42 and compared to the unaffected parent metal. There exists an obvious difference in the grain structure and presence of bright particles in the parent metal (Laves phase) which are absent in the HAZ image.

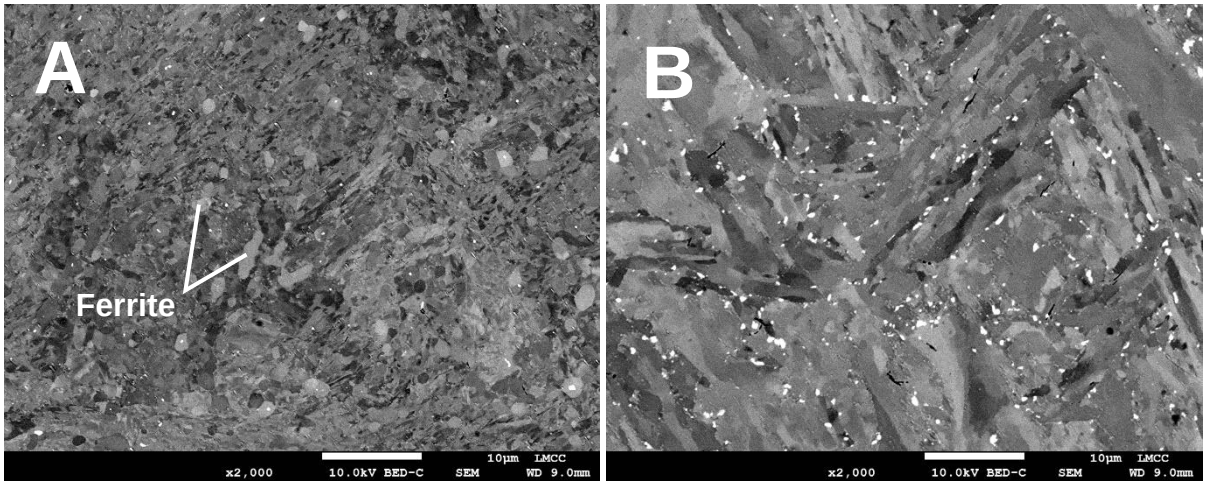

Figure 5-42. Comparison of the heat affected zone microstructure (A) 1.0 mm from the fusion line (T_{peak} = 995°C) and the unaffected parent material (B) in weld 8C (AWS type -B8 under-matching filler metal, as-welded condition, and martensitic parent metal TP1); magnification 2,000X; scale width = 10 µm

The local composition of the ferrite grains to the martensitic matrix in the HAZ and the martensitic parent metal matrix is compared in Figure 5-43. The ferrite grains are enriched in Cr and Mo (e.g. spot locations 1, 3, 4 and 5) relative to the local measurement in the HAZ and to the matrix (e.g. spot location 2 and 'parent metal area'). Furthermore, the unaffected parent material composition should possess a composition between the extreme bounds for Cr and Mo in the martensitic HAZ and ferrite grains. The data in Figure 5-43 support this claim. It is thus the case that local enrichment of both Cr and Mo is explained by the dissolution of $M_{23}C_6$ and Laves leading to stabilization of ferrite in the HAZ for service-exposed materials. For virgin materials, the presence of ferrite in the HAZ would be a result of only $M_{23}C_6$ dissolution as discussed in (Sawada et al. 2015).

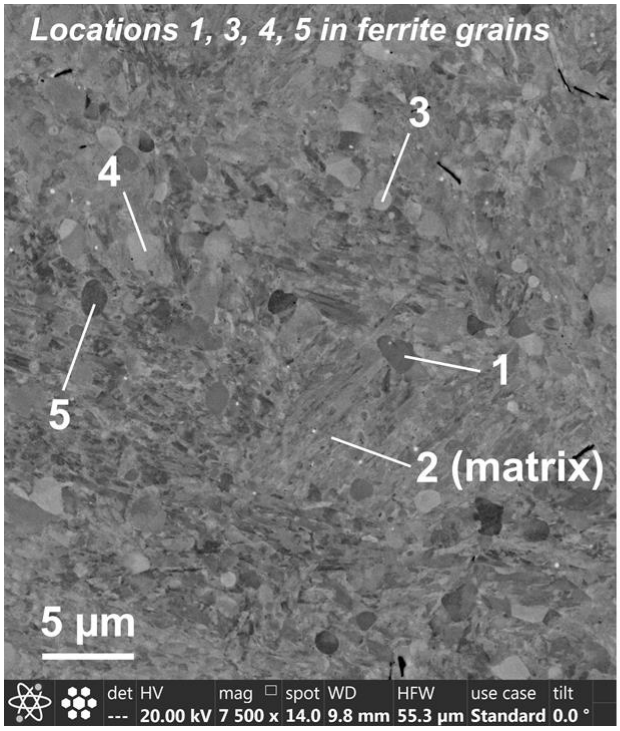

Spot Location	Cr (wt. %)	Mo (wt. %)	V (wt. %)	Fe (wt. %)
1	11.25	2.46	0.59	85.71
2	8.67	0.22	0.19	90.92
3	10.32	1.16	0.29	88.23
4	10.46	2.64	0.20	86.69
5	10.01	1.75	0.23	88.02
Parent metal area	9.60	0.63	0.23	89.53

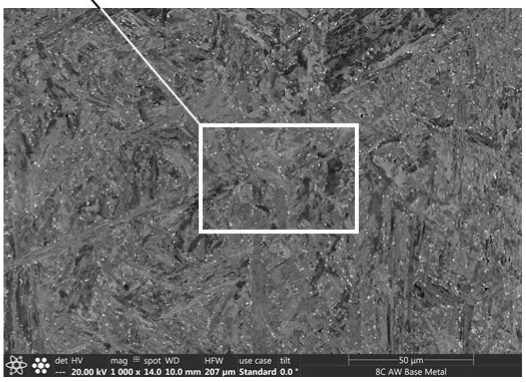

Figure 5-43. Comparison of the heat affected zone microstructure in weld 8C (AWS type -B8 under-matching filler metal, as-welded condition, and martensitic parent metal TP1); 7,500X magnification in the heat affected zone image (left) and 1,000X magnification in the unaffected parent metal (bottom right)

Confirmation of the measurements reported in Figure 5-43 included a systematic evaluation of ~10 locations in the weld 8C parent metal or HAZ for coarse Laves phase, coarse $M_{23}C_6$, HAZ martensite, HAZ ferrite and parent metal martensite. Details regarding the identification of suitable locations to carry out this assessment are provided below:

- Locations in the HAZ with a martensitic matrix including evidence for substructure consistent with a packet/block/lath morphology;
- Featureless grains in the HAZ with a consistent morphology of ferrite were singled out for evaluation;
- In BED mode, bright particles are identified as Laves phase;
- In BED mode, 'coarse' $M_{23}C_6$ particles possess a dull gray appearance.

The SEM-EDS procedure utilized for this process included the following parameters: 15 kV for the matrix assessment in the HAZ or parent metal resulting in approximately 50,0000 cps; 5 kV for the particle assessment of Laves or $M_{23}C_6$ (to reduce the interaction volume with the matrix) resulting in approximately 12,000 cps; 10 mm

working distance; 100s dwell time for either small maps (such as in the ferrite grains or matrix readings) or spots (such as for the Laves or $M_{23}C_6$ particles). The assessed elements varied with the constituent of interest, for example:

- Cr, Mo, Fe, Si were assessed for the HAZ martensite matrix, HAZ ferrite matrix, parent metal martensite matrix and laves phase;
- Cr, Mo, Fe, Si, V, Mn and C were assessed for $M_{23}C_6$ particles;
- Construction of ternary element plot comparisons only considered the elements Cr, Mo and Si.

Evaluation of the parent metal martensite matrix including ten unique locations is provided in Figure 5-44A and for selected areas in a magnified view in Figure 5-44B. The results for this analysis resulted in a consistent set of data, given in Figure 5-45.

Evaluation of the HAZ ferrite and HAZ martensite is detailed for individual locations in Figure 5-46 to Figure 5-46C. A magnified view of selected sites for SEM-EDS analysis is given in Figure 5-46D. The results for the HAZ ferrite composition and HAZ martensite composition are given in Figure 5-47 and Figure 5-48, respectively.

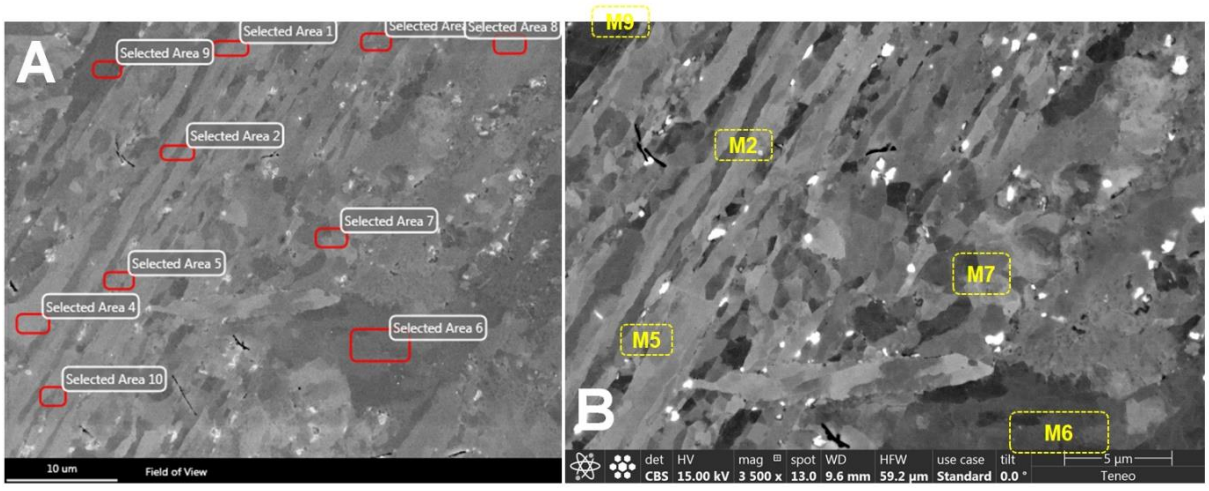

Figure 5-44. Representative locations for measurement of composition in the martensitic parent metal matrix including all areas (A) and selected locations shown in the analyzed area (B)

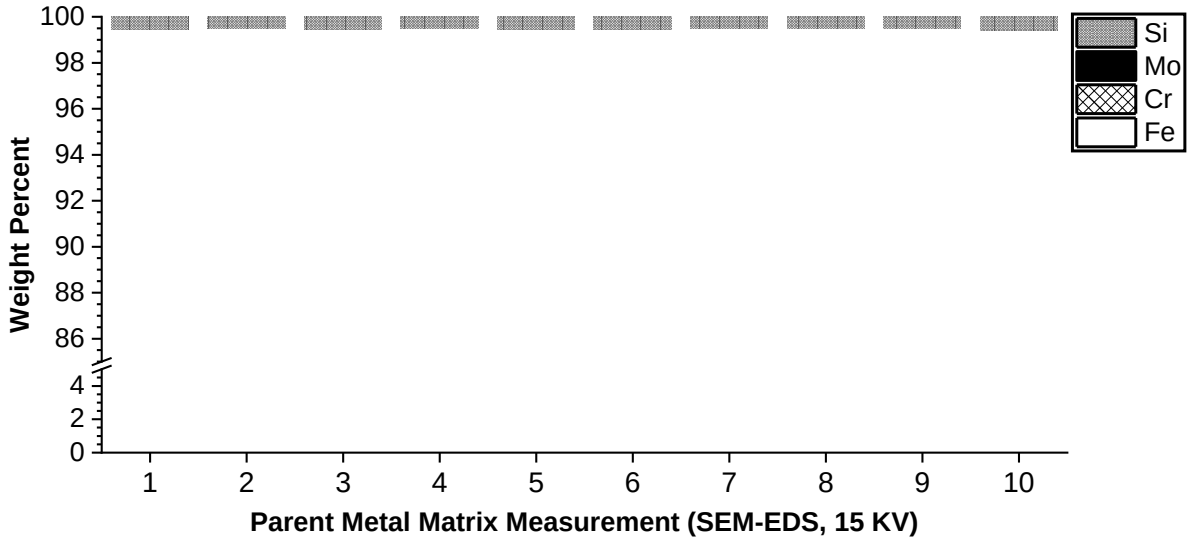

Figure 5-45. Results for the measurement of ten locations in the martensitic parent metal matrix for Si, Mo, Cr and Fe (in weight percent)

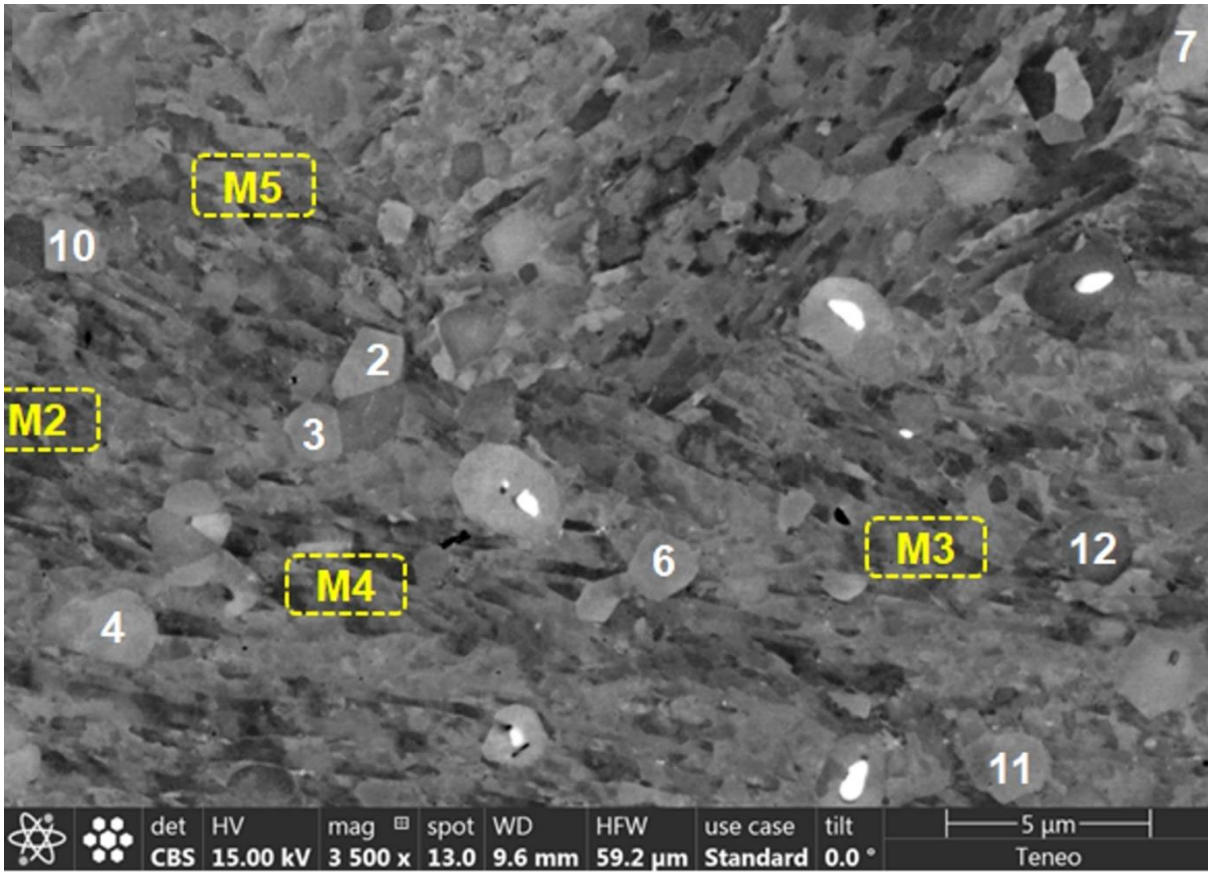

Figure 5-46. Representative locations for measurement of composition in the martensitic heat affected zone (HAZ) matrix locations (A, B), ferritic HAZ locations (C) and a combined image showing martensitic HAZ measurements (yellow) and ferritic HAZ measurements (white numbers) (D)

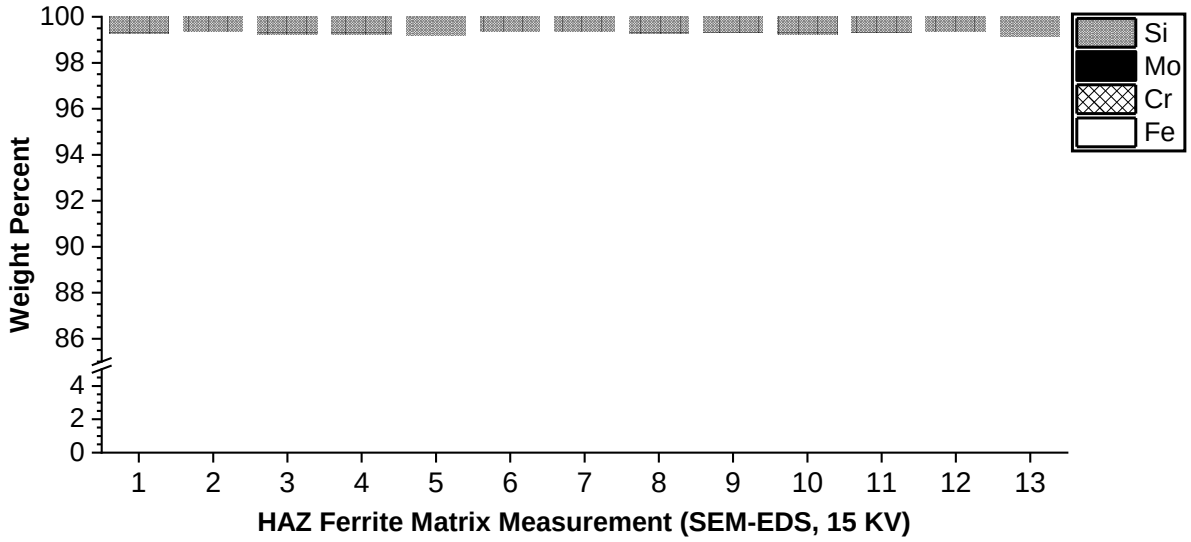

Figure 5-47. Results for the measurement of thirteen locations in the ferritic heat affected zone matrix for Si, Mo, Cr and Fe (in weight percent)

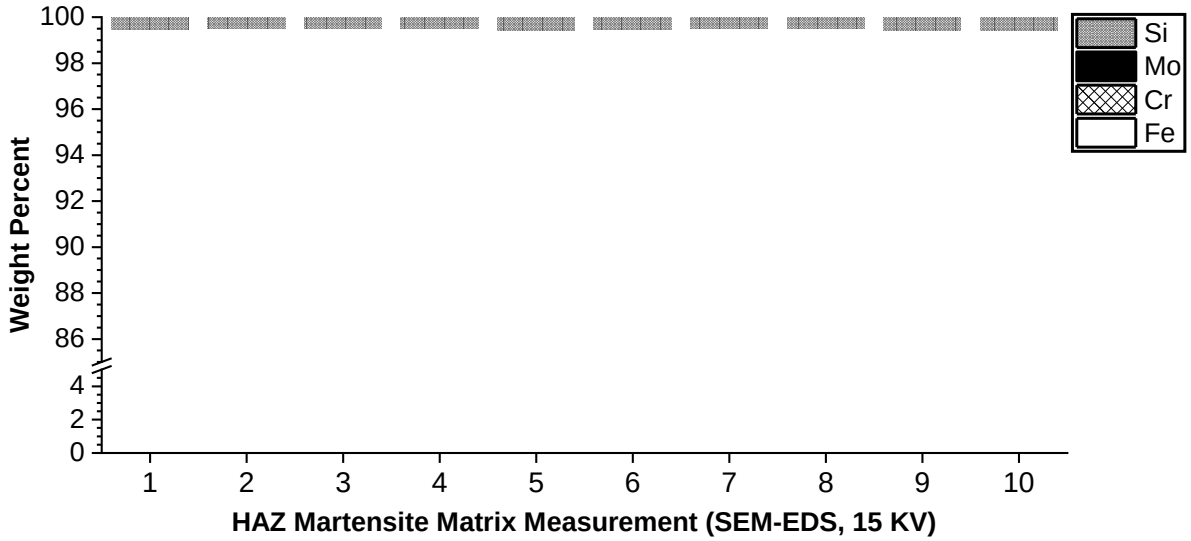

Figure 5-48. Results for the measurement of ten locations in the martensitic heat affected zone matrix for Si, Mo, Cr and Fe (in weight percent)

A summary of the particle analysis is provided in Figure 5-49 to Figure 5-51. Locations for the Laves phase analysis are detailed in Figure 5-49. The results of the Laves phase particles and $M_{23}C_6$ particles are given in Figure 5-50 and Figure 5-51, respectively. The values for these particles are compared to data in the literature for Grade 91 steel from Panait (2010), who reported mean compositional data for four Laves particles in the crept condition, 128 $M_{23}C_6$ particles in the as-received condition and 120 $M_{23}C_6$ particles in the crept condition (see Table 5-2). The composition information provided in Panait's study the data were obtained using TEM-EDX

analysis on carbon extractive replicas and in the crept condition for a broken sample obtained after 113,431 hours at 600°C and 80 MPa was utilized.

For the Laves particles the agreement in the composition information was very good (Figure 5-50). With respect to the $M_{23}C_6$ particles there is a notable decrease in the reported Cr content, which is displaced by the higher Fe content compared to Panait's results. This indicates that the interaction volume of the beam in the matrix is larger than the size of the coarse $M_{23}C_6$ particles (generally >200 nm diameter in this assessment compared to Laves phase which is ~>500 nm). The reported compositions in Figure 5-51 do offer a means by which to clearly distinguish particles even if the values cannot be regarded as absolute.

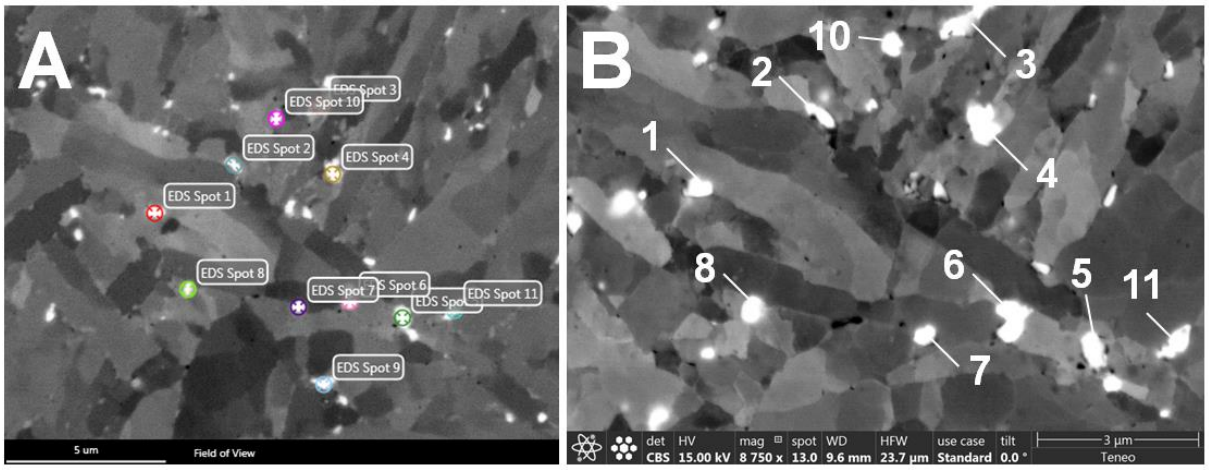

Figure 5-49. Representative locations for measurement of composition in the Laves phase particles for all particles (A) and a higher magnification image (B)

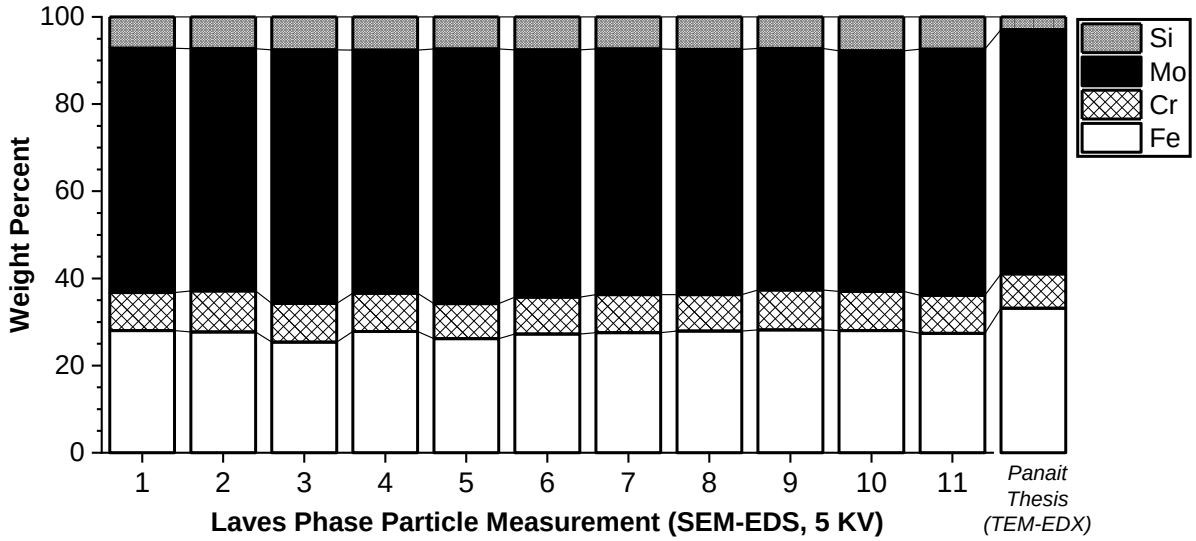

Figure 5-50. Results for the measurement of eleven Laves phase particles for Si, Mo, Cr and Fe (in weight percent) and compared to the results reported by Panait (2010)

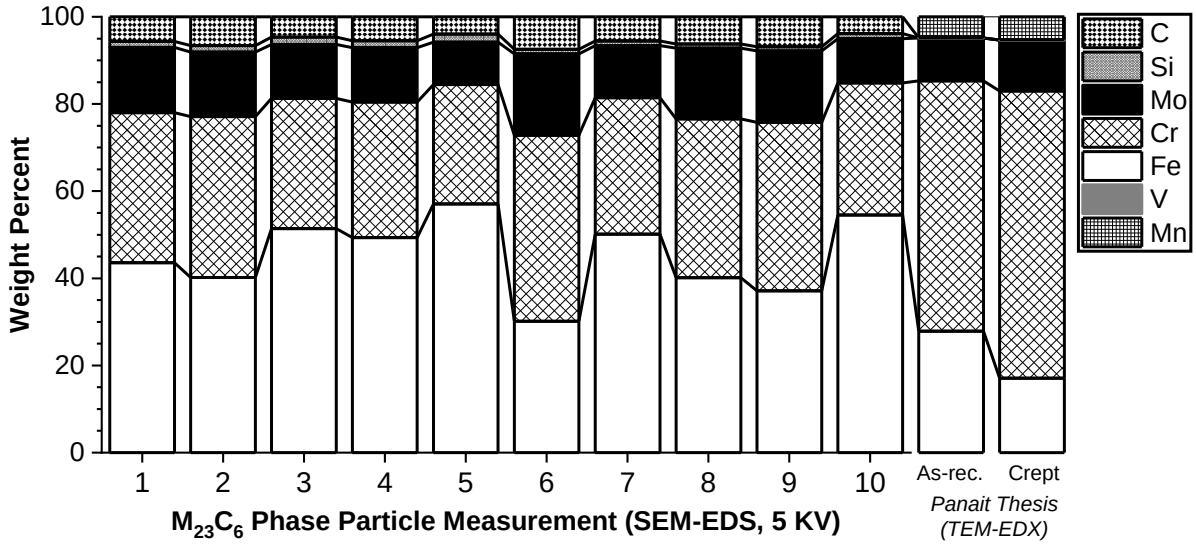

Figure 5-51. Results for the measurement of ten $M_{23}C_6$ particles for C, Si, Mo, Cr, Fe, V and Mn (in weight percent) and compared to the results reported by Panait (2010) in the pre-test and post-test conditions

The comparison of composition is represented in Figure 5-52 as a ternary composition diagram for Mo, Fe and Cr. Figure 5-52A provides a comparison of the notable particles in the Grade 91 HAZ or parent metal: Laves phase, $M_{23}C_6$ and matrix (either ferrite or martensite). The magnified view in Figure 5-52B compares the data for the matrix compositions: HAZ ferrite, HAZ martensite and HAZ parent metal. It is observed in Figure 5-52B that the parent metal martensite and HAZ martensite are removed from the population for the HAZ ferrite measurements. To assess if this observation is statistically significant, a set of analyses were performed including a t-Test.

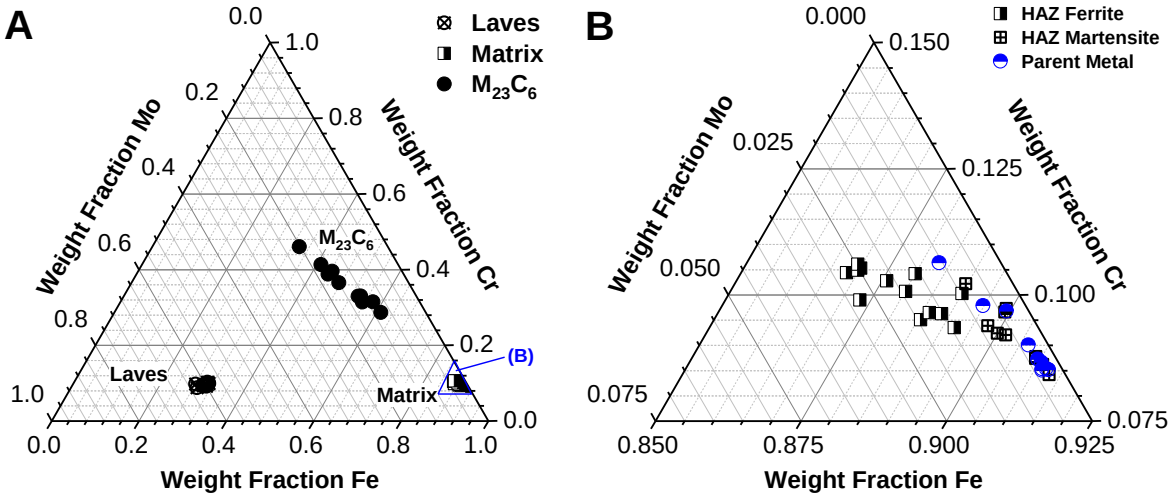

Figure 5-52. Comparison of all measurements for Mo, Cr and Fe (weight percent) in the Laves phase, $M_{23}C_6$ and matrix constituents (A) and a magnified view of the matrix measurements for the heat affected zone ferrite, heat affected zone martensite and parent metal martensite (B)

A summary of the Mo and Cr concentrations in the matrix constituents is compared in Figure 5-53A and Figure 5-53B, respectively. A simple comparison of mean values suggests that the values for Cr or Mo are indeed different, but it should be emphasized that:

- Descriptive statistics only describes the existing sample dataset;
- Inferential statistics allow for use of calculations like the t-Test to assess populations beyond the existing data to make generalizations;
- The p-value is a value provided by the t-Test for comparison to a critical value to evaluate whether the pattern of data in the sample could be produced at random;
- If p = 0.05 there is a 5% chance the data are 'random' or *are not statistically significant.* A typical threshold value is 0.05, but for this assessment a more rigorous value of 0.01 was utilized.

The results of a t-Test for the comparison of the parent metal martensite to the HAZ martensite and the HAZ martensite to the HAZ ferrite is provided in Table 5-3. The t-Test results show that the parent metal martensite and HAZ martensite compositions do not significantly vary for Cr and Mo. However, when evaluating the HAZ martensite and HAZ ferrite compositions there is statistically significant variation in the Cr and Mo content. P-values for parent metal to HAZ martensite comparisons suggest there is a 75% or 51% probability that the data is random for Cr and Mo mean values, respectively. In contrast, the difference in the HAZ ferrite to HAZ martensite shows for Cr there is a 99.8% and for Mo a >99.999999% likelihood the values are statistically significant.

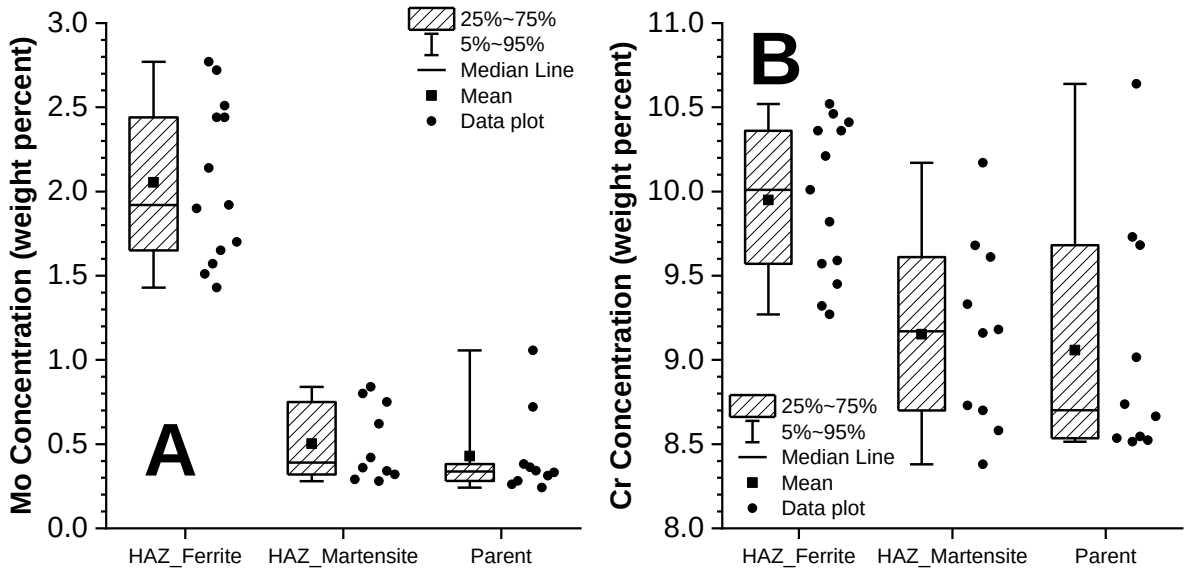

Figure 5-53. Distribution of the Mo (A) and Cr (B) concentration (weight percent) in the matrix measurements

Table 5-3. Results for the t-Test of the parent metal martensite to heat affected zone martensite Cr and Mo levels and for the heat affected zone martensite to heat affected zone ferrite Cr and Mo levels

Constituent 1	Constituent 2	Element	df	$p-value$	Is comparison statistically significant? (significance level = 0.01)
Parent Metal	HAZ Martensite	Cr	18	0.751	No
Parent Metal	HAZ Martensite	Mo	18	0.509	No
HAZ Martensite	HAZ Ferrite	Cr	21	0.00204	Yes
HAZ Martensite	HAZ Ferrite	Mo	21	5.35E-9	Yes

Variation in the Cr and Mo content for the HAZ microstructure was previously suggested by Sawada et al. (2015) to be a result of local $M_{23}C_6$ dissolution. Since both Laves phase and $M_{23}C_6$ particles were present in the ex-service material in which the weldments were made, it was important to assess if Laves phase dissolution might also be contributing to the ferrite evolution in the HAZ. Support for $M_{23}C_6$ being the primary contributor to local ferrite formation is provided in Figure 5-54 where Laves phase is observed in the center of a ferrite grain in five unique locations.

Further explanation of the ferrite formation is provided by Yu (2015), who rationalized the evolution of ferrite during the welding process using thermodynamic simulations. In his discussion, he noted the influence that Cr and C have on the evolution of the ferrite. During the welding thermal cycle when the peak temperature is sufficient to begin the dissolution process, both Cr and C diffuse into austenite. Since the solubility

of Cr in austenite is reduced, Cr accumulates at the carbide-austenite interface and results in an austenite to ferrite transformation on-cooling. Because C has a higher diffusion rate and its solubility in austenite is increased the potential effect of C on ferrite formation can be disregarded. It can thus be concluded that the SEM-EDS maps provided in Figure 5-35 to Figure 5-41 highlight relevant, local variation in the Cr and Mo content in selected weldments.

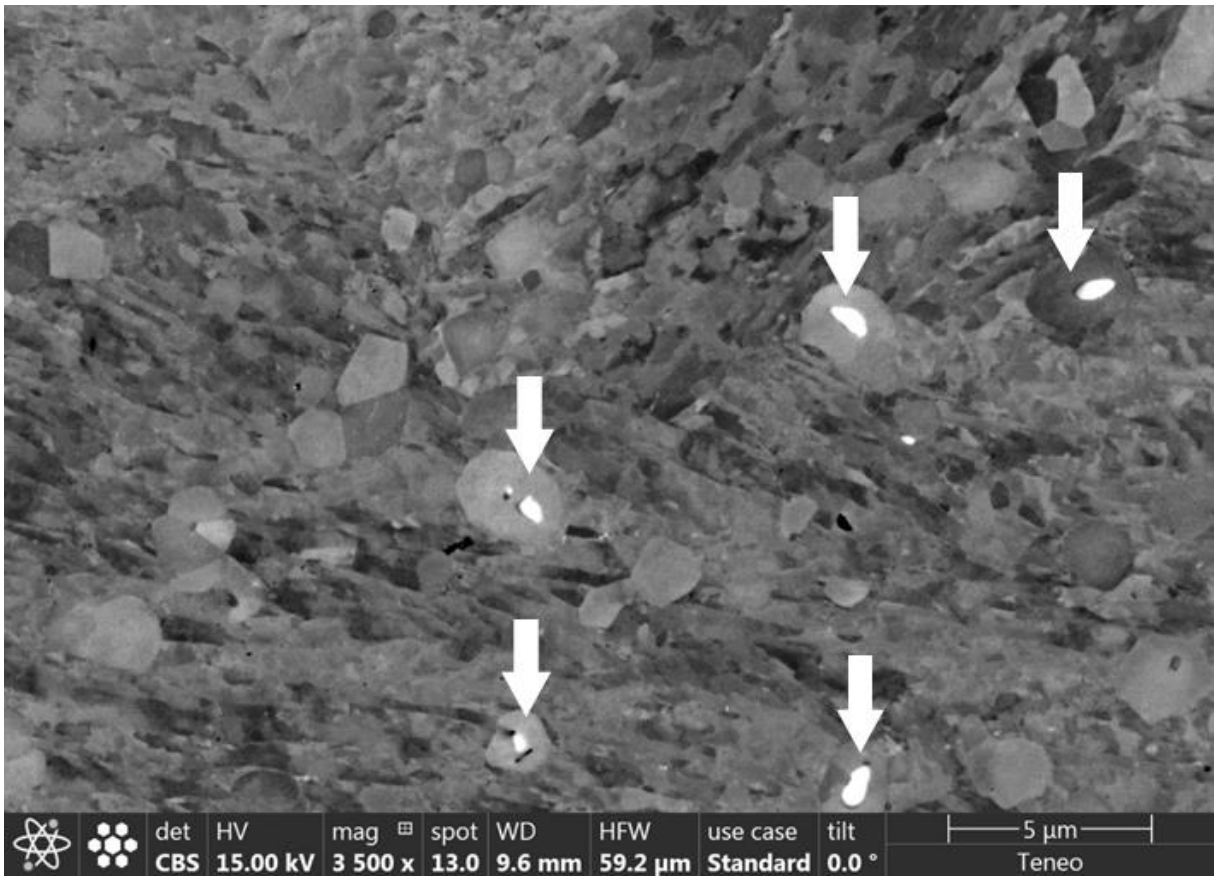

Figure 5-54. Presence of Laves phase in ferrite grains in the heat affected zone

5.7.2 Analysis of the fusion line for weld 9C

Compositional mapping across the fusion line of weld 9C in the location shown in Figure 5-55 is provided in Figure 5-56A to Figure 5-56D for Cr, Ni, Fe and Mo, respectively. The selected location for the composition assessment is identical to that previously provided for the EBSD mapping in Figure 5-34.

As noted in Figure 5-56A, the composition for Cr does not vary markedly across the fusion line. Reasons for this include: 1) the composition of the EPRI P87 filler metal closely matches (~9.0 wt. %) that of the TP1 material (~8.3 wt. %); and 2) the weldment

was not subjected to PWHT, which might be expected to precipitate carbides in the Ni-base filler metal along the observed grain boundaries in the weld metal.

The variation in the alloying elements Fe, Ni and Mo is more pronounced. The Fe and Ni show a ‘stepped’ variation where the composition remains constant until the approximate location of the fusion line. The change is first subtle, with slight Ni enrichment and Fe-depletion followed by a second zone that is still distinct from either the weld metal or parent metal and that of the first zone. Finally, the weld metal reaches a content for Ni and Fe that is globally representative of the deposited bulk composition for EPRI P87. The variations in composition near the fusion line are consistent with the prior-introduced descriptions for the partially mixed or transition zone (Table 1-3).

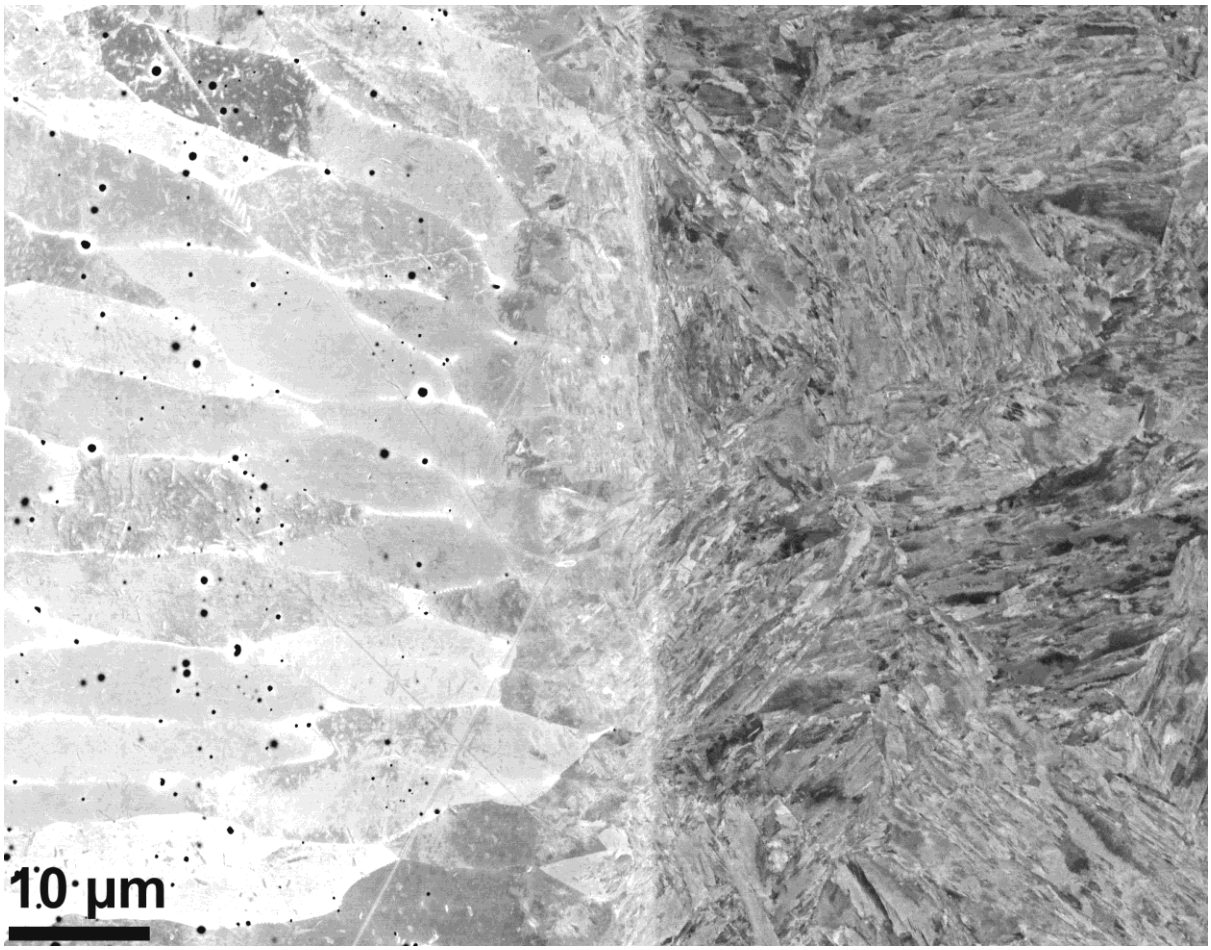

Figure 5-55. Location for SEM-EDS and SEM-EBSD at the fusion line in the as-fabricated condition for weld 9C (EPRI P87 weld metal on left-hand side and Grade 91 on the right-hand side of each image)
Note: *SEM-EBSD results presented in Figure 5-34*

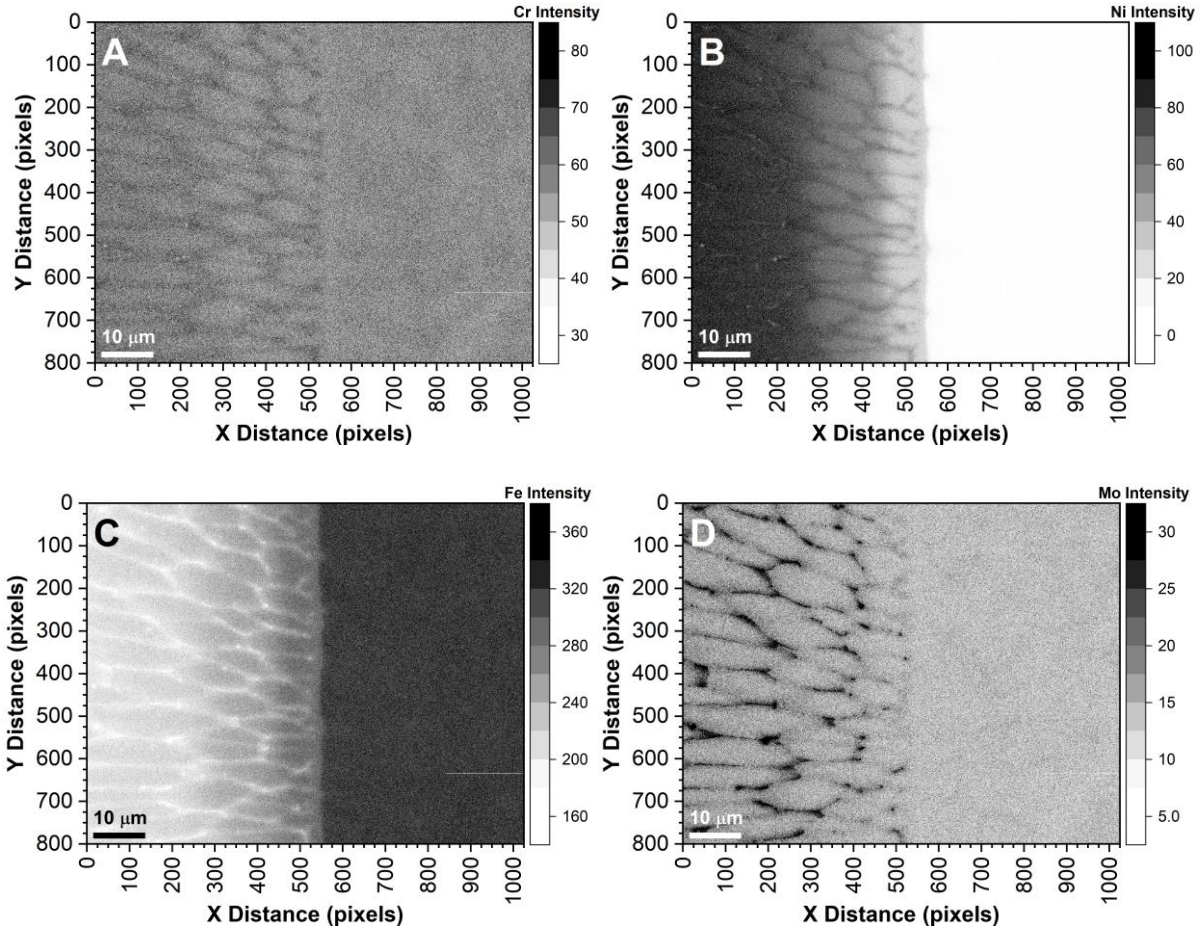

Figure 5-56. Results for SEM-EDS at the fusion line in the as-fabricated condition for weld 9C (EPRI P87 weld metal on left-hand side and Grade 91 on the right-hand side of each image) and for Cr intensity (A); Ni intensity (B); Fe intensity (C) and Mo intensity (D)

5.8 Discussion

A selection of grain boundary maps collected for weld 7C is provided in Figure 5-57. The change in the microstructure starting in the unaffected base metal and moving through the HAZ is clear. The local, hardness minimum value for weld 7C, as with the other evaluated welds, occurs in a location where the microstructure is martensitic. Figure 5-58 provides EBSD grain boundary maps for the weldments fabricated in the martensitic parent materials in the location where the local minimum in the hardness profile given in Figure 5-10 to Figure 5-14. Each figure contains a matrix characterized by extensive, substructure, providing evidence that the local soft zone cannot be associated with the PTZ. The figures given for AR-B2 and RNT-B2 appear to be less martensitic (e.g. less substructure boundaries), although this observation is complicated by a finer prior austenitic grain size for this material when compared to the TP1 material utilized for welds 7C, 8C and 9C (~20 versus >100 μm).

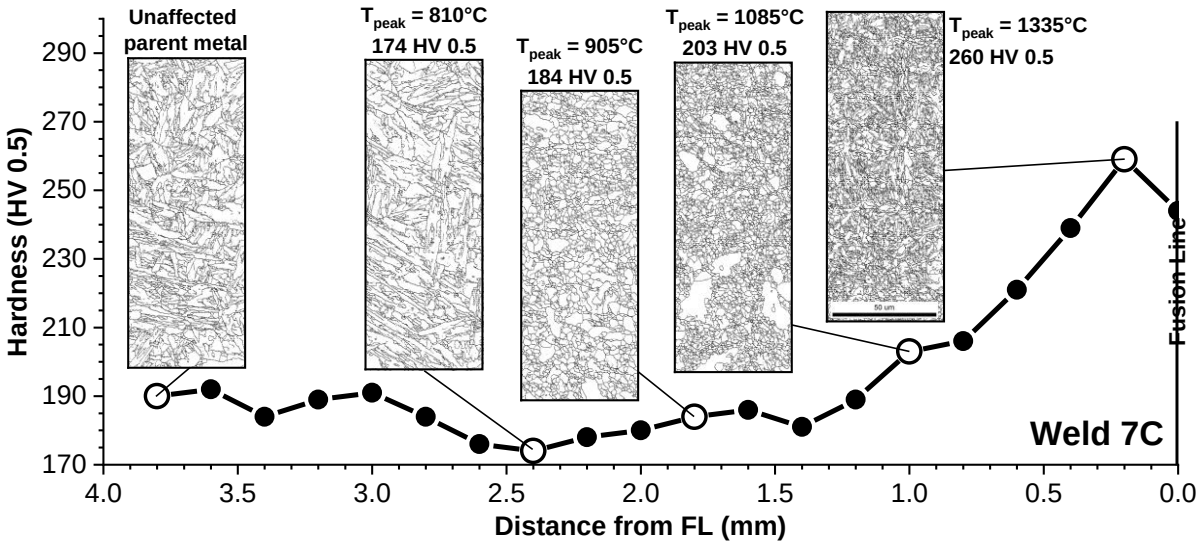

Figure 5-57. Electron backscatter diffraction (EBSD) images for all boundaries with misorientation of 2-180 degrees in selected locations through the heat affected zone for weld 7C (E9015-B9 matching filler metal, PWHT at 675°C for 2 hours, and martensitic parent metal TP1)

The martensitic matrix that is documented in the location of lowest hardness for this set of data gives credence to the early studies in Grade 91 steel regarding the association of the region to the OTZ. This infers the OTZ has not experienced a peak temperature above the Ac_1 value and is consistent with prior explanations (Biss 1982, Ferranti 1989). It is thus the case that the commonly referred to soft zone is best characterized as the OTZ and consistent with the definition provided in Table 1-4.

Figure 5-59 provides additional evidence regarding the association of the soft zone with the OTZ. The conventional argument that the soft zone is linked to a thermal cycle that exceeds the Ac_1 temperature is difficult to rationalize. If this was indeed the case, the as-welded condition should be mostly absent of this zone, yet there exists a notable, even if discontinuous soft zone in Figure 5-59B. For a thermal cycle which exceeds the Ac_1, a partial transformation of the HAZ to austenite and subsequent transformation on-cooling to either ferrite or fresh martensite or a mixed microstructure (rate dependent) must occur. Thus, an as-welded microstructure might be expected to be mostly if not completely devoid of a soft zone due to the accelerated cooling rate from welding.

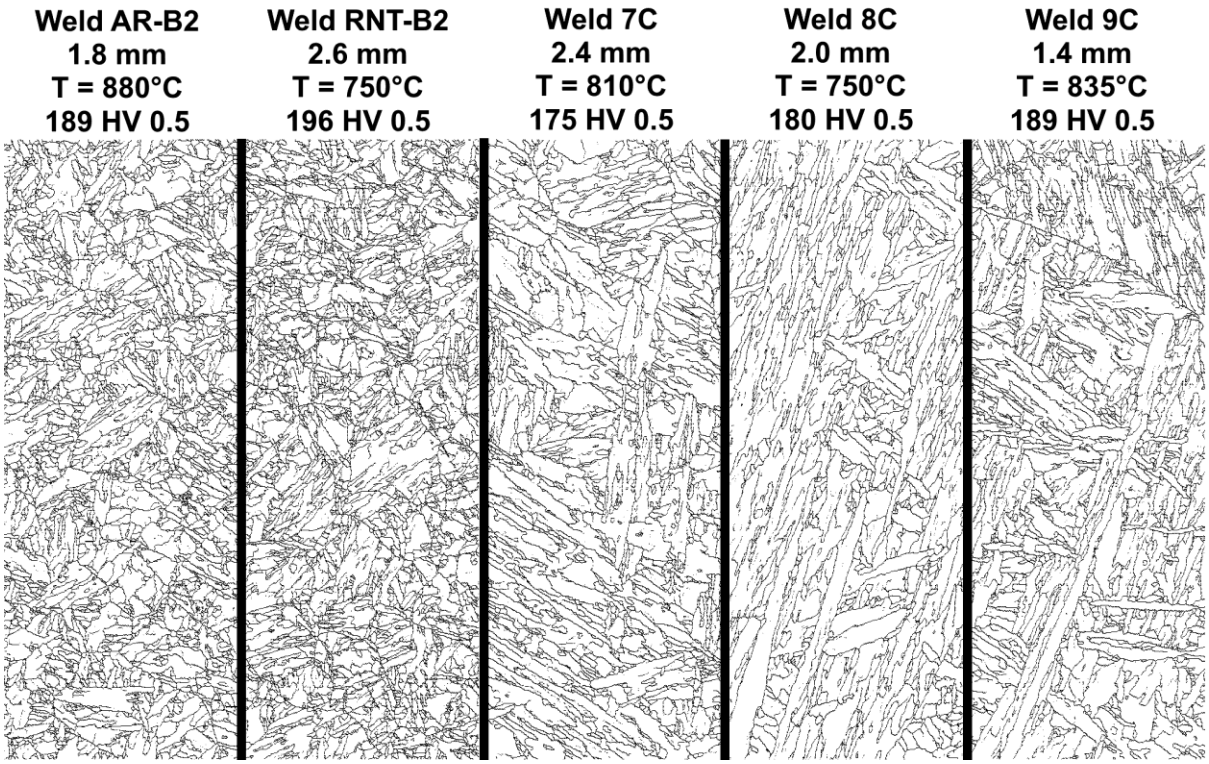

Figure 5-58. Electron backscatter diffraction (EBSD) images for all boundaries with misorientation of 2-180 degrees in the lowest hardness location in the heat affected zone for the weldments made in martensitic parent material
Note: *in all examples the heat affected zone has a martensitic microstructure with apparent packet and lath boundaries***.** *Indicated hardness and calculated peak temperature is taken from Figure 5-10 to Figure 5-14.*

It might be argued that the complexity of a multi-pass weld could allow for the superimposition of multiple thermal cycles that would induce accelerated tempering in a susceptible region in the HAZ even in the as-welded condition. However, there are three arguments to the contrary. Firstly, and as prior detail shows in Figure 5-58, the region with the local minimum hardness value contains extensive substructure boundaries characteristic of martensite. Secondly, the growth of the OTZ after PWHT is occurring in the parent material and not the PTZ or CTZ. This is observed in the comparison provided in Figure 5-59 providing evidence that the evolution of the OTZ in a preferential direction away from the HAZ. Lastly, the OTZ has been documented in single pass welds in Grade 92, as reported in (Xu 2017).

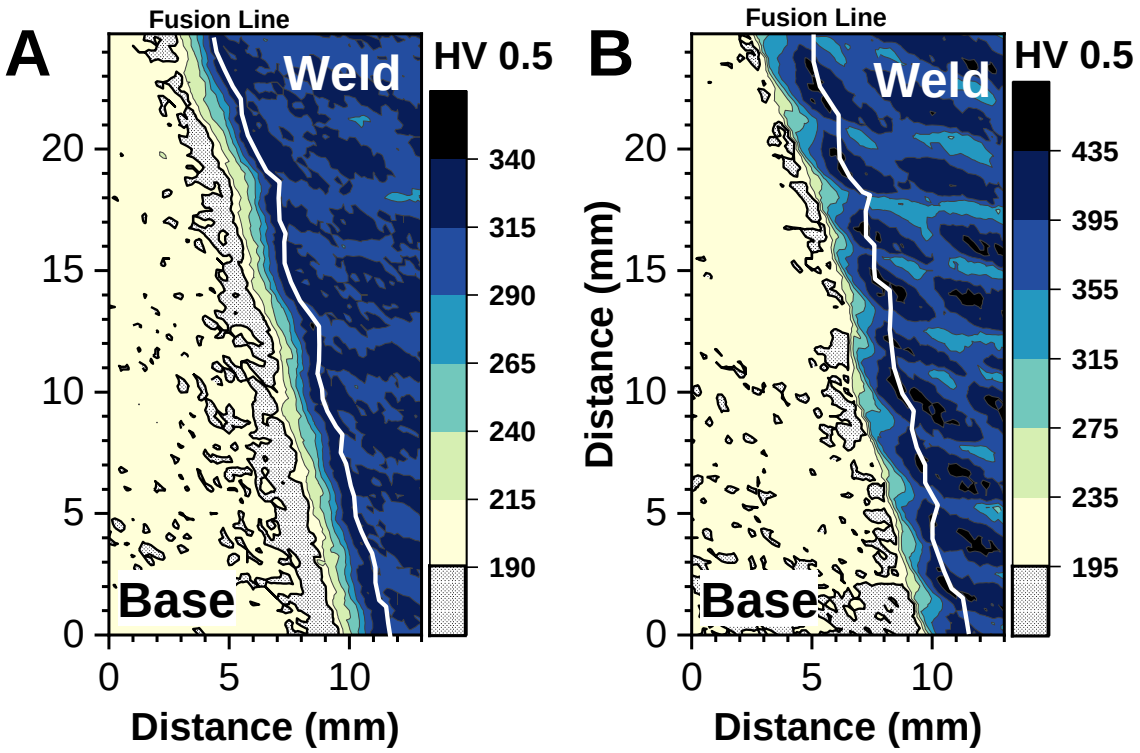

Figure 5-59. Comparison of hardness values in the post weld heat treated (675°C/2h) condition (A) and as-welded condition (B) for weld 7C (E9015-B9 matching filler metal, PWHT at 675°C for 2 hours, and martensitic parent metal TP1)
Note: *Indents consistent with soft zone outlined in black dotted regions*

One explanation for the evolution of the OTZ is associated with the complexity of the phase transformations that occur in the adjacent PTZ. Easterling explains this phenomenon, "The effect of $\delta \rightarrow \gamma \; and \; \gamma \rightarrow \alpha$ transformations with their associated latent heat changes, have been shown to produce slight 'kinks' on the thermal cycle curves..." (Easterling 1992). Supporting this statement are the data in Figure 3-10 and provided below in Figure 5-60 for a monitored, thick-section multi-pass weldment (Bauer et al. 2010). There exists a notable plateau in the data for a peak temperature approximated by the Ac_1. This temperature remains constant does not consistently change over about a 600 µm distance and the values in the HAZ, which are sustained above the maximum PWHT temperature of 790°C where tempering is expected to occur more rapidly is a comparable distance. It is thus proposed that the width of the OTZ can be explained by the latent heat of the phase transformation which serves to stabilize a temperature near the Ac_1 temperature. This results in either accelerated tempering during the welding cycle (noted in Figure 5-59B) or subsequent PWHT (such as noted in the hardness map data, Figure 5-1, Figure 5-4 and Figure 5-5).

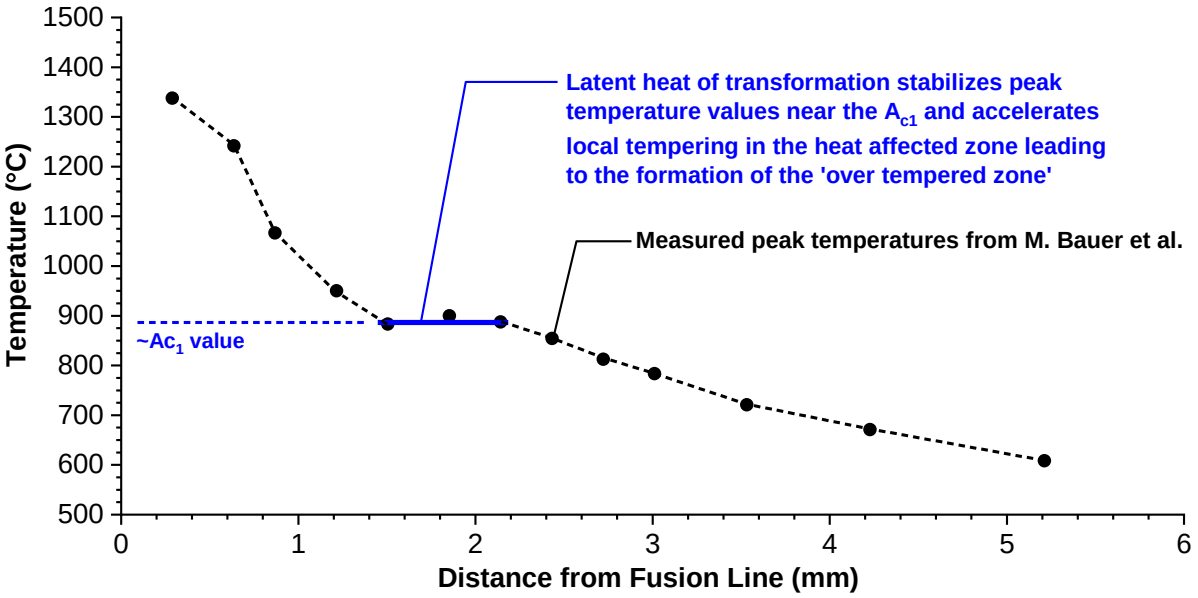

Figure 5-60. Observed 'kink' in the measured thermal history for a monitored, thick-section weldment detailed by (Bauer et al. 2010)

Association of the microstructural change moving from the unaffected parent material into the HAZ can be compared to available information for calculating the theoretical, equilibrium A_1 temperature. The theoretical A_1 temperature in Table 5-4 for each parent metal composition is calculated using two equations in the literature, and compared to the reported values in section 4.3 using ThermoCalc TCFe7 database.

Equation 5.1 (Santella et al. 2010). $A_1(°C) = 805°C + 2.5(\%Cr) + 18.1(\%Mo) + 19.1(\%Si) + 37.1(\%V) + 19.2(\%Nb) - 63.7(\%C) - 130.6(\%N) - 60.5(\%Mn) - 72.3(\%Ni)$

Equation 5.2 (Wang 2010). $A_1(°C) = 2120 - 243(\%C) - 174(\%N) + 87.5(\%Si) - 24.4(\%Mn) + 16.676(\%Cr)^2 - 271.81(\%Cr) - 365.45(\%Ni)^2 + 153.05(\%Ni) + 164(\%Mo)^2 - 299.2(\%Mo) + 1320(\%V)^2 - 570(\%V)$

Table 5-4. Comparison of theoretical A_1 and A_3 temperatures for the investigated parent materials.

Parent Metal	A_1 (°C) [ThermoCalc, Ch. 4]	A_1 (°C) [Eq. 5.1]	A_1 (°C) [Eq. 5.2]	A_3 (°C) [ThermoCalc, Ch. 4]
B2	812	815	828	850
TP1	805	808	818	840

The available methods for determining the A_1 temperaure are in generally good agreement, with a deviation of about 15°C.

In the following assessment, the experiments reported by (Gaffard 2004) for Grade 91 steel are utilized. Since welding generates non-equilibrium heating rates, the A_1 and

A_3 can be expected to shift to Ac_1 and Ac_3 values. Using ThermoCalc to assess the A_1 and A_3 for the reported composition given in Gaffard's thesis, the values are 811 and 855°C, respectively. Gaffard has considered the effect of heating rate in his experimental work and the reported data are summarized in Figure 5-61.

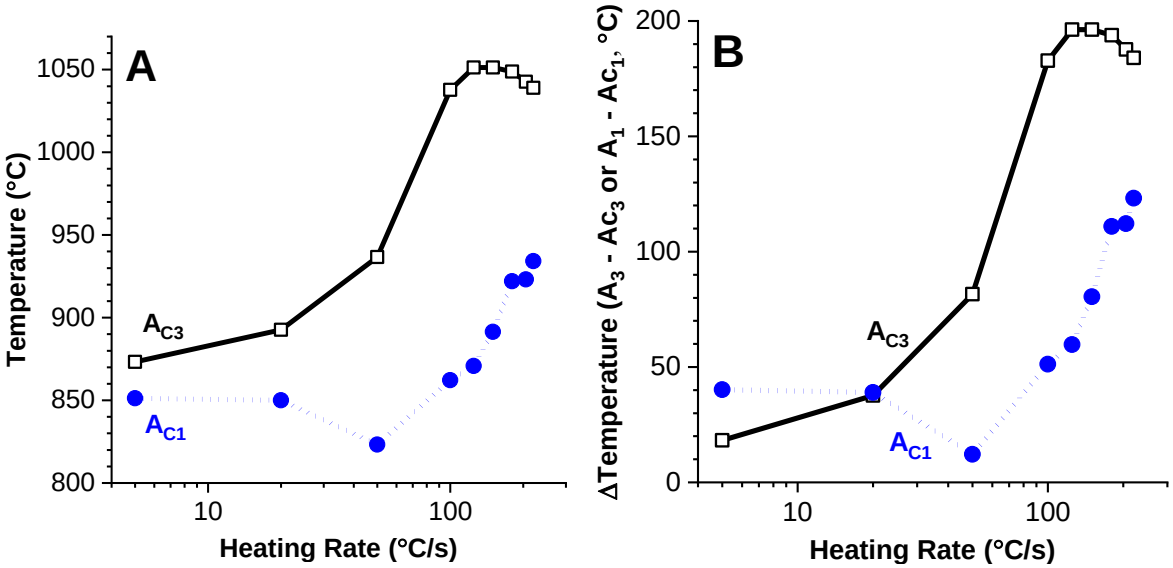

Figure 5-61. Comparison of the influence of heating rate (°C/s) on the absolute value for the Ac_1 and Ac_3 temperatures in Grade 91 steel (A) and the calculated shift in these values using the equilibrium temperature A_1 or A_3 and as a function of heating rate (B) (Gaffard 2004)

The welding thermal cycle detailed in section 3.3.4 is recreated using the open source software SmartWeld and the 1018 steel database (note: a Grade 91 database is not available in the SmartWeld software), and is shown in Figure 5-62. It is apparent that the heating rate can be expected to be of the order of 1,000°C/s. Although this rate is outside the investigated range in Figure 5-61, the shift in the Ac_1 and Ac_3 values appear to saturate for heating rates ≥100°C/s. If the shift at the 'saturation heating rate' is assumed to be ~100°C for Ac_1 and ~180°C for Ac_3, as indicated in Figure 5-61B, then the assessed values in Table 5-5 are believed to approximate the lower and upper critical temperatures in the evaluated weldments.

The absolute value for the Ac_3 reported by Gaffard appears to be considerably higher than might be expected if the shift from the A_1 to Ac_1 are representative for the A_3 to Ac_3. While the procedure for determining the reported Ac_1 and Ac_3 values is not reported in (Gaffard 2004), and it has been shown that this is potentially an important consideration (Siefert et al. 2015). Recent data generated on multiple Grade 91 steel heats and relevant to the present research suggest that the Ac_3 value for a heating

rate of ~1,000°C/s is ~980°C and thus slightly lower than the saturated value reported in Table 5-5.

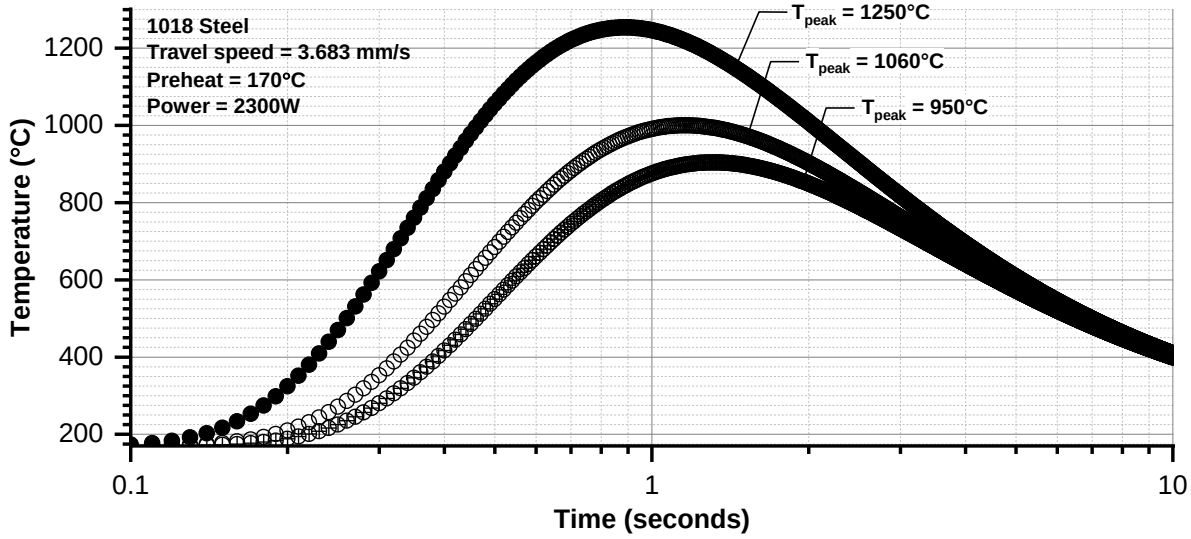

Figure 5-62. Determination of the time to reach a peak temperature of 1250, 1060 or 950°C using the correlation in SmartWeld open source software and the database for 1018 steel (SmartWeld 2016)

Table 5-5. Consideration of heating rate on the assessed Ac_1 and Ac_3 values for the investigated parent materials.

Parent Metal	Approximate A_1 (°C)	Ac_1 (°C)	Approximate A_3 (°C)	Ac_3 (°C)
B2	820	920	850	1030
TP1	810	910	840	1020

The assessment of weldments using EBSD in Figure 5-22 to Figure 5-26 and Figure 5-28 to Figure 5-32 provides perspective on the calculated peak temperature (T_{peak}) in which the microstructural change is noted. The T_{peak} values for each weldment where the microstructural change is reflected in the EBSD grain boundary maps and is summarized for each weldment in Table 5-6.

Combined information from Table 5-5 and Table 5-6 suggests there is a correlation between the microstructural change and the A_1 value (8C and RNT-B2) or the Ac_1 temperature (7C, 9C, AR-B2). The discrepancy in the observed behavior is likely a function of at least two factors: the procedure utilized to evaluate the T_{peak} value through the width of the HAZ (section 3.3.4) and the heterogeneity that exists in a multi-pass, thick-section weldment. To the later point, an exact understanding of the specific thermal history where the documented EBSD data is given in Figure 5-28 to Figure 5-33 is impossible.

Table 5-6. Consideration of the EBSD data and welding thermal cycle on the observed change in microstructure in the heat affected zone

Weld	T_{peak} (°C) where Microstructural Change in EBSD grain boundary maps is noted
7C	905
8C	800
9C	885
AR-B2	880
RNT-B2	800
F-TP1	1030

The comparison of data and selected experiments in the literature suggest more work is needed to evaluate these steels under non-equilibrium thermal cycles. In general, the balance of results show that the onset of microstructural change coincides with a temperature approximated by the Ac_1 value (~850 or 880°C for B2 and TP1, respectively) and not the A_1 value (~820°C depending on method of determination). Furthermore, if the values for the measured Ac_3 are overlaid on the microstructural images, in most cases the microstructure exhibits a visible change before this value is reached.

The width of the HAZ is summarized in Table 5-7 and will be utilized as a benchmark for future observations regarding the evolution of damage. The width of the HAZ presented by the EBSD data is sufficient to document the width of the CTZ + PTZ. For example, weld 7C is observed to exhibit a distinct change in the plotted grain boundaries in Figure 5-28 for a T_{peak} of 905°C (Table 5-6) corresponding to 1.8 mm from the fusion line. The width of the HAZ using the hardness map data is sufficient to capture the entire width of the HAZ, e.g. the CTZ + PTZ + OTZ. For this assessment the hardness map data were analyzed to provide an approximate, maximum extent of the HAZ.

For the data presented in Table 5-7, the weld 9C fabricated with a Ni-base filler material possesses a narrow HAZ width. This observation can be explained based on the lower melting temperature for the Ni-base filler material compared to the Grade 91 steel (e.g. 1395 versus 1500°C, Table 3-5). This requires lower heat input to melt the filler metal, and thus reduces the HAZ width. In general, the PWHT'ed weldments exhibit the widest HAZ, particularly since the OTZ is more developed. The exception to this observation is the F-TP1 weldment which is observed to possess a narrow HAZ. In this context, the 'narrow HAZ' in the F-TP1 weldment is defined by the reported

characterization techniques which did not observe a marked change in microstructure until a peak temperature of ~1030°C was noted.

Table 5-7. Comparison of the heat affected zone (HAZ) width for data generated using electron back scatter diffraction (EBSD) and hardness mapping

Weld	Width of HAZ, EBSD (μm) [CTZ + PTZ]	Width of HAZ, hardness (μm) [CTZ + PTZ + OTZ]
7C	1,800	4,000
8C	<1,800	3,000
9C	1,200	2,000
AR-B2	1,800	4,500
RNT-B2	2,200 to 2,600	4,500
F-TP1	1,200	N/A

Local compositional heterogentiy was observed on a macro-basis in the assessment of the weld 8C composition for a large micro-XRF map starting in the parent metal and moving through the HAZ and into the deposited weld metal. Dilution between the AWS type -B8 filler metal and the parent metal was noted for the first layer deposited against the machined groove, particularly for elements like V which are not intentionally added to the filler material. For subsequent weld passes there was little dilution, but segregation was noted in the weld metal. The observed segregation on a macro-scale or micro-scale may be important pending the observed damage that is devleoped in the feature cross-weld creep test samples.

Within the HAZ, compositional heterogeneity was noted in several evaluated welds. In the as-welded HAZ microstructure, ferrite grains were noted with a composition rich in Cr and Mo suggesting the decomopstion of $M_{23}C_6$ and/or Laves (Figure 5-43). As the material utilized in welds 7C, 8C and 9C was the service-exposed TP1 material, the presence of Laves phase was expected and documented in section 4.4. In the ferritic F-TP1 HAZ, extensive carbide necklacing was noted in the HAZ around formerly ferritic grains. This same structure was observed to a lesser extent in weld 7C; as these welds were evaluated in the PWHT condition it is not unreasonbale to assume that similar ferrite grains existed in these weldments prior to the PWHT at 675°C for 2 hours.

5.9 Summary

Characterization of the weldments in the as-fabricated condition included assessment of hardness using large-scale mapping, macro-scale compositional mapping, local

mapping in the HAZ using SEM-EDS, SEM-EBSD through the HAZ, and linking these observations to the calculated temperature profile through the HAZ. The evaluated weldments showed considerable variability resulting from several key factors including:

- Condition of parent metal, such as ferritic versus martensitic or renormalized and tempered versus service-exposed. For the evaluated service-exposed material, the presence of Laves phase may contribute to the stabilization of ferrite in the HAZ. However, Laves phase was present inside some ferrite grains in the HAZ suggesting that $M_{23}C_6$ decomposition was the dominant factor in the observed ferrite grain formation.
- Selection of welding consumable can change the width of the HAZ. For example, the use a Ni-base filler metal with a lower melting temperature reduced the width of the HAZ whether the CTZ, PTZ and/or OTZ were considered in the assessment.
- In the as-welded or PWHT condition clear differences in the observed features in the HAZ were noted, such as the presence of ferrite grains in the as-welded condition or carbide necklacing around ferrite grains (or the lack of ferrite grains altogether) in the PWHT condition.

Important conclusions in this section are summarized as follows:

- The formation of a soft zone in the HAZ is not linked to the classical descriptions for regions in the HAZ such as the ICHAZ or FGHAZ. The soft zone is best described as an over-tempered zone (OTZ) consistent with the definition in Table 1-4.
- The formation of the OTZ is most realistically linked to the complexity of the phase transformations that occur in the PTZ. It is rationalized that these phase transformations, particularly the $\gamma \rightarrow \alpha$ transformation result in a latent heat of transformation that can stabilize relatively high temperatures near the Ac_1 over a substantial length beyond the PTZ.
- EBSD effectively quantifies the abrupt change in the HAZ associated with the PTZ. This occurs at a calculated peak temperature that is approximated by the A_1 or Ac_1 for the investigated materials and weldments. Disagreement as to the

exact temperature is a function of the utilized equations to estimate this temperature, the rationale used to estimate the Ac_1 and the variability that exists in the selection of a suitable location for the evaluation in multi-pass weldments.

- Composition heterogeneity exists on a macro- and micro-level which were characterized for selected weldments using micro-XRF and SEM-EDS, respectively. The contribution of this heterogeneity will be evaluated in following chapters where attempts are made to link microstructural features to the accumulation of damage.

Future chapters, particularly Chapter 7, will build on the as-fabricated assessment to link the macro-damage observations to key findings provided in this section. This link will provide a basis for consolidation of efforts in Chapters 8 and 9 which will focus on the identification of specific features in the microstructure linked to the formation of damage.

6 Influence of Parent Metal Deformation and Damage Resistance on Cross-weld Creep Performance

6.1 Introduction

Previous chapters have provided a context for the selection of materials and test conditions (Chapter 4) and the assessment of each weldment in the as-fabricated condition (Chapter 5). This chapter begins with a review of the parent material composition and condition before detailing the mechanical test results for each parent material and fabricated weldment. The primary objective of this chapter is to characterize the mechanical response of the evaluated materials and the discussion emphasizes the contribution that the parent material deformation and damage response has on feature cross-weld creep test behavior. The time-dependent, systematic test program is assessed through analysis of the strain versus time data, including the shape of the curve, post-test macro-ductility, comparison to available databases using the Larson Miller parameter (LMP) relationship, and perspective on damage tolerance using the lambda parameter. The evaluation of the data will provide a clearer context in which to analyze the failure response and location of failure in each sample in Chapter 7.

6.2 Review of Parent Materials

The parent materials investigated in this research are limited to two heats of Grade 91 steel (see Chapter 4 for full details regarding the in-service operation of the component and complete chemical composition). The two heats of material, as shown in Table 6-1, possess clear differences in commonly referenced embrittlement factors, particularly in relation to the composition of minor elements, which are used to rank the susceptibility of heat-specific behavior. Equations for widely utilized factors for assessing low alloy steels or martensitic steels are given below:

Equation 6.1. $\text{J Factor (Watanabe Factor)} = (\text{Mn} + \text{Si}) \times (\text{P} + \text{Sn}) \times 10^4\ [\text{wt.\%}]$ (Watanabe et al. 1980)

Equation 6.2. $\text{Mod. J Factor} = (\text{Mn} + \text{Si}) \times (\text{P} + \text{S} + \text{Sb} + \text{Sn} + \text{As}) \times 10^4\ [\text{wt.\%}]$ (Mayer 1991)

Equation 6.3. $\text{X factor (Bruscato Factor)} = \frac{(10\text{P} + 5\text{Sb} + 4\text{Sn} + \text{As})}{100}\ [\text{ppm}]$ (Bruscato 1970)

Equation 6.4. $\text{Creep Embrittlement Factor (CEF)} = \text{P} + 3.57\text{Sn} + 8.16\text{Sb} + 2.43\text{As}$ (King 1980)

Equation 6.5. $\mathrm{SUM} = \mathrm{As} + \mathrm{Sn} + \mathrm{Sb}\ [\mathrm{wt.\%}]$ (EPRI 2014a)

Equation 6.6. $\text{Nitrogen to Aluminum Ratio} = \frac{\mathrm{N}}{\mathrm{Al}}\ [\mathrm{wt.\%}]$ (Brett 2008)

The data in Table 6-1 show that the B2 parent steel used to fabricate the AR-B2 and RNT-B2 weldments has a higher value for all calculated embrittlement factors and a lower N/Al ratio compared to the TP1 and F-TP1 parent material. It may thus be suspected that the susceptibility to damage for the weldments in AR-B2 and RNT-B2 is potentially greater; the extent and nature of the developed damage in the cross-weld creep samples is quantified in Chapter 7. The N/Al value for both steels is not ideal, e.g. ~≤2 and according to data in (Brett 2007 and Komai et al. 2017) this ratio should be >4. No guidance is given for the other embrittlement factors in material specifications although for low alloy steels the J-factor or X-factor are desired to be in a maximum range of 90 to 150 or 12 to 15, respectively (ArcelorMittal USA 2013). The X-factor, commonly specified for welding consumables, is routinely specified for ferritic steels to values <15. The condition of the parent materials in the evaluated state (for uniaxial, plain bar tests and feature, cross-weld tests) is reviewed in Table 3-2.

Table 6-1. Comparison of common embrittlement factors for the investigated parent materials in this study

Material	N/Al	J Factor	Mod. J Factor	X Factor	CEF	SUM
AR-B2, RNT-B2	1.1	147.6	345.2	14.6	8.7	0.0231
TP1, F-TP1	2.1	36.5	159.4	13.9	3.8	0.00783

Table 6-2. Heat treatment procedures for the parent material prior to fabricating weldments.

Designation	Microstructure	Condition	Heat Treatment
AR-B2	Tempered Martensite	Ex-service	Service-exposed at 570°C for 79,000 hours
TP1	Tempered Martensite	Ex-service	
RNT-B2	Tempered Martensite	Renormalized and Tempered	1065°C/0.5h/AC 765°C/2h/AC
F-TP1	Ferritic	Fully ferritic	950°C/0.5h cool at 100°C/h to 760°C/2h/AC

The parent metal microstructure was assessed using electron backscatter diffraction (EBSD) in Figure 6-1 (image quality maps) and Figure 6-2 (auto grain map). The AR-B2 and RNT-B2 steels are shown to possess a tempered martensitic microstructure

with a PAG diameter of about 20 µm. The TP1 material exhibits a tempered martensitic microstructure, but the PAG diameter is much larger and >100 µm. The substructure inside each grain is thus coarser and elongated relative to the AR-B2 and RNT-B2 materials. The F-TP1 has a ferritic microstructure with a grain size of ~50 µm with no substructure. The set of heat treatments reviewed in Table 6-2 are confirmed to have achieved the objectives to evaluate materials with an expected variability in deformation and damage resistance. This behavior is overlaid on a previously introduced matrix, Figure 6-3.

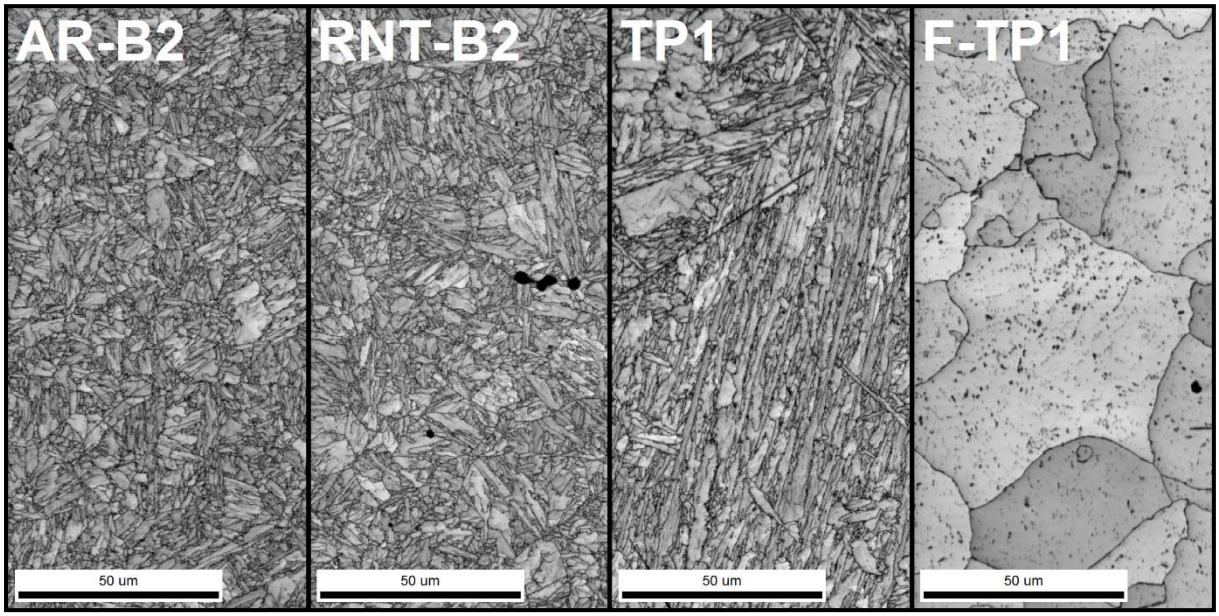

Figure 6-1. Electron backscatter, image quality map for grain boundaries with misorientation of 2-180° for the investigated parent materials

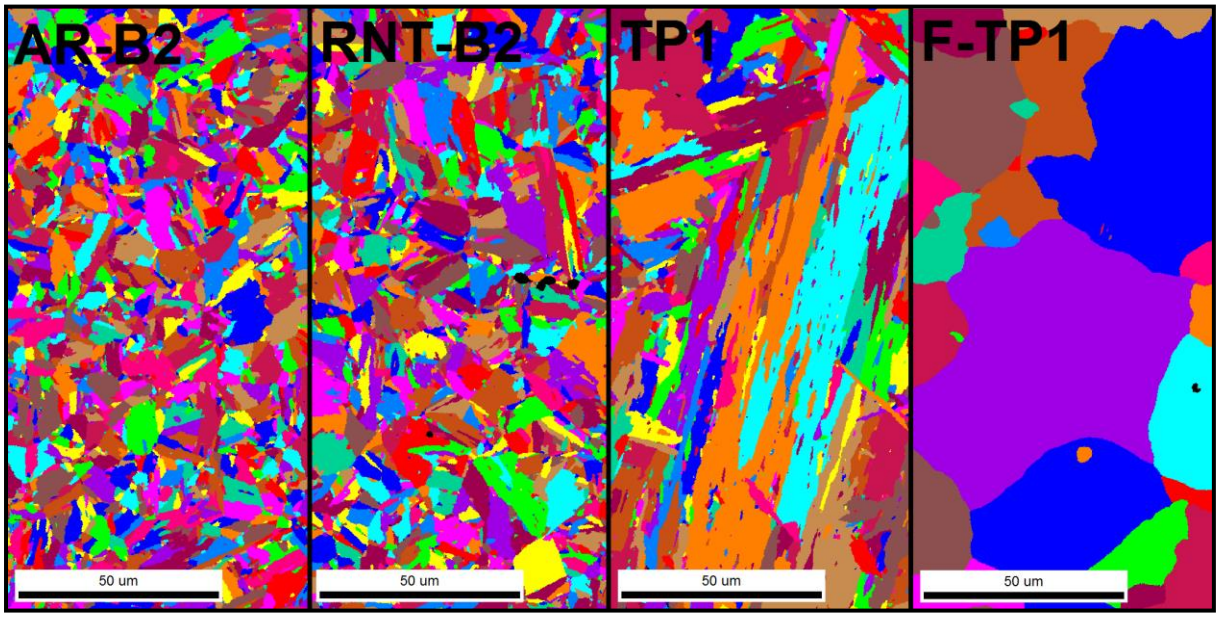

Figure 6-2. Electron backscatter, auto grain map for each of the investigated parent materials

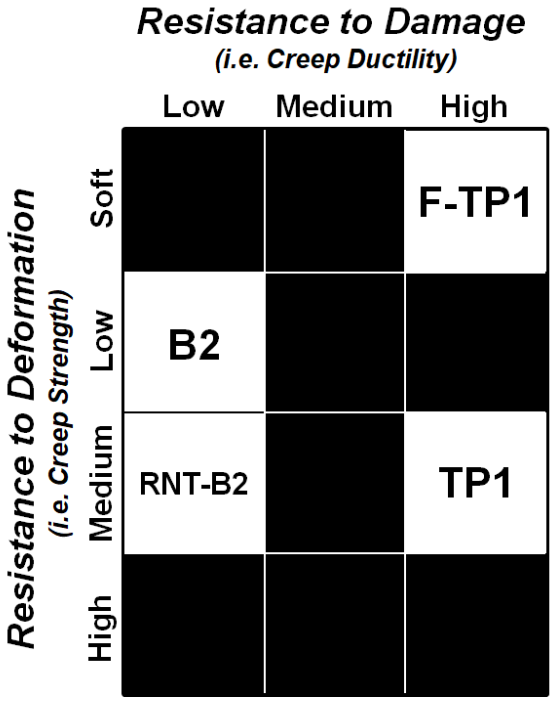

Figure 6-3. Parent metal creep behavior, as assessed in the strength-ductility matrix
Note: *under-matching, matching and over-matching filler materials were used to make a total of three weldments in TP1*

6.3 Parent Metal Creep Behavior

To ensure the expectation of parent metal behavior was realized through the combination of ex-service and reheat treated material, it was necessary to evaluate the performance in uniaxial, plain bar creep tests. The tests were performed at two test conditions; for the martensitic parent metal, a typical screening test condition of 625°C and 100 MPa was utilized. The applied stress at this temperature is too high for the ferritic, F-TP1 material as it is close to the yield stress. Thus, a reduced stress value of 60 MPa was employed and will be rationalized in a later section in this Chapter. Performance for the four parent materials was evaluated with respect to deformation and damage resistance. The results for parent metal creep tests are given in Table 6-3; the times to failure are compared in Figure 6-4; and the cross-sectional area upon failure is compared in Figure 6-5.

Regarding the RNT-B2 and TP1 material performance, the failures in the plain bar uniaxial tests lie within the bounds given for minimum and mean material. The AR-B2 material lies at the minimum bound and the F-TP1 material lies at the minimum bound for ‘soft’ Grade 91 steel. As time-temperature-parameter relationships do not consider ductility, the values provided in Figure 6-4 cannot account for the potential effect that

stress-state may have on cross-weld creep performance. The reported ductility values vary significantly as illustrated in Figure 6-5; this is true for materials which are martensitic and exhibit very similar times to failure and minimum creep rates (e.g. RNT-B2 and TP1).

Table 6-3. Parent metal creep test results for plain bar uniaxial tests at 625°C

Sample	Stress (MPa)	Time to Failure (hours)	Elong. (%)	ROA (%)	Minimum Creep Rate (%/h × 10^{-4})	λ
AR-B2	100	1,083	15.9	26	28.4	5.2
RNT-B2	100	3,360	10.5	15	7.43	4.2
TP1	100	2,950	26.0	83	6.89	12.8
F-TP1	60	1,828	37.1	90	94.8	2.1

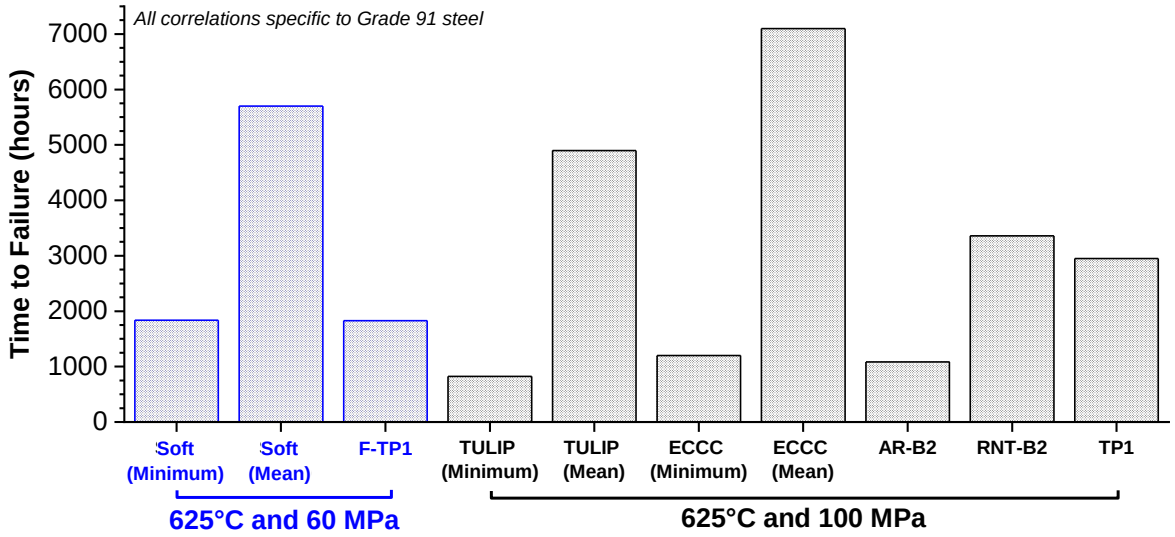

Figure 6-4. Comparison of the time to failure for the investigated parent materials F-TP1, AR-B2, RNT-B2 and TP1 to known material relationships for minimum and mean bounds (EPRI 2013c)

The strain-time behavior in Figure 6-6 is normalized for both strain and time in Figure 6-7 to facilitate comparison of the shape of the creep curve. The behavior in Figure 6-6 is similar for each material in that a very short and minimum amount of primary creep is observed before reaching a steady state (F-TP1) or pseudo steady-state region (AR-B2, RNT-B2 and TP1). While the times to failure are notably different, the amount of tertiary creep and the recorded strain at failure is very different for the comparison presented in Figure 6-6 and Figure 6-7. This observation is partially

accounted for by the lambda calculation documented in Table 6-3 using Equation 2.7 (e.g. $\lambda = \frac{\varepsilon_f}{\dot{\varepsilon}_{min} \times t_r}$).

The observed behavior in the normalized plot in Figure 6-7 provides an interesting perspective. Because for this dataset the TP1 material exhibits high strength and good creep ductility, the normalized behavior is removed from the other data (e.g. to the lower right-hand region of the chart). The two martensitic steels AR-B2 and RNT-B2 are biased to the F-TP1 data not because of low creep strength, but because of the relatively low elongation. The F-TP1 data, although exhibiting good ductility, possess very low creep strength, hence the relative grouping of the AR-B2, RNT-B2 and F-TP1 data.

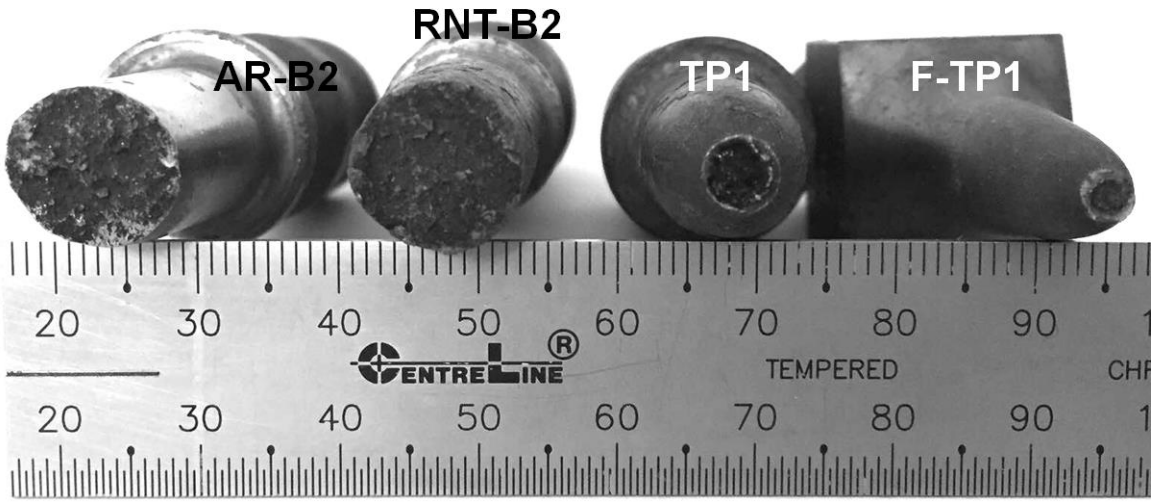

Figure 6-5. End-on view of creep ductility for parent metal plain bar creep tests

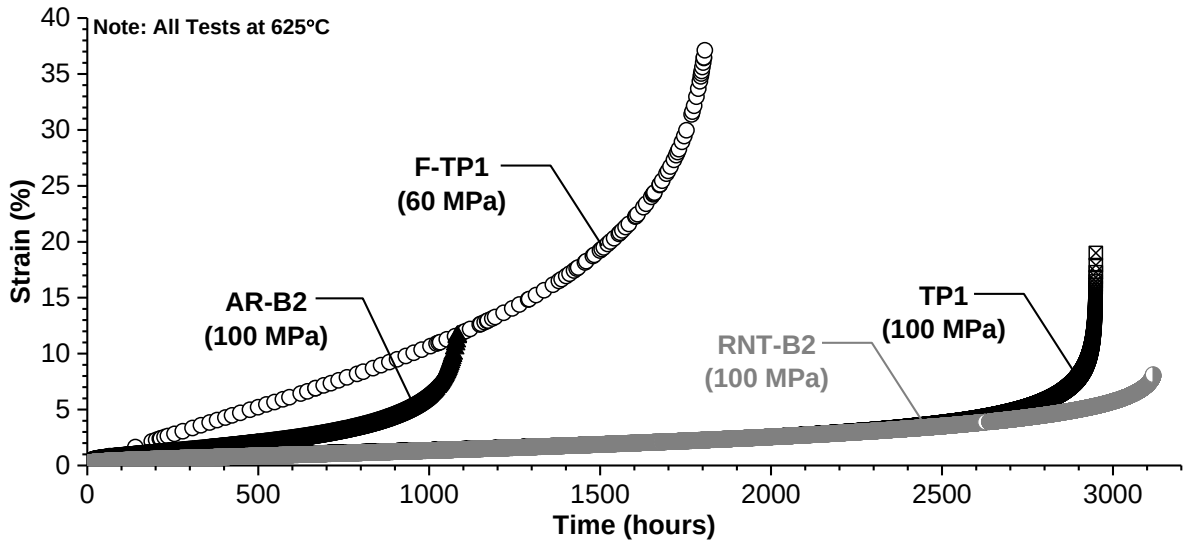

Figure 6-6. Strain versus time behavior for parent metal plain bar uniaxial tests for tests conducted at 625°C

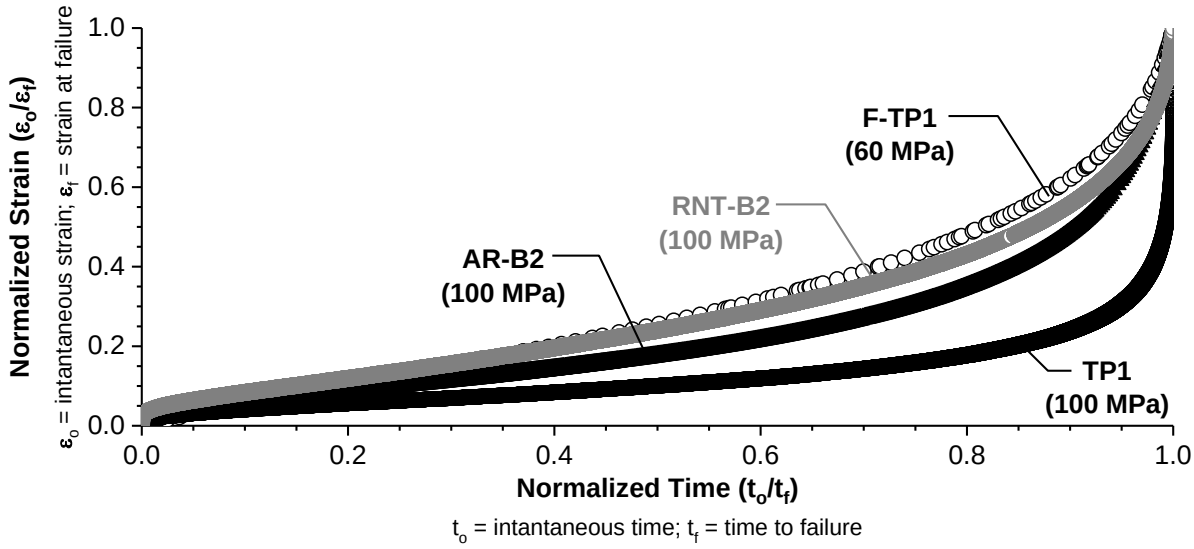

Figure 6-7. Normalized strain versus time behavior for parent metal plain bar uniaxial tests

Figure 6-8 and Figure 6-9 provide a comparison of the strain rate behavior against time or strain, respectively. For the F-TP1 material, a constant and uniform increase in the strain is noted with time; this behavior is further reinforced in Figure 6-8 and Figure 6-9 where the minimum creep rate remains relatively unchanged with time until very high strain values are reached (e.g. ~10%). In this regard, the martensitic parent materials pass through a minimum creep rate while the F-TP1 exhibits a steady state creep rate. The martensitic materials showed a decreasing strain rate with time until a threshold strain value of about 1.5% is achieved, after which the strain rate is observed to increase dramatically. Comparison of the RNT-B2 and TP1 data in Figure 6-6 to Figure 6-9 show similar behavior, although these materials exhibit marked differences in creep ductility (whether assessed as elongation, ROA or λ).

The ductility of the failed parent metal creep samples is shown macroscopically in Figure 6-5 and for the mounted cross-sections in Figure 6-10. It is apparent that the samples which exhibit low ductility AR-B2 and RNT-B2 have a higher density of creep voids. In contrast, the TP1 and F-TP1 failures exhibit classic cup-and-cone failures and it is likely that the limited amount of damage in these cross-sections is a result of local tearing around inclusions near to the end of failure. The extensive necking in these samples locally increases the stress further promoting the development of very localized damage.

Based on the parent metal creep deformation and damage susceptibility, the investigated parent materials have been placed into the risk matrix in Figure 6-3. Note

that for the TP1 material, multiple weldments were made which included under-matching, matching and over-matching filler material. In this context, 'matching' is defined on an approximate strength-basis with respect to the parent metal. Thus, the over-matching filler material is the Ni-base filler metal ERPI P87, the matching filler material is AWS Type -B9 filler metal and the under-matching filler metal is AWS type -B8 filler metal. This assessment of parent metal creep performance supports the placement of each parent material in the matrix in Figure 6-3. The remaining set of results will detail the cross-weld creep behavior.

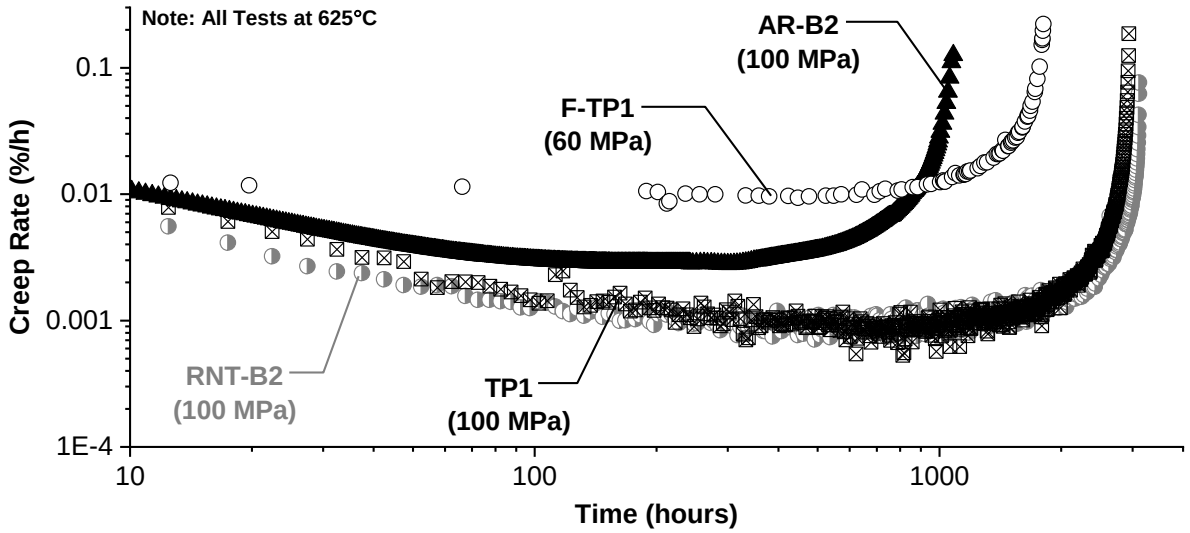

Figure 6-8. Time (hours) and minimum creep rate (%/h) at 625°C for the parent materials of interest

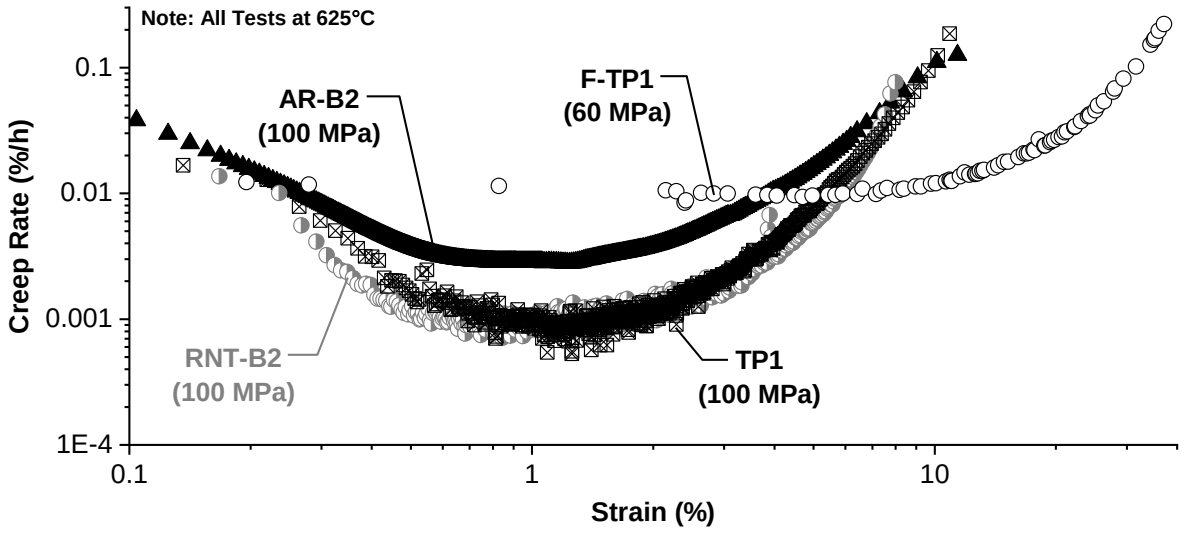

Figure 6-9. Strain (%) and minimum creep rate (%/h) at 625°C for the parent materials of interest

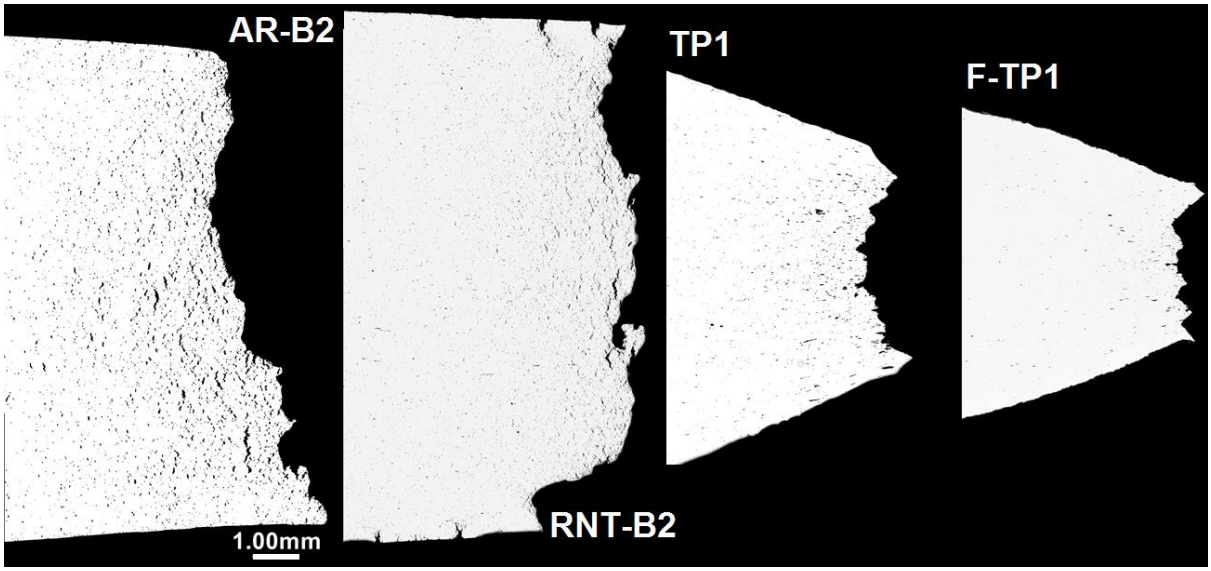

Figure 6-10. Macro, cross-section assessment of creep damage for parent metal plain bar creep tests

6.4 Feature Cross-weld Creep Results

The benefit of using a feature cross-weld creep test geometry and the selection of test conditions was summarized in sections 4.5 and 4.6. A complete set of results for the feature cross-weld creep tests are provided in Table 6-4. This test program achieved 146,500 total hours of testing and except for the matching weldment in TP1 (weld 7C) there were three or more tests per weldment, including the evaluation of an applied stress value that is representative of a realistic hoop stress value for a modern, in-service piping system (e.g. 50 or 60 MPa).

The determination of failure location in Table 6-4 is based on a simple, macroscopic failure criterion and examples of the different failure-types are given in Figure 6-11 to Figure 6-13. Figure 6-11 provides an example of a parent metal dominated failure; the necking in the gauge sample is clearly away from the weld metal and HAZ. Figure 6-12 provides an example of necking and damage which is macroscopically weld metal dominated and Figure 6-13 provides an example of a HAZ dominated failure.

Table 6-4. Feature cross-weld creep test results.

Sample	Parent Metal and/or Filler Metal Details	Stress (MPa)	Temp. (°C)	Time (hours)	Min. Creep Rate (%/h)	λ	Failure Location*
AR-B2-1	AR-B2; low strength and ductility	80	625	426	5.42E-04	0.83	HAZ
AR-B2-2		60	625	1,685	7.10E-05	1.71	HAZ
AR-B2-3		80	600	1,822	9.00E-05	1.23	HAZ
AR-B2-4		50	625	4,816	1.40E-05	2.87	HAZ
RNT-B2-1	RNT-B2; medium strength and low ductility (Renormalized and Tempered AR-B2)	80	625	842	2.37E-04	1.01	HAZ
RNT-B2-2		60	625	2,596	6.15E-05	1.67	HAZ
RNT-B2-3		80	600	3,617	2.42E-05	2.54	HAZ
RNT-B2-4		50	625	6,101	1.58E-05	1.77	HAZ
F-TP1-1	F-TP1; very low strength and high ductility (Ferritic TP1)	80	625	269	4.56E-01	0.08	Parent metal
F-TP1-2		60	625	4,553	1.50E-03	1.24	HAZ; parent metal deformation
F-TP1-3		80	600	1,503	4.84E-03	1.79	Parent metal
F-TP1-4		50	625	15,472	4.60E-05	3.69	HAZ; parent metal deformation
7C-1	TP1; medium strength and high ductility	80	625	3,743	5.40E-05	1.41	HAZ
7C-2		60	625	13,201	1.50E-05	1.69	HAZ
8C-1	• TP1; medium strength and high ductility • Under-matching filler metal (e.g. 9Cr-1Mo)	80	625	1,509	6.50E-04	1.56	HAZ, weld metal damage
8C-2		80	600	5,179	1.13E-04	1.53	HAZ, weld metal damage
8C-3		60	625	4,064	2.81E-04	1.15	Weld metal, HAZ damage
8C-4		50	625	7,703	7.57E-05	2.66	Weld metal, HAZ damage
8C-5		70	600	10,461	5.27E-05	1.63	HAZ, weld metal damage
8C-6		60	600	20,234	1.27E-05	3.06	Weld metal, HAZ damage
8C-7		90	575	13,101	2.20E-05	2.37	HAZ, weld metal damage
9C-1	• TP1; medium strength and high ductility • Over-matching filler metal (e.g. Ni-base)	80	625	2,129	6.05E-05	1.56	HAZ
9C-2		80	600	8,348	1.23E-05	1.92	HAZ, isolated fusion line damage
9C-3		60	625	13,130	6.65E-06	1.41	HAZ, isolated fusion line damage

***HAZ = heat affected zone**

Figure 6-11. Example of parent metal dominated failure (sample F-TP1-3)

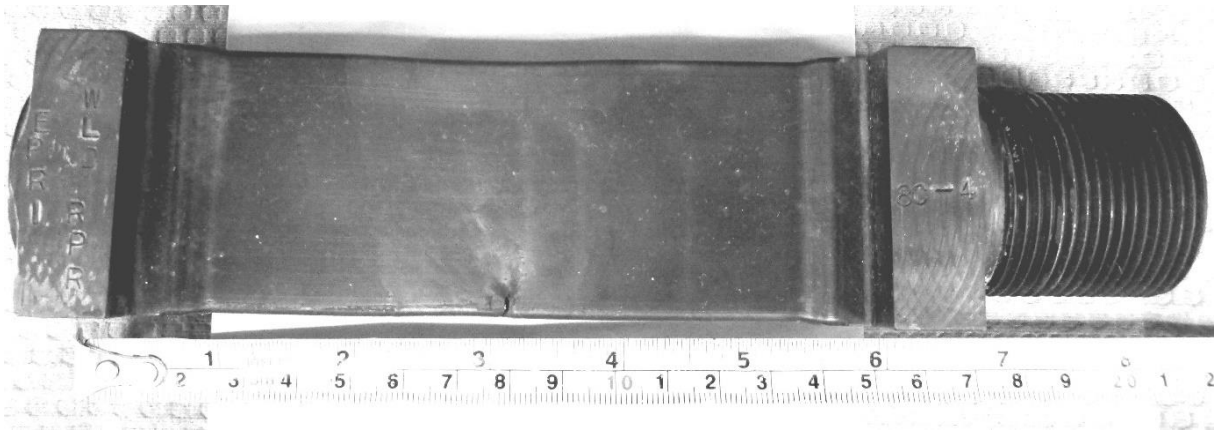

Figure 6-12. Example of a weld metal dominated failure (sample 8C-4)

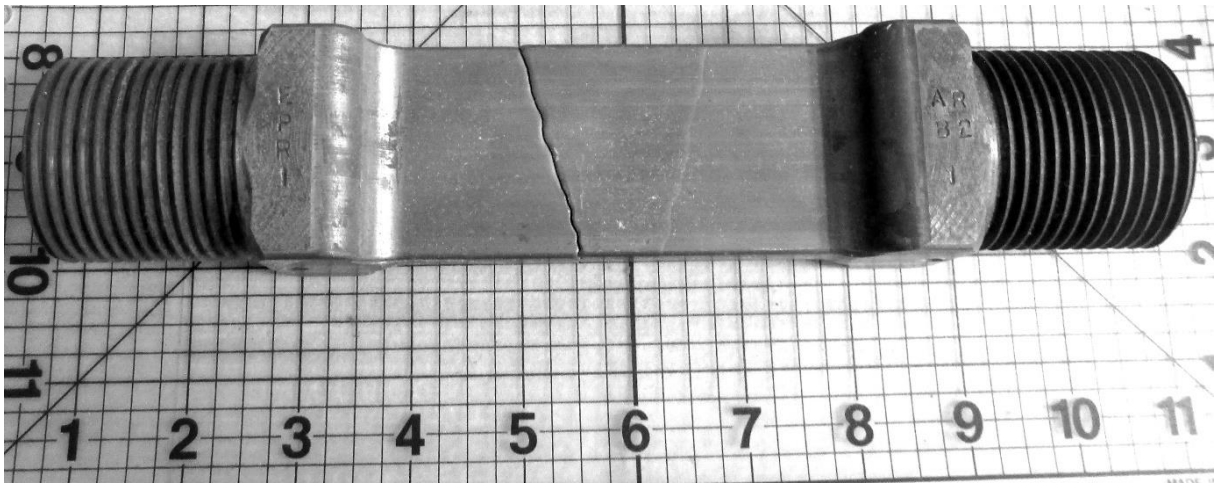

Figure 6-13. Example of a heat affected zone dominated failure (sample AR-B2-1)

Comparisons of the strain versus time data are detailed for the two common test conditions of 625°C and 80 MPa (Figure 6-14) and 625°C and 60 MPa (Figure 6-15) that were used to assess the six investigated weldments. For five of the six weldments,

supplementary results were generated using test conditions optimized from the initial set of results; the strain versus time data are not provided for these additional tests.

The comparisons in Figure 6-14 and Figure 6-15 are plotted on an unconventional logarithmic strain y-axis as the total strain accumulated in the F-TP1 and under-matching weldment in TP1 (weld 8C) is approximately an order of magnitude greater than for the balance of the evaluated weldments. In this regard, it should be emphasized that only the F-TP1 and 8C series of tests exhibited an appreciable structural, tertiary creep response in the strain versus time data.

The balance of the cross-weld tests where the parent material was martensitic and the filler material was matching or over-matching failed with very little appreciable tertiary creep. This reality is reflected in most of the short-term tests where the test could not be terminated prior to failure. For the longer duration tests, the onset of tertiary creep was noted in the best case after ~95% life and such tests are terminated before plastic tearing ruined the potential for an informative evaluation of damage in its advanced state.

Assessment of the lambda parameter was performed using the methodology provided in section 2.4. The cross-weld creep test strain versus time data contained a large amount of primary creep and this was subtracted from the final strain at failure in a manner consistent with the recommended practice in (Wilshire and Burt 2005). Determination of the minimum creep rate was in many cases approximated by a steady state creep rate where there was little deviation with increasing time, unlike the behavior for martensitic parent material data in Figure 6-8. Although it is recognized that the calculation of the lambda value for the cross-weld creep test might have some limitations, these are rationalized below.

The strain accumulation can be expected to occur in a very localized region in the HAZ. Assessment conducted by Parker and Parson for a CrMoV weld test indicated that the strain accumulation occurred over about 1 mm in the HAZ, with intense localization confined to about 0.5 mm wide band within the gauge section. For these welds, the evaluation of damage in Chapter 7 will establish the distance over which damage accumulates in the HAZ, but it is expected that this width is a fraction (e.g. a couple or few mm) of the total gauge length (125 mm).

In the results presented in Table 6-4, for some welds the strain accommodation occurred over a larger section (or fraction) of gauge length due to either weld metal deformation (as for the weld 8C tests) or parent metal deformation (e.g. F-TP1 weldment). In these cases, the partitioning of strain is more complicated due to the global nature of the deformation.

If the strain is assumed to accumulate in a narrow region in the HAZ, then the local elongation can be considered to increase. Additionally, the creep rate will also increase by a relative amount as the measured strain ($\varepsilon \propto \frac{\Delta L}{L_o}$) increases as the initial gauge length will be reduced. Since $\lambda \propto \frac{\varepsilon_f}{\dot{\varepsilon}_{min}}$, it can be expected that values for both ε_f and $\dot{\varepsilon}_{min}$ will increase proportionally and the relative value for λ will not change substantially from that calculated using the data presented in Table 6-4. When this calculation was performed assuming a gauge length of 2 mm, the values for λ did not change markedly from the reported values in Table 6-4. Furthermore, and as reported by (Goodall et al. 1975), the assessment of ductility was made for parent metal multiaxial, notch bar or hole in plate parent metal tests. The analogy here is that a metallurgical notch in a constrained, feature-type cross-weld test sample provides a similar effect to a geometric notch in a parent material.

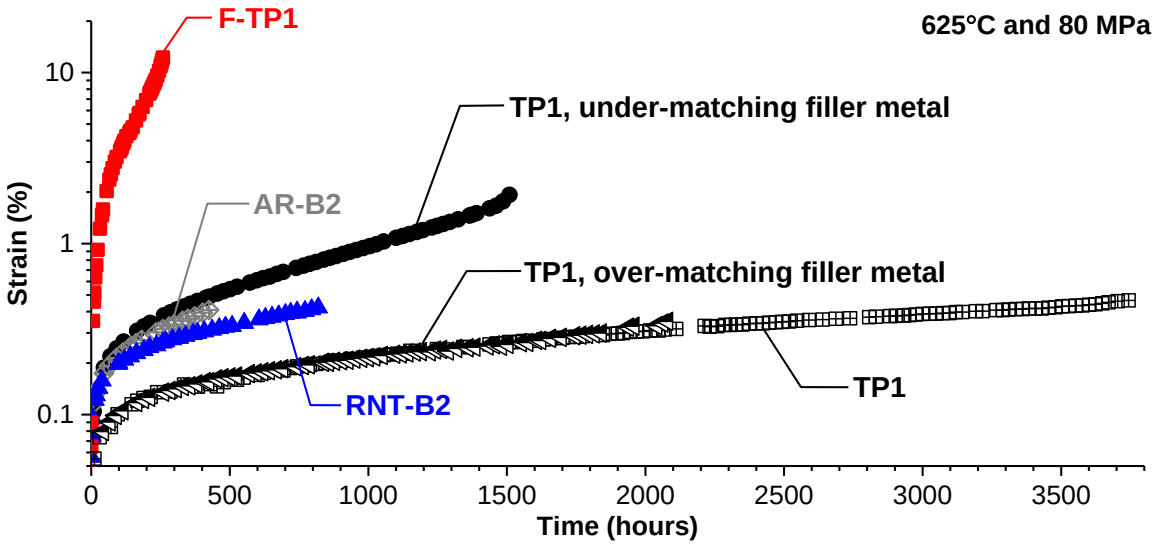

Figure 6-14. Strain versus time behavior for feature cross-weld creep tests conducted at 625°C and 80 MPa

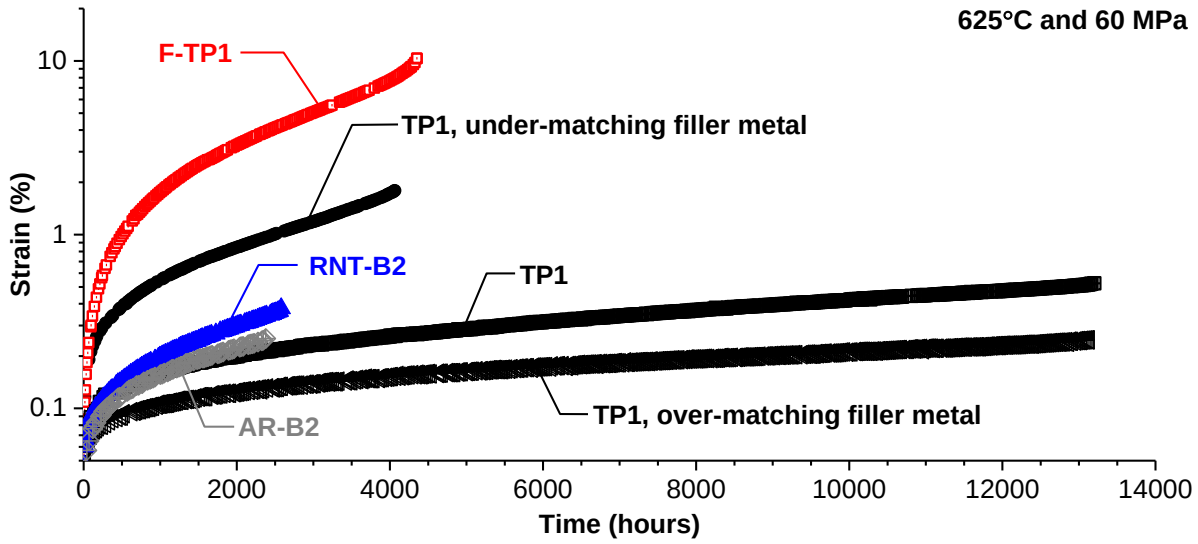

Figure 6-15. Strain versus time behavior for feature cross-weld creep tests conducted at 625°C and 60 MPa

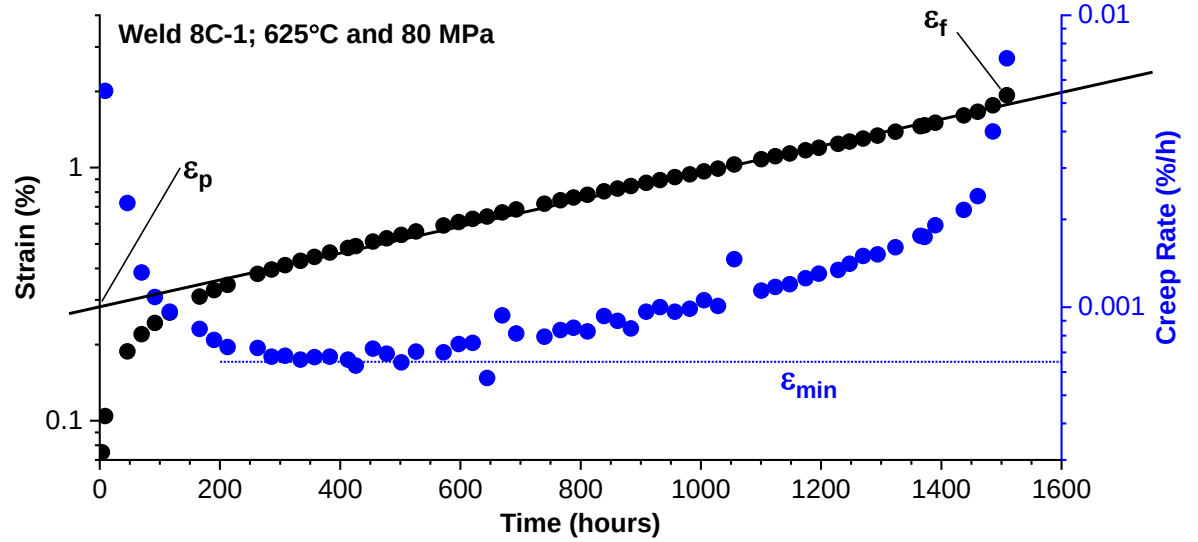

Figure 6-16. Assessment of cross-weld creep data for the data inputs needed (t_r, $\dot{\varepsilon}_{min}$, ε_f, ε_p) to calculate λ

6.5 Larson Miller Parameter Comparison

The cross-weld creep test performance assessment in this section utilizes a Larson-Miller approach, previously developed by Bell, reviewed in (Abson and Rothwell 2013) and detailed in section 4.2. Bounds for the mean, mean-20%, mean-40% or mean-50% are illustrated in Figure 6-17 and are derived from modifications of the stress value. The bounds and are plotted against an existing database for HAZ failures in Grade 91 steel (EPRI 2015g). As shown, the general minimum bound is approximated by the mean-20% line, whilst an absolute minimum bound to all data is given by the mean-40% line.

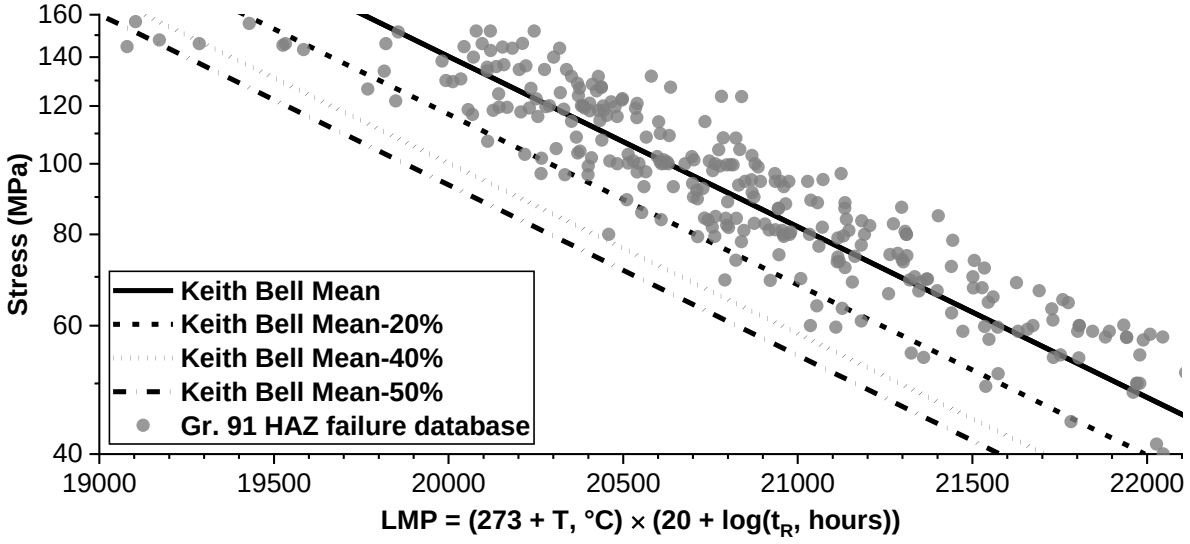

Figure 6-17. Comparison of the mean, mean-20%, mean-40% and mean-50% against a database for cross-weld creep tests in Grade 91 steel

The weldments made with matching filler material are displayed in Figure 6-18. This comparison provides perspective regarding the effect of the parent metal deformation and damage resistance (Figure 6-3) on cross-weld response. For the TP1 material, which is classified as having medium strength and high creep ductility, the cross-weld creep response slightly exceeds mean behavior. For the AR-B2 and RNT-B2 material, both of which possess low creep ductility, the cross-weld creep performance is clearly reduced from the mean-20% bound. This is significant because, as provided in Table 6-3 and Figure 6-4, the parent metal time to failure for the AR-B2 sample was slightly above the minimum bound for Grade 91 parent metal steel, while for the RNT-B2 parent material the time to failure was well-above the minimum bound. This comparison is clear evidence that the parent metal deformation characteristics alone are not a good indicator of cross-weld creep behavior.

For the F-TP1 weldment, the higher stress tests at 80 MPa are clearly the lowest performing tests in this study. For a reduced applied stress of 60 MPa the cross-weld behavior begins to merge with the mean-20% bound and for 50 MPa exceeds the minimum bound. This behavior is consistent with strain-hardening behavior and in this example, the applied test stress of 50 or 60 MPa is sufficiently low that it does not overwhelm the deformation resistance of the parent material. In the 80 MPa tests the failure mode was clearly dominated by necking in the parent metal with little or no apparent damage in the HAZ or weld metal.

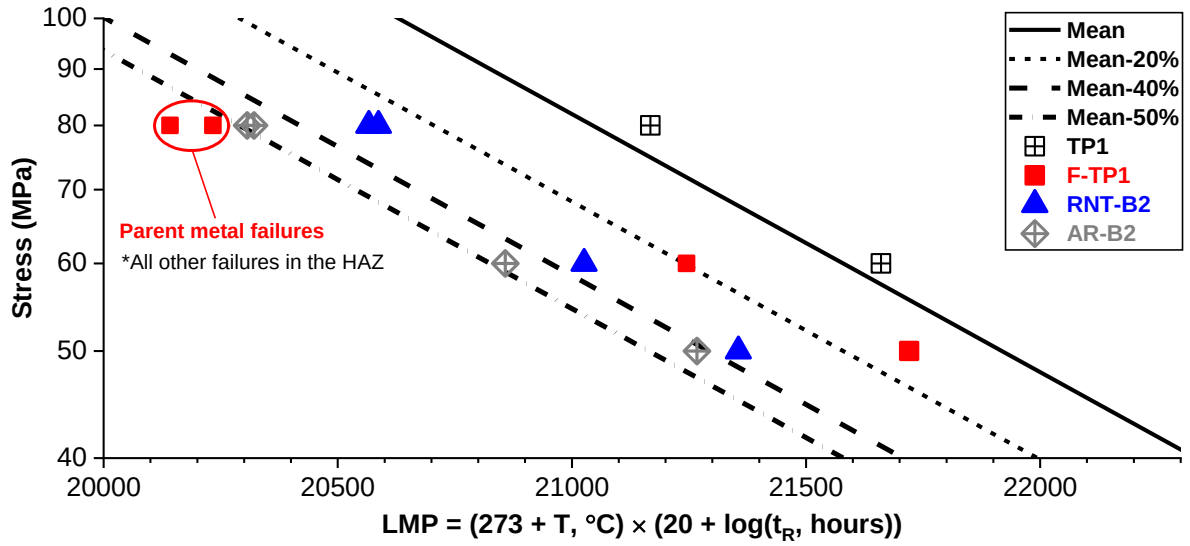

Figure 6-18. Cross-weld creep data plotted as a function of Larson Miller Parameter (LMP) and stress (MPa) for weldments made with matching filler metal (AWS type -B9 filler metal) and given a post weld heat treatment at 675°C for 2 hours
Note: *failures in F-TP1 in the parent material for 80 MPa tests; all other failures in the image were in the HAZ*

Figure 6-19 evaluates the influence of filler metal strength on cross-weld creep performance. For the under-matching filler material, the cross-weld creep tests achieve the mean-20% bound and exhibit both HAZ and weld metal damage. For the matching or over-matching filler material, the welds exceed the mean-20% line and in multiple tests achieve or slightly exceed the mean performance. The over-matching filler material at the higher stress tests (80 MPa) deviates from mean bound indicating that the over-matching weld metal may play a role in reducing the performance at higher applied stresses. The potential role that the over-matching filler material might play on a reduction in performance is questionable since even 'matching' filler material is over-matching relative to the HAZ where damage occurs. Thus, although the over-matching, Ni-base filler metal presents an extreme variation there is not convincing evidence in this study to support a dramatic reduction in behavior for failures dominated by HAZ damage (note that all the cross-weld tests for the Ni-base filler metal failed in the HAZ).

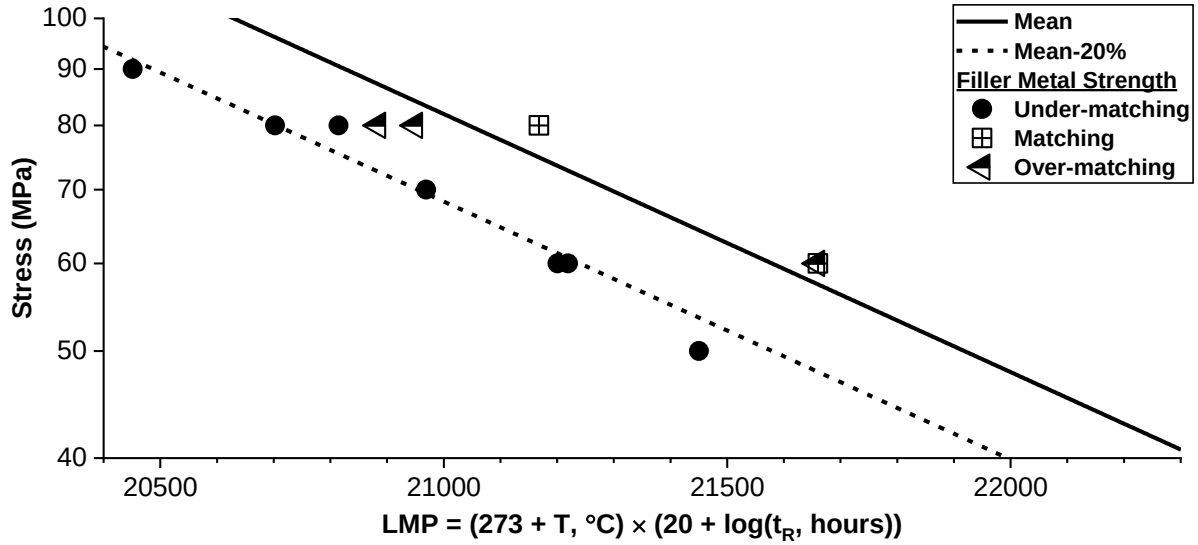

Figure 6-19. Cross-weld creep data plotted as a function of Larson Miller Parameter (LMP) and stress (MPa) for weldments made in the TP1 parent material evaluating the impact of filler metal strength on performance
Note: *under-matching = AWS type –B8 filler metal; matching = AWS type –B9 filler metal; over-matching = Ni-base (EPRI P87)*

6.6 Effect of parent metal deformation and damage resistance on observed feature, cross-weld creep behavior

The inherent deformation response in the HAZ is consistent over the applied test stress range in this study for the F-TP1 and B2 steels. At 625°C and 80 MPa, the failure time for AR-B2-1 was 426 hours, whilst for F-TP1-1 this life was 269 hours. Similarly, at 600°C and 80 MPa the failure time for AR-B2-3 is 1,822 hours while for F-TP1-3 the test duration is 1,503 hours. A key difference in this comparison is the final strain value achieved, e.g. for the AR-B2 tests a value of ~0.4% and for the F-TP1 the strain is >10%. Thus, the accommodation of strain for these two different sets of test results is very different.

The accommodation of strain in the F-TP1 tests is more global in nature, as evidenced by the general necking (Figure 6-11). For the 80 and 60 MPa tests, the general concentration of strain in the parent metal resulting a local neck is accelerated for the tests at 80 MPa (relative to the 60 MPa test) such that the test lives do not achieve the mean-20% of the scatter-band for cross-weld behavior. This result is linked to the relative ratios between the yield stress and the applied stress. The yield strength at 625°C for F-TP1 material is given in Table 6-5 and compared below:

- For an applied uniaxial test stress of 80 MPa and at 625°C, the ratio of the applied stress to the yield stress is 0.68. For perspective, the ratio between the

applied stress to the yield stress for martensitic Grade 91 steel, the ratio is 0.46 using reported tensile data in (Vallourec 1992).

- Similarly, but for an applied uniaxial test stress of 60 MPa and at 625°C, the ratio of the applied stress to the yield stress is 0.51. By comparison to the mean-20% bound for martensitic Grade 91 steel, the ratio is 0.35 using reported tensile data in (Vallourec 1992).

Table 6-5. Tensile tests at ambient and elevated temperature for the F-TP1 material*

F-TP1 Tensile Test Temp.	UTS (MPa)	YS (MPa)	Elong. (%)	ROA (%)
Ambient	502	237	32.3	70.7
625°C (1157°F)	190	118	65.4	91.4

*strain rate at yield = 0.005 mm/mm/min.

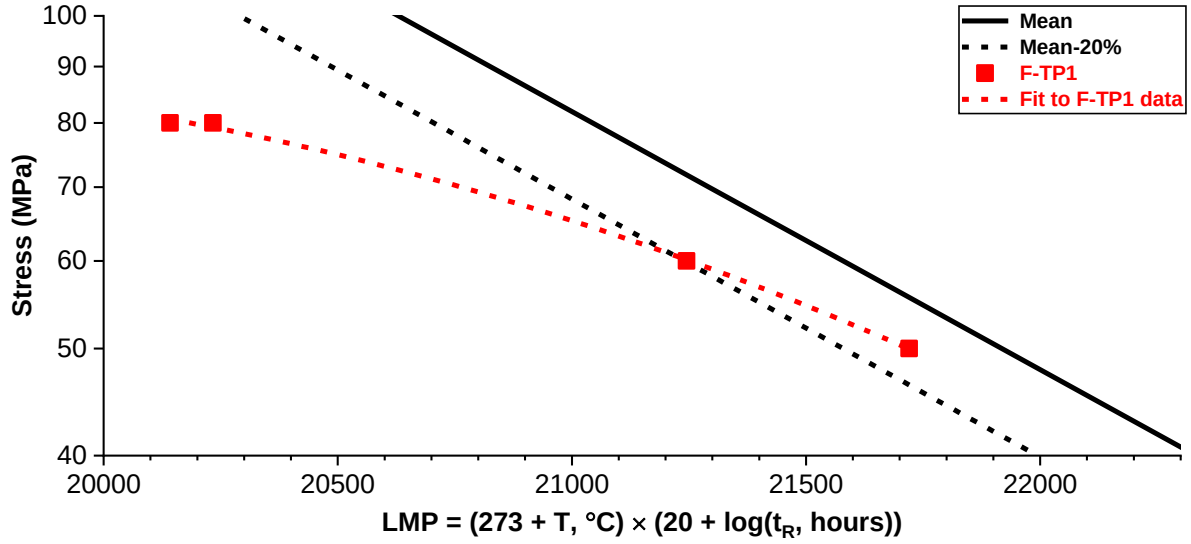

Figure 6-20. Comparison of Cross-weld creep data plotted as a function of Larson Miller Parameter (LMP) and stress (MPa) for weldments made in the ferritic parent material

Cross-weld creep testing for a material which possesses low deformation resistance (such as ferritic Grade 91 steel) needs to consider the potential effect of test conditions on observed behavior; this is discussed with respect to the uniaxial creep stress to yield stress ratio (CS:YS). Given the test conditions and parent metal constituents, the test condition of 625°C and 60 MPa in the F-TP1 results in a CS:YS value (0.51) that is approximated by the test condition of 625°C and 80 MPa for the balance of tests in the martensitic parent material (0.46). For perspective, the test conditions at 625°C, 80 MPa and F-TP1 material, the ratio of CS:YS is 0.68; this same ratio applied to

martensitic Grade 91 and for a test temperature of 625°C would result in an applied test stress of 120 MPa.

Testing at the reduced stress value of 50 or 60 MPa in the F-TP1 material not only resulted in a merging of mean-20% data (Figure 6-20), but also a migration in the failure location from the parent metal to the HAZ even despite the notable deformation in the parent metal gauge section, Figure 6-21. The results highlight both the sensitivity of parent material with low creep strength to stress state and the potential for acceptable behavior that can be achieved provided an understanding of the in-service stress is known. The damage in the HAZ appears to be crack-growth dominated and the assessment of damage in these tests will be summarized in Chapter 7.

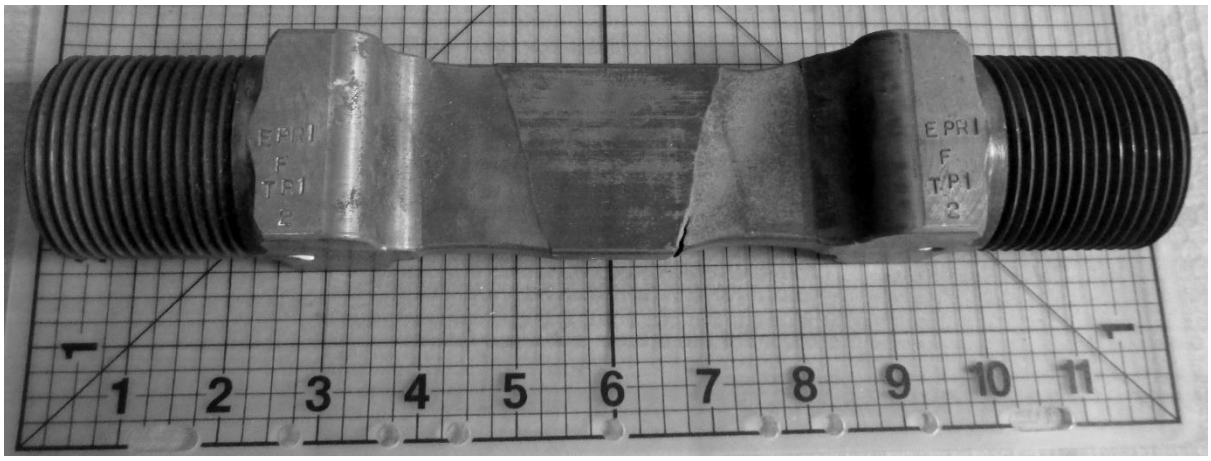

Figure 6-21. Example of parent metal dominated failure (sample F-TP1-2)

The data for the AR-B2 and RNT-B2 tests remains clearly offset from the mean-20% bound unlike for the F-TP1 tests, Figure 6-22. The improved deformation resistance, which is achieved by a renormalized and tempered heat treatment in the RNT-B2 parent material, appears to play a role in the 80 MPa tests. However, as the test stress decreases, the apparent difference in performance for the AR-B2 and RNT-B2 cross-weld tests is negligible and the trends in data are seen to merge near 50 MPa. This observation indicates that for specific stress regimes, the inherent resistance to damage in the parent material is manifested in. the HAZ. This resistance to damage cannot be modified either by a conventional, commercial heat treatment inherent in common material specifications or by the thermal cycle from welding. Furthermore, any increase in parent metal strength because of the controlled heat treatment can be expected to be undone by the welding thermal cycle resulting in an eventual reduction in behavior to the ‘weakest’ condition possible.

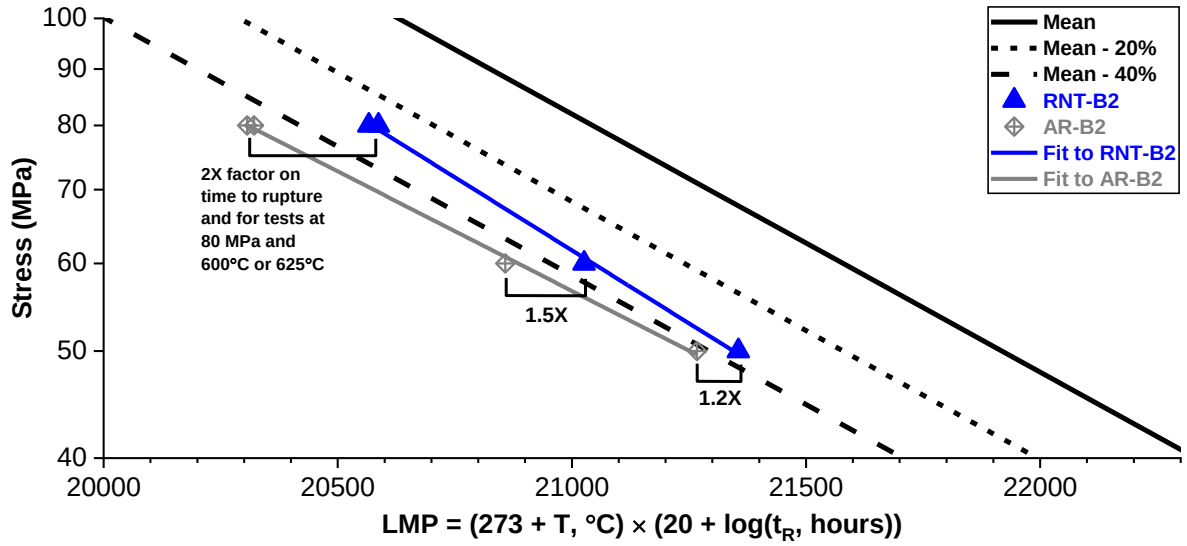

Figure 6-22. Comparison of Cross-weld creep data plotted as a function of Larson Miller Parameter (LMP) and stress (MPa) for weldments made in low ductility parent material

The macro-response of the strain versus time data is plotted in Figure 6-23 for a normalized representation of the strain and time behavior since the measurements varied by about a factor of ten for the tests of interest. With respect to the weldments made in the martensitic Grade 91 steel, and irrespective of the parent metal damage or deformation response, the behavior is identical. The onset of tertiary creep and an indication of the relative damage tolerance is only noted at the very end of the test at ~95% of consumed life. In contrast, the F-TP1 weldment shows a dramatically different response and it is observed that a consistent increase in the strain is observed after about 80% of consumed life. It is important to emphasize that whilst previous comparisons emphasize the potential impact of resistance to damage on ***when*** the test fails, the comparison in Figure 6-23 provides detail on ***how*** the test fails. In the context of component performance, there is considerable need to illustrate test results using both basic concepts; e.g. when and how structures might fail.

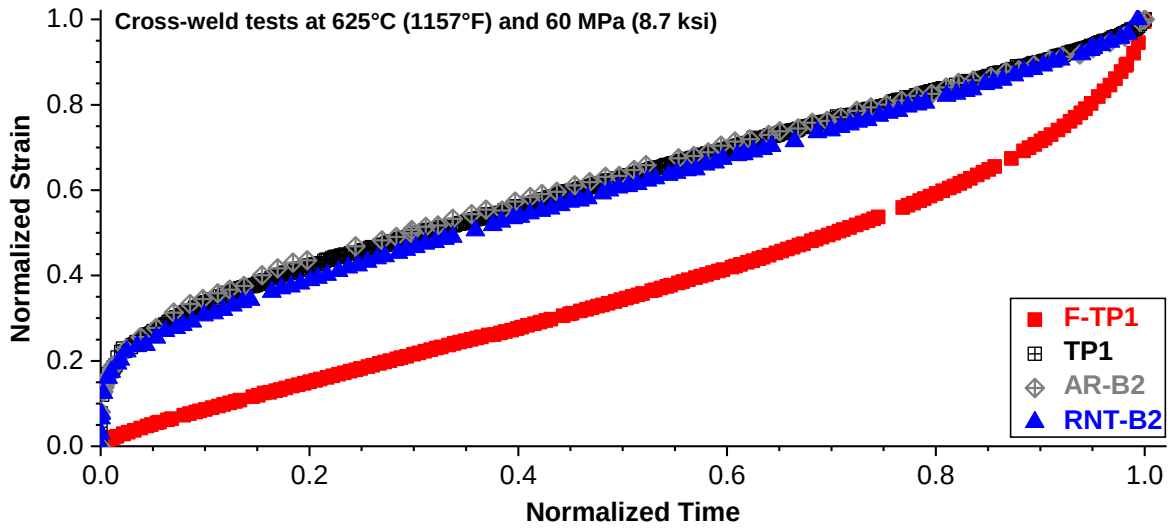

Figure 6-23. Comparison of normalized strain versus time data for selected cross-weld creep tests at 625°C and 60 MPa which evaluate the effect of parent metal deformation resistance on performance

A second comparison examining the damage tolerance of the cross-weld creep behavior is provided in Figure 6-24 for the calculated λ parameter. In all examples, $\lambda < 5$, a threshold specified by R5 and other researchers as a general demarcation for material behavior as damage tolerant or damage intolerant (e.g. see Goodall et al. 1975). This result suggests that regardless of parent metal condition, cross-weld performance for conventional weld geometries (in this study a single-vee with a 15° bevel).

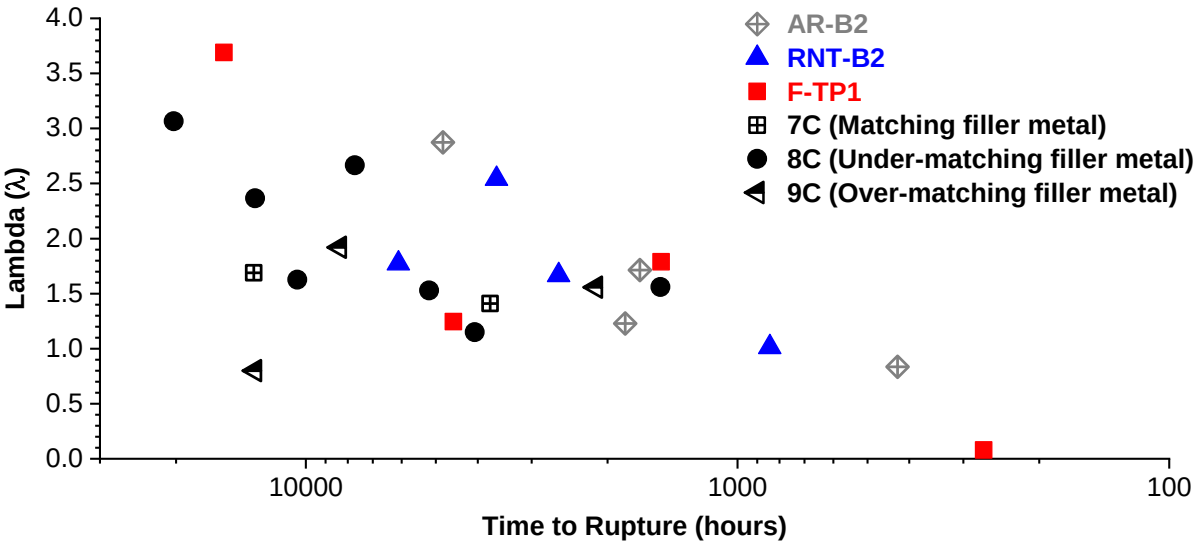

Figure 6-24. Variation in the material parameter λ as a function of time to rupture for the evaluated, feature cross-weld creep tests

6.7 Effect of Filler Metal Strength on the Observed Feature, Cross-weld Creep Behavior

The effect of filler metal strength on cross-weld creep behavior was evaluated in the TP1 material for under-matching, matching and over-matching filler materials. With respect to the under-matching filler material (weld 8C), the performance for the feature-type cross weld creep tests is compared in Figure 6-25 to data for simulated HAZ creep tests and a cross-weld creep database in Grade 91 steel. The relationship for the simulated HAZ and weld 8C data very closely follows the mean-20% bound.

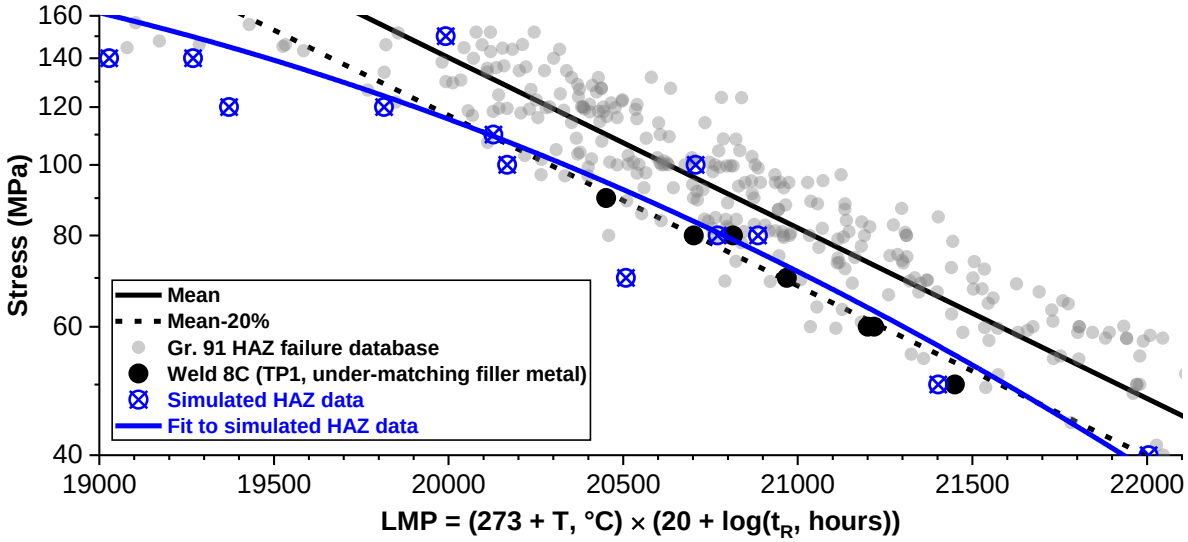

Figure 6-25. Comparison of Cross-weld creep data plotted as a function of Larson Miller Parameter (LMP) and stress (MPa) for weldment made with under-matching (black filled circles) and plotted against data in for simulated HAZ tests (blue circles) (Hongo et al. 2012 and Koukal et al. 2010)

The consistent trend for the under-matching filler material cross-weld tests which meet the mean-20% of the database can be explained based on the reduced constraint that is present because of the reduced creep strength of the filler material. A similar observation was made by Mayr is his assessment of filler metal strength in E911 cross-weld tests (Mayr et al. 2011). The utilized filler metal in weld 8C, an AWS-type -B8 consumable containing nominally 9 wt. % Cr and 1 wt. % Mo without purposeful additions of V, Nb or N, is effectively the same as the strength for the Grade 91 steel HAZ. Similar to the F-TP1 samples, this allows for more global deformation that is noted in the assessment of the strain versus time behavior (Figure 6-26) and in the macro-observations (see necking in the weld metal, centerline of gauge in Figure 6-12). This effectively reduces the constraint and does not allow the HAZ or weld metal to offload stress to the adjacent, stronger constituents and as is the case for HAZ-

dominated failures. While this might be interpreted as inferior behavior if judgment is based merely on a time to failure standpoint, the damage tolerance of the structure is increased and the normalized strain versus time behavior for test samples 8C-4 and F-TP1-2 overlap.

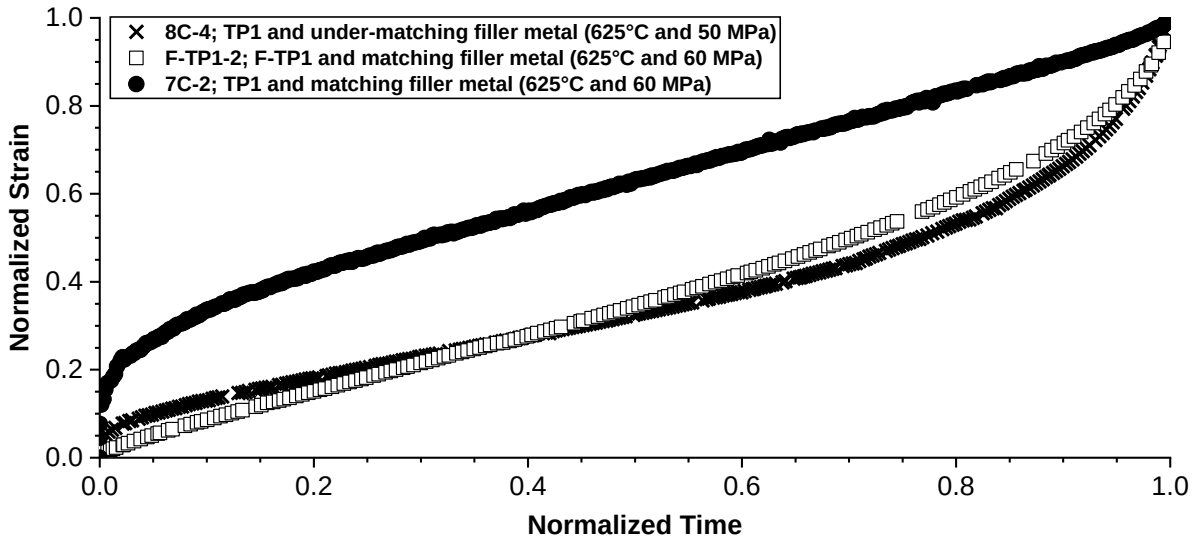

Figure 6-26. Comparison of normalized strain versus time data for selected cross-weld creep tests at 625°C and 60 MPa or 50 MPa which evaluate the composite effect of parent metal and filler metal strength on performance

As previously noted, the under-matching weldment exhibited more damage tolerance than for either matching or over-matching weldments. A set of comparisons is provided in Figure 6-27 and Figure 6-28. For Figure 6-27 and similar to that of F-TP1 in Figure 6-23, there is clear transition to tertiary creep, e.g. global deformation with the key difference being the material constituent which is deforming (e.g. for F-TP1 the constituent is the low creep strength parent metal while for the under-matching filler metal it is the 9Cr-1Mo weld metal). Like the matching weldment, the over-matching filler metal shows a similar effect where tertiary creep is only noted at the end of life. For the over-matching case, this response may be even more pronounced as there is effectively no indication of failure until the end of life, Figure 6-28.

As the Ni-base weld metal is over-matching to the Grade 91 steel parent metal and might be considered *very over-matching* to the PTZ for the assessed test conditions, it is not unreasonable to expect the weld metal to be offloaded with much of the stress, thereby maximizing the constraint on the HAZ. In this study, and for the lower stress tests at 60 MPa, the failure time for the matching and over-matching tests was identical. For the higher stress tests at 80 MPa and either 600°C or 625°C, there is no

supporting evidence for a slight acceleration of damage evolution. However, the tests are still well within reason, e.g. within the mean-20% and mean of the cross-weld creep scatter-band. It is not known if failures would have been further accelerated by a higher stress test above 80 MPa and if the parent metal pedigree would further accelerate the development of damage.

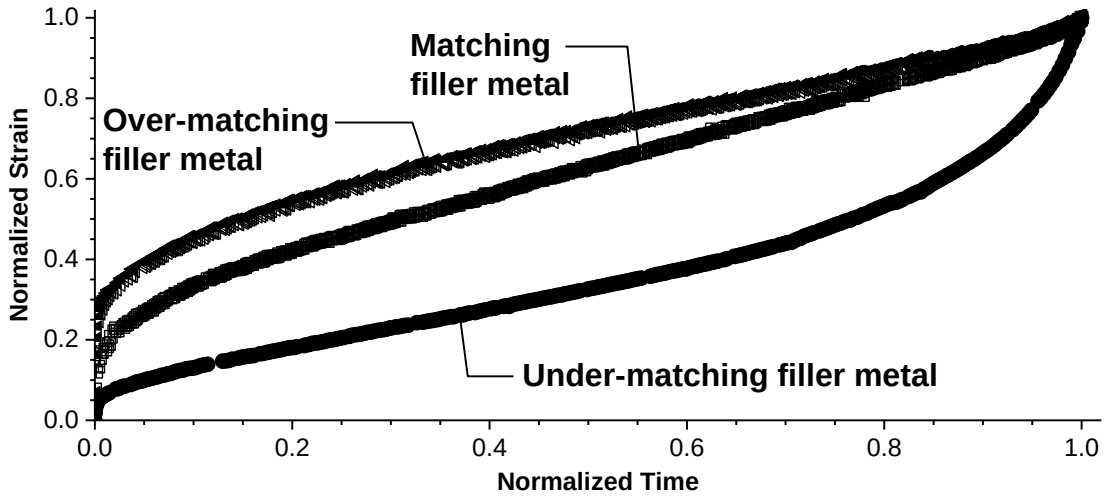

Figure 6-27. Comparison of normalized strain versus time data for selected cross-weld creep tests at 625°C and 60 MPa which evaluate the effect of filler metal strength on performance

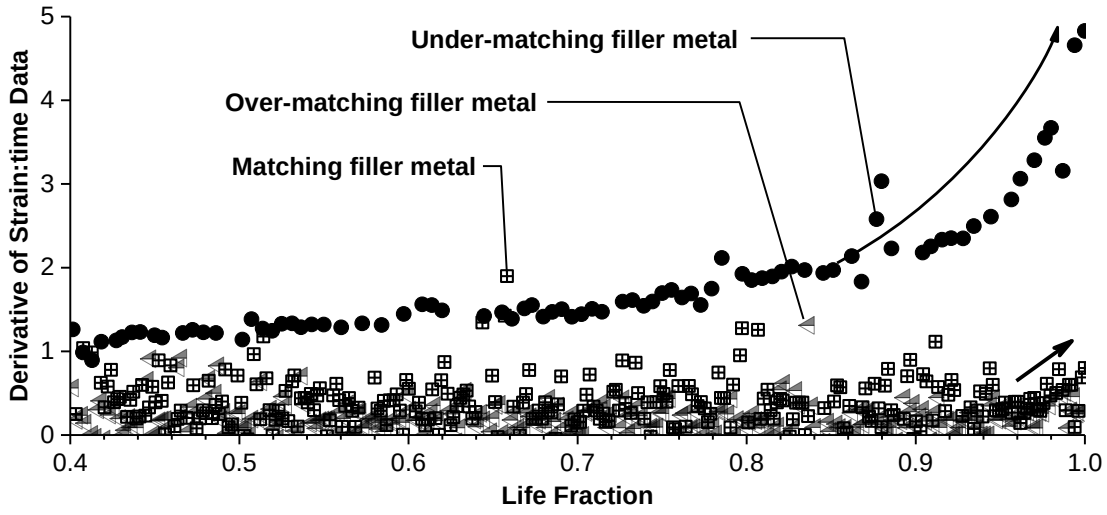

Figure 6-28. Assessment of damage tolerance using the derivative of the strain versus time data as a function of time fraction and as compared for the weldments which investigated the influence of the filler metal strength (625°C and 60 MPa)

6.8 Discussion

The results for the parent material utilized in this study showed dramatic differences relative to the time to failure and the assessed creep ductility for uniaxial, plain bar creep test specimens. The variability in life for the martensitic parent material was a

factor of 3 for a test condition of 625°C and 100 MPa. Larger deviations in the parent metal ductility were noted, particularly with respect to the ROA and the nature in which damage was manifested. For samples AR-B2 and RNT-B2, which exhibited ROA values of ~25%, there was evidence of a large density of creep voids in the failed test specimen, indicating a lower barrier to the nucleation of creep damage in this heat of material. In contrast, the TP1 material in the ferritic or martensitic condition, exhibited very high creep ductility with ROA values >80% although the time to failure for these conditions varied significantly. The F-TP1 material was not evaluated at 625°C and 100 MPa, although the estimated time to failure using an available correlation might be expected to be ~35 hours, e.g. about 100X lower than the observed time to failure for the martensitic TP1 material (2,950 hours). It is emphasized that this reduction in performance was not observed in the feature, cross-weld creep tests and reasons for this will be reviewed in the following discussion.

A single, martensitic parent material welded with selected filler materials to produce a set of controlled weldment responses for under-matching, matching and over-matching filler metals was evaluated. Perspective should be provided regarding the time to failure for the under-matching weldment made in the martensitic parent metal which consistently failed at the mean-20% bound. The potential life of a girth weld is detailed in Table 6-6 using the mean-20% bound and the previously calculated hoop stress of 65.5 MPa for an ex-service header (section 4.6) as an upper bound for stress and the axial stress of 32.7 MPa for a lower bound on stress-state.

Table 6-6. Assessment of cross-weld creep life (hours to crack initiation using Equation 4.3) for an axial- or hoop-stress dominated condition in weldments which possess performance consistent with the mean-20% bound to a cross-weld database for Grade 91 steel.

Stress	625°C	600°C	575°C	550°C
Hoop (65.5 MPa)	7,060	36,100	185,000	945,000
Axial (32.7 MPa)	194,000	751,000	>1,000,000	>1,000,000

The results in Table 6-6 highlight that an acceptable expectation on performance can be achieved for notionally ‘under-matching’ weldments provided the condition of the parent metal is known to place a given weld in a mean-20% bound. For matching or over-matching weldments there was considerably less observed damage tolerance in the form of tertiary creep, although the time to failure for both weldments was greater than the mean-20% bound.

Recent, well-controlled simulations which recreate a HAZ microstructure in Grade 91 steel and for three of the steel conditions evaluated were previously presented in Figure 2-62. Interestingly, and although the times to failure are very similar, the shortest life is for that of the TP1 simulated HAZ (identified as 'CC'). Although the creep ductility values are generally good, e.g. ~60% ROA, there is a notable increase in the creep ductility for the TP1 material which exhibited excellent creep ductility in the uniaxial parent metal tests. AR-B2 (identified as 'BB') and RNT-B2 (identified as 'DD') have lower creep ductility and nearly identical times to failure. These results reinforce the assertion from the authors in (Kimmins et al. 1993) that the accumulation of damage in cross-weld creep samples is the primary concern regarding behavior and that the manifestation of damage is only explained based on cavitation susceptibility of the parent metal.

The appreciation of the difference in deformation and damage in ferritic steels is not a new concept and has been reviewed by previous researchers in section 2.14.1. An example of these findings, and specific to simulated HAZ samples for a set of 1¼Cr-½Mo, showed that although the parent materials exhibited similar deformation responses, the extent of cavitation in interrupted samples and at failure varied considerably (Fujibayashi and Endo 2002). For the material that exhibited a higher density of cavitation, the absolute values for the As, Cu and Sn were clearly elevated resulting in an increase in the CEF value (see equation 6.4). The evaluated Grade 91 steels in this thesis show a similar trend, e.g. the parent metal B2 exhibits a higher weight percent of As, Cu, Sn and other tramp elements (e.g. Pb, S, Sb) in comparison to TP1.

Consideration of the results in Figure 6-24 bear some additional explanation. Although the F-TP1 weldment shows a low value for the λ parameter that never exceeds 5, the reality of in plant behavior should be considered in the context of how these tests were observed to fail. Although the lifetime for this set of welds was low, and the assessed minimum creep rate relatively high, there was extensive deformation in the parent metal in all tests. In a plant setting, it might be expected that this would be reflected in the parent material in the form of swelling in the pipe assuming there was a sufficient and uniform length of ferritic material. This behavior would likely be highlighted provided the location or affected system was subjected to routine inspection such that sufficient time between detection of geometric instability and the leak exists occurs.

For the weld 8C made in the TP1 with the under-matching filler metal there is a general trend for the longest-term tests to possess increased values for the λ parameter. For the shorter-term tests, the values for weld 8C are biased to lower values for λ because the test samples exhibited considerable tertiary creep (relative to the matching and over-matching weldments in the martensitic parent metal). Because of the extensive tertiary creep, none of the weld 8C tests were taken entirely to failure leading to a bias of the value for ε_f and thus the λ parameter.

The importance of material ductility and damage tolerance of the structure is summarized by Goodall et al. (1975). In structures the presence of low damage tolerance or materials with very poor creep ductility can promote rapid propagation of initiated cracks through creep damaged material. In these cases, the estimation of component life is initiation-dominated. There is a macro- and a micro- perspective in this behavior that should be considered in the context of component assessment. For example, a desired life determination of the structure might rely on an initiation-based criterion, but the constitutive model used to make this assessment should be properly calibrated. This perspective has been considered by Ashby and Dyson and Dyson and Gibbons in the context of the λ parameter (Ashby and Dyson 1984 and Dyson and Gibbons 1987). Application of relevant constitutive models to weld performance remains an active area of research within the weld-performance and component assessment communities including recent assessment in (Pritchard et al. 2018).

The increased creep ductility in the parent metal serves to increase the time to failure, but the inherent realities of structural behavior will necessitate the placement of a creep weak region (e.g. the PTZ) in a constrained condition leading to a multiaxial stress state. This multiaxial stress state will assist in the development and growth of creep damage, regardless of parent metal condition. Reported evaluation of constrained, notch bar creep tests in HAZ material from Grade 91 steel have suggested that the maximum principal stress is linked to cavity initiation, while the stress triaxiality ratio provides a better correlation to cavity growth (Tsuruta et al. 2017). With respect to macro performance of welded structures, particularly in girth weld, seam weld or end-cap configurations, improvement in how the structure will fail will only be realized if novel weld geometries are considered for locations at risk to leak or break. One such concept, identified as a ‘step weld’ design, has been recently shown to provide such benefit (EPRI 2014c).

There exists a clear need to utilize the generated information in this Chapter for the development and calibration of material models which provide relevant perspective on damage initiation in structures. This focus is a primary driver for continued research and future focus to better elucidate factors governing void initiation, growth and the manifestation of damage as an ‘initiation criterion’ in a model used for component screening and assessment.

6.9 Summary

The results in this chapter have detailed a systematic set of feature, cross-weld creep tests in well-pedigreed parent materials. The fabricated weldments were produced using the welding procedures detailed in Chapter 3 and assessed in the pre-test condition in Chapter 5. The results in Chapter 6 have not only used the prior information as a foundation, but show that the cross-weld creep lives can be dramatically changed through an alteration of the damage response of the parent metal.

The cross-weld behavior for a parent material in its weakest state, e.g. for Grade 91 steel in the fully ferritic condition, showed the sensitivity of the test result to stress state. For applied stress values that were ~≤50% of the yield stress at the test temperature, the cross-weld life merged with the minimum of the scatter-band. For applied stress values that were ~70% of the yield stress at the applied test temperature, the offset in life was approximated in the cross-weld creep database by a mean-50% bound.

The use of a filler material which matches the strength of the PTZ (e.g. AWS type -B8) was shown to provide creep lives in martensitic parent material that were approximated by a mean-20% bound to the cross-weld creep database. Furthermore, these weldments showed increased damage tolerance, as assessed by the increase in tertiary creep strain, an increase in the calculated λ parameter and consideration of the macro-state of damage; e.g. damage in the weld metal and HAZ and extensive deformation in the weld metal. The performance relative to the mean-20% was substantiated to provide perspective for in-service application including a consideration of the dominate stress acting across the weldment (e.g. hoop versus axial) and an expected range of realistic operating temperatures for Grade 91 steel components. This assessment clearly demonstrated the need for engineers to

consider the specifics of fabrication and operation on the estimated performance for a given weldment.

For a weldment made with a filler material that is over-matching to the parent material (e.g. the Ni-base filler metal EPRI P87) there was not a notable shift in the failure location to the fusion line nor was a debit in cross-weld performance noted for the evaluated test conditions. Thus, for the temperature and stresses applied in this study (e.g. 600 or 625°C and 60 or 80 MPa), there was not an apparent, detrimental effect of the Ni-base weld metal.

Assessment of cross-weld creep behavior and a link to the parent metal deformation and damage resistance summarized in Figure 6-3 is provided in Figure 6-29 for the matching weldments fabricated in martensitic parent material (e.g. AR-B2, RNT-B2 and TP1). Figure 6-29 clearly links the deformation and damage characteristics of the parent material to cross-weld creep performance, where it is emphasized that the effect of creep ductility inherent to the parent material clearly has a dominant effect on behavior. The comparison of the two parent materials RNT-B2 and TP1 for which the parent material deformation response documented as time to failure only varied by 10%, while the variation in cross-weld creep response is a factor 5 on life alone. This deviation can only be explained by the difference in creep ductility, which for the RNT-B2 and TP1 parent metal steels varies with respect to ROA by a factor of 5 (Table 6-3).

Martensitic CSEF steels are widely utilized in components with complex geometries, and it is important that the scientific community assess not only ‘when’ the damage might initiate but also appreciate the distribution and evolution of damage, e.g. ‘how’ the component may fail. It is only through this combined understanding of deformation (when a structure fails) and damage (how a structure fails) that a sensible life management approach be developed and grounded in a full appreciation of the factors which affect weldment behavior.

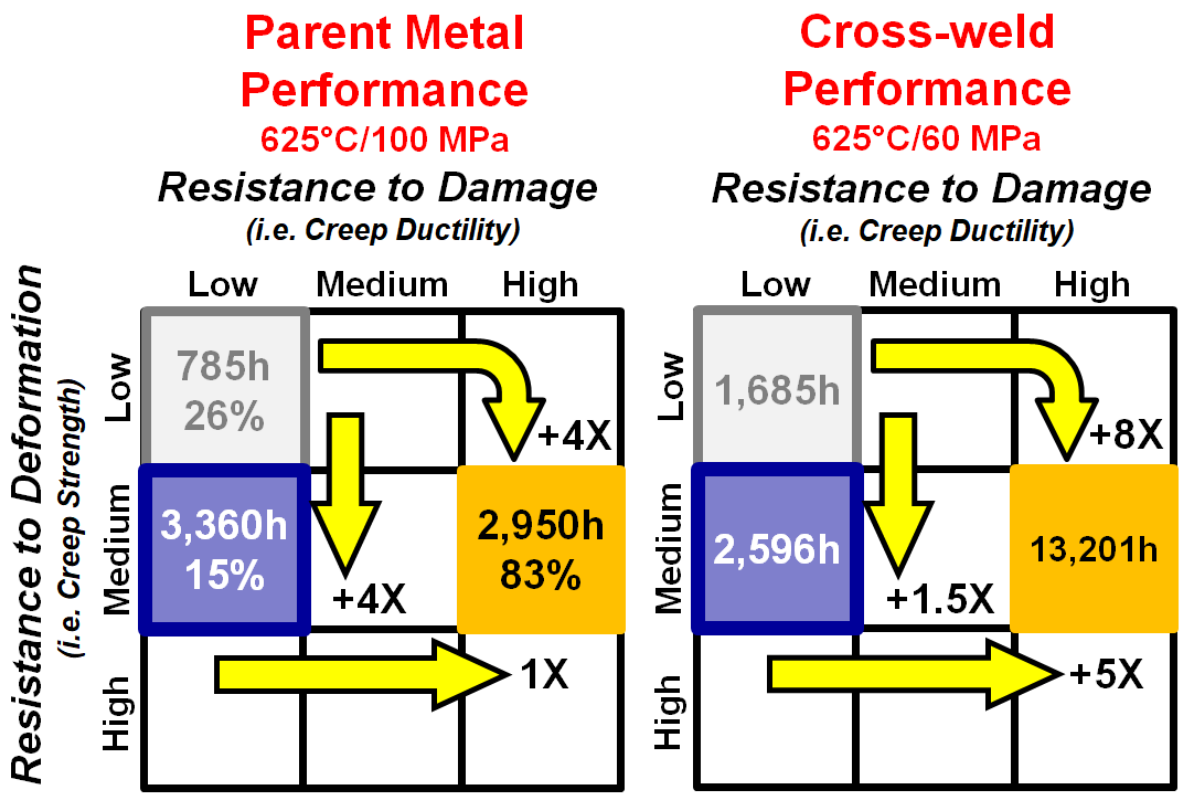

Figure 6-29. The link between parent metal classification in the deformation-damage matrix to parent metal uniaxial, plain bar creep test results at 625°C and 100 MPa and to feature-type cross-weld creep tests at 625°C and 60 MPa
Note: *the arrows indicate the increase in lifetime for key variations in the damage-deformation matrix*

The following chapters will focus on the assessment of the present damage in selected feature, cross-weld creep test samples including evaluation of the nature of the damage in a macro-, micro- and nano-scale. Chapter 7 provides the assessment of damage through the HAZ and linking the observed void density to specifics of the welding thermal cycle and hardness map data. Chapter 8 assesses the local nature of cavitation within the PTZ and finally Chapter 9 provides clarity on the manifestation of damage for an interrupted sample in the AR-B2 material. It is through this comprehensive understanding of the parent materials possessing dramatically different responses to deformation and damage, and detailed in this Chapter, will attempt to be understood in the context of feature, cross-weld creep performance on a macro- and local-basis.

7 Macro-Characterization of Damage in Cross-weld Creep Tests

7.1 Introduction

The assessment of cross-weld creep performance must not only consider the mechanical behavior, but also evaluate the extent and nature of the observed damage in the sample. For samples which fail in the heat affected zone (HAZ) it is possible to analyze the location of failure as well as the distribution of damage because the feature cross-weld creep tests contain the entire weld region, including both HAZs. The application of a consistent and well-defined procedure is equally important in this regard as the current chapter will leverage the findings for the as-fabricated condition in Chapter 5 and the detailed assessment of the cross-weld creep test data in Chapter 6.

The results presented in Chapter 5 provided clear and distinct evidence that the partially transformed zone (PTZ) was offset from the location of the so-called soft zone in the HAZ. The results in the current chapter will attempt to provide perspective regarding the failure location and the distribution of damage through the HAZ. This will enable specific comparison to important findings including:

- Distribution of hardness indents in the so-called ‘soft zone’;
- Location of macro-failure or macro-cracking in the HAZ;
- Distribution of peak temperatures through the HAZ;
- Contribution of parent metal creep strength and creep ductility to the observed trends and
- The influence of filler metal strength to the observed trends.

Chapter 6 documented the observed failure locations in the cross-weld creep test samples. The assessment of damage in selected cross-weld creep test samples will provide additional information regarding the nature and morphology of damage on the macro-scale using light optical microscopy. The association of damage on the micro-scale will be the subject of following Chapters 8 and 9.

7.2 Location of Failure in Feature-type Cross-weld Creep Tests

The general macro-failure location for each sample which exhibited HAZ damage is provided in Table 6-4. This information includes basic detail for sample failures which did not occur in the HAZ is noted for completeness (e.g. parent metal or weld metal). The additional detail for failure location in the HAZ provided in Table 7-1 is specific to the distance of failure relative to the fusion line. The classification of the sample as 'ruptured' or 'terminated' refers to the nature of the completed test condition. In some cases, the test was unable to be stopped prior to the complete failure through one of the HAZ regions. For samples that did not rupture, and are classified as terminated, the presence of macro-cracking and/or a very high density of creep voids through one or both HAZs was present such that the life fraction of these tests was likely to be ≥95%.

Table 7-1. Macro-failure assessment of the distance between failure and the fusion line in the feature cross-weld creep tests

Sample	Parent Metal and/or Filler Metal Details	Stress (MPa)	Temp. (°C)	Time to Failure (hours)	Failure Location in the HAZ as a function of Distance from the Fusion Line (μm) [R] = Ruptured [T] = Terminated
AR-B2-1	AR-B2; low strength and ductility	80	625	426	1,315 [R]
AR-B2-2		60	625	1,685	1,225 [T]
AR-B2-3		80	600	1,822	1,110 [R]
AR-B2-4		50	625	4,816	1,153 [T]
RNT-B2-1	RNT-B2; medium strength and low ductility (Renormalized and Tempered AR-B2)	80	625	842	1,300 [R]
RNT-B2-2		60	625	2,596	1,482 [R]
RNT-B2-3		80	600	3,617	1,412 [R]
RNT-B2-4		50	625	6,101	1,250 [T]
F-TP1-1	F-TP1; very low strength and high ductility (Ferritic TP1)	80	625	269	Parent metal
F-TP1-2		60	625	4,553	375 [T]
F-TP1-3		80	600	1,503	Parent metal
F-TP1-4		50	625	15,472	850 [T]
7C-1	TP1; medium strength and high ductility	80	625	3,743	1,440 [R]
7C-2		60	625	13,201	1,625 [T]
8C-1	• TP1; medium strength and high ductility • Under-matching filler metal (e.g. 9Cr-1Mo)	80	625	1,509	1,070 [T]
8C-2		80	600	5,179	950 [T]
8C-3		60	625	4,064	1,210 [T]
8C-4		50	625	7,703	***
8C-5		70	600	10,461	1,060 [T]
8C-6		60	600	20,234	***
8C-7		90	575	13,101	1,115 [T]
9C-1	• TP1; medium strength and high ductility	80	625	2,129	820 [R]
9C-2		80	600	8,348	960 [R]
9C-3		60	625	13,130	1,040 [T]

	• Over-matching filler metal (e.g. Ni-base)				

***There was not sufficient macro-cracking damage in the HAZ to measure the macro failure location

Select cross-sections in the as-polished condition are provided in Figure 7-1 to Figure 7-5 which detail the extent of damage in the parent metal, HAZ or weld metal. One macro sample is presented for each set of cross-weld tests performed in the six weldments.

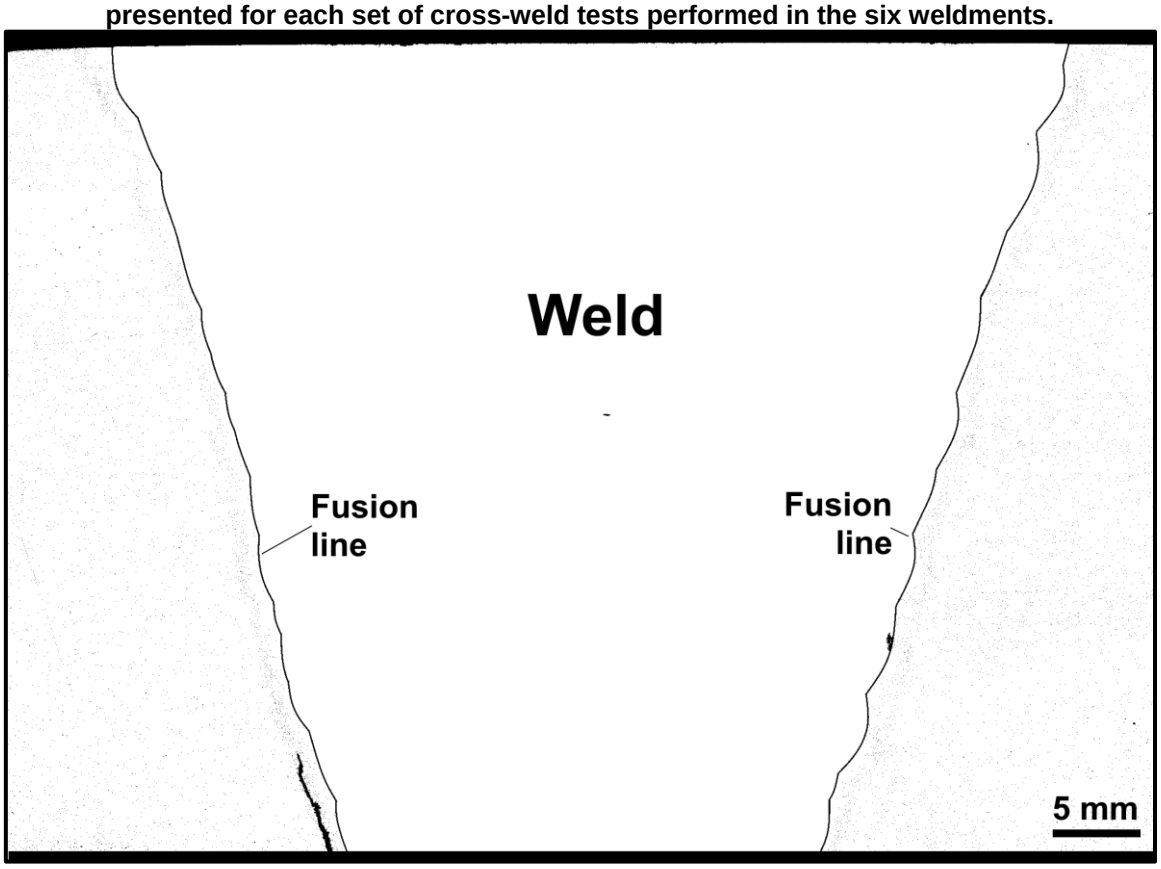

Figure 7-1Figure 7-1 provides an example of failure in the F-TP1 material where extensive necking is present in the parent metal and is accompanied by the formation of a single, dominant surface-connected crack in the HAZ.

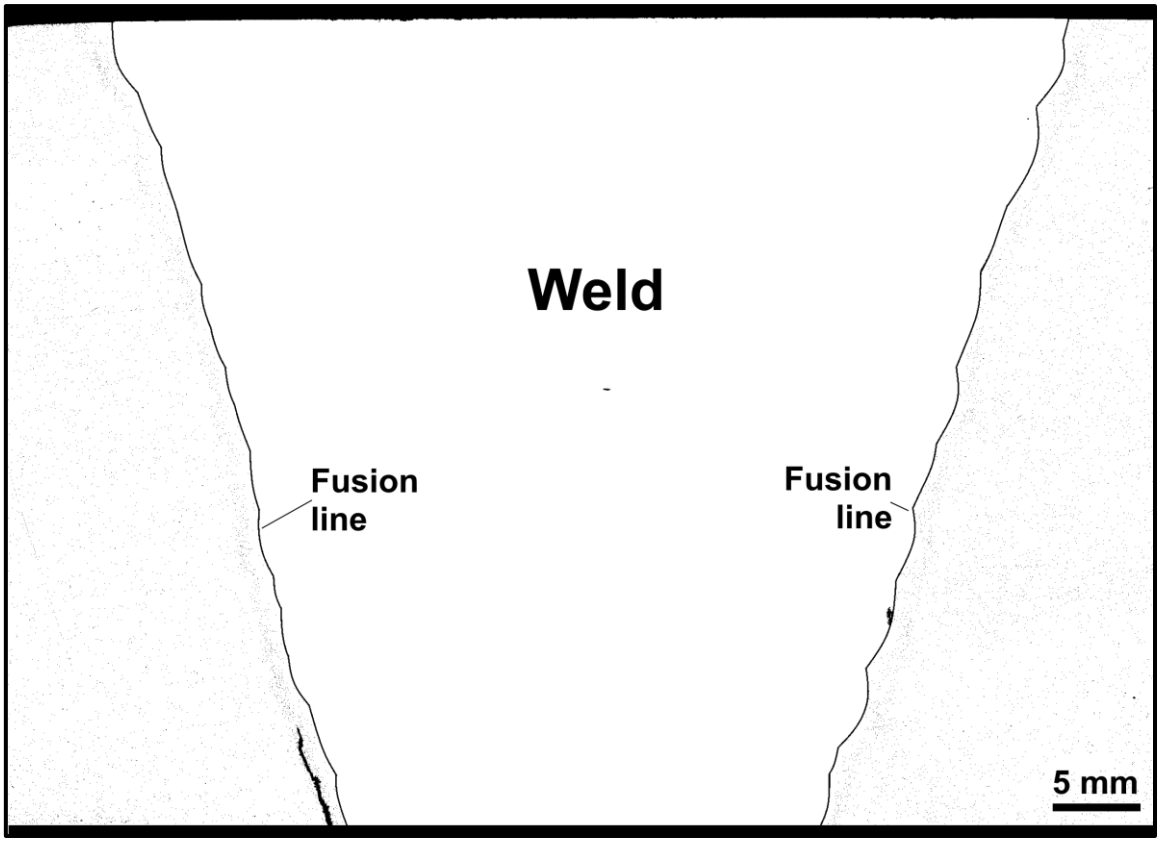

Figure 7-1. Macro-image of damage in feature-type cross-weld test sample F-TP1-4

Figure 7-2 to Figure 7-5 highlight damage that has evolved almost exclusively in the HAZ. In some cases, isolated damage in the form of voids is noted in the weld metal; Figure 7-2 provides the clearest example. The apparent damage in the weld metal volume in Figure 7-5 is an elevated concentration of slag inclusions due to the filler material (e.g. EPRI P87).

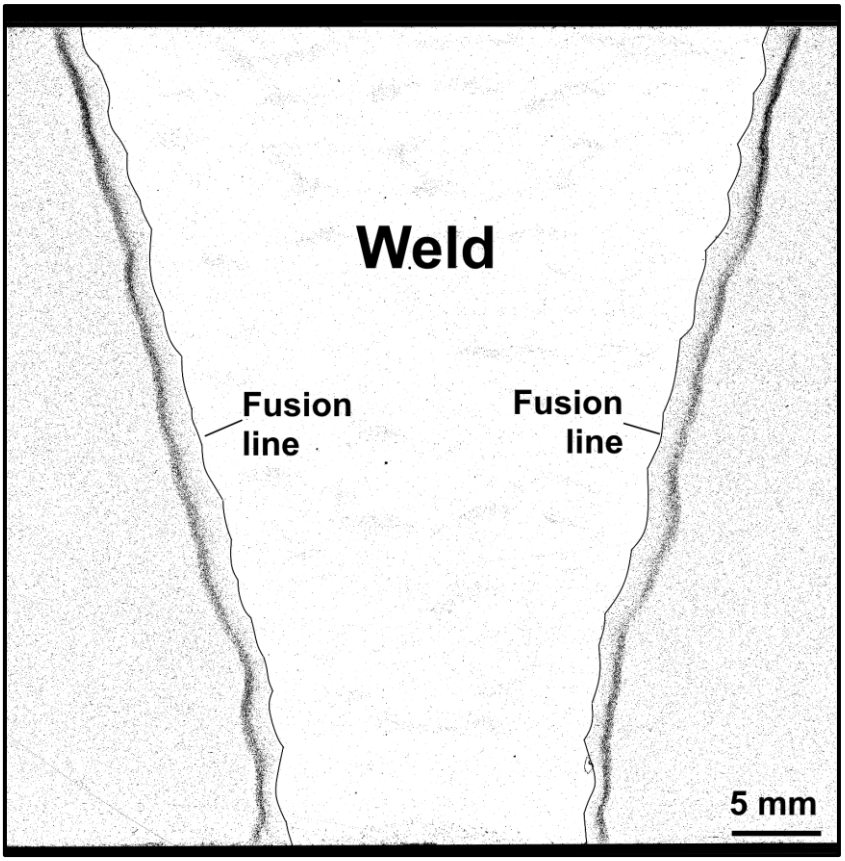

Figure 7-2. Macro-image of damage in feature-type cross-weld test sample AR-B2-2

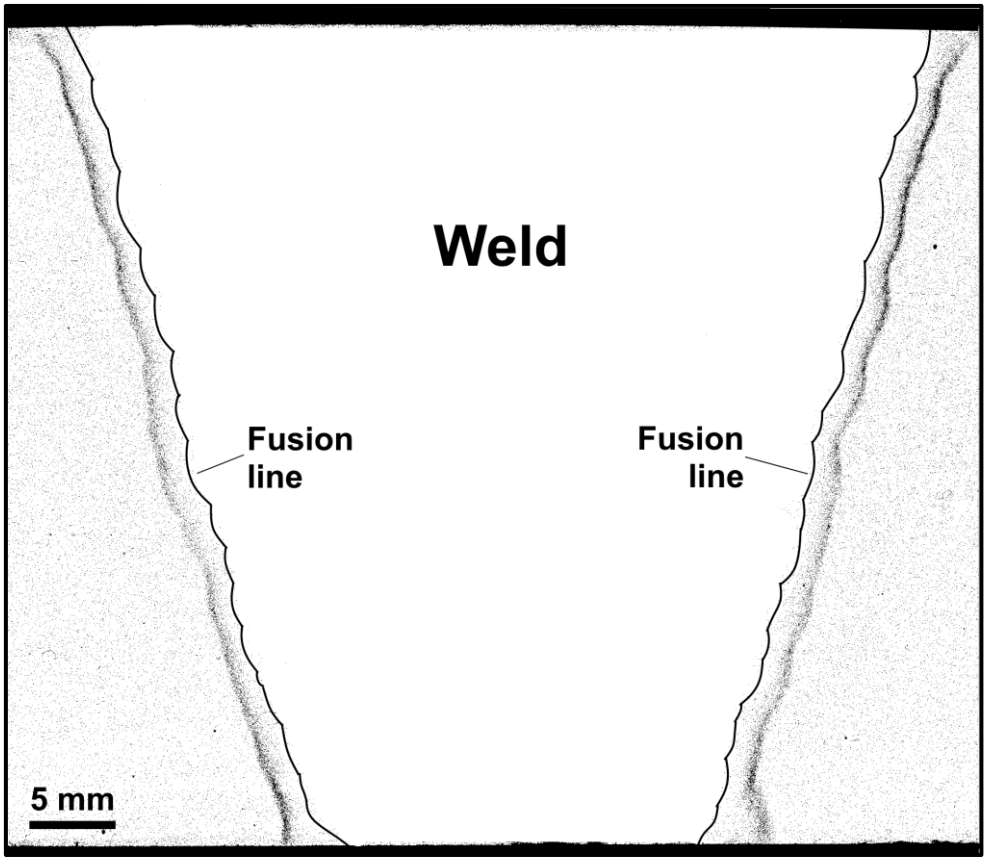

Figure 7-3. Macro-image of damage in feature-type cross-weld test sample RNT-B2-4

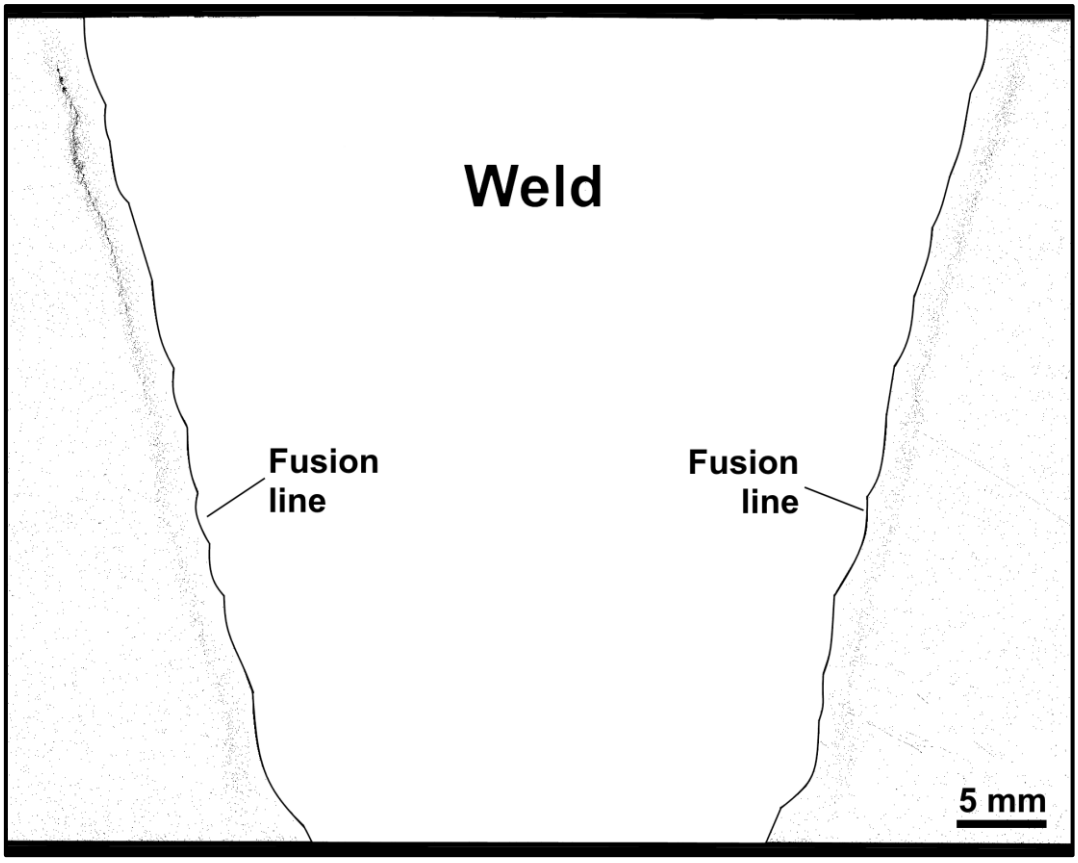

Figure 7-4. Macro-image of damage in feature-type cross-weld test sample 7C-2

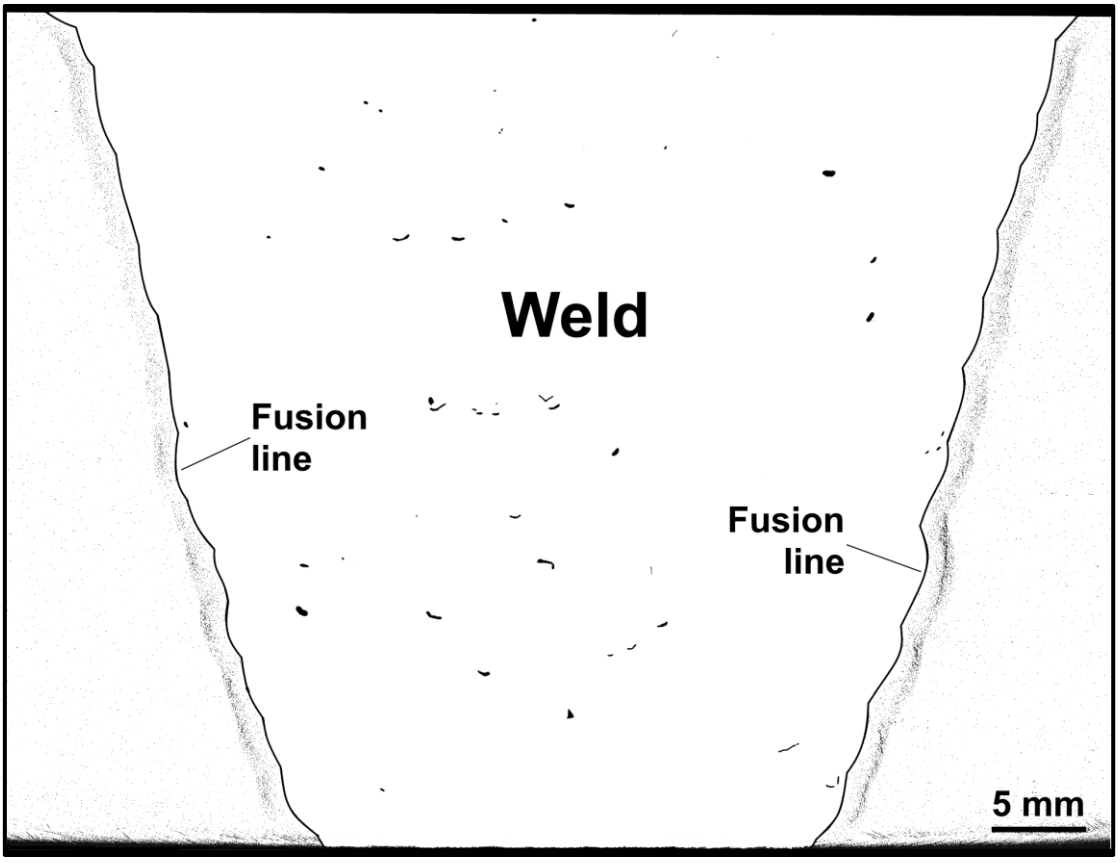

Figure 7-5. Macro-image of damage in feature-type cross-weld test sample 9C-3

Figure 7-6 provides an example of failure which is predominately in the weld metal, as noted by the extensive cracking and a clear neck which has formed in the weld metal centerline. In addition to the weld metal damage, less extensive HAZ damage is also present in Figure 7-6 near the cap region (e.g. top of the image) in the form of high void density and near the left-hand side of the root portion a macro-crack that is approximately 3 mm in length.

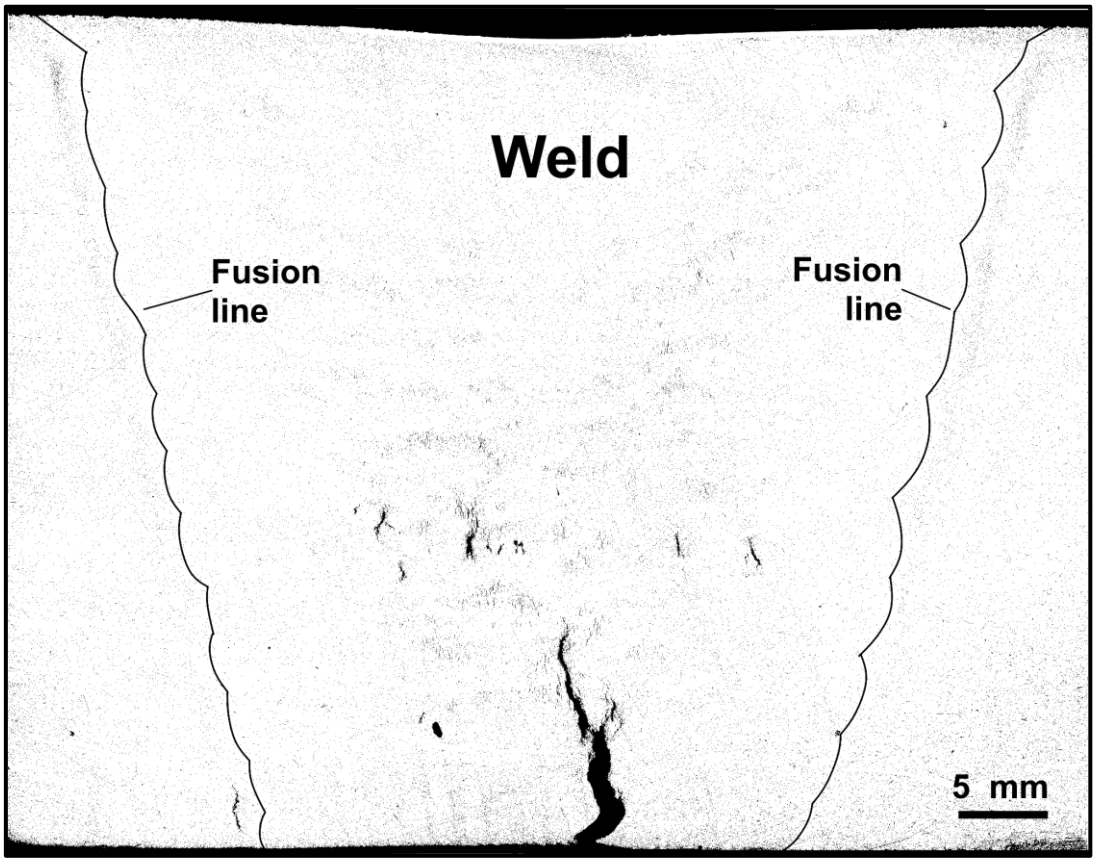

Figure 7-6. Macro-image of damage in feature-type cross-weld test sample 8C-4

7.3 Macro-damage in the Weld Metal and Heat Affected Zone

An example of weld metal macro-damage in the as-polished condition is provided in Figure 7-7 for sample 8C-4. This localization of damage is apparently associated with coarse columnar grain boundaries, such as those seen in Figure 7-8 to Figure 7-10 in the etched condition. Cracking is primarily isolated to these boundaries which are formed during the solidification process and do not undergo subsequent refinement by successive welding thermal cycles.

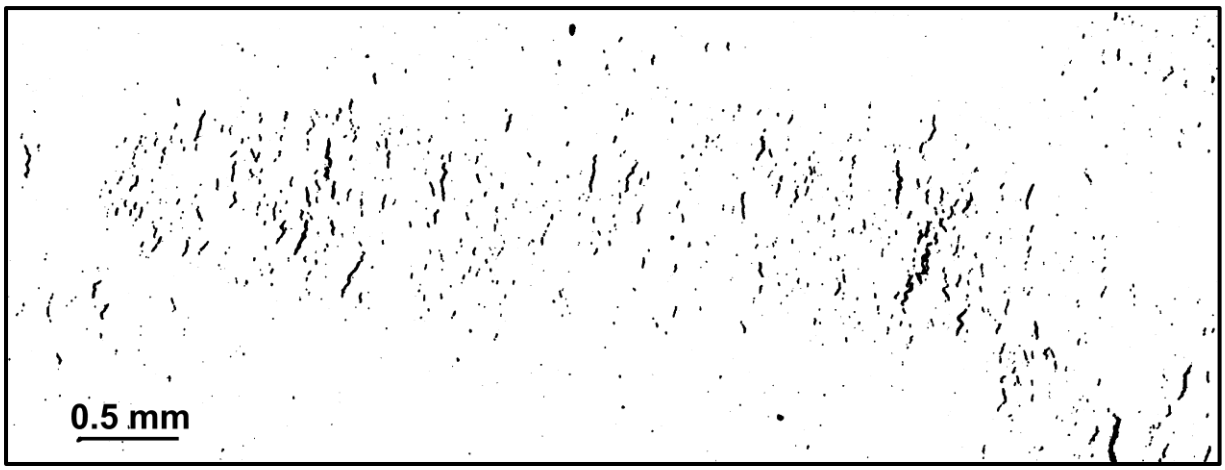

Figure 7-7. Weld metal damage in feature-type cross-weld test sample 8C-4

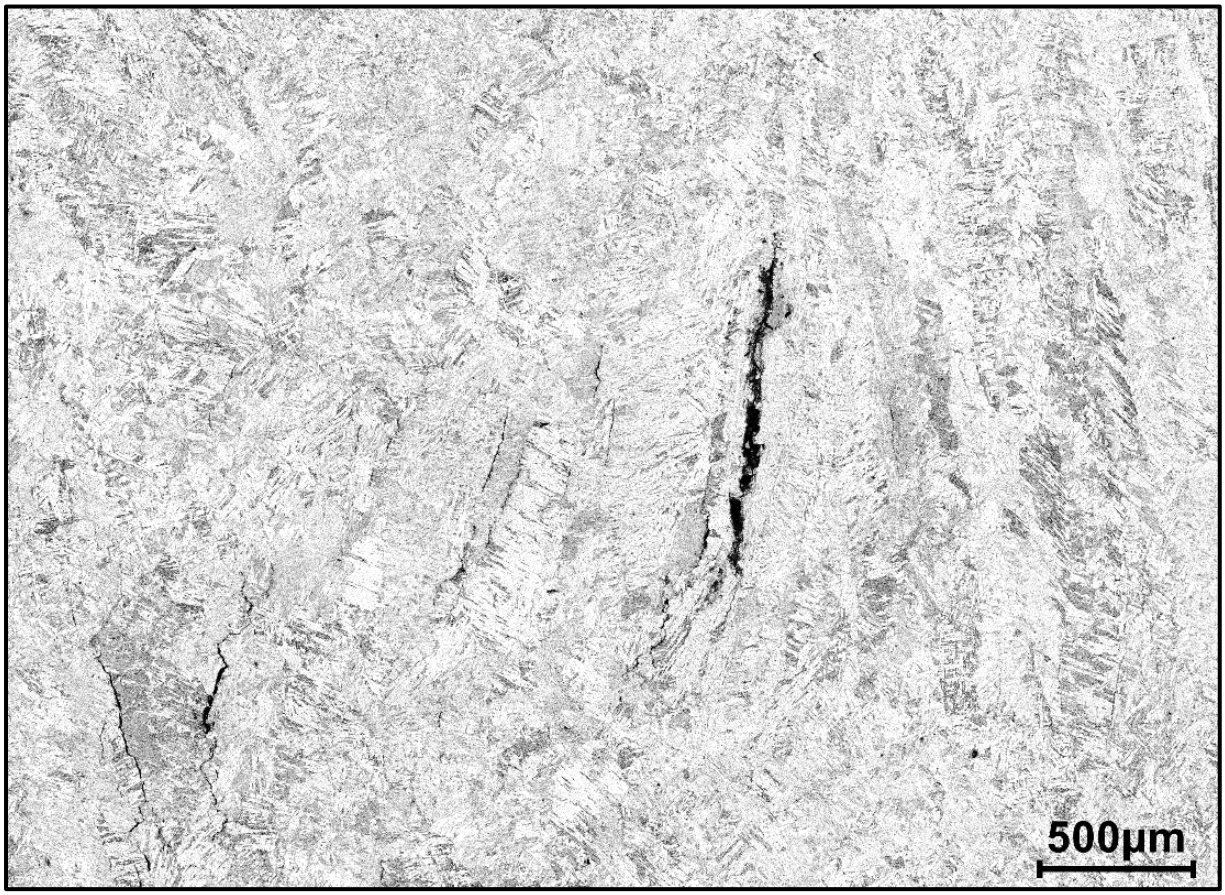

Figure 7-8. Weld metal damage in feature-type cross-weld test sample 8C-6
Note: *formation of macro-cracking appears to be concentrated at coarse-columnar grain boundaries. Sample etched in Villella's reagent*

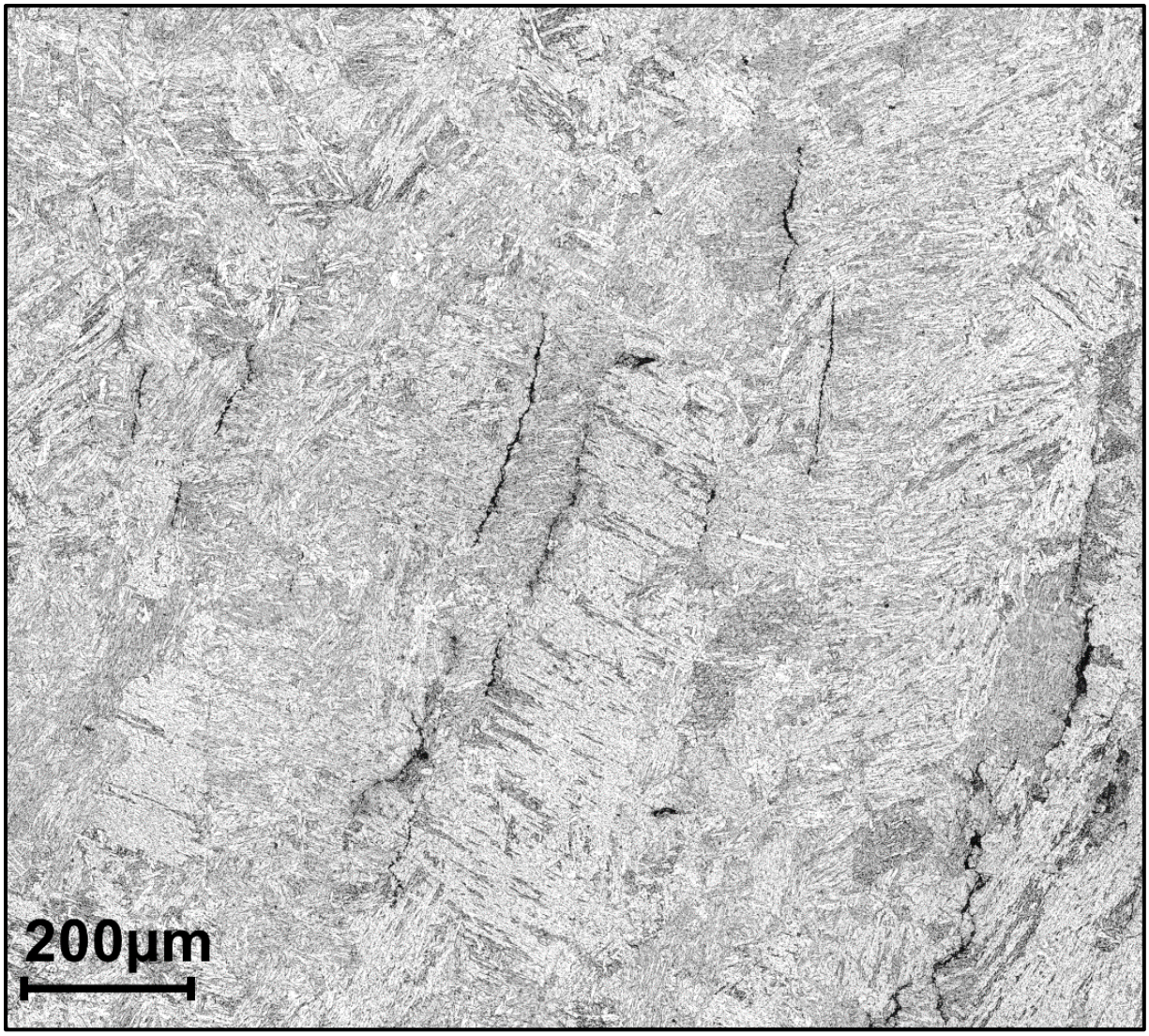

Figure 7-9. Weld metal damage in feature-type cross-weld test sample 8C-6 (Villella's reagent)

Figure 7-10. Weld metal damage in feature-type cross-weld test sample 8C-6 (Villella's reagent)

Figure 7-11 provides a comparison of representative damage in the HAZ for samples which failed exclusively through the HAZ and which show the effect of parent metal creep strength and creep ductility on the evolution of damage. The highest level of damage is clearly observed in Figure 7-11A and Figure 7-11B for the B2 parent material which exhibits very low creep ductility. There is considerably less HAZ damage present in Figure 7-11C for the TP1 parent material which exhibits very high creep ductility.

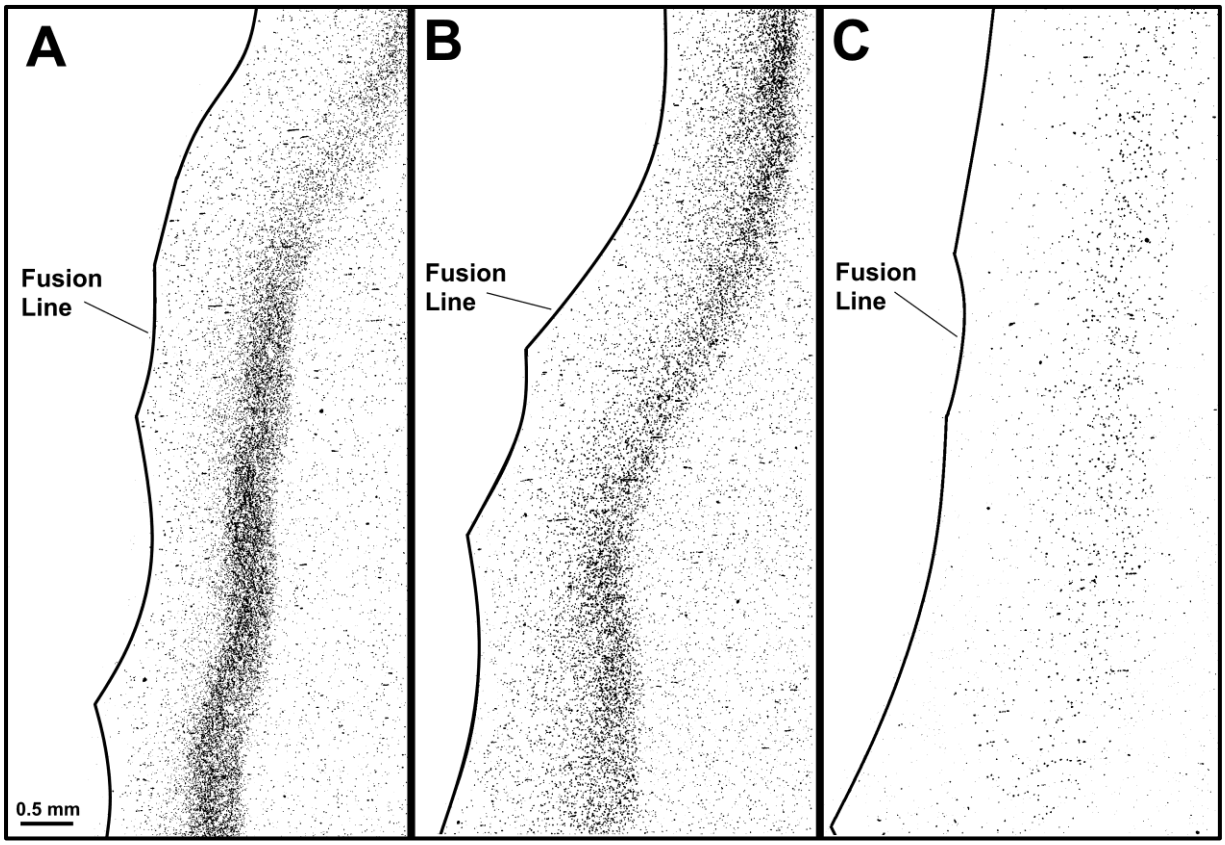

Figure 7-11. Comparison of damage in the heat affected zone for low creep strength and low creep ductility parent metal weldment sample AR-B2-2 (A), for medium creep strength and low creep ductility parent metal weldment sample RNT-B2-2 (B) and for medium creep strength and high creep ductility parent metal weldment sample 7C-2 (C).
Note: *all weldments manufactured using matching filler metal and a post weld heat treatment of 675°C for two hours.*

Figure 7-12 compares the influence of filler metal strength on the evolution of damage. The lowest level of damage is in the under-matching filler metal HAZ, Figure 7-12A. As the strength of the filler metal is increased relative to the HAZ, there is an increase in the extent of damage which is most clearly shown for the Ni-base weldment, Figure 7-12C. Future sections will provide detailed measurements and comparisons for the level of peak damage and the distribution of the damage through the HAZ in all of the samples highlighted in Figure 7-11 and Figure 7-12.

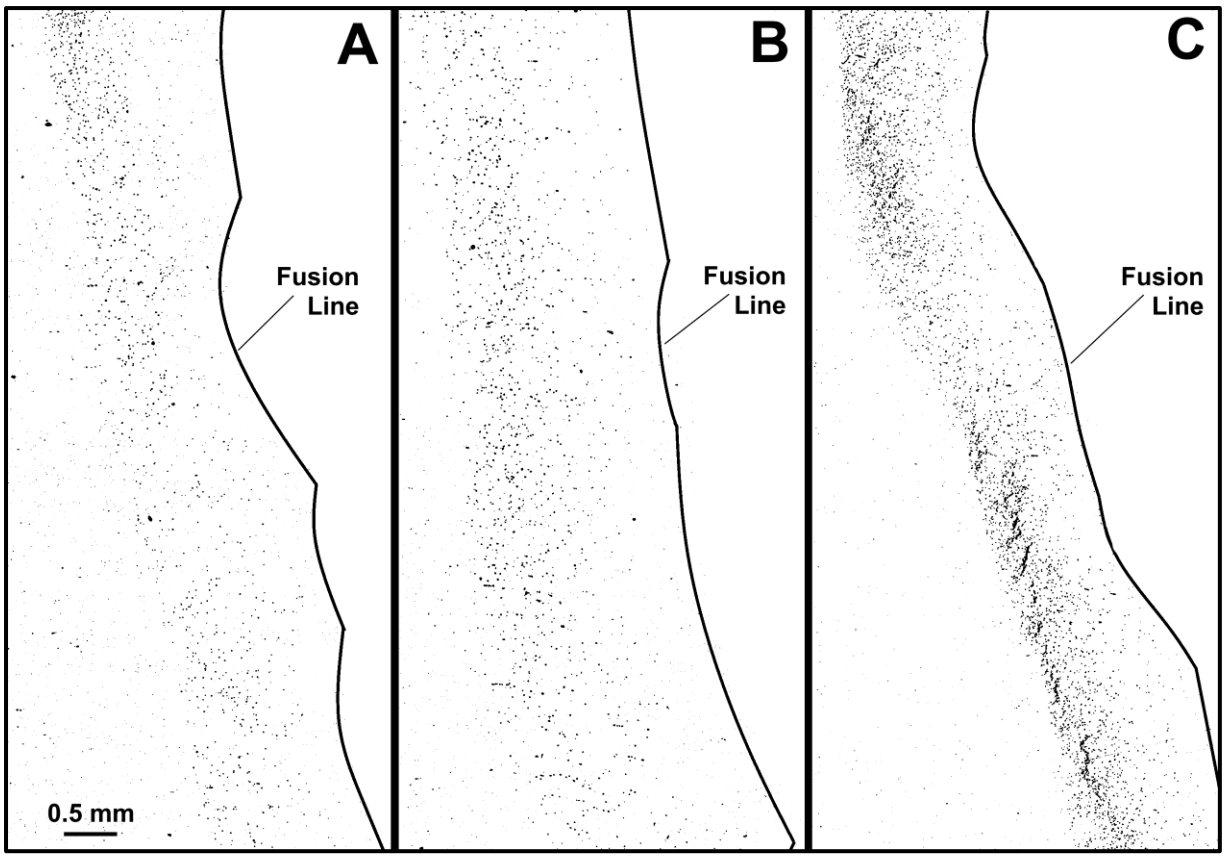

Figure 7-12. Comparison of damage in the heat affected zone for under-matching filler metal sample 8C-4 (A), matching filler metal sample 7C-2 (B) and over-matching filler metal sample 9C-3 (C).
Note: *all weldments manufactured in parent metal TP1. Increasing filler metal strength left to right.*

7.4 Selection of Test Samples

Detailed evaluation of damage in post-test samples is focused on the five samples listed in Table 7-2. A sample from the F-TP1 series of weldments is not included because the extent of cavitation in either F-TP1-2 or F-TP1-4 where HAZ cracking is noted is minimal or effectively non-existent. For the balance of the cross-weld samples, the evaluated test condition is consistent across each sample; e.g. the applied test temperature is identical (625°C) and the applied stress is 60 MPa except for 8C-4 (applied stress is 50 MPa). The selection of test sample 8C-4 for evaluation is predicated on the extent of damage, and particularly in the HAZ and of the 8C series of samples, 8C-4 contains the most advanced state of damage in the HAZ.

Table 7-2. Evaluated samples for the extent of damage through the HAZ

Sample	Stress (MPa)	Temp. (°C)	Time to Failure (hours)	Failure Location
AR-B2-2	60	625	1,685	HAZ
RNT-B2-2	60	625	2,596	HAZ
7C-2	60	625	13,201	HAZ
8C-4	50	625	7,703	Weld metal; HAZ damage
9C-3	60	625	13,130	HAZ; isolated fusion line damage

7.5 Linking of Macro-Damage to Hardness Map Data

The hardness maps performed in the as-fabricated condition, e.g. either in the as-welded condition for weldments 8C or 9C or in the PWHT condition for the balance of the weldments, have been previously presented in section 5.2. The assessment of these maps included the separation of hardness data associated with a so-called soft zone as a function of distance from the fusion line (procedure provided in 3.3.2). A representative soft zone from the analyzed weldments is identified in Figure 7-13. In this image, it is noted that the soft zone is a continuous region with a distinct and uniform hardness range that is below that of the unaffected parent material.

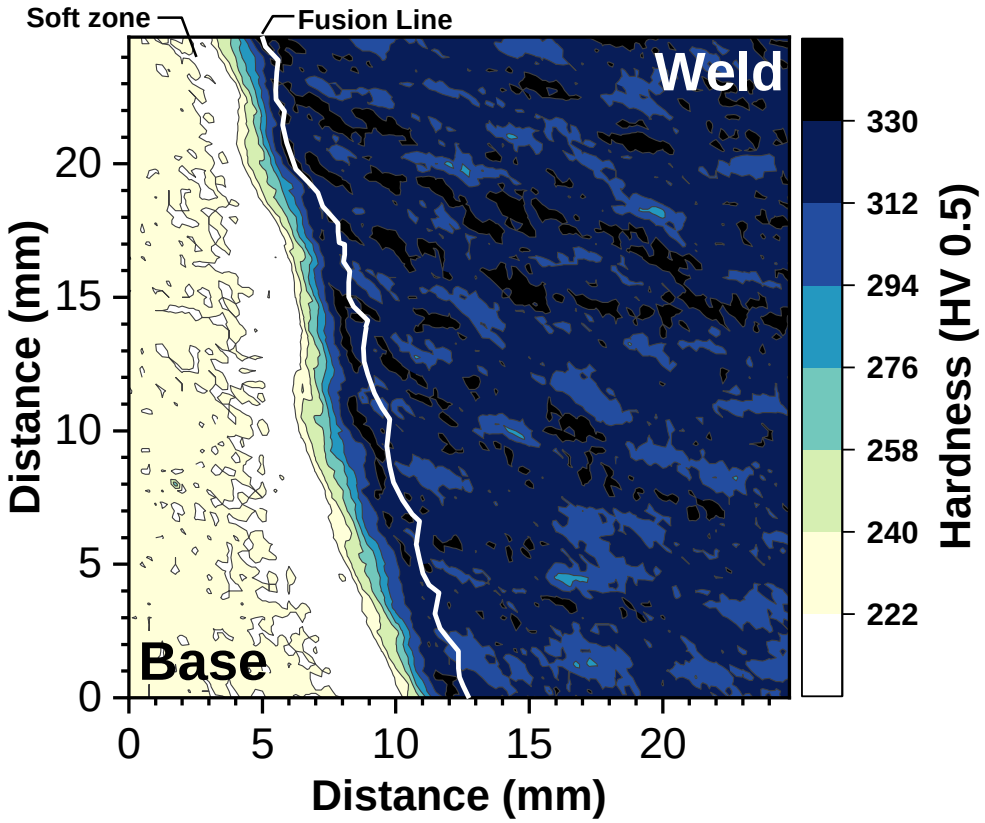

Figure 7-13. Representative color hardness map and identification of the soft zone. Weldment RNT-B2 (E9015-B9 matching filler metal, PWHT at 675°C for 2 hours, and re-normalized and tempered, martensitic parent metal B2, PWHT at 675°C for 2 hours)

The distribution of hardness indents in the soft zone are compared to the distribution of damage through the HAZ in Figure 7-14 to Figure 7-18. For each distribution, the plots provide either a ‘hardness count’ or ‘void count’ as a function of distance from the fusion line. The hardness count represents the number of indents below a threshold hardness value; this threshold value varies for each weldment as the condition of the parent metal and weld needs to be taken into consideration (see section 3.3.2). The void count represents the number of voids for a given location relative to the fusion line. The bin size is 250 and 50 μm for the hardness count and void count, respectively and these were the same for all comparisons. For weldments AR-B2 (Figure 7-14) and RNT-B2 (Figure 7-15), the void count is 5 to 10X higher than for the other assessed weldments. The extent of damage is presented on a log scale in Figure 7-19 comparing the test samples 7C-2 and AR-B2-2. As will be discussed, this dramatic increase in damage is not an artifact. In all cases the distribution of damage and hardness indents in the soft zone are offset and do not overlap. Thus, the maximum extent of damage did not correlate with a region in the HAZ produced in the as-fabricated condition that is markedly reduced in hardness.

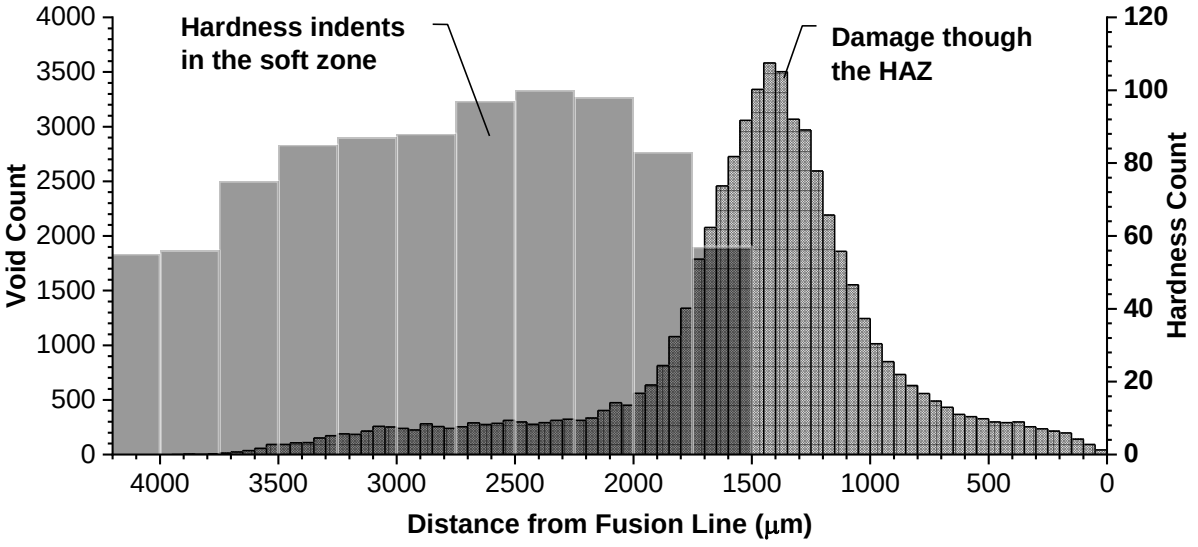

Figure 7-14. Comparison of damage in the heat affected zone for feature-type cross-weld creep sample AR-B2-2 to the distribution of hardness indents in the soft zone for weld AR-B2

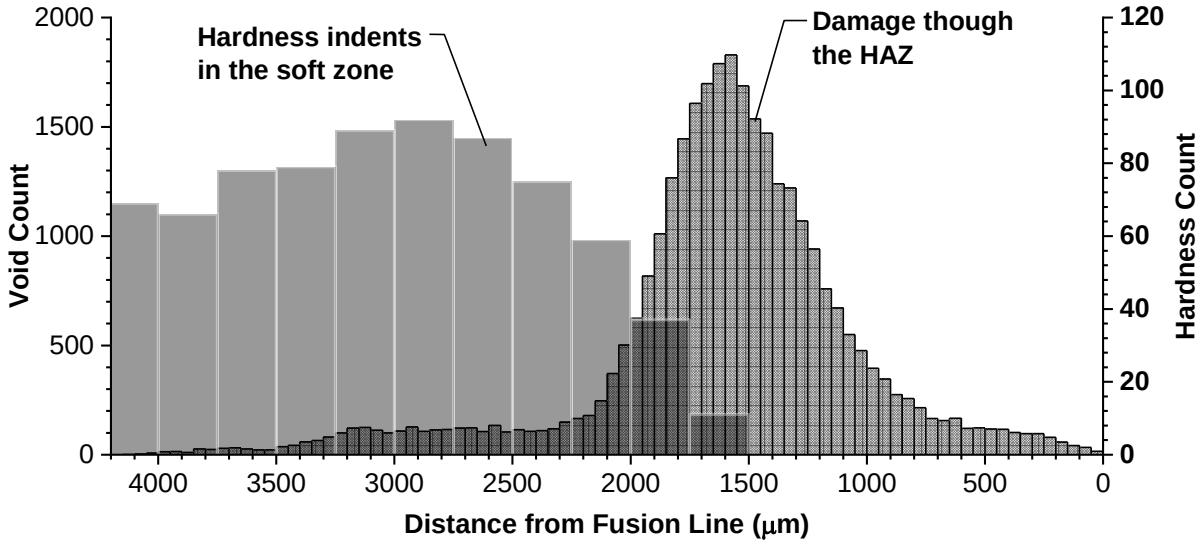

Figure 7-15. Comparison of damage in the heat affected zone for feature-type cross-weld creep sample RNT-B2-2 to the distribution of hardness indents in the soft zone for weld RNT-B2

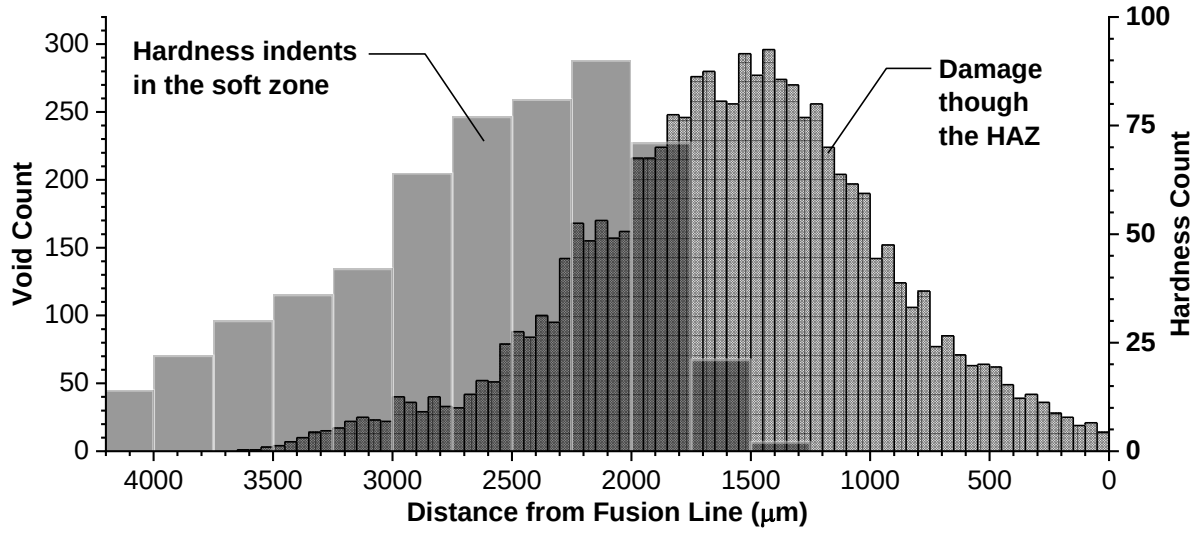

Figure 7-16. Comparison of damage in the heat affected zone for feature-type cross-weld creep sample 7C-2 to the distribution of hardness indents in the soft zone for weld 7C

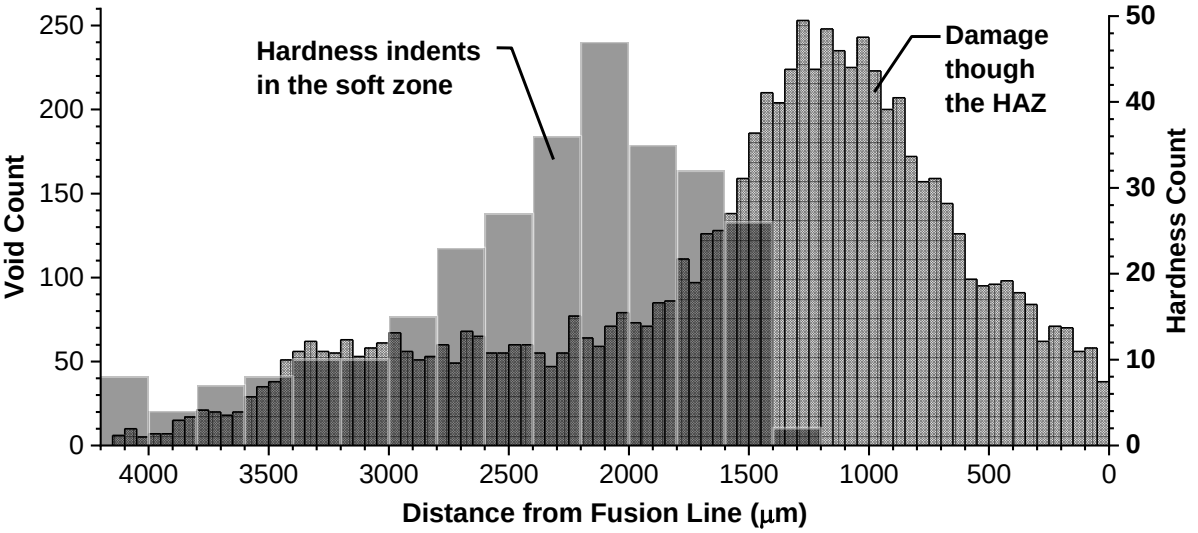

Figure 7-17. Comparison of damage in the heat affected zone for feature-type cross-weld creep sample 8C-4 to the distribution of hardness indents in the soft zone for weld 8C

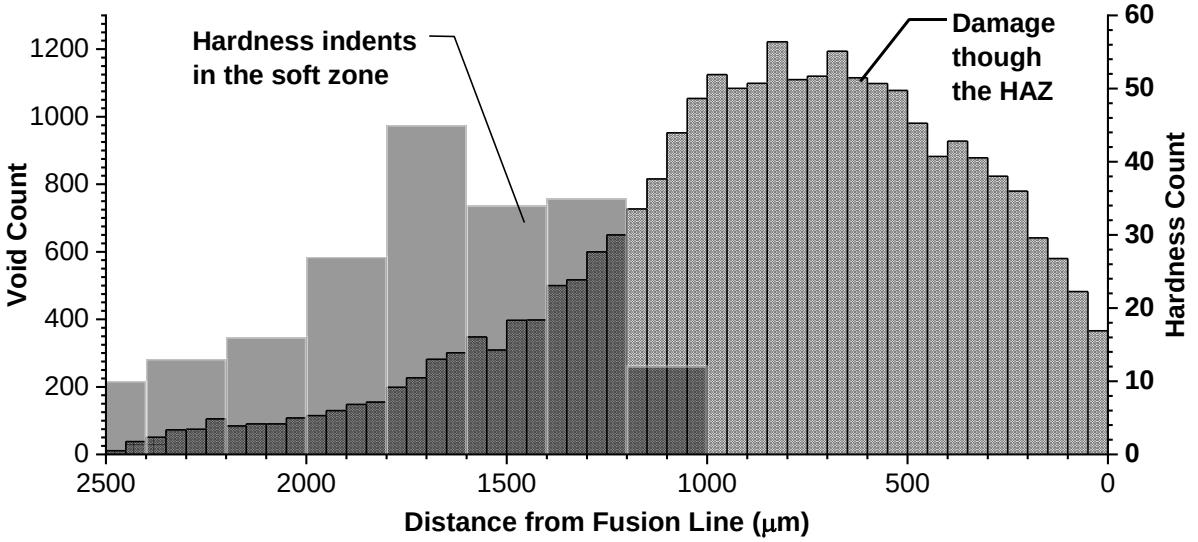

Figure 7-18. Comparison of damage in the heat affected zone for feature-type cross-weld creep sample 9C-3 to the distribution of hardness indents in the soft zone for weld 9C

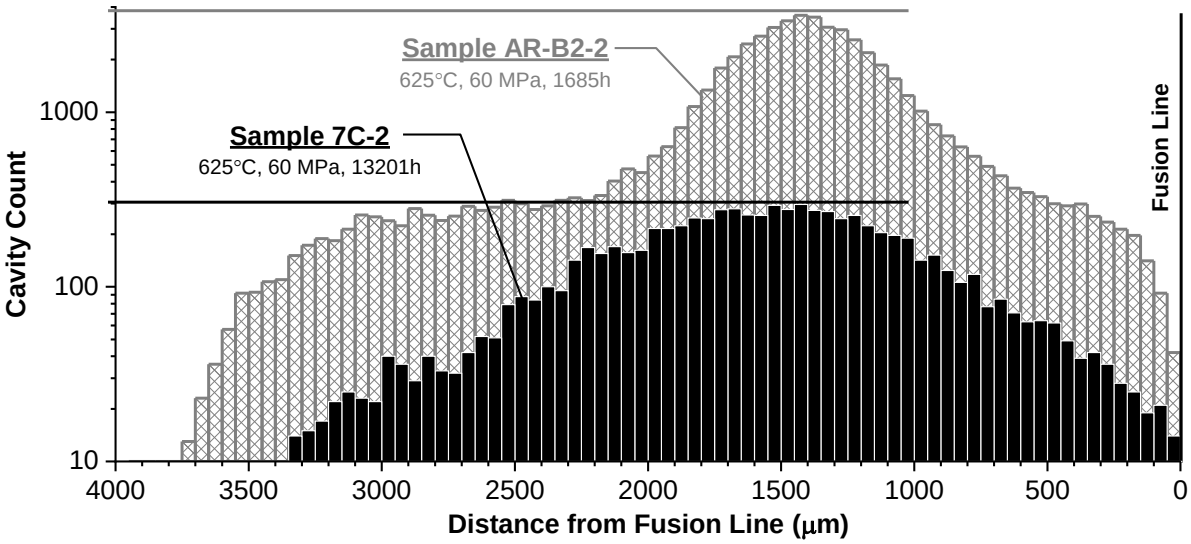

Figure 7-19. Comparison of samples AR-B2-2 and 7C-2 on a log scale for cavity count

7.6 Linking of Macro-Damage to the Welding Thermal Cycle

The relative location of peak damage with the initiation of the soft zone (as determined by hardness mapping), the calculated peak temperature associated with peak damage and the measured macro failures are given in Table 7-3. The extent of damage with respect to the calculated temperature distribution and the macro-failure location is plotted in Figure 7-20 to Figure 7-24. In each of these figures, the location of peak damage, a concept which highlights the distribution of damage between the 25th and 75th percentiles for location relative to the fusion line, is highlighted in red. A more detailed evaluation of the concept of peak damage is presented in (Parker and Siefert 2016b). The calculated peak temperature is represented as a solid blue line and as a function of distance from the fusion line; the procedure for performing this assessment is detailed in section 3.3.4 and was utilized in Chapter 5 for the comparisons of the as-fabricated condition through the HAZ.

Table 7-3. Comparison of locations for the initiation of the soft zone determined by hardness mapping, the location of peak damage, the calculated temperature range determined by a simplified Rosenthal solution and the location of macro failure in the heat affected zone

Sample	Initiation of Soft Zone Location (μm)	Peak Damage Location (μm)	Temperature in HAZ Associated with Peak Damage (°C)	Macro Failure Locations (μm)
7C-2	1,500	1,175 to 1,970	875 to 1,035	1,440 to 1,625
8C-4	1,250	905 to 2,045	865 to 1,105	950 to 1,210
9C-3	1,000	480 to 1,060	925 to 1,120	820 to 1,040
RNT-B2-2	1,750	1,310 to 1,810	890 to 1,010	1,300 to 1,482
AR-B2-2	1,500	1,200 to 1,690	905 to 1,020	1,110 to 1,315

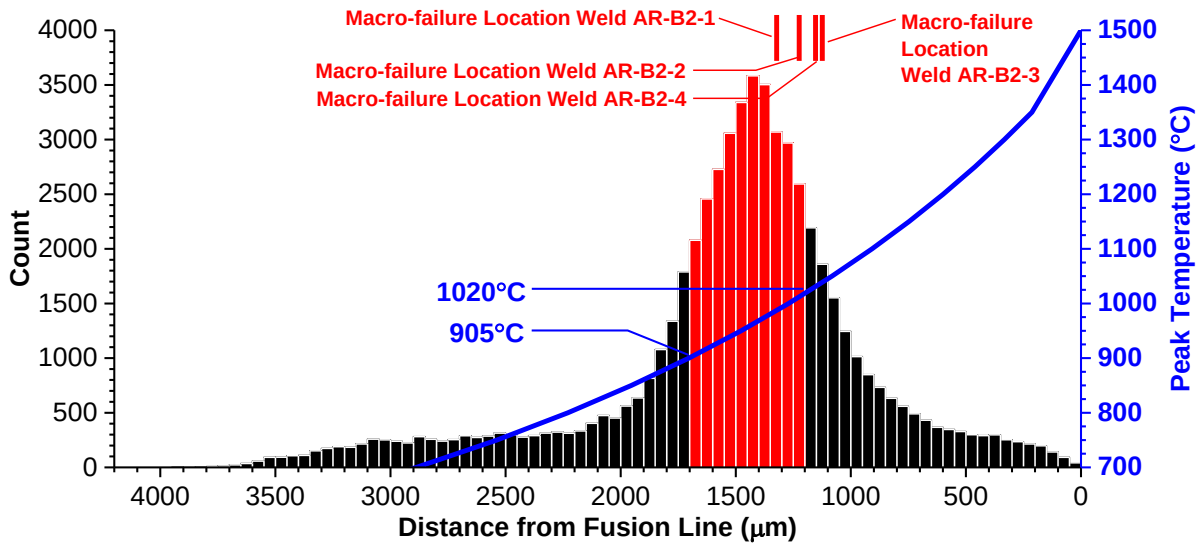

Figure 7-20. Distribution of damage and peak temperature in the heat affected zone in sample AR-B2-2 and as compared to the balance of macro-failure locations in the heat affected zone for the AR-B2 series of tests

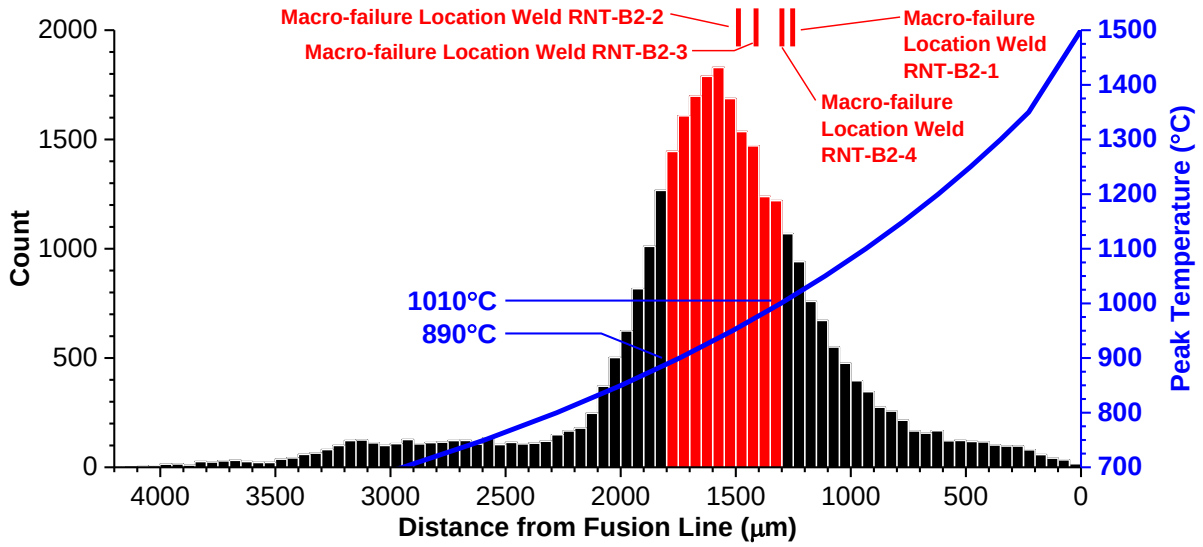

Figure 7-21. Distribution of damage and peak temperature in the heat affected zone in sample RNT-B2-2 and as compared to the balance of macro-failure locations in the heat affected zone for the RNT-B2 series of tests

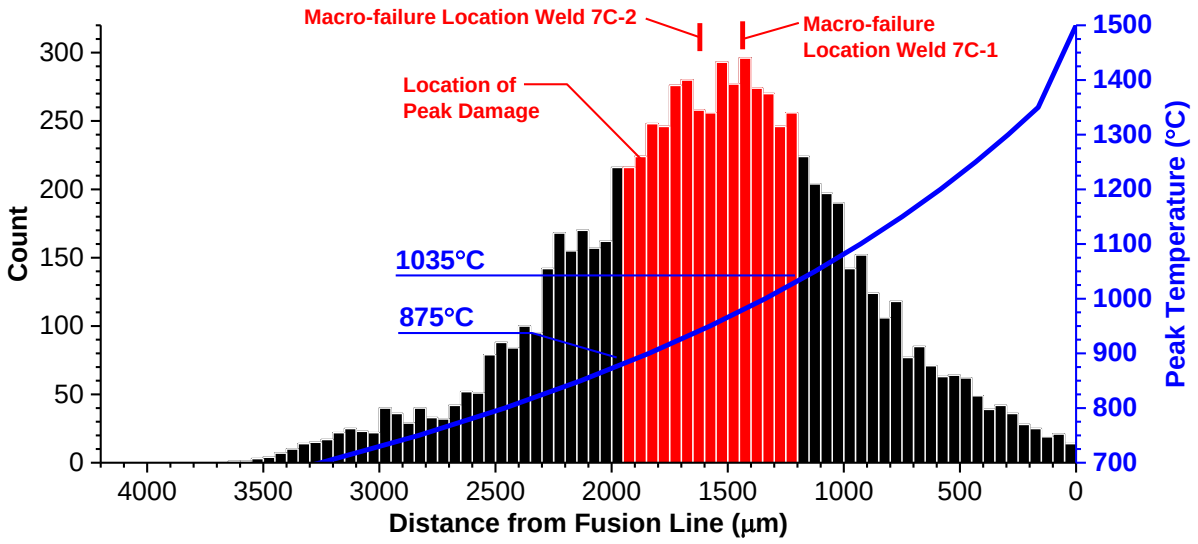

Figure 7-22. Distribution of damage and peak temperature in the heat affected zone in sample 7C-2 and as compared to the balance of macro-failure locations in the heat affected zone for the 7C series of tests

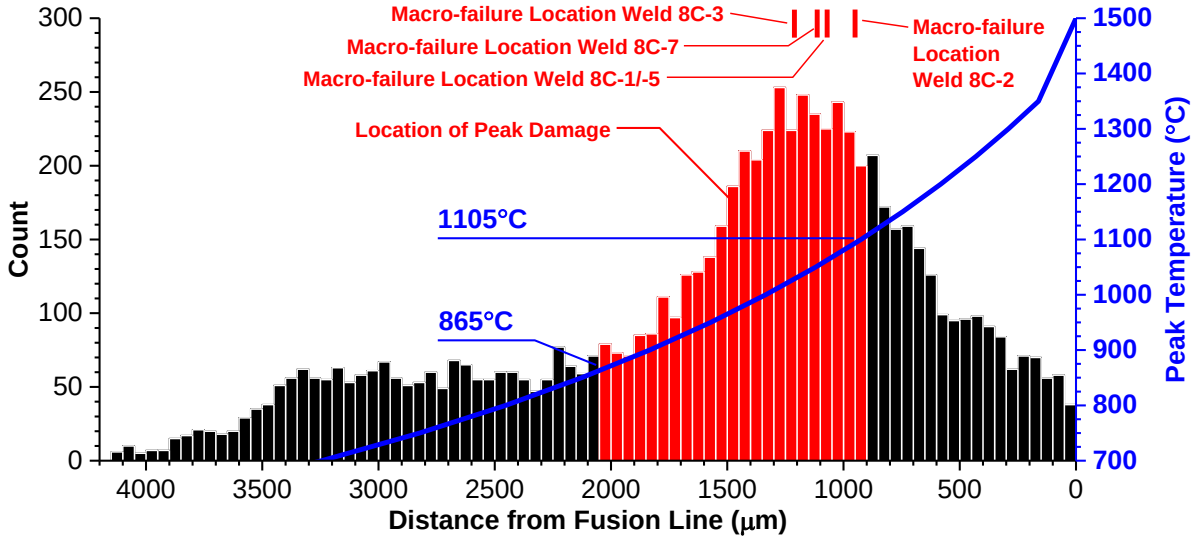

Figure 7-23. Distribution of damage and peak temperature in the heat affected zone in sample 8C-4 and as compared to the balance of macro-failure locations in the heat affected zone for the 8C series of tests

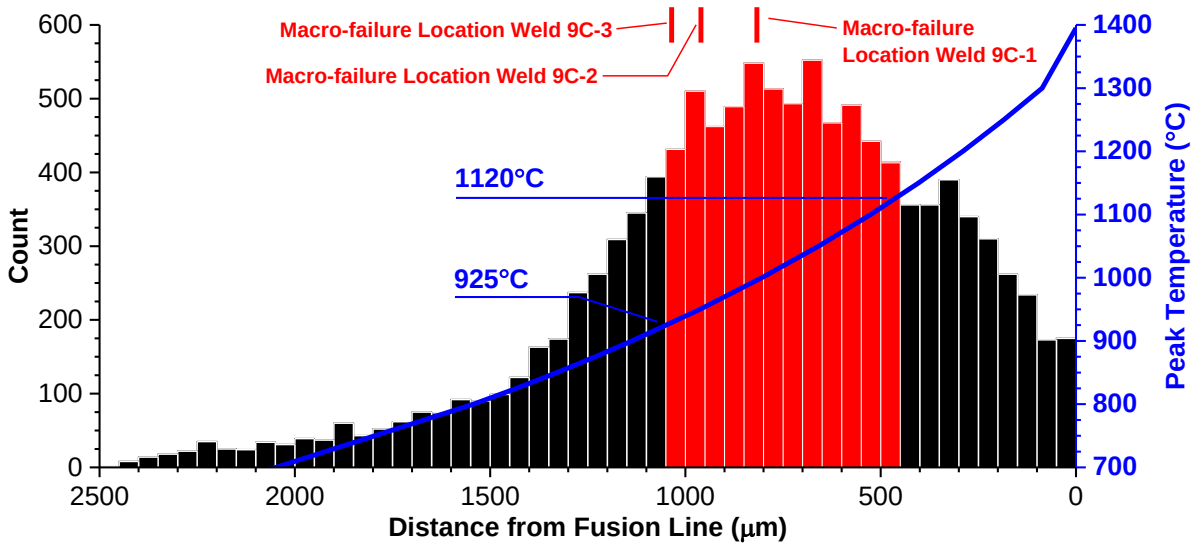

Figure 7-24. Distribution of damage and peak temperature in the heat affected zone in sample 9C-3 and as compared to the balance of macro-failure locations in the heat affected zone for the 9C series of tests

In general, the distribution of damage through the HAZ exhibits a normal distribution. The data in weld 9C-3 (Figure 7-24) deviate from this behavior, a point which is discussed in the following paragraph. In some cases, particularly for sample AR-B2-2 and RNT-B2-2, a long tail is present into the unaffected parent material. This is not an artifact, rather a low level of accumulated damage in the parent material due to its inherently low resistance to the nucleation of creep damage. Note that this tail is not present in the evaluation of sample 7C-2 (e.g. a parent metal with high creep ductility [see Table 6-3 for a comparison of plain bar parent metal creep data]).

The behavior in sample 9C-3 shows a different distribution where the damage forms more readily through the entirety of the HAZ. This is a function of the over-matching, Ni-base weld metal which potentially creates a higher triaxial stress state in the HAZ compared to either the matching or under-matching weldments. This increased triaxiality is not only a function of the filler metal strength, but may also be attributed to the narrower HAZ resulting from the reduced heat input from welding, a point which was noted in section 5.8.

Perspective on the estimated Ac_1 and Ac_3 values compared to the peak temperature range in the HAZ associated with peak damage is provided in Table 7-4. This assessment builds on the information presented in Table 5-5, which used equations 5.1 and 5.2, ThermoCalc simulations to estimate the A_1 and A_3 values and published data from (Gaffard 2004) to evaluate the potential shift to the Ac_1 and Ac_3 temperatures

resulting from the non-equilibrium weld thermal cycle. The critical phase transformation temperatures under equilibrium and non-equilibrium conditions are compared to the temperature in the HAZ associated with peak damage (from Table 7-3).

Table 7-4. Comparison of locations for the initiation of the soft zone determined by hardness mapping, the location of peak damage, the calculated temperature range determined by a simplified Rosenthal solution and the location of macro failure in the heat affected zone

Parent Metal	Approx. A_1 (°C)	Ac_1 (°C)	Approx. A_3 (°C)	Ac_3 (°C)	Cross-weld Sample	Temperature in HAZ Associated with Peak Damage (°C)	Temperature in HAZ Associated with Macro Failure Location (°C)
TP1	810	910	840	1020	7C-2	875 to 1,035	~970
					8C-4	865 to 1,105	~965
					9C-3	925 to 1,120	~970
B2	820	920	850	1030	RNT-B2-2	890 to 1,010	~980
					AR-B2-2	905 to 1,020	~1,020

In all cases, *the location of peak damage* corresponds more closely to a calculated peak temperature approximated by the Ac_1. The extent of damage is observed to extend slightly beyond the Ac_3 value, particularly for the samples evaluated in the as-welded condition (e.g. 8C-4 and 9C-3). The association of damage with this temperature range would thus be characterized as Type IV failure or Type IV damage and is often associated with the ICHAZ or the FGHAZ. *The documented macro failure* location is biased to a temperature more characteristic of the Ac_3 value.

The description of the failure location to an exact location in the HAZ is confusing considering the classification of the HAZ regions is most often done so using the classical diagram from Easterling (Figure 1-9). The definition of 'intercritical' in the context of non-equilibrium welding conditions cycle shifts the A_1 and A_3 to Ac_1 and Ac_3 values. Under equilibrium conditions, the ICHAZ would be defined as a peak temperature between 815 to 850°C for the AR-B2 material, while for nonequilibrium welding heating rates this range is shifted considerably to values ~920 to 1030°C.

Furthermore, the data show that the association of damage with a region in the HAZ recently classified as the PTZ is more accurate considering the difficulty in defining the regions of the HAZ associated with a purely ICHAZ or FGHAZ thermal cycle. While the PTZ extends through a considerable portion of the HAZ, the peak temperature region where damage is observed in accordance with the peak damage concept, is

approximated by the range of temperatures between the Ac_1 value (which can be compositionally and welding thermal cycle dependent) and the minimum temperature for normalization (e.g. 1040°C for Grade 91 steel). Although damage is observed outside of this temperature regime, the position of macro failure in all samples coincides with the location of peak damage and is nearer to the Ac_3 temperature (than the Ac_1 temperature). This subtle difference in the distribution of damage and the ultimate failure location is perhaps one reason why there exists widespread disagreement within the literature regarding the precise location for failure in Grade 91 steel cross-weld tests.

Comparison of the cross-weld test samples made with matching filler material, given a PWHT and in martensitic parent metal is provided in Figure 7-25. The center of each distribution is not observed to change dramatically, but the density of damage is markedly different. Note that the comparison of samples AR-B2-2 and 7C-2 was provided in Figure 7-19 for a log scale of cavity count to show the factor of ten difference in absolute density that was observed between these two cross-weld tests.

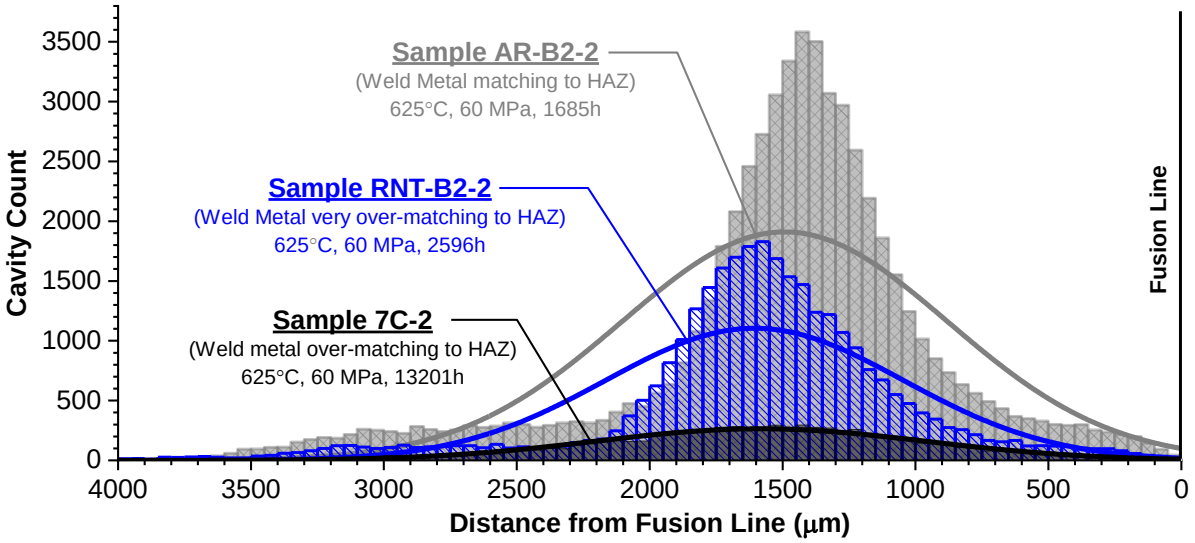

Figure 7-25. Comparison of evaluated weldments made with matching filler metal and given a post weld heat treatment at 675°C for 2 hours.
Note: *AR-B2-2 is a low creep strength and low creep ductility parent material, RNT-B2-2 is a medium creep strength and low creep ductility parent material and 7C-2 is a medium creep strength and high creep ductility parent material*

Where conditions are altered based on filler metal strength, the constraint on the HAZ is observed to alter the distribution of damage, most notably the overall width over which damage is seen to accumulation, Figure 7-26. In the case of the under-matching filler metal cross-weld creep test 8C-4, the damage through the HAZ forms over a

larger width compared to the matching test sample 7C-2. Furthermore, the extent of damage is accommodated by a cross-sectional area that is larger than for the other investigated samples since the weld metal is observed to possess damage.

For the over-matching filler metal sample 9C-3 the distribution of damage is shifted to higher overall peak cavity count values and biased closer to the fusion line. As documented previously in Figure 7-12 the accumulated damage at termination of the test in sample 9C-3 is higher and possesses multiple micro-cracks through the evaluated region in the HAZ. This does not change the apparent failure mode from a Type IV failure although it does highlight the importance of structural behavior in cross-weld creep test evaluations. As the strength of the filler metal increases and becomes *very* over-matching relative to the parent metal, the damage in the HAZ is increased. The damage is seen to increase in absolute density, as well as with respect to the width, e.g. damage is seen more broadly through the HAZ up to the fusion line.

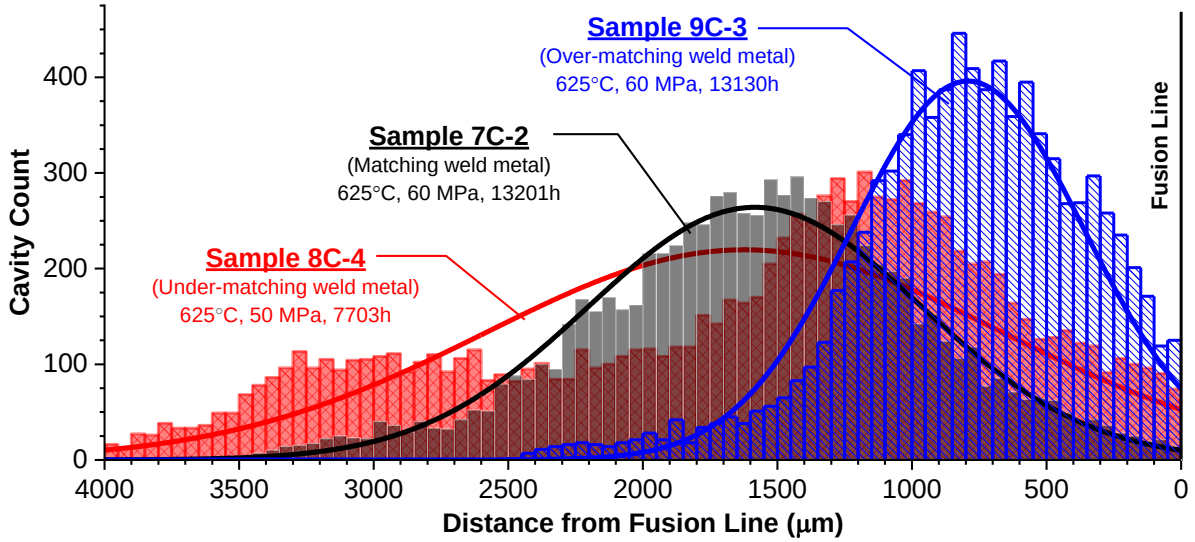

Figure 7-26. Comparison of evaluated weldments made with variable filler metal strength.
Note: *sample 9C-3 made with an over-matching filler material, sample 7C-2 with a matching filler metal and sample 8C-4 with an under-matching filler metal.*

7.7 Density of Cavitation in the Heat Affected Zone

Comparison of individual images in the HAZ to the global density of damage are summarized in Table 7-5. The global peak cavitation density is calculated from the histograms of damage presented previously in Figure 7-20 to Figure 7-24. In each figure, the width of the bin is 50 μm. The highest damage count value is utilized and this value is divided by the product of the bin width and the height of the analyzed image (e.g. either 22.0 mm for sample 9C-3 or 23.2 mm for samples AR-B2-2, RNT-

B2-2, 7C-2 and 8C-4). This global value is compared to local images taken using a 20X objective (~400X magnification) which are provided in Figure 7-27 to Figure 7-31. In general, the distribution of damage is observed to subtly change through the thickness. Locations for documenting the 'local high cavitation' or 'local low cavitation' regions were based on this observation. An example of such variation is provided in Figure 7-32. Thus, an attempt is made in Table 7-5 and Figure 7-27 to Figure 7-31 to document the variability in damage distribution that was observed in the cross-weld creep test samples.

Table 7-5. Comparison of cavity densities in the evaluated feature-type cross-weld creep samples

Sample	Global Peak Cavitation (voids/mm^2)	Local, High Cavitation Region (voids/mm^2)	Local, Low Cavitation Region (voids/mm^2)
AR-B2-2	3,103	3,060	2,505
RNT-B2-2	1,573	1,255	625
7C-2	254	435	240
8C-4	215	435	180
9C-3	500	725	260

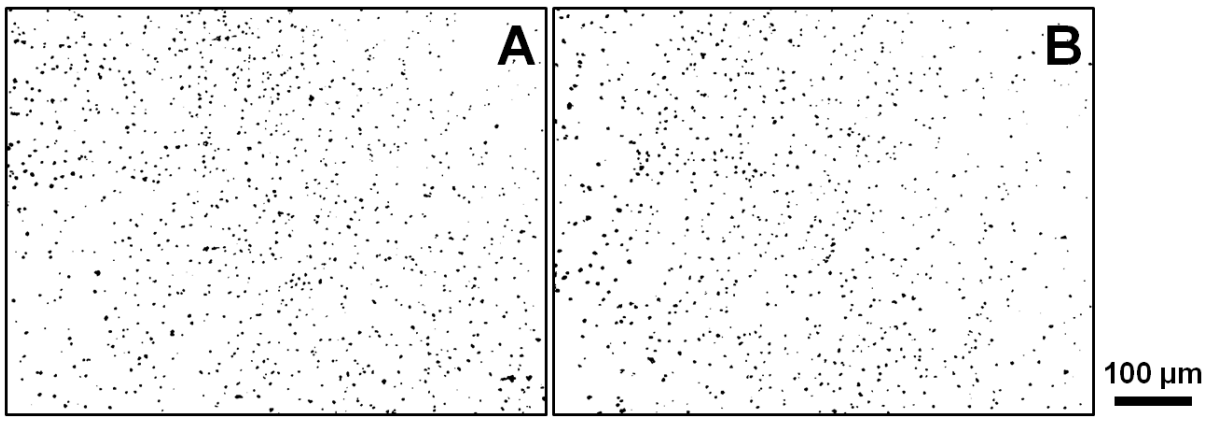

Figure 7-27. Representative damage in AR-B2-2 for a high damage Location (A) and a low damage location (B)

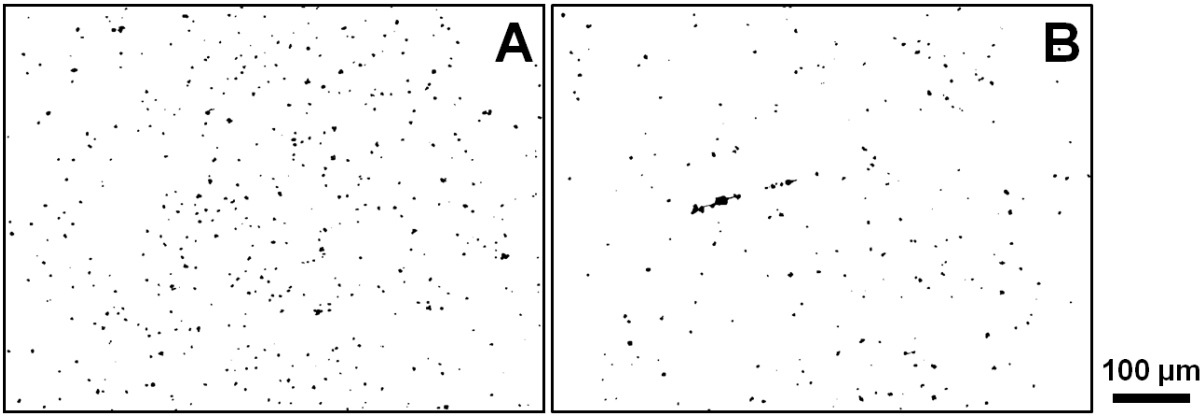

Figure 7-28. Representative damage in RNT-B2-2 for a high damage Location (A) and a low damage location (B)

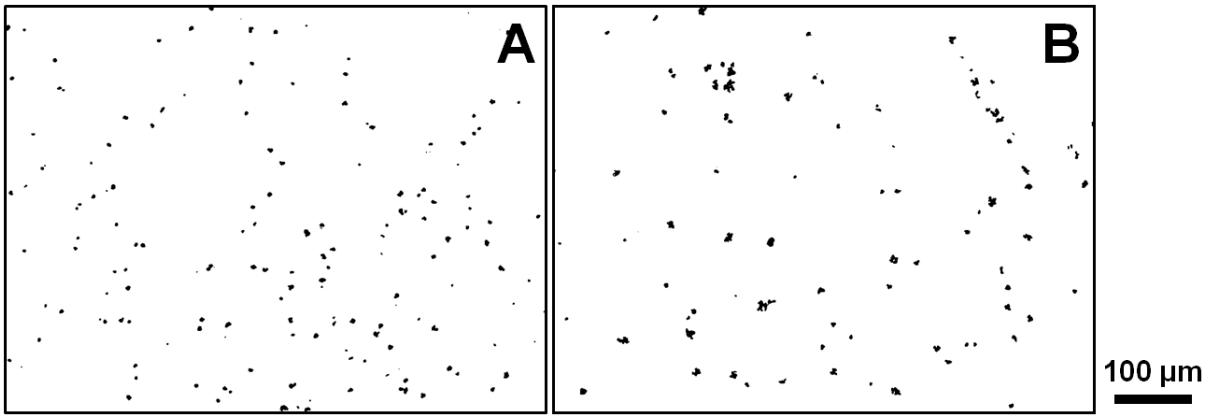

Figure 7-29. Representative damage in 7C-2 for a high damage Location (A) and a low damage location (B)

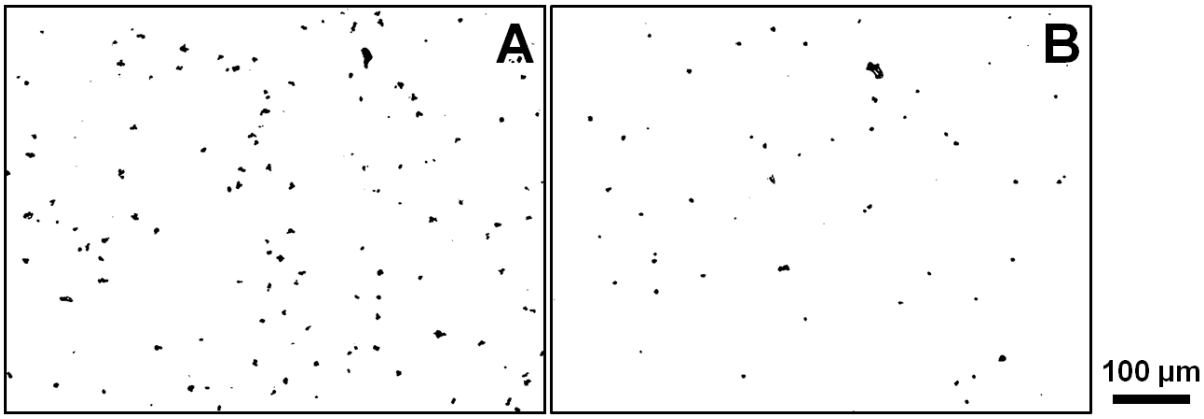

Figure 7-30. Representative damage in 8C-4 for a high damage Location (A) and a low damage location (B)

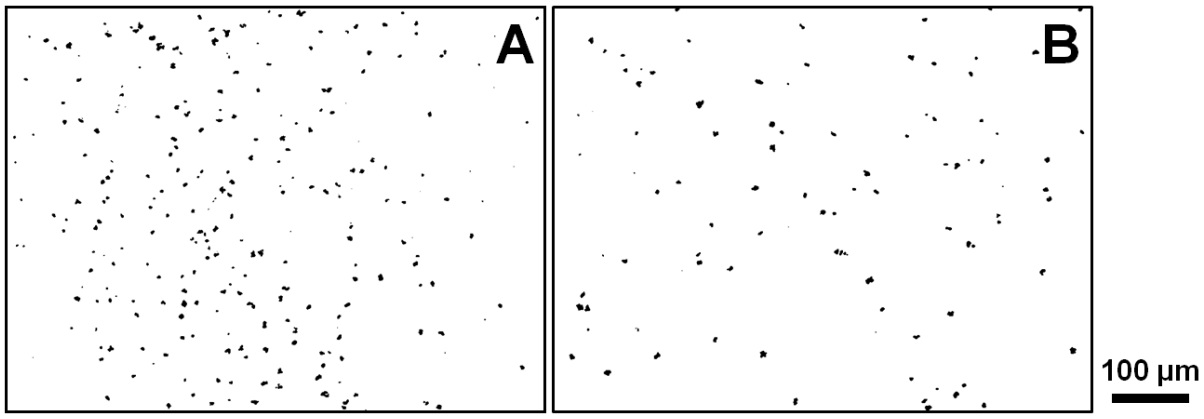

Figure 7-31. Representative damage in 9C-3 for a high damage Location (A) and a low damage location (B)

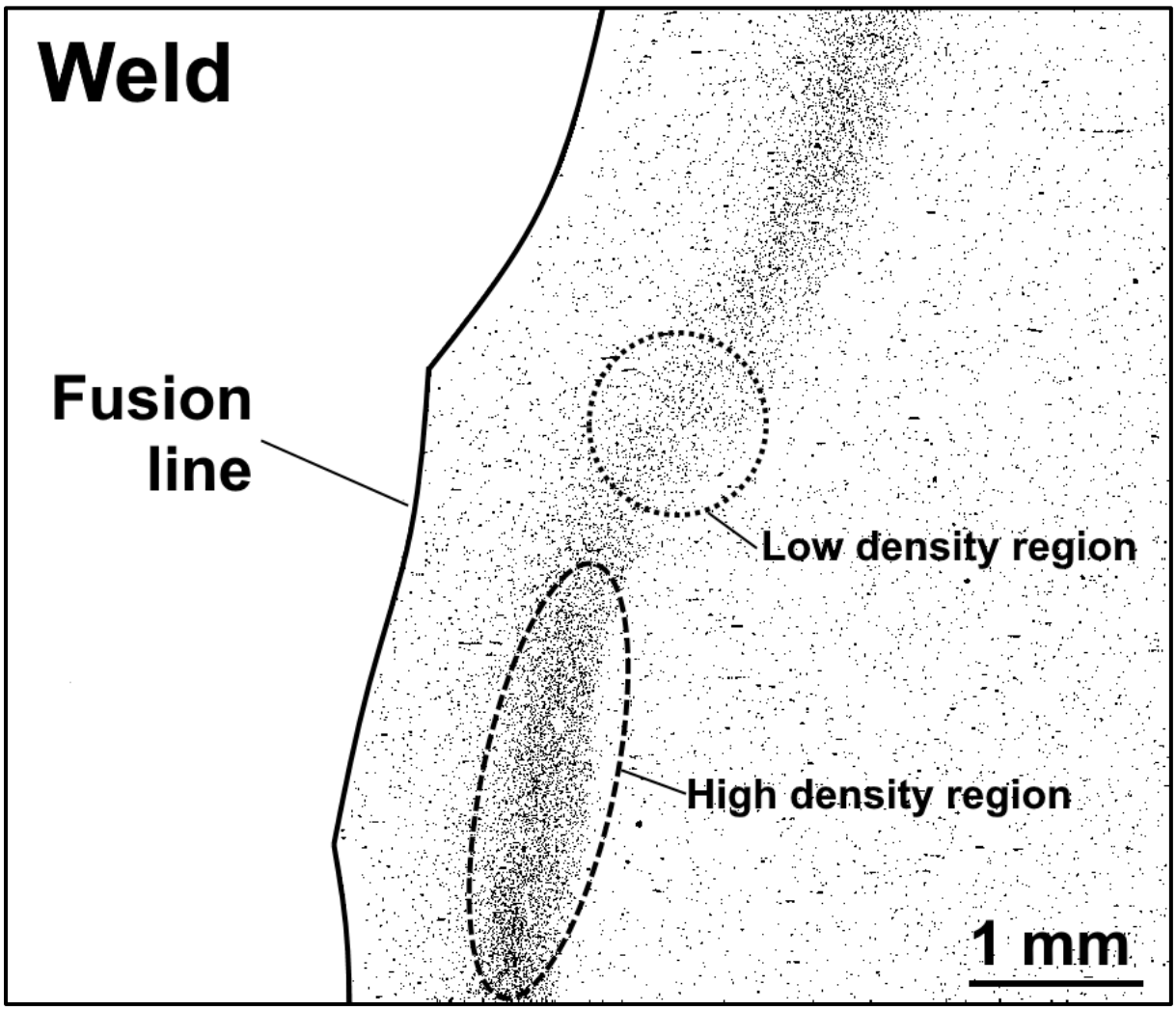

Figure 7-32. Comparison of relative low and high-density regions of damage in the heat affected zone (image taken from sample AR-B2-2)

7.8 Discussion

One weld exhibited consistent, macro-level damage in the weld metal associated with the fact that the AWS type -B8 filler metal possesses a deformation resistance very

comparable to that of the Grade 91 PTZ (Figure 6-25). The damage in the weld metal was noted along coarse columnar grain boundaries aligned normal to the applied stress axis (Figure 7-7 to Figure 7-10).

A second weld, F-TP1, exhibited failure in the parent material unless the applied stress was ≤60 MPa for a test temperature of 625°C. At an applied stress of 50 MPa the behavior of the cross-weld creep test exhibited less parent metal deformation compared to the test at 60 MPa (Figure 7-33) suggesting that the formation of a HAZ-dominated crack will become a more important consideration under certain service conditions. Furthermore, the location of failure in the HAZ in these tests was closer to the fusion line compared to the weldments made in the martensitic parent metal.

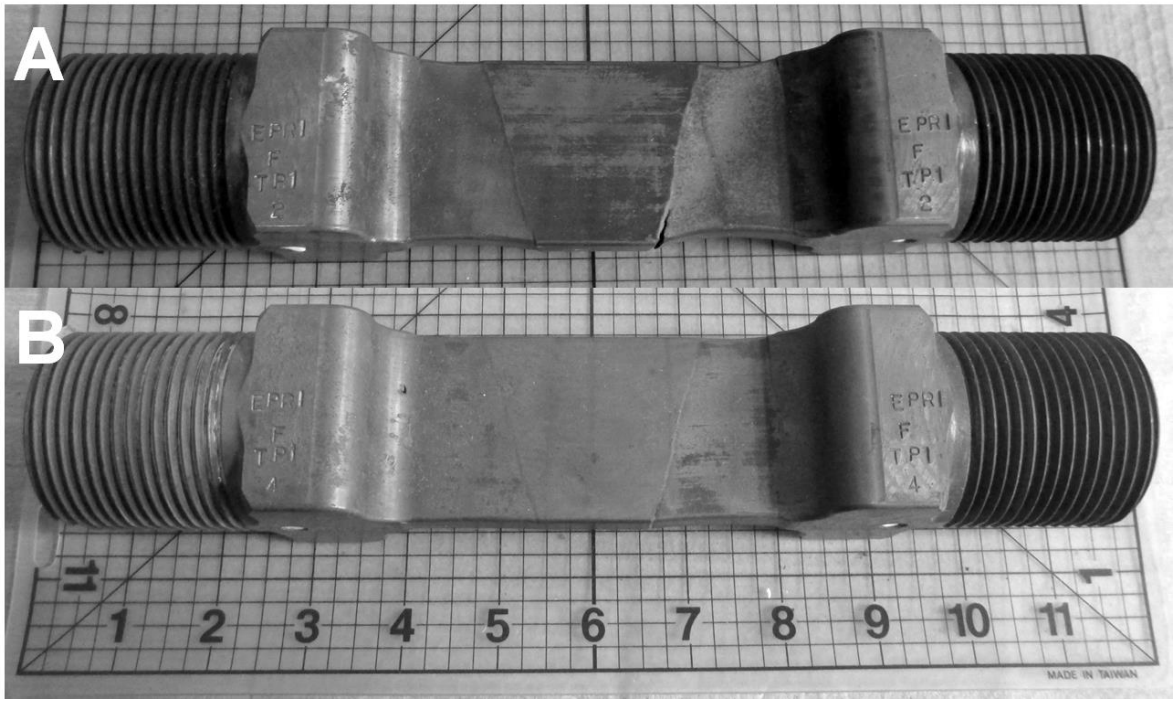

Figure 7-33. Comparison of feature cross-weld creep tests in F-TP1 parent material; test at 625°C and 60 MPa (A) and test at 625°C and 50 MPa (B)

For the cross-weld creep samples which failed by the evolution of damage and/or cracking in the HAZ (e.g. so-called Type IV failures) the location coincided with a bias to a temperature approximated by the Ac_3 (see Table 7-4). This same comparison showed, however, that a distribution of damage was observed through the HAZ and dominated by the presence of damage in a specific region of the HAZ called the PTZ. The field of damage which overlapped a zone called the region of 'peak damage' was 500 to 800 µm in width for tests in martensitic parent metal, fabricated with matching filler materials and given a PWHT. The peak damage was concentrated in a location

in the HAZ (Figure 7-34) that experienced a peak temperature approximated by the Ac_1 temperature and extended to a temperature that overlaps the minimum normalization temperature (1040°C).

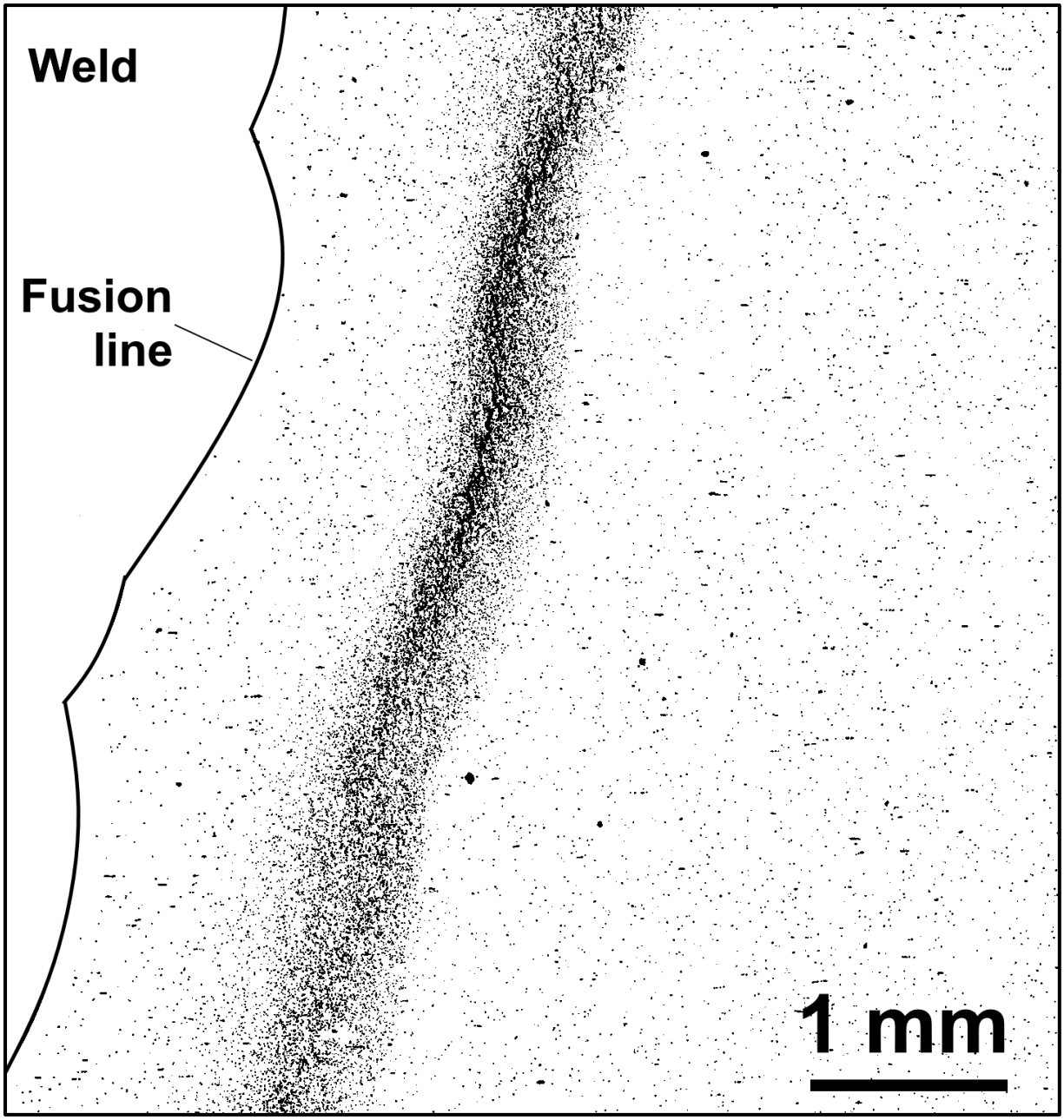

Figure 7-34. Representative field of damage in the heat affected zone for a low ductility parent metal (AR-B2-2 shown)

The comparison of damage through the HAZ and the hardness indents identified as being in a soft zone adjacent to the HAZ did not overlap completely. In fact, the distributions provided in Figure 7-14 to Figure 7-18 provide a consistent story; the association of damage in the HAZ cannot be linked to a soft zone since this region is

not clearly linked to the PTZ. Evidence continues to emphasize that the soft zone is best characterized as the OTZ (section 5.8).

For the welds evaluated in the parent material with low creep ductility (AR-B2 and RNT-B2), the extent of damage was notably higher through the HAZ even for test durations that were 5-8X less compared to the high creep ductility base metal (TP1), Figure 7-25. The observed behavior in Figure 7-25 is interesting with respect to several points. These cross-weld test were conducted at identical test conditions, and for otherwise identical weldments, with the primary difference being the parent material condition. The factor of ~8 on life links strongly to the cavity density and the development of a high density of cavities. Thus, for the AR-B2 and RNT-B2 materials, there must exist a larger density of nucleation sites for damage. It is considered that the density of such sites must be high, since the PTZ will be susceptible to the nucleation and growth of voids owing to the multiaxial stress state that develops in this region. Once a critical density of voids exists, and provided a uniform damage field is present (likely for a controlled, cross-weld test under uniform axial stress), the time between crack initiation and failure will be very low. This point was highlighted in sections 6.6 and 6.8.

A very similar conclusion is detailed in (Parker and Parsons 1995) and reviewed in section 2.14.1, where the authors conducted a controlled study assessing cross-weld behavior of an ex-service weld. This ex-service weld had been fabricated from two unique heats of CrMoV and welded with 2.25Cr-1Mo filler metal. With respect to the main alloying elements, the CrMoV steels were effectively the same and exhibited a similar volume fraction of inclusions. However, upon a more detailed area fraction assessment of the inclusion density, it was clear that the CrMoV steel B, which had exhibited the HAZ failures in the cross-weld creep tests, contained a larger density of fine inclusions. Interestingly, uniaxial creep tests in both parent materials – and again like the response in this study for parent materials TP1 and RNT-B2 – showed that the CrMoV steel B, in which HAZ failures occurred, was slightly stronger than the CrMoV steel A (by ~30%). Although the deformation response was similar, the creep ductility in steel A was about 10% whereas for steel B the values were greater than 20%. The authors rationalized these observations, “Since the tendency for an inclusion to be present on the boundary will increase for fine grain sizes, the observed susceptibility

for HAZ failures is directly related to the base material ductility, rather than simply being a consequence of the microstructure modifications developed during welding."

A comparison of the PTZ microstructure, assessed using EBSD and reported in section 5.6, is provided for the weldments in the martensitic parent materials (e.g. AR-B2, RNT-B2 and 7C) in Figure 7-35. The overall grain boundary size and morphology appears similar for each of these weldments, and for a location that is in the as-fabricated condition and approximated by the location of macro failure reported in Table 7-1. This again emphasizes the need to more fully characterize the nature and extent of damage on the micro-scale to help elucidate the features which contribute to damage and ultimately Type IV failure.

AR-B2 HAZ; EBSD map collected at 1.2 mm from fusion line (FL).
Macro failures 1.1 to 1.3 mm from FL.
Image centered T_{peak} ~1020 ± 25°C

RNT-B2 HAZ; EBSD map collected at 1.2 mm from fusion line (FL).
Macro failures 1.25 to 1.5 mm from FL
Image centered T_{peak} ~1030 ± 25°C

TP1 HAZ; EBSD map collected at 1.2 mm from fusion line (FL).
Macro failures 1.4 to 1.6 mm from FL
Image centered T_{peak} ~985 ± 25°C

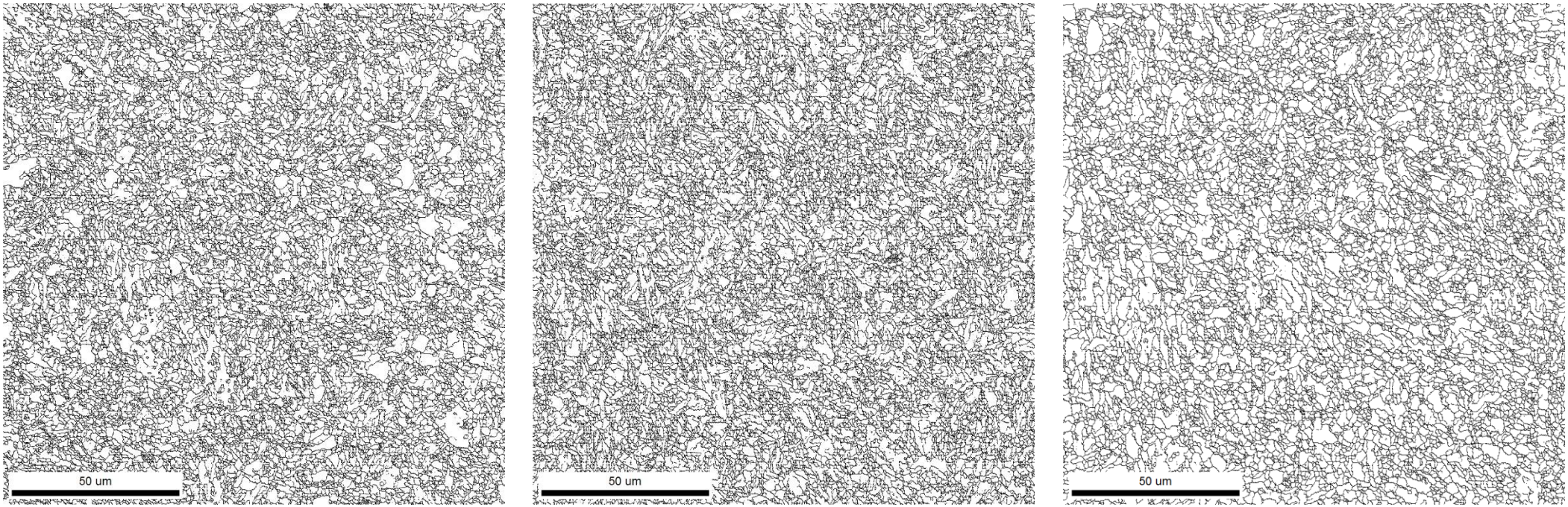

Figure 7-35. Comparison of microstructures for grain boundary maps collected using SEM-EBSD and for boundaries 2-180° at a position in the as-fabricated heat affected zone where macro-failure was documented in the post-test evaluation; scale = 50 µm

7.10 Summary

In Chapter 5, the as-fabricated microstructure was detailed. In Chapter 6, the mechanical performance of the cross-weld creep test program assessed and in the most recent chapter the macro failure nature of select cross-weld creep tests were provided. The assessment in this Chapter supports several key conclusions regarding the macro-characteristics of damage in the HAZ in Grade 91 steel:

- Damage is not associated with a so-called soft-zone often identified through routine hardness evaluation in the as-fabricated HAZ (Figure 7-14 to Figure 7-18);
- Damage is consistently identified in a region defined in Table 1-4 as the PTZ;
- Peak damage is observed in a temperature range equivalent to the Ac_1 value (e.g. ~900°C) to just below the minimum value for normalization (~1040°C), Figure 7-20 to Figure 7-24. For weldments which are not subjected to PWHT, the distribution of damage is slightly increased to temperatures approximated by the upper end of normalization for Grade 91 steel (e.g. ~1100°C).
- Macro-failures are consistently observed in the 50^{th} to 75^{th} percentiles in the damage distribution (e.g. biased to the Ac_3 value as opposed to the Ac_1 value or soft zone)
- Damage is ~an order of magnitude greater for the low creep ductility parent material as compared to the high ductility parent metal heat, Figure 7-19;
- The use of over-matching filler material is observed to increase the overall extent of damage in the HAZ and shift elevated levels of damage to a region biased to the fusion line, Figure 7-26. HAZ dominated failures in the PTZ are still observed.
- The use of under-matching filler material widens the distribution of damage in the HAZ and extends into the weld metal where damage is concentrated along coarse columnar grain boundaries, Figure 7-7 to Figure 7-10.

Future Chapters will evaluate damage on a finer length scale, attempting to link the evolution of creep voids to specific features and/or particles in the HAZ. To accomplish

this, the assessments will focus on selected samples highlighted in Table 7-2 as well as the evaluation of the interrupted sample AR-B2-5 described in Chapter 4.

8 Micro-characterization of Damage using Scanning Electron Microscopy

8.1 Introduction

The macro failure evaluation presented in Chapter 7 quantified the dramatic difference in cavity density for weldments fabricated using nominally identical welding procedures. The current chapter utilizes several methods for quantifying damage on the micro-scale, such as:

- Imaging of representative damage utilizing backscatter and/or secondary electron detectors;
- Quantitative assessment of local composition and confirmation of particles inside or adjacent to cavities using SEM-EDS;
- SEM-EBSD to identify if recrystallization associated with strain localization can be quantified and to locate the cavities relative to the grain boundary profile in the HAZ; and
- For the dissimilar metal weld (e.g. weld 9C), assessment of compositional changes across the fusion line.

8.2 Selection of Test Samples

The detailed evaluation of damage in post-test samples has focused on seven samples, Table 8-1. Apart from the weld 8C series of cross-weld tests, the assessment of damage on the micro-scale for samples AR-B2-2 (low strength, low ductility), RNT-B2-2 (medium strength, low ductility), 7C-2 (medium strength, high ductility) and 9C-3 (medium strength, high ductility, over-matching filler metal) in the present Chapter is consistent among this set of samples. Regarding the weld 8C, the selected samples 8C-5 and 8C-7 (medium strength, high ductility, under-matching filler metal) possess a combination of HAZ and weld metal damage. The evaluation of fusion line damage is provided for sample 9C-3 although the dominate failure mode was the development of damage in the HAZ. The sample F-TP1-4 (low strength, high ductility, ferritic parent metal) was included in this evaluation as it contained a more evolved set of damage in the HAZ compared to the F-TP1-2 sample.

Table 8-1. Evaluated samples for the evaluation of damage

Sample	Stress (MPa)	Temp. (°C)	Time to Failure (hours)	Evaluated Regions
AR-B2-2	60	625	1,685	HAZ
RNT-B2-2	60	625	2,596	HAZ
7C-2	60	625	13,201	HAZ
8C-5	70	600	10,461	HAZ and weld metal
8C-7	90	575	13,101	
9C-3	60	625	13,130	HAZ and fusion line
F-TP1-4	50	625	15,472	HAZ

8.3 Damage in the Weld Metal

Damage in the deposited weld metal was noted for the weld 8C series of tests. The damage was present near the center of the gauge (Figure 7-6), and independent of a macro-variation in the composition (see Figure 5-7 to Figure 5-9). The macro-appearance of the damage is provided in Figure 8-1 where the damage is oriented normal to the applied stress axis. Images obtained in the etched condition using traditional light optical microscopy can be found in Figure 7-7 to Figure 7-10. Based on these low magnification images, it was originally suggested that damage was concentrated in the coarse columnar regions of the weld metal in Section 7.3. This assertion will be revisited in the subsequent information.

At higher magnifications (Figure 8-3), the damage present in the weld metal suggests that individual cavities are nucleating along grain boundaries normal to the stress axis, then growing and coalescing into micro- and eventual macro-cracks, for example as shown in Figure 8-3D. This behavior is consistent with the classical description proposed by Neubauer for the development of damage in CrMo, low alloy steels where damage is first present as isolated cavities, then oriented cavities which link to form microcracks and eventually macrocracks (Neubauer 1984). The observed, spherical ‘voids’ that are not present on boundaries are likely to be gas pores (e.g. “weld porosity”) developed from the welding process and not necessarily ‘damage’ (see Figure 8-2).

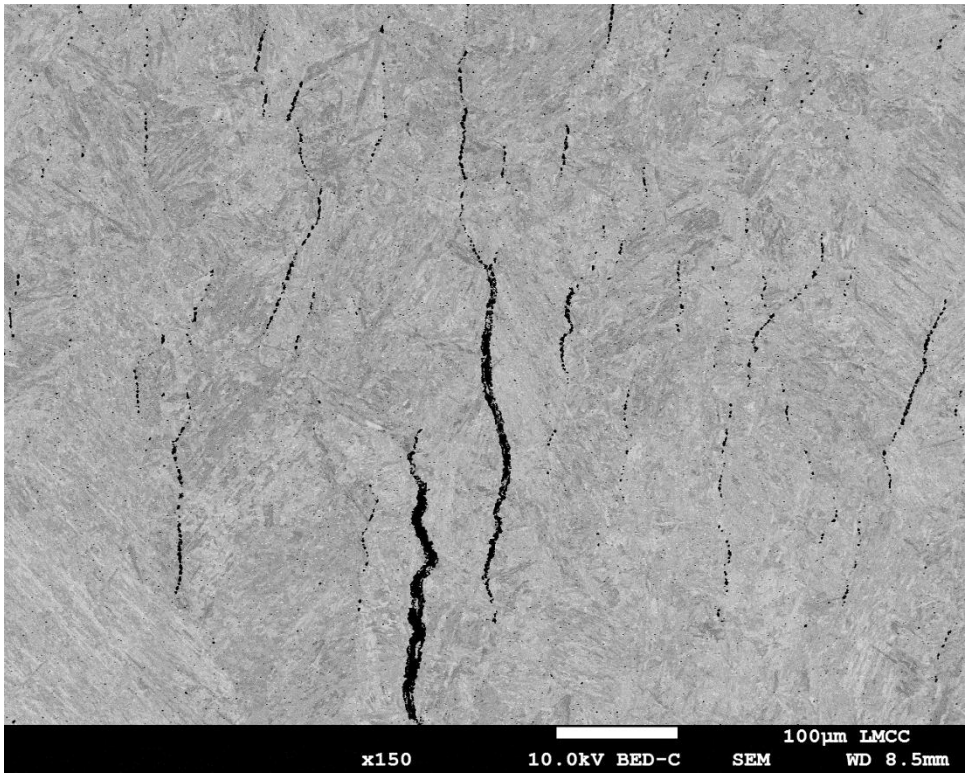

Figure 8-1. Sample 8C-7 (575°C, 90 MPa, 13,101 hours), SEM backscatter electron image of damage in the weld metal on macro scale, 150X; scale = 100 µm
Note: *Stress axis is left-to-right*

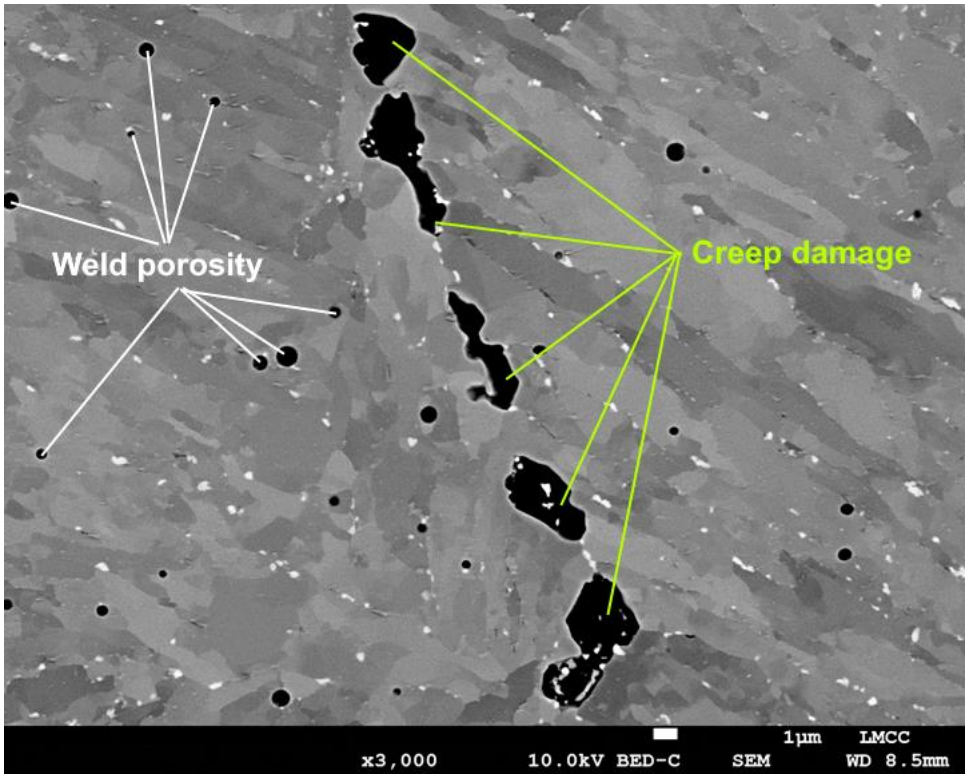

Figure 8-2. Clarification of the difference between weld porosity resulting from the welding process during fabrication (noted as intragranular, spherical voids) and the presence of creep damage along grain boundaries; scale = 1 µm

Distinction between the rate-governing step in the formation of cavities in this series of damage in the weld metal is difficult to determine since the individual cavities in Figure 8-3H are already >1 μm in diameter and of the order of ~5 μm in diameter. The size and extent of damage is such that the original nucleation source or a microstructural zone adjacent to the cavity is not easily observable and thus impossible to quantify.

Characterization of damage in the weld metal is presented on a larger scale using backscatter imaging in Figure 8-4 and using SEM-EBSD in Figure 8-5. Figure 8-4A was purposely taken using a large field of view to include damage through a region in the weld metal with coarse columnar and refined regions. The coarse columnar region is clearly present through the center of the image. In the regions above and below this location, the grain structure is more refined. As shown in Figure 8-4B using an adjusted brightness and contrast image to highlight the damage as black and the matrix as white, the damage is documented in both the coarse and refined grain regions. The damage is aligned normal to the stress axis and is neither preferentially distributed in a higher density in the columnar nor in the refined regions. The extent of macro-cracking is greatest in the coarse columnar region, but this does not suggest that this region is ‘more damaged.’ The extent of cracking is greater in the coarse columnar region since the mean grain boundary length is higher. Damage thus does not seem to prefer a single region in the weld; it simply occurs throughout the weld, is aligned normal to the stress axis and is solely intergranular.

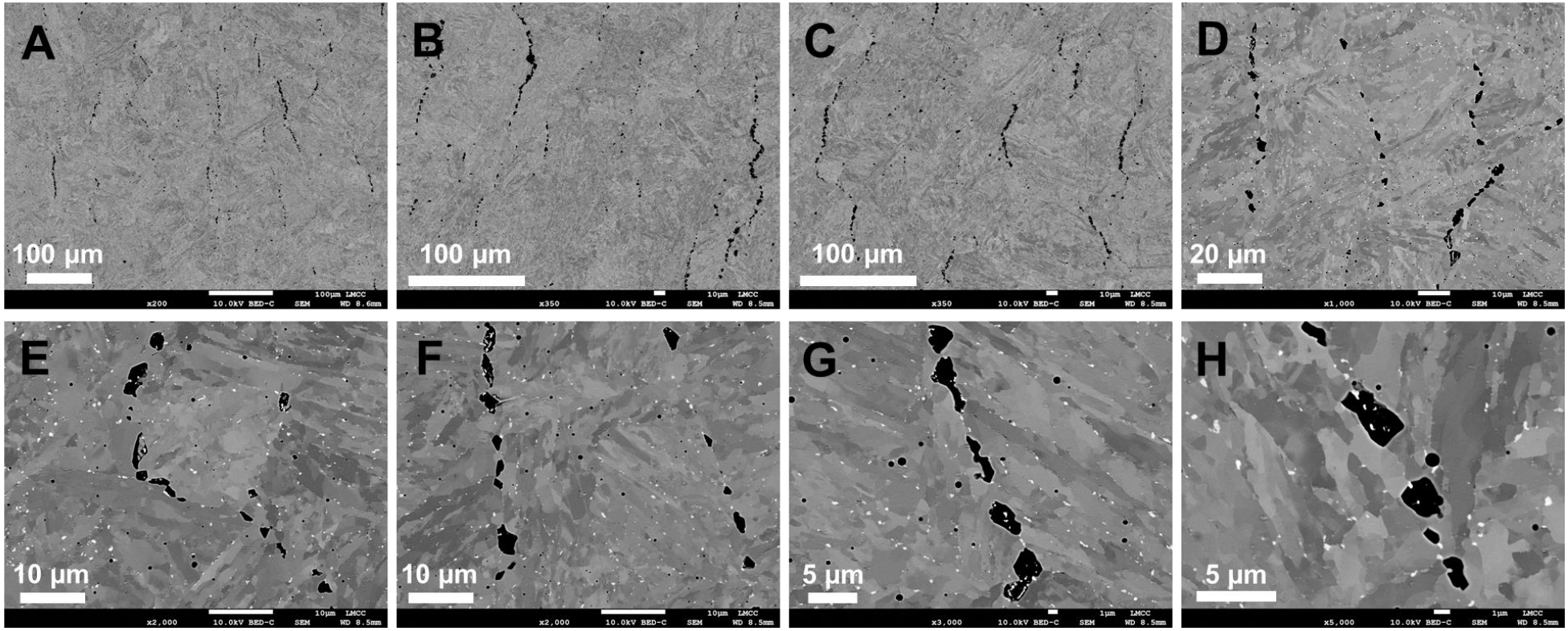

Figure 8-3. Sample 8C-7 (575°C, 90 MPa, 13,101 hours), SEM backscatter electron images of damage in the weld metal and not associated with inclusions, 200X (A), 350X (B, C), 1,000X (D), 2,000X (E, F), 3,000X (G) and 5,000X (H)
Note: *Stress axis is left-to-right*

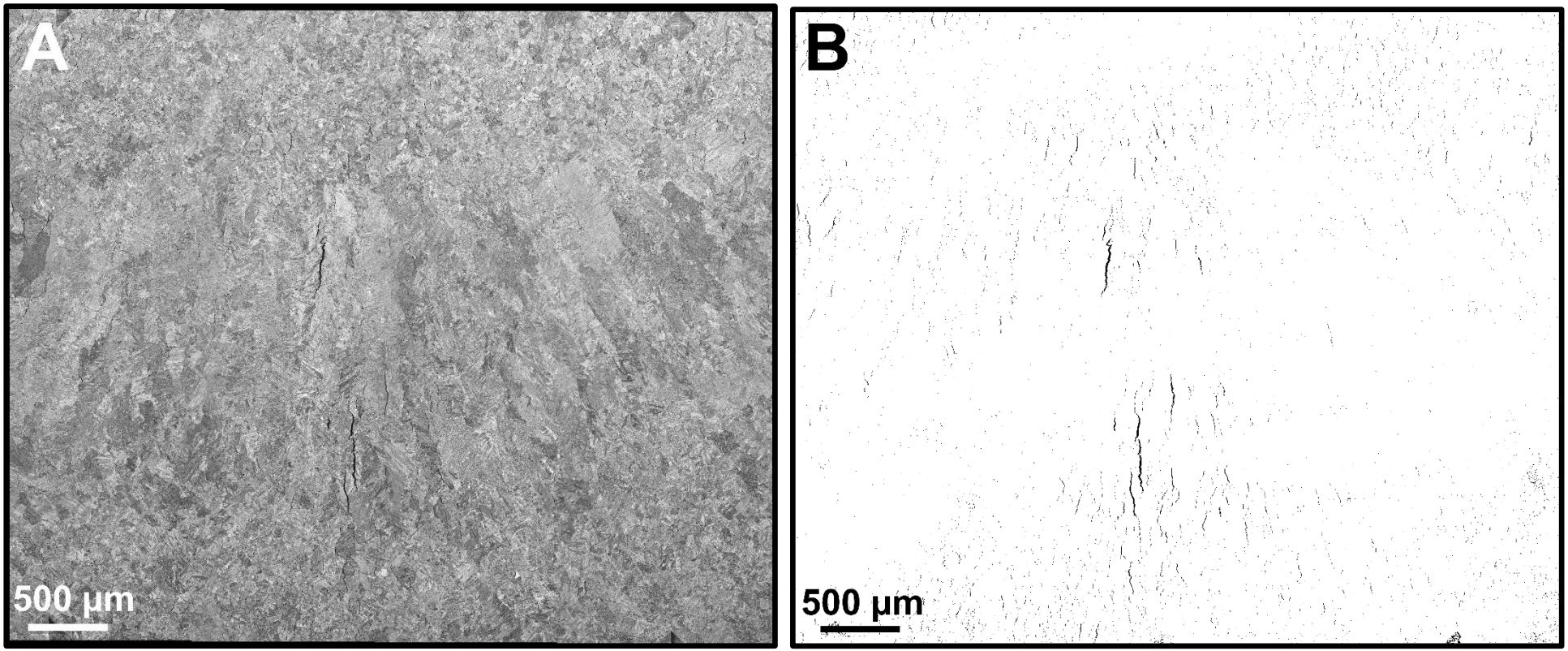

Figure 8-4. Assessment of damage in sample 8C-5 (600°C, 70 MPa and 10,461 hours). Compiled in images created from 20 individual images in the weld metal including a backscatter image (A) and an adjusted contrast and brightness image highlights the creep damage in (B)

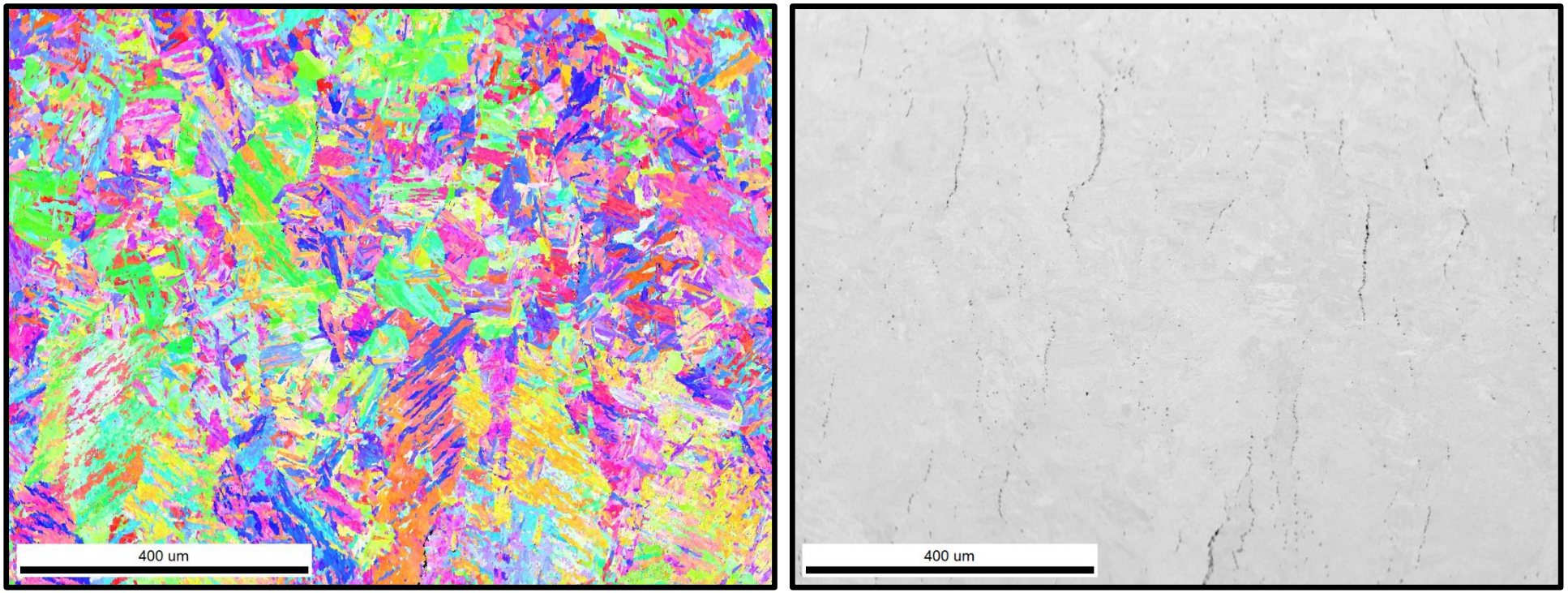

Figure 8-5. SEM-EBSD results for representative damage in the weld metal in sample 8C-5 (600°C, 70 MPa and 10,461 hours). Inverse pole figure provided on the left and the SEM image highlighting the present damage on the right

8.4 Damage in the Heat Affected Zone

The following sections discuss the evaluation of damage in the heat affected zone for the set of weldments fabricated in martensitic parent material (AR-B2, RNT-B2 or TP1) or for the weldment generated in the ferritic parent material (F-TP1). The purpose in separating these sections is to make a distinction consistent with the macro-evaluation provided in Chapter 7 (Table 7-1) where failure in the F-TP1 set of tests is in a HAZ location closer to the fusion line compared to the balance of the cross-weld tests. As highlighted in Chapter 7 the failure in the F-TP1-2 and F-TP1-4 tests occurred in a position 375 or 850 μm from the fusion line, respectively whereas the failures in the AR-B2, RNT-B2 and weld 7C tests in a position ranging from ~1,100 to 1,600 μm.

8.4.1 Damage in the heat affected zone for cross-weld samples in martensitic parent metals

The nature and extent of damage in the HAZ was a primary focus in the evaluation of the feature cross-weld creep tests since it has been well-documented that Grade 91 steel components have failed or exhibited in-service damage due to the accumulation and linking of damage resulting in Type IV failures (Brett et al. 1999, EPRI 2009, Parker and Brett 2013, EPRI, 2015e, Nitsche et al. 2015). The association of damage in the HAZ with specific features in the microstructure was assessed in this section using SEM imaging, SEM-EDS and SEM-EBSD.

Images at the same magnification are provided in Figure 8-6 for sample 7C-2 and sample RNT-B2-2. These images show the markedly different density of damage that is observed in the HAZ for these two weldments fabricated in unique parent materials.

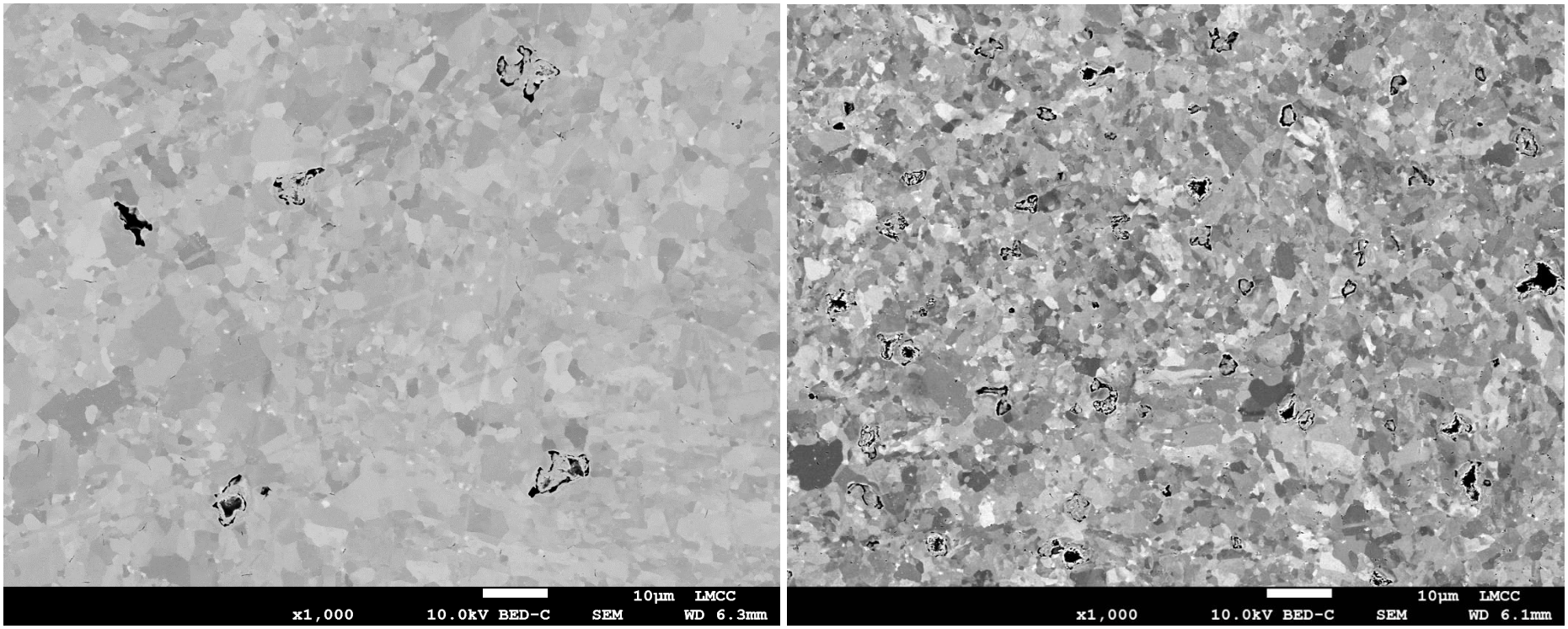

Figure 8-6. Representative field of heat affected zone damage in a high ductility parent metal (TP1 material). Test sample 7C-2 (625°C, 60 MPa, 13,201 hours) [left] and Representative field of heat affected zone damage in a low ductility parent metal (RNT-B2 material). Test sample RNT-B2-2 (625°C, 60 MPa, 2,596 hours) [right]; scale = 10 µm
Note: *Stress axis is left-to-right*

Two populations of creep cavities are noted in the HAZ for all feature cross-weld creep test samples. One population is not clearly linked to a nucleation source and may appear to simply grow from a grain boundary in the HAZ. A second population shows clear association with a nucleation source such as a carbide (e.g. $M_{23}C_6$ or NbC), Laves phase or an inclusion. In this second population, there is a consistent, observed evolution of damage from inclusions and EDS analysis in Figure 8-7 to Figure 8-10 provides context for this observation. The observed damage in these figures is present on inclusions which are sometimes clustered as MnS and Al_2O_3 (Figure 8-7), MnS stringers (Figure 8-8), complex structures with MnS, AlN and Laves (Figure 8-9) or MnS with an AlN 'shell' (Figure 8-10). Aside from showing the association of damage with these particles, the complex nature of the morphologies shows a clear link for some inclusions as trap sites for segregation of elements like Al, Mo, S, etc. during billet solidification.

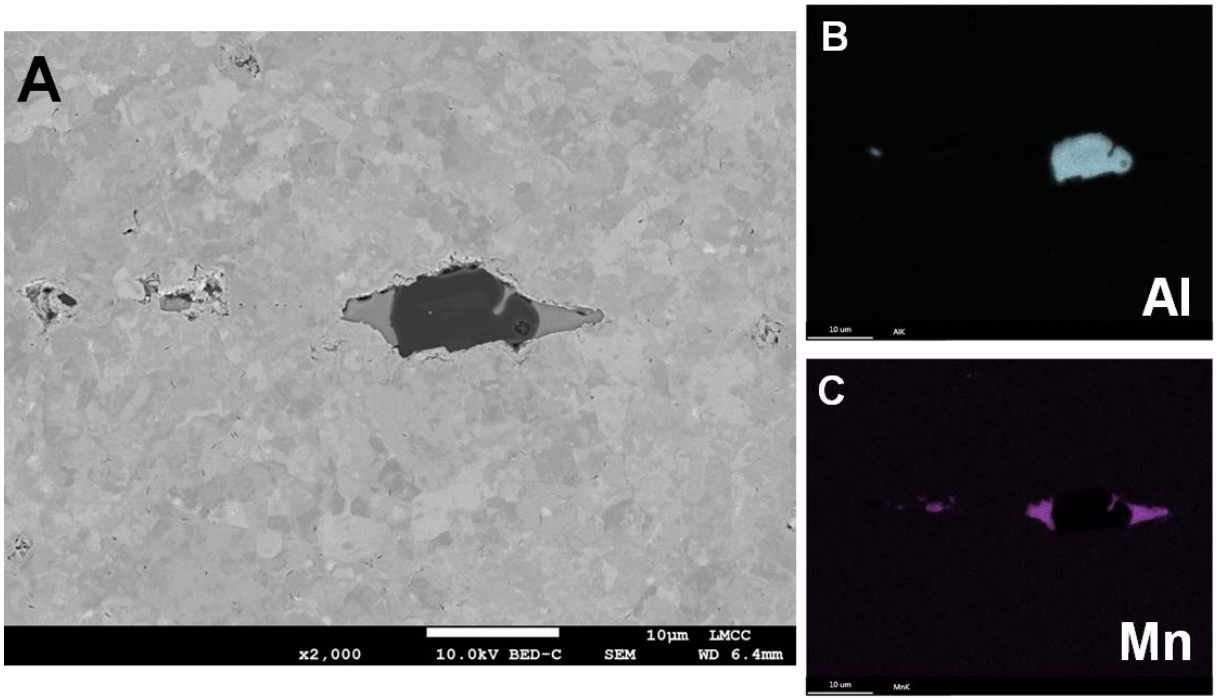

Figure 8-7. Example of SEM-EDS map at damage associated with an inclusion cluster. In this example the intensities for Al Kα and Mn Kα are utilized as an indicator for alumina and MnS, respectively. Sample AR-B2-2 (625°C, 60 MPa, 1,685 hours)

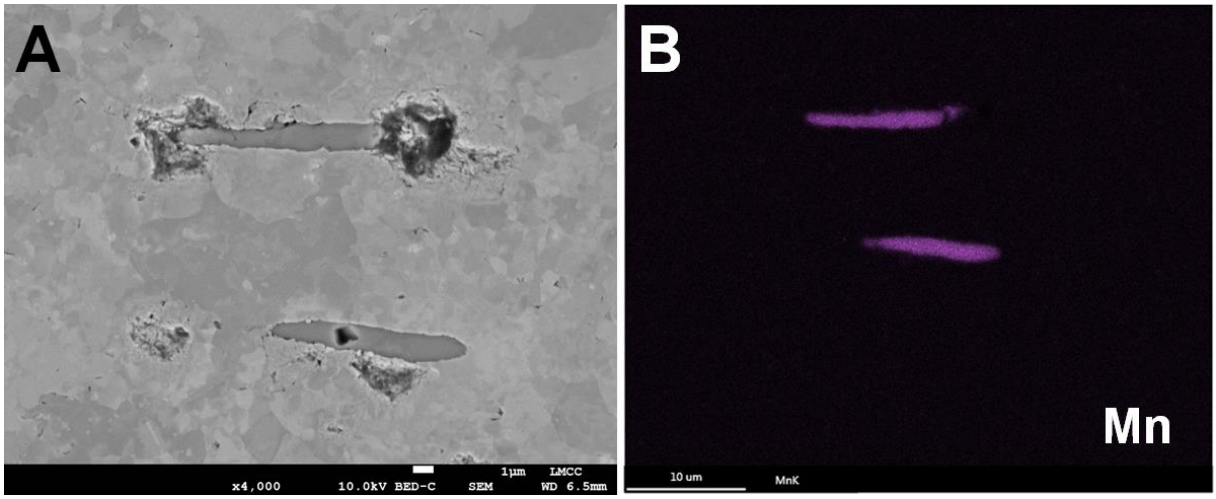

Figure 8-8. Example of SEM-EDS map at damage associated with an inclusion cluster. In this example the intensity for Mn Kα are utilized as an indicator for alumina and MnS, respectively. Sample AR-B2-2 (625°C, 60 MPa, 1,685 hours)

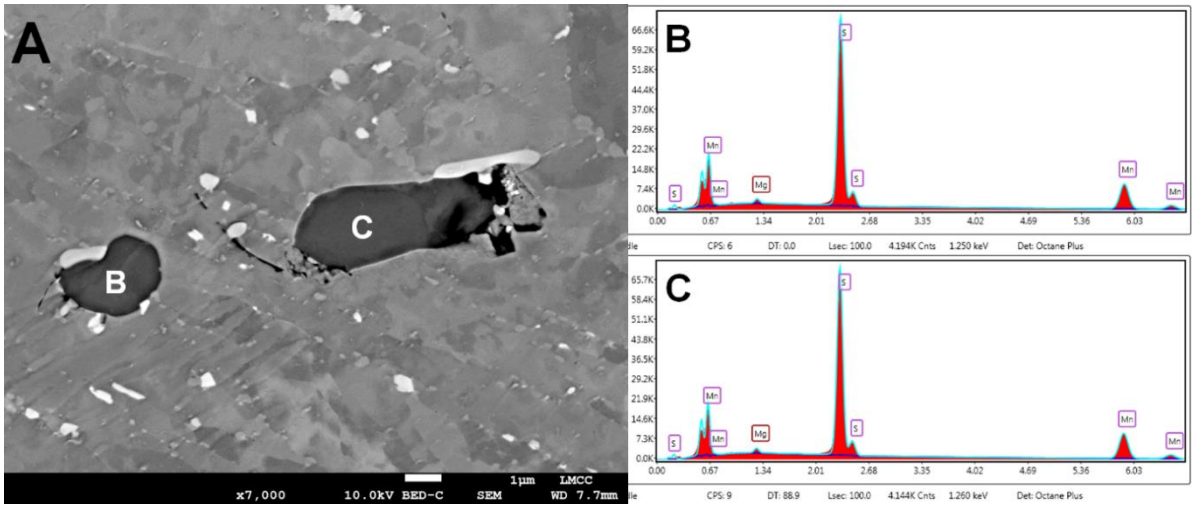

Figure 8-9. Location of SEM-EDS spot analysis (A) and the spectra (B, C). In this example the spectra show association of composition with Mn and S. Sample 8C-7 (575°C, 90 MPa, 13,101 hours).

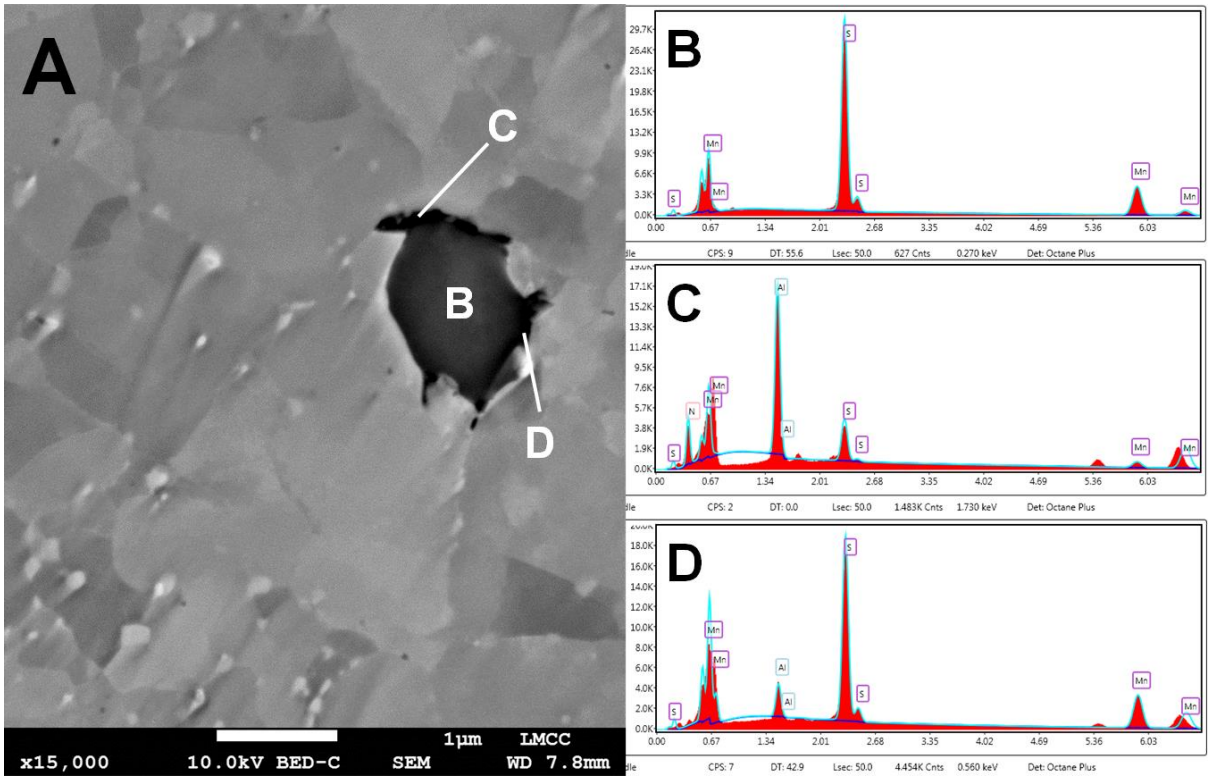

Figure 8-10. Location of SEM-EDS spot analysis (A) and the spectra (B, C, D). In this example the spectrum for (B) shows association of composition with Mn and S, the spectrum for (C) shows signals for Al, N and S and the spectrum for (D) possesses peaks for Al, Mn, N and S. Sample 8C-7 (575°C, 90 MPa, 13,101 hours).

The identification of particles shown in these figures makes repeated EDS analysis unnecessary since in backscatter imaging these particles possess a consistent contrast for identification of particles. The observed damage in the HAZ for the evaluation samples in Table 8-1 is provided in Figure 8-11 to Figure 8-20. For each cross-weld creep test (7C-2, 8C-5, 9C-3, AR-B2-2 and RNT-B2-2) a set of images are provided for damage that is not associated with inclusions and a set of images show the association of damage with inclusions. The exception to this series of images is the relatively few, apparent sites in sample 9C-3 which were identified to be linked to second phase particles. The overall size of the voids in 9C-3 was notably larger, and more developed compared to the balance of the samples, such as to RNT-B2. The comparison of damage in the HAZ for 9C-3 and RNT-B2-2 is provided in Figure 8-21 and Figure 8-22 for context.

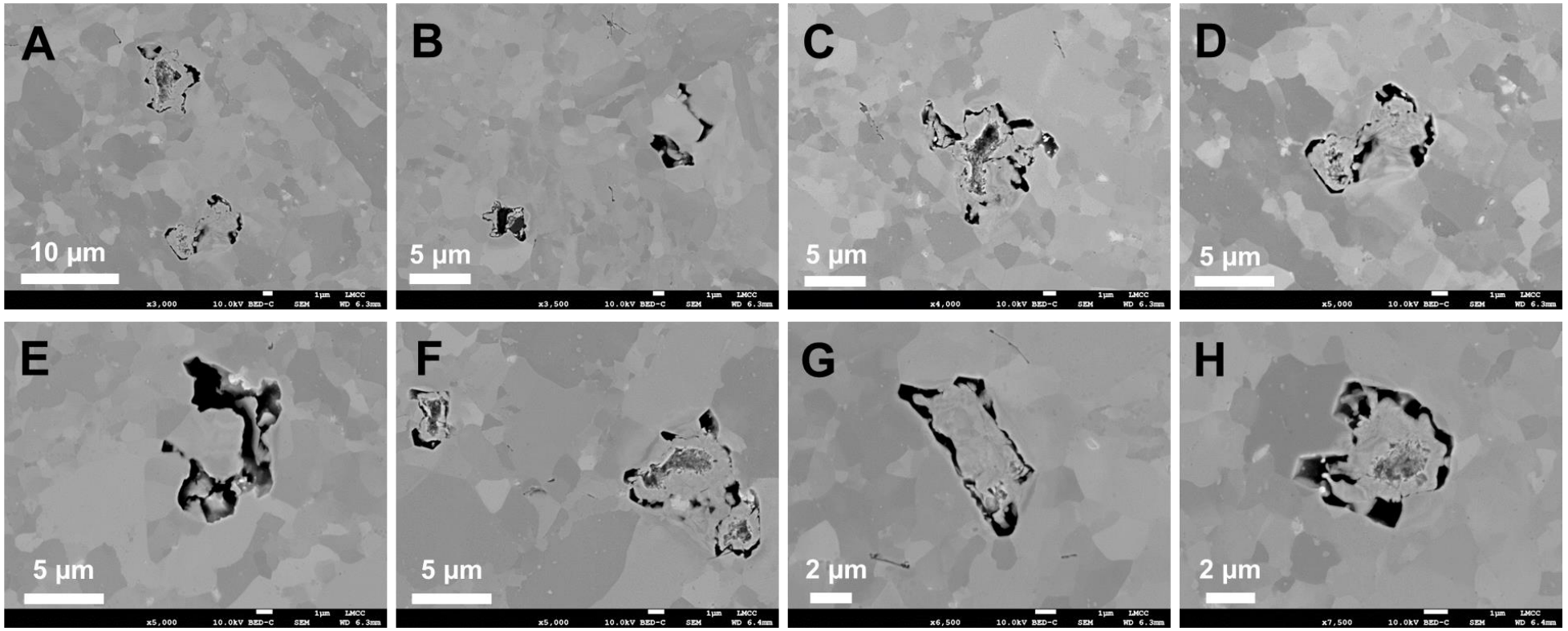

Figure 8-11. Sample 7C-2 (625°C, 60 MPa, 13,201 hours), SEM backscatter electron images of damage in heat affected zone not associated with inclusions, 3,000X (A), 3,500X (B), 4,000X (C), 5,000X (D, E, F), 6,500X (G) and 7,500X (H)
Note: *Stress axis is left-to-right*

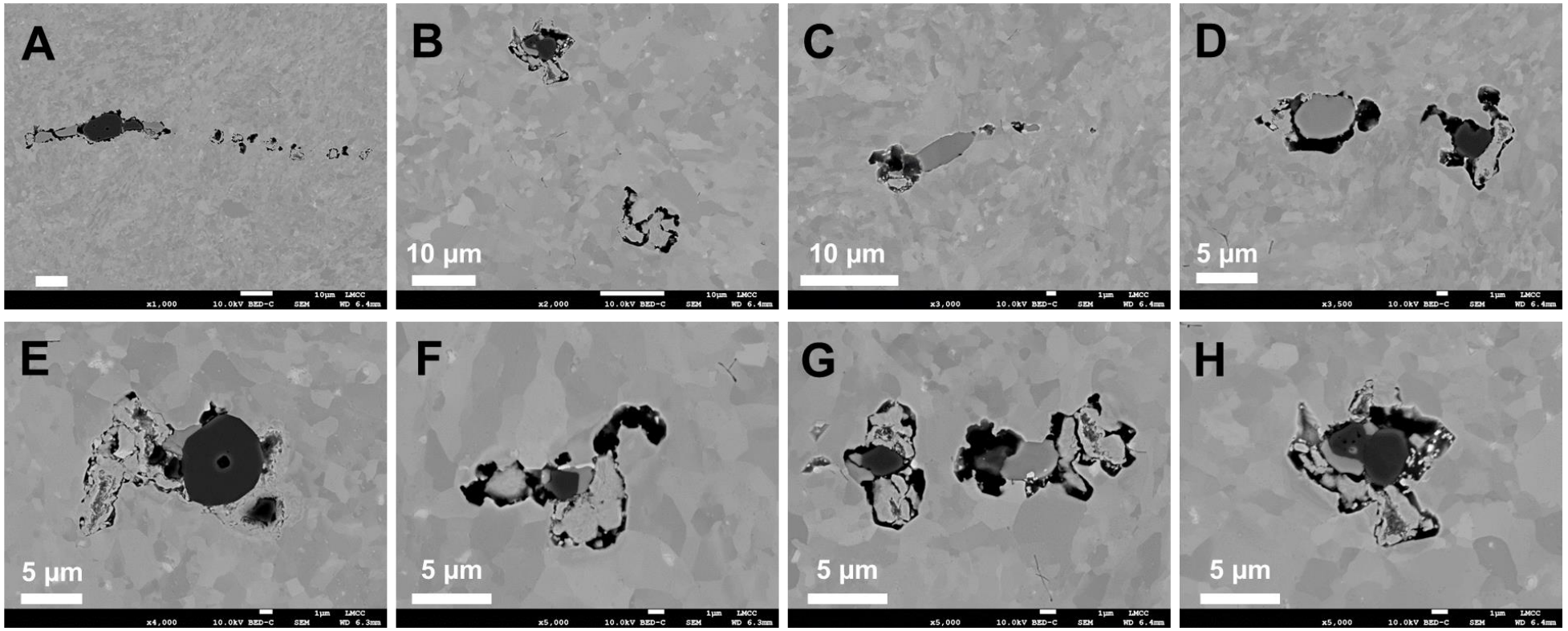

Figure 8-12. Sample 7C-2 (625°C, 60 MPa, 13,201 hours), SEM backscatter electron images of damage in heat affected zone associated with inclusions, 1,000X (A), 2,000X (B), 3,000X (C), 3,500X (D), 4,000X (E), 5,000X (F, G, H)
Note: *Stress axis is left-to-right*

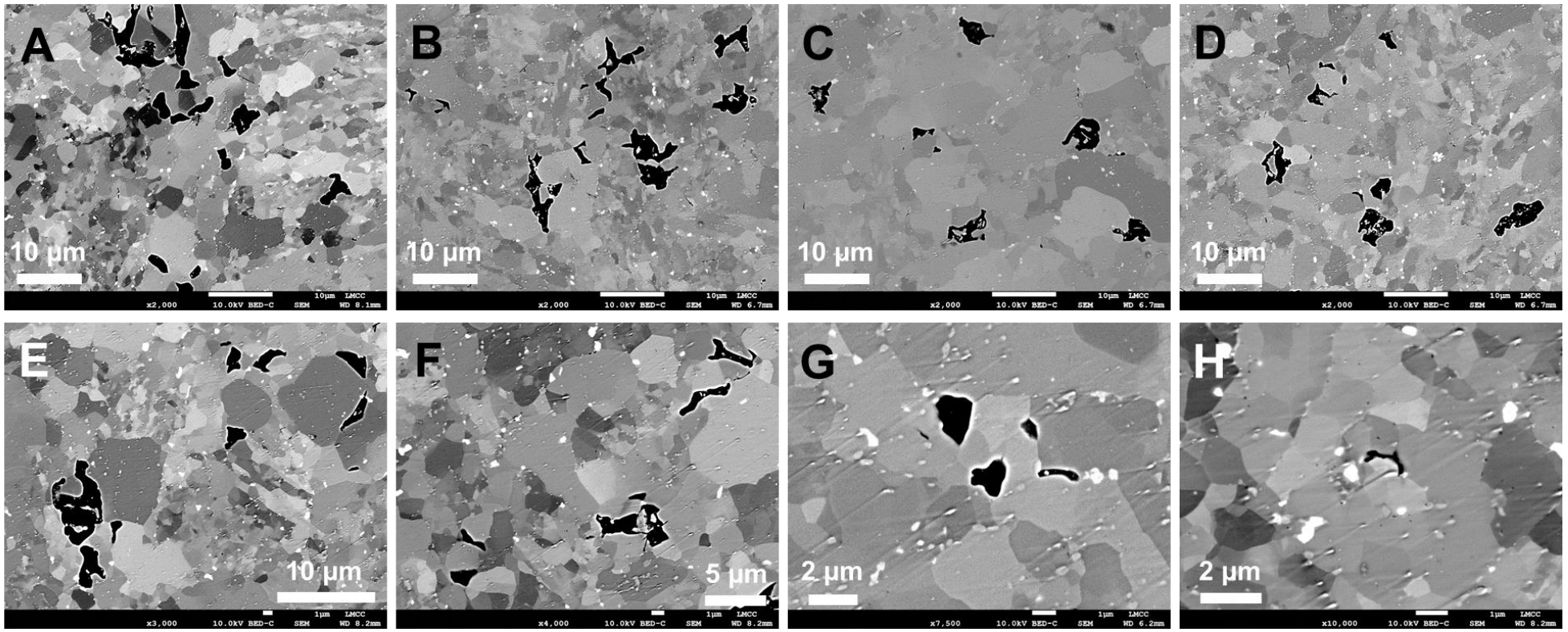

Figure 8-13. Sample 8C-5 (600°C, 70 MPa, 10,461 hours), SEM backscatter electron images of damage in heat affected zone not associated with inclusions, 2,000X (A, B, C, D), 3,000X (E), 4,000X (F), 7,500X (G), 10,000X (H)
Note: *Stress axis is left-to-right*

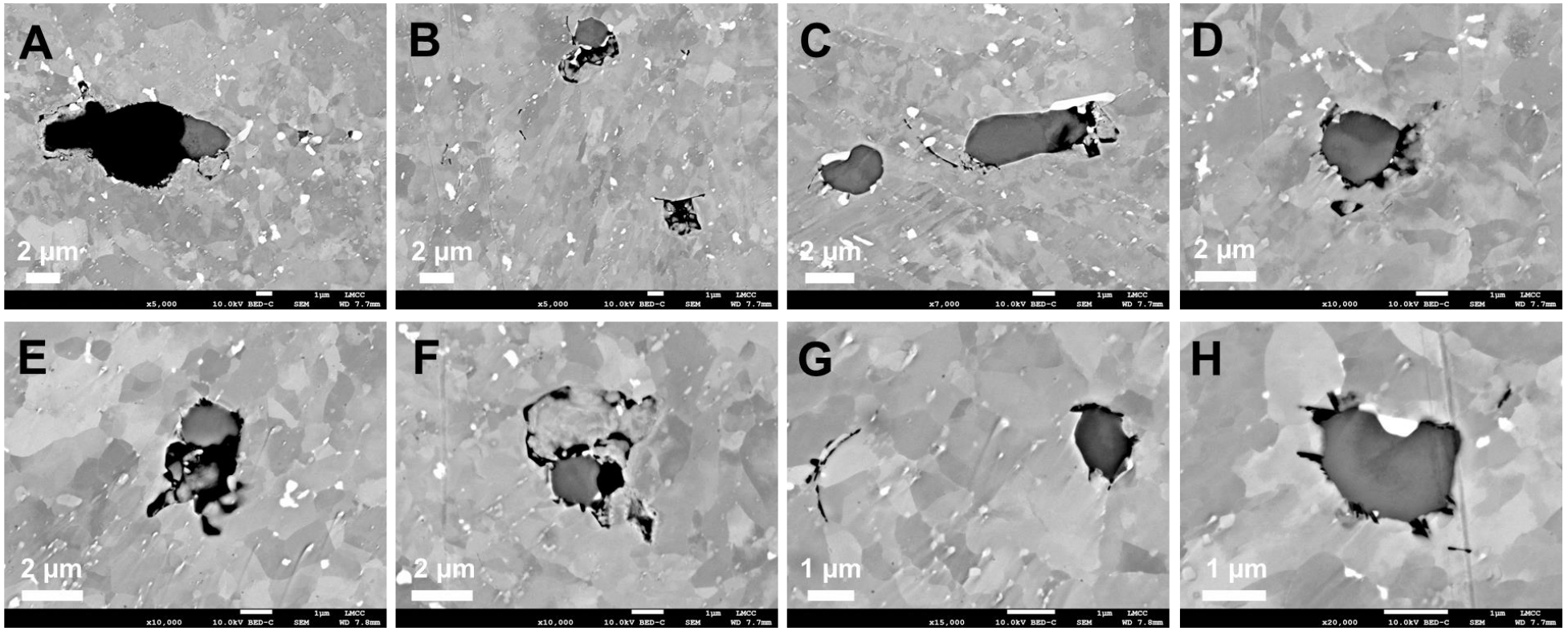

Figure 8-14. Sample 8C-5 (600°C, 70 MPa, 10,461 hours), SEM backscatter electron images of damage in heat affected zone associated with inclusions, 5,000X (A, B), 7,000X (C), 10,000X (D, E, F), 15,000X (G), 20,000X (H)
Note: *Stress axis is left-to-right*

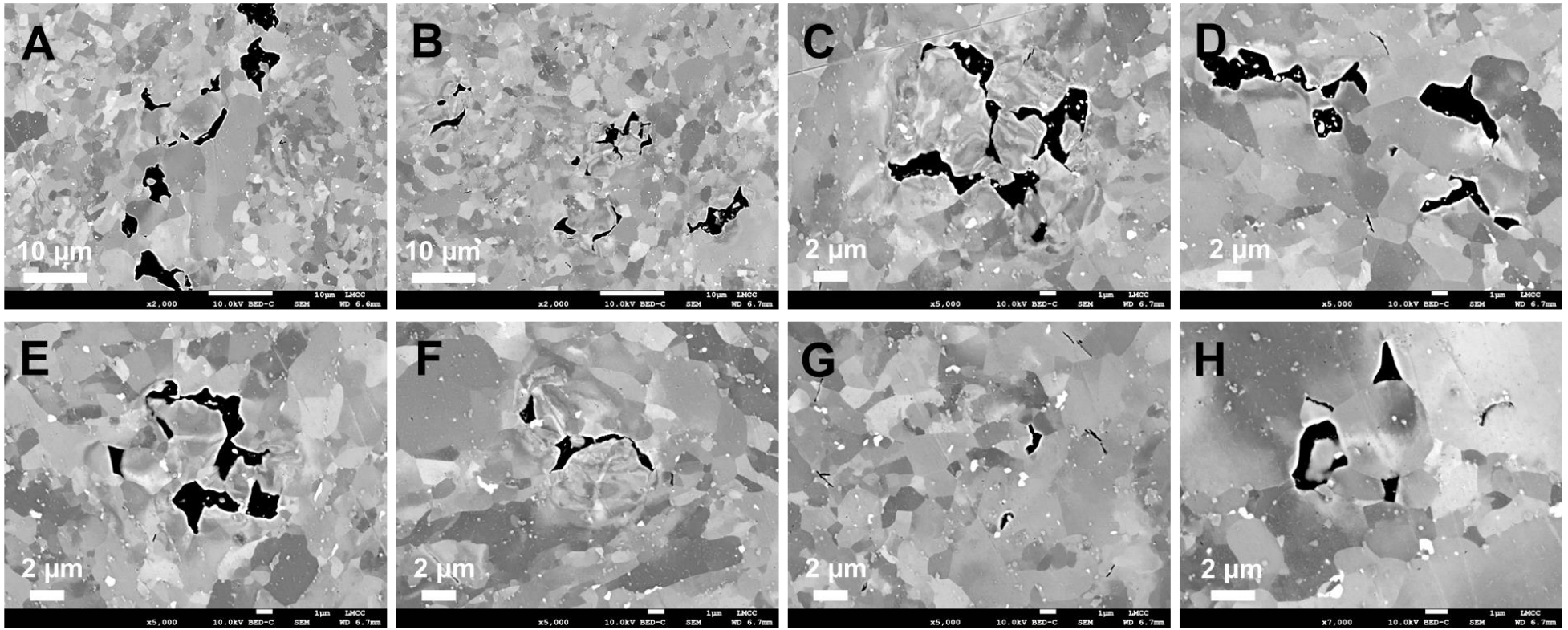

Figure 8-15. Sample 9C-3 (625°C, 60 MPa, 13,130 hours), SEM backscatter electron images of damage in heat affected zone not associated with inclusions, 2,000X (A, B), 5,000X (C, D, E, F, G), 7,000X (H)
Note: *Stress axis is left-to-right*

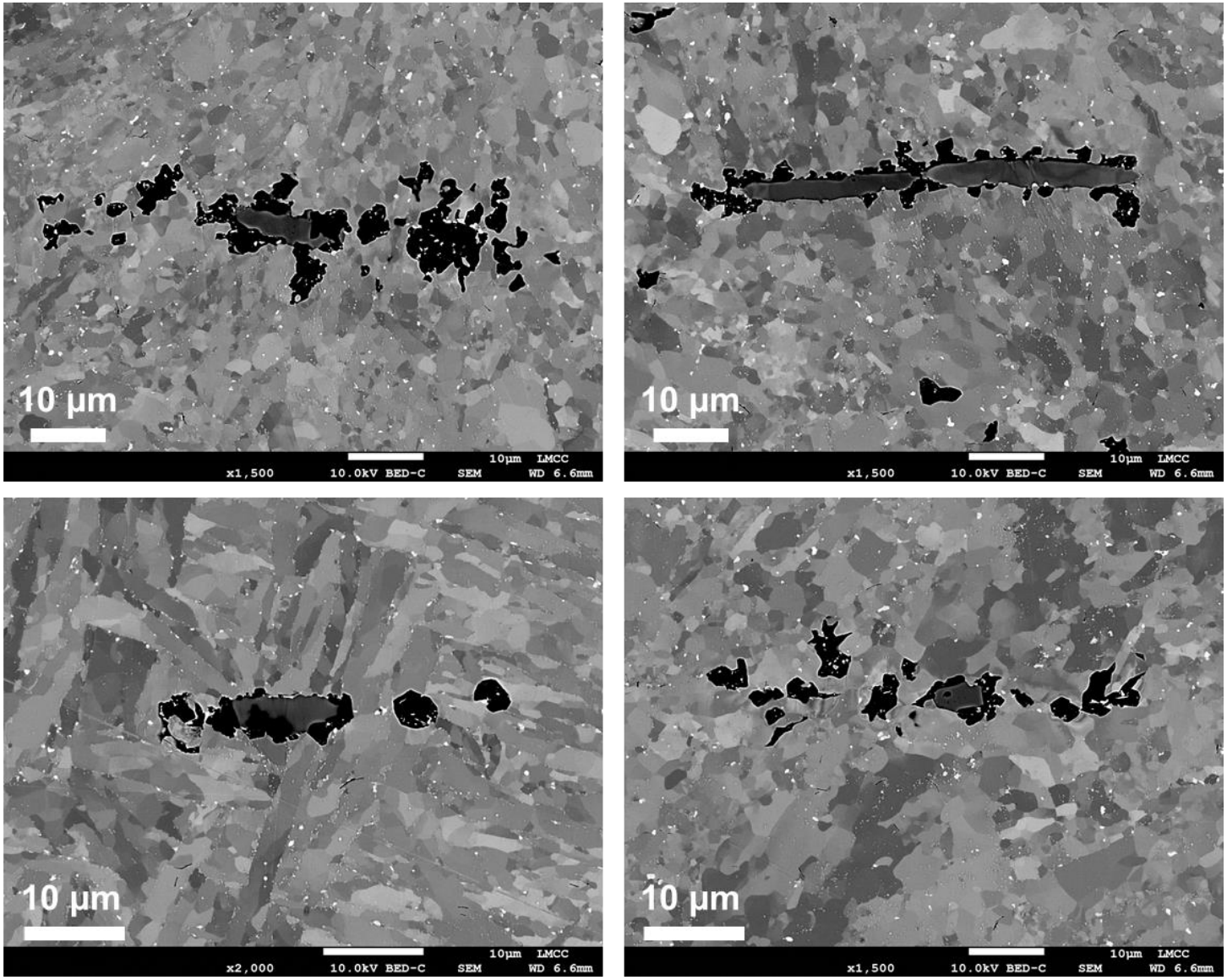

Figure 8-16. Sample 9C-3 (625°C, 60 MPa, 13,130 hours), SEM backscatter electron images of damage in heat affected zone associated with inclusions, 1,500X (A, B, C) and 2,000X (D)
Note: *Stress axis is left-to-right*

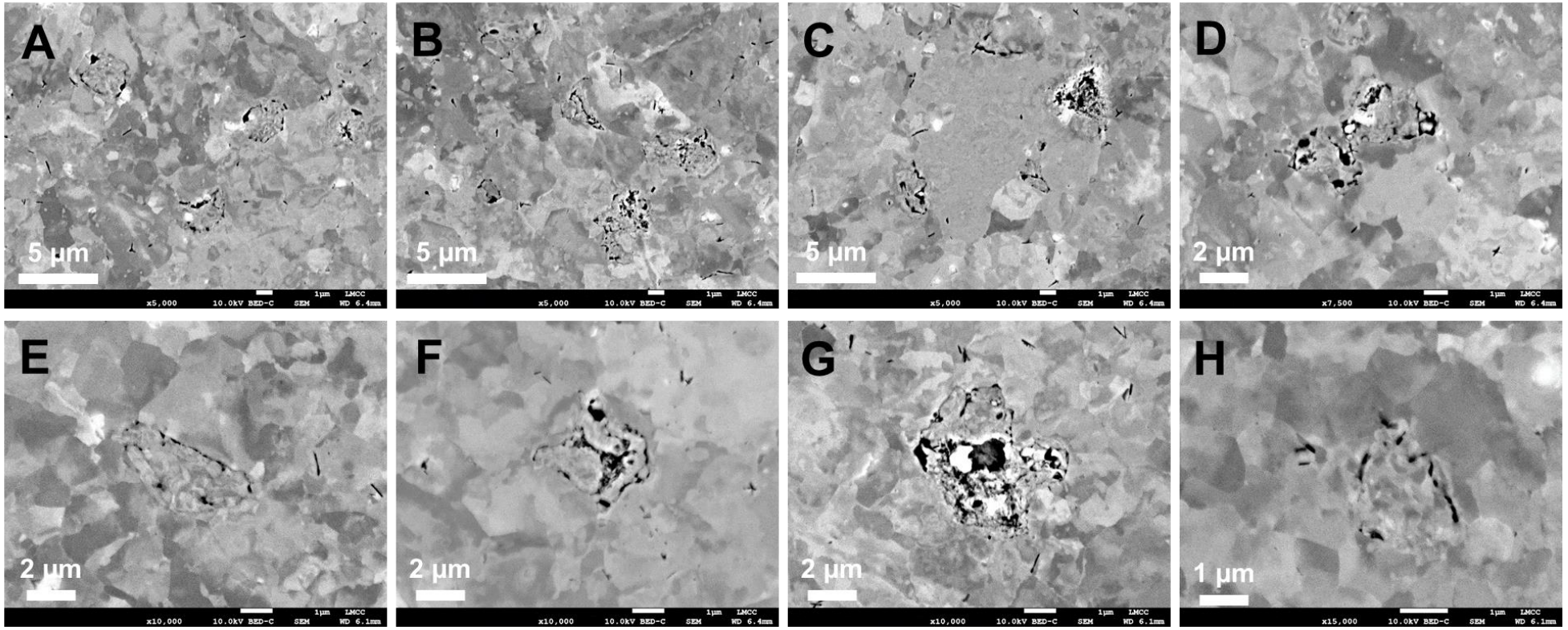

Figure 8-17. Sample AR-B2-2 (625°C, 60 MPa, 1,685 hours), SEM backscatter electron images of damage in heat affected zone not associated with inclusions, 5,000X (A, B, C), 7,500X (D), 10,000X (E, F, G) and 15,000X (H)
Note: *Stress axis is left-to-right*

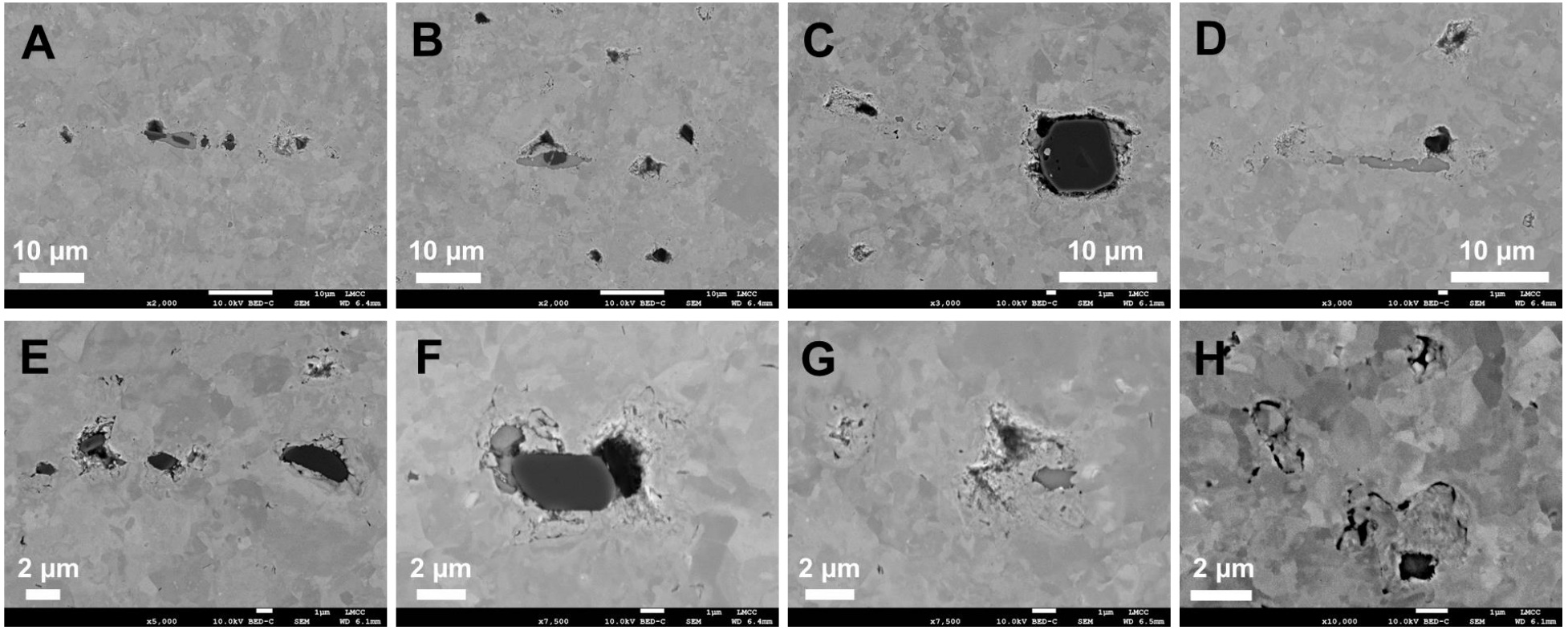

Figure 8-18. Sample AR-B2-2 (625°C, 60 MPa, 1,685 hours), SEM backscatter electron images of damage in heat affected zone associated with inclusions, 2,000X (A, B), 3,000X (C, D), 5,000X (E), 7,500X (F, G) and 10,000X (H)
Note: *Stress axis is left-to-right*

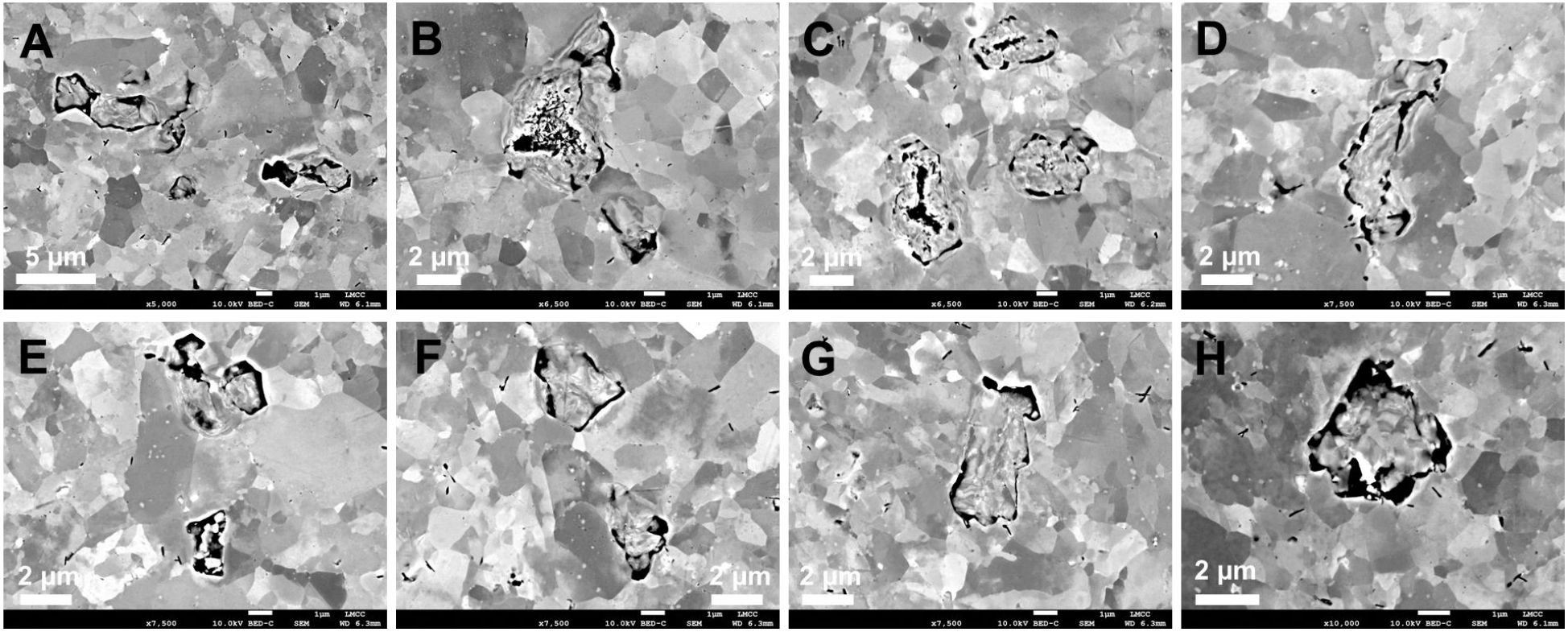

Figure 8-19. Sample RNT-B2-2 (625°C, 60 MPa, 2,596 hours), SEM backscatter electron images of damage in heat affected zone not associated with inclusions, 5,000X (A), 6,500X (B, C), 7,500X (D, E, F, G) and 10,000X (H)
Note: *Stress axis is left-to-right*

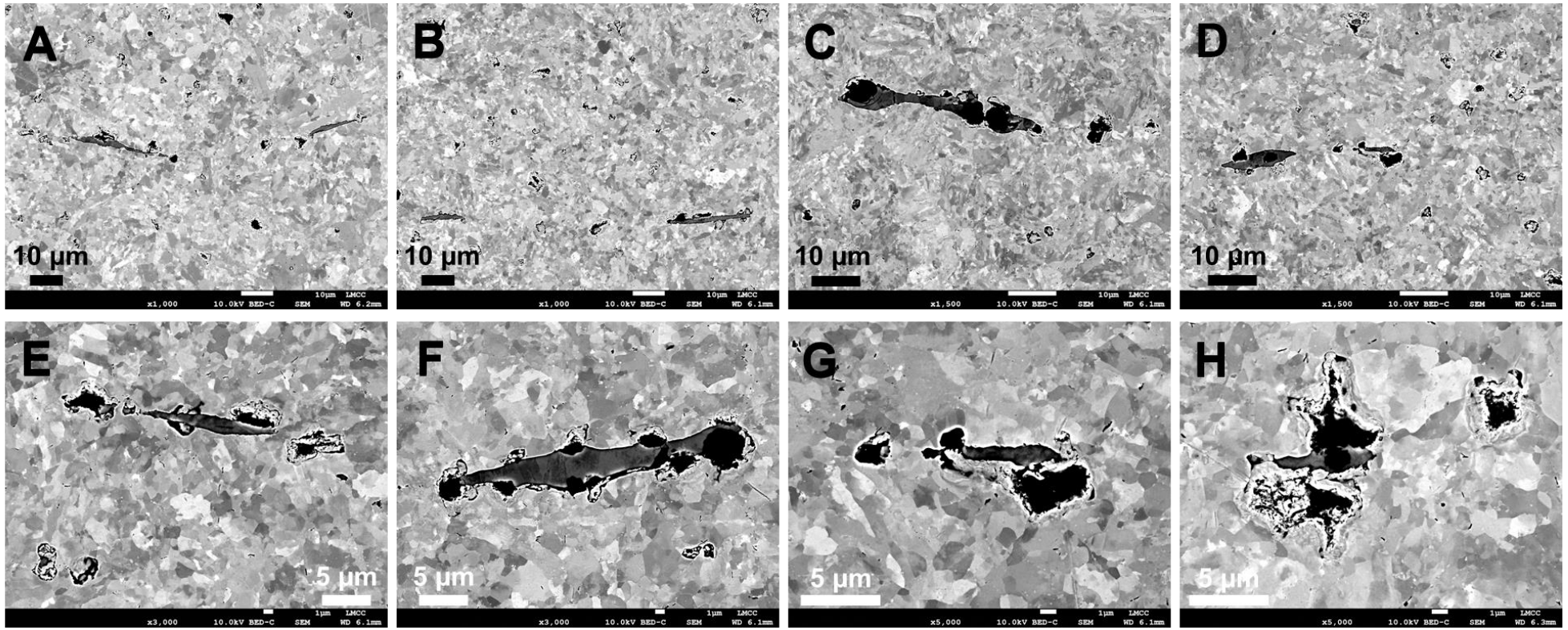

Figure 8-20. Sample RNT-B2-2 (625°C, 60 MPa, 2,596 hours), SEM backscatter electron images of damage in heat affected zone associated with inclusions, 1,000X (A, B), 1,500X (C, D), 3,000X (E, F), 5,000X (G, H)
Note: *Stress axis is left-to-right*

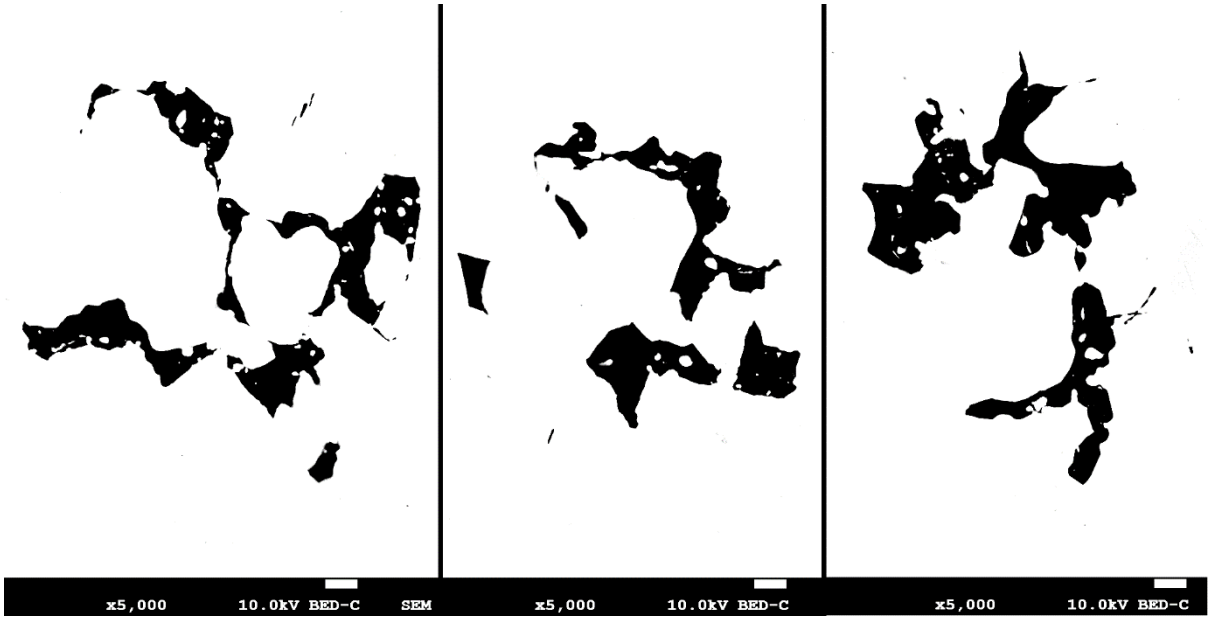

Figure 8-21. Networks of representative creep voids in weld 9C-3; note scale = 1 µm

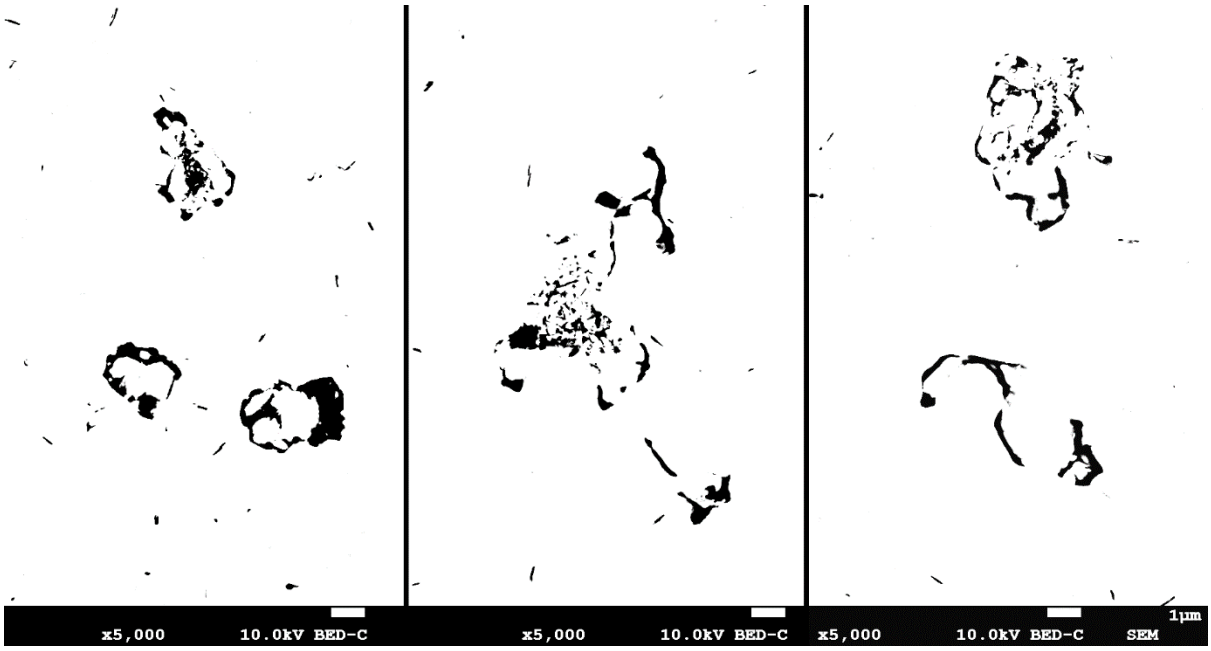

Figure 8-22. Networks of representative creep voids in weld RNT-B2-2; note scale = 1 µm

The association of damage in the HAZ, whether at an inclusion or apparently in the HAZ matrix, suggested that the localization of strain could be responsible for the nucleation and/or growth of the cavity or network of damage. If this is the case then it might follow that recrystallization should be observed adjacent to the cavity. An example of this process is highlighted in Figure 8-23 where damage is clearly present at the location of MnS inclusion stringers (see Figure 8-8 for SEM-EDS information) and there may be a field of recrystallization adjacent to the damage.

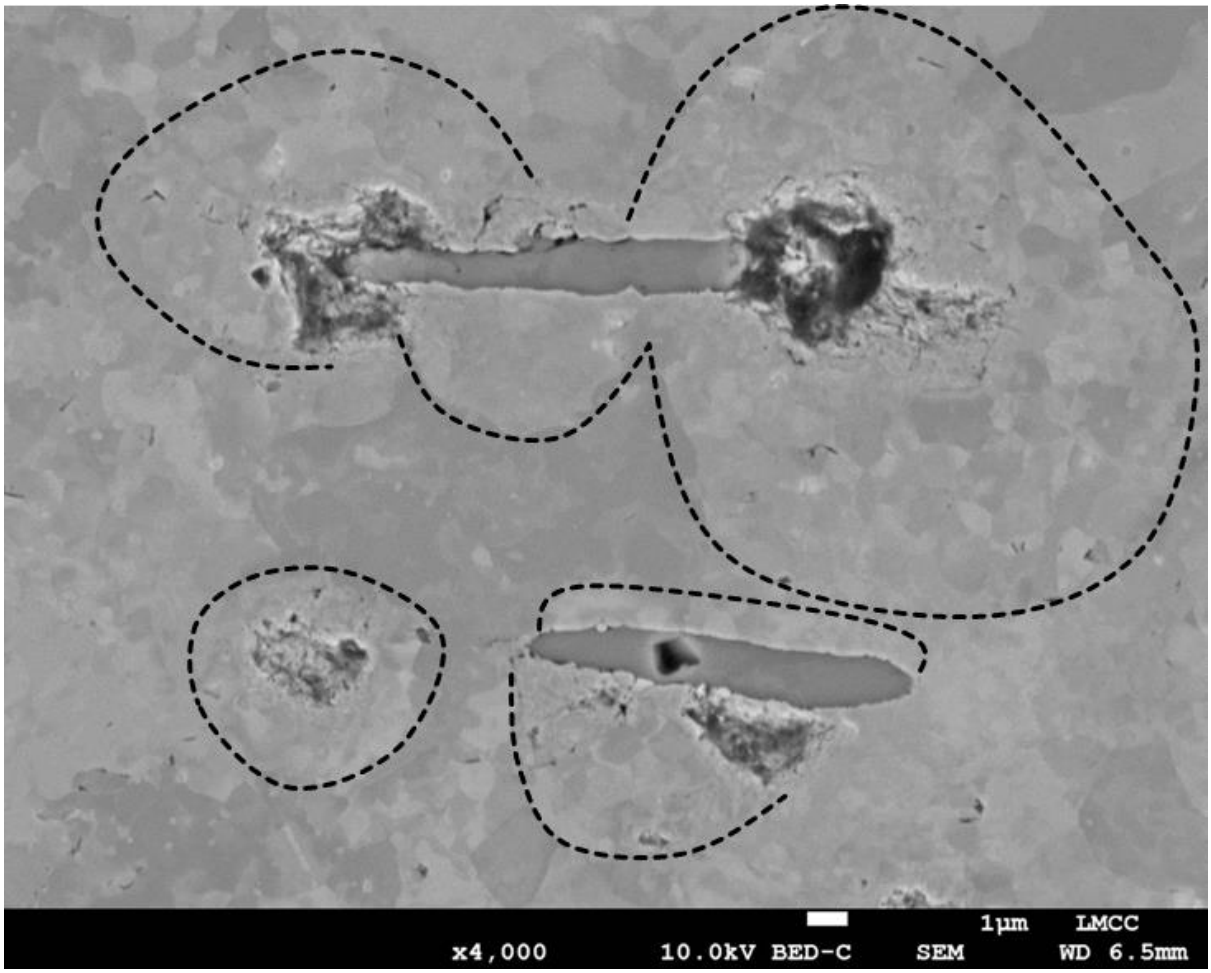

Figure 8-23. Example of apparent strain localization around MnS inclusions in sample AR-B2-2 (625°C, 60 MPa, 1,685 hours). SEM-EDS information for this location is provided in Figure 8-8 and SEM-EBSD information in Figure 8-24.
Note: *stress axis is left-to-right*

An attempt was made to use SEM-EBSD to map the fields of grain refinement around the MnS stringers using a *relatively small* step size (0.15 µm). As observed in Figure 8-23 many of the individual grains in the HAZ are <1 µm in diameter. The results provided in Figure 8-24 do not provide unequivocal evidence regarding the apparent grain refinement in the backscatter image in Figure 8-23. This observation is revisited in the following Chapter 9 using a revised approach with a much finer step size.

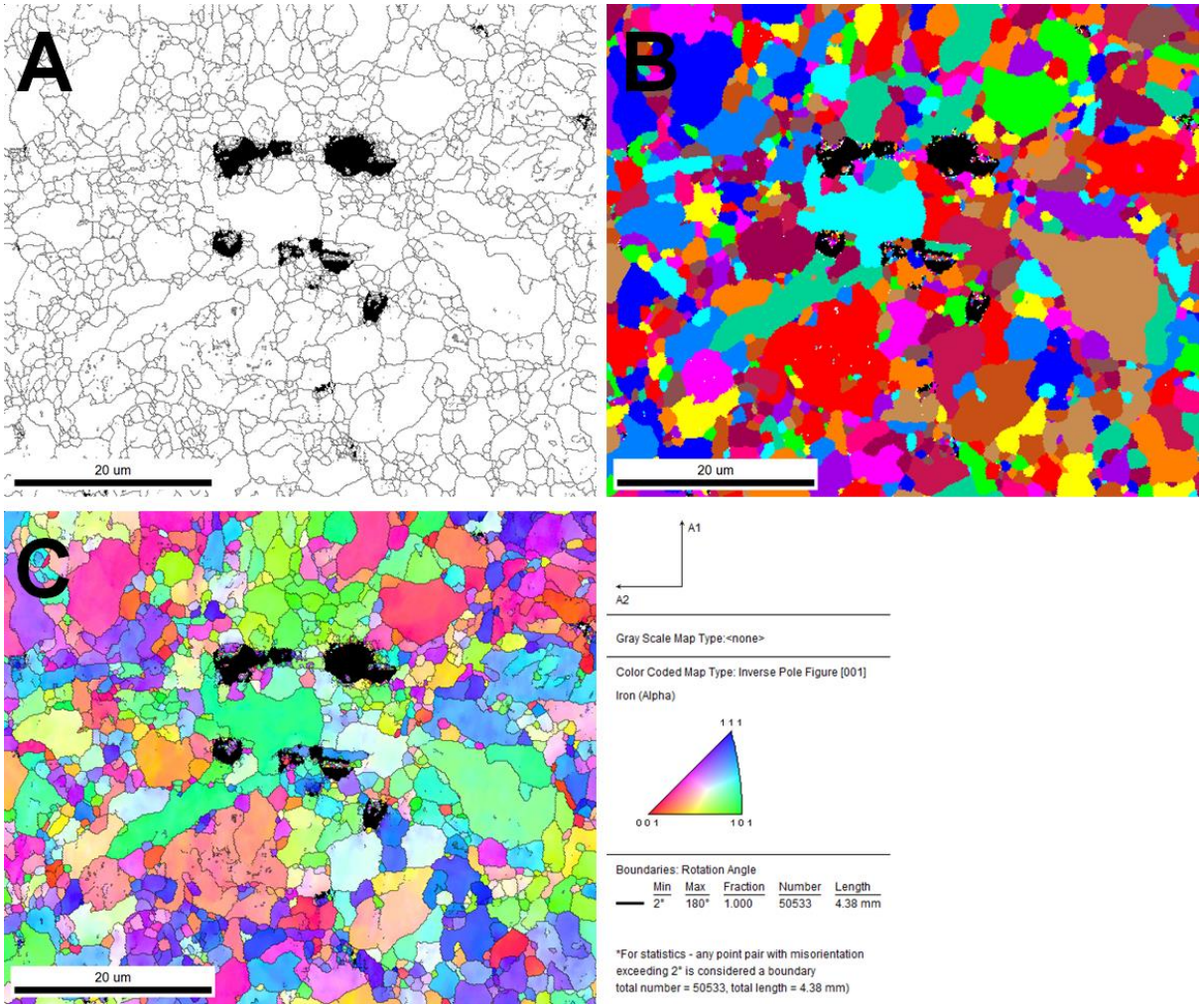

Figure 8-24. SEM-EBSD in the heat affected zone of sample AR-B2-2 (625°C, 60 MPa, 1,685 hours) to assess potential for strain localization at an inclusion; scale = 20 µm
Note: *Stress axis is left-to-right*

A second, large scale EBSD map was performed in sample 8C-7 in the HAZ (Figure 8-25). The size of the cavities (~2 to 5 µm) relative to the grain size (variable in the range of 1 to 20 µm) means that the likelihood of a cavity on a grain boundary is high. Furthermore, although there is a large difference in grain size, there does not appear to be a clear link between the size of the grain and the association of damage. The results in this section elaborate the need for refined procedures and context when assessing damage in the HAZ dependent on the objective of the evaluation.

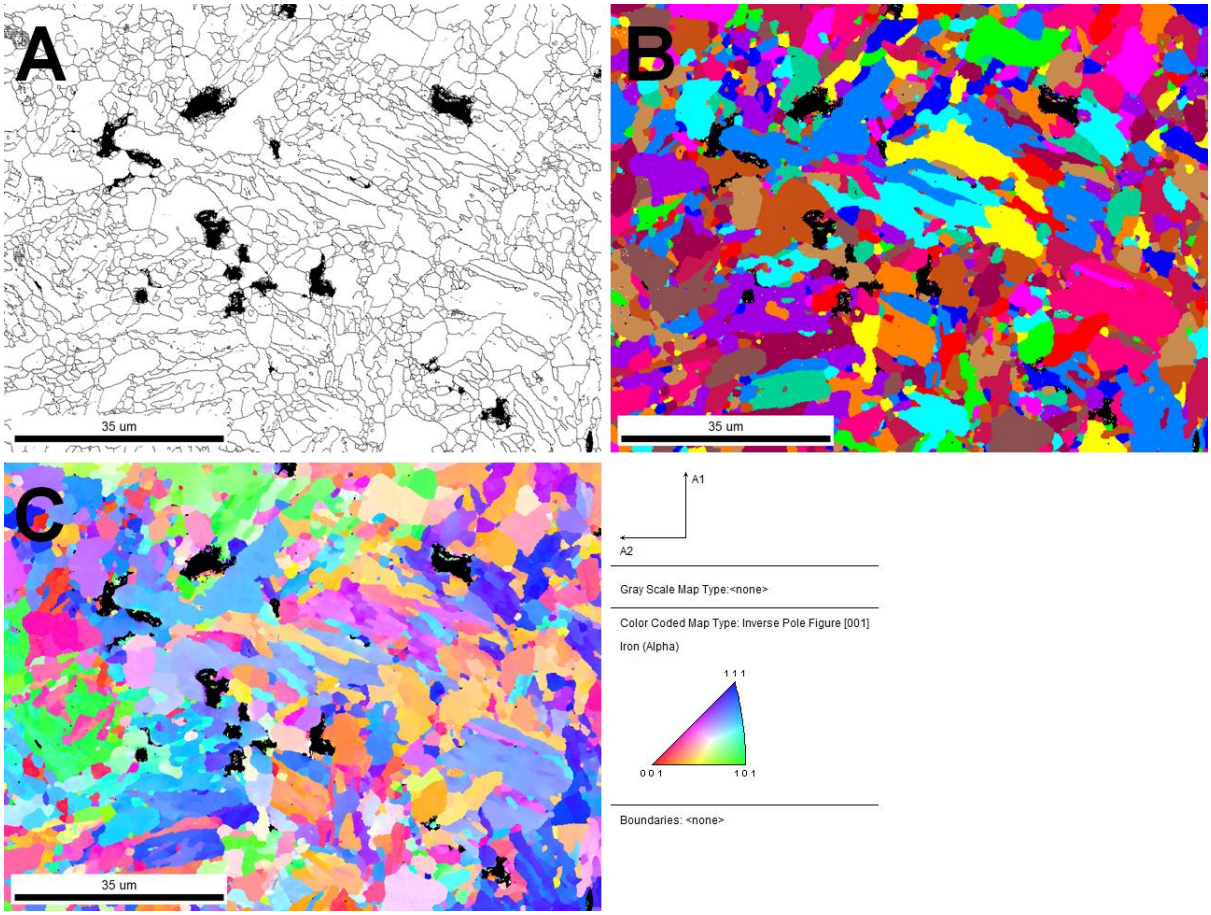

Figure 8-25. SEM-EBSD in the heat affected zone of sample 8C-7 (575°C, 90 MPa, 13,101 hours) to assess localization of damage at intersection of large and small grains; scale = 20 µm
Note: *Stress axis is left-to-right*

8.4.2 Damage in the heat affected zone for Sample F-TP1-4

The evaluation of damage in the sample F-TP1-4 was warranted as the parent material utilized in the cross-weld creep tests was ferritic and thus in its theoretical weakest condition. Furthermore, macro-failure assessment of cracking in the samples F-TP1-2 and F-TP1-4 showed that macro-cracks were evolving in the HAZ, but in a position relative to the fusion line that was different from that in the weldments assessed in the prior section 8.4.1.

An assessment of damage in the HAZ of sample F-TP1-4 and for a distribution of damage associated with or without second phase particles is provided in Figure 8-26. Damage that does not contain a clear particle in or adjacent to the cavity is detailed in Figure 8-26A to Figure 8-26H while examples for the presence of a second phase particle inside the void are provided in Figure 8-26I to Figure 8-26L.

Two examples of damage and second phase particles were analyzed using EDS mapping, the results provided in Figure 8-27 and Figure 8-28. The inclusion cluster in Figure 8-27 is a complex arrangement where an Al-Mg-O-rich center is surrounded by an Al-O rich shell. A Mn-rich particle exists in the lower right corner of the inclusion, suggesting the presence of MnS. The morphology of the inclusion in Figure 8-28 is markedly different from prior documentation; in this example the inclusion has a cubic shape. The formation of the Ti-V-N-rich inclusion appears to have nucleated on a prior existing Al_2O_3 particle in the center of the inclusion cluster.

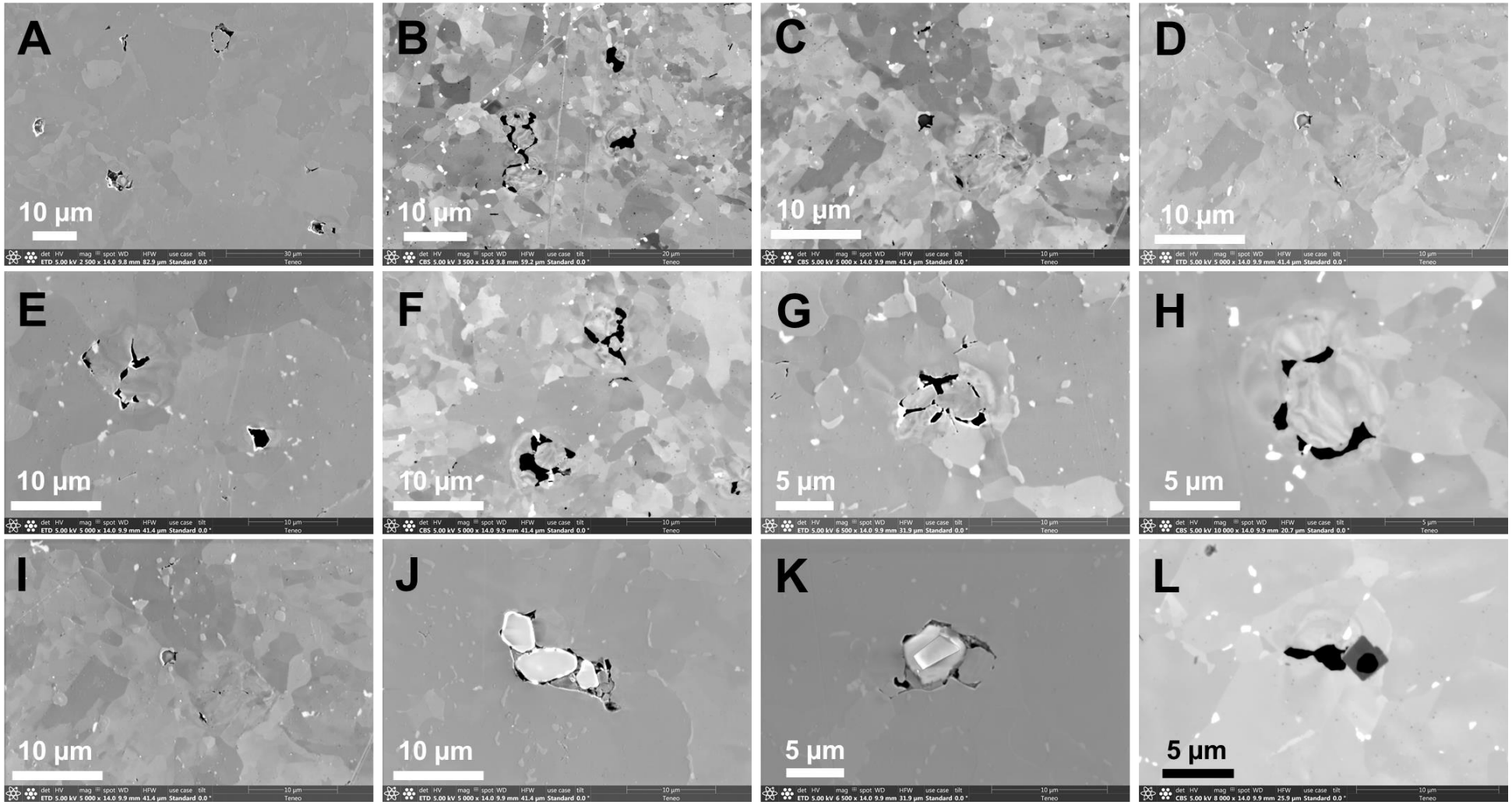

Figure 8-26. Sample F-TP1-4 (625°C, 50 MPa, 15,472 hours), SEM backscatter electron images of damage in heat affected zone not associated with inclusions, 2,500X (A), 3,500X (B), 5,000X (C, D, E, F), 6,500X (G), 10,000X (H) or associated with inclusions, 5,000X (I, J), 6,500X (K), 8,000X (L)
Note: *Stress axis is left-to-right*

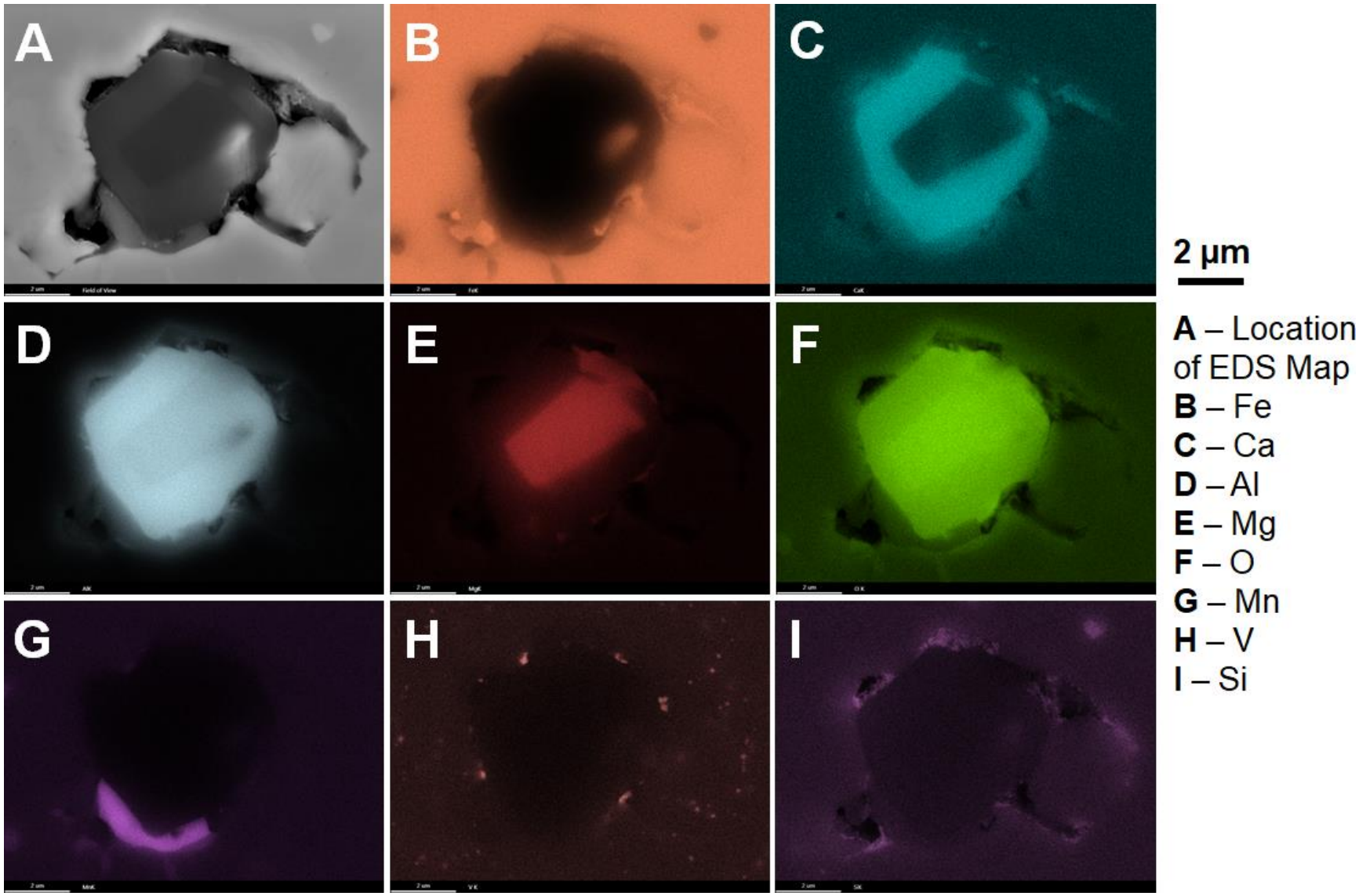

Figure 8-27. Sample F-TP1-4 (625°C, 50 MPa, 15,472 hours), SEM backscatter electron images of damage in heat affected zone associated with an inclusion, Location of EDS Map (A), Fe (B), Ca (C), Al (D), Mg (E), O (F), Mn (G), V (H) and Si (I)
Note: *Analysis performed in the location shown in Figure 8-26K*

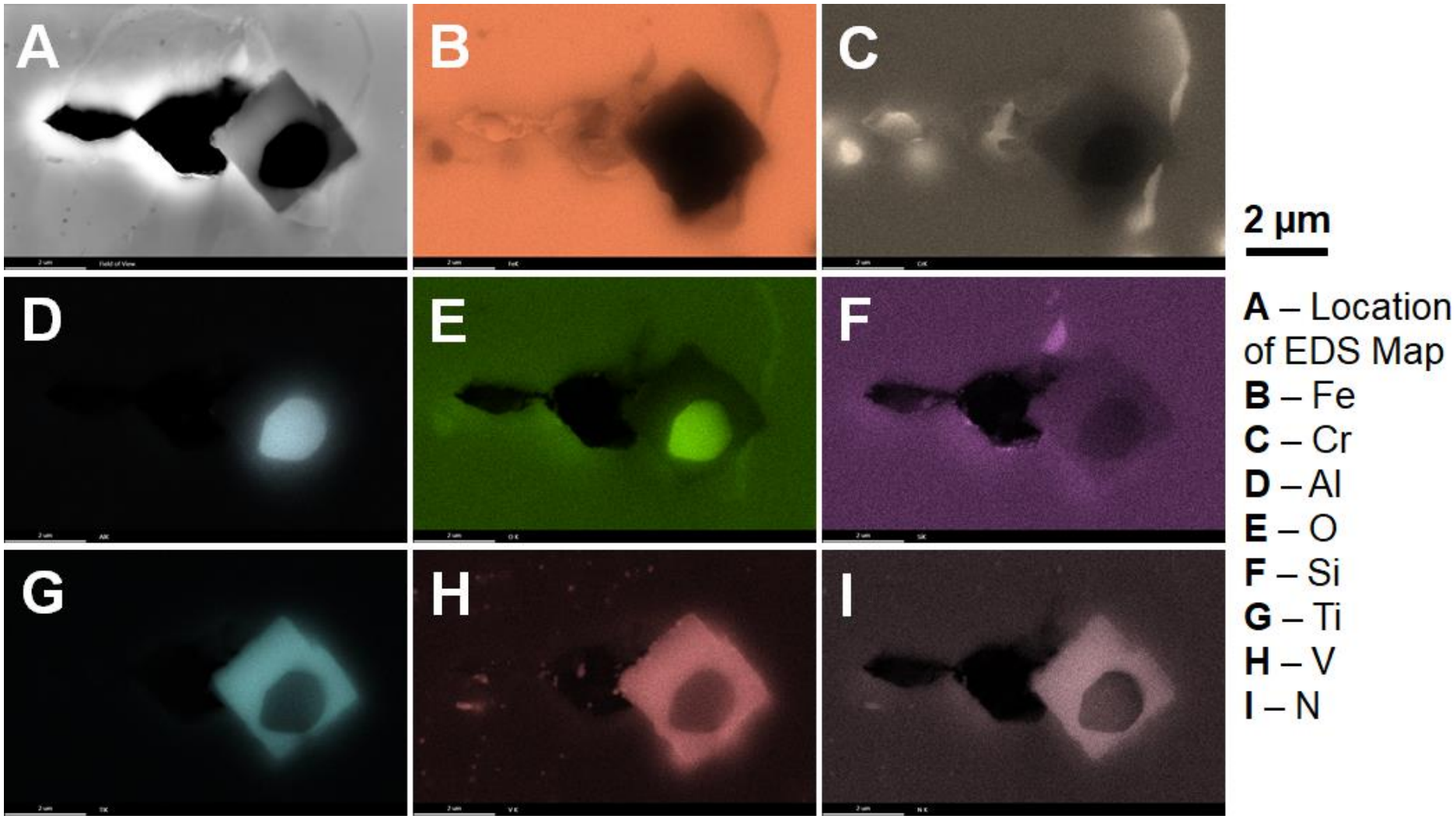

Figure 8-28. Sample F-TP1-4 (625°C, 50 MPa, 15,472 hours), SEM backscatter electron images of damage in heat affected zone associated with an inclusion, Location of EDS Map (A), Fe (B), Cr (C), Al (D), O (E), Si (F), Ti (G), V (H) and N (I)
Note: *Analysis performed in the location shown in Figure 8-26L*

8.5 Damage at the Fusion Line in Sample 9C-3

Isolated cavities were noted at the fusion line in sample 9C-3. This provided a unique opportunity to assess contributing factors to the evolution of damage in this location. Numerous, catastrophic failures have been observed along the fusion line in Grade 91 steel welded with a Ni-base filler material and typically to a stainless steel (EPRI 2009, Matherne et al. 2010 and Fabricius and Jackson 2016). The joining of Grade 91 steel with a Ni-base filler metal would normally classify such a weld as a ‘dissimilar metal weld (DMW).’ Although DMWs installed in power generating plants typically involve a stainless steel on the opposite side to the Grade 91, failure is most often reported along the fusion line against the Grade 91 to Ni-base filler metal.

Examples of damage at the fusion line are provided in Figure 8-29. The association of damage in these images is associated with a distinct phase that does not possess the extent of substructure noted in the microstructures adjacent to this region. It is apparent that the observed damage is not biased to a boundary or location as the featureless phase is only ~5 µm in width. Where damage is documented it is generally within the featureless constituent observed in Figure 8-29, later identified as ferrite.

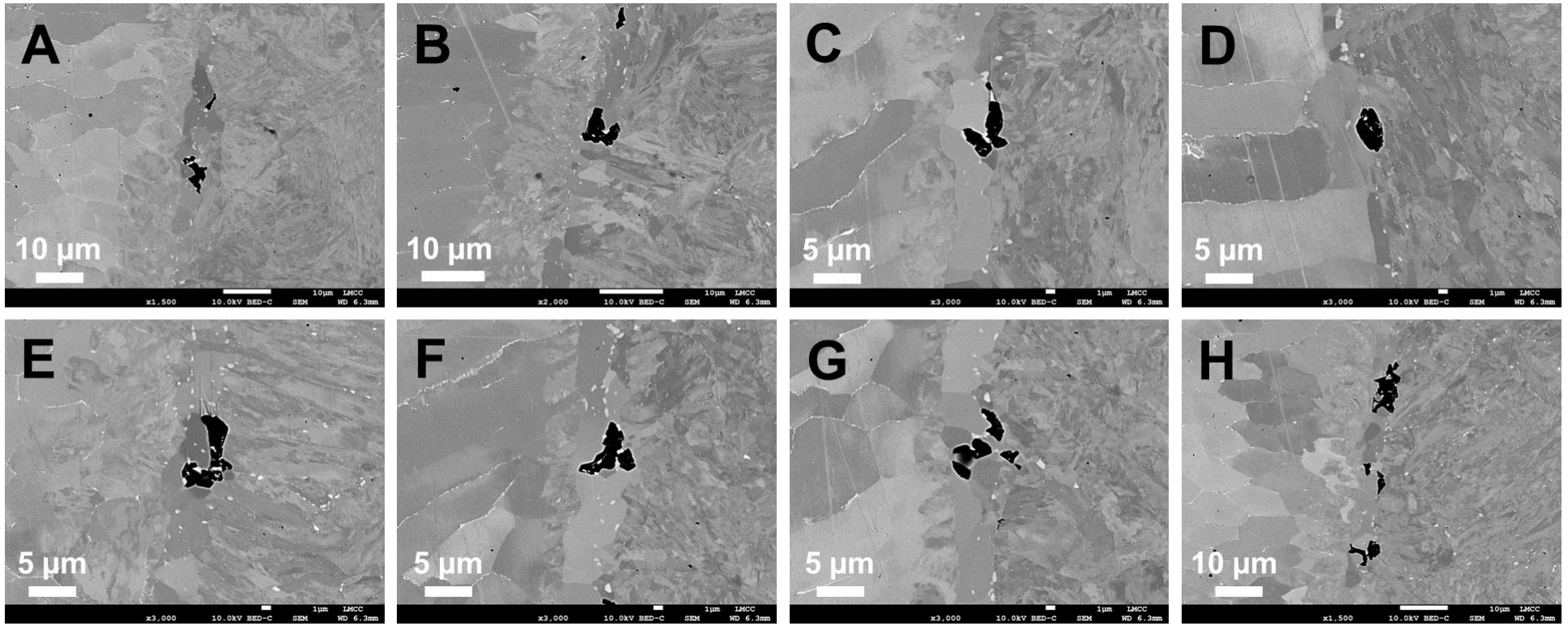

Figure 8-29. 9C-3, SEM backscatter electron images of damage in fusion line, 1,500X (A), 2,000X (B), 3,000X (C, D, E, F, G) 1,500X (H)
Note: *Stress axis is left-to-right*

An understanding of the damage observed in Figure 8-29 is linked to the as-fabricated state and the fundamental regions in the weld metal provided in Chapter 1 in Figure 1-8 and Table 1-3 and to the previous EBSD and EDS results in the as-fabricated condition, Figure 5-34 and Figure 5-56. Compositional mapping using EDS, and presented in Figure 8-30 to Figure 8-33, shows four distinct regions in the immediate vicinity of the fusion line boundary. These regions are identified in Figure 8-30 as the fully fusion zone, the martensite band, the ferrite band/HAZ and the HAZ in the Grade 91 steel. The location of the creep cavities in Figure 8-30 is superimposed on the elemental maps in Figure 8-31 to Figure 8-33.

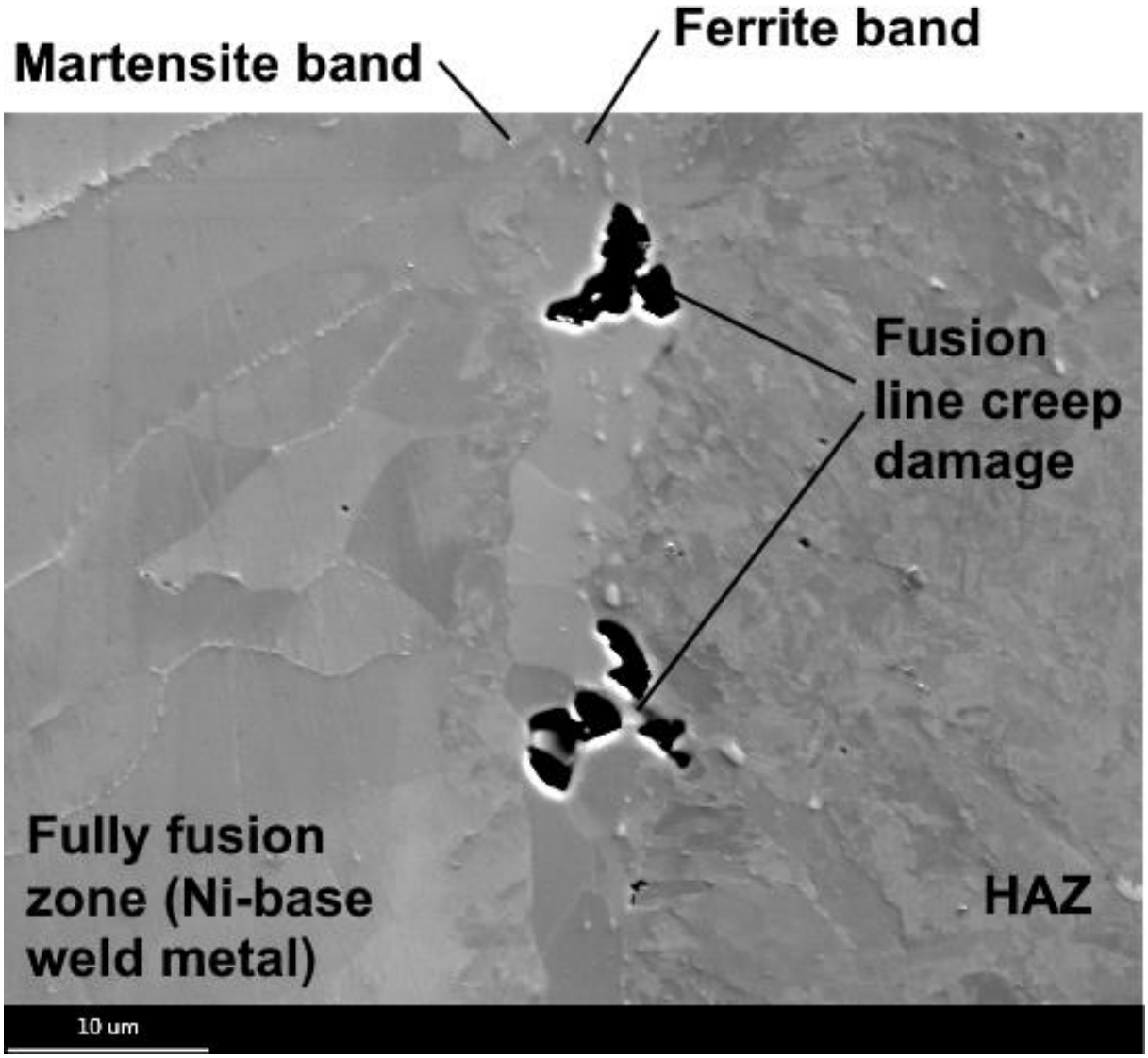

Figure 8-30. Location of SEM-EDS mapping at the fusion line in the location of creep voids in the post-test condition for sample 9C-3 (625°C, 60 MPa, 13,130 hours)

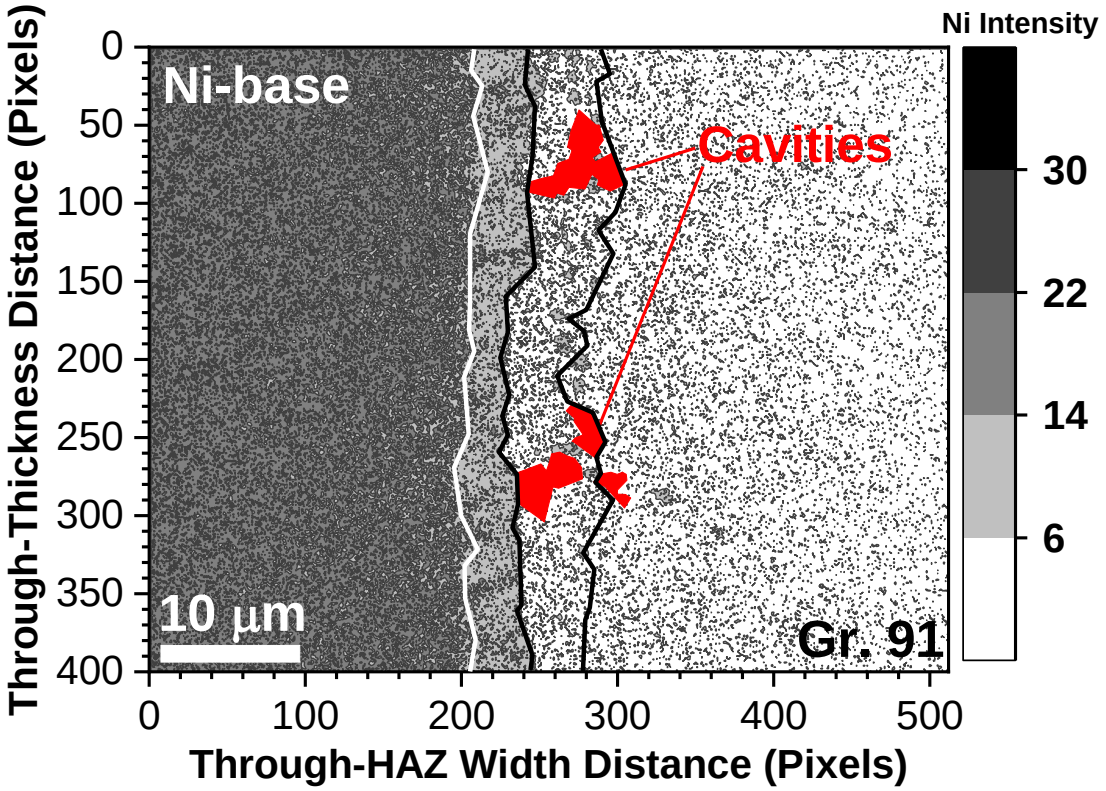

Figure 8-31. Location of SEM-EDS mapping at the fusion line in the location of creep voids in the post-test condition for sample 9C-3 (625°C, 60 MPa, 13,130 hours) and for Ni-intensity

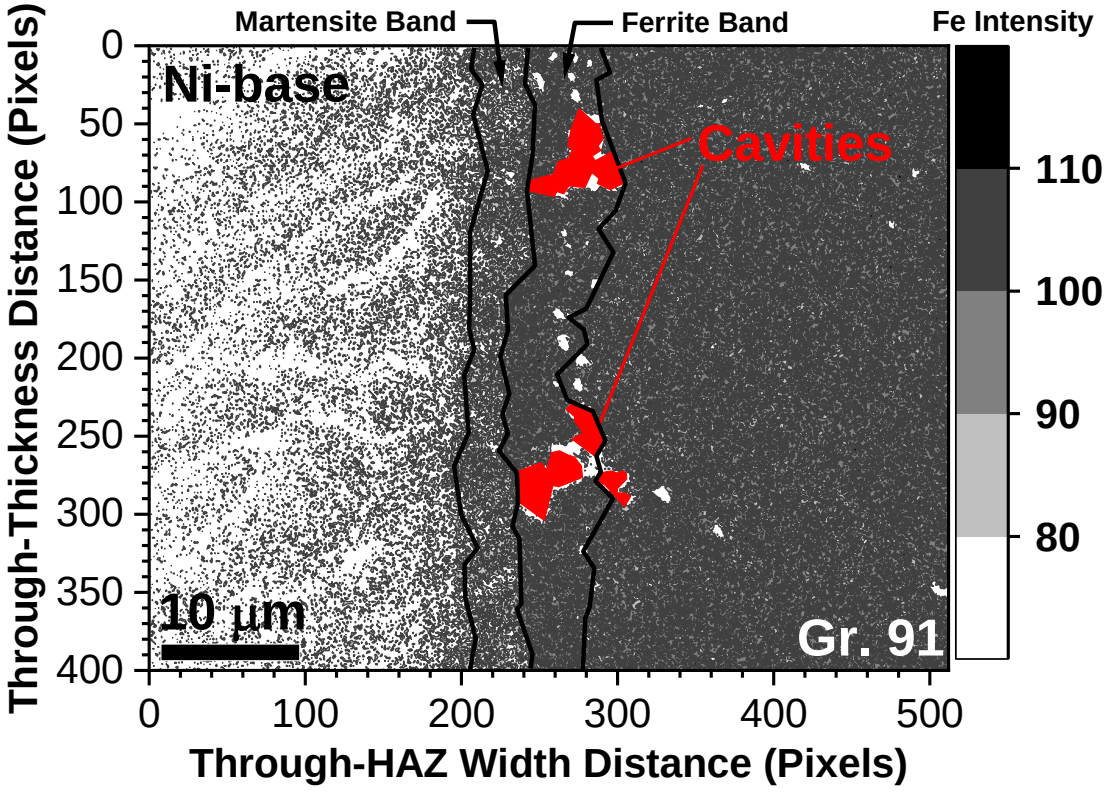

Figure 8-32. Location of SEM-EDS mapping at the fusion line in the location of creep voids in the post-test condition for sample 9C-3 (625°C, 60 MPa, 13,130 hours) and for Fe-intensity

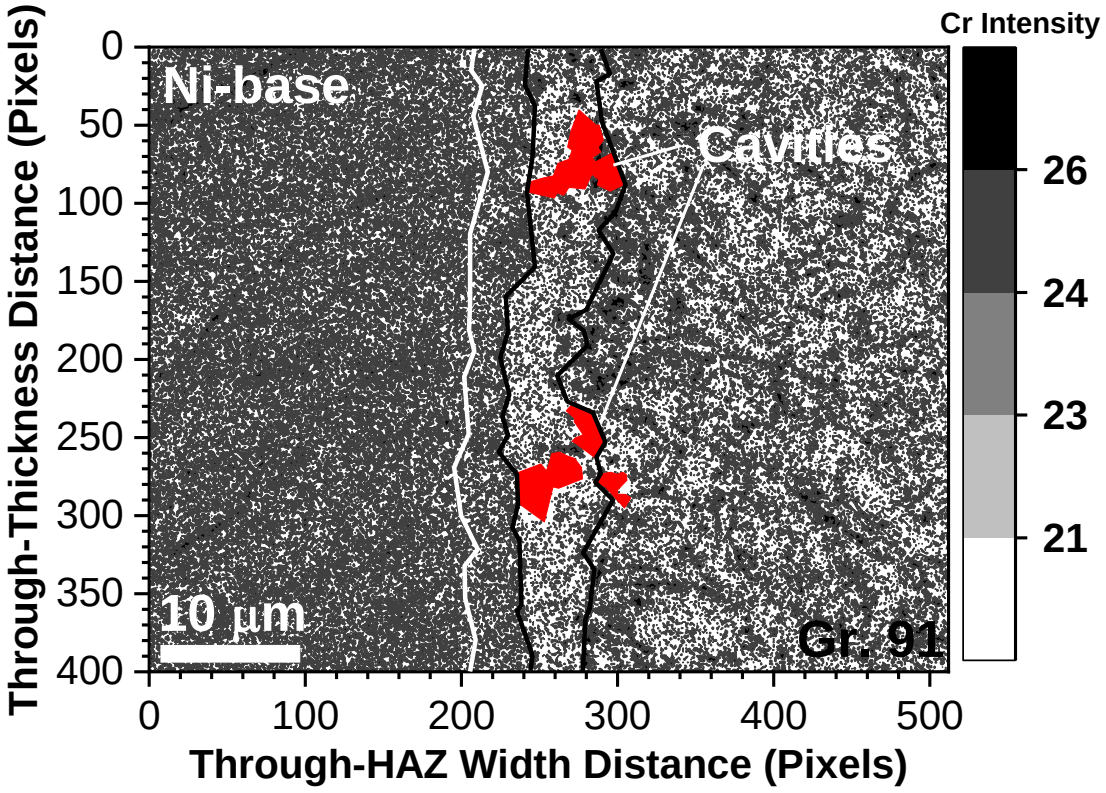

Figure 8-33. Location of SEM-EDS mapping at the fusion line in the location of creep voids in the post-test condition for sample 9C-3 (625°C, 60 MPa, 13,130 hours) and for Cr-intensity

The exact location of the creep damage near the fusion line is not a straightforward interpretation. The results provided in Figure 8-29 show that damage is consistently concentrated in a region that appears in backscatter imaging to be ferrite. Furthermore, this ferrite region possesses a composition on a macro-scale that is indistinguishable from the Grade 91 HAZ. Reference to the definitions in Table 1-3 provide context for these observations. The region possessing a composition identical to that of the parent material and adjacent to the fusion line in the weld metal is the unmixed zone (UMZ).

Additional clarification of the compositional variation in Figure 8-31 to Figure 8-33 shows that the observed, martensitic phase present between the damaged region and the fully fusion zone has a composition that is between that of the parent metal and fully fusion zone and consistent with the description of the TZ in Table 1-3. This observation is most obvious for the Ni and Fe maps where the relative intensity of each element changes to an intermediate gray-scale color as compared to the fully fusion zone or the HAZ.

An attempt to link these findings to the as-fabricated state is provided in Figure 8-34. This figure overlaps the SEM-BED with a narrowed location where the EBSD data and EDS data were collected. As shown in this image, there exists a continuous band in the Ni intensity map (Figure 8-34C) centered at the 500-pixel location (x-axis). It is proposed this region is the TZ; to the right of this region lies the UMZ where damage develops in-service and to the right of the UMZ would lie the fusion line.

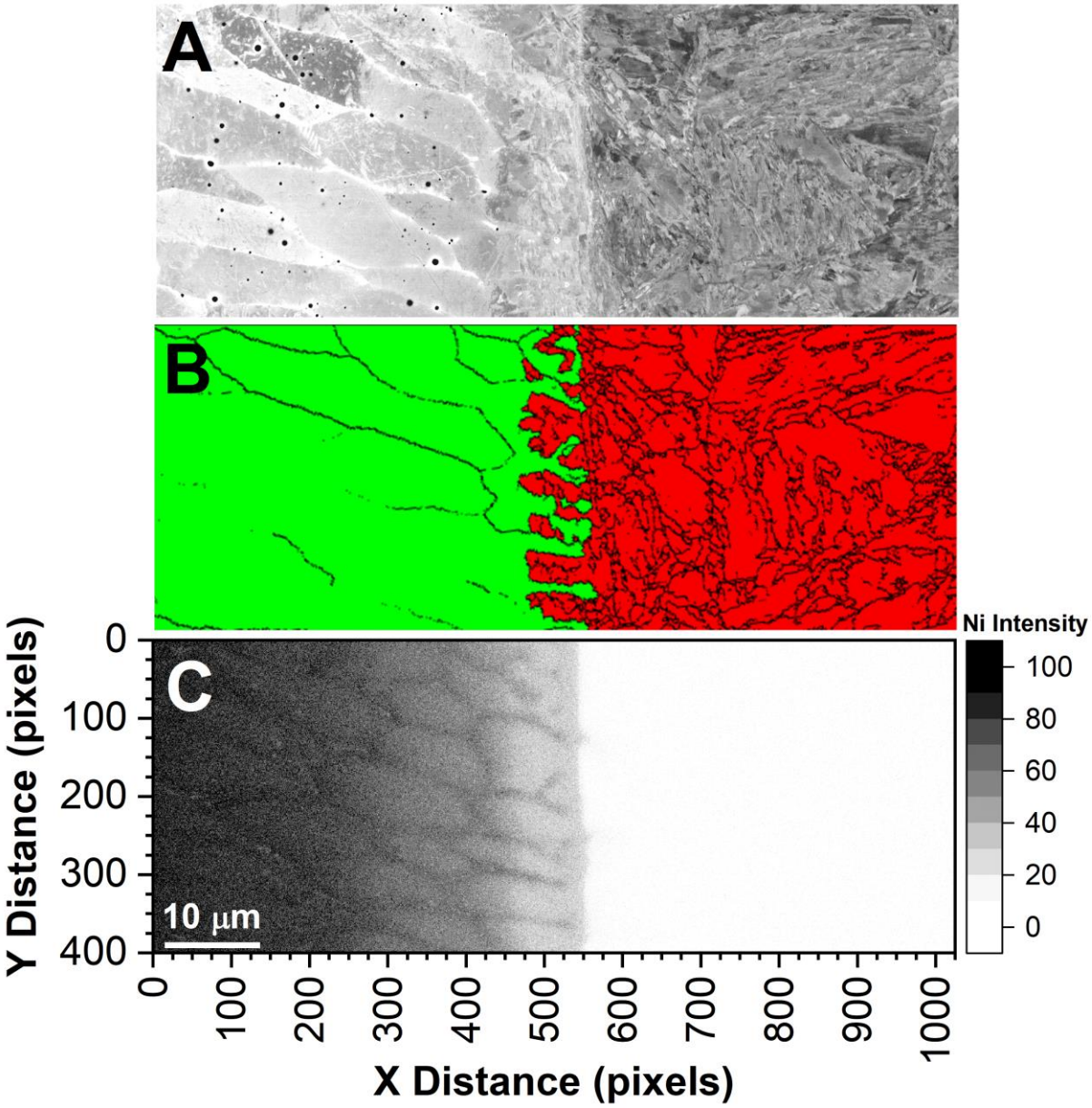

Figure 8-34. Results for SEM-EDS at the fusion line in the as-fabricated condition for weld 9C (EPRI P87 weld metal on left-hand side and Grade 91 on the right-hand side of each image). SEM image of the boundary (A), the distribution of FCC (green) and BCC (red) phases and overlay of boundaries (B) and EDS results for Ni (C)

8.6 Discussion

For the evaluated set of feature cross-weld creep tests, damage was observed in multiple locations including the weld metal for the under-matching weld 8C, the HAZ in all test samples or the fusion line for the over-matching weld 9C. In most cases, the dominant failure mode was associated with a highly localized failure path or high density of damage through the length of the HAZ in a zone that was ~500 to 1,000 µm in width. The F-TP1 series of welds were susceptible to parent metal failure and where damage in the HAZ was noted, the density was considerably lower than for the balance of the cross-weld tests. Furthermore, failure for the two of the F-TP1 cross-weld tests occurring in the HAZ appeared to be dominated by a crack growth mechanism. The weld 8C tests sometimes exhibited a combination of weld metal and HAZ damage. The following sections will summarize the findings for the damage present in each region including the weld metal, HAZ and fusion line.

8.6.1 Damage in the weld metal

The composition for the AWS type -B8 filler metal does not contain V, Nb, N or other alloying additions and thus results in a dominant carbide of the form M_6C or $M_{23}C_6$ (Furtado et al. 2007). Formation of coarse carbides and Laves phase results in local depletion adjacent to these particles and particularly for the solid solution strengthening element Mo. Thus, the evolution of damage may occur at the grain boundary in a location absent of a precipitate or adjacent to a particle where local depletion of solid solution strengthening elements exists. EBSD data confirmed that damage was concentrated at grain boundaries preferentially aligned normal to the stress axis. The size of the cavities at the grain boundaries did not permit a more evolved interpretation of the sequence of events including the responsible feature for nucleation, which subsequently leads to stable cavity growth. Prior investigations by Middleton, primarily in the assessment of reheat cracking susceptibility for controlled alloying additions in CrMoV steel, suggests boundary zone deformation is suppressed in 9 wt. % Cr steels due to the similarity in strength for the grain boundary zone and matrix (Middleton 1981). This might imply that formation of a composition-depleted zone adjacent to the boundary is not be readily present, although more work on interrupted samples would be required to confirm this.

The formation of localized conditions in the weld metal necessary to assist void nucleation was not biased to the refined or the coarse columnar regions. This statement is supported by the widespread damage in the weld 8C tests in both the refined and coarse columnar regions. The seemingly controlling features are the grain boundary, its relative length which determines the extent of coalesced cavities able to develop into observable cracks and its orientation relative to the stress axis (the more normal the boundary the more likely damage is present).

8.6.2 Damage in the heat affected zone

In the HAZ, two populations of creep voids were observed. There existed a population associated with inclusions and a second population not clearly linked to a second phase particle or an inclusion. The assessment of damage in a 2D, single plane complicates the interpretation provided in this Chapter. Furthermore, the evaluation of cross-weld creep tests is most frequently performed (as in this study) in the 'failed' condition resulting in cavities which are large relative to the primary or preferred site(s) for nucleation. The diameters for the observed grains and the cavities in the HAZ overlap, such as documented in the EBSD overlay image in Figure 8-25.

Assessment of the void size, irrespective of the nucleation source, is not a straightforward exercise since it is observed that the cavities consistently possess a highly irregular shape (e.g. Figure 8-11, Figure 8-15, and Figure 8-19). An attempt to determine or rationalize the relative cavity size among the assessed samples would require assumptions to be made for what constitutes the *actual size of the cavity* and significant image editing to accommodate the assumption. For example, the consideration of cavity area where an inclusion is still present (such as Figure 8-14D) or if it is reasonable to include the apparent grain deformation (such as Figure 8-19G) in the assessment is not a trivial consideration and can lead to significant discrepancies procedure-to-procedure. As such, no attempt was made to quantify the cavity size in this section. The sometimes-complex manifestation of damage in the HAZ is well-documented in the literature; an example provided by Masuyama is given in Figure 8-35. The complicated interpretation of cavitation in interrupted creep tests in Grade 91 steel has been previously detailed in (Yadav et al. 2015).

A general focus on particles or features in the microstructure which affect the deformation resistance has resulted in an overall set of results in the literature which attempt to link damage in the HAZ of 9-12 wt. % Cr CSEF steels to:

- Grain boundaries (such as in Masuyama 2017b, Lee et al. 2005, Tanaka et al. 2013, Wang and Li 2016) or
- $M_{23}C_6$ (Lee et al. 2005, Zhao et al. 2012, Sakthivel et al. 2016) or Laves phase (Zhang et al. 2015) or
- General coarse precipitates including Z-phase, Laves or $M_{23}C_6$ (Abd El-Azim et al. 2013) or
- Inclusions and/or nitrides (Yadav et al. 2015).

It is generally the case that little attention has been given to the potential contribution that inclusions or nitrides may have (e.g. AlN in Grade 91 or BN in grade 92) and the relative contribution of these particles to void nucleation and growth.

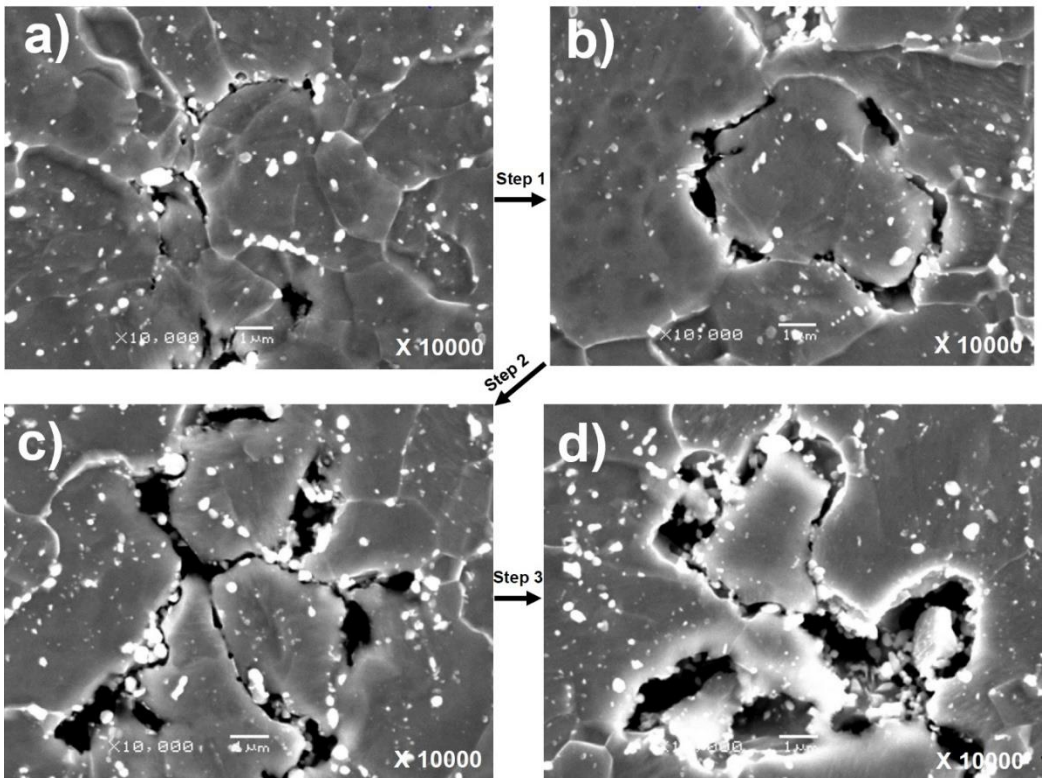

Figure 8-35. Complex growth of creep damage in the heat affected zone for Grade 91 steel (Masuyama 2017b)
(a) The initiation of a critical defect
(b) growth of the defect to include the entire, local grain boundary length
(c) extension of the damage to adjacent grains
(d) and the consumption of local grains by the formation of a single, interconnected cavity

The interaction of particles in the matrix under creep processes is reviewed by Goods and Brown (1979), who provide perspective on how a particle might contribute to cavity development at the particle-matrix interface. They suggest for approximately equiaxed particles there will be some influence of interfacial decohesion or for elongated particles the particle will fail by internal fracture (Goods and Brown 1975). In the present research, there is evidence for contaminant effects; e.g. the presence of multiple inclusions in a cluster (Figure 8-18E) or as part of a single particle (Figure 8-18F) or a 'shell' of AlN or other precipitates around MnS (Figure 8-14C and Figure 8-14H). The localized nature of elemental segregation in the MnS particles has been independently documented for Al and Cu (Figure 2-41) in Grade 91 steel. The formation of MnS near the end of the melting process may partially explain why the presence of other particles are observed at MnS; see section 4.3. These observations could support the reduction in interfacial strength leading to decohesion, particularly during the steel making process where the local deformation at an inclusion or cluster may be sufficient to promote local decohesion. Such an effect has been identified in Grade 92 by Gu (2017).

Consideration of the effect of inclusions on cavity nucleation has been more routinely appreciated in the literature for low alloy steels, such as in the assessment of time-dependent behavior in 1Cr-0.5Mo or 1.25Cr-0.5Mo including ex-service weldments (Lee and Muddle 1995 and Fubyashi 2003). These two examples show a clear association of damage with MnS, and build on the shorter-term observations for multiple reheat cracking studies in the CEGB where the influence of MnS on the nucleation of damage is well-documented (Cane and Middleton 1981).

There is little, documented information in the recent literature for the role that inclusions might play in the cavitation process in martensitic CSEF steels. This research has documented a significant difference in the number density of inclusions for a commercially available inclusion-counting process (Table 4-6) and for an optimized procedure (Table 4-7 and Figure 4-19). This is a notable result because the steels of interest, at the time of component fabrication, were Code-compliant meeting the basic acceptance testing requirements including hardness, tensile, and impact properties. The documented damage in Chapter 7 shows the density is highest in the HAZ for the B2 steel which possesses a higher inclusion density. This increased

susceptibility to damage in B2 coincides with a reduction in cross-weld creep performance that is nearly a factor of 10 compared to the TP1 material. While inclusions are not generally observed to contribute to a dramatic loss of creep deformation resistance, there is substantial inferential evidence in Chapters 6 and 7 that such particles are affecting the damage susceptibility in the HAZ, leading to a reduction in cross-weld creep life. This point is emphasized not only by the mechanical assessment of the data which clearly show that deformation alone cannot explain the dramatic difference in cross-weld creep performance. The importance of damage is emphasized in the current chapter as individual cavities were often associated with a second phase particle or inclusion.

Each individual void in the HAZ was typically of the order of 1 to 10 μm in diameter. Generally, for a parent material with low creep ductility, the number density of cavities was higher and the local deformation field reduced compared to the parent metal with the higher creep ductility (this is compared in Figure 8-36 and Figure 8-37). The size of the cavity, relative to the microstructure, matches well with the median size of MnS in the parent materials of interest (Figure 4-19, ECD of ~500 nm). Furthermore, it is demonstrated that a statistically-significant difference in the parent metal inclusion population exists. The association of this finding is reasonable since inclusions cannot be resolutionized in the HAZ during the welding process in the location where peak damage is observed. Furthermore, there is still a sizeable amount of AlN present in the HAZ where damage is observed, Figure 8-36. The association of damage with AlN appears to be a random event as the extent of AlN far exceeds the cavity density and there are many examples in Figure 8-36 where a cavity is not present at AlN. It is recognized that AlN formation may decrease the amount of MX present in the HAZ and compound the development of damage using a deformation-based argument.

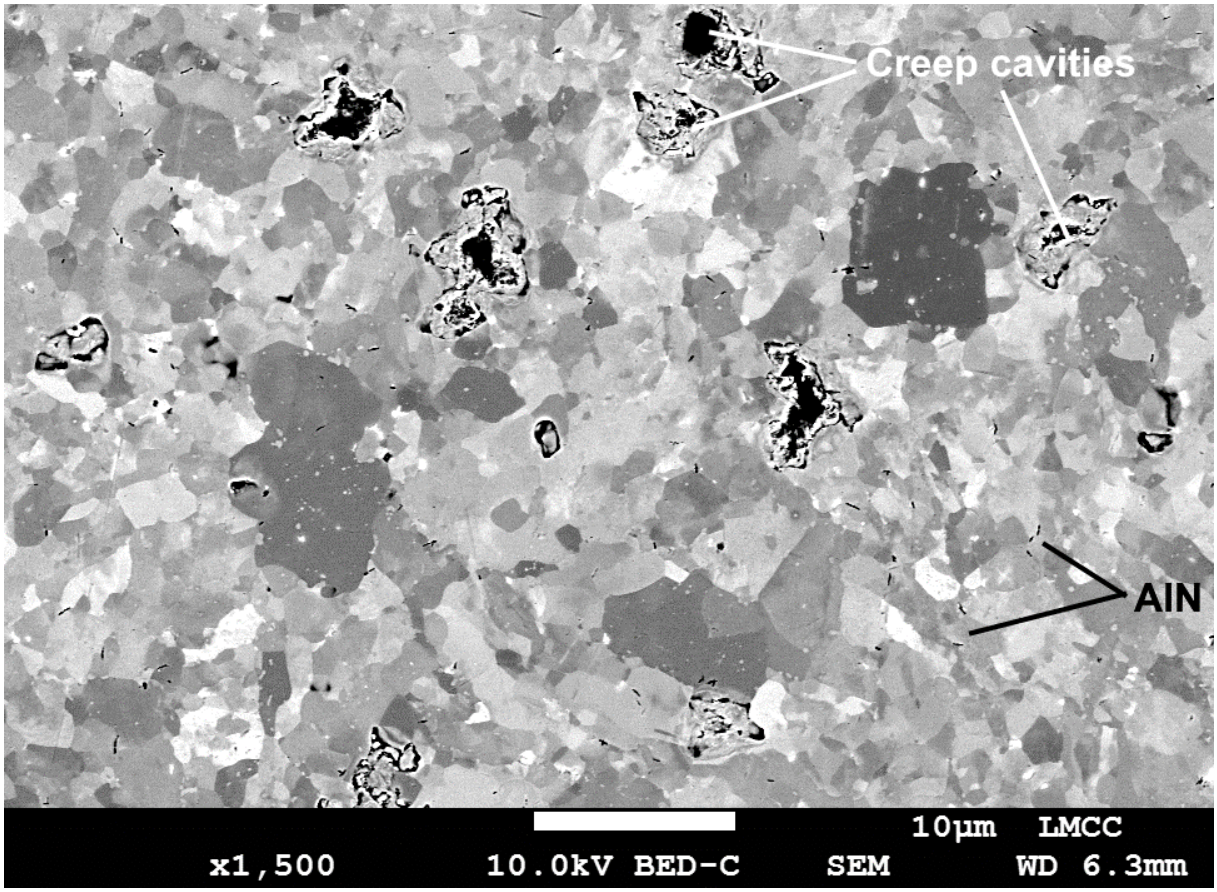

Figure 8-36. Identification of creep cavities and AlN in a representative field of damage in the heat affected zone for sample RNT-B2-2 (625°C, 60 MPa, 2,586 hours).
Note: *the extensive amount of AlN in the field of view.*

The localized nature of the strain accumulation was noted in the HAZ and manifested as local areas of recrystallization (Figure 8-37). Although an attempt was made to quantify and measure this using SEM-EBSD at the location of two MnS inclusions (Figure 8-24), the results did not provide clear support for this observation. However, the literature provides more convincing evidence (Figure 8-38) and there exists many theories as to the reason for strain localization. The distribution of second phase particles in the matrix may account for this strain localization. Alternatively, it has been postulated the local deformation of the matrix occurs at intersections of hard and soft grains (Masuyama 2017b) or 'creep strong' and 'creep weak' grains (Wang and Li 2016). The 'creep strong' grains are characterized by higher densities of $M_{23}C_6$ and/or MX carbonitrides with some evidence of substructure and the 'creep weak' grains by a featureless, fully ferritic matrix. The strain localization, whether due to a local particle or a hard-soft grain interaction is postulated to create a local multiaxial stress state as schematically represented in Figure 8-39 (Masuyama 2017b). The combination of the susceptible microstructure in the presence of a multiaxial stress state thus leads to the

necessary conditions for void nucleation and growth. In the following chapter a refined procedure will be utilized to document this strain localization using SEM-EBSD.

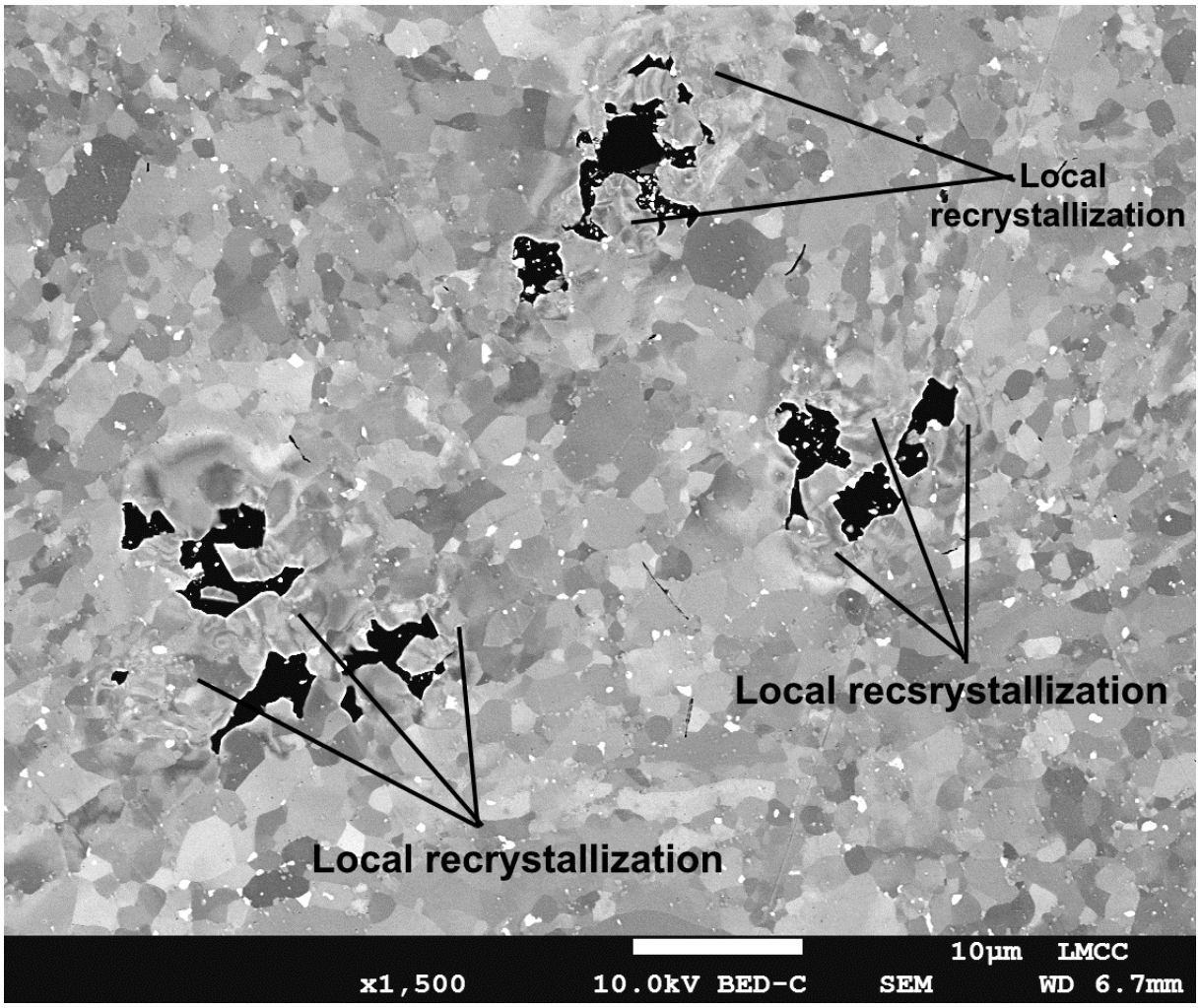

Figure 8-37. Evidence of local recrystallization and/or deformation at the location of creep cavities in the heat affected zone for sample 9C-3 (625°C, 60 MPa, 13,130 hours)

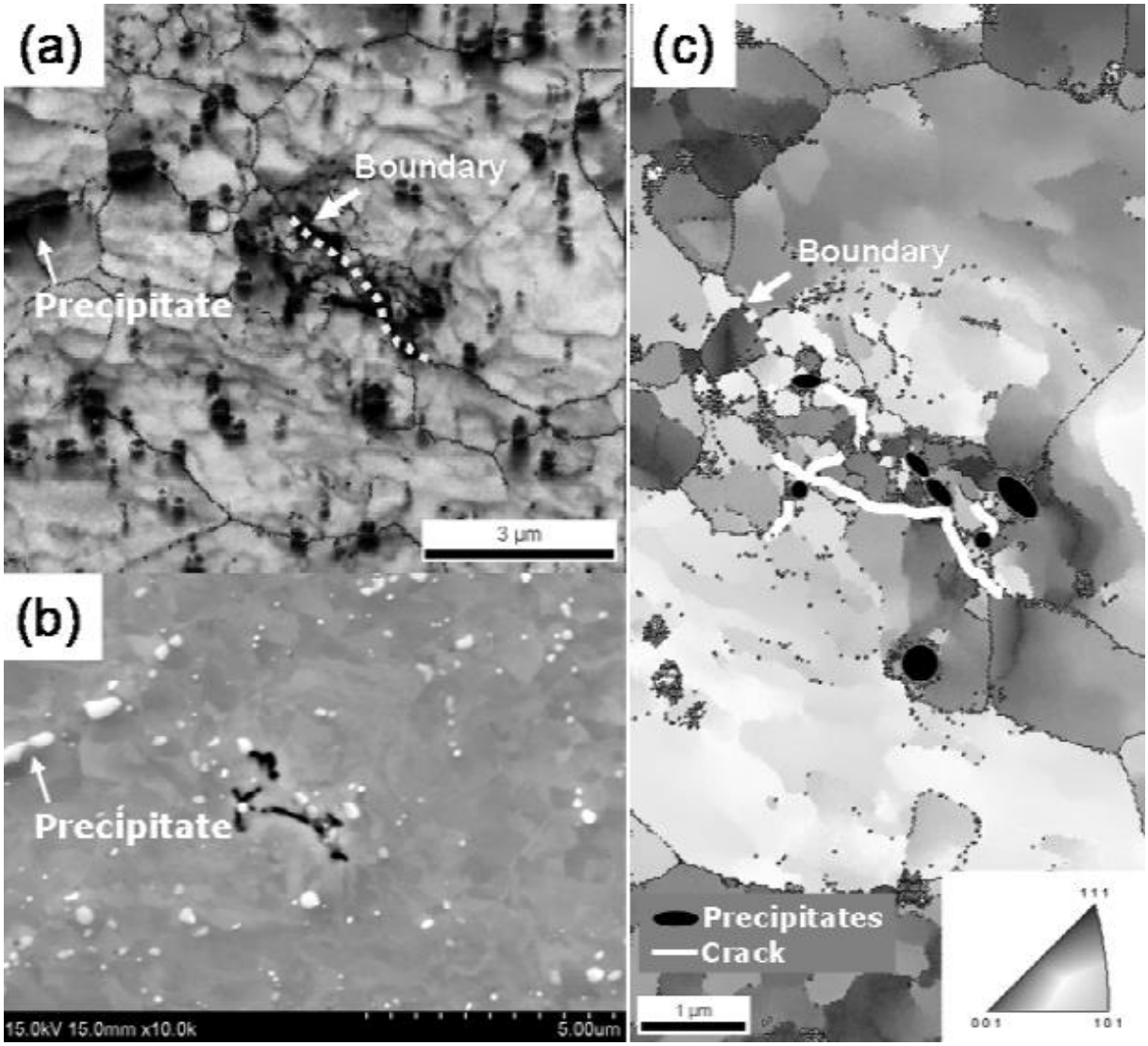

Figure 8-38. Reported recrystallization in the heat affected zone for a Grade 91 steel cross-weld creep test conducted at 650°C and 60 MPa to 25%-time fraction and documented using electron backscatter diffraction, from (Tanaka et al. 2013).

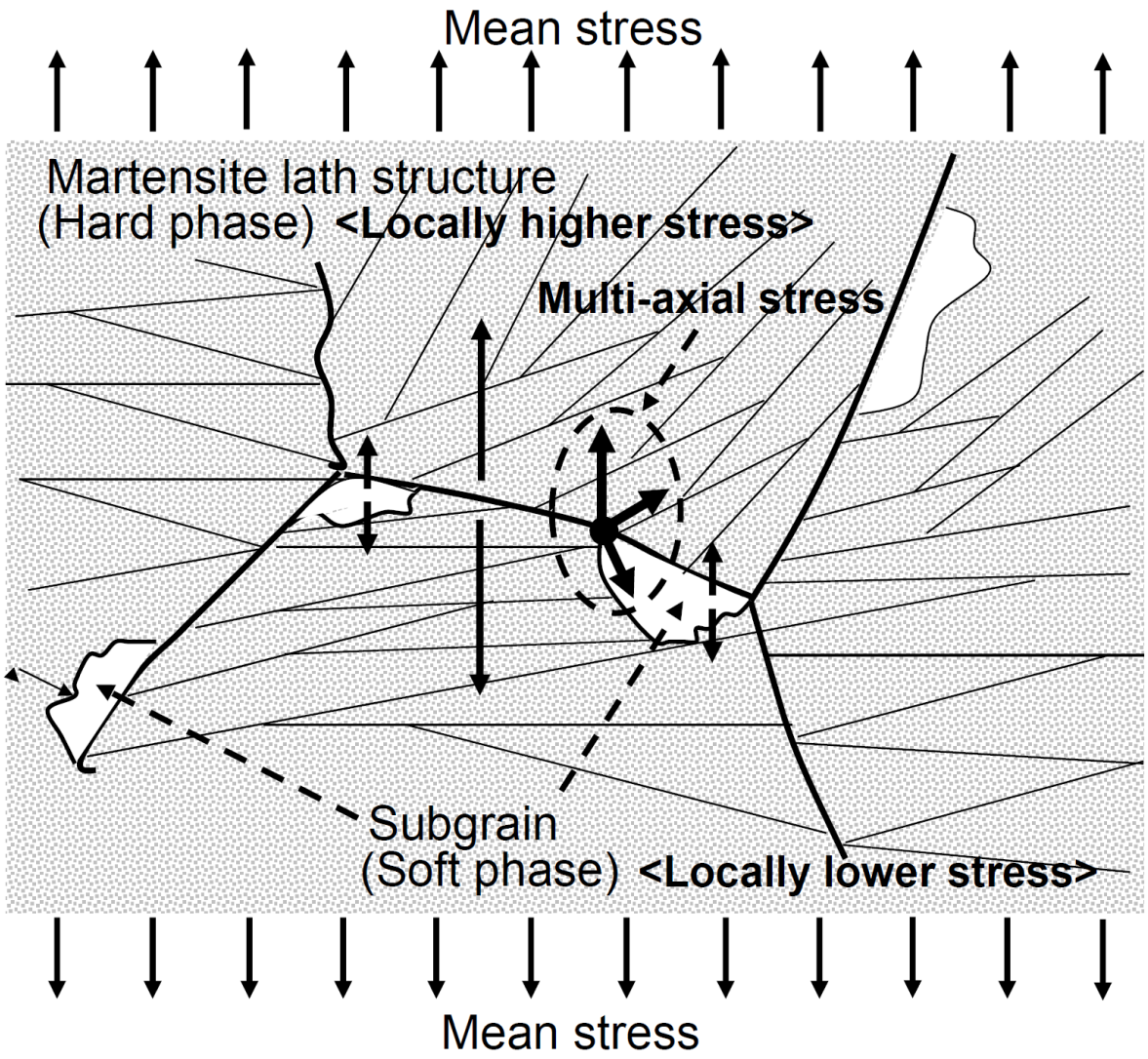

Figure 8-39. Postulated stress state which develops in the HAZ for locations where a martensitic, hard phase is adjacent to a ferritic, soft phase (Masuyama 2017b)

The nucleation of creep damage at coarsened or large particles in the HAZ of 9 wt. % Cr CSEF steels was investigated by Li and Shinozaki who utilized a 3D model of a precipitate in the matrix (Li and Shinozaki 2005). The purpose of modeling the particle-matrix interaction was to evaluate the critical strain required to nucleate a void. In this work, the size of the precipitate and the Young's modulus of the precipitate were systematically varied between 0.10 to 0.25 μm and 400 to 800 GPa, respectively. They did not consider the effect of interfacial strength (which might be reduced by the presence of segregated elements, for example). In their work, the equivalent strain around the precipitate increased with the increasing radius of the precipitate. This indicates that large precipitates promote a wider field of elevated strain compared to small precipitates. It can be concluded that 'coarsened precipitates' or more generally 'large particles' leads to an increased susceptibility for creep void initiation.

The role of ‘coarse precipitates’, and more specifically $M_{23}C_6$, has been explained by Lee et al. (Lee et al. 2005). In the evaluation of a cross-weld creep test in Grade 91 steel after testing at 650°C and 83 MPa (failure in 442 hours) the association of damage was noted at the interface of coarse $M_{23}C_6$ cavities where these particles resided on grain boundaries and in the junction between small and large grains (Figure 2-57). The large grains were fully recovered ferrite whereas the finer grains were reported to contain some substructure representative of martensite. The presented argument for the development of damage in the highlighted locations suggested the deformation of the soft grains was more likely to induce rotation of the hard grains creating a sharp, island-like crack. The heterogeneity of local strain accommodation was postulated to assist in the cavity nucleation and consistent with the schematic presented in Figure 8-39 and the analysis of Li and Shinozaki. Lee et al. additionally note several observations were made in the microstructure where the presence of ‘hard’ and ‘soft’ grains were clearly detected but no cavity was observed. They surmised that the different image quality indices between neighboring grains may assist cavity nucleation, but were not the critical microstructure feature.

While damage is routinely associated with $M_{23}C_6$ or Laves phase in the literature, such observations were not readily identified through the course of routine microstructure examination in the current study. Two examples of such observations are provided in Figure 8-40 where a small cavity has nucleated at a $M_{23}C_6$ particle and for damage concentrated at a complex cluster of $M_{23}C_6$ and Laves phase particles Figure 8-41. In both cases, the particles reside at grain boundaries in the HAZ.

The appearance of the cavities in the HAZ show a tendency to faceted cavity walls, such as shown in Figure 8-40, Figure 8-42 and Figure 8-43. This morphology is a point documented in fundamental studies of cavitation in alpha-iron (Wingrove and Taplin 1969 and Cane and Greenwood 1975), in CrMo steel weld metal in Figure 8-44 (Lundin et al. 1998) and more recently in 9 wt. % Cr CSEF steels in Figure 8-45 (Gaffard 2004) and Figure 8-46 (Gu 2017). The formation of faceted cavities is evidence for a diffusion-assisted mechanism, but the exact reasons for this are often insufficiently described.

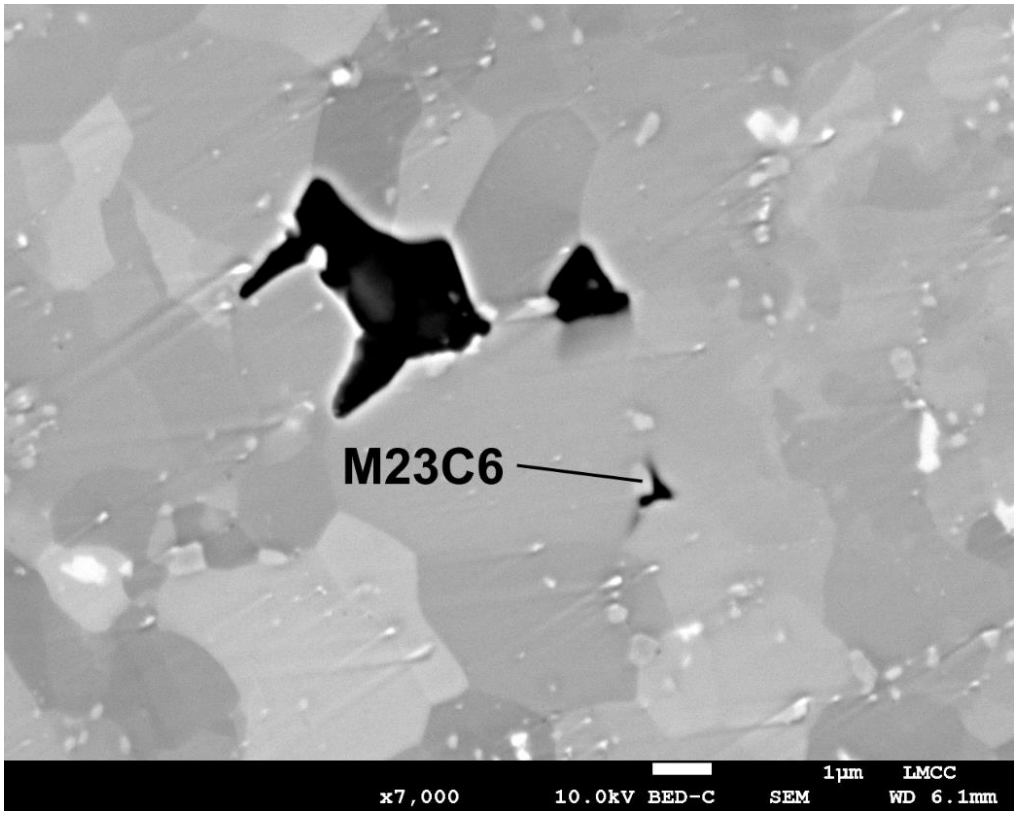

Figure 8-40. Example of void nucleation at $M_{23}C_6$ in the heat affected zone for sample 8C-5 (600°C, 70 MPa, 10,461 hours)

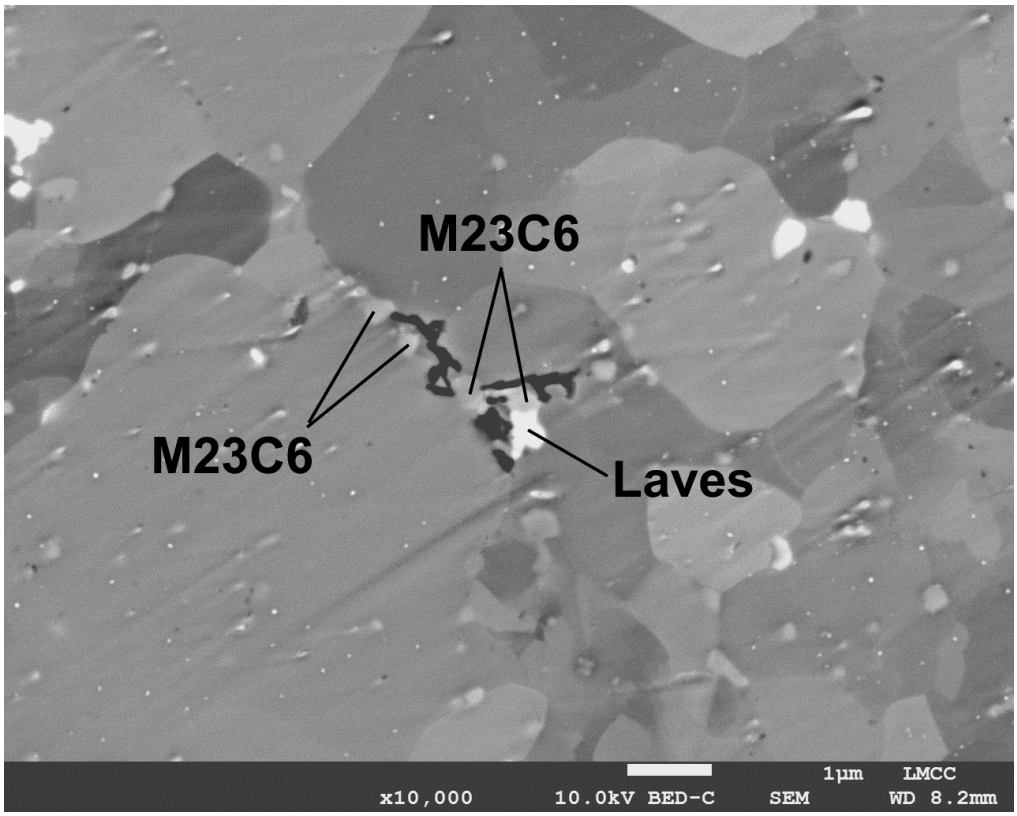

Figure 8-41. Example of void nucleation at a cluster of $M_{23}C_6$ and Laves phase particles in the heat affected zone for sample 8C-5 (600°C, 70 MPa, 10,461 hours)

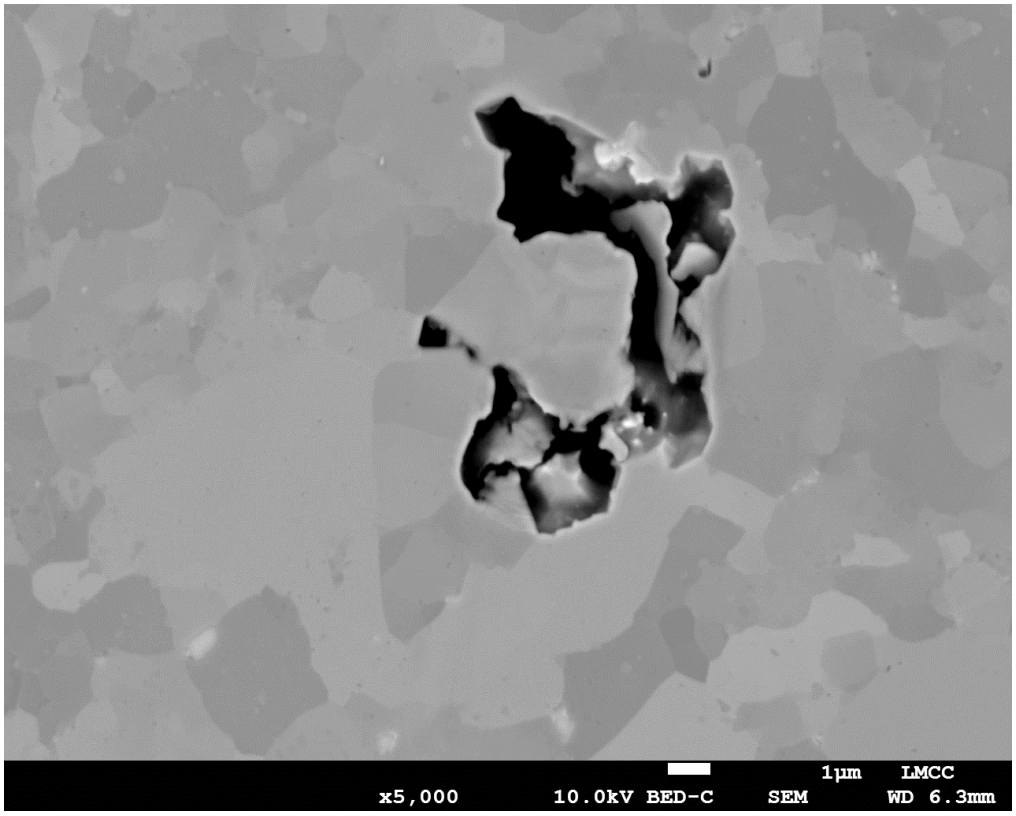

Figure 8-42. Faceted appearance of void growth for a single cavity at high magnification (5,000X) in the heat affected zone for sample 7C-2 (625°C, 60 MPa, 13,201 hours)

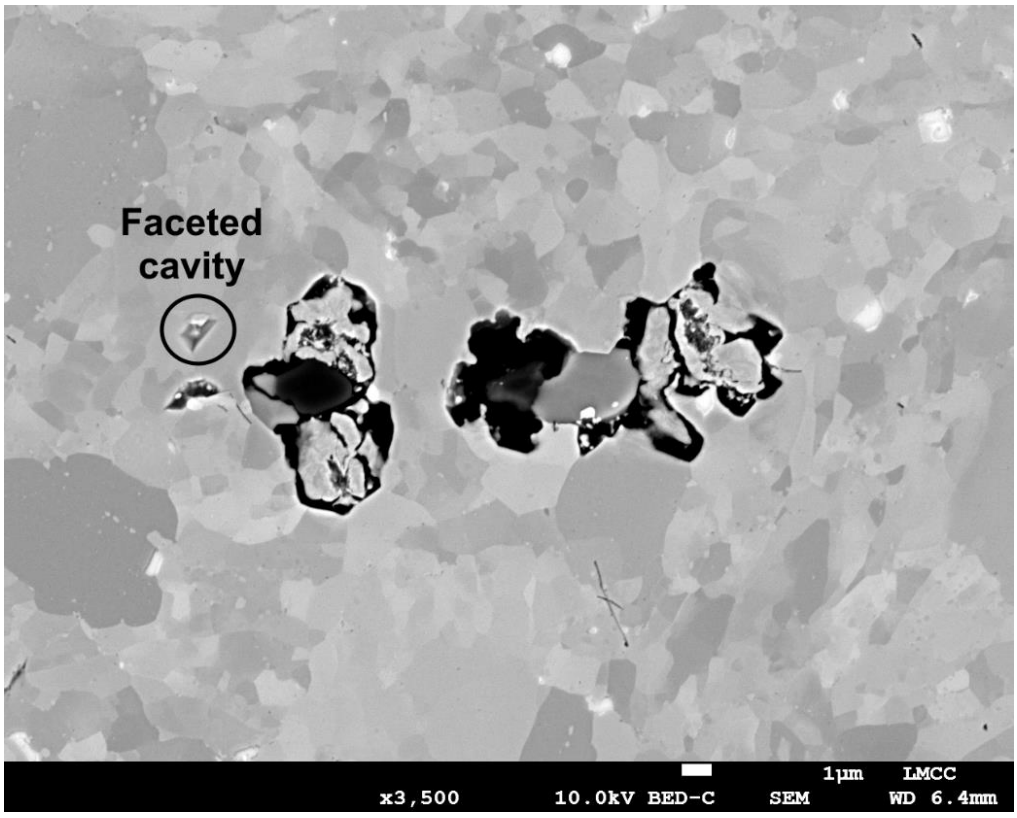

Figure 8-43. Example of faceted cavity in the heat affected zone for sample 7C-2 (625°C, 60 MPa, 13,201 hours)

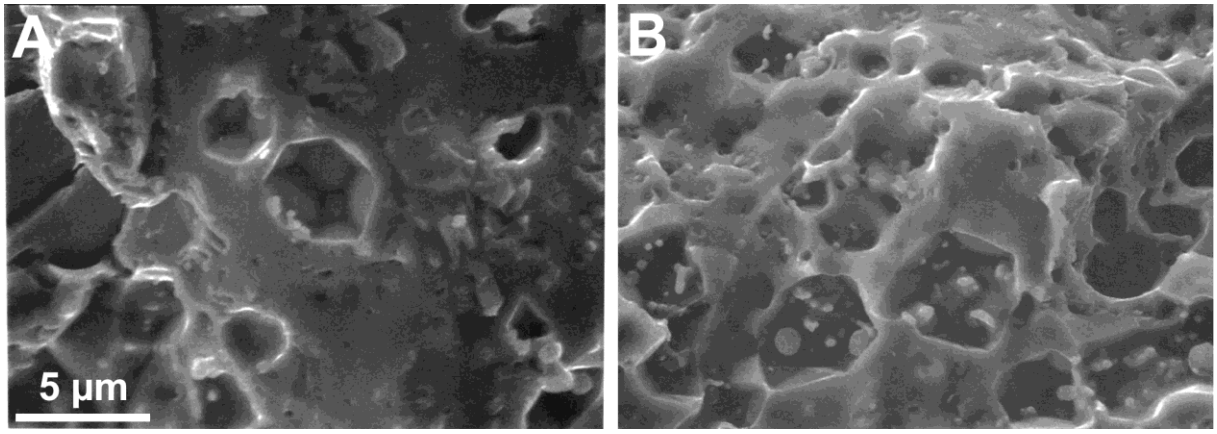

Figure 8-44. Examples of faceted cavities in CrMo steel weld metal taken in a SEM at 5,000X (Lundin et al. 1998)

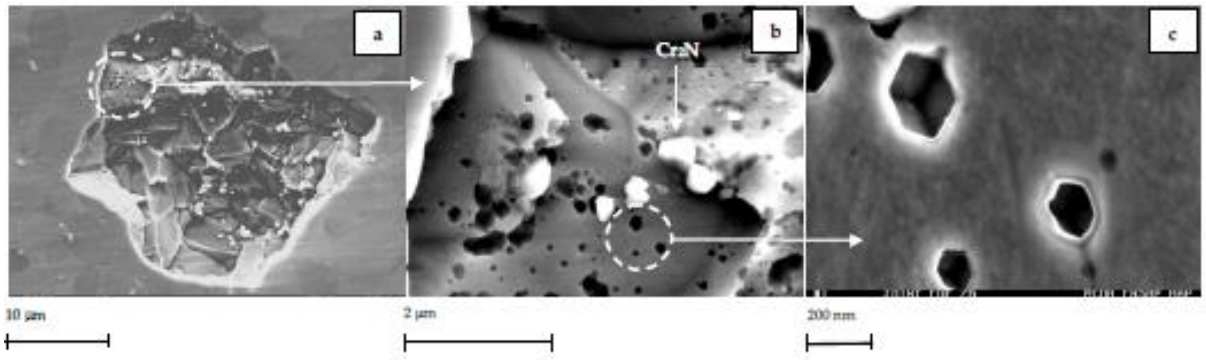

Figure 8-45. Documented faceted cavities in Grade 91 steel heat affected zone cross-weld creep tests (Gaffard 2004).

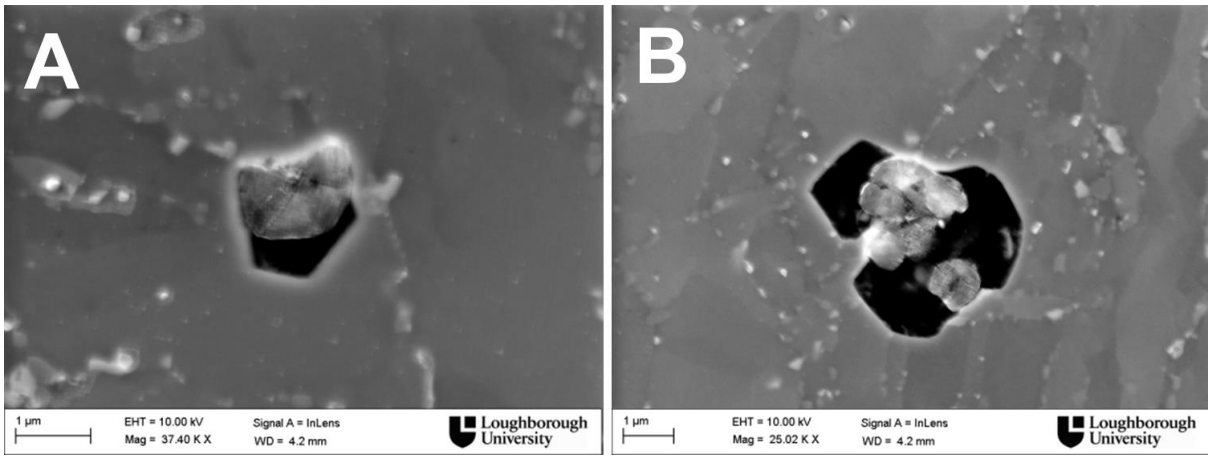

Figure 8-46. Examples of faceted cavities in Grade 92 steel parent metal taken in a SEM at 37,400X (A) or 25,000X (B) (Gu 2017)

The observed damage in the HAZ can be summarized using a similar set of conclusions proposed by Cane and Greenwood (1975). In their assessment of damage in iron they demonstrate the nucleation of damage is most favorable at inclusions and the development of damage is assisted by grain boundary sliding. With

increasing strain, the development of damage is possible at less favorable sites suggesting there exists a clear hierarchy of susceptibility. The observed damage in the evaluated samples follow a similar logic such that damage can be expected to form at less favorable sites as the test duration increases and the growth of the cavities early in the process reaches a sufficient size inducing local stress concentrations in the matrix.

8.6.3 Damage in the fusion line

The accumulation of damage at the fusion line in sample 9C-3 was shown to be in a zone consistent with the classical description for the unmixed zone (UMZ). The composition of the location where damage is identified does not show a local increase in the content for Ni nor Cr nor a local depletion in Fe. Adjacent to this region, in the partially mixed zone or transition zone (TZ), there is notable enrichment in Ni and Cr. However, damage is not identified in the UMZ and this region possesses substructure representative of martensite whereas the UMZ has a fully ferritic microstructure. The localization of damage in the UMZ was not associated with damage at an interface or boundary; examples of damage were provided which show a more random association of damage in the UMZ. The UMZ was ~5 μm in width.

The evolution of the UMZ to ferrite has at least two, potential rationalizations. The first, relies on an explanation resulting from processing during fabrication and is not a plausible explanation. The cross-weld creep testing for weld 9C was conducted in the as-welded condition and there is no evidence in the SEM imaging or in the SEM-EBSD information provided in Figure 8-34 that the ferrite band is present after welding. It is more credible the compositional heterogeneity present in the as-fabricated state (see Figure 8-34C and Figure 5-56) contributes to the formation and stability of this zone. It is thus potentially the case that any fabricated weldment involving a 9 wt. % Cr CSEF steel joined with a Ni-base filler metal will be inherently susceptible to the formation of this region.

The second, and more probable explanation for the evolution of the UMZ requires the local diffusion of carbon during the cross-weld creep test. Where the compositional gradient is steep, carbon diffuses down the chemical potential gradient during creep exposure leading to a gradual depletion of carbon in the UMZ. This has two effects; the stabilization of martensite in the Ni-enriched TZ and the formation of so-called

Type I carbides along the fusion line. Formation of such carbides in the provided documentation is relatively diffuse, and is most clearly observed in Figure 8-29F and to a lesser extent in Figure 8-33. This evaluation is the subject of a recent manuscript utilizing detailed observations in multiple, controlled experiments where Ni-base filler metals were deposited on a Grade 91 steel substrate and compared microstructurally using SEM-EBSD to the predictions provided by kinetic modeling simulations using DICTRA (Orzolek et al. 2019).

8.7 Summary

The assessment of damage in the evaluated samples provided examples of time-dependent damage generated in the weld metal for an AWS type -B8 filler metal (weld 8C), at the fusion line for a weldment fabricated with the Ni-base filler metal EPRI P87 (weld 9C) and in the HAZ for all weldments. Damage in the weld metal was observed through the deposited weld metal and was not preferentially located in a specific region characterized by grain size. Rather, the association of voids or cracks was associated with grain boundaries normal to the applied stress axis and the extent of observed cracking was a function of grain boundary length such that for low magnification imaging it *might appear* that damage is concentrated in the coarse columnar region. However, no definitive association could be made with the coarse columnar region and an increased level of damage when compared to the refined regions.

Damage in the HAZ was associated with second phase particles such as inclusions and few voids were clearly identified at Laves phase or $M_{23}C_6$. An equal, if not larger, population of voids were documented in locations where no particle could be clearly identified in the cavity or at the cavity wall. It is important to emphasize that the evaluation of cavity-particle association in 2D only assesses a single plane. For cavities which do not show a clear association with a second phase particle it cannot be ascertained whether a particle existed above the cavity (and was removed by polishing) or a particle exists below the cavity (and is impossible to evaluate).

Damage in the fusion line was concentrated within a single zone identified as the UMZ and possessing ferritic microstructure with no substructure. The UMZ, about 5 μm in width, contained damage throughout the zone and did not exhibit a marked tendency to the development of damage at ‘Type I carbides’ or other features adjacent to the

zone. It was postulated the evolution of the UMZ may be a result of local carbon diffusion during the creep test.

The assessment of damage is a 3D-problem; ideally a statistically relevant set of 3D-observations can provide confidence in a 2D-assessment. However, the process for performing 3D assessment is still not well-developed for the scale of the features present within the microstructure. It should be noted that although many examples of cavity-inclusion association are provided in the prior slides the clear majority of cavities were empty. Thus, the next series of experiments will attempt to perform a series of optimized investigations using focused ion beam (FIB) milling to expose subsurface cavities unaffected by the polishing process and for an interrupted sample. This will be complemented by fractography and EDS to confirm whether there are nucleation sources inside the cavity.

9 Micro- and Nano-characterization of Damage using Advanced Microscopy Techniques for an Interrupted Cross-weld Creep Test

9.1 Introduction

As previously pointed out the creep deformation and fracture behavior of Grade 91 steels varies with composition and heat treatment. The traditional view of “classic” long term creep fracture behavior of engineering steels is that ductility tends to be generally the inverse of strength, i.e. as the strength of the steel increases the deformation to fracture decreases. However, it has been established in Grade 91 steel that these general trends do not apply. Thus, the factors which control deformation are different to the factors which control creep cavitation. In the HAZ of multipass welds the thermal cycles introduced will significantly modify the microstructure. Detailed characterization has shown that these thermal cycles invariably result in a partially transformed zone (PTZ) of low strength. If this is universally true, then it can be proposed that the factor of ten variation in creep performance of cross weld tests is a consequence of differences in fracture behavior.

The current research examines this hypothesis by undertaking detailed examination of weldment creep behavior for a steel which exhibits relatively poor ductility in both base metal and cross weld testing. Indeed, experience has shown that there is a category of steels which have exhibited early-in-service failures (Brett et al. 1999, EPRI 2009, Parker and Brett 2013, EPRI 2015e, Nitsche et al. 2015). There are several factors which make this investigation unique:

1. Tests were performed on feature cross-weld test samples (specific test identification for the characterization described is AR-B2-5);
2. Weld procedures were carefully designed and monitored so that so far as practicable the microstructures were uniform across the section (and there was no general scatter from sample to sample);
3. The creep tests were performed under conditions which produced low ductility creep fractures consistent with features expected in long term service, and;

4. The AR-B2-5 cross-weld creep test was terminated at a known life fraction to permit detailed examination and characterization of the size, distribution and features of creep cavities present.

The benefits in undertaking an interrupted test link directly to information detailed in Chapter 8. Consideration of fractured specimens showed that details of early stage cavitation could not be identified because there was extensive cracking in the failed HAZ. The damage in the failed test samples (e.g. ≥95% life fraction) is already well-evolved in comparison to the features in the microstructure which might be responsible for the nucleation of creep cavities. There exists an overlap in the relative grain size in the HAZ, which is of the order of 2 to 20 µm, and the cavity diameter (~1 to 5 µm). This makes it highly probable that voids resulting from a creep process nucleate on grain boundaries. Similarly, the distribution of second phase precipitates like $M_{23}C_6$ or Laves phase are found in the 100,000s or 1,000,000s in number (Table 4-5). Again, this makes it likely that a creep cavity is associated with such a phase or precipitate. It is thus the case that more clarity needs to be obtained through not only optimized microscopy procedures but also for the examination of interrupted samples which should contain a less-evolved distribution of damage.

9.2 Selection of Test Sample AR-B2-5 and Relevant Background

The selected sample AR-B2-5 was interrupted after 1,006 hours test duration at 625°C and 60 MPa. The assessment of the strain versus time data in Figure 4-22 suggests that this test was terminated at a strain fraction of 72% and the time fraction basis is 61%. A macro-image of the cross-section from the center plane of the specimen in the post-test and etched condition is provided in Figure 9-1. It is clear from this image that there is no presence of a macro-crack or otherwise noted distress. Images of the local damage in the HAZ were previously detailed in Figure 4-26 to Figure 4-29.

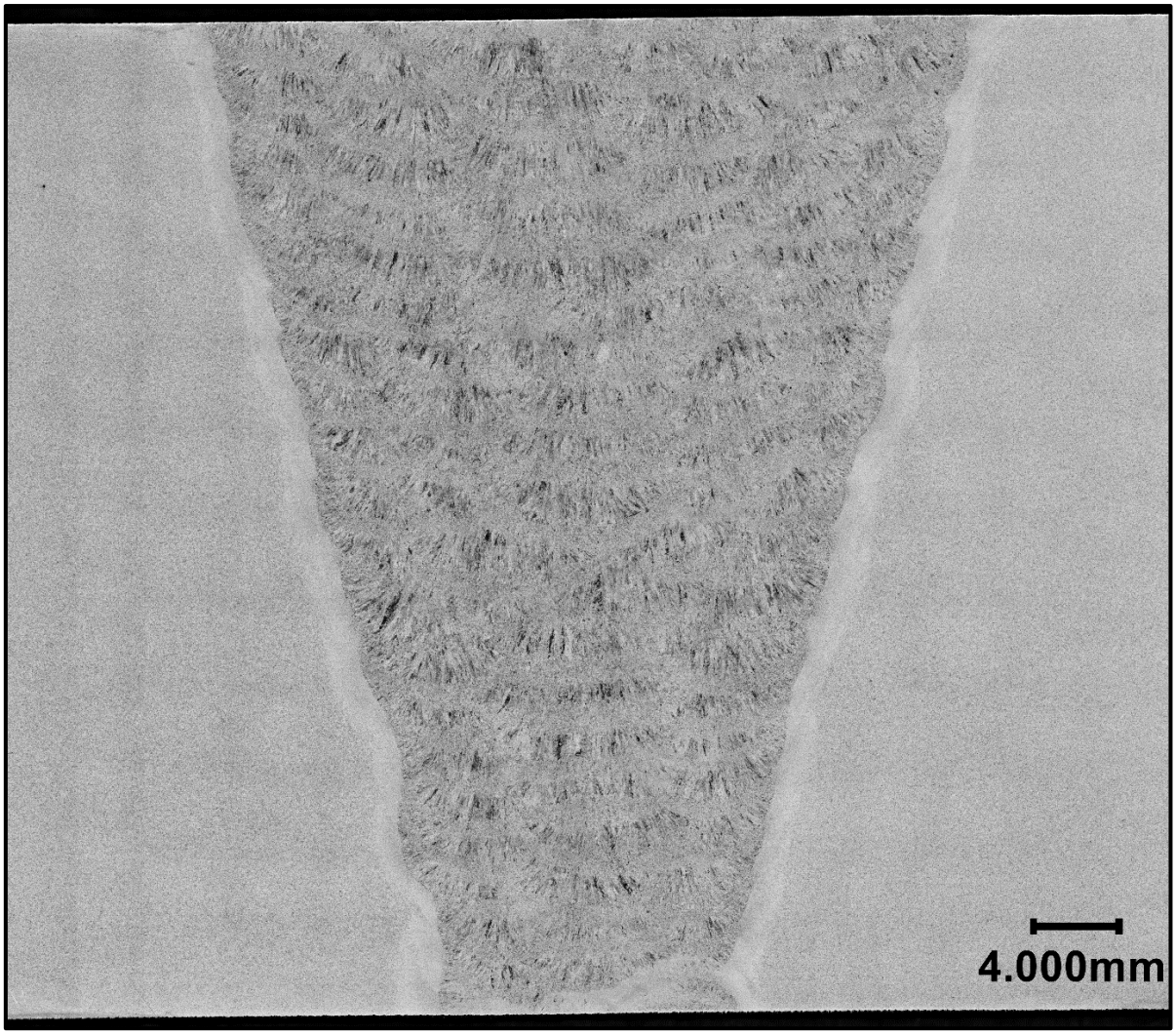

Figure 9-1. Macro image of sample AR-B2-5 (625°C, 60 MPa, 1,006 hours) interrupted at 61% time fraction and 72% strain fraction. There is no obvious sign of micro- or macro-damage.

9.3 Scanning Electron Microscope (SEM) Imaging of Damage

An extensive amount of damage was identified in the HAZ using scanning electron microscopy. Example micrographs are shown in Figure 4-30C and Figure 9-2. A progressively-increasing field of damage was observed traversing the HAZ, i.e. moving from the parent metal starting on the left-side of Figure 9-2, through the PTZ where a high density of cavities was observed in a field ~440 µm wide, and through the remaining HAZ until the weld metal was reached.

Representative fields of damage in the HAZ for sample AR-B2-5 are provided in Figure 9-3 to Figure 9-5. The macro-appearance of cavitation in Figure 9-3 and Figure 9-4 and is shown on a more local scale in Figure 9-5. For the field of damage present in

Figure 9-3 the calculated cavity density at this magnification (500X) is 6,400 cavities/mm^2.

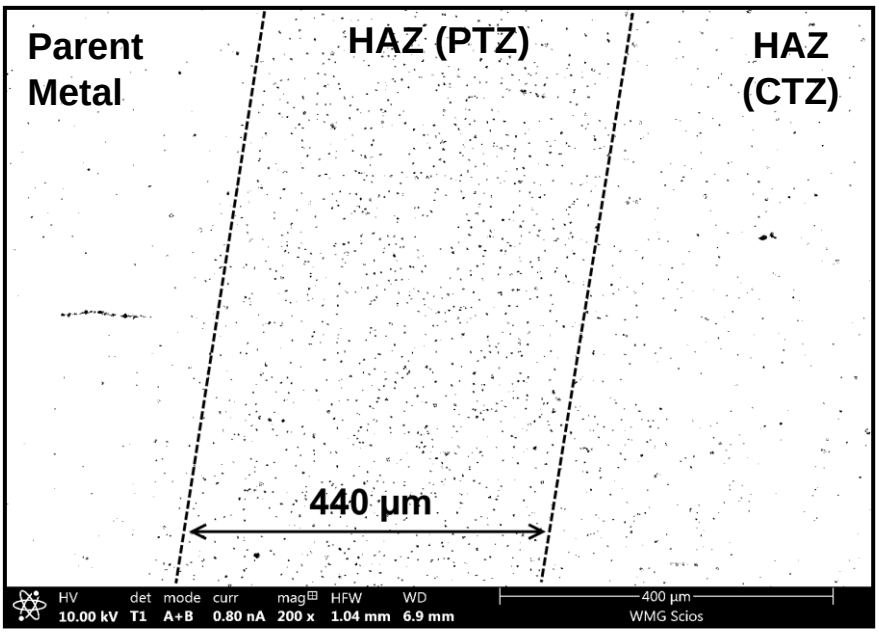

Figure 9-2. Macro-characterization of damage in the heat affected zone for sample AR-B2-5 (625°C, 60 MPa, 1,006 hours), 200X.

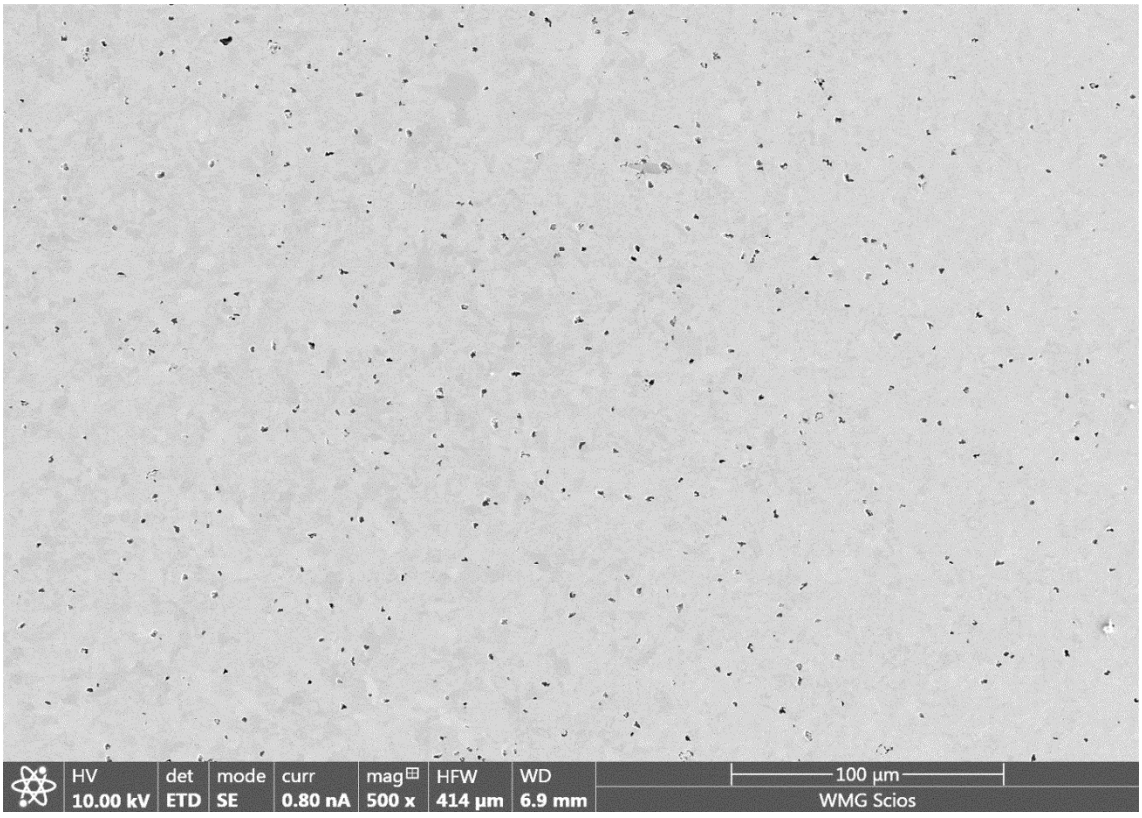

Figure 9-3. Representative field of damage in the heat affected zone for sample AR-B2-5 (625°C, 60 MPa, 1,006 hours), 500X.

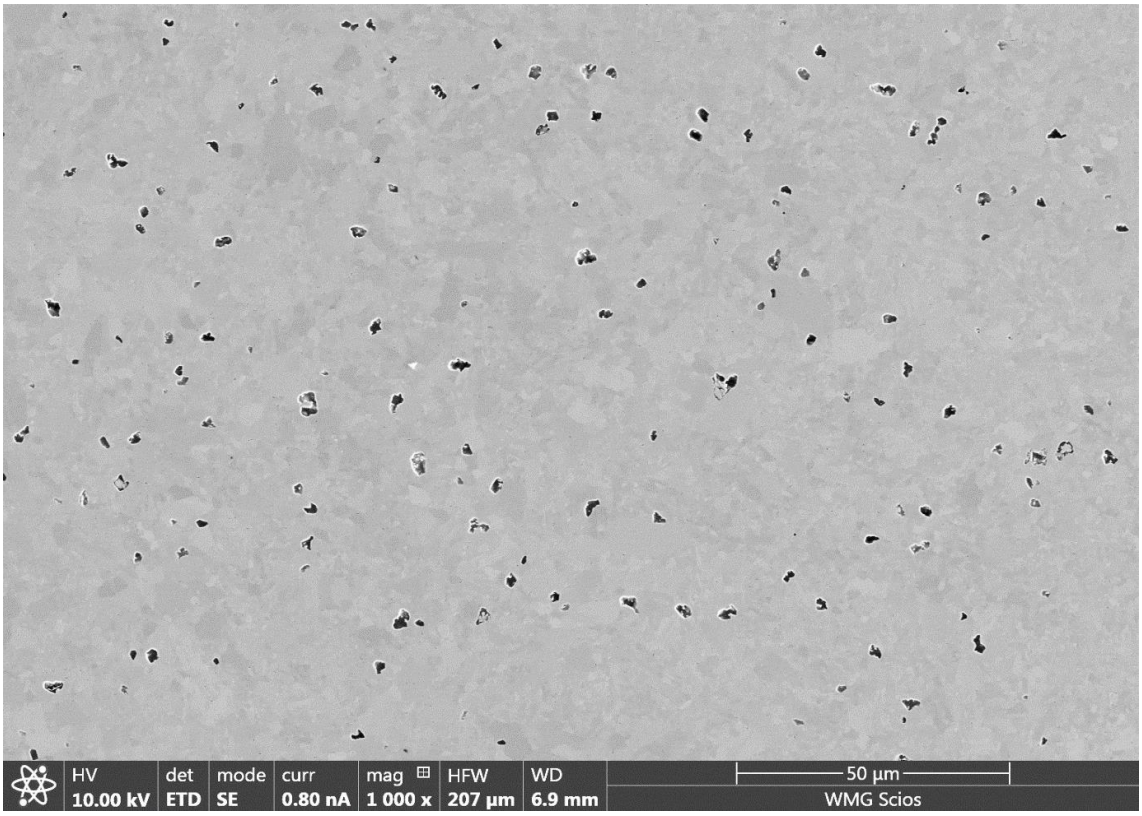

Figure 9-4. Representative field of damage in the heat affected zone for sample AR-B2-5 (625°C, 60 MPa, 1,006 hours), 1,000X.

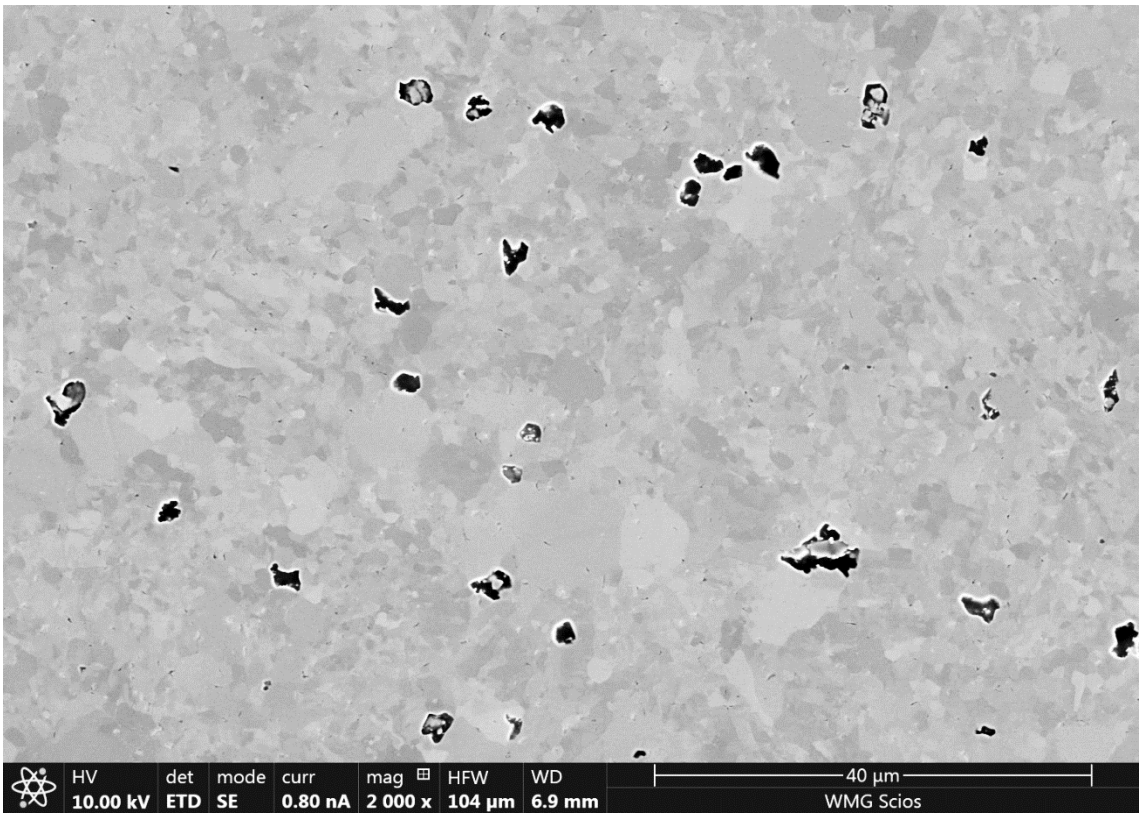

Figure 9-5. Representative field of damage in the heat affected zone for sample AR-B2-5 (625°C, 60 MPa, 1,006 hours), 2,000X.

The size distribution of creep cavities in Figure 9-6 are provided for ~80 individual cavities measured in ten unique fields of view. Examples of the images utilized to evaluate the cavity size are provided in Figure 9-7. The data suggest that the mean or median value is about 2 μm.

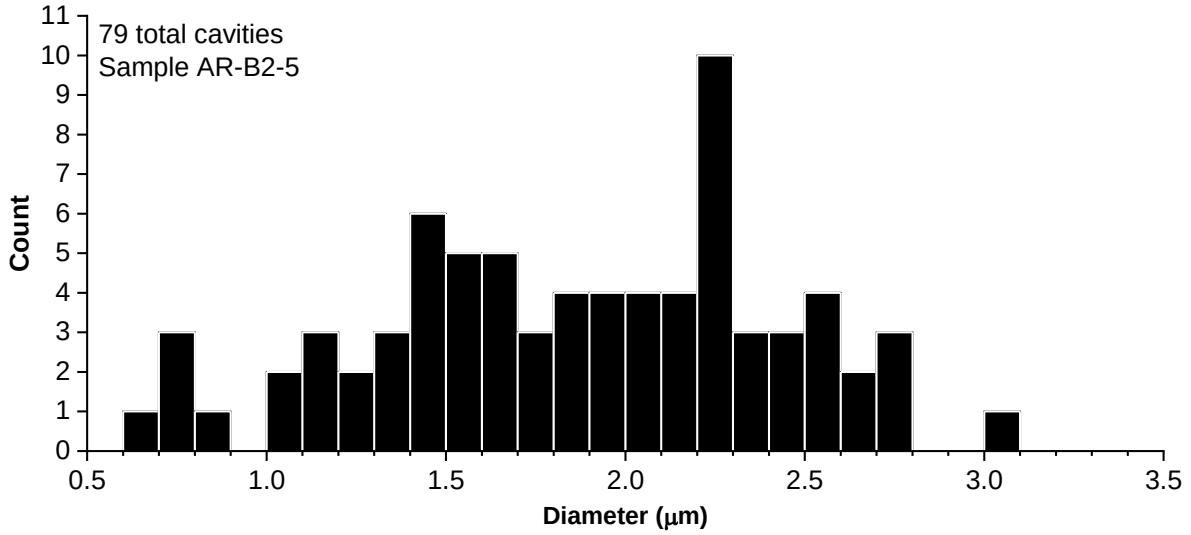

Figure 9-6. Results for the assessment of cavity diameter for ten images taken at 5,000X in the heat affected zone; four representative fields give in Figure 9-8

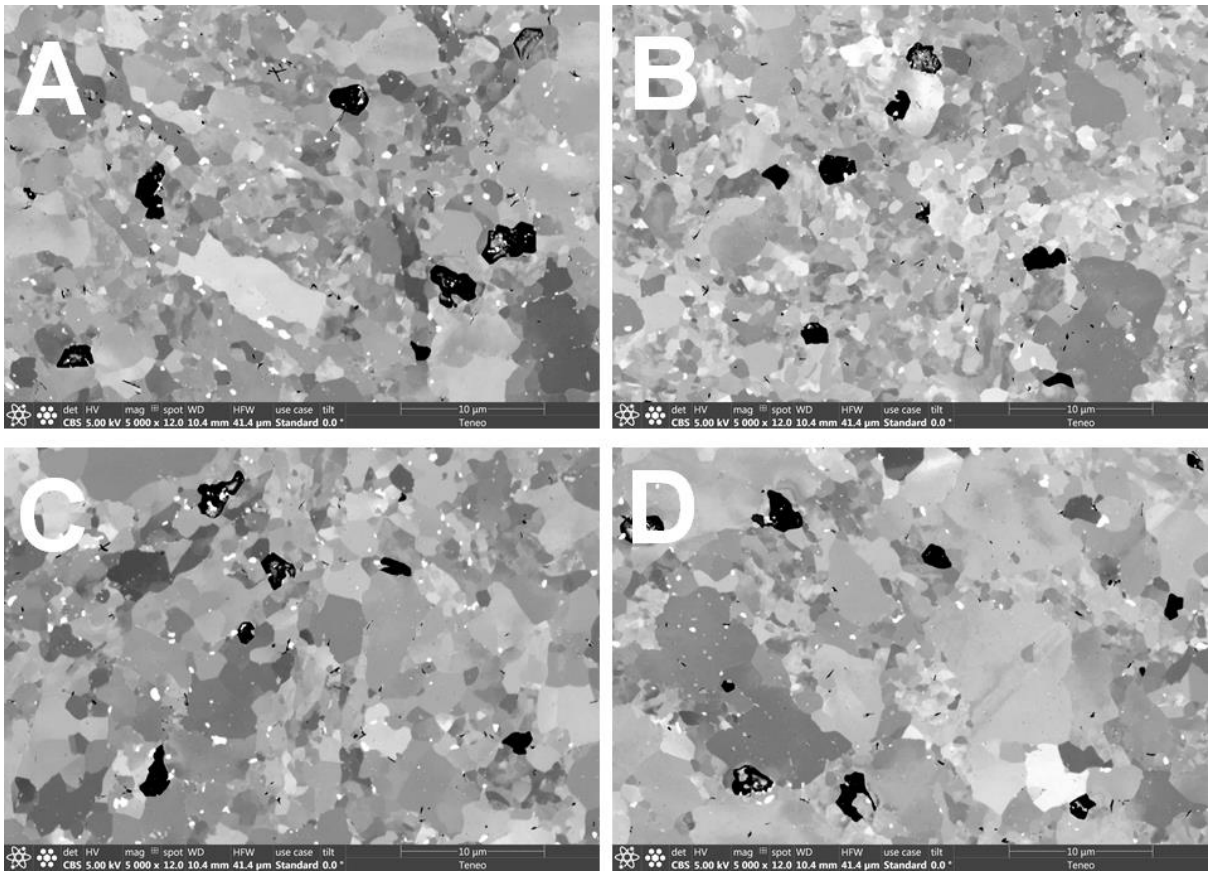

Figure 9-7. Representative cavities in the heat affected zone for sample AR-B2-5 (625°C, 60 MPa, 1,006 hours), 5,000X.

Assessment of representative cavities in the HAZ that were not clearly associated with second phase particles and examples associated with inclusions are provided in Figure 9-8 and Figure 9-9, respectively. As previously noted, there are several consistent observations summarized below:

- Most cavities appear to have a faceted morphology (see Figure 9-8D, Figure 9-8E, Figure 9-8K, Figure 9-8L, Figure 9-9A, Figure 9-9I, Figure 9-9K);
- For cavities which are associated with inclusions there is sometimes a co-contaminant effect where multiple inclusions exist in the same cluster (Figure 9-9A, Figure 9-9C, Figure 9-9D, Figure 9-9E, Figure 9-9L);
- There is extensive AlN that does not appear to have nucleated damage (Figure 9-7, Figure 9-8, and Figure 9-9);
- Local cavity evolution appears to be assisted by strain concentration. This is noted by the deformation present within or adjacent to the observed voids.

These features and observations will be explored in more detail in the following sections utilizing a variety of SEM-based qualitative and quantitative techniques.

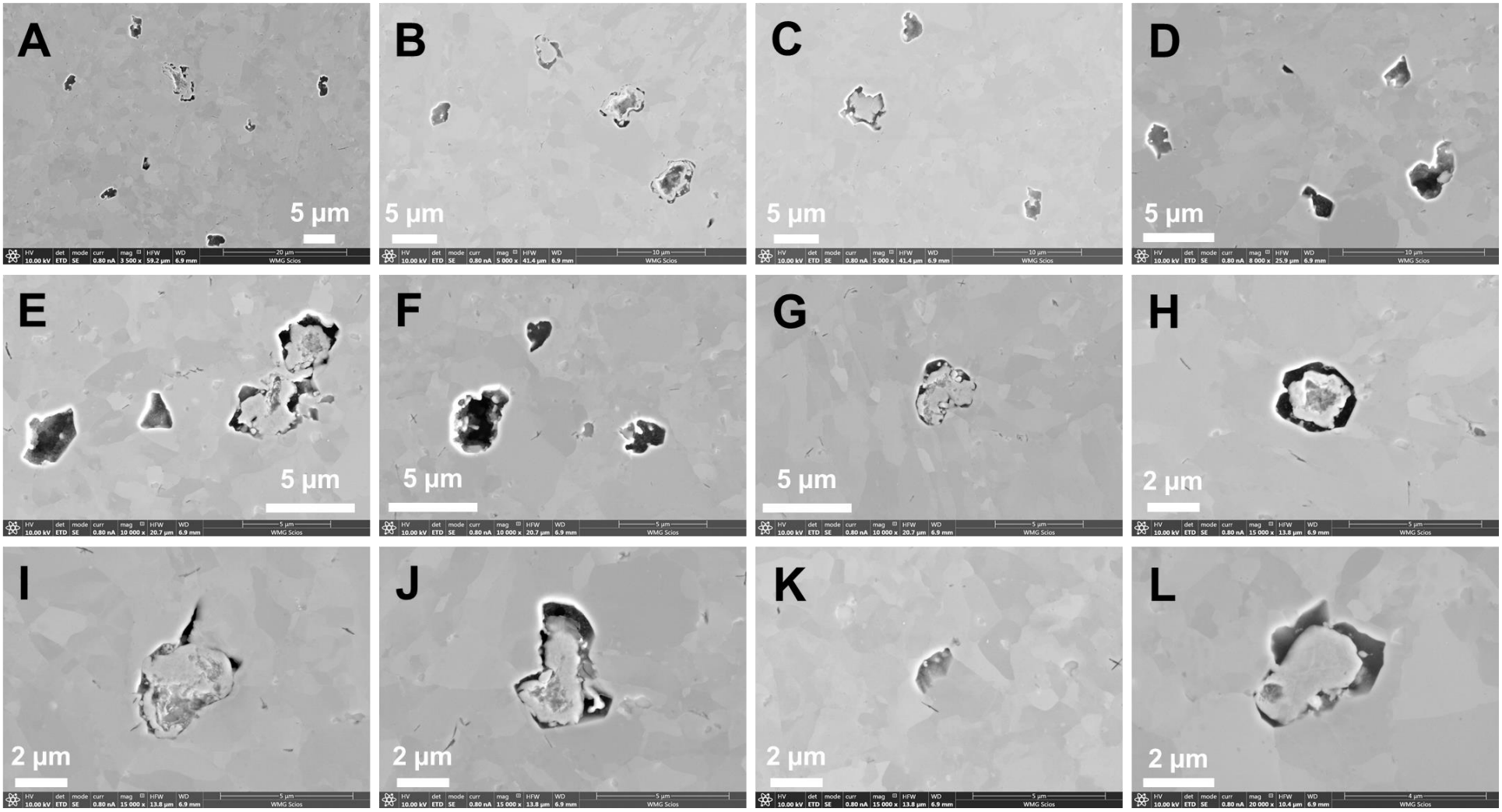

Figure 9-8. Examples of cavities in the heat affected zone for sample AR-B2-5 (625°C, 60 MPa, 1,006 hours) not associated with inclusions, 3,500X (A), 5,000X (B, C), 8,000X (D), 10,000X (E, F, G, H), 15,000X (I, J, K) and 20,000X (L)

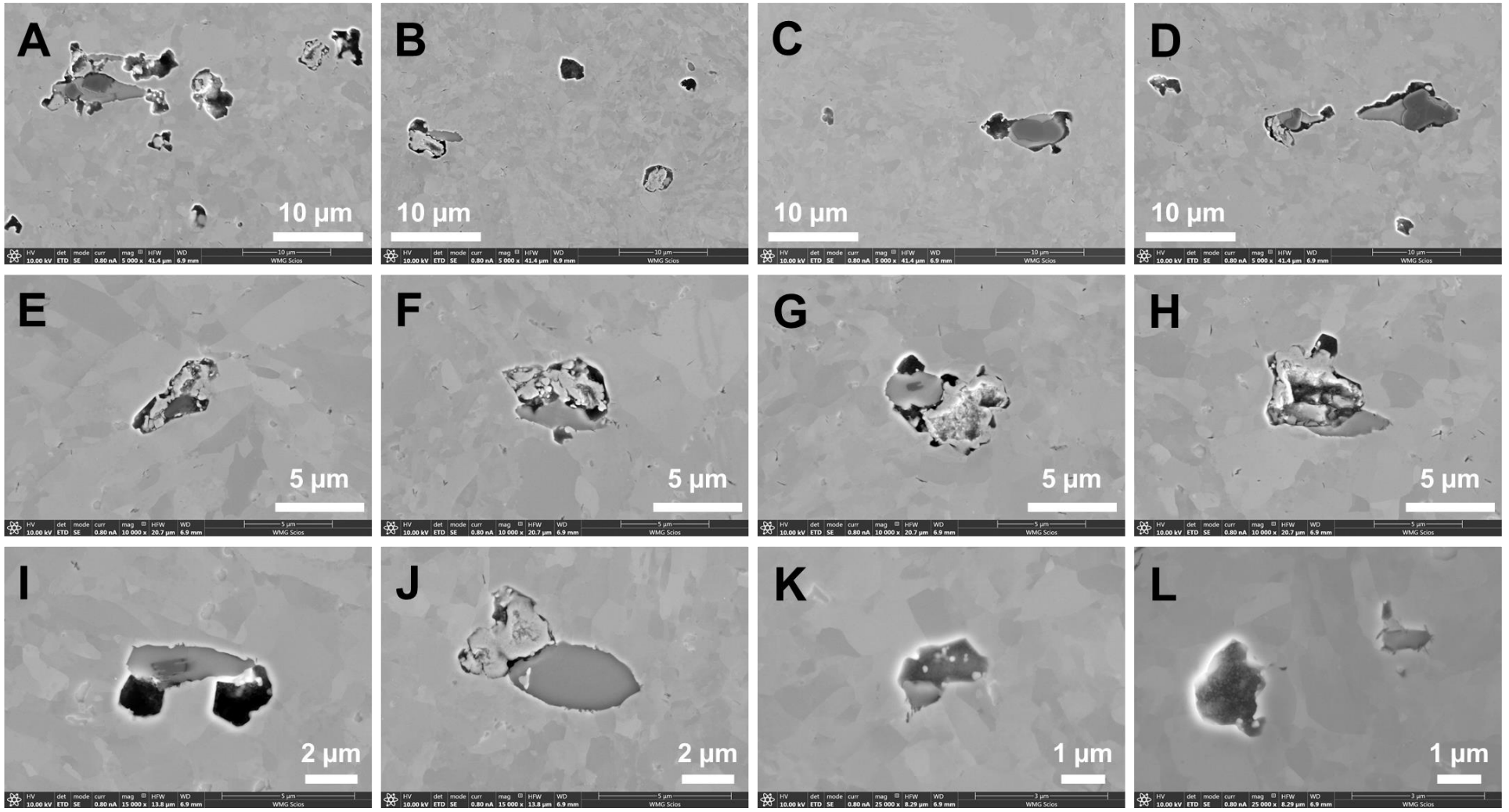

Figure 9-9. Examples of cavities in the heat affected zone for sample AR-B2-5 (625°C, 60 MPa, 1,006 hours) associated with inclusions, 5,000X (A, B, C, D), 10,000X (E, F, G, H), 15,000X (I, J) and 25,000X (K, L)

9.4 Energy Dispersive X-ray Spectroscopy (SEM-EDS)

Analysis of local cavities using SEM-EDS is provided in Figure 9-10 and Figure 9-11. These areas of local damage were previously reported in Figure 9-9G and Figure 9-9D, respectively. The EDS map provided in Figure 9-10 shows the formation of a complex inclusion cluster where a MnS particle has nucleated from the Al_2O_3. With respect to the steel making process, the stability of Al_2O_3 is much higher than for MnS, resulting in the formation of Al_2O_3 earlier in the process (at a higher temperature). This can account for the observed MnS formation from existing Al_2O_3 particles. An additional ring of Al is present around the MnS particle, likely present as AlN.

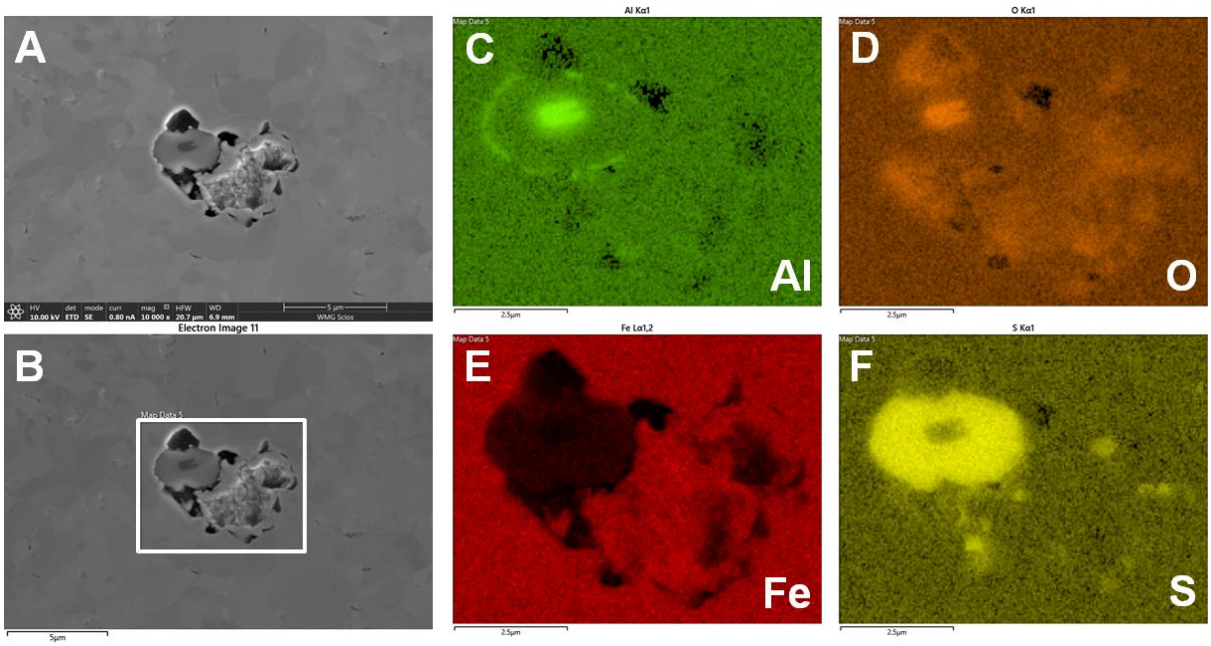

Figure 9-10. SEM-EDS map for a location of damage (A, B) and for aluminum (C), oxygen (D), iron (E), and sulfur (F). Sample AR-B2-5 (625°C, 60 MPa, 1,006 hours).

The EDS map presented in Figure 9-11 shows an inclusion cluster of Al_2O_3, and MnS. There appears to be some association of Mg with the particles highlighting the compositional complexity that can exist in these clusters. The identification of the predominately Al_2O_3 and MnS particles in the matrix using SEM-EDS and linking this to the primary imaging mode (secondary electron or 'ETD') provides for the possibility to interpret additional sites without the need for repeated EDS measurements. This approach is demonstrated in Figure 9-12 to Figure 9-15. In these figures several examples of damage around second phase particles (predominately inclusions) are shown and identified.

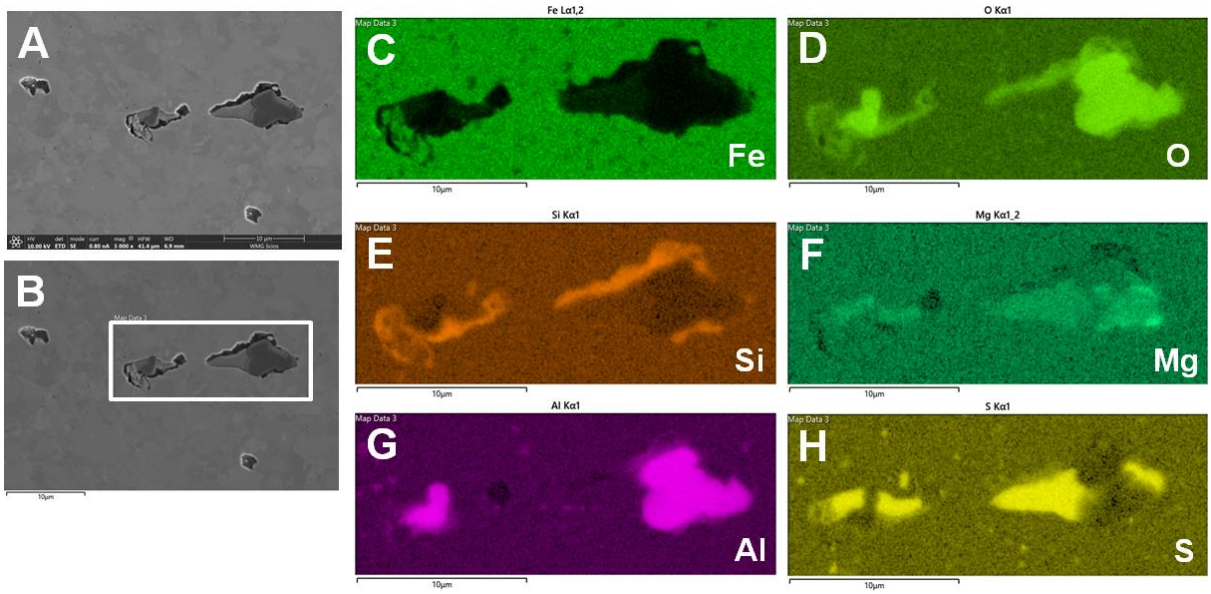

Figure 9-11. SEM-EDS map for a location of damage (A, B) and for iron (C), oxygen (D), silicon (E), magnesium (F), aluminum (g), and sulfur (h). Sample AR-B2-5 (625°C, 60 MPa, 1,006 hours).

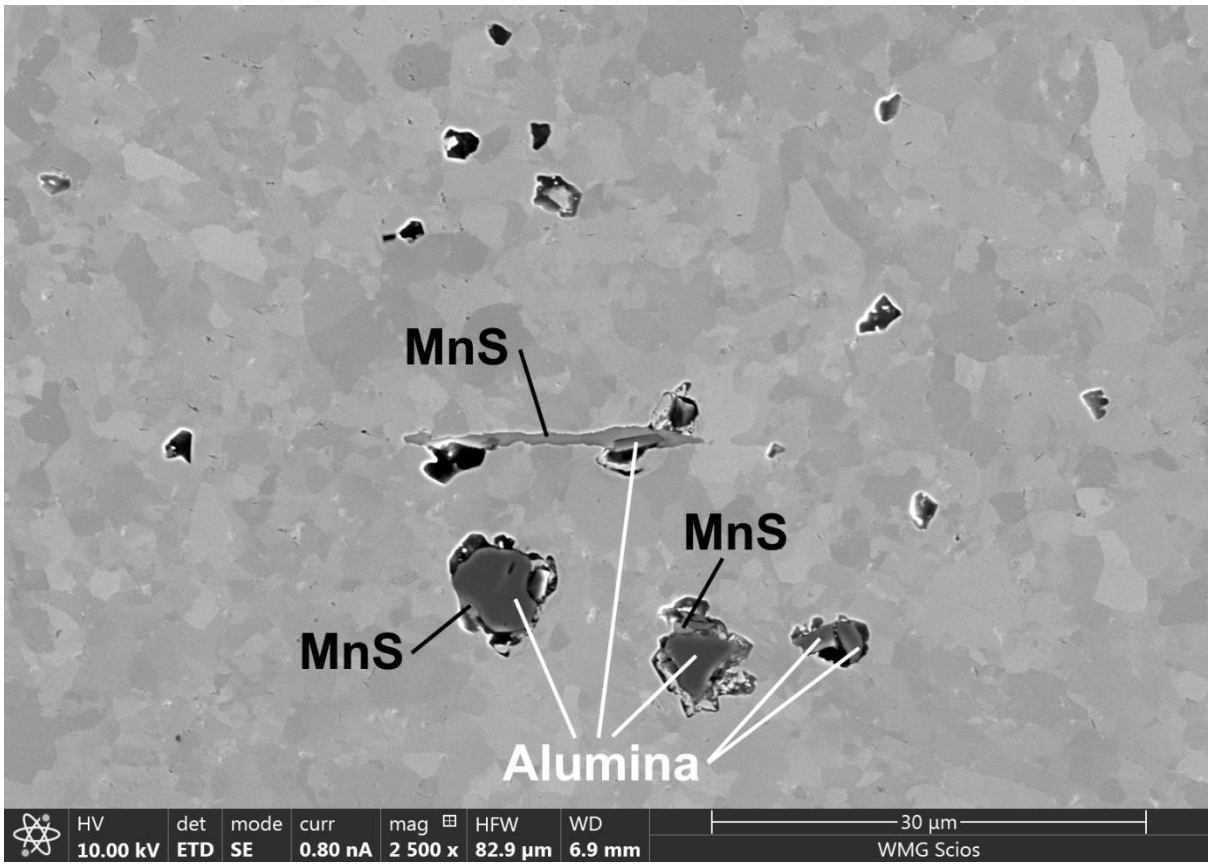

Figure 9-12. Association of damage with inclusion clusters (MnS and Al_2O_3) in sample AR-B2-5 (625°C, 60 MPa, 1,006 hours)

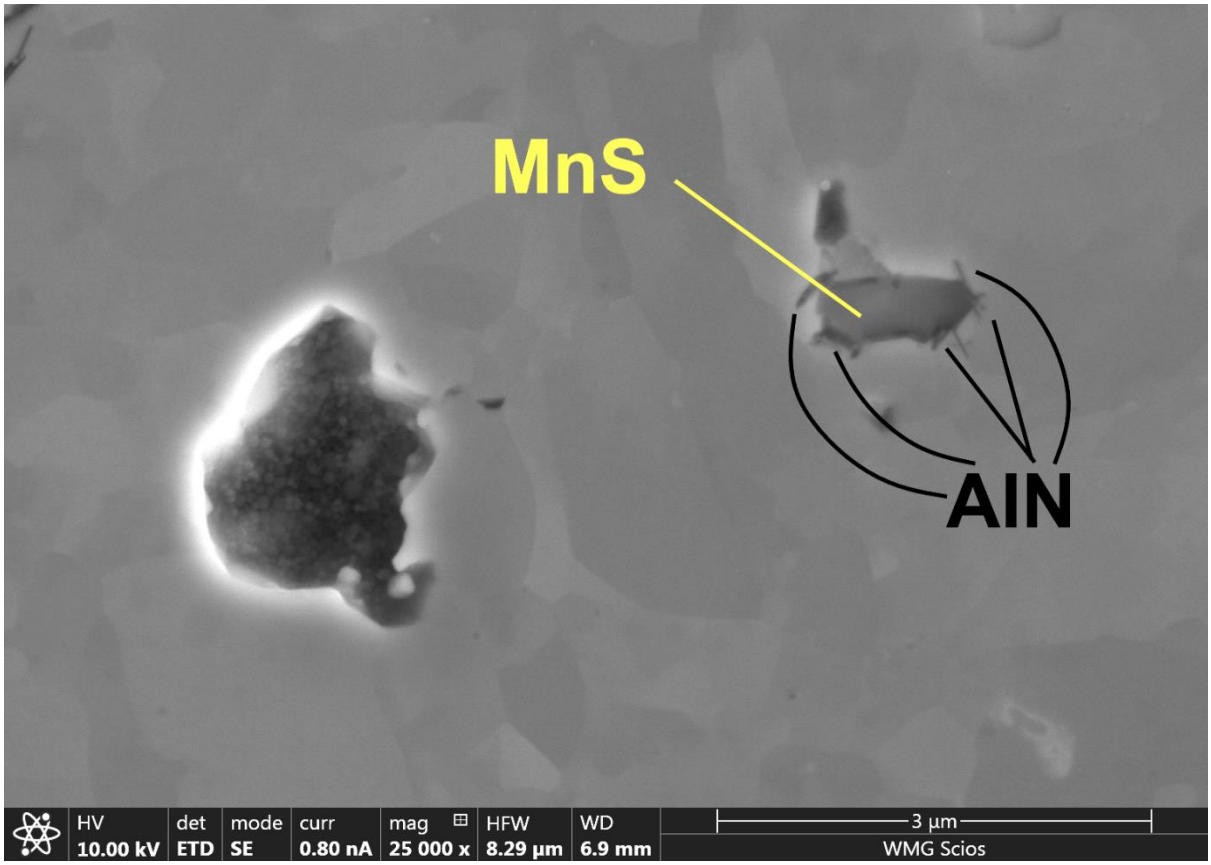

Figure 9-13. Association of damage with an inclusion cluster (MnS and AlN) in sample AR-B2-5 (625°C, 60 MPa, 1,006 hours)

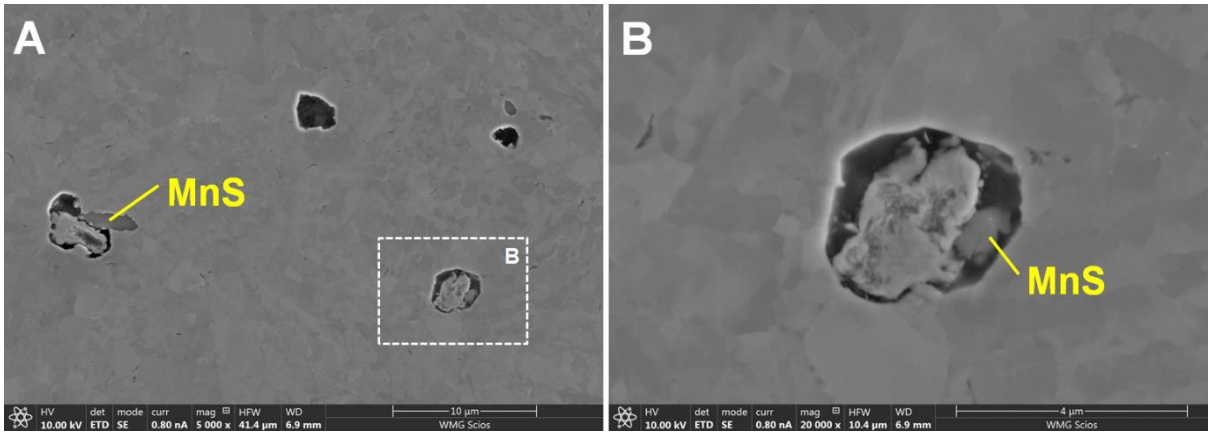

Figure 9-14. Examples of cavities in the heat affected zone for sample AR-B2-5 (625°C, 60 MPa, 1,006 hours) associated with inclusions, 5,000X (A) and 20,000X (B)

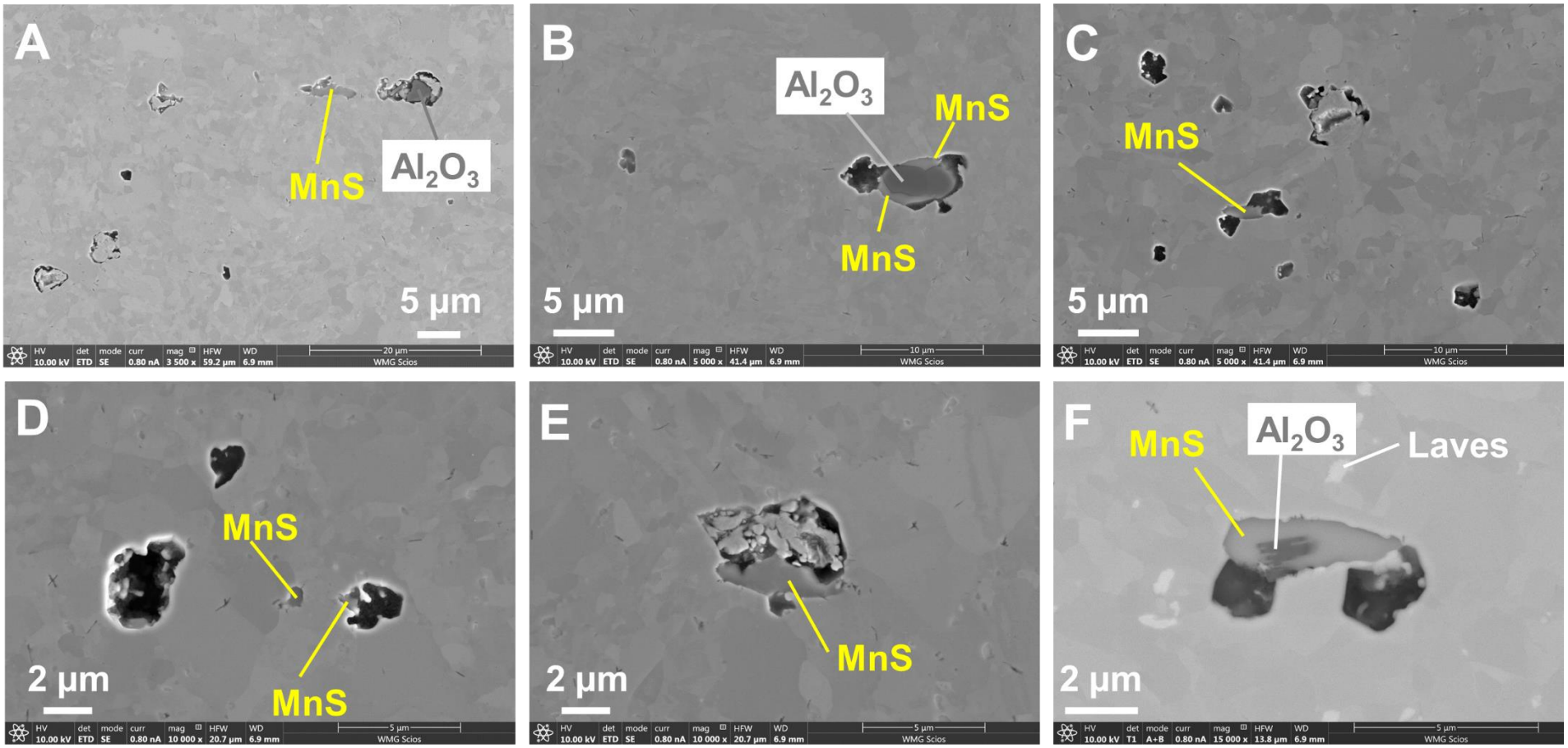

Figure 9-15. Identification of nucleation source for cavities in the heat affected zone for sample AR-B2-5 (625°C, 60 MPa, 1,006 hours); 3,500X (A), 5,000X (B, C), 10,000X (D, E) and 15,000X (F)

9.5 Electron Backscatter Diffraction (EBSD)

Figure 9-16 provides a representative field of damage in the HAZ. Figure 9-16A shows the general, large variability of grain size in the HAZ where damage is present. In this location it is apparent that the mean grain diameter ranges from ~1 to 20 µm. Local assessment of cavities, such as those highlighted in Figure 9-16B and Figure 9-16C using backscatter imaging, clearly highlight the observed deformation linked to the formation of voids. The observation in Figure 9-16C is reinforced by the fact that the entirety of the deformed region is still connected to the matrix; e.g. it is impossible for this material to have been deposited as deformed or foreign material introduced by the preparation procedure.

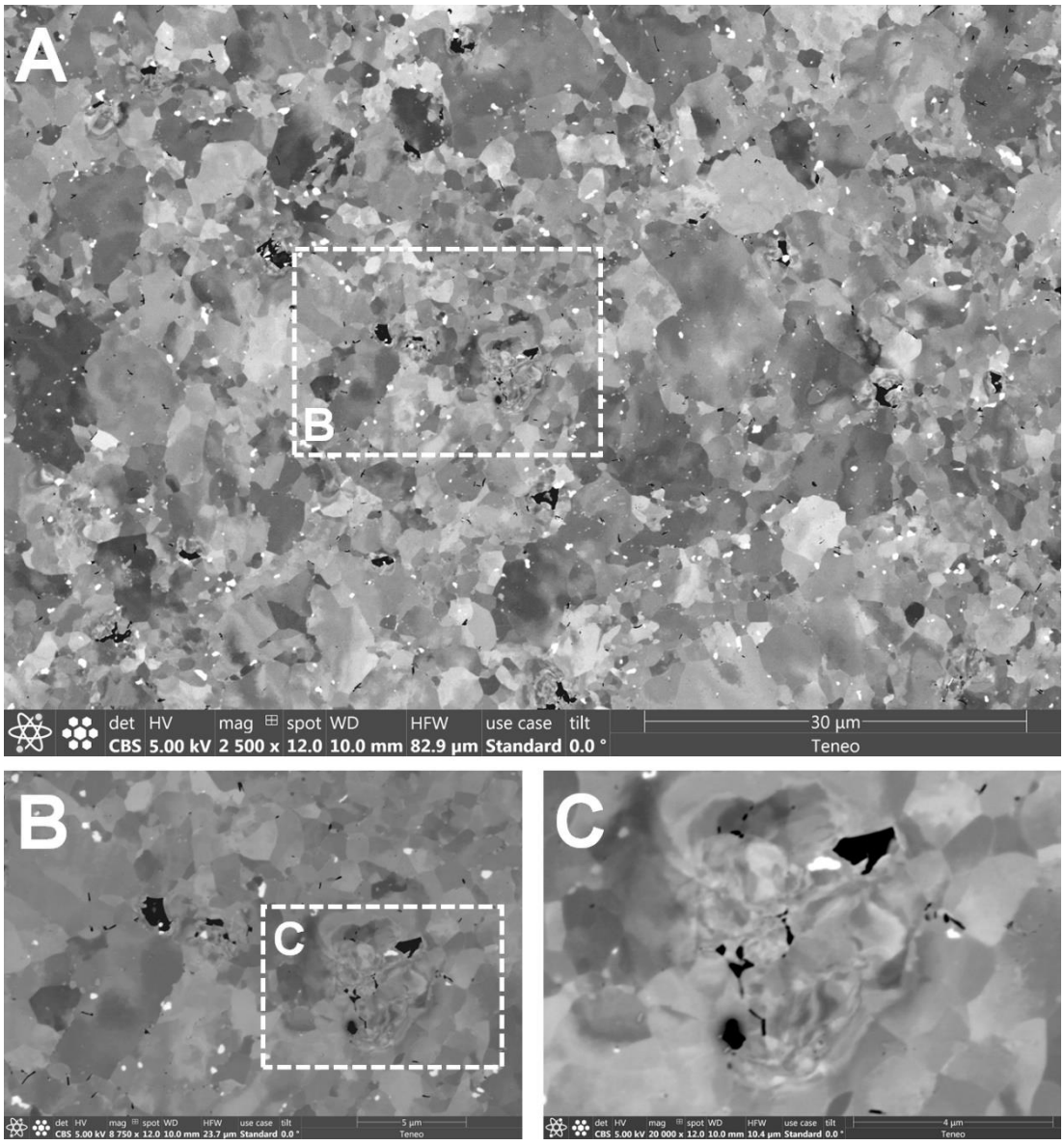

Figure 9-16. Representative location in sample AR-B2-5 heat affected zone (A) highlighting the apparent grain recrystallization at cavity sites in the microstructure (B, C)

Figure 9-16 shows that many of the large, ferrite grains contain a notable variation in grain contrast without a clear presence of a subgrain boundary. This suggests that the location where this is observed has not yet fully developed to the point of local grain recrystallization. High densities of very fine grains are also observed. This is further support for the notion that these regions are associated with concentrated, local deformation. Lastly, there exist fine grains away from damage in locations where grains may have been recrystallized but without the formation of voids.

9.5.1 Macro-scale analysis for a representative field of damage

Assessment of damage in the HAZ for sample AR-B2-5 is provided in Figure 9-17 to Figure 9-19. In total, about 50 cavities are present in this image (141 µm wide X 106 µm tall [0.015 μm^2]). Observations linked to the microstructure and cavitation shown in these images are summarized below:

- There are local regions of recrystallization present by a high density of very fine grains that are ≤1 µm in diameter (Figure 9-18);
- The locations where void development is most pronounced do not always coincide with intersections between large and small grains nor in locations where there exists clear evidence for recrystallization (Figure 9-17 or Figure 9-18).
- The region around cavities is characterized by high densities of low angle grain boundaries (Figure 9-19).

To better elucidate the trends in local strain intensification, individual cavities are analyzed in the following section.

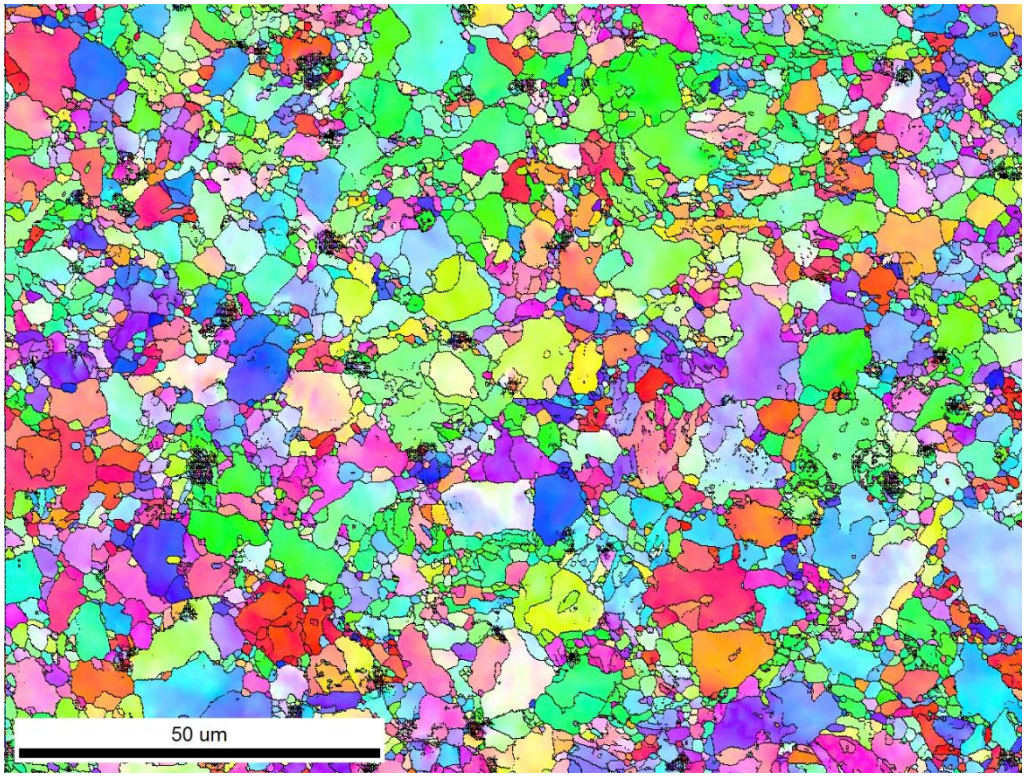

Figure 9-17. Representative, damaged heat affected zone location in sample AR-B2-5 (625°C, 60 MPa, interrupted at 1,006 hours); overlay of inverse pole figure and all grain boundaries with misorientation of 2 to 180°

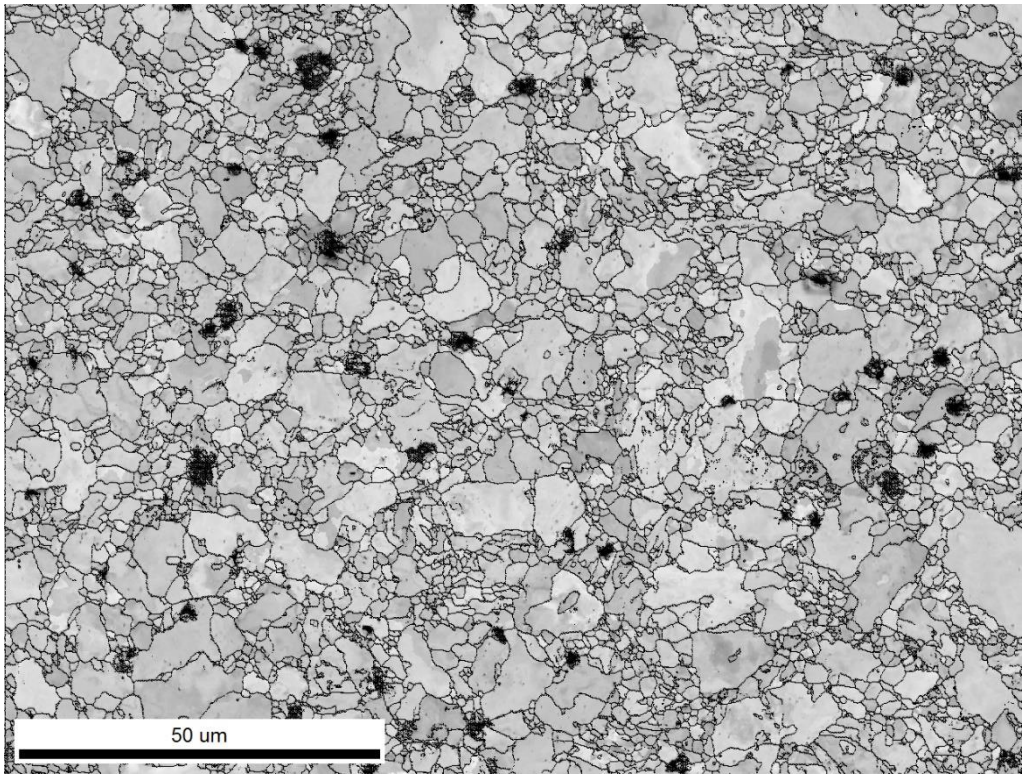

Figure 9-18. Representative, damaged heat affected zone location in sample AR-B2-5 (625°C, 60 MPa, interrupted at 1,006 hours); overlay of image quality map and all grain boundaries with misorientation of 2 to 180°

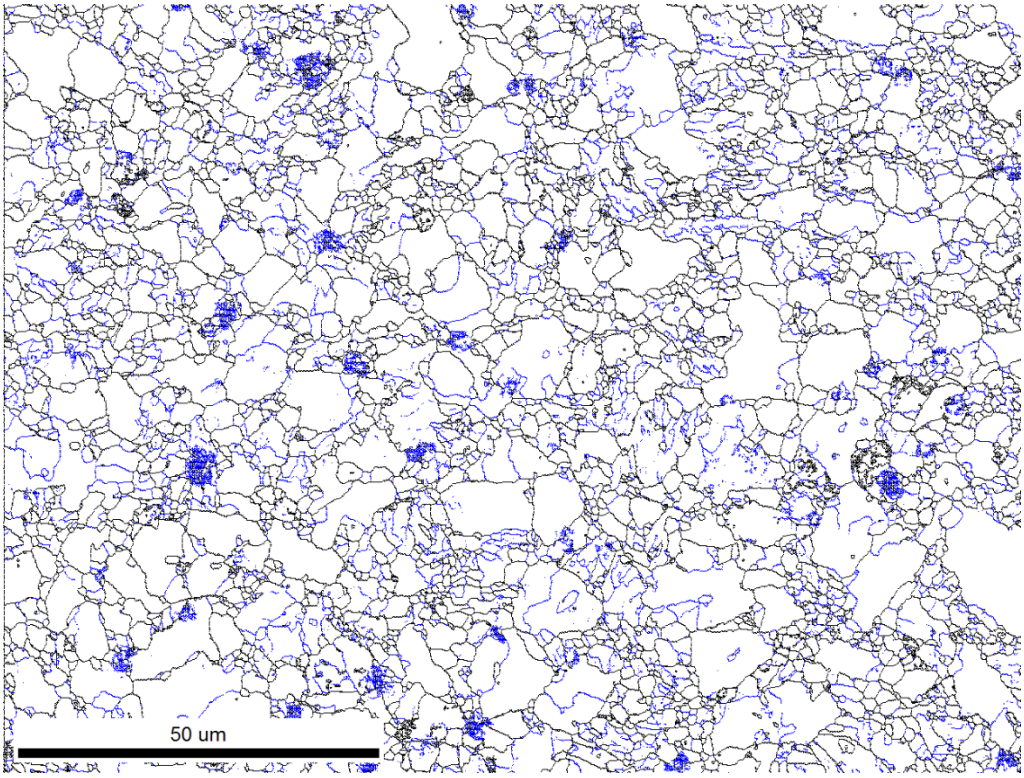

Figure 9-19. Representative, damaged heat affected zone location in sample AR-B2-5 (625°C, 60 MPa, interrupted at 1,006 hours); grain boundary map only with highlighted blue boundary misorientation = 2 to 15° and black boundary misorientation = 15 to 180°

9.5.2 Micro-scale analysis for individual cavities

Assessing the local variation in grain orientation and recrystallization in the present sample is performed using SEM-EBSD and employing a refined procedure detailed in sections 3.6.6 and 3.6.7. The initial attempt to evaluate local grain refinement which were described in Chapter 8 (see Figure 8-24 and Figure 8-25) did not utilize a sufficient step size in the collection of EBSD data (e.g. 0.15 µm versus the 0.03 or 0.05 µm in the refined approach used in the present section). The refined step size used here provided a more complete assessment at the cavity location to qualitatively image subgrains and boundaries at each cavity location.

The results for an optimized EBSD assessment are provided in Figure 9-20, Figure 9-22, and Figure 9-24. In two analyzed cavities, particles were noted inside the cavity and were analyzed using -EDS, in Figure 9-21 and Figure 9-23. The documentation of the local cavity area includes a backscatter image or a secondary electron image, the image quality (IQ) map, the inverse pole figure (IPF) and the kernel average misorientation (KAM) map. Documentation of the KAM has been used in previous

research to provide evidence for the localization of strain at the cavity (Wang and Li 2017).

The results for location 1 provided in Figure 9-20 and Figure 9-21 document a location where two cavities are present and are not linked together in the prepared plane. The presence of a MnS particle in the cavity that is centered in the image is confirmed in Figure 9-22. The documented EDS spectrum contains notable peaks for Mn, Al and S. The deformation observed in the CBS image (Figure 9-20A) is more clearly shown in the IQ map (Figure 9-20C). The IPF image (Figure 9-20D) shows the variation in grain orientation within the grain for grains adjacent to the cavities. Localization of strain is suggested by the KAM map in the adjacent region around the cavities with decreasing intensity moving away from this immediate location. Interesting, for the two AlN particles identified in the right edge of Figure 9-20B there is no suggestion in the KAM map that a localization of strain is present at these particles.

The results for location 2 provided in Figure 9-22 and Figure 9-23 show the evolution of damage at a grain boundary, a Laves phase particle (bright, angular particle in Figure 9-22), and a location of increased Cr at the cavity wall inferring association with a carbide (Figure 9-23). In this example the KAM map shows a strongly oriented zone of misorientation for the grain above the cavity with considerably less concentration in other locations adjacent to the cavity.

Two locations of damage are fully captured in Figure 9-24. In the analyzed plane no particle is identified. Several Laves phase particles are observed in Figure 9-24A. Comparison of this image with either the IQ map (Figure 9-24B) or the KAM map (Figure 9-24D) does not suggest a consistent and clear link between these particles and the localization of strain.

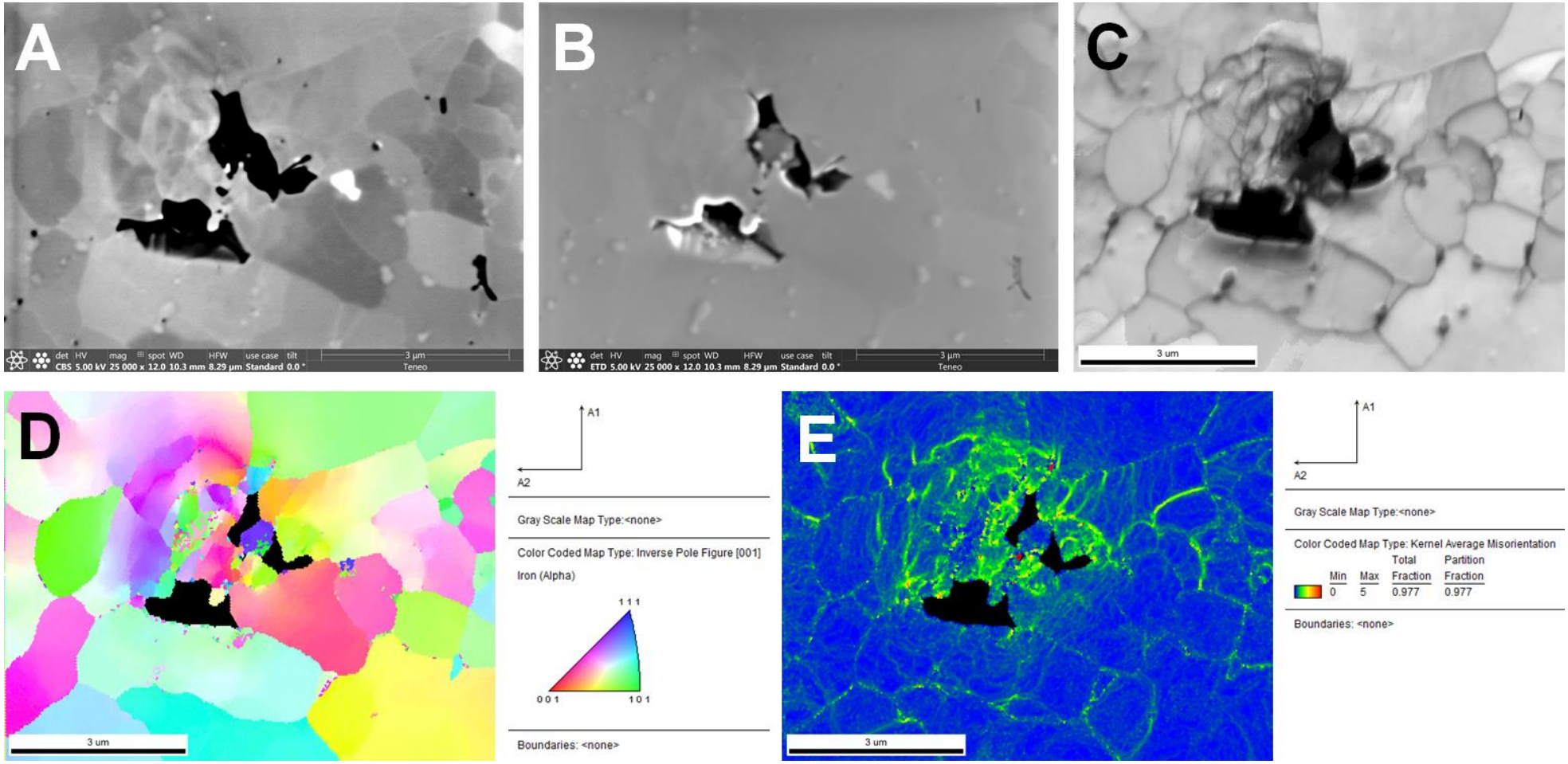

Figure 9-20. Location 1 backscatter image (A), scanning electron image (B), image quality map (C), inverse pole figure image (D) and kernel average misorientation map (E)

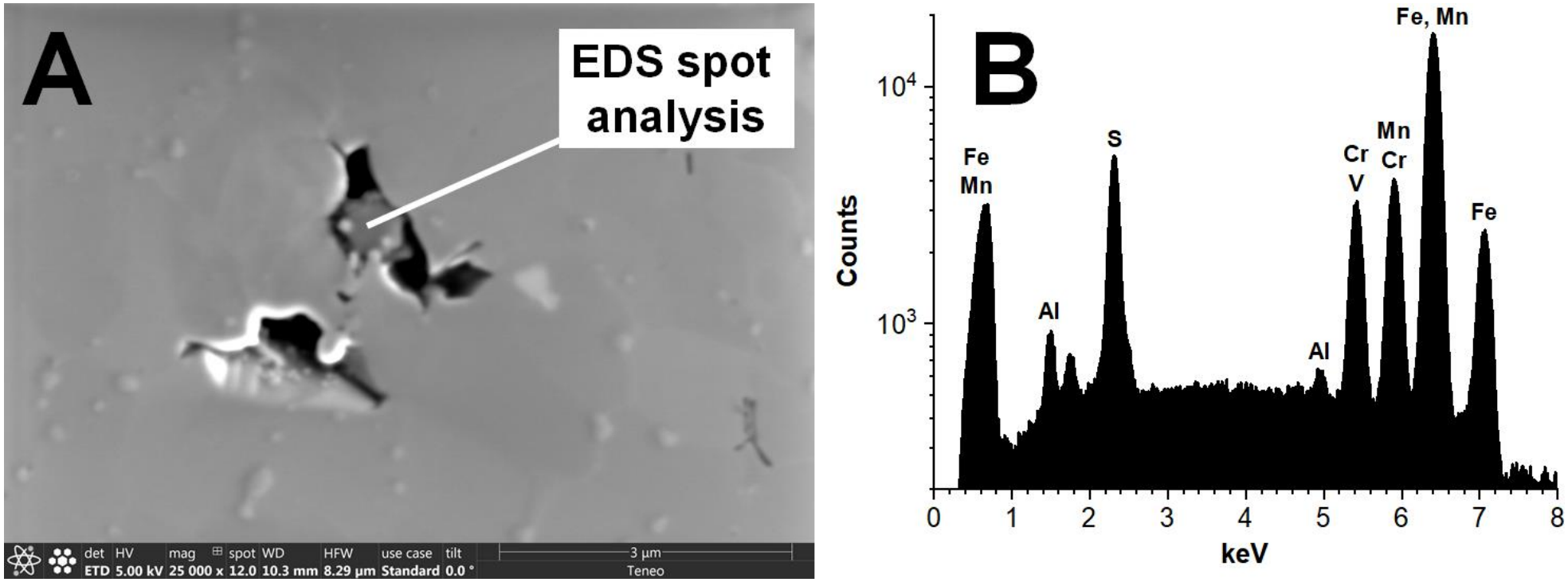

Figure 9-21. Cavity location 1 scanning electron image highlighting the apparent particle in the upper cavity (A) and SEM-EDS spectrum for particle identified in the cavity (B) showing association with MnS

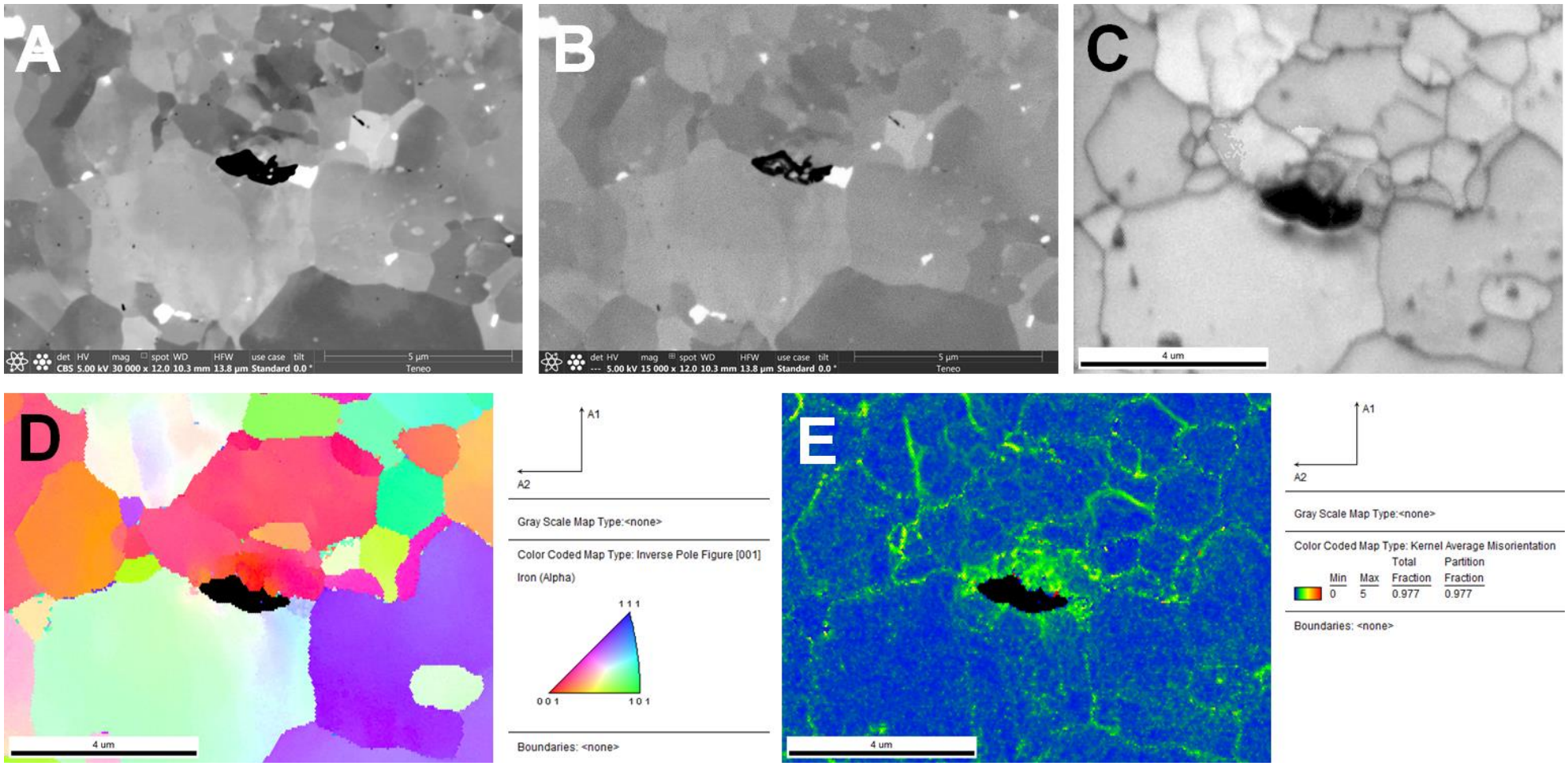

Figure 9-22. Location 2 backscatter image (A), scanning electron image (B), image quality map (C), inverse pole figure image (D) and kernel average misorientation map (E)

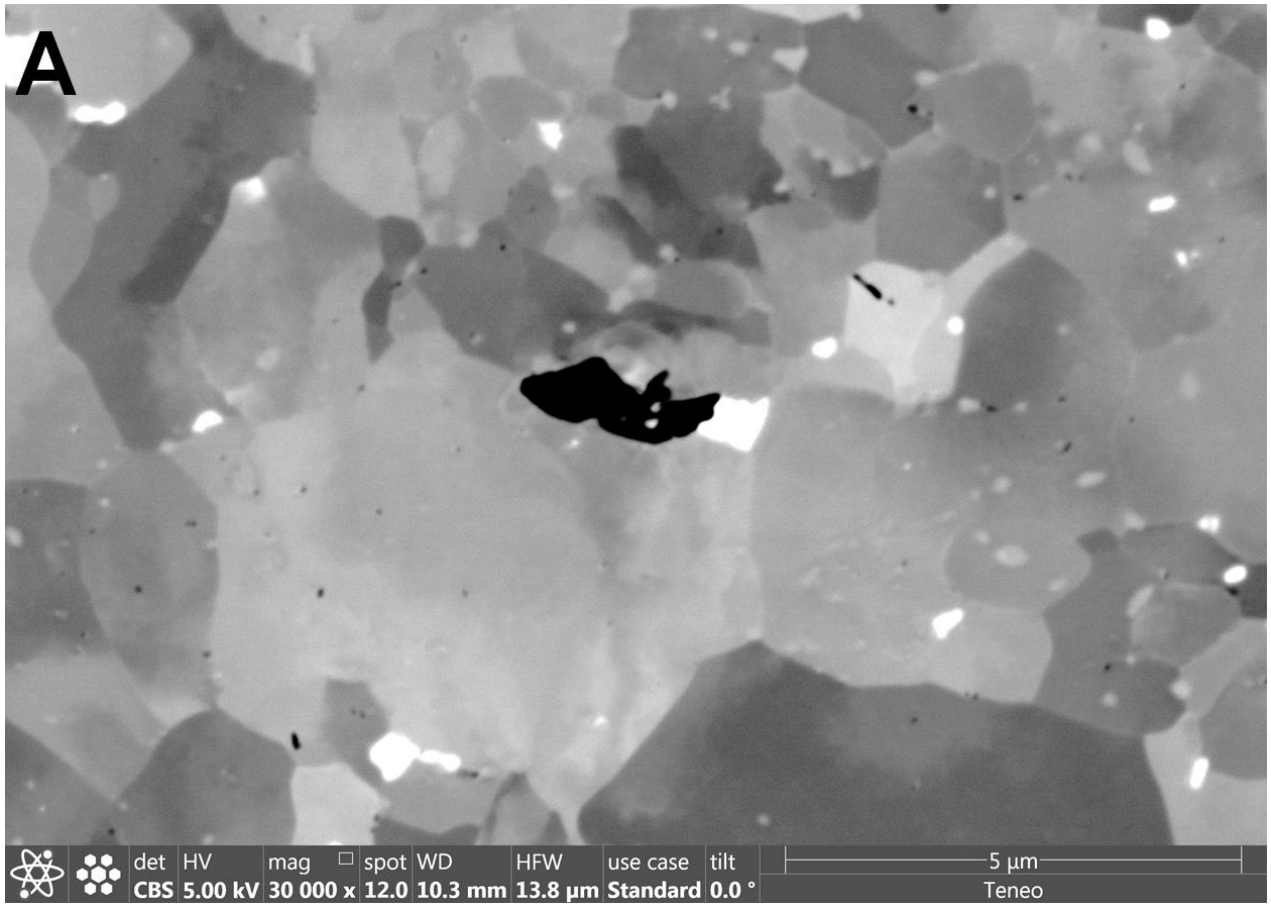

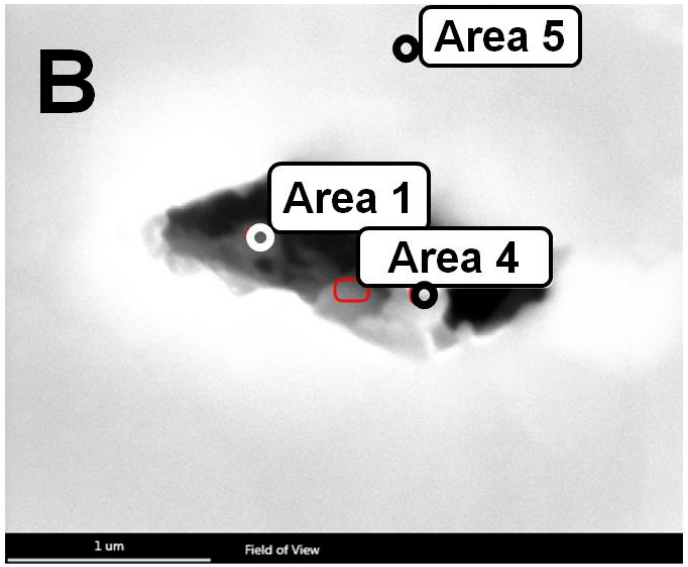

Element	Area 1	Area 4	Area 5
Mo	0.85	2.1	0.54
V	0.38	0.27	0.21
Cr	16.19	21.63	10.61
Mn	0.26	0.48	0.04
Fe	82.31	75.5	88.6

Figure 9-23. Cavity location 2 backscatter image (A) and SEM-EDS results for particles identified in the cavity (B) and table for highlighted areas 1, 4 (Cr-enriched) and 5 (matrix)

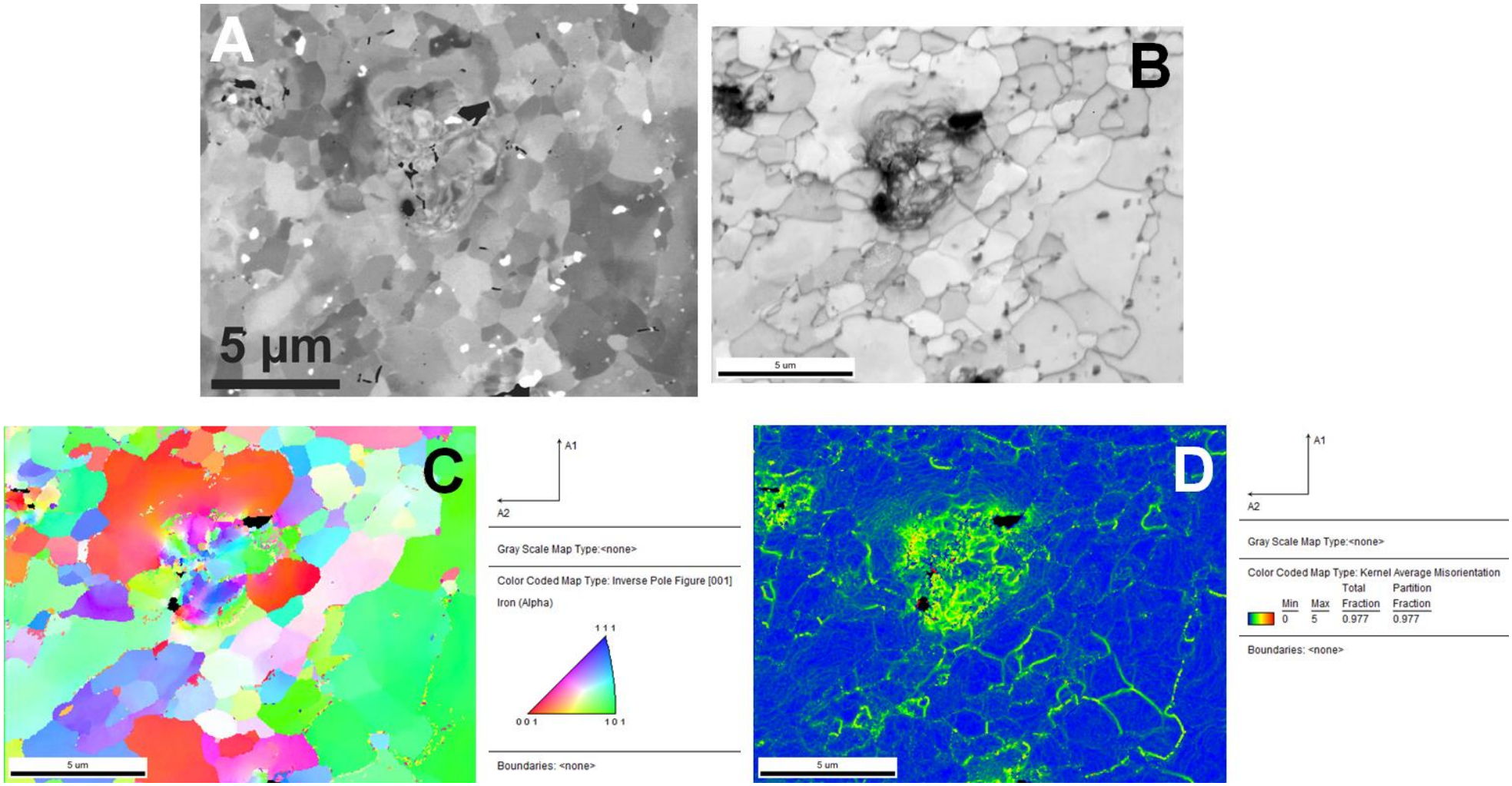

Figure 9-24. Location 3 backscatter image (A), image quality map (B), inverse pole figure image (C) and kernel average misorientation map (D)

9.6 Fractography

A sample from the HAZ was carefully machined using EDM and notched in the plane of damage to provide a sample for fractography. The fractured sample possessed a large variation to topography and was characterized by local ductility in the regions between creep cavities. A representative field of cavitation in the HAZ is presented in Figure 9-25. A higher magnification image is provided in Figure 9-26. This includes the outline of cavities in the fractured plane. There exists a general distribution of particles in all cavities including a larger nucleation source for the indicated cavity near the bottom of the image.

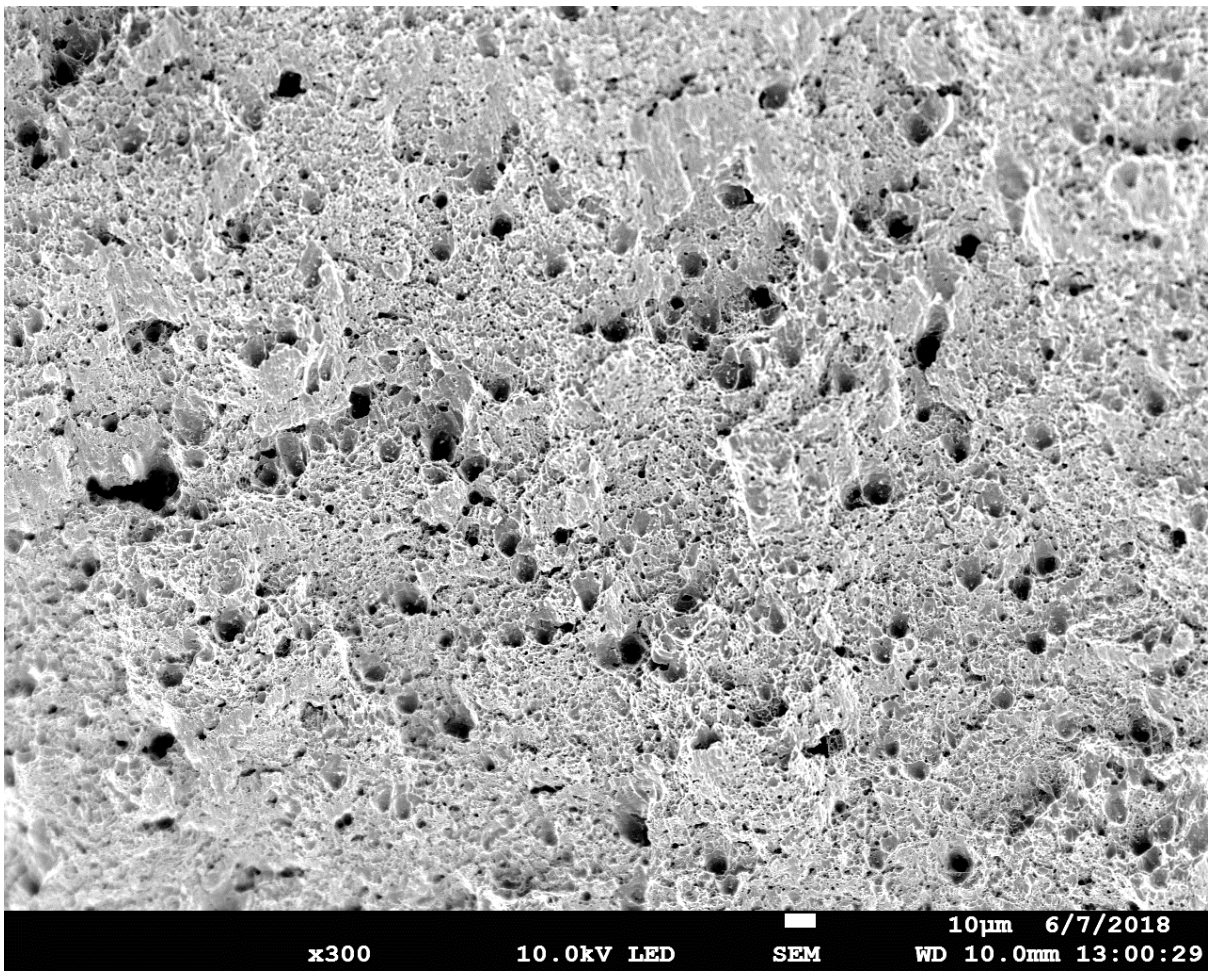

Figure 9-25. Fractography in sample AR-B2-5 (625°C, 60 MPa, 1,006 hours) showing a field of large cavities in the heat affected zone, 300X

The fractured plane was not flat and exhibited considerable changes in topography which did not permit SEM-EDS measurements to be carried out in some locations of the sample. Furthermore, some of the cavities, even in the interrupted HAZ, were still large on a micro-scale and the nucleation source was embedded deep in the cavity.

This prevented the acquisition of sufficient signal for processing. Nevertheless, examples of identified cavity nucleation sources are presented in Figure 9-27 and Figure 9-28; in both examples the particle in the cavity is identified by the EDS spectra as MnS. In the cavities presented in Figure 9-29 and Figure 9-31 there is an association with MnS as well as some particles identified as carbides (probably $M_{23}C_6$) or Laves phase. In several locations, documented in Figure 9-31, a boron peak was noted in the spectra at the MnS particle.

Figure 9-26. Fractography in sample AR-B2-5 (625°C, 60 MPa, 1,006 hours) highlighting the cavities in the heat affected zone formed because of time-dependent damage, 2,500X

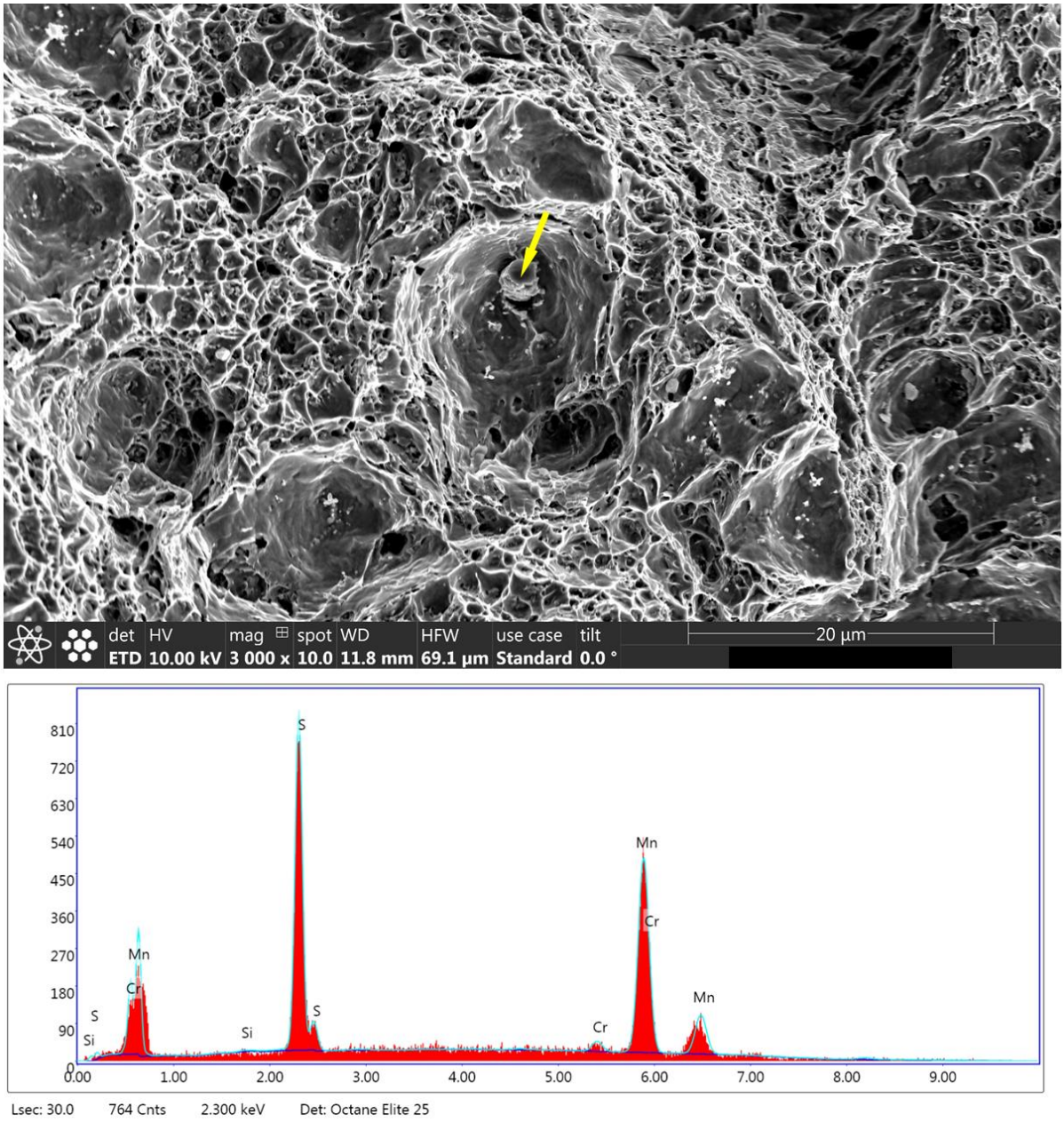

Figure 9-27. Fractography in sample AR-B2-5 (625°C, 60 MPa, 1,006 hours) including a particle (A) analyzed by SEM-EDS (B) and showing association with MnS (3,000X)

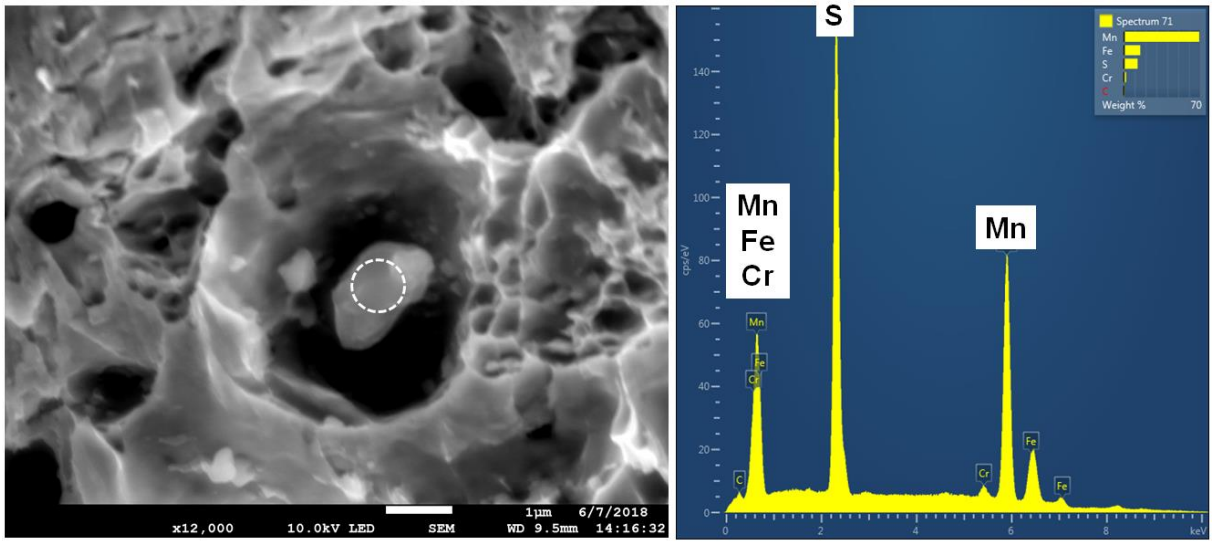

Figure 9-28. Fractography in sample AR-B2-5 (625°C, 60 MPa, 1,006 hours) including a particle (A) analyzed by SEM-EDS (B) and showing association with MnS (12,000X)

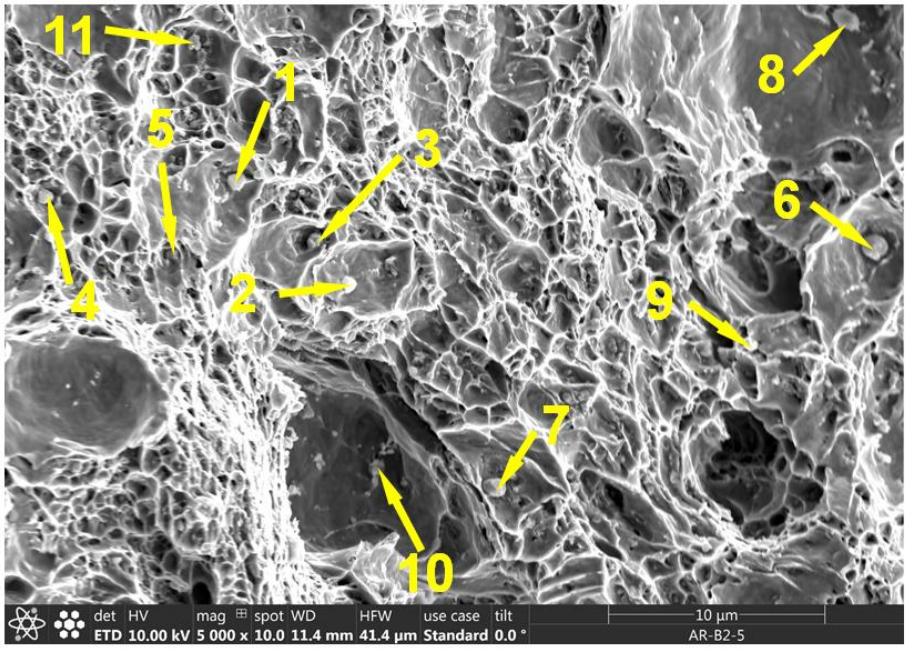

Particle	Type
1	MnS
2	MnS
3	MnS
4	MnS
5	Laves
6	MnS
7	MnS
8	MnS
9	Matrix
10	Carbide
11	Laves

Figure 9-29. Fractography in sample AR-B2-5 (625°C, 60 MPa, 1,006 hours) and assessment of 11 particles in the field of view at 5,000X

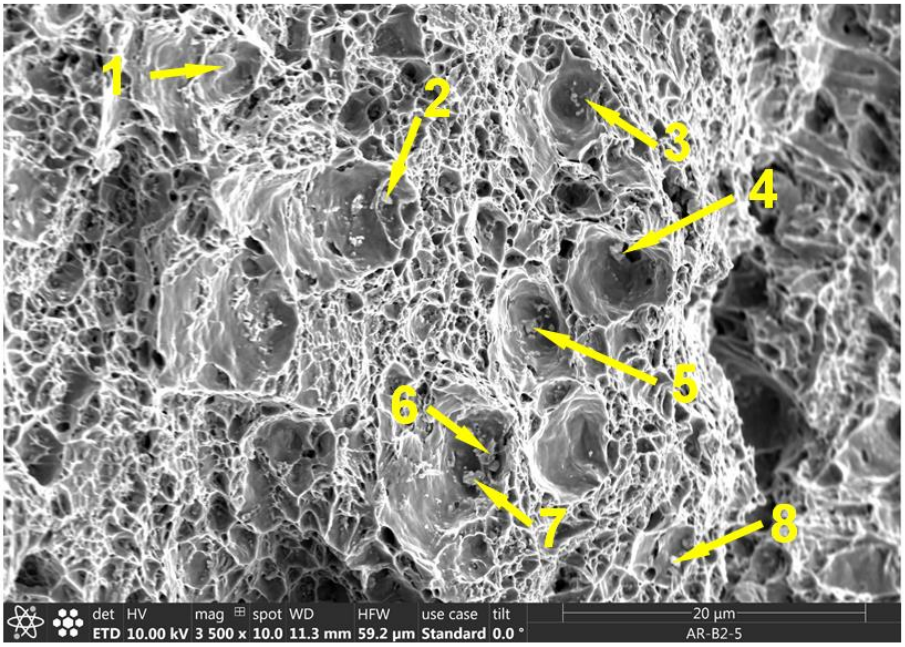

Particle	Type
1	MnS
2	MnS
3	Carbide
4	Carbide
5	MnS
6	Laves
7	MnS
8	Carbide

Figure 9-30. Fractography in sample AR-B2-5 (625°C, 60 MPa, 1,006 hours) and assessment of 8 particles in the field of view at 3,500X

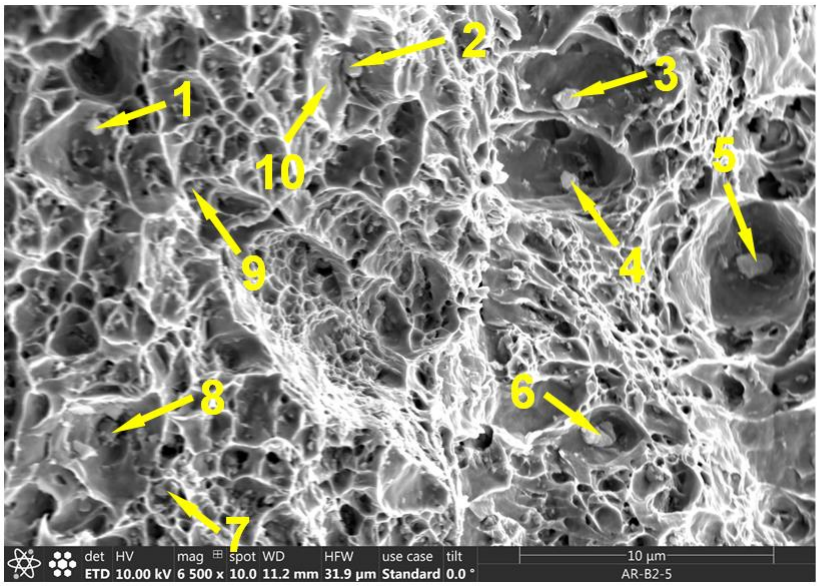

Particle	Type	Notes
1	MnS	B peak
2	MnS	
3	MnS	B peak
4	MnS	
5	MnS	
6	MnS	B peak
7	Laves	
8	MnS	
9	Unknown	
10	MnS	

Figure 9-31. Fractography in sample AR-B2-5 (625°C, 60 MPa, 1,006 hours) and assessment of 10 particles in the field of view at 6,500X

9.7 Dual-beam Focused Ion Beam Milling and SEM-EDS Analysis

An area representative of the creep cavities in the HAZ was locally prepared for FIB. Each slice removed ~100 nm of material. The process was periodically interrupted as new cavities were opened to perform EDS spot or small SEM-EDS map assessments. A total of 98 slices were taken through the section revealing 31 subsurface cavities. For 12 of the cavities, detailed in Table 9-1, there was an association with elemental

peak(s) that may indicate the presence of a coarse particle such as MnS, AlN, $M_{23}C_6$, V-rich (perhaps Z-phase), Nb-rich (probably NbC).

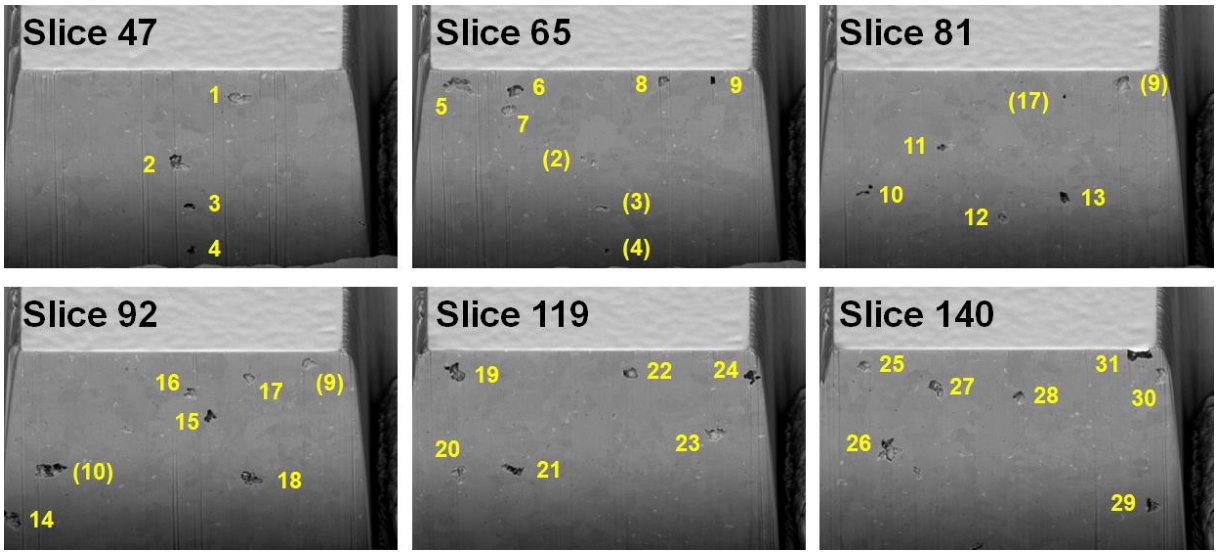

Figure 9-32. Identified cavities in the serial sectioning of a plane through sample AR-B2-5 (625°C, 60 MPa, 1,006 hours)
Note: *width of the plane is ~50 µm*

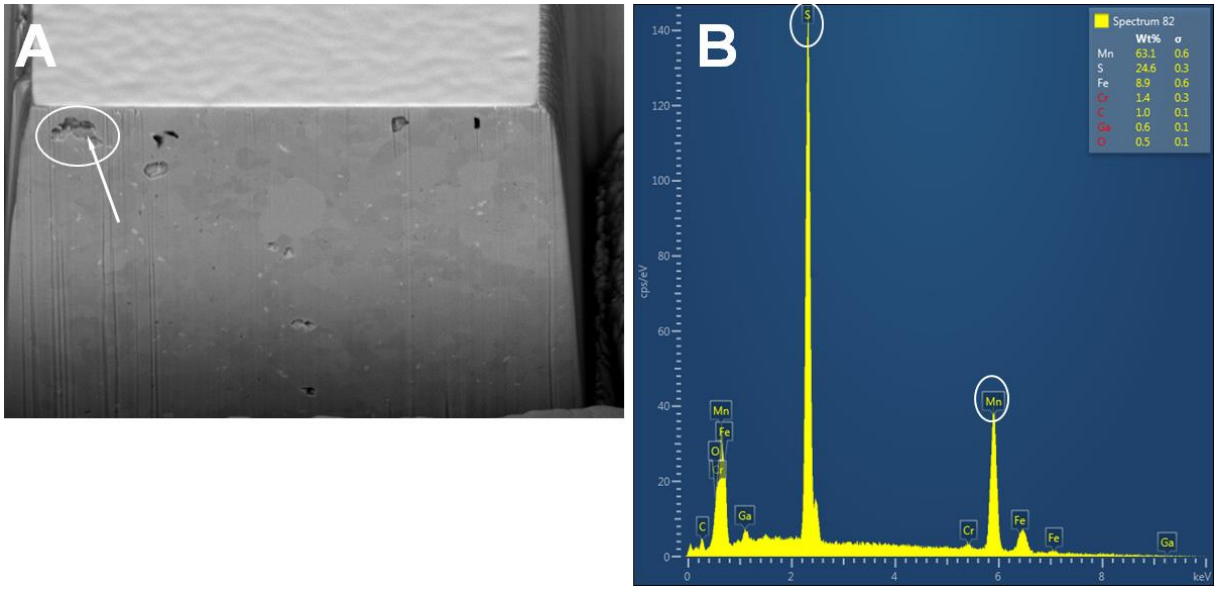

Figure 9-33. Example of SEM-EDS at cavity 5 in the sectioning detailed in Figure 9-32 for sample AR-B2-5 (625°C, 60 MPa, 1,006 hours)

Table 9-1. Association of cavities in Figure 9-32 with particles identified by SEM-EDS

Cavity	General Observations
1	Elevated V and Cr; weak S peak
2	V, Al- and Nb-peaks
3	Potential evidence for S-peak
5	Clear MnS association
12	Weak Al-peak
13	V-peak
15	Mn- and S-peaks
19	Al-, Nb-association; weak Mn- and S-association
21	V-association
27	V-association
29	Nb-association
30	V- and Al-association

9.8 Plasma Focused Ion Beam (P-FIB) Milling and SEM-EDS Mapping

In the prior-detailed FIB procedure only ~30 cavities in the HAZ were revealed. A larger volume of material in the HAZ was prepared and removed for P-FIB assessment. Key advantages of the P-FIB process over the dual beam FIB is that the amount of material analyzed is greater and the collection of EDS map data for sectioned planes is facilitated. In the current research a total of 813 slices were taken through the HAZ, and every fourth slice was analyzed using SEM-EDS (e.g. 204 total EDS maps). For the representative, 3D-reconstructed image given in Figure 9-35 the dark features are MnS, the blue features are creep cavities and the light features are Al-rich (AlN or Al_2O_3). In addition to the 3D-reconstructed data given in Figure 9-34 to Figure 9-38, each sectioned plane was evaluated and linked to the individual map data for Mn Kα, Mo Kα, S Kα, Al Kα and O Kα. A representative dataset is provided in Figure 9-39 to Figure 9-42 for slice 781, Comparison of the results obtained provides a link of the information to individual cavities and composition and cavitation was classified by cavity size as coarse or fine.

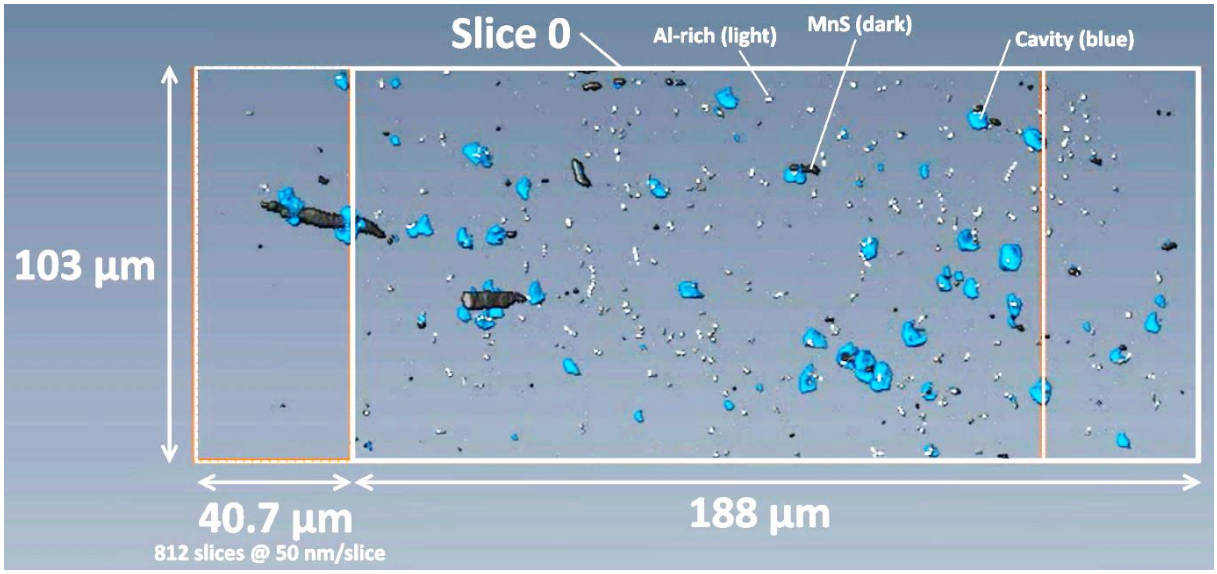

Figure 9-34. Corner view of representative data for P-FIB evaluation; information for Al-rich (light particles), MnS (dark particles) and cavities (blue volume) are provided

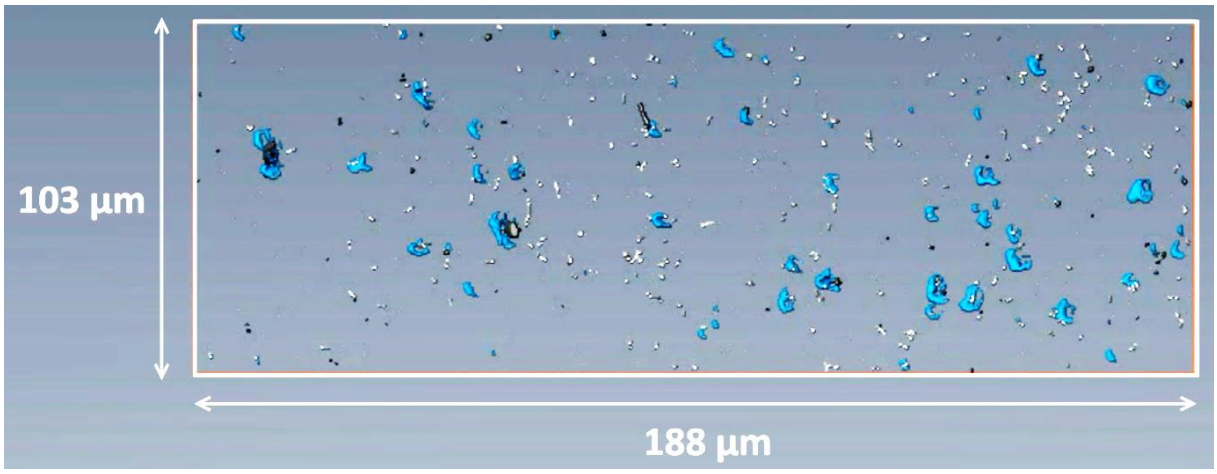

Figure 9-35. Slice 0; note information for Al-rich (light particles), MnS (dark particles) and cavities (blue volume) are provided

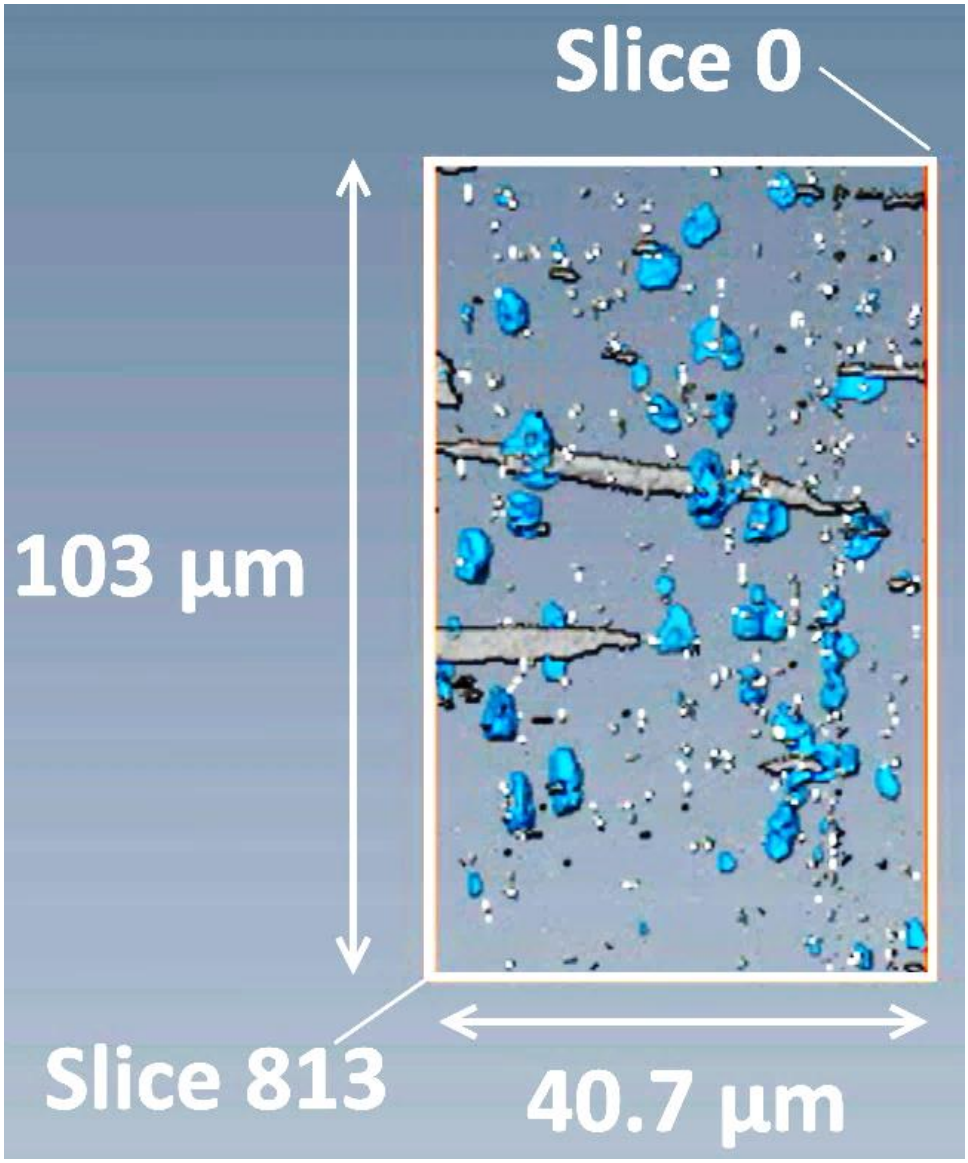

Figure 9-36. Side view of analyzed volume; note information for Al-rich (light particles), MnS (dark particles) and cavities (blue volume) are provided

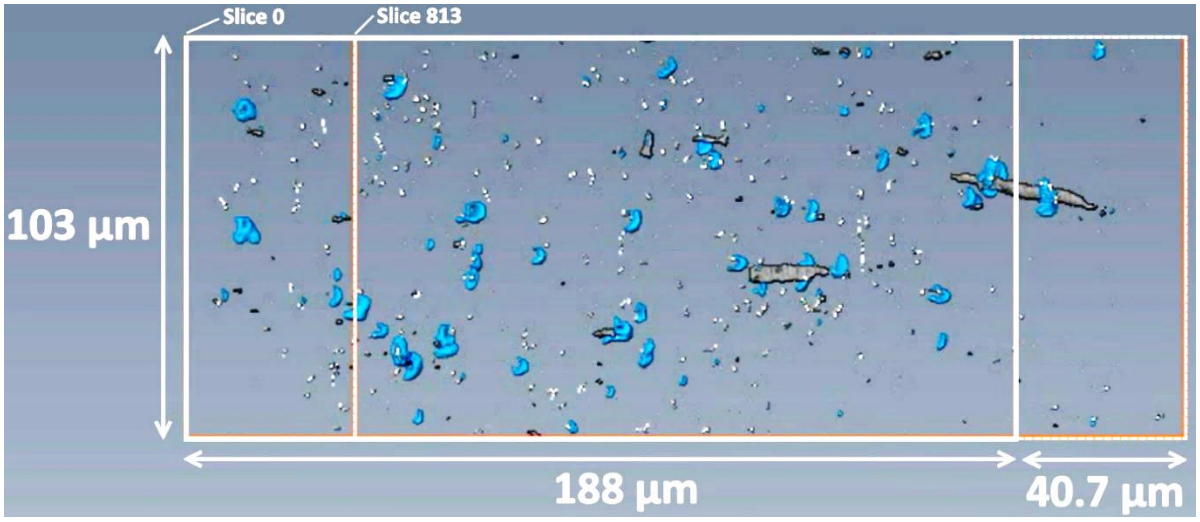

Figure 9-37. Corner view of analyzed volume; note information for Al-rich (light particles), MnS (dark particles) and cavities (blue volume) are provided

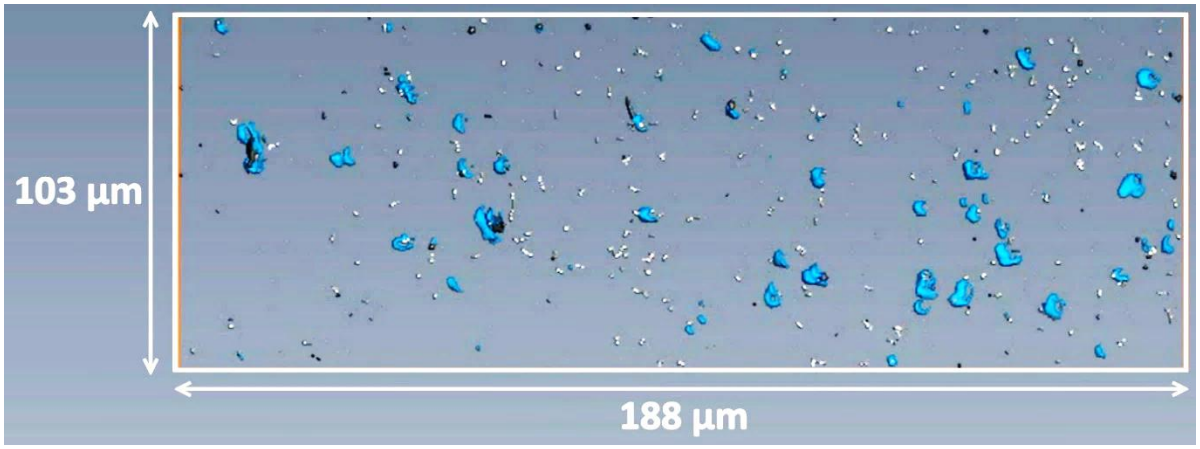

Figure 9-38. Slice 813; note information for Al-rich (light particles), MnS (dark particles) and cavities (blue volume) are provided

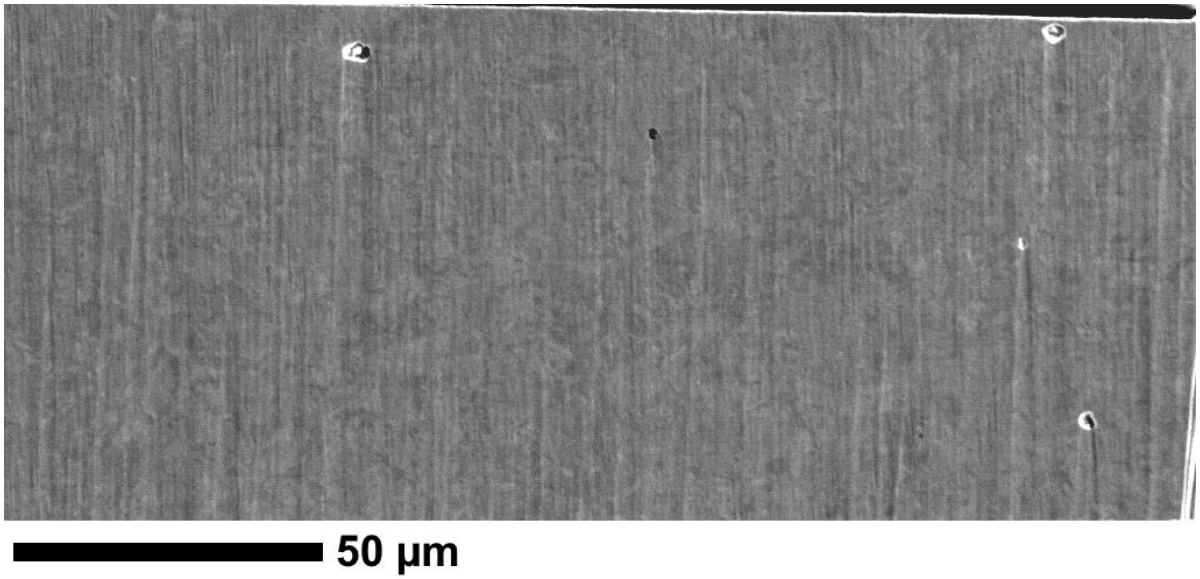

Figure 9-39. Representative secondary electron image; Slice 781 (EDS Map 196)

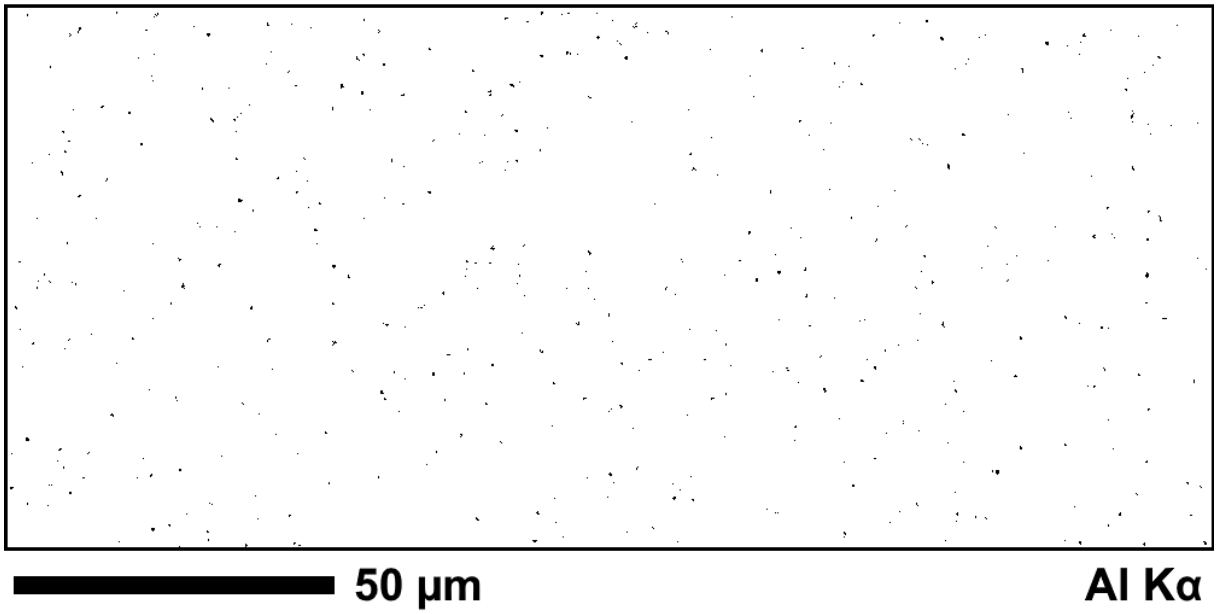

Figure 9-40. Representative EDS map for Al Kα; Slice 781 (EDS Map 196)

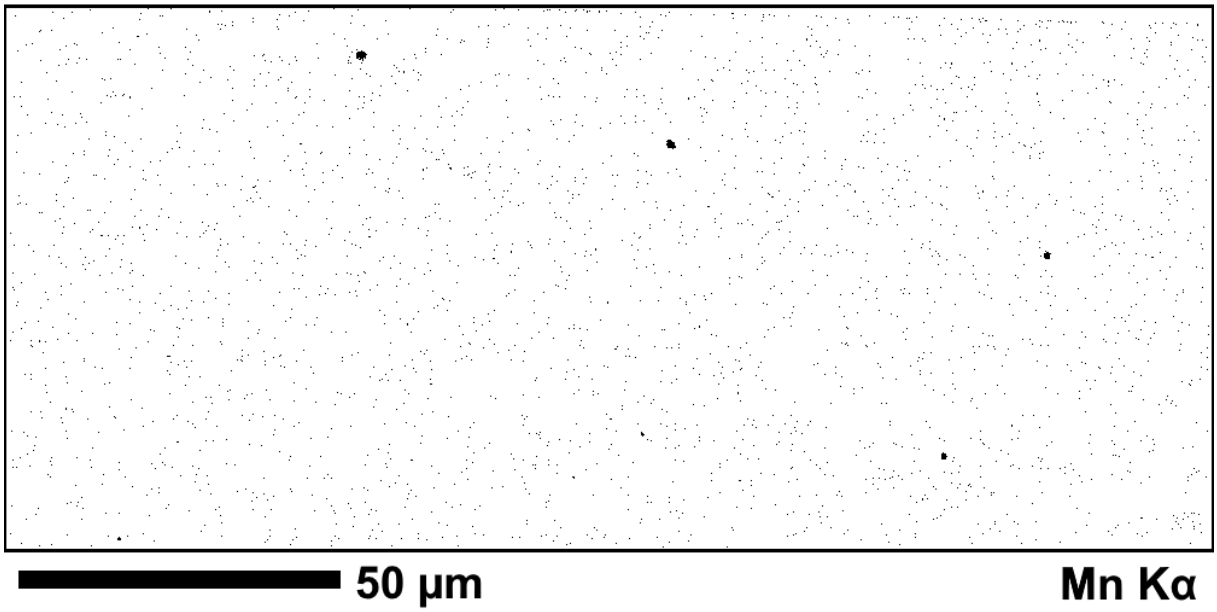

Figure 9-41. Representative EDS map for Mn Kα; Slice 781 (EDS Map 196)

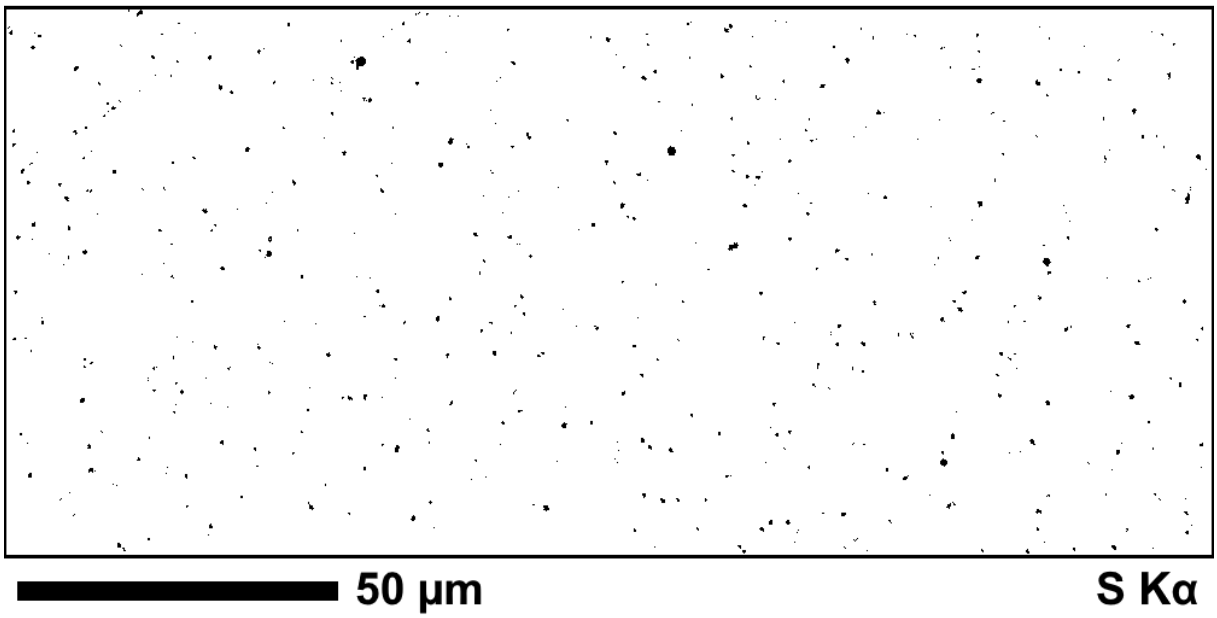

Figure 9-42. Representative EDS map for S Kα; Slice 781 (EDS Map 196)

For the data given in Table 9-2 there is an association of damage with second phase particles. This observation is clear for the coarse cavities (~>1 µm) where the link between Al-rich or Mn-rich particles is 98%. Furthermore, the coarse cavities tend to show a complex cluster association of Laves phase and/or $M_{23}C_6$ present in the same cavity morphology. A similar comparison between the fine cavities (~≤1 µm) and the Al-rich and Mn-rich particles is 58%. In general, there exists a clear association of cavity to particle damage, and the summarized data shows an overall link with Al or Mn of 98% for coarse cavities and 58% for fine cavities.

Table 9-2. Association of cavity size with EDS peaks for Al K, Mn K, O K, Al+Mn or Al or Mn peaks. Note,

Cavity Size	Number	Al Kα	Mn Kα	O Kα	Al+Mn	Total Linked to Al or Mn	Notes
Fine	55	20 (36%)	18 (33%)		7 (13%)	32 (58%)	
Coarse	50	46 (92%)	28 (56%)	3 (6%)	28 (56%)	49 (98%)	For 12 of 22 cavities not associated with Mn, there is evidence for a complex cluster of Laves, $M_{23}C_6$ or another phase

9.9 Scanning Transmission Electron Microscopy (TEM/STEM)

A thin foil was extracted from the PTZ region of the HAZ using FIB. This examination allowed local composition analysis and an assessment of particles linked to cavity nucleation which were captured in the volume of the foil. The thinned region evaluated using TEM and STEM is documented in Figure 9-43 for the bright and dark field images. The cavity is represented as the black or white void near the top of each image. The EDS results are provided in Figure 9-44. The field of view captured three AlN particles (see Al map in Figure 9-44B), one which is present adjacent to the cavity in a small cluster of carbides and a V-rich particle. There is a non-uniform distribution of Cr-rich carbides at the observed grain boundaries. The documentation of the cavity location was not able to capture a potential nucleation source, unless the association of damage in this location is linked to the cluster of AlN particles.

A second EDS analysis performed in the immediate vicinity of the cavity is detailed in Figure 9-45. The documented EDS results show the plate-like morphology of the AlN and it is apparent that two such particles exist in the same location. In some cases, such as observed in Figure 9-9H the same morphology is observed in SEM analysis of a single plane. The presence of Cu is observed in the location of the AlN particles, Figure 9-47. These Cu precipitates are extremely fine and <50 nm in diameter.

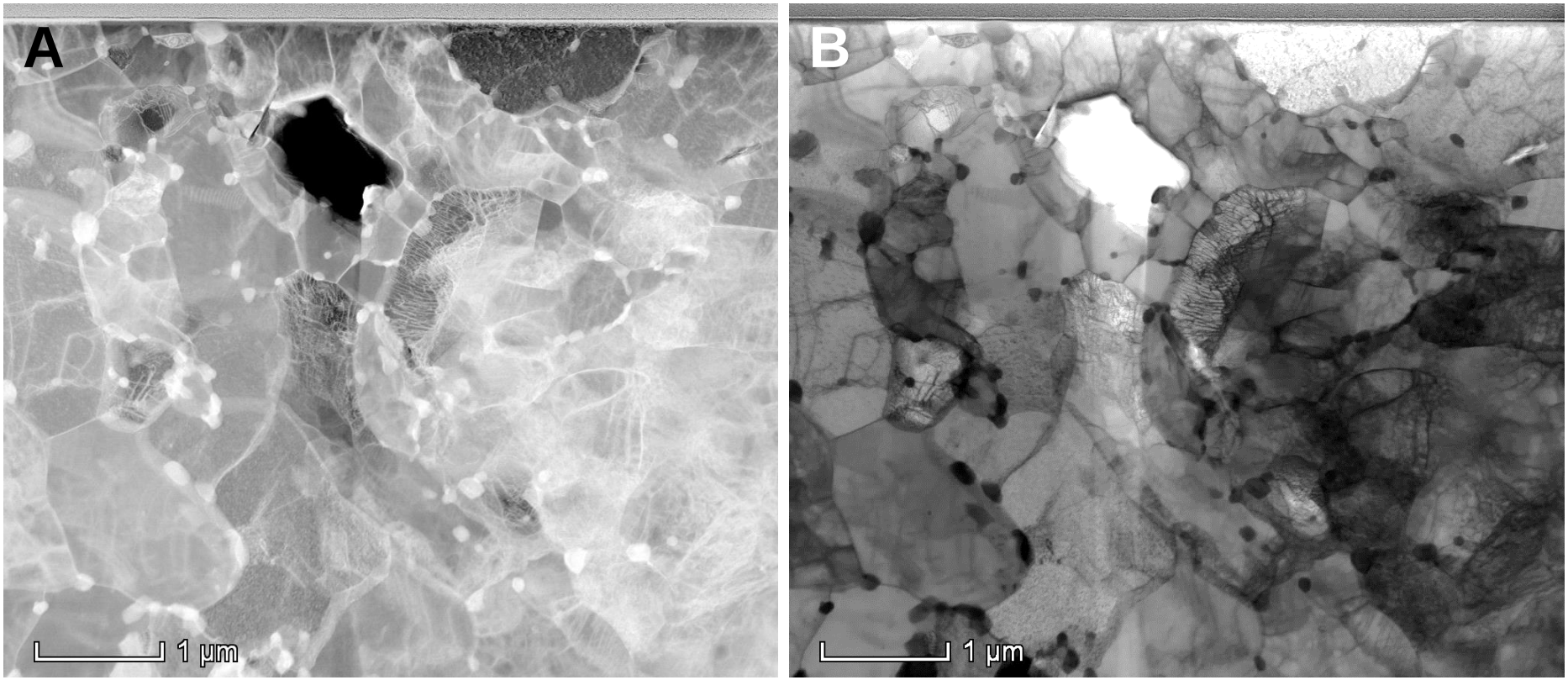

Figure 9-43. TEM bright-field image (A) and dark-field image (B) for the extracted thin foil sample taken from the heat affected zone of sample AR-B2-5 (see Figure 3-22 for location)

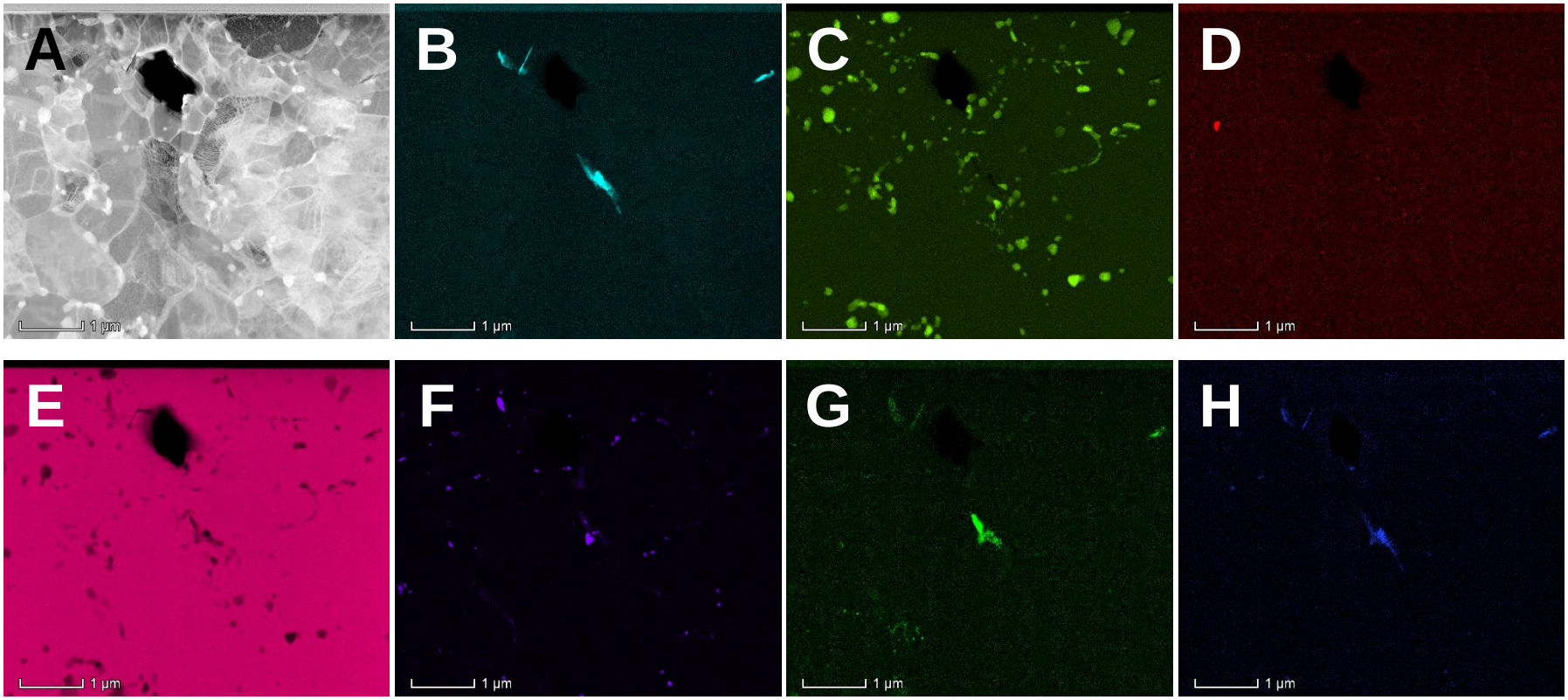

Figure 9-44. STEM analysis for the location documented in Figure 9-43 (A) and for aluminum (B), chromium (C), copper (D), iron (E), vanadium (F), niobium (G) and nitrogen (H)

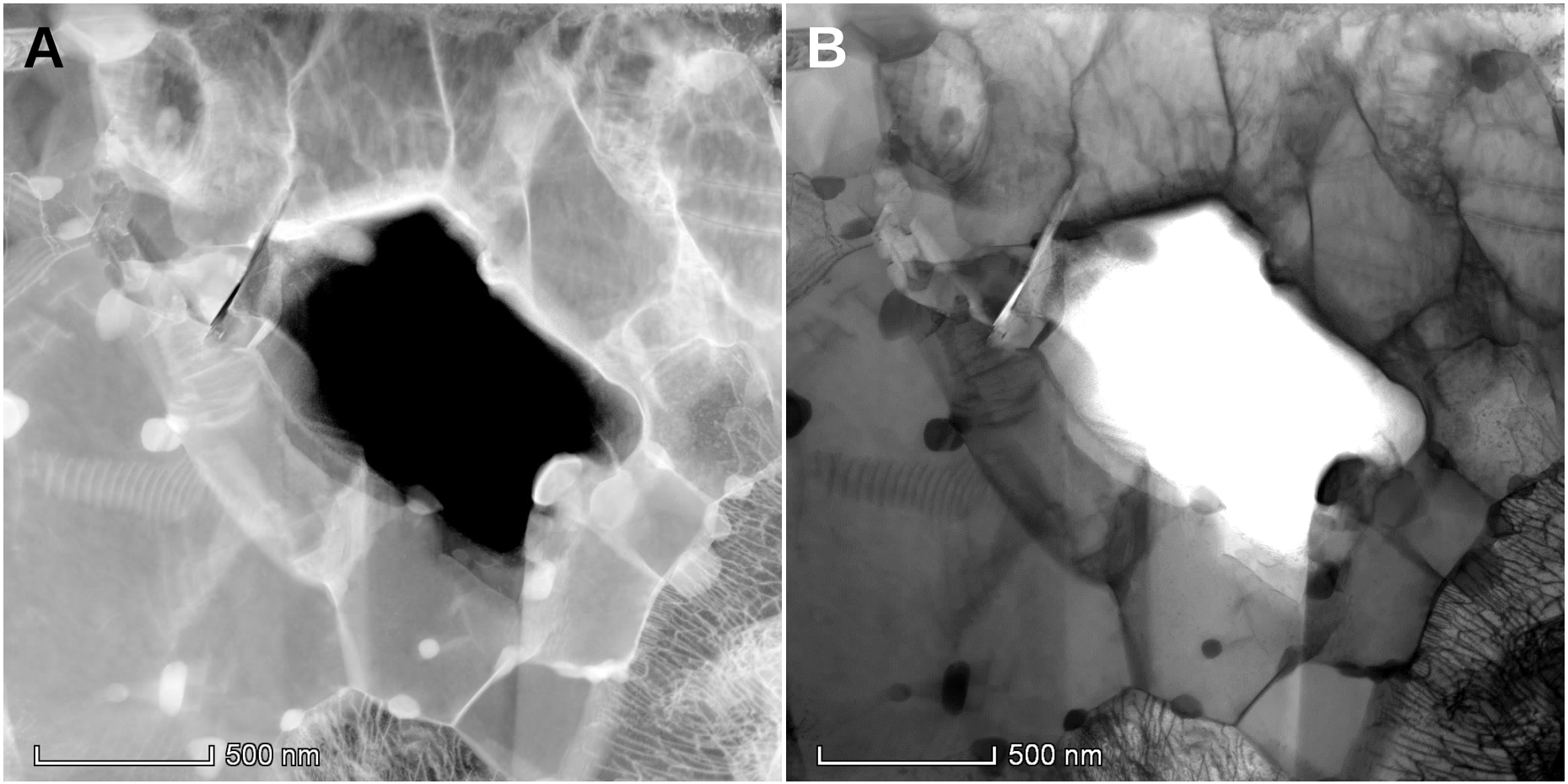

Figure 9-45. TEM bright-field image (A) and dark-field image (B) for the extracted thin foil sample taken from the heat affected zone of sample AR-B2-5 (see Figure 9-43 for location)

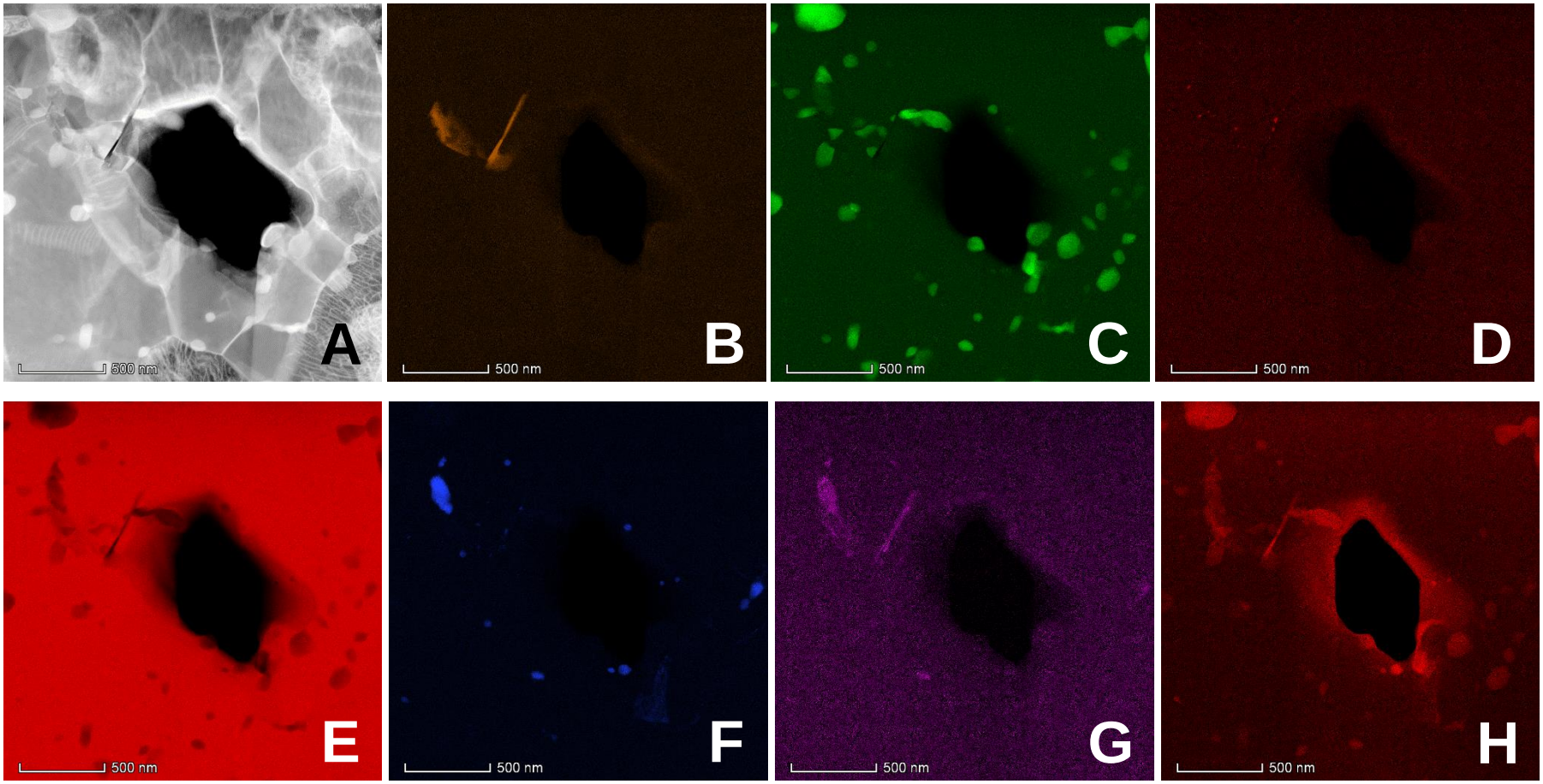

Figure 9-46. STEM analysis for the location documented in Figure 9-45 (A); aluminum (B), chromium (C), copper (D), iron (E), vanadium (F), niobium (G) and nitrogen (H)

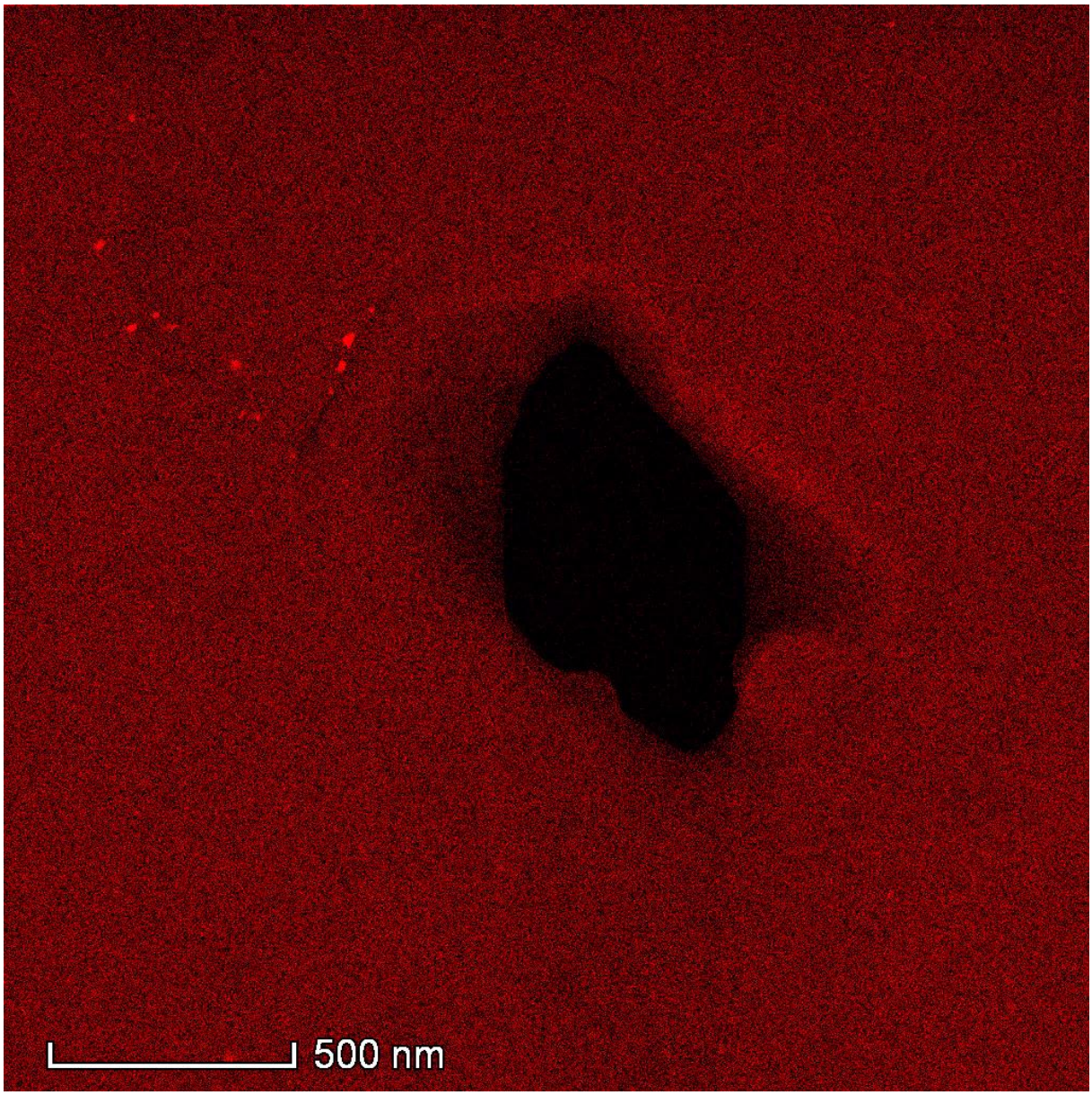

Figure 9-47. Copper map for the location in Figure 9-45 highlighting the nano-scale precipitation of Cu in the vicinity of the AlN and Carbonitride cluster adjacent to the cavity

9.10 Discussion

The summary of results generated in the current chapter will be placed into a context that closely follows the evolution of a stable creep cavity and its subsequent growth rationalized by the information generated in the early 1980s for low alloy steel behavior (CEGB 1980, Cane and Middleton 1981). From a simplistic point of view, the authors argue that the application of a stress normal to the grain boundary is the governing factor in cavity growth and that the nucleation process is a relatively unimportant event.

This basic premise is relevant in the current thesis and the implications of the findings are paraphrased below:

- The nucleation process can be effectively modeled using classical nucleation theory such that the stable cavity size is inversely proportional to the maximum principal stress (e.g. $r_c > \frac{2\gamma}{\sigma_1}$).
- The susceptibility of bainitic low alloy steels to the formation of creep damage leading to low ductility failure can be controlled independently of mechanical strength, and more preferably by a modification of the density of incoherent particles residing on grain boundaries.
- Under conditions where plasticity contributes to cavity growth, low-ductility failure may be avoided by elimination of the boundary-deformation zone such as in higher-chromium steels (e.g. 9Cr-1Mo).
- The creep cavity nucleation occurs independent of creep strength and the associated boundary-shear behavior.

The following discussion therefore places the current research in the context of these earlier findings, informed by detailed microstructural analysis at a fine scale which was not possible in the early 1980s and illustrates how these conclusions can be modified and developed to account for creep failure in this important class of high chromium steels examined in this research.

In the present research, the details for the nucleation event in the HAZ could not be evaluated since the samples were fabricated from ex-service material and the potential for decohesion could not be easily decoupled from the virgin condition. However, the evaluation of the parent metal in the post-service condition, and as detailed in Chapter 4, did not suggest that extensive creep damage was present in the material utilized for the cross-weld test evaluations. Calculations for the consumed life of the parent metal further supported this observation, e.g. that the parent metal exhibited at most a life fraction consumed of 5% and more likely on the order of 1%. Additionally, extensive damage was noted in the interrupted sample that had already progressed to a relatively mature condition after ~70% life fraction. Thus, there exists inferential evidence for the damage-susceptible material that nucleation event is not an important

event. More conclusive and recent findings from the literature support this point for 9 wt. % Cr CSEF steels.

The nucleation of damage at second phase particles has recently been investigated by Xu (2017) and Gu (2017) in Grade 92 parent metal and cross-weld samples including interrupted creep tests and assessment in the as-received condition. In the as-received material, it is clearly shown that BN is decohered from the matrix. Evidence for the nucleation of creep damage in cross-weld creep samples in Grade 91 steel after 20% life fraction is detailed in the experiments presented by Hongo et al. (2012), Figure 9-48. It is thus the case that arguments made for early-in-life nucleation, if not instantaneous, are well-supported even if not well-understood.

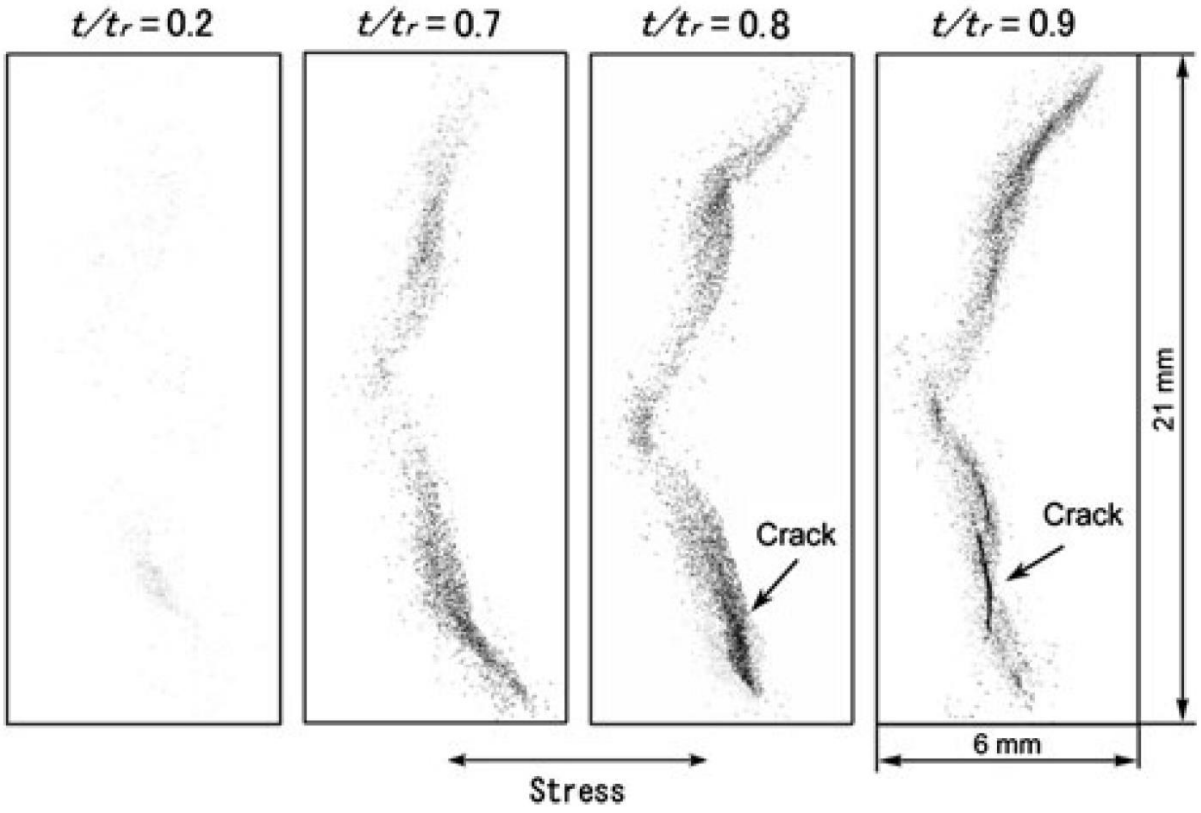

Figure 9-48. Distribution of damage through the heat affected zone for a series of interrupted tests performed at 600°C and 90 MPa.
Note: *that the ultimate failure time for this weldment and stated test condition is 8,853 hours (Hongo et al. 2012).*

Recent assessment of an extensive cross-weld creep database generated by NIMS suggests that the maximum principal stress is an important factor in rationalizing behavior. Using a multiaxial damage mechanics approach proposed by Hayhurst and given in Equation 9.1, the experimental cross-weld creep result to the predicted time to failure is given in Figure 9-49 (Tabuchi et al. 2017).

Equation 9.1. $$\frac{d\omega}{dt} = \frac{M[\alpha\sigma_1+(1-\alpha)\sigma_{eq}]^{\chi}}{(1+\phi)(1-\omega)^{\phi}} t^m$$

For the relationship in Equation 9.1, σ_1 is the maximum principal stress, σ_{eq} is the equivalent stress, ω is the damage variable, and A, n, m, M, ϕ and χ are the material constants. Determination of the material constants was made possible by a comprehensive test program including tests in the same parent material for: unaffected base metal; cross-weld; and simulated HAZ.

In the present research, the development of a dataset to drive the necessary material constants for a similar assessment is not reported although continuing research in EPRI is generating the type of information required to perform such an evaluation. It is important to emphasize that the data illustrated in Figure 9-49 (previously provided in the literature review) show a clear over-prediction of lifetime in the long-term test data using the relationship in Equation 9.1 and assuming a value for α = 0.3 or 0.4. A reduction in the over-conservative behavior is only possible using values for α which are closer to 1 (e.g. maximum principal stress controlled).

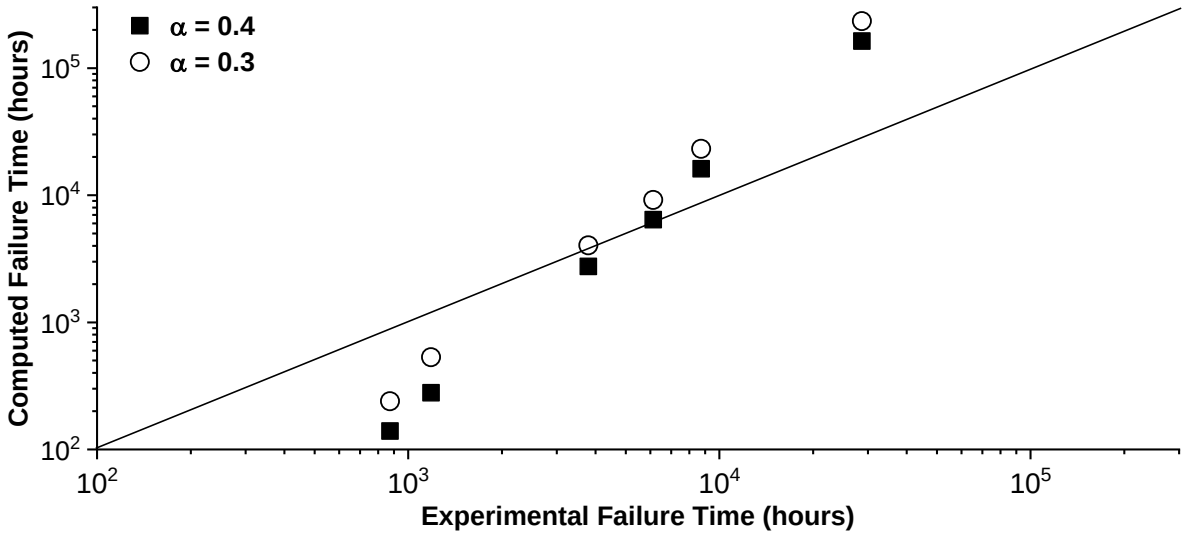

Figure 9-49. Comparison of the computed time to failure using equations 2.20 and 2.21 to the experimental failure time reported in (Tabuchi et al. 2017)

Additional evidence regarding the importance of stress-state is provided in the literature by a recent experiment performed by (Tsuruta et al. 2017). This study, although only briefly reviewed in the present thesis, is relevant to the discussion of stress-state and the authors made two very important conclusions. Through the application of a multiaxial notch bar test geometry in HAZ material and simultaneous measurement of creep damage evolution using x-ray micro-tomography (resolution of

~1 μm), the void number density correlated to the maximum principal stress and the average void growth rate is linked to the stress multiaxiality (defined in their study by a triaxiality factor, $TF = \frac{\sigma_h}{\sigma_{eq}}$ where σ_h is the hydrostatic stress and σ_{eq} is the Mises equivalent stress). It is thus the case that the dependency of damage evolution (e.g. whether cavity growth and/or nucleation are considered) is dependent on the maximum principal stress and the multiaxial stress state. Interpretation of the results suggests the importance of sample geometry and that the extensive field of damage observed after an estimated consumed life of 70% in the interrupted sample in Chapter 9 is not accidental. The consideration of stress-state and the factors which affect weld behavior are important considerations for life management where large variations on predicted behavior can occur depending on the assumed stress.

It was highlighted in Chapter 7 that the development of damage in the HAZ shows a distinct correlation with heat-to-heat dependency. Invoking the argument presented by Cane and Middleton (1981) for low alloy steels suggests that incoherent, grain boundary particles are a primary driver for creep damage. The evidence for a damage-susceptible heat of Grade 91 steel material, and in the PTZ, shows a very strong dependence on the distribution of second phase particles. Since the grain size in the PTZ is very fine, the likelihood for large inclusions to be present at the grain boundary is high. This is emphasized in the P-FIB assessment where the association of coarse creep voids with MnS or Al-rich precipitates is 98%. For the coarse cavity population, 56% were associated only with Mn, representing a considerable fraction of the damage present in the HAZ with MnS inclusions. In the distribution of the fine cavities, 58% were associated with Mn or Al-rich precipitates and 33% with Mn-rich alone. It is thus the case that a considerable distribution of damage in the PTZ for a damage susceptible heat of Grade 91 are either linked to inclusions produced during steel making (MnS or Al_2O_3) or potentially to a distribution of particles evolved during the processing to the final product form (e.g. AlN).

Cane and Middleton observed that the MnS coherency in the ferrite matrix increases considerably with increasing Cr content ≥ 5 wt. %. This observation is not directly relevant in the current study, where MnS is often present as a complex cluster of particles (for example Figure 9-13 and Figure 9-15). The present findings and

unpublished research continue to evolve methods to assess the inclusion distribution in 9 wt. % Cr steels.

It is important to emphasize the difficulty in rationalizing the evolution of damage in the current Chapter based on creep strength alone. It has been suggested, for example in (Wang and Li 2016; Masuyama 2017b), that the presence of precipitate-free and precipitate-rich grains in adjacent HAZ boundaries generates the necessary mismatch in deformation resistance to generate the strain needed for cavity nucleation. A strength-based argument cannot explain the localized nature of damage in the PTZ since the number of boundaries between precipitate-free and precipitate-rich grains can be expected to far exceed the number of observed cavities. The SEM-EBSD data given in Figure 9-17 contained more than a dozen instances of large ferrite grains with clear evidence of deformation and yet there is not a consistent link to the association of damage in these examples. Whilst it is acknowledged that cavity formation is most certainly a 3D problem, the argument made in this discussion is that the local deformation characteristics can only result in the formation of a cavity if there also exists a susceptible particle at the boundary.

For a strength-based rationale regarding the nucleation and generation of creep damage in the HAZ, it should follow that the generation of a welding thermal cycle in *any* Grade 91 steel heat will create the necessary conditions described in (Wang and Li 2017) to generate a creep cavity. The argument presented throughout this thesis follows a simple logic that a simulated HAZ – regardless of the parent metal – should possess a similar strength, yet when placed in multiaxial test condition the behavior must be observed to change considerably. This assertion is grounded in the reality that a parent metal sensitive to the evolution of damage will exhibit a high density of cavities when subjected to a relevant, multiaxial stress state. Recent data generated by Takahashi et al. (2019) and a more recent, unpublished set of data (Siefert 2019) provides the context for this assertion in Figure 9-50 to Figure 9-52. In Figure 9-50A the total variation in the evaluated heats of parent metal strength for a standard screening test condition of 625°C and 100 MPa is ~16X with respect to the time to failure. However, for the simulated HAZ condition in the same parent metals (e.g. a controlled reproduction of the material condition in the PTZ) in Figure 9-50B an absolute variation for the time to failure is only 2.3X. It is thus clear that the variability in the parent metal strength is not directly correlated to the HAZ strength. Although

this point is not well-understood nor documented, it is nonetheless vital to the discussion. If the variability in strength present in the unaffected parent metal cannot explain the dramatic difference in a relevant set of cross-weld creep tests, then what constitutes the dominant characteristic for behavior?

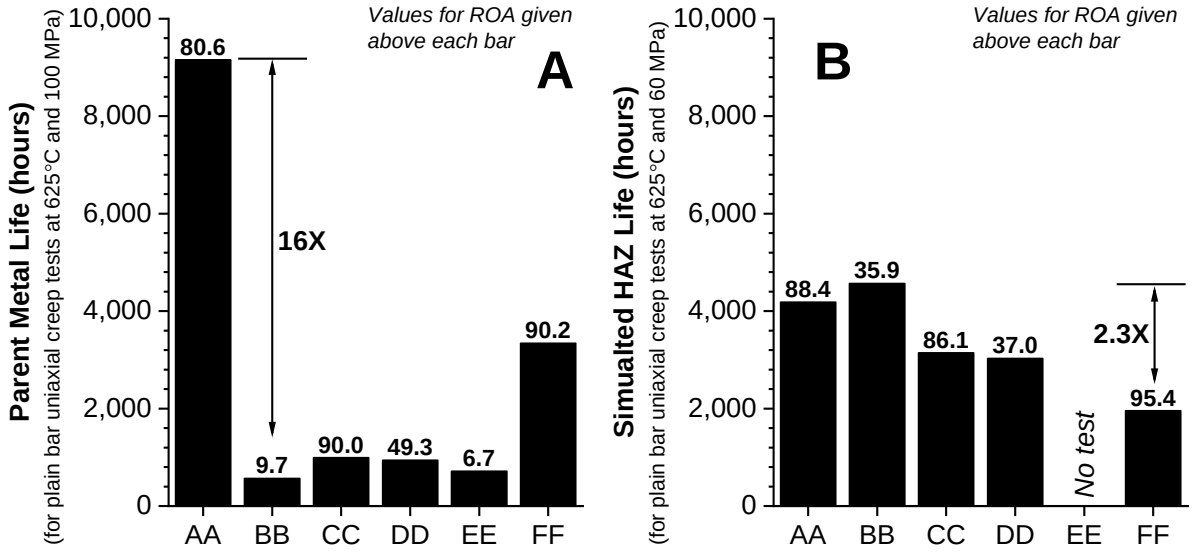

Figure 9-50. Comparison of the parent metal life at 625°C and 100 MPa (A) and the simulated heat affected zone (HAZ) life at 625°C and 60 MPa (B) for a unique set of parent metal samples.
Note: *sample 'BB' in this figure is B2 and sample 'CC' is TP1 for correlation with behavior assessed in the present thesis*

The data provided in the comparisons in Figure 9-51 and Figure 9-52 provide a comprehensive set of results which demonstrate that the cross-weld behavior is more clearly linked to the parent metal creep ductility (Figure 9-51) and not to the parent metal creep strength (Figure 9-52). Although parent metal ductility is utilized in the context of reduction of area, this screening parameter approximates the susceptibility of the parent material to the development of creep damage such that it is routinely observed for Grade 91 steel that low ROA values correlate to high densities of creep voids. The simple linear relationship in Figure 9-51 reinforces the correlation between the cross-weld creep life to the parent metal ROA whereas there exists no correlation to the parent metal strength in Figure 9-52. The outcome of this comparison is supported by the previous observation for the P-FIB analysis where a significant population of coarse and fine cavities are linked to second phase inclusion particles.

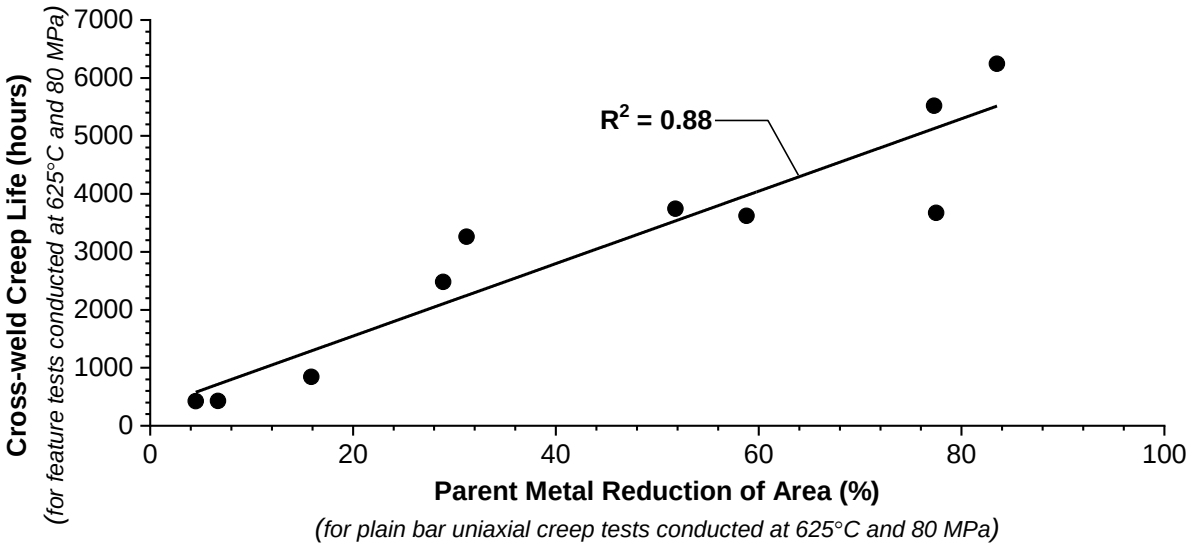

Figure 9-51. Correlation of cross-weld creep life (hours) to the parent metal reduction of area (%) value for testing conducted at 625°C and 80 MPa

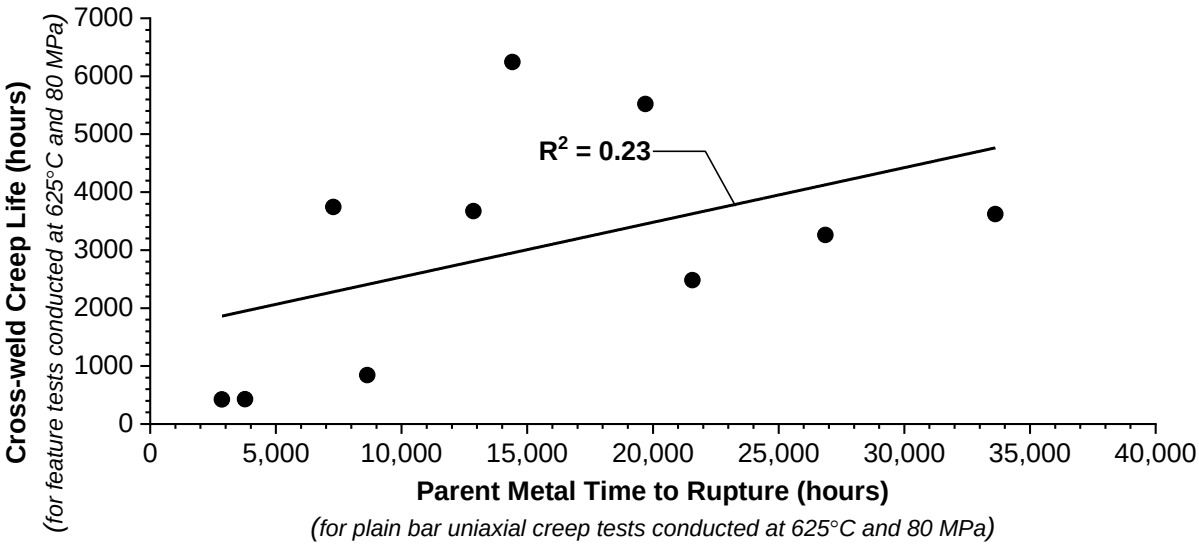

Figure 9-52. Correlation of cross-weld creep life (hours) to the parent metal life (hours) for testing conducted at 625°C and 80 MPa

Considering the present findings in Chapter 6, Figure 9-51, and Figure 9-52 the reduction in cross-weld creep behavior is linked to the susceptibility of the formation of creep damage that is reasonably classified by the parent metal creep ductility expressed as ROA. Considering the present findings, this is not a well-documented nor appreciated finding in the literature for Grade 91 steel where it is widely assumed that this steel exhibits creep ductile behavior, for example in (Hosseini et. al. 2013).

The findings in this research clearly suggest a link between cavitation density and a reduced time to failure for relevant, cross-weld creep tests. This assessment is shown to be clearly linked to the population of second phase particles for an interrupted cross-

weld creep test interrupted after an estimated life fraction of 70%. The implications for these findings must incorporate a more stringent level of control on elements which affect the distribution of second phase inclusion particles, and the level of Al and S. The reduction in Al directly affects the distribution of AlN and to a lesser extent for Al_2O_3. Reducing the S content is important with respect to decreasing the number density of MnS particles. The complexity of the interaction between inclusions and other particles is not well-established. However, extensive evidence is presented for a co-contaminant effect which enforces an overall need to restrict composition for materials operating in the time-dependent regime. It is thus the case for future research that a heat dependency on creep behavior should be more thoroughly linked to the distribution and hierarchy of second phase particles which affect strength and ductility. In Grade 91 steel optimization for long-term behavior is needed through identifying the role of inclusions (including type or classification if present as a complex cluster), the evolution of phases in service (Laves), the link between phases/particles and segregation, and whether intentional phases (such as carbides and particularly $M_{23}C_6$) are effective sites for promoting in-service damage.

9.11 Summary

The assessment of damage in an interrupted cross-weld creep test for a damage-susceptible material presented in this chapter has described the application of advanced electron techniques to assess factors affecting the nucleation of creep cavities. The work performed is unique because optimized approaches have allowed comparison of data produced using methods to quantify and/or illustrate contributing factors for damage in the HAZ for an interrupted cross-weld creep sample. The utilized methods included: SEM imaging; SEM-EDS; EBSD; dual-beam FIB; P-FIB; STEM and fractography.

Although the initial objective to utilize an interrupted sample was to provide a set of HAZ damage which was less evolved than in the failed samples, the interrupted sample with a consumed life of ~70% already possessed a well-developed distribution of damage. This suggested that the damage formed well before the interruption and provided evidence that for damage susceptible (e.g. low creep ductility) material, the cavities nucleated and began to grow relatively early in life.

The applied techniques presented in this Chapter were optimized from procedures previously utilized for the evaluation of failed samples in Chapter 8. The modified approach was necessary to enable several key findings: quantifiable evidence for recrystallization in the microstructure adjacent to cavities and in other areas of the HAZ microstructure; 3D evaluation of damage for a fractured sample face and reconstructed volume removed by the FIB or P-FIB process; and localized compositional evaluation at a subsurface cavity by STEM. This important set of results are briefly reviewed in the following summary of information.

In the interrupted test condition, a high density of creep cavitation was observed in the PTZ. Similar to the previous test results obtained in 2D using a combination of SEM imaging in secondary electron mode, backscatter mode and SEM-EDS composition mapping, cavities were observed to contain secondary phases such as inclusions and in other examples the cavities were clearly ‘empty’.

EBSD evaluation was initially inconclusive when utilized to evaluate the observed recrystallization at the damage sites when discussed in Chapter 8. However, when a very fine step size was utilized (e.g. 0.03 or 0.05 µm compared to the previous 0.15 µm) the maps showed clear examples of misorientation variations inside large ferrite grains, recrystallization around cavity sites and recrystallization at grain boundaries without an apparent nucleation source in the 2D plane. The result suggested that although the accommodation of strain is widespread on a microstructural scale, there was very localized development of creep voids.

Fractographic evaluation requires additional optimization, namely to ensure a clean and ideally flat fracture surface. Although not explicitly detailed in this Chapter nor in the experimental procedure, the fracture of a plane through the HAZ damage was not trivial and several attempts were required to produce an acceptable surface for examination. The difficulties in fracturing the sample included the alignment of notches in the heavily damaged PTZ (which only is only ~500 to 1,000 µm in width), the orientation of the notch(es) relative to the HAZ, the toughness of the HAZ even after prolonged exposure in liquid nitrogen, and achieving repeatable results for a procedure. Even when an acceptable sample was eventually created, the fracture plane exhibited considerable topography necessitating a more thorough human-machine interaction than would allow for an automated analysis of a large area.

However, there remains merit in continued exploration of a routine procedure that can take advantage of this relatively simple type of assessment. In the examples provided, fractography was sufficient to show some association of cavities with inclusions like MnS.

The results detailed in this Chapter provide a promising set of information to build on regarding the application of large volume removal and reconstruction using 3D material removal processes. 3D techniques employing FIB or P-FIB were helpful to generate a unique compilation of data and to analyze subsurface damage which was not affected by the polishing procedure removing the potential for surface contamination. However, when utilizing such approaches, it was important to consider several items to provide sufficient perspective on the procedure:

- The size and number density of cavities were first well-established in 2D to determine the necessary volume of material required for removal of a set number of statistically relevant density of cavities;
- It was necessary to balance the number of SEM-EDS maps with the size of the nucleation source to better establish the rate at which the maps were collected through the FIB process. This not only affected the potential for capturing the nucleation source in the map, but also the length of the data collection process;
- An optimized P-FIB 3D reconstruction process with periodic SEM-EDS mapping linked a significant number of cavities to inclusions. 98% of the coarse cavities were linked to Al or Mn peaks (e.g. AlN, Al_2O_3 or MnS) and 56% of the coarse cavities were linked to MnS. The fine cavities were linked in 58% of the examples to Al or Mn peaks and 33% of the damage to MnS.

STEM analysis of a thin foil sample containing a local cavity just below the polished surface provided insufficient volume to fully capture a nucleation source. A cluster of AlN particles with nanoscale Cu-rich precipitates was observed adjacent to one cavity wall. Cu-rich nanoscale particles were observed elsewhere in the foil. Cr-rich precipitates were randomly distributed throughout the volume with no apparent association of damage with coarse or high density of such particles. The difficulty in targeting the cavities, its relative size to the thin foil volume and the unknown location of nucleation sources make the removal, preparation and analysis very challenging.

It should be emphasized that a routine procedure, with the potential or eventual standardization, will always be a preferred means for data development. However, the information provided in this summary emphasizes the need to often consider data collection on a sample-by-sample basis and that for very refined procedures it may not be possible to standardize the technique. Procedure-optimization is possible provided a set of well-pedigreed information is generated at relevant length scales to inform the assumption. Such considerations are becoming very important for microstructural analysis because the tools are easy-to-use, large datasets are now possible to collect, open-source software exists to analyze the data, and the potential exists for the researcher to produce a set of unique and impactful data *provided the procedures are relevant*. It is hoped then that the approaches demonstrated herein provide a foundation on which to build for future assessment of damage mechanisms in 9 wt. % Cr CSEF steels.

10 Conclusions

10.1 Summary of Learnings

Linking metallurgical risk factors in Grade 91 steel to creep ductility continues to be a primary focus for life management research. The creep ductility of the parent material is an important consideration since it is inevitable that mechanical notches present as stress concentrations and metallurgical notches present as welds are introduced through design and fabrication of complex components. Furthermore, and increasingly throughout the world it is expected that components will be subjected to cyclic operation (e.g. creep-fatigue). In each of these three scenarios (mechanical notch, metallurgical notch and creep-fatigue), it has been well documented that poor creep ductility can dramatically and detrimentally influence component performance.

For the purposes of this PhD thesis and discussed in the literature review provided in Chapter 2, the metallurgical risk factors in Grade 91 steel were fundamentally divided into factors which influence creep strength or creep ductility. It was highlighted that potential metallurgical factors affecting creep ductility in 9 wt. % Cr steels had not been sufficiently defined and that the vast majority of investigations focused solely on the factors contributing to deformation behavior. A review of the literature thus provided sufficient justification to investigate three primary themes in this thesis:

- The influence of the parent metal creep strength (deformation) and parent metal creep ductility (damage) on the cross-weld creep response using a feature-type test geometry;
- Establishing the effect of the welding process on the macro-distribution of damage through the HAZ;
- Association of damage with particles or features in the HAZ on a micro-level.

The performance of an ex-service Grade 91 steel header that operated in a power plant in the UK at a nominal steam temperature of ~570°C (1058°F) and for ~79,000 hours served as the donor material for the evaluations. A thorough review of this well-pedigreed material was provided in Chapter 4. Two specific heats of material in the ex-service condition were utilized for the experiments and were shown to have markedly different responses to creep deformation and creep damage (Chapter 6). The selected parent materials were compared for chemical composition, thermodynamic assessment and the inclusion type and density. For common second

phases particles, such as Laves, $M_{23}C_6$, and AlN, comparable densities between the two variants were reported in Chapter 4. A key distinction in the inclusions present was the elevated density of MnS in the low ductility material. This result was confirmed using a commercially available analysis procedure and an optimized approach.

Evaluation of the parent materials included the ex-service condition as well as two heat-treated conditions (the low ductility parent metal was renormalized and tempered and the high creep ductility parent metal was given a fully ferritic microstructure for comparison purposes). The final set of four parent metal conditions provided a unique opportunity to establish a relevant set of HAZ-responses. The HAZ-response was assessed for a total of six weldments where the parent metal condition, filler material and post weld heat treatment (PWHT) were systematically varied. The distribution of microstructure through the HAZ was evaluated using large-scale hardness mapping, macro-scale local assessment in the HAZ using SEM-EDS, SEM-EBSD through the HAZ, and linking these observations to the calculated temperature profile through the HAZ (Chapter 5). The evaluation of the six weldments prior to feature cross-weld testing provided several important observations:

- The formation of a soft zone in the HAZ was best described as an over-tempered zone (OTZ) whereby little or none of this region was associated with a transformed region;

- The formation of the OTZ, and its overall width, was most realistically linked to the complexity of the phase transformations that occur in the adjacent partially transformed zone (PTZ). It was rationalized that these phase transformations, particularly the $\gamma \rightarrow \alpha$ transformation on-cooling resulted in a latent heat of transformation that stabilized an elevated temperature range approximated by the Ac_1 and over a substantial width beyond the OTZ/PTZ boundary.

- Selection of the welding consumable can change the width of the HAZ. For example, the use a Ni-base filler metal with a lower melting temperature reduced the width of the HAZ whether the CTZ, PTZ and/or OTZ were considered in the measurement.

- EBSD was utilized to quantify the abrupt change in the HAZ associated with the PTZ. The PTZ initiated in a region where the calculated peak temperature

approximated by the A_1 or Ac_1 for the investigated materials and weldments. Disagreement as to the exact temperature was a function of the used equations to estimate this temperature.

The cross-weld creep behavior of the fabricated weldments was assessed using a feature-type test geometry, which provided a stress-state more representative of thick-section components. It was shown in Chapter 4 that the larger, feature-type test geometry provided a distribution and density of creep damage through the HAZ that was very different from the documented damage in the small diameter round bar test geometry (6.35 mm diameter) characteristic of most studies. This result was an important consideration in the evaluation of cross-weld creep behavior in martensitic 9 wt. % Cr steels and emphasized the importance test geometry may have on the evolution of HAZ damage in lab testing.

Assessment of cross-weld creep behavior and a link to the parent metal deformation and damage resistance was summarized in Chapter 6. It was emphasized in this set of results that parent metal creep ductility had a dominant effect on cross-weld creep behavior. This point was emphasized by the comparison of the two parent materials RNT-B2 and TP1 for which the parent material deformation response was nearly identical (the variability in time to failure was only 10%), and yet the variation in the cross-weld creep time to failure was a factor of 5. This deviation was only plausibly explained by the difference in the parent metal creep ductility; the RNT-B2 and TP1 parent metal steels varied with respect to ROA by a factor of 5 (15% versus 83%, respectively). The arrival at this conclusion was made possible by the fact that the weldments were fabricated using an identical welding procedure including the weld geometry, filler metal, PWHT and feature cross-weld test geometry.

The assessment of the cross-weld test samples provided extensive examples of time-dependent damage. The test matrix was designed to evaluate a large range of potential variables contributing to cross-weld behavior, and damage was reported in each of the four major constituents: parent metal, fusion line, weld metal and HAZ. Clarification for this observation is summarized below:

- Damage was noted in the parent metal for high stress tests (80 MPa) for 600 or 625°C tests in the ferritic parent metal cross-weld tests (F-TP1). This behavior was linked to the applied stress value, which was >50% of the yield

stress at the given test temperature. The behavior of the F-TP1 weldment approached the minimum of the cross-weld database for an applied stress of 50 or 60 MPa at 625°C. This behavior was attributed to the resistance of the material to damage initiation and the fact that behavior for cross-weld test data and ferritic parent metal behavior begins to merge for test conditions sufficiently below the yield strength of the ferritic material.

- Where an under-matching AWS type -B8 filler metal (weld 8C) was utilized, damage was widely present through the weld metal. Damage in the weld metal was not preferentially located in a specific region characterized by grain size. Rather, the association of voids or cracks with grain boundaries normal to the applied stress axis and the extent of observed cracking was a function of grain boundary length such that for low magnification imaging it *might appear* that damage is concentrated in the coarse columnar region. However, no definitive association could be made with the coarse columnar region and an increased level of damage when compared to the grain refined regions.

- Isolated and discontinuous fusion line damage was noted in the weldment fabricated with the Ni-base filler metal EPRI P87 (weld 9C). It should be noted that the extent of damage at the fusion line in these tests (600°C and 80 MPa, 625°C and 80 MPa or 625°C and 60 MPa) was not sufficient to result in a micro- or macro-level crack. Failure in all cases was reported in the HAZ.

- In the HAZ damage was observed for nearly all the evaluated weld samples. The macro-distribution of damage assessed in Chapter 7 provided several key conclusions summarized below:

    - Damage was not linked to a so-called soft-zone, often identified through routine hardness evaluation as the OTZ. As explained in prior information, the OTZ is often erroneously described as the fine-grained HAZ (FGHAZ) or inter-critical HAZ (ICHAZ) in the literature.

    - Damage is consistently identified in a region best defined as the PTZ. The definition for the PTZ in Table 1-4 was consistent with the findings in the current PhD thesis, e.g. “the original matrix is only partially re-austenitized along with a partial dissolution of the pre-existing precipitate particles.”

- Maximum damage is observed in a peak temperature range equivalent to the measured Ac_1 value (e.g. ~900°C) to just below the minimum value for normalization (~1040°C). For weldments evaluated in the as-welded condition, the distribution of damage was slightly biased to a higher temperature range approximated by the upper end of normalization for Grade 91 steel (e.g. ~1100°C).
- Macro-failures were consistently observed in the 50^{th} to 75^{th} percentiles of the damage distribution (e.g. failure occurred in a location more similar to the Ac_3 value as opposed to the Ac_1 value or the OTZ);
- Damage is ~an order of magnitude greater for the low creep ductility parent material as compared to the high ductility parent metal heat;
- The use of an over-matching filler material (Ni-base) was observed to increase the overall extent of damage through the width of the HAZ for a parent material with good creep ductility. However, the damage was not concentrated in a region at the fusion line or adjacent to the fusion line such as in the CTZ. HAZ dominated failures in the PTZ were still observed in cross-weld tests using the Ni-base filler metal. This result was a function of the selected test conditions, which under isothermal test conditions, promoted the HAZ failures (e.g. 600°C/80 MPa, 625°C/80 MPa and 625°C/60 MPa).
- The use of under-matching filler material increased the macro-distribution of damage such that damage extended into the weld metal. This resulted in a variability in failure location (weld metal or HAZ). Regardless of the reported failure location, extensive damage was identified in both the weld metal and HAZ constituents.

Assessment of damage in Chapters 8 and 9 in the HAZ was associated with second phase particles such as inclusions. The identification of damage with high-density particles such as Laves phase or $M_{23}C_6$ was attributed to the increased probability of damage association. Where damage was identified with these particles, it was apparent that the damage developed in locations where clusters of these particles existed. It is important to emphasize that the evaluation of cavity-particle association in 2D only assesses a single plane. For cavities which did not show a clear association

with a second phase particle it cannot be ascertained whether a particle existed above the cavity (and was removed by polishing) or a particle exists below the cavity (and is impossible to evaluate).

Purposeful extraction of a sub-surface cavity, and analysis of the local thin foil using TEM provided perspective regarding a potential nucleation of damage associated with AlN. However, the length scale of this assessment did not provide definitive nor conclusive statistical evidence for the association of damage with a population of second phase particles. It is for this reason that more sophisticated procedures were employed to evaluate damage in 3D and fractography (focus of Chapter 9).

The results for techniques designed to explore damage in the HAZ in 3D showed that a substantial population of voids were linked to second phase particles consistent with MnS or Al-rich (oxides or AlN). The use of the P-FIB process to remove a large section of material in the HAZ showed that for a population of ~100 cavities in the HAZ, there was an equal distribution of fine and coarse cavities. For the coarse population, 92% of the cavities were linked to Al-rich phases, 56% of the cavities were linked to MnS and 98% of the cavities were linked to either Al-rich or MnS particles. For the fine cavities, ~33% of the cavities were linked to MnS or Al-rich phases and 58% of the total cavity distribution was linked to either MnS or Al-rich particles. It is thus the conclusion that a notable distribution of cavities in the HAZ for low creep ductility parent material was associated with particles that might be controlled by modifying material specifications for composition (e.g. a reduction in the S or Al content).

10.2 Perspective on the need for Future Work

The primary driver linking the damage to specific features in the microstructure is a universal need to reduce heat-to-heat variability in 9 wt. % Cr CSEF steels. The widely documented variability in component performance complicates the life management process and sometimes makes this impossible. This point is underscored by an emerging need to increase plant efficiency or design for cyclic behavior and therefore an inherent reality that materials are being pushed to the limits of their respective performance envelope.

The disparity in plant component performance arises from two steps in the component or system fabrication stage:

1. The application of a minimum set of standards or requirements during production of common material product forms and
2. The application of a minimum set of standards or requirements at the design and fabrication stages of these materials into complex components and systems.

Whether explicit or implicit, there is an expectation that the design life for such components and systems is in the 100,000s of hours.

In some new construction or component replacement cases, it is widely understood that the minimum set of requirements at the material-manufacture or component-fabrication stages are insufficient. To supplement this ‘understood’ assumption, OEM or end-user specifications exist as documents which serve to increase the overall quality and design-for-intended application of the installed component(s). The emerging and recent global emphasis to produce plants capable of flexible operation while reducing CO_2 emissions through increased efficiency would seem to drive all stakeholders in the plant design process towards a higher level of inherent quality. This statement should be especially true given the reality that manufacturers are designing fabricated components from complex 9 wt. % Cr CSEF steels and within the maximum permissible design envelope. However, there is a growing emphasis within the power generation industry to contain cost at all stages of the life management process, including the upfront design and procurement of materials. This results in an attitude that treats current requirements as *the standard* as opposed to a *minimum standard*. Simply stated, this reality is challenging current research emphasis since for materials designed to operate close to or at a recognized limit, there is a real and present need to more completely link metallurgical risk factors in the manufactured product to its potential in-service performance for an anticipated life >100,000 hours.

In countless service experience examples, an overwhelming need arises in the evaluation of weldment performance for critical components and/or features. This point must emphasize the assessment of damage in cross-weld creep samples in CSEF steels with specific microstructural features. Grade 91 steel possesses several types of particles; Laves phase, MX carbonitrides, $M_{23}C_6$, inclusions and potentially Z-phase (if Cr is elevated or segregation in the product is present) or BN (if B is not controlled). For a distribution of particles there may exist variability with the present compositional

segregation resulting from the steel-making process. For commonly observed particles, either in the as-fabricated or post-service state, statistical methods for assessing particle type and density are desperately needed to assist life management practices. These approaches should consider the potential for segregation in the steel and emphasize standardized procedures that can be universally applied for new, post-service or lab-evaluated materials.

When a weld is superimposed on the final product form, the evaluation of microstructural features which might contribute to component behavior is complicated by the introduction of the HAZ which creates a second set of potentially important factors. In the minimum, the literature claims the following factors *might be* relevant to cross-weld creep behavior:

1. Grain boundary size or length;
2. Presence of particles on boundaries (which is very likely given the typical grain size and size of particle) and the potential for coarse particles at grain boundary features like triple points;
3. Interaction of adjacent, martensitic grains with a clear substructure grain interior with ferrite grains that are featureless;
4. Interaction of adjacent grains in the HAZ with a measurable density of second phase $M_{23}C_6$ or MX phases with grains that are precipitate-free.

The illustration above and in the prior discussion emphasizes that a single procedure cannot rationalize a set of observations in a meaningful context. Similar procedures, if not standardized, are vital for researchers to provide common observations or to challenge the status quo in these complex materials.

Linking damage in a structure to the phases present, grain boundaries or other features presents a 3D-problem. A statistically relevant set of 3D-observations can provide confidence in a more simplistic 2D-assessment. However, the process for performing 3D assessment is still not well-developed. As procedures become more widespread, for example large volume removal and in-situ quantitative assessment using P-FIB, the confidence in routine observations should be increased by systematic evaluation.

Recent assessments reported by Abe (2019), Xu (2017) and reassessment of a sample conducted by Masuyama et al. (Masuyama 2017b) show for an additional set of test results in 9 wt. % Cr CSEF steels there is an evolving set of learnings which both support and apparently are at odds with the findings presented in the current thesis. Clarification is provided below to shed light on the need for continued research.

- There is well-documented evidence for Grade 91 steel that heat-to-heat variability must be considered in weldment behavior. For parent metal with poor creep ductility and documented high levels of S and Al, such as examined in this PhD thesis, the cross-weld creep behavior was poor. The on-going evaluation of a sample provided from a Grade 91 sample, with exceptionally low S and tramp elements, the nucleation of cavities may be isolated to grain boundary features in the microstructure which manifest as a ‘spider web’ cluster of linked micro-cracks. It is clearly the case that extremes in behavior should be understood as opposed to a focus on heats of material which represent ‘mean behavior.’
- The balance of information available for Grade 92 steel shows that the formation of BN is a dominant consideration in the cavity nucleation behavior and this is reflected in parent metal and cross-weld testing. The difficulty in removing BN from this steel is demonstrated by the work of Sakuraya et al. (2006) and a recent evaluation of behavior by Abe et al. (2019). Additional work building on the thesis of Xu reflects a very strong association of damage in cross-weld creep tests in Grade 92 with BN (Xu 2017).

In summary, the association of damage in Grade 91 and Grade 92 CSEF steels is linked to a hierarchy of susceptible particles. This reality is manifested by a link to the parent material where a critical density of susceptible particles is linked to a reduction in the creep ductility. In cross-weld creep tests, there can exist a more marked reduction in cross-weld creep life when susceptible particles are present. This reality, whether detailed in the current PhD research in Grade 91 steel or in the literature, has identified a need for continued application of conventional, state-of-the-art, and evolving electron-based microstructural techniques. This need is predicated on an overall reality that faces end-user/owner/operators, who are expected to manage

components fabricated from 9 wt. % Cr steels over the next several decades. As such, a summarized set of needs are summarized below:

1. Understanding the consequence of major steel making processes on the final product form. These processes are very simply divided into: casting of billet; forging of billet into the final product form; and final heat treatment.

2. Emphasis on relevant, perhaps standardized, test conditions to permit comparison of data produced in a global research environment to address issues specific to screening for heat-to-heat or material-to-material behavior and development of relevant data to support new construction best practices.

3. Characterization of damage in test samples to link the development of damage to specific features in the microstructure responsible for damage or deformation. The emphasis in this point is irrelevant if the material is not well-characterized by a given steel-making process nor if the selected test conditions do not result in relevant damage.

4. Development of standardized procedures for analysis of microstructure and damage in steels using conventional electron-microscopy-based techniques. This might include open-source software to allow for the evaluation of Laves phase, $M_{23}C_6$ and inclusions or other relevant second phase particles (such as BN).

5. Linking 3D analysis to more-easily-produced results using 2D techniques.

It is often the case that researchers come to believe that the research for a given material may reach ‘maturity’ resulting in a less-justifiable need for continued or sustained research and development. However, steel-making practices may change, fabrication steps once widely-employed as ‘best practice’ might be eliminated, and subtle economic drivers (such as the need to use scrap metal) can drive changes in the manufactured product. We must appreciate these realities and recognize an over-arching need to push a sustained philosophy for research in widely utilized materials and not for merely focus on ‘new’ or emerging steels or materials. If history is a precursor to the future, then for Grade 22, a relatively simple low alloy CrMo steel which saw its initial widespread use in the 1940s, 1950s and 1960s, is still widely specified today – some 75 years later. By comparison Grade 91 saw widespread use

in the early 1990s (30 years ago) and Grade 92 in the late 2000s (15 years ago). It is thus the case that much remains to be discovered and learned even for materials which might be widely regarded to be well-understood.

11 References

F. Abe and M. Tabuchi. “Microstructure and Creep Strength of Welds in Advanced Ferritic Power Plant Steels.” *Science and Technology of Welding and Joining 9* (1), 2004. pp. 22 to 30.

F. Abe. “Precipitate Design for Creep Strengthening of 9% Cr Tempered Martensitic Steel for Ultra-supercritical Power Plants.” *Science and Technology of Advanced Materials 9* (1), 2008. pp. 1 to 15.

Creep Resistant Steels, 1st edition, ed. F. Abe, T. Kern and R. Viswanathan. Woodhead Publishing: 2008. B. Wilshire and H. Burt. “Chapter 15: Creep Strain Analysis for Steel.”

F. Abe, M. Tabuchi, S. Tsukamoto and T. Shirane. "Microstructure Evolution in the HAZ and Suppression of Type IV Fracture in Advanced Ferritic Power Plant Steels," in International Conference WELDS 2009, Fort Myers, FL, July 2009.

F. Abe. “Grade 91 Heat-Resistant Martensitic Steel” *in Coal Power Plant Materials and Life Assessment: Developments and Applications* ed. A. Shibli. Woodhead Publishing, United Kingdom: 2014. pp. 3 to 46.

F. Abe. "Grade 91 Heat-resistant Martensitic Steel." in *Coal Power Plant Materials and Life Assessment*, Cambridge, UK, Woodhead Publishing, 2014, pp. 1 to 51.

F. Abe, T. Ohba, H. Miyazaki, Y. Toda and M. Tabuchi. “Effect of W-Mo Balance and Boron Nitrides on Creep Rupture Ductility of 9Cr Steel.” *Materials at High Temperatures*, published online February 2, 2019.

D. J. Abson and J. S. Rothwell. “Review of Type IV Cracking of Weldments in 9-12 wt. % Cr Creep Strength Enhanced Ferritic Steels.” *International Materials Review* 58 (8), 2013. pp. 437 to 473.

R. Agamennone, W. Blum, C. Gupta and J.K. Chakravartty. "Evolution of microstructure and deformation resistance in creep of tempered martensitic 9–12 wt. % Cr–2%W–5%Co steels." *Acta Materialia* 54 (11), 2006. pp. 3003 to 3014.

P. J. Alberry and W. K. C. Jones. “Diagram for the Prediction of Weld Heat-affected Zone Microstructure.” *Metal Science* 4 (1), 1977. pp. 360 to 364.

S. K. Albert, M. Matsui, T. Watanabe, H. Hongo, K. Kubo and M. Tabuchi. “Microstructural Investigations on Type IV Cracking in a High Cr Steel.” *ISIJ International* 42 (12), 2002. pp. 1497 to 1504.

B. T. Alexandrov, L. Wang L., J. A. Siefert, J. K. Tatman, J. C. Lippold. "Phase Transformations In Creep Strength Enhanced Ferritic Steel Weld," *Machines, Technologies, Materials* 4 (1), 2012. pp. 33 to 36.

D. J. Allen and S. T. Fenton. “A hardness-based creep rupture model for new and service aged P91 steel.” *Proceedings of the International Conference on Life Management and Maintenance for Power Plants BALTICA VII*, VTT, 2007. pp. 156–170.

F. Arav, H. J. M. Lentferink, C. F. Etienne and J. C. van Wortel. “Effect of Fabrication Processes on the Creep Behavior of 9-12% Chromium Steels.” *Proceedings of the Fifth International Conference on Creep of Materials*, 1992. pp. 117 to 125.

“Plate. A516 and A387 Pressure Vessel Steels: A Technical Overview.” ArcelorMittal USA, September 2013.

H. G. Armaki, R. Chen, K. Maruyama and M. Igarashi. "Creep Behavior and Degradation of Subgrain Structures Pinned by Nanoscale Precipitates in Strength-Enhanced 5 to 12 Pct Cr Ferritic Steels." *Metallurgical and Materials Transactions A* 42A (10), 2011. pp. 3084 to 3094.

M. F. Ashby and B. F. Dyson. “Creep Damage Mechanics and Micromechanisms.” *Proceedings of the 6th International Conference on Fracture*, 1984. pp. 3 to 30.

M. F. Ashby and K. E. Easterling. “A First Report on Diagrams for Grain Growth in Welds.” *Acta Materialia* 30, 1982. pp. 1969 to 1978.

ASME Boiler and Pressure Vessel Code Section I: Rules for Construction of Power Boilers. The American Society of Mechanical Engineers, New York, NY. Interpretation I-89-30 issued September 18, 1989.

American Society of Mechanical Engineers Boiler and Pressure Vessel Code Section I. New York: 2017. Table PW-39-5.

American Society of Mechanical Engineers Boiler and Pressure Vessel Code Section I. Appendix A-317.

American Society of Mechanical Engineers Boiler and Pressure Vessel Code Section II, Part A. New York: 2017.

American Society of Mechanical Engineers Boiler and Pressure Vessel Code Section II, Part D. New York: 2017.

“Case 2179: 9Cr-1Mo-1W-Cb Material.” *Cases of American Society of Mechanical Engineers Pressure Vessel.* Code Case 2179-8, Approved June 28, 2012.

“Case 2180: Seamless 12Cr-2W Material.” *Cases of American Society of Mechanical Engineers Pressure Vessel.* Code Case 2180-6. Approval Date: August 11, 2010.

“Case 2199: 9Cr-1Mo-1W-Cb Material.” *Cases of American Society of Mechanical Engineers Pressure Vessel.* Code Case 2199-6, Approved April 4, 2011.

“Case 2327: 9Cr-1Mo-1W-Cb Material.” *Cases of American Society of Mechanical Engineers Pressure Vessel.* Code Case 2327-2, Approved January 29, 2009.

“Case 2540: 2.25Cr-1Mo-V-B-Ti Material.” *Cases of American Society of Mechanical Engineers Pressure Vessel.* Code Case 2540, Approved July 2, 2010.

“Case 2781: 12Cr-1.5W-1.6Co-B Material.” *Cases of American Society of Mechanical Engineers Pressure Vessel.* Code Case 2781, Approved October 23, 2013.

ASTM E384-11e1, Standard Test Method for Knoop and Vickers Hardness of Materials, ASTM International, West Conshohocken, PA, 2011, www.astm.org. DOI: 10.1520/E0384-11E01.

R. W. Bailey. Creep of Steel Under Simple Compound Stress. *Engineering* 121, 1930. pp. 265.

W. T. Bakker and B. Nath. “Development and Testing of Ferritic Steels for Advanced Power Plants.” In *New Steels for Advanced Power Plants II, Phase 2: Development of Advanced 9-12 Cr Steels for Thick Section Boiler Applications*. EPRI, Palo Alto, CA: 2001. 1006281. pp. 1-5.

M. Bauer, E. Roos, A. Klenk and K. Maile. “Investigations on the High Temperature Behaviour of Welded Martensitic Joints.” *Engineering Fracture Mechanics 77* (15), 2010. pp. 3000 to 3010.

W.Bendick, B. Hahn and W. Schendler. “Development of Creep Damage in Steel Grades X10CrMoVNb9-1 (P/T 91) and X20CrMoV12-1.” *Advances in Material Technology for Fossil Power Plants, Proceedings of the 3rd Conference*, CRC Press: 2001. pp. 299 to 308.

H. K. D. H. Bhadeshia. “Mechanisms and Models for Creep Deformation and Rupture” in *Comprehensive Structural Integrity Volume 5: Creep and High-temperature Fatigue*, ed. I. Milne, R. O. Ritchie and B. Karihaloo. Elsevier, 2003. pp. 1 to 23.

V. Biss. “Metallographic Investigation of Soft Regions near Heat Affected Zones of Modified 9Cr-1Mo, HT-9 and 2-1/4Cr-1Mo Steel Weldment.” Climax Molybdenum Compony of Michigan Status Report J-4747, March 1982.

A. M. Bissell, B. J. Cane and J. F. DeLong. “Remnant Life Assessment of Seam Welded Pipework.” *Proceedings of the International Conference on Life Assessment and Extensio*n, 1988. pp. 203 to 211.

N. R. Blount and J. W. Taylor. “Current Status and Application of Steel P.91 in the UK Boiler Programme.” *Third International Conference on Improved Coal-Fired Power Plants*, EPRI, Palo Alto, CA: 1992. TR-100848. pp. 31-1 to 31-17.

S. J. Brett, D. J. Allen and J. Pacey. “Failure of a Modified 9 wt. % Cr Header Endplate.” *Case Histories on Integrity and Failures in Industry*. EMAS Engineering Materials Advisory Services Limited, 1999. pp. 873 to 884.

S. J. Brett. “Type IIIa Cracking in 1/2CrMoV Steam Pipework Systems.” Science and Technology of Welding and Joining 9 (1), 2004. pp. 41 to 45.

S. J. Brett, J. S. Bates and R. C. Thomson, “Aluminum Nitride Precipitation in Low Strength Grade 91 Power Plant Steels.” *Proceedings of the 4th International Conference on Advances in Materials Technology for Fossil Power Plants*, ASM International: 2004. pp. 1183 to 1197.

S. J. Brett. “In-Service Type IV Cracking in a Modified 9 wt. % Cr (Grade 91) Header-Update.” ETD Workshop on Industry & Research Experience in the use of T/P91, P/T92, P/T122, T23 T24 & other new Steels in HRSG & Conventional Boilers. June 2007, London, UK.

S. J. Brett, D. J. Allen and L. W. Buchanan. “The Type IV Creep Strength of Grade 91 Materials.” *Proceedings of the 3rd International Conference on the Integrity of High Temperature Welds*. IOM, 2007.

S. J. Brett. “Early Type IV Cracking on Two Retrofit Grade 91 Steel Headers.” *IIW International Conference: Safety and Reliability of Welded Components in Energy and Processing Industry*, Graz, Austria, July 10–11, 2008.

S. J. Brett. “Estimated Timescale for the Onset of Type IV Cracking in Grade 91 Power Plant Components.” *Proceedings of the 6th International Conference on Advances in Materials Technology for Fossil Power Plants*, ASM International: 2010. pp. 752 to 761.

M. Brookes. “Microstructural Characterisation of an Ex-service Steel Header with Poor Creep Resistance.” Senior project supervised by Dr. G. West, Loughborough University, 2015.

R. Bruscato. “Temper Embrittlement and Creep Embrittlement of 2 1/4Cr1Mo Shielded Metal Arc Weld deposits,” *Welding Research Supplement*, 1970. pp.148s–156s.

B. J. Cane. “Estimating the Remnant Creep Life of Power Plant Components.” *High Temperature Technology* 1 (4), 1983. pp. 215 to 228.

B. J. Cane and G. W. Greenwood. “The Nucleation and Growth of Cavities in Iron during Deformation at Elevated Temperatures.” *Metal Science* 9 (1), 1975. pp. 55 to 60.

B. J. Cane and C. J. Middleton. “Intergranular Creep-cavity Formation in Low-alloy Bainitic Steels.” *Metal Science* 15 (7), 1981. pp. 295 to 301.

G. M. D. Cantin, W. Mazur, H. K. D. H. Bhadeshia and J. A. Francis. “Effects of Weld Preheat Temperature and Heat Input on Type IV Failure.” *Science and Technology of Welding and Joining 14* (5), 2009. pp. 436 to 442.

B. J. Cane and C. J. Middleton. “Intergranular Creep Cavity Formation in Low Alloy Bainitic Steels.” CEGB Laboratory Note No. RD/L/N 195/80.

H. Cerjak and P. Mayr and C. Schlacher. “Creep Strength of Welded Joints of Ferritic Steels” in *Creep Resistant Steels*, ed. F. Abe, T. Kern and R. Viswanathan. Woodhead Publishing Limited: 2008. pp. 477.

H. Chilukuru, K. Durst, S.Wadekar, M. Schwienheer, A. Scholz, C. Berger, K.H. Mayer and W. Blum. "Coarsening of Precipitates and Degradation of Creep Resistance in Tempered Martensite Steels," *Materials Science and Engineering A* 510-511, 2009. pp. 81 to 87.

L. Cipolla, A. Di Gianfrancesco, G. Cumino, and S. Caminada. “Long Term Creep Behaviour and Microstructural Evolution of ASTM Grade 91 steel.” *Proceedings of the 4th International Conference on Advances in Materials Technology for Fossil Power Plants*, ASM International: 2004. pp. 1071 to 1085.

L. Cipolla, A. Di Gianfrancesco, D. Venditti, G. Cumino and S. Caminada. “Microstructural Evolution during Long Term Creep Tests of 9 wt. % Cr Steel Grades.” *Proceedings of CREEP8, 8th International Conference on Creep and Fatigue at Elevated Temperatures*. July 22-26, 2007, San Antonio, TX. Paper PVP2007-26030.

L. Cipolla, S. Caminada, D. Venditti, H. K. Danielsen and A. Di Gianfrancesco. "Microstructural Evolution of ASTM P91 after 100,000 hours Exposure at 550C and 600C," in *9th Liege Conference: Materials for Advanced Power Engineering* 2010, Liege, Belgium, 2010.

A. C. F. Cocks. “The Nucleation and Growth of Voids in a Material Containing a Distribution of Grain-Boundary Particles.” *Acta Metallurgica* 33 (1), 1985. pp. 129 to 137.

S. A. David, J. A. Siefert, and Z. Feng. “Welding and Weldability of Candidate Ferritic Alloys for Future Advanced Ultrasupercritical Fossil Power Plants.” *Science and Technology of Welding and Joining 18 (8), 2013*. pp. 631 to 651.

A. Di Gianfrancesco, O. Tassa and S. Spigarelli. “Correlation between Microstructural Evolution and Creep Response in 9Cr-1Mo and 9Cr-1Mo-NbVW Heat-Resistant Steels” in *Modelling of Microstructural Evolution in Creep Resistant Materials*, ed. A. Strang. IOM Communications, London: 1999. pp. 161 to 176.

V. Dudko, A. Belyakov, D. Molodov and R. Kaibyshev. "Microstructure Evolution and Pinning of Boundaries by Precipitates in a 9 pct Cr Heat Resistant Steel during Creep." *Metallurgical and Materials Transactions A* 44A (1), 2013. pp. S162 to S172.

B. F. Dyson and M. F. Ashby. "Creep Damage Mechanics and Micromechanisms." in *Advances in Fracture Research*, vol. 1, Oxford, UK, Pergamon Press, 1984, p. 3 to 30.

B. F. Dyson and T. B. Gibbons. “Tertiary Creep in Nickel- base Superalloys: Analysis of Experimental data and Theoretical Synthesis.” *Acta Metallurgica* 35 (9), 1987. pp. 2355 to 2369.

K. Easterling. *Introduction to the Physical Metallurgy of Welding, 2nd Edition*. Butterworth-Heinemann Ltd., 1992.

G. Eggeler, J. C. Earthman, N. Nilsvang and B. Ilschner. “Microstructural Study of Creep Rupture in a 12% Chromium Ferritic Steel.” *Acta Metallurgica* 37 (1), 1989. pp. 49 to 60.

F. V. Ellis, S. O. Hilton, J. F. Henry and J. E. Bynum. “Influence of Service Experience on Base and Weld Metal of ½Cr-½Mo-¼V High-Pressure Steam Inlet Piping.” *Transactions of the ASME* 104, 1982. pp. 120 to 129.

P.J. Ennis, A. Zielińska-Lipiec and A. Czyrska-Filemonowicz. “Influence of heat treatments on microstructural parameters and mechanical properties of P92 steel.” *Materials Science and Technology* 16 (10), 2000. pp. 1226 to 1233.

P.J. Ennis. “Creep Strengthening Mechanisms in High Chromium Steels.” *Advances in Materials Technology for Fossil Power Plants: Proceedings of the 3rd International Conference,* ed. R. Viswanathan, W. T. Bakker and J. D. Parker. IOM Communications, London: 2001. pp. 187 to 194.

Review of Type IV Cracking in Piping Welds. EPRI, Palo Alto, CA: 1997. TR-108971.

Grade 22 Low Alloy Steel Handbook: 2-1/4Cr-1Mo, 10CrMo9 10, 622, STPA24. EPRI, Palo Alto, CA: 2005. 1012840.

X20 CrMoV12-1 Steel Handbook. EPRI, Palo Alto, CA: 2006. 1012740. (EPRI 2006a)

TULIP 2.0: A Computer Code for Probabilistic Analysis of Superheater/Reheater Tubing. EPRI, Palo Alto, CA: 2006. 1010621. (EPRI 2006b)

Service Experience with Grade 91 Components. EPRI, Palo Alto, CA: 2009. 1018151.

Life Management of Creep-Strength- Enhanced Grade 91 Steels—Atlas of Microstructures: Base Metal. EPRI, Palo Alto, CA: 2013. 3002000080. (EPRI 2013a).

Life Management of Creep Strength Enhanced Grade 91 Steel – Atlas of Microstructures and Welds. EPRI, Palo Alto, CA: 2013. 3002000081. (EPRI 2013b).

Life Management of Creep Strength Enhanced Grade 91 Steel: Damage Calculator. EPRI, Palo Alto, CA: 2013. 3002000082. (EPRI 2013c).

The Benefits of Improved Control of Composition of Creep-Strength-Enhanced Ferritic Steel Grade 91. EPRI, Palo Alto, CA: 2014. 3002003472. (EPRI 2014a).

The Influence of Steel Making and Processing Variables on the Microstructure and Properties of Creep-Strength-Enhanced Ferritic (CSEF) Steel Grade 91. EPRI, Palo Alto, CA: 2014. 3002004370. (EPRI 2014b).

Best Practice Guideline for Well-Engineered Weld Repair of Grade 91 Steel. EPRI, Palo Alto, CA: 2014. 3002003833. (EPRI 2014c).

Well-Engineered Weld Repair of Grade 91 Steel: Results for Through-thickness Repair Welds. EPRI, Palo Alto, CA: 2014. 3002004476. (EPRI 2014d).

Life Management of Creep Strength Enhanced Ferritic Steels: *Solutions for the Performance of Grade 91 Steel – Overview*. EPRI, Palo Alto, CA: 2014. 3002000083. (EPRI 2014e).

Well-Engineered Weld Repair of Grade 91 Steel: Analysis of Welding Geometry on Creep Performance. EPRI, Palo Alto, CA: 2015. 3002004484. (EPRI 2015a).

A Perspective on the Selection of Preheat, Interpass and Post-weld Cool Temperatures Using Grade 91 Steel as an Example. EPRI, Palo Alto, CA: 2015. 3002005351. (EPRI 2015b).

A Well-Engineered Approach for Establishing the Minimum Allowable Post Weld Heat Treatment for Power Generation Applications of Grade 91 Steel. EPRI, Palo Alto, CA: 2015. 3002005350. (EPRI 2015c).

Nondestructive Methods for Detection of High-Temperature Damage in Creep-Strength-Enhanced Ferritic Steels (Grades 91 and 92) as a Basis for Life Evaluation. EPRI, Palo Alto, CA: 2015. 3002005187. (EPRI 2015d).

Service Experience with CSEF Steels in Power Plants in the Asia-Pacific Region. EPRI, Palo Alto, CA: 2015. 3002005089. (EPRI 2015e).

Guidelines and Specifications for High-Reliability Fossil Power Plants, 2nd Edition: Best Practice Guideline for Manufacturing and Construction of Grade 91 Steel Components. EPRI, Palo Alto, CA: 2015. 3002006390. (EPRI 2015f).

Data Compilation for Grade 91 Steel Creep-Fatigue Datasheets. EPRI, Palo Alto, CA: 2015. 3002003260. (EPRI 2015g).

An Informed Perspective on the Use of Hardness Testing in an Integrated Approach to the Life Management of Grade 91 Steel Components. EPRI, Palo Alto, CA: 2016. 3002007320. (EPRI 2016a).

Well-Engineered Weld Repair of Grade 91 Steel: Analysis of the Effect of Welding Geometry on Creep Performance and a Summary of Lessons Learned. EPRI, Palo Alto, CA: 2016. 3002004484. (EPRI 2016b).

Life Management of 9 wt. % Cr Steels: Evaluation of Metallurgical Risk Factors in Grade 91 Steel Parent Material. EPRI, Palo Alto, CA: 2018. 3002009678.

R. W. Evans, J. D. Parker and B. Wilshire. *Recent Advances in Creep and Fracture of Engineering Materials and Structures*, B. Wilshire and D. R.J. Owen, eds., Pineridge Press, Swansea, UK, 1982. pp. 135–84.

A. Fabricius and P. S. Jackson. “Premature Grade 91 Failures – Worldwide Plant Operational Experiences.” *Engineering Failure Analysis* 66, 2016. pp. 398 to 406.

I. Fedorova, A. Belyakov, P. Kozlov, V. Skorobogatykh, I. Shenkova and R. Kaibyshev. "Laves-phase Precipitates in a Low-carbon 9% Cr Martensitic Steel during Aging and Creep at 923K." *Materials Science and Engineering A* 614, 2014. pp. 153 to 163.

M. Ferranti. “Weld Simulated US Mod 9Cr1Mo Steel – Part 2: Softening Phenomenon at the Base Metal – Heat Affected Zone Interface. CEGB Report RD/M/1712/RR88, January 1989.

Private Correspondence with Jude R. Foulds, February 2017.

J. A. Francis, W. Mazur and H. K. D. H. Bhadeshia. “Type IV Cracking in Ferritic Power Plant Steels.” *Materials Science and Technology 22* (12), 2006. pp. 1387 to 1395.

J. A. Francis, H. K. D. H. Bhadeshia and P. J. Withers. “Welding Residual Stresses in Ferritic Power Plant Steels.” *Materials Science and Technology* 23 (9), 2007. pp. 1009 to 1020.

S. Fujibayashi. “Grain Boundary Damage Evolution and Rupture Life of Service-exposed 1.25Cr-0.5Mo Steel Welds.” *ISIJ International* 43 (12), 2003. pp. 2054 to 2061.

S. Fujibayashi and T. Endo. “Creep Behavior at the Intercritical HAZ of a 1.25Cr-0.5Mo Steel.” *ISIJ International* 42 (11), 2002. pp. 1309 to 1317.

H. C. Furtado, L. H. de Almeida and I. Le May. “Precipitation in 9Cr-1Mo Steel after Creep Deformation.” *Materials Characterization* 58 (1), 2007. pp. 72 to 77.

V. Gaffard. “Experimental Study and Modelling of High Temperature Creep Flow and Damage Behaviour of 9Cr1Mo-NbV Steel Weldments.” Thesis accepted by Paris Institute of Technology, December 2004.

E. P. George, P. L. Li and D. P. Pope. “Creep Cavitation in Iron – I. Sulfides and Carbides as Nucleation Sites.” *Acta Metallurgica* 35 (10), 1987. pp. 2471 to 2486.

E. P. George, P. L. Li and D. P. Pope. "Creep Cavitation in Iron: Impurity Effects." in *Creep and Fracture of Engineering Materials and Structures,* Swansea, 1987.

E. P. George, R. L. Kennedy and D. P. Pope. “Review of Trace Element Effects on High-Temperature Fracture of Fe- and Ni-base Alloys.” *Physica Status Solida (A) Applied Research* 167 (2), 1998. pp. 313 to 333.

M. Gold, J. Hainsworth and J. M. Tanzosh. “Service Experience with Design and Manufacturing Approaches with T/P91 Materials.” *EPRI Conference on 9 wt. % Cr*

Materials Fabrication and Joining Technologies. EPRI, Palo Alto, CA: 2001. 1006299. pp. 15-1 to 15-20.

I. W. Goodall, R. D. H. Cockroft and E. J. Chubb. “An Approximate Description of the Creep Rupture of Structures.” *International Journal of Mechanical Sciences* 17 (5), 1975. pp. 351 to 360.

I. W. Goodall and R. A. Ainsworth. “Failure of Structures by Creep.” *Proceedings of the Conference on Materials and Fabrication*, 1977. pp. 871 to 885.

S. H. Goods and L. M. Brown. “The Nucleation of Cavities by Plastic Deformation, Overview No. 1.” *Acta Metallurgica* 27, 1979. pp. 1 to 15.

G. J. Grant, J. Darsell and D. Catalani. “Solid State Joining of Creep Enhanced Ferritic Steels.” Presented at the Department of Energy and National Energy Technology Laboratory Crosscutting Technology Research Review Meeting, April 27 to May 1, 2015. Pittsburgh, PA.

O. Grong. *Metallurgical Modelling of Welding, 2nd Edition*. Editor H. K. D. H. Bhadeshia. The Institute of Materials, Cambridge, UK: 1997. pp. 3, 35, 40.

Y. Gu, G. D. West, R. C. Thomson and J. D. Parker. "Investigation of Creep Damage and Cavitation Mechanisms in P92 Steels," in *Proceedings of the 7th International Conference on Advances in Materials Technology for Fossil Power Plants*, Waikoloa, Hawaii, 2013.

Y. Gu. “Microstructural Investigation of Creep Behaviour in Grade 92 Power Plant Steels.” Thesis accepted by Loughborough University in 2017.

J. Hald. "Microstructure and Long-Term Creep Properties of 9-12% Cr Steels," in *Proceedings of the ECCC Creep Conference on Creep and Fracture in High Temperature Components*, London, UK, September 2005.

J. Hald and H. K. Danielsen. "On the Nulceation and Dissolution Process of Z-phase Cr(V, Nb)N in Martensitic 12 wt. % Cr Steels." *Materials Science and Engineering A* 505, 2009. pp. 169 to 177.

E. M. Haney, F. Dalle, M. Sauzay, L. Vincent, I. Tournie, L. Allias and B. Fournier. “Macroscopic Results of Long-term Creep on a Modified 9 wt. % Cr-1Mo steel (T91).” *Materials Science and Engineering A* 510-511, 2009.pp. 99 to 103.

J. J. Sanchez-Hanton, “Microstructural Evolution in Grade 91 (9Cr1MoVNb) Power Plant Steels.” PhD Thesis, University of Loughborough, October 2007.

Y. Hasegawa, M. Sugiyama and K. Kawakami. “Type IV Damage Mechanism due to the Microstructure Weakening in the HAZ of a Multi-Layer Welded Joint of the W Containing 9 wt. % Cr Ferritic Creep Resistant Steel.” *2nd ECCC Conference on Creep and Fracture in High Temperature Components: Design and Life Assessment Issues*, DSTech Publications Inc., 2009. pp. 995 to 1006.

J. H. Hollomon and L. C. Jaffe. “Time-Temperature Relations in Tempering Steel.” *Transactions of AIME* 162 (1945). pp. 223 to 249.

H. Hongo, M. Tabuchi and T. Watanabe. “Type IV Creep Damage Behavior in Gr.91 Steel Welded Joints.” *Metallurgical and Materials Transactions A* 43A, 2012. pp. 1163 to 1173.

E. Hosseini, S. R. Holdsworth and E. Mazza. “The LICON Methodology for Predicting Long-time Uniaxial Creep Rupture Strength of Materials.” *International Journal of Pressure Vessels and Piping* 111-112, 2013. pp. 27 to 35.

T. H. Hyde, W. Sun, A. A. Becker and J. A. Williams. “Effect of Weld Angle and Axial Load on the Creep Failure Behaviour of an Internally Pressurized Thick Walled CrMoV Pipe Weld.” *International Journal of Pressure Vessels and Piping* 78 (5), 2001. pp. 365 to 372.

DIN EN ISO 6507: Metallic Materials – Vickers Hardness Test Part 1: Test Method. ISO, Geneva, Switzerland: 2005. pp. 1-19.

D. Jandova, J. Kasl and V. Kanta. “Influence of Substructure on Creep Failure of P91 Steel Weld Joints.” *2nd ECCC Conference on Creep and Fracture in High Temperature Components: Design and Life Assessment Issues*, DSTech Publications Inc., 2009. pp. 177 to 188.

D. Jandova and J. Kasl. “Influence of Precipitation on Dislocation Substructure and Creep Properties of P91 Steel Weld Joints.” *Materials at High Temperatures* 27 (2), 2010. pp. 135 to 140.

D. R. Jara. “9-12% Cr Heat Resistant Steels: Alloy Design, TEM Characterisation of Microstructure Evolution and Creep Response at 650C.” Thesis accepted by Ruhr University Bochum, 2011.

Private conversation with Mahmud Jarrar, 2016.

W. K. C. Jones and P. J. Alberry. “The Role of Phase Transformations in the Development of Residual Welding Stresses.” CEGB Report R/M/R244.

K. Kaneko, S. Matsumura, A. Sadakata, K. Fujita, W. J. Moon, S. Ozaki, N. Nishimura and Y. Tomokiyo. "Characterization of Carbides at Different Boundaries of 9Cr-steel." *Materials Science and Engineering A* 374, 2004. pp. 82 to 89.

S. T. Kimmins, M. C. Coleman and D. J. Smith. “An Overview of Creep Failure Associated with Heat Affected Zones of Ferritic Weldments.” *Proceedings of the Fifth International Conference on Creep and Fracture of Engineering Materials and Structures*, 1993. pp. 686.

K. Kimura. “Assessment of Long-term Creep Strength and Review of Allowable Stress of High Cr Ferritic Creep Resistant Steels.” Proceedings of the ASME Pressure Vessels and Piping Conference 2005. PVP2005-71039, pp. 237 to 244.

K. Kimura. “Present Status and Future Prospect of NIMS Creep Data Sheet.” *Proceedings of the Creep Deformation and Fracture, Design and Life Extension Symposium held at the Materials Science and Technology 2005 (MS&T 2005) Conference*, MS&T: 2005. pp. 97 to 106.

K. Kimura, K. Sawada and H. Kushima. "Creep Rupture Ductility of Creep Strength Enhanced Ferritic Steels." Journal of Pressure Vessel Technology 134 (3), 2012. Article Number 031403.

K. Kimura and K. Sawada. “Influence of Chemical Composition and Materials Processing on Creep Strength of Grade 91 Steels.” *Proceedings to the 4th International ECCC Conference on Creep and Fracture*, September 2017.

B. L. King. “Intergranular embrittlement in CrMoV steels: An assessment of the effects of residual impurity elements on high temperature ductility and crack growth,” *Philosophical Transactions of the Royal Society A*, 1980. pp. 235 to 251.

A. Kipelova, R. Kaibyshev, A. Belyakov and D. Molodov. "Microstructure Evolution in a 3% Co Modified P911 Heat Resistant Steel under Tempering and Creep Conditions." *Materials Science and Engineering* A 528, 2011. pp. 1280 to 1286.

H. Kitahara, R. Ueji, N. Tsuji and Y. Minamino. "Crystallographic Features of Lath Martensite in Low-Carbon Steel." *Acta Materialia* 54 (3), 2006. pp. 1279 to 1288.

S. Kobayashi, K. Sawada, T. Hara, H. Kushima and K. Kimura. "Heat-to-Heat Variation in Creep Rupture Ductility of ASME Gr.91 Steels in the Long-term - Investigation into Recovery of Microstructure and Void Formation." in *Proceedings of the 7th International Conference on Advances in Materials Technology for Fossil Power Plants*, Waikoloa, Hawaii, 2013.

S. Kobayahsi, K. Sawada, T. Hara, H. Kushima and K. Kimura. "The Formation and Dissolution of Residual Delta Ferrite in ASME Grade 91 Steel Plates." *Materials Science and Engineering A* 592, 2014. pp. 241 to 248.

T. Kojima, K. Hayashi and Y. Kajita. “HAZ Softening and Creep Rupture Strength of High Cr Ferritic Steel Weldments.” *ISIJ International* 35 (10), 1995. pp. 1284 to 1290.

N. Komai, T. Tokiyoshi, T. Igari, H. Ohyama, F. Masuyama and K. Kimura. “Experimental Observation of Creep Damage Evolution in Seam-welded Elbows of Mod. 9Cr-1Mo Steel.” *Materials at High Temperature 33* (6), 2016. pp. 617 to 625.

N. Komai, K. Arisue, N. Saito, K. Tominaga and M. Fujita. “Effect of Alloying Elements on Creep Rupture Strength in Mod.9Cr-1Mo Steel Weldments.” *Proceedings to the 4th International ECCC Conference on Creep and Fracture*, September 2017.

L. Korcakova and J. Hald. "Precipitate Stability in Creep Resistant Ferritic Steels - Experimental Investigations and Modelling." *ISIJ International* 43 (3), 2003. pp. 420 to 427.

A. Kosta, K. G. Tak, R. J. Hellmig, Y. Estrin and G. Eggeler. "On the Contribution of Carbides and Micrograin Boundaries to the Creep Strength of Tempered Martensite Ferritic Steels." *Acta Materialia* 55 (2), 2007. pp. 539 to 550.

J. Koukal, M. Sondel and D. Schwarz. “Correlation of Creep Properties of Simulated and Real Weld Joints in Modified 9 wt. % Cr Steels.” *Welding in the World 54* (1/2), 2010. pp. R28 to R34.

R. Krein, A. Klenk and J. Schubert. “Weld Strength Reduction in Modern Tempered Martensitic 9% Chromium Creep Resistant Steels.” 4th International European Creep Collaborative Committee Conference on Creep and Fracture, Dusseldorf, Germany. September 2017.

H. Kushima, K. Kimura and F. Abe. “Degradation of Mod. 9Cr-1Mo Steel during Long-term Creep Deformation.” *Tetsu-to-Hagane* 85 (11), 1999. pp. 841 to 847.

K. Laha, K. S. Chandravathi, P. Parameswaran, K. Bhanu Sankara Rao and S. L. Mannan. “Characterization of Microstructures across the Heat-Affected Zone of the Modified 9Cr-1Mo Weld Joint to Understand its Role in Promoting Type IV Cracking.” *Metallurgical and Materials Transactions A* 38A, 2007. pp. 58 to 68.

F. R. Larson and J. Miller. “A Time-Temperature Relationship for Rupture and Creep Stresses.” *Transactions of the ASME* 74 (5), 1952. pp. 765 to 775.

F. A. Leckie and D. R. Hayhurst. “Creep Rupture of Structures.” *Proceedings of the Royal Society* A 340 (1622), 1974. pp. 323 to 347.

F. A. Leckie and D. R. Hayhurst. “Constitutive Equations for Creep Rupture.” *Acta Metallurgica* 25 (9), 1977. pp. 1059 to 1070.

J. S. Lee, K. Maruyama, I. Nonaka and T. Ito. “Mechanism of Type IV Failure in Weldment of a Mod. 9Cr-1Mo Steel.” *Creep Deformation and Fracture, Design, and Life Extension*, ed. R. S. Mishra, J. C. Earthman, S. V. Raj and R. Viswanathan; Materials Science and Technology, 2005. pp. 139 to 148.

Y. J. Lee and B. C. Muddle. “Creep Damage of Weldments in 1Cr-0.5Mo during Long Term Service at Elevated Temperature.” *Scripta Metallurgica et Materialia* 33 (5), 1995. pp. 355 to 362.

D. Li and K. Shinozaki. “Simulation of Role of Precipitate in Creep Void Occurrence in Heat Affected Zone of High Cr Ferritic Heat Resistant Steels.” *Science and Technology of Welding and Joining 10* (5), 2005. pp. 544 to 549.

M. Lind. “Mechanism and Kinetics of Transformation of Alumina Inclusions in Steel by Calcium Treatment.” Thesis accepted by Helsinki University of Technology, 2006.

J. C. Lippold. *Welding Metallurgy and Weldability*. Wiley and Sons, Inc., New Jersey: 2015. pp. 10 to 12.

Y. Liu, S. Tsukamoto, T. Shirane and F. Abe. “Formation Mechanism of Type IV Failure in High Cr Ferritic Heat-Resistant Steel-Welded Joint.” *Metallurgical and Materials Transactions A* 44A, 2013. pp. 4626 to 4633.

C. D. Lundin, G. Zhou and M. Prager. “Cryo-cracking: a Technique for Creep Damage Assessment in High Temperature Components.” *Materials at High Temperatures* 15 (3-4), 1998. pp. 167 to 173.

C. D. Lundin, B. J. Kruse, R. Menon and M. W. Richey. “Investigation of the Transformational Characteristics and Weldability of Modified 9Cr-1Mo Steel.” Subcontract 7685 X77, WBS Element UTN-3.1, 1982. pp. 1 to 55.

H. Magnusson and R. Sandström. “Dislocation climb of particles at creep conditions in 9-12% Cr steel.” *Metallurgical Materials Transactions 38A*, 2007. pp. 2428-2434.

H. Magnusson and R. Sandstrom. “Creep Strain Modeling of 9 to 12 Pct Cr Steels Based on Microstructure Evolution.” *Metallurgical and Materials Transactions A* 38A, 2007. pp. 2033 to 2039.

S. S. Manson and A. M. Haferd. “A Linear Time-Temperature Relation for Extrapolation of Creep and Stress-Rupture Data.” National Advisory Committee for Aeronautics, NACA Technical Note 2890, March 1953.

S.S. Manson and W.F. Brown. “Time Temperature Stress Relations for Correlation and Extrapolation of Stress Rupture Data.” *Proc. ASTM* 53 (1953). pp. 683 to 719.

S. S. Manson and C. R. Ensign. “A Quarter-Century of Progress in the Development of Correlation and Extrapolation Methods for Creep Rupture Data.” *Journal of*

Engineering Materials and Technology, Transactions of the ASME 101 (4), 1979. pp. 317 to 325.

K. Maruyama, K. Sawada and J. Koike. "Strengthening Mechanisms of Creep Resistant Tempered Martensitic Steel." *ISIJ International* 41 (6), 2001. pp. 641 to 653.

K. Maruyama. “Fundamental Aspects of Creep Deformation and Deformation Mechanism Map” in *Creep-resistant Steels*, ed. F. Abe, T. U. Kern and R. Viswanathan. Woodhead Publishing Limited, Cambridge, England: 2008. pp. 265 to 278.

K. Maruyama, J. Nakamura and K. Yoshimi. “Prediction of Long-Term Creep Rupture Life of Grade 122 Steel by Multiregion Analysis.” *Journal of Pressure Vessel Technology, Transactions of the ASME* 137 (2), 2015. Article number 21403.

K. Maruyama, J. Nakamura and K. Yoshimi. “Assessment of Long-Term Creep Rupture Strength of T91 Steel by Multiregion Rupture Data Analysis.” *Journal of Pressure Vessel Technology* 138 (3), 2016.

F. Masuyama. “Creep Rupture Life and Design Factors for High Strength Ferritic Steels.” *Proceedings of the European Creep Collaborative Committee Conference on Creep and Fracture in High Temperature Components – Design and Life Assessment Issues*. DSTech Publications, Lancaster, PA: 2005. pp. 983 to 996.

F. Masuyama. “Advances in Creep Damage/Life Assessment Technology for Creep Strength Enhanced Ferritic Steels.” *Procedia Engineering* 55, 2013. pp. 591 to 598.

F. Masuyama. “Development History and New Generation of Creep Strength Enhanced Ferritic Steels.” *ETD Conference Fabrication and use of P91 Steel: International Industry and Plant Experience Conference.* New Castle, Australia, October 11-12, 2017.

F. Masuyama. “P91/P92 Component Integrity/Life Assessment.” *ETD Conference Fabrication and use of P91 Steel: International Industry and Plant Experience Conference.* New Castle, Australia, October 11-12, 2017.

C. Matherne, D. DeRouen and W. Baxter. “Catastrophic Failure of a Dissimilar Metal Weld in a High Pressure Steam Venturi.” Presented at the 2010 AIChE Spring National Meeting, San Antonio, TX, 2010.

M. Matsui, M. Tabuchi, T. Watanabe, K. Kubo, J. Kinugawa and F. Abe. “Degradation of Creep Strength in Welded Joint of 9 wt. % Cr Steel.” *ISIJ International* 41, 2001. pp. S126 to S130.

K. H. Mayer. “Progress Report on MAN Investigations of Boehler and JSW Superclean Trial Forgings.” *Proceedings of the EPRI Conference Superclean Rotor Steels*, ed. R. I. Jaffe, Pergamon Press: 1991. Pp. 155 to 175.

P. Mayr, S. Mitsche, H. Cerjak and S. M. Allen. “The Impact of Weld Metal Creep Strength on the Overall Creep Strength of 9 wt. % Cr Steel Weldments.” *Journal of Engineering Materials and Technology 133* (2), 2011. pp. 87 to 93.

C. J. Middleton. “Reheat Cavity Nucleation and Nucleation Control in Bainitic Creep-resisting Low-alloy Steels: Roles of Manganese Sulphide, Residual, and Sulphurstabilizing Elements.” *Metal Science* 15 (4), 1981. pp. 154 to 167.

C. J. Middleton and B. J. Cane. “Intergranular Creep-Cavity Formation in Low-Alloy Bainitic Steels.” *Metal Science* 15 (7), 1981. pp. 295 to 301.

F. C. Monkman and N. J. Grant. “An Empirical Relationship between Rupture Life and Minimum Creep Rate in Creep-Rupture Tests.” Proceedings of the ASTM, Volume 56: 1956. pp. 595 to 605.

S. Morito, X. Huang, T. Furuhara, T. Maki and N. Hansen. "The Morphology and Crystallography of Lath Martensite in Alloy Steels," *Acta Materialia* 54 (19), 2006. pp. 5323 to 5331.

O. R. Myhr and O. Grong. “Dimensionless Maps for Heat Flow Analyses in Fusion Welding.” *Acta Metallurgica et Materialia 38* (3), 1990. pp. 449 to 460.

B. Nath, E. Metcalfe and J. Hald. “Microstructural Development and Stability in New High Strength Steels for Thick Section Applications at up to 620°C” in *Microstructural Development and Stability in High Chromium Ferritic Power Plant Steels*, ed. A. Strang and D. J. Gooch. The Institute of Materials, London: 1997. pp. 123 to 143.

B. Neubauer. “Creep Damage Evolution in Power Plants.” Proceedings of the Second International Conference on Creep and Fracture of Engineering Materials and Structures, Pineridge Press: 1984. pp. 1217 to 1226.

National Board Inspection Code Part 3 Repairs and Alterations. National Board, USA, 2017.

Data Sheets on the Elevated-Temperature Properties of 9Cr-0.5Mo-1.8W-V-Nb Steel Tube for Power Boilers (ASME SA-213/SA-213M Grade T92) and 9Cr-0.5Mo-1.8W-V-Nb Steel Pipe for High Temperature Service (ASME SA-335/SA-335M Grade P92). Datasheet 48A. National Institute for Materials Science, Japan: 2012.

Data Sheets on the Elevated-Temperature Properties of 11Cr-2W-0.4Mo-1Cu-Nb-V Stainless Steel Pipe for High Temperature Service (KA-SUS 410J3 TP), 11Cr-2W-0.4Mo-1Cu-Nb-V Stainless Steel Plate for Power Plants (KA-SUS 410J3) and 11Cr-2W-0.4Mo-1Cu-Nb-V Stainless Steel Tube for Power Boilers (KA-SUS 410J3 TB). Datasheet 51A. National Institute for Materials Science, Japan: 2013.

Data Sheets on the Elevated Temperature Properties of 9Cr-1Mo-V-Nb Steel Tubes for Boilers and Heat Exchangers (ASME SA-213/SA-213M Grade T91), 9Cr-1Mo-V-Nb Steel Plates for Boilers and Pressure Vessels (ASME SA-387/SA-387M Grade 91) and 9Cr-1Mo-V-Nb Steel Seamless Pipe for High Temperature Service (ASME SA-335/SA-335M Grade P91). Datasheet 43A. National Institute for Materials Science, Japan: 2014.

E. F. Nippes. “The Weld Heat-Affected Zone.” *Welding Journal* 38 (1), 1959. pp. 1s to 17s.

A. Nitsche, D. Allen and P. Mayr. "Damage Assessment of Creep Affected Weldments of a Grade 91 Header Component after Long-term High Temperature Service." *Welding in the World* 59 (4), 2015. pp. 675 to 682.

F. H. Norton. The Creep of Steel at High Temperatures, McGraw Hill, New York, 1929.

F. K. G. Odqvist. “Historical Survey of the Development of Creep Mechanics from its Beginnings in the Last Century to 1970” in *Creep in Structures*, ed. A. R. S. Ponter and D. R. Hayhurst. Springer-Verlag, Berlin: 1981. pp. 1 to 12.

J. R. DiStefano and V. K. Sikka, et al. *Summary of Modified 9 wt. % Cr-1Mo Steel Development Program, 1975-1986.* ORNL, Oak Ridge, TN: October 1986. ORNL 6303.

J. F. King, V. K. Sikka, M. L. Santella, J. F. Turner and E. W. Pickering. “Weldability of Modified 9 wt. % Cr-1Mo Steel.” ORNL Report 6299, September 1986.

R. L. Orr, O. D. Sherby and J. E. Dorn. “Correlation of Rupture Data for Metals at Elevated Temperatures.” *Transactions of ASM* 46, 1954. pp. 113.

S. Orzolek, J. DuPont and J. Siefert. “Microstructural Evolution of Dissimilar Metal Welds involving Grade 91.” Submitted to Metallurgical and Materials Transactions A, manuscript E-TP-19-119A, submitted on January 31, 2019.

Private conversation with Ohio State

C. Panait, "Microstructure of P91 Steel after more than 10^5h Exposure to Creep at 600°C," in *ECCC Conference on Creep and Fracture in High Components*, Zurich, Switzerland, April 2009.

C. G. Panait. “Metallurgical Evolution and Creep Strength of 9-12% Cr Heat Resistant Steels at 600C and 650C.” Thesis accepted by Paris Institute of Technology, September 2010.

C. Panait, A. Lipiec, T. Koziel, A. Czyrska-Filemonowicz, A. Gourgues-Lorenzon and W. Bendick. "Evolution of Dislocation Density, Size of subgrains and MX-type Precipitates in a P91 Steel during Creep and during Thermal Ageing at 600°C for more than 100,000h," *Materials Science and Engineering A* 527, 2010. pp. 4062 to 4069.

C. G. Panait, W. Bendick, A. Fuchsmann, A. F. Gourgues-Lorenzon and J. Besson. "Study of the Microstructure of the Grade 91 Steel after more than 100,000 h of Creep Exposure at 600C." *International Journal of Pressure Vessels and Piping* 87 (6), 2010. pp. 326 to 335.

J. D. Parker. “The Effect of Specimen Size on Creep Behaviour.” *Welding in the World* 37 (5), 1996. pp. 233 to 241.

J. D. Parker. “Factors affecting Type IV Creep Damage in Grade 91 Steel Welds.” *Materials Science and Engineering A* 578, 2013. pp. 430 to 437.

J. D. Parker. “Creep Ductility Considerations for High Energy Components Manufactured from Creep Strength Enhanced Steels.” *Materials at High Temperatures* 34 (2), 2017. pp. 109 to 120.

J. D. Parker and S. Brett. “Creep Performance of a Grade 91 Header.” *International Journal of Pressure Vessels and Piping* 111-112 (2013). pp. 82 to 88.

J. D. Parker and A. W. J. Parsons. “High Temperature Deformation and Fracture Processes in 2¼Cr1Mo – ½Cr½Mo¼ Weldments.” *International Journal of Pressure Vessels and Piping* 63, 1995. pp. 45 to 54.

J. D. Parker and J. A. Siefert. “Weld Repair of Grade 91 Piping and Components in Power Generation Applications, Creep Performance of Repair Welds.” *Materials at High Temperatures 33* (1), 2016. pp. 58 to 67.

J. D. Parker and J. A. Siefert. “Evaluation of the Creep Cavitation Behavior in Grade 91 Steels.” *International Journal of Pressure Vessels and Piping* 138 (2), 2016. pp. 31 to 44.

J. D. Parker and J. A. Siefert. “The Creep and Fracture Behaviour of Tempered Martensitic Steels.” *Materials at High Temperatures* 35 (6), 2018. pp. 491 to 503.

J. D. Parker, K. Coleman, J. A. Siefert and J. P. Shingledecker. "Challenges with NDE and Weld Repair of Creep-Strength Enhanced Ferritic Steels." *Advanced Materials & Processes* 170, 2012. pp. 20 to 23.

P. Parameswaran, K. Laha, K. S. Chandravathi and K. Bhanu Sankara Rao. “Microstructural Aspects of the Causes of Type IV Cracking in Cr-Mo Steel Weld Joints.” *Transactions of the Indian Institute of Metals 63* (2-3), 2010. pp. 479 to 483.

P. A. Pellicani, J. C. Vaillant, J. Gabrel, and A. Vanderschaeghe. “Modified 9Cr (T91/P91) Steel Tubes and Pipe: Shop Production and Fabrication Datas.” *Proceedings of the EPRI Third International Conference on Improved Coal-Fired Power Plants*, August 1992. EPRI Report TR-100848, April 2-4, 1991, San Francisco, CA. pp. 18-2 and 18-10.

A. J. Perry. “Cavitation in Creep.” *Journal of Materials Science 9* (1974). pp. 1016 to 1039.

J. Pesicka, R. Kuzel, A. Dronhofer and G. Eggeler. “The Evolution of Dislocation Density during Heat Treatment and Creep of Tempered Martensite Ferritic Steels.” *Acta Materialia* 51, 2003. pp. 4847 to 4862.

J. Pesicka, A. Aghajani, Ch. Somsen, A. Hartmaier and G. Eggeler. “How Dislocation Substructures Evolve during Long-term Creep of a 12% Cr Tempered Martensitic Ferritic Steel.” *Scripta Materialia* 62 (6), 2010. pp. 353 to 356.

F. B. Pickering. “Historical Development and Microstructure of High Chromium Ferritic Steels for High Temperature Applications” in *Microstructural Development and Stability in High Chromium Ferritic Power Plant Steels*, ed. A. Strang and D. J. Gooch. The Institute of Materials, London: 1997. pp. 1 to 29.

M. Prager. “Development of the MPC Omega Method for Life Assessment in the Creep Regime.” *Proceedings of the Pressure Vessels and Piping Conference* 288, 1994. pp. 1–20.

G. Pritchard, I. Perrin, J. D. Parker and J. A. Siefert. “Application of a Physically-based Creep Continuum Damage Mechanics Constitutive Model to the Serviceability Assessment of a Large Bore Branch Connection.” *Proceedings of the ASME 2018 Elevated Temperature Application and Materials Conference*, April 2018. ETAM2018-6719.

C. Punshon. “Reduced Pressure Electron Beam Welding in the Power Generation Industry.” *Presented at the 6th EPRI International Conference on Welding and Repair Technology for Power Plants*, June 16-18, 2004, Sandestin, FL, USA.

(R5). An Assessment Procedure for the High Temperature Response of Structures: Assessment Procedure R5.

M. Abd El-Rahman, Abd El-Salam, I. El-Mahallawi and M. R. El-Koussy. “Influence of Heat Input and PWHT of Boiler Steel P91 (9Cr-1Mo-V-Nb) Weld Joints, Part 1 –

Microstructure.” *International Heat Treating and Surface Engineering 7* (1), 2013. pp. 23 to 31.

M. Abd El-Rahman, Abd El-Salam, I. El-Mahallawi and M. R. El-Koussy. “Influence of Heat Input and PWHT of Boiler Steel P91 (9Cr-1Mo-V-Nb) Weld Joints, Part 2 – Mechanical Properties.” *International Heat Treating and Surface Engineering 7* (1), 2013. pp. 32 to 37.

M. Rauch, K. Maile, P. Seliger and A. Reuter. “Creep damage development in martensitic 9Cr steels.” *VGB PowerTech*, September 2004. pp. 71 to 75.

H. Riedel. *Fracture at High Temperatures.* Springer-Verlag: Heidelberg, 1987.

D. F. Roan and B. B. Seth. “A Metallographic and Fractographic Study of the Creep Cavitation and Fracture Behavior of 1Cr-1Mo-0.25V Rotor Steels with Controlled Residual Impurities.” *Ductility and Toughness Considerations in Elevated Temperature Service*, ASME, 1978. pp. 79 to 98.

J. D. Robson and H. K. D. H. Bhadeshia. “Modelling the Development of Microstructure in Power Plant Steels” in *Microstructural Development and Stability in High Chromium Ferritic Power Plant Steels*, ed. A. Strang and D. J. Gooch. Institute of Materials, London: 1997. pp. 179 to 207.

D. Rosenthal. “Mathematical theory of heat distribution during welding and cutting.” *Welding Journal 20* (5), 1946. pp. 220-s to 234-s.

D. Rosenthal. “The theory of moving sources of heat and its application to metal treatments.” *Transactions of the ASME* 48, 1946. pp. 848 to 866.

J. S. Rothwell and D. J. Abson. “Effect of Thermal History during Fabrication on the Mechanical Properties of Weldments in Grade 91 Creep Resistant Steel.” *Creep and Fracture of Engineering Materials and Structures.* The Japan Institute of Metals, 2012.

R. Sandstrom and R. Wu. "Creep Cavity Nucleation and Growth in 12Cr-Mo-V Steel." *Materials Science and Technology* 11 (6), 1995. pp. 579 to 588.

T. Sakthivel, S. Panneer and K. Laha. “An Assessment of Creep Deformation and Rupture Behavior of 9Cr-1.8W-0.5Mo-VNb.” *Materials Science and Engineering A* 640, 2015. pp. 61 to 71.

T. Sakthivel, K. Laha, M. Vasudevan, M. Koteswara Rao and S. Panneer Selvi. “Type IV Cracking Behaviour of Modified 9Cr-1Mo Steel Weld Joints.” *Materials at High Temperatures 33* (2), 2016. pp. 137 to 153.

K. Sakuraya, H. Okada and F. Abe. “BN Type Inclusions formed in High Cr Ferritic Heat Resistant Steel.” *Energy Materials 1* (3), 2006. pp. 158 to 166.

W. F. Savage, E. F. Nippes and E. S. Szekers. “A Study of Weld Interface Phenomena in a Low Alloy Steel.” *Welding Journal* 55 (9), 1976. pp. 260s to 268s.

K. Sawada, K. Miyahara, H. Kushima, K. Kimura and S. Matsuoka. "Contribution of Microstructural Factors to Hardness Change during Creep Exposure in Mod.9Cr-1Mo Steel." *ISIJ International* 45 (12), 2005. pp. 1934 to 1939.

K. Sawada, H. Kushima, K. Kimura and M. Tabuchi. "TTP Diagrams of Z Phase in 9-12% Cr Heat-resistant Steels." *ISIJ International* 47 (5), 2007. pp. 733 to 739.

K. Sawada, K. Suzuki, H. Kushima, M. Tabuchi and K. Kimura. “Effect of Tempering Temperature on Z-phase Formation and Creep Strength in 9 wt. % Cr-1Mo-V-Nb-N Steel.” *Materials Science and Engineering A* 480 (2008), pp. 558 to 563.

K. Sawada, H. Kushima, M. Tabuchi and K. Kimura. “Effect of Creep Deformation on Z phase Formation in Gr.91 steel.” *Materials Science and Technology* 30 (1), 2014. pp. 12 to 16.

K. Sawada, T. Hara, M. Tabuchi, K. Kimura and K. Kubushiro. “Microstructure Characterization of Heat Affected Zone after Welding in Mod.9Cr-1Mo Steel.” *Materials Characterization* 101, 2015. pp. 106 to 113.

K. Sawada, K. Sekido, H. Kushima and K. Kimura. “Microstructural Degradation during Long-term Creep in 9-12 wt. % Cr Steels.” *Proceedings to the 4th International ECCC Conference on Creep and Fracture*, September 2017.

C. Schlacher, C. Beal, C. Sommitsch, S. Mitsche and P. Mayr. “Creep and Damage Investigation of Advanced Martensitic Chromium Steel Weldments for High Temperature Applications in Thermal Power Plants.” *Science and Technology of Welding and Joining* 20 (1), 2015. pp. 82 to 90.

H. J. Schuller, J. Haigh and A. Woitscheck. “Cracking in the weld region of shaped components in hot steam lines – Materials investigations.” Der Maschinenschaden 47 (1), 1974, pp. 1–13.

M. P. Seah, "Adsorption-Induced Interface Decohesion." Acta Metallurgica 28 (7), 1980. pp. 955 to 962

H. Semba, B. Dyson and M. McLean. “Microstructure-based Creep Modelling of a 9 wt. % Cr Martensitic Steel.” *Materials at High Temperatures* 25 (3), 2008. pp. 131 to 137.

H. Shigeyama, Y. Takahashi, J. D. Parker. “Prediction of Creep Life on Notched Bar Specimens of Grade 92 Steel.” *Proceedings of the ASME 2016 Pressure Vessels and Piping Conference*. PVP2016-63964.

J. A. Siefert, J. P. Shingledecker and J. D. Parker. “Optimization of Vickers Hardness Parameters for Micro and Macro Indentation of Grade 91 Steel.” *Journal of Testing and Evaluation 41* (5), 2013. pp. 778 to 787.

J. A. Siefert, B. M. Leister and J. N. DuPont. “Considerations in the Development of CCT Diagrams for Complex Ferritic Materials.” *Materials Science and Technology*, 31 (6), 2015. pp. 651 to 660.

J. A. Siefert, J. D. Parker and R. C. Thomson. “Linking Performance of Parent Grade 91 Steel to the Cross-weld Creep Performance using Feature Type Tests.” *Proceedings from the Eighth International Conference on Advances in Materials Technology for Fossil Power Plants*, ASM International, 2016. pp. 531 to 544.

P. W. Fuerschbach and G. R. Eisler. “SmartWeld: Open Source Applications for Weld Analysis and Optimization.” Presentation accessed on November 30, 2016. http://smartweld.sourceforge.net/Pdf_docs/slides_SAND2010_4731C.pdf

S. H. Song, Y. W. Xu and H. F. Yang. "Effect of Impurity Tin on the Creep Properties of a P91 Heat-Resistant Steel." *Metallurgical and Materials Transactions A* 45 (9), 2014. pp. 4361 to 4370.

S. Spigarelli. “Microstructure-based Assessment of Creep Rupture Strength in 9Cr Steels.” *International Journal of Pressure Vessels and Piping* 101 (1), 2013. pp. 64 to 71.

Rupture Ductility of Creep Resistant Steels, ed. A. Strang. Institute of Materials, 1991.

A. Strang and V. Vodarek. “Precipitation Processes in Martensitic 12CrMoVNb Steels During High Temperature Creep.” *Microstructural Development and Stability in High Chromium Ferritic Power Plant Steels*, Institute of Materials: 1997. pp. 31 to 51.

A. Strang, V. Vodarek and H.K.D.H. Bhadeshia. “Modelling of Microstructural Degradation in Creep Resistant 12 wt. % Cr Power Plant Steels” in *Modelling of Microstructural Evolution in Creep Resistant Materials*, ed. A. Strang. IOM Communications, London: 1999. pp. 129 to 150.

M. Subanovic, "Grade 91: Influence of Residual Elements on Creep Properties." Presented to the ASME Task Group on Creep Strength Enhanced Ferritic Steels, January 2015.

On-cooling value as provided through private conversation with Bob Swindeman, December 2015.

M. Tabuchi, H. Hongo and T. Matsuaga. “Long-term Creep Strength and Fracture of Gr. 91 Steel Welds.” *Materials at High Temperatures 34* (5-6), 2017. pp. 466 to 472.

Y. Takahashi, H. Shigeyama, J. Siefert and J. Parker. “Effect of Simulated Heat Affected Zone Thermal Cycle on the Creep Deformation and Damage Response of Grade 91 Steel including Heat-to-Heat Variation.” *Proceedings of the ASME 2018 Pressure Vessels and Piping Conference*, ASME, 2018. PVP2018-85012.

Y. Tanaka, K. Kubushiro, S. Takahashi, N. Saito and H. Nakagawa. “Creep-induced Microstructural Changes in Large Welded Joints of High Cr Heat Resistant Steel.” *Procedia Engineering* 55, 2013. pp. 41 to 44.

D. W. J. Tanner, W. Sun and T. H. Hyde. “The Effect of Weld Fusion Zone Angle in a Cross-weld Specimen under Creep.” *12th International Conference on Creep and Fracture of Engineering Materials and Structures*. March 27 to 31, 2012 in Kyoto, Japan.

Thermo-Calc Software TCFE-5 TCS Steels/Fe-Alloys Database. Stockholm, Sweden: Thermo-Calc Software AB. in ThermoCalc (TCFe7 Steels/Fe-Alloys v7.0)

Y. Tsuchida, K. Tokuno, and K. Hashimoto. “Development and BOF Manufacture of Modified 9Cr-1Mo Steel Plates with Excellent Strength and Toughness.” Nippon Steel Technical Report No. 58, July 1993. pp. 27 to 35.

H. Tsuruta, K. Yoshida, H. Toda, A. Takeuchi and M. Uesugi. “3D Quantitative Evaluation of Creep Void in 9Cr Steel Welded Joint with X-ray Micro Tomography.” *Proceedings to the 4th International ECCC Conference on Creep and Fracture*, September 2017.

E. T. Turkdogan and J. Pearson. “The Solubility of Sulphur in Iron and Iron-Manganese Alloys.” *Journal of the Iron and Steel Institute 180* (1955). pp. 349 to 354.

F. Vakili-Tahami, D. R. Hayhurst and M. T. Wong. “High-temperature Creep Rupture of Low Alloy Ferritic Steel Butt-welded Pipes subjected to Combined Internal Pressure

and End Loadings.” *Philosophical Transactions of the Royal Society A* 363, 2005. pp. 2629 to 2661.

The P91 Book: Ferritic Pipe for High Temperature Use in Boilers and Petrochemical Applications. Vallourec Industries, France: 1992.

R. Viswanathan. *Damage Mechanisms and Life Assessment of High-Temperature Components*, ASM International: 1995. pp. 59 to 103.

R. Viswanathan and J. R. Foulds. “Failure Experience with Seam-welded Hot Reheat Pipes in the USA” in Service Experience, Structural Integrity, Severe Accidents and Erosion in Nuclear and Fossil Plants, ed. S. R. Paterson. ASME, New York: 1995. pp. 187 to 205.

Y. Wang and L. Li. “Microstructure Evolution of Fine-Grained Heat-Affected Zone in Type IV Failure of P91 Welds.” *Welding Journal* 95 (1), 2016. pp. 27 to 36.

T. Ishiguo, Y. Murakami, K. Ohnishi and J. Watanabe. "2.25%Cr-1%Mo pressure vessel steels with improved creep rupture strength." *Proceedings of the Symposium on Applications of 2.25%Cr-1%Mo steel for Thick-wall Pressure Vessels*, ASTM STP 755, 1980. pp. 129-147.

H. J. Westwood, M. A. Clark and D. Sidey. “Creep Failure and Damage in Main Steamline Weldments.” Proceedings of the Fourth International Conference on Creep and Fracture of Engineering Materials and Structures, The Institute of Metals, London, 1990. pp. 621 to 634.

C. L. White, J. H. Schneibel and M. H. Yoo. “Sulfur and Antimony Segregation to Creep Cavity Surfaces in Ni and an FCC Fe-Ni-Cr Alloy." in *Proceedings of the Second International Conference on Creep and Fracture of Engineering Materials and Structures*, Part I, Swansea, UK, 1984.

J. A. Williams. “Methodology for High Temperature Failure Analysis.” *Behavior of Joints in High Temperature Materials*, Applied Science, NY, NY: 1982. pp. 187 to 215.

B. Wilshire and H. Burt. “Damage Evolution during Creep of Steels.” *Proceedings of the European Creep Collaborative Committee Conference on Creep and Fracture in High Temperature Components – Design and Life Assessment Issues*. DSTech Publications, Lancaster, PA: 2005. pp. 191 to 200.

A. L. Wingrove and D. M. R. Taplin. “The Morphology and Growth of Creep Cavities in α-iron.” *Journal of Materials Science* 4, 1969. pp. 789 to 796.

X. Xu. “Microstructural Evolution and Creep Damage Accumulation in Grade 92 Steel Weld for Steam Pipe Applications.” Thesis accepted by Loughborough University in 2017.

X. Xu, G. West, J. A. Siefert, J. D. Parker, and R. C. Thomson. “The Influence of Thermal Cycles on the Microstructure of Grade 92 Steel.” *Metallurgical and Materials Transactions A* 48 (11), 2017. pp. 5396 to 5414.

S. D. Yadav, B. Sonderegger, B. Sartory, C. Sommitsch and C. Poletti. "Characterisation and Quantification of Cavities in 9Cr Martensitic Steel for Power Plants." *Materials Science and Technology* 31 (5), 2015. pp. 554 to 564.

S. D. Yadav, B. Sonderegger, M. Stracey and T. Poletti. “Modelling the Creep Behaviour of Tempered Martensitic Steel based on a Hybrid Approach.” *Materials Science and Engineering A* 662, 2016. pp. 330 to 341.

M. Yaguchi, T. Matsumura, and K. Hoshino. “Evaluation of Long-term Creep Strength of Welded Joints of ASME Grades 91, 92 and 122 Type Steels.” *Proceedings of the ASME 2012 Pressure Vessels and Piping Conference*, Toronto, CA. Paper PVP2012-78393.

M. Yaguchi, K. Nakamura and S. Nakahashi. “Re-evaluation of Long-term Creep Strength of Welded Joint of ASME Grade 91 Type Steel.” Proceedings of the ASME Pressure Vessels and Piping Conference 2016. PVP2016-63316.

K. Yamada, M. Igarashi, S. Muneki and F. Abe. "Effect of Heat Treatment on Precipitation Kinetics in High-Cr Ferritic Steels." *ISIJ International* 42 (7), 2002. pp. 779 to 784.

K. Yamamoto, H. Hamatani, K. Umetsu, S. Takeuchi, T. Toh, K. Tsunenari, Y. Maruki and Y. Yamada. “Development of Steel Surface Melting Technology for Improvement of Hot Shortness Caused by Tramp Elements.” Nippon Steel Publication, August 2013.

M. Yamazaki, T. Watanabe, H. Hongo and M. Tabuchi. “Creep Rupture Properties and fracture Type of 9Cr-1Mo-V-Nb/18Cr-8Ni Steel Dissimilar Joints.” Welding in the World 55 (1-2), 2011. pp. 67 to 77.

V. A. Yardley, S. Fahimi and E. J. Payton. "Classification of Creep Crack and Cavitation Sites in Tempered Martensite Ferritic Steel Microstructures using MTEX Toolbox for EBSD." *Materials Science and Technology* 31 (5), 2015. pp. 547 to 553.

X. Yu. “Correlation of Ferrite Formation to Creep Properties of Cr-Mo Steel Welds.” *Welding in the World* 59, 2015. pp. 251 to 259.

L. Zhao, H. Jing, L. Xu, Y. Han and J. Xiu. “Experimental Study on Creep Damage Evolution Process of Type IV Cracking in 9Cr-0.5Mo-1.8W-VNb Steel Welded Joint.” *Engineering Failure Analysis* 19, 2012. pp. 22 to 31.

J. Zhao, J. Gong, A. Saboo, D. C. Dunand and G. B. Olson. “Dislocation-based Modeling of Long-term Creep Behaviors of Grade 91 Steels.” *Acta Materialia* 149, 2018. pp. 19 to 28.

Q. Zhang, J. Zhang, P. Zhao, Y. Huang, Y. Yang and Y. Zhao. “Microstructure of 10% Cr Martensitic Heat-resistant Steel Welded Joints and Type IV Cracking Behavior during Creep Rupture at 650°C.” Materials Science and Engineering A 638, 2015. pp. 30 to 37.